frontiers | Research Topics

Model organisms in plant science: *Arabidopsis thaliana*

Edited by
Valya N. Vassileva, Ali Ferjani and Hironaka Tsukagoshi

Published in
Frontiers in Plant Science

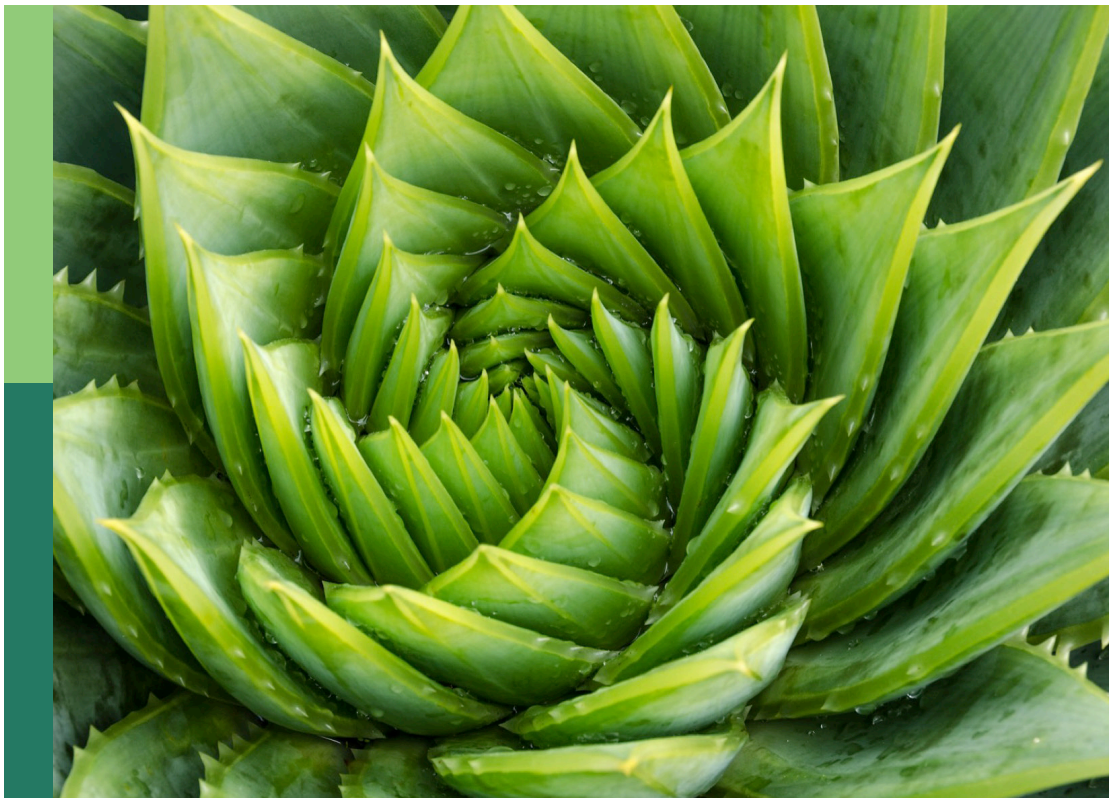

ISSN 1664-8714
ISBN 978-2-8325-3562-2
DOI 10.3389/978-2-8325-3562-2

About Frontiers

Frontiers is more than just an open access publisher of scholarly articles: it is a pioneering approach to the world of academia, radically improving the way scholarly research is managed. The grand vision of Frontiers is a world where all people have an equal opportunity to seek, share and generate knowledge. Frontiers provides immediate and permanent online open access to all its publications, but this alone is not enough to realize our grand goals.

Frontiers journal series

The Frontiers journal series is a multi-tier and interdisciplinary set of open-access, online journals, promising a paradigm shift from the current review, selection and dissemination processes in academic publishing. All Frontiers journals are driven by researchers for researchers; therefore, they constitute a service to the scholarly community. At the same time, the *Frontiers journal series* operates on a revolutionary invention, the tiered publishing system, initially addressing specific communities of scholars, and gradually climbing up to broader public understanding, thus serving the interests of the lay society, too.

Dedication to quality

Each Frontiers article is a landmark of the highest quality, thanks to genuinely collaborative interactions between authors and review editors, who include some of the world's best academicians. Research must be certified by peers before entering a stream of knowledge that may eventually reach the public - and shape society; therefore, Frontiers only applies the most rigorous and unbiased reviews. Frontiers revolutionizes research publishing by freely delivering the most outstanding research, evaluated with no bias from both the academic and social point of view. By applying the most advanced information technologies, Frontiers is catapulting scholarly publishing into a new generation.

What are Frontiers Research Topics?

Frontiers Research Topics are very popular trademarks of the *Frontiers journals series*: they are collections of at least ten articles, all centered on a particular subject. With their unique mix of varied contributions from Original Research to Review Articles, Frontiers Research Topics unify the most influential researchers, the latest key findings and historical advances in a hot research area.

Find out more on how to host your own Frontiers Research Topic or contribute to one as an author by contacting the Frontiers editorial office: frontiersin.org/about/contact

Model organisms in plant science: *Arabidopsis thaliana*

Topic editors

Valya N. Vassileva — Biological Sciences, Bulgarian Academy of Sciences, Bulgaria
Ali Ferjani — Tokyo Gakugei University, Japan
Hironaka Tsukagoshi — Meijo University, Japan

Citation

Vassileva, V. N., Ferjani, A., Tsukagoshi, H., eds. (2023). *Model organisms in plant science: Arabidopsis thaliana*. Lausanne: Frontiers Media SA.
doi: 10.3389/978-2-8325-3562-2

Table of contents

frontiers | Frontiers in Plant Science

TYPE Editorial
PUBLISHED 11 September 2023
DOI 10.3389/fpls.2023.1279230

OPEN ACCESS

EDITED AND REVIEWED BY
Anna N Stepanova,
North Carolina State University,
United States

*CORRESPONDENCE
Valya Vassileva
valyavassileva@bio21.bas.bg

RECEIVED 17 August 2023
ACCEPTED 28 August 2023
PUBLISHED 11 September 2023

CITATION
Ferjani A, Tsukagoshi H and Vassileva V (2023) Editorial: Model organisms in plant science: *Arabidopsis thaliana*. *Front. Plant Sci.* 14:1279230. doi: 10.3389/fpls.2023.1279230

Editorial: Model organisms in plant science: *Arabidopsis thaliana*

Ali Ferjani[1], Hironaka Tsukagoshi[2] and Valya Vassileva[3]*

[1]Department of Biology, Tokyo Gakugei University, Tokyo, Japan, [2]Faculty of Agriculture, Meijo University, Nagoya, Japan, [3]Department of Molecular Biology and Genetics, Institute of Plant Physiology and Genetics, Bulgarian Academy of Sciences, Sofia, Bulgaria

KEYWORDS

model organisms, *Arabidopsis thaliana*, fundamental research, plant development, molecular mechanisms, plant-environment interactions

Editorial on the Research Topic
Model organisms in plant science: *Arabidopsis thaliana*

Studies of model organisms not only identify fundamental biological mechanisms but also provide valuable hints and resources for translational research. In the plant kingdom, *Arabidopsis thaliana*, a Brassicaceae family member, holds particular importance due to its distinct advantages for studying plant development and responses to environmental cues. Despite its limited agricultural value, Arabidopsis remains highly favored for physiological, biochemical, genetic, and molecular investigations because of its compact, well-characterized genome, ease of cultivation and manipulation, short life cycle, and prolific seed production (Koornneef and Meinke, 2010). Extensive research on this model organism has advanced plant science globally, giving rise to innovative concepts and methodologies (Chen et al., 2004; Soltis et al., 2007; Van Norman and Benfey, 2009; Krämer, 2015).

The objective of the current Research Topic was to elucidate the importance of Arabidopsis as a model system by presenting recent studies with this species and emphasizing its pivotal role in the progress of plant research.

This Research Topic comprises diverse research articles, including one review, one mini-review, 10 original research papers, and a corrigendum. Together, these contributions explore fundamental aspects of Arabidopsis cell and developmental biology, employing various approaches, including genetics, metabolomics, and phenotypic analysis.

The mini-review by Zhao and Long summarizes the current understanding of how plants respond to mechanical stimuli and translate mechanical information into three-dimensional structures using Arabidopsis organs as a model. Also, the article raises questions about distinguishing mechanical cues, their involvement in cell specification, the management of heterogeneity and robustness, the establishment of mechanochemical hotspots, organ polarity, and the evolutionary preservation of plant shapes under environmental forces.

The review authored by Tabeta et al. focuses on the intricate control of plant leaf size, arising from the complex interplay between genetic and environmental factors. The authors accentuate the pivotal molecular and cellular processes governing organ-wide regulation and the

compensatory mechanisms that modulate the leaf size of Arabidopsis (Ferjani et al., 2008). The review also explores novel mechanisms of metabolic and hormonal crosstalk, providing a new research frontier in leaf size regulation.

Soda et al. investigate the molecular basis of stomatal movements in Arabidopsis using the *rtl2* mutant with constitutively open stomata and reduced levels of the enzyme tryptophan synthase ß subunit 1 (TSB1). The *TSB1* gene is involved in the tryptophan biosynthetic pathway, which is also linked to auxin biosynthesis. The authors demonstrate that tryptophan deficiency, not auxin, is responsible for the open stomatal phenotype in the mutant and that external tryptophan application restores the normal stomatal aperture.

The study by Dukic et al. examines the role of chloroplast magnesium (Mg^{2+}) in plant and algae photosynthesis. The authors pinpoint three transporters, MGT10, MGR8, and MGR9, in the inner envelope of Arabidopsis chloroplasts. Each of these transporters displays distinct functions in maintaining chloroplast Mg^{2+} homeostasis and regulating photosynthesis. The research shows the significance of MGR8 and MGT10 as key Mg^{2+} transporters while emphasizing the role of MGR9 in plant adaptation to Mg^{2+} fluctuations. Importantly, the authors identify an MGT10 homolog in *Chlamydomonas reinhardtii*, named MRS4, as essential for photosynthesis and cell growth, suggesting an evolutionarily conserved role for these magnesium transporters across species.

An et al. investigate the growth-promoting effects of the brassinosteroid brassinolide (BL) and the fungicide pyraclostrobin (Pyr) on Arabidopsis. The authors demonstrate that the combined application of BL and Pyr increases leaf biomass and inflorescence growth, attributable to improved photosynthetic performance and increased sugar accumulation. The synergistic effect of co-applying BL and Pyr outperforms the effects of individual BR or Pyr treatments. This strategy could potentially offer an environmentally friendlier alternative to mitigate the ecotoxicological impact of Pyr.

A study conducted by Kim et al. explores the role of the root cortex in nutrient and water transport and its selective storage capabilities. The authors examine cortex development and find that cortical cells do not divide during root apical meristem development; however, auxin could trigger cortical cell division, suggesting the role of this hormone in determining the fate of root cortical cells.

Jiang et al. investigate the role of tonoplast proton pumps in plant gametophyte development. The authors observe that the absence of two types of vacuolar proton pumps or a sole deficiency of V-ATPase leads to abnormal development and misplacement of female gametophytes. The lack of V-ATPase activity results in a slowed division of endosperm nuclei following the fertilization of the central cell. This research also reveals that V-ATPase plays a crucial role in regulating auxin levels in ovules, thereby affecting the spacing between the central cell and egg cell nuclei, and subsequently influencing endosperm development.

Regulating intracellular inorganic pyrophosphate (PPi) levels is vital for proper growth and development in living organisms of all kingdoms. In Arabidopsis, an enzyme called vacuolar membrane-bound H^+-translocating pyrophosphatase (H^+-PPase)/FUGU5 is important for controlling PPi balance. The study by Tojo et al. focuses on the regulation of PPi levels by examining the impact of H^+-PPase/FUGU5 deficiency on Arabidopsis. Through phenotypic and metabolomic analyses, this research demonstrates the essential role of H^+-PPase/FUGU5 in maintaining PPi homeostasis, particularly during the initial stages of seedling establishment, while revealing the minor contribution of the other soluble PPases.

Gunji et al. explore the effects of elevated PPi levels on plant development by taking advantage of the well-characterized loss-of-function H^+-PPase mutant *fugu5*. The authors demonstrate that excess PPi inhibits gluconeogenesis, disrupts cell division, and triggers compensatory cell enlargement (CCE) in cotyledonary palisade tissue (Ferjani et al., 2011). Excess PPi reduces the complexity of pavement cells and the patterning and functioning of stomata. By selectively removing PPi from specific tissue types, the authors observe improved overall plant growth and suppressed CCE, although this only partially restores epidermal abnormalities. Together, these findings deepen our understanding of leaf metabolic changes, showing tissue- and cell-autonomous growth inhibition due to excess PPi.

Plant micronutrient boron is crucial for rhamnogalacturonan-II (RG-II) pectin polysaccharide crosslinking in the Golgi apparatus, where AVP2;1, a type II H^+-PPase, is located. Onuh and Miwa study how mutations in the Golgi-localized H^+-PPase AVP2;1 impact Arabidopsis growth and cell wall components. By applying forward genetics, they find that *AVP2;1* mutations alleviate the inhibition of root cell division and elongation under boron deficiency with no effect under normal conditions. The authors observe a tendency of a reduction in RG-II specific sugars in mutant cell walls, supporting the role of AVP2;1 in pectin synthesis in the Golgi apparatus. Unlike the vacuolar H^+-PPase FUGU5/AVP1 essential for PPi homeostasis, this study underscores the potential of Golgi-localized H^+-PPase AVP2;1 in Golgi acidification and cell wall synthesis.

The article contributed by Sotta et al. examines the mechanisms by which overexposure to boron triggers DNA damage and cell death in the root meristems of Arabidopsis. The authors show that in the *rpt5a* mutant of the 26S proteasome, increased boron leads to reduced root elongation, more DNA damage, and cell death. However, introducing a mutation in the NAC domain-containing transcription factor *NAC103*, which is a proteasome target, alleviates these effects. The *nac103* mutation also reduces the accumulation of superoxide in the root tips under boron stress. These outcomes imply that NAC103 contributes to maintaining a healthy root meristem, even in the absence of the RPT5A proteasome subunit under excessive boron.

Uchida et al. employ a metabolome genome-wide association study (mGWAS) to identify genes influencing primary and secondary metabolite contents in Arabidopsis. By analyzing seed metabolomic data acquired through liquid chromatography-mass spectrometry, the authors identify single nucleotide polymorphisms in genes linked to flavonoid and glucosinolate biosynthesis. These researchers also discover an uncharacterized methyltransferase gene associated with N-methylhistidine content and confirm its importance for N-methylhistidine biosynthesis in Arabidopsis through knockout and overexpression experiments.

In summary, the accepted publications provide a comprehensive overview of the recent findings and novel mechanisms that expand

our insights into Arabidopsis and plant biology in general. The articles elucidate vital molecular and cellular events that impact plant structure and function, considerably advancing our understanding of plant-environment interactions. These insights hold great promise for driving innovation in crop yield enhancement and opening new avenues of exploration in the field.

Author contributions

AF: Writing – review & editing. HT: Writing – review & editing. VV: Writing – original draft, Writing – review & editing.

Acknowledgments

We thank the authors for their valuable contributions to this Research Topic and extend our gratitude to the reviewers for their thorough assessments and dedicated efforts towards the Research Topic.

Conflict of interest

The authors declare that the research was conducted in the absence of any commercial or financial relationships that could be construed as a potential conflict of interest.

Publisher's note

References

Chen, Z. J., Wang, J., Tian, L., Lee, H. S., Wang, J. J., Chen, M., et al. (2004). The development of an Arabidopsis model system for genome-wide analysis of polyploidy effects. *Biol. J. Linn. Soc Lond.* 82, 689–700. doi: 10.1111/j.1095-8312.2004.00351.x

Ferjani, A., Segami, S., Horiguchi, G., Muto, Y., Maeshima, M., and Tsukaya, H. (2011). Keep an eye on PPi: the vacuolar-type H^+-pyrophosphatase regulates postgerminative development in *Arabidopsis*. *Plant Cell* 23, 2895–2908. doi: 10.1105/tpc.111.085415

Ferjani, A., Yano, S., Horiguchi, G., and Tsukaya, H. (2008). "Control of leaf morphogenesis by long- and short-distance signaling: differentiation of leaves into sun or shade types and compensated cell enlargement," in *Plant growth signaling*, vol. 10 . Eds. L. Bögre and G. Beemster (Berlin, Heidelberg: Springer), 47–62. doi: 10.1007/7089_2007_148

Koornneef, M., and Meinke, D. (2010). The development of Arabidopsis as a model plant. *Plant J.* 61, 909–921. doi: 10.1111/j.1365-313X.2009.04086.x

Krämer, U. (2015). The natural history of model organisms: planting molecular functions in an ecological context with *Arabidopsis thaliana*. *eLife* 4, e06100. doi: 10.7554/eLife.06100

Soltis, D. E., Chanderbali, A. S., Kim, S., Buzgo, M., and Soltis, P. S. (2007). The ABC model and its applicability to basal angiosperms. *Ann. Bot.* 100, 155–163. doi: 10.1093/aob/mcm117

Van Norman, J. M., and Benfey, P. N. (2009). *Arabidopsis thaliana* as a model organism in systems biology. *Wiley Interdiscip. Rev. Syst. Biol. Med.* 1, 372–379. doi: 10.1002/wsbm.25

frontiers | Frontiers in Plant Science

TYPE Original Research
PUBLISHED 04 August 2022
DOI 10.3389/fpls.2022.945225

OPEN ACCESS

EDITED BY
On Sun Lau,
National University of Singapore, Singapore

REVIEWED BY
Soon-Ki Han,
Daegu Gyeongbuk Institute of Science and Technology (DGIST), South Korea
Mingyuan Zhu,
Duke University, United States

*CORRESPONDENCE
Ali Ferjani
ferjani@u-gakugei.ac.jp

†PRESENT ADDRESS
Akira Oikawa,
Graduate School of Agriculture, Kyoto University, Kyoto, Japan

Mariko Asaoka,
Department of Biological Sciences, Faculty of Science, Kanagawa University, Hiratsuka, Kanagawa, Japan

SPECIALTY SECTION
This article was submitted to Plant Development and EvoDevo, a section of the journal Frontiers in Plant Science

RECEIVED 16 May 2022
ACCEPTED 30 June 2022
PUBLISHED 04 August 2022

CITATION
Gunji S, Kawade K, Tabeta H, Horiguchi G, Oikawa A, Asaoka M, Hirai MY, Tsukaya H and Ferjani A (2022) Tissue-targeted inorganic pyrophosphate hydrolysis in a *fugu5* mutant reveals that excess inorganic pyrophosphate triggers developmental defects in a cell-autonomous manner. *Front. Plant Sci.* 13:945225. doi: 10.3389/fpls.2022.945225

Tissue-targeted inorganic pyrophosphate hydrolysis in a *fugu5* mutant reveals that excess inorganic pyrophosphate triggers developmental defects in a cell-autonomous manner

Shizuka Gunji[1,2], Kensuke Kawade[3,4,5], Hiromitsu Tabeta[1,5], Gorou Horiguchi[6,7], Akira Oikawa[5,8†], Mariko Asaoka[1†], Masami Yokota Hirai[5,9], Hirokazu Tsukaya[10] and Ali Ferjani[1*]

[1]Department of Biology, Tokyo Gakugei University, Koganei, Tokyo, Japan, [2]United Graduate School of Education, Tokyo Gakugei University, Tokyo, Japan, [3]National Institute for Basic Biology, Okazaki, Aichi, Japan, [4]Department of Basic Biology, School of Life Sciences, Graduate University for Advanced Studies (SOKENDAI), Okazaki, Aichi, Japan, [5]RIKEN Center for Sustainable Resource Science, Yokohama, Japan, [6]Department of Life Science, College of Science, Rikkyo University, Tokyo, Japan, [7]Research Center for Life Science, College of Science, Rikkyo University, Tokyo, Japan, [8]Faculty of Agriculture, Yamagata University, Tsuruoka, Japan, [9]Department of Applied Biosciences, Graduate School of Bioagricultural Science, Nagoya University, Nagoya, Japan, [10]Department of Biological Sciences, Graduate School of Science, The University of Tokyo, Tokyo, Japan

Excess PPi triggers developmental defects in a cell-autonomous manner. The level of inorganic pyrophosphate (PPi) must be tightly regulated in all kingdoms for the proper execution of cellular functions. In plants, the vacuolar proton pyrophosphatase (H^+-PPase) has a pivotal role in PPi homeostasis. We previously demonstrated that the excess cytosolic PPi in the H^+-PPase loss-of-function *fugu5* mutant inhibits gluconeogenesis from seed storage lipids, arrests cell division in cotyledonary palisade tissue, and triggers a compensated cell enlargement (CCE). Moreover, PPi alters pavement cell (PC) shape, stomatal patterning, and functioning, supporting specific yet broad inhibitory effects of PPi on leaf morphogenesis. Whereas these developmental defects were totally rescued by the expression of the yeast soluble pyrophosphatase IPP1, sucrose supply alone canceled CCE in the palisade tissue but not the epidermal developmental defects. Hence, we postulated that the latter are likely triggered by excess PPi rather than a sucrose deficit. To formally test this hypothesis, we adopted a spatiotemporal approach by constructing and analyzing *fugu5-1 PDF1*$_{pro}$*::IPP1*, *fugu5-1 CLV1*$_{pro}$*::IPP1*, and *fugu5-1 ICL*$_{pro}$*::IPP1*, whereby PPi was removed specifically from the epidermis, palisade tissue cells, or during the 4 days following seed imbibition, respectively. It is important to note that whereas PC defects in *fugu5-1 PDF1*$_{pro}$*::IPP1* were completely recovered, those in *fugu5-1 CLV1*$_{pro}$*::IPP1* were not. In addition, phenotypic analyses of *fugu5-1 ICL*$_{pro}$*::IPP1* lines demonstrated that the immediate removal of PPi after

seed imbibition markedly improved overall plant growth, abolished CCE, but only partially restored the epidermal developmental defects. Next, the impact of spatial and temporal removal of PPi was investigated by capillary electrophoresis time-of-flight mass spectrometry (CE-TOF MS). Our analysis revealed that the metabolic profiles are differentially affected among all the above transgenic lines, and consistent with an axial role of central metabolism of gluconeogenesis in CCE. Taken together, this study provides a conceptual framework to unveil metabolic fluctuations within leaf tissues with high spatio–temporal resolution. Finally, our findings suggest that excess PPi exerts its inhibitory effect *in planta* in the early stages of seedling establishment in a tissue- and cell-autonomous manner.

KEYWORDS

***fugu5* mutant, leaf morphogenesis, metabolism, pyrophosphate homeostasis, pyrophosphatase, cell-autonomous regulation**

Introduction

Pyrophosphate (PPi) is ubiquitously released within living cells as a byproduct of nearly 200 metabolic reactions, such as DNA, RNA, protein, and saccharide polymerization (Stitt, 1998; Maeshima, 2000; Heinonen, 2001; Ferjani et al., 2014a,b). In plant cells, PPi is used as an intracellular energy donor by several enzymes, such as the tonoplastic PPi-dependent proton pump (H^+-PPase; Rea and Poole, 1985, 1993; Rea et al., 1992; Sarafian et al., 1992; Maeshima, 2000; Drozdowicz and Rea, 2001), UDP-glucose pyrophosphorylase (UGPase, EC 2.7.7.9), fructose-6-phosphate 1-phosphotransferase (PFP, EC 2.7.1.90; Stitt, 1990; Dennis et al., 1997), and pyruvate phosphate dikinase (PPDK, EC 2.7.9.1; Parsley and Hibberd, 2006; Eastmond et al., 2015). Controlling the PPi level is essential to sustaining cellular activity. The loss of function of soluble PPase (sPPase) in several organisms, such as *Escherichia coli* (Chen et al., 1990), *Saccharomyces cerevisiae* (Lundin et al., 1991), and *Caenorhabditis elegans* (Ko et al., 2007), leads to severe growth arrest and/or cell death due to excess PPi. Such severe phenotype or lethality has for decades hampered corroboration of the effects of a perturbed PPi level *in planta*.

We reported that excess PPi in the H^+-PPase loss-of-function *fugu5* mutant severely compromises gluconeogenesis from seed storage lipids and inhibits a hypocotyl elongation in etiolated seedlings (Ferjani et al., 2011, 2014a, 2018), arrests cell division in cotyledonary palisade tissue, and triggers a compensated cell enlargement (CCE; Tsukaya, 2002, 2008; Horiguchi et al., 2005, 2006a,b; Ferjani et al., 2007, 2008, 2010, 2011, 2013a,b; Amano et al., 2015; Katano et al., 2016; Takahashi et al., 2017; Tabeta et al., 2021; Nakayama et al., 2022). It is important to note that these phenotypes were recovered by exogenous sucrose (Suc) supply or specific removal of PPi from the *fugu5* background by the yeast cytosolic PPase IPP1 under the control of the vacuolar H^+-pyrophosphatase *AVP1/FUGU5* promoter in *fugu5-1 AVP1*$_{pro}$*::IPP1* transgenic lines (Ferjani et al., 2011, 2014a,b; Asaoka et al., 2019; Gunji et al., 2020). Consistently, CE-TOF MS analyses of the major metabolites characteristic of gluconeogenesis from seed storage lipids identify UGPase as the major target of the inhibitory effects of excess PPi *in planta* (Ferjani et al., 2018). Moreover, UGPase, a ubiquitous enzyme found in bacteria, animals, and plants catalyzes the production of UDP-glucose (UDP-Glc), the major glycosyl donor for Suc synthesis, as well as cellulose and callose formation and is the precursor of other nucleotide sugars (Kleczkowski, 1994; Gibeaut, 2000; Winter and Huber, 2000; Johansson et al., 2002).

The *Arabidopsis thaliana* (hereafter, Arabidopsis) genome encodes five cytosolic sPPases (*AtPPa1* to *AtPPa5*), and one isoform (*AtPPa6*) was reported to be targeted to the chloroplast stroma (Schulze et al., 2004; Öztürk et al., 2014; Gutiérrez-Luna et al., 2016). Moreover, sPPases and H^+-PPase cooperatively regulate the PPi level: H^+-PPase is essential for maintaining adequate PPi content, and the cytosolic AtPPa isozymes, in particular, AtPPa1, prevent its increase to a toxic level (Ferjani et al., 2014a; Segami et al., 2018).

In plants, H^+-PPase mediates the hydrolysis of PPi and the acidification of the vacuole (Rea and Poole, 1985; Rea et al., 1992; Sarafian et al., 1992; Maeshima, 2000; Drozdowicz and Rea, 2001). It has long been thought that H^+-PPase is important as an H^+-pump; however, analyses of *fugu5 AVP1*$_{pro}$*::IPP1* provided evidence that the hydrolysis of inhibitory PPi, rather than vacuolar acidification, is the major contribution of this enzyme during the establishment of Arabidopsis

Abbreviations: H^+-PPase, H^+-translocating pyrophosphatase; sPPase, soluble inorganic pyrophosphatase; PPi, inorganic pyrophosphate; PFP, PPi-dependent phosphofructokinase; UGPase, UDP-glucose pyrophosphorylase; PPDK, pyruvate orthophosphate dikinase; DAS, days after seed sowing; DAI, days after induction of seed germination.

seedlings (Ferjani et al., 2011; Segami et al., 2018). However, until recently, the key questions concerning the effects of excess PPi on leaf tissue other than the palisade and other cell types have gone unanswered.

Examination of the outermost cotyledon layer in *fugu5* revealed an increase in stomatal density (i.e., the number of stomata per unit area) in violation of the one-cell-spacing rule, a defect in stomata closure (Asaoka et al., 2019), and showed that pavement cells (PCs) exhibit defective puzzle-cell formation (Gunji et al., 2020). It is important to note that specific removal of PPi in *fugu5-1 AVP1*$_{pro}$*::IPP1* transgenic lines restored these epidermal phenotypic aberrations in the *fugu5* background (Gunji et al., 2020). Furthermore, in *fugu5 GC1*$_{pro}$*::IPP1* transgenic lines, which exclusively express IPP1 in guard cells, stomatal closure recovered, which suggests a role for H^+-PPase in stomatal function (Asaoka et al., 2019). It is surprising that PCs in mutants with defects in gluconeogenesis (*pck1-2*; Eastmond et al., 2000) or the glyoxylate cycle (*icl-2* and *mls-2*; Cornah et al., 2004; Penfield et al., 2004, respectively) showed no phenotypic change, which indicates that reduced Suc production from seed storage lipids is not the cause of *fugu5* epidermal developmental defects (Gunji et al., 2020). The subsequent live imaging revealed that cortical microtubules (MTs) in PCs exhibited a reduced velocity and were slightly fragmented and sparse in *fugu5* compared to the wildtype (WT; Gunji et al., 2020). Consistently, the addition of PPi *in vitro* leads to a dose-dependent delay in tubulin polymerization, thus, supporting a link between PPi and MT dynamics (Gunji et al., 2020). Taken together, these findings suggest that whereas CCE is triggered by decreased Suc production, epidermal defects are likely triggered by an overaccumulation of PPi. Hence, whereas PPi homeostasis is a prerequisite for proper leaf organogenesis, excess PPi has differential effects on the growth and development of palisade tissue cells and epidermal cells.

Here, we used a spatiotemporal approach to unpack the molecular process underlying the inhibitory effects of PPi on the key leaf tissues and at the key developmental stages. More specifically, we constructed *PDF1*$_{pro}$*::IPP1*, *CLV1*$_{pro}$*::IPP1*, and *ICL*$_{pro}$*::IPP1* lines in which PPi was removed, on the *fugu5-1* background, from the epidermis, palisade tissue cells, or during the 4 days following seed imbibition, respectively. The phenotypic and metabolomics approaches showed that excess PPi *in planta* has its inhibitory effect in the early stages of seedling establishment and in a tissue-autonomous manner.

Materials and methods

Plant materials and growth conditions

The WT used in this study was *A. thaliana* Colombia-0 (Col-0), and mutants and all transgenic plants were on the Col-0 background. Also, *fugu5-1* was isolated and characterized as a loss-of-function mutant of the vacuolar type H^+-PPase (Horiguchi et al., 2006b; Ferjani et al., 2007, 2011). In addition, the two previously described independent transgenic lines expressing yeast sPPase IPP1 on the *fugu5-1* mutant background (*AVP1*$_{pro}$*::IPP1*#8-3 and #17-3) were used (Ferjani et al., 2011). The seeds were sown on rockwool (Nippon Rockwool), watered daily with 0.5 g L^{-1} Hyponex solution, and grown under a 16-h light and 8-h dark cycle with white light from fluorescent lamps at approximately 50 μmol m^{-2} s^{-1} and 22°C. The sterilized seeds were sown on Suc-free Murashige and Skoog (MS) medium (Wako Pure Chemical) or MS medium with 2% (w/v) Suc, where indicated. 0.1% (w/v) 2-(N-morpholino) ethanesulfonic acid (MES) was added, then pH was adjusted to 5.8 with KOH, and solidified with 0.2–0.5% (w/v) gellan gum (Murashige and Skoog, 1962) to determine the effects of medium composition on phenotype. The seeds were sown on MS plates and stored at 4°C in the dark for 3 days as cold treatment. After the cold treatment, the seedlings were grown in the light (as above) or in the dark for the indicated periods of time.

Generation of *PDF1*$_{pro}$*::IPP1* and *CLV1*$_{pro}$*::IPP1* transgenic plants

About 1.5 kbp of the upstream region of the *PDF1* gene and about 2.0 kbp of the upstream region of the *CLV1* gene that had been cloned into the pDONR P4-P1R were used (Kawade et al., 2013). The coding region of *IPP1* from *S. cerevisiae* was fused into pDONR201 (Ferjani et al., 2011), and the vectors were subjected to the LR reaction with the R4 gateway binary vector R4pGWB501 (Nakagawa et al., 2008). The resultant final constructs were used to transform *fugu5-1* mutant plants by the floral–dip method (Clough and Bent, 1998). Several independent T_3 homozygous lines expressing the *IPP1* gene under the control of *PDF1*$_{pro}$ (*PDF1*$_{pro}$*::IPP1*#6-7, *PDF1*$_{pro}$*::IPP1*#9-1, and *PDF1*$_{pro}$*::IPP1*#20-5 lines) or *CLV1*$_{pro}$ (*CLV1*$_{pro}$*::IPP1*#8-3, *CLV1*$_{pro}$*::IPP1*#10-2, and *CLV1*$_{pro}$*::IPP1*#12-3 lines) from a single T-DNA insertion locus on the *fugu5-1* background were used for analyses.

Obtaining *PDF1*$_{pro}$*::GUS* and *CLV1*$_{pro}$*::GUS*

On the *an3-4* background, *PDF1*$_{pro}$*::GUS* and *CLV1*$_{pro}$*::GUS* were described elsewhere (Kawade et al., 2013). To obtain *PDF1*$_{pro}$*::GUS* and *CLV1*$_{pro}$*::GUS* on the *fugu5-1* background, we crossed *fugu5-1* with the above lines and used the resultant F_3 generation to select double homozygous lines based on hygromycin resistance and *fugu5-1* genotyping, as described previously (Takahashi et al., 2017).

Generation of *ICL*$_{pro}$*::GUS* and *ICL*$_{pro}$*::IPP1* transgenic plants

For *ICL* promoter *GUS* construction, the *ICL* promoter was amplified by PCR with the pICL-F: 5′-TATATGTTTGAAGCTCATCCACGAGCTAAGCAAGT-3′ and pICL-R: 5′-GGACTGACCTACCCGGGCTTTAACTTTTATAAATTGG-3′ primer set. The binary vector pSMAB704 was digested with *Sma*I and *Hind*III to remove the 35S promoter. The PCR-amplified *ICL* promoter fragments were cloned into the *Sma*I and *Hind*III sites of pSMAB704 by infusion (TaKaRa). The resulting vectors were treated with *Sma*I and *Sac*I to remove the *GUS* cDNA coding region. Using the IPP1-F: 5′-TAAAAGTTAAAGCCCATGACCTACACTACCAGACA-3′ and IPP1-R: 5′-GATCGGGGAAATTCGTTAAACAGAACCGGAGATGA-3′ primer set, we cloned amplified *IPP1* into the *ICL*$_{pro}$*::GUS Sma*I and *Sac*I sites by infusion (TaKaRa). The resultant final construct was used to transform *fugu5-1* mutant plants by the floral–dip method (Clough and Bent, 1998). Several independent T_3 homozygous lines expressing *IPP1* under the *ICL* promoter were identified on the *fugu5-1* background. The *ICL* promoter lines *ICL*$_{pro}$*::IPP1*#9-2, *ICL*$_{pro}$*::IPP1*#11-2, *ICL*$_{pro}$*::IPP1*#13-1, and *ICL*$_{pro}$*::IPP1*#24-1 were used in the further experiments.

The GUS Histochemical Staining

The seedlings were treated with 90% (v/v) acetone on ice. For GUS staining, the samples were incubated in staining solution [sterile distilled water, 750 μg/ml X-Gluc (5-bromo-4-chloro-3-indolyl-β-D-glucuronide), 100-mM sodium phosphate buffer (pH 7.0), 3-mM potassium ferrocyanide, 10-mM ethylenediaminetetraacetic acid buffer (pH 8.0), and [0.1% (v/v) Triton X-100] overnight at 37°C in a desiccator. The GUS-stained samples were washed once with sterile Milli-Q, cleared with chloral solution, and observed under a light stereomicroscope (Leica Microsystems).

Microscopy and phenotypic analysis

The photographs of gross plant morphology at 10 days after seed sowing (DAS) and 12 DAS were taken with a stereoscopic microscope (M165FC; Leica Microsystems) connected to a CCD camera (DFC300FX; Leica Microsystems) and a digital camera (D5000 Nikkor lens AF-S Micro Nikkor 60 mm; Nikon). The gross plant morphology at 25 DAS was photographed with a digital camera (D5000 Nikkor lens AF-S Micro Nikkor 60 mm; Nikon). After sampling, the leaves were fixed in formalin/acetic acid/alcohol [FAA; 4% (v/v) formalin, 5% (v/v) acetic acid, and 50% (v/v) ethanol] and cleared with chloral solution (200-g chloral hydrate, 20-g glycerol, and 50-ml deionized water) to measure the leaf area and cell number, as described previously (Tsuge et al., 1996). The whole leaves were observed with a stereomicroscope equipped with a CCD camera. The leaf palisade tissue cells were observed and photographed under a light microscope (DM-2500; Leica Microsystems) equipped with Nomarski differential interference contrast optics and a CCD camera. The cell size was determined as the mean palisade cell area of 20 palisade cells per leaf on a paravermal view (Ferjani et al., 2011).

Observation and quantitative analysis of epidermal cells

For scanning electron microscopy (SEM), cotyledons were dissected from the plants at the indicated growth stages. The samples were fixed overnight in FAA at room temperature. The fixed specimens were dehydrated in an ethanol series [50, 60, 70, 80, 90, 95, 99.5, and 100% (v/v); 60 min per step] and stored overnight in 100% (v/v) ethanol at room temperature. The ethanol was replaced with 3-methylbutyl acetate, and the samples were dried in a critical-point dryer (JCPD-5; JEOL), sputter-coated with gold–palladium using an anion sputter (JFC-1100; JEOL), and examined under an S-3400N scanning electron microscope (Hitachi) as described previously (Maeda et al., 2014). The SEM images of the adaxial side of cotyledons were used to quantify PC complexity. The area and perimeter of individual PCs (n = 20–30 cells from one cotyledon; a total of six cotyledons) were measured with ImageJ (v.1.63). We quantified their complexity by calculating the undulation index (UI; Thomas et al., 2003) using the following equation (Kürschner, 1997):

$$\mathrm{UI} = \frac{Ce}{2\pi\sqrt{Ae/\pi}},$$

where UI (dimensionless) is the undulation index, C (μm) is the cell perimeter, and A (μm^2) is the cell area. Note that an increased UI indicates an increased PC complexity and *vice versa*.

Stomatal index (SI) is the percentage of the number of stomata to the total number of epidermal cells. Stomatal index was calculated using the following equation:

$$\mathrm{SI} = \frac{St\ x\ 100}{E + S},$$

where St is the number of stomata per unit area, and E is the number of epidermal cells within the same unit area.

Metabolite profiling by capillary electrophoresis time-of-flight mass spectrometry (CE-TOF MS)

Three-day-old etiolated seedlings were immediately frozen in liquid nitrogen after sampling and stored at −80°C prior to CE-TOF MS analysis. The CE-TOF MS analysis was performed as described previously (Ferjani et al., 2018); further details are presented elsewhere (Oikawa et al., 2011a,b). The raw CE-TOF MS data were converted, and the peaks were automatically identified, aligned, and annotated with our in-house software Masterhands (Sugimoto et al., 2010).

Quantitative analysis of total triacylglycerol (TAG)

We measured the quantities of seed lipid reserves in dry seeds and in 1-, 2-, 3-, and 4-day-old etiolated seedlings by determining total TAG using a Triglyceride E-Test Assay Kit (Wako Pure Chemical). Either 20 dry seeds or 20 seedlings were homogenized with a mortar and pestle in 100 μl sterile distilled water. The homogenates were mixed with 0.75 ml of the reaction buffer provided in the kit as described previously (Arai et al., 2008; Ferjani et al., 2011). The sample TAG concentration was determined according to the manufacturer's protocol. The lengths of etiolated seedlings were determined as described previously (Ferjani et al., 2011).

Quantification of Suc

A total of 100 etiolated seedlings at 3 days after induction of seed germination (DAI) were collected in a tube in liquid nitrogen and lyophilized. The samples were extracted with a bead shocker in a 2 ml tube with 5 mm zirconia beads and 80% MeOH for 2 min at 1000 rpm (Shake Master NEO; Biomedical Sciences). The extracted solutions were centrifuged at 104 g for 1 min, and 150-μl centrifuged solution and 10-μl 2 mg/L (UL-$^{13}C_6^{glc}$)-Suc (Omicron Biochemicals, South Bend, IN, United States) were dispensed into a 1.5-ml tube. After the solution was dried with a centrifuge evaporator (Speed vac; Thermo), 100-μl Mox reagent (2% methoxyamine in pyridine; Thermo) was added to the 1.5-ml tube, and the metabolites were methoxylated at 30°C and 1,200 rpm for approximately 6 h with a thermo-shaker (BSR-MSC100; Biomedical Sciences). After methoxylation, 50-μl 1% v/v trimethylchlorosilane (TMS; Thermo) was added to the 1.5-ml tube. For TMS derivatization, the mixture was incubated for 30 min at 1,200 rpm at 37°C as above. Finally, 50 μl of the derivatized samples were dispensed into vials for GC-QqQ-MS analysis (AOC-5000 Plus with GCMS-TQ8040; Shimadzu) as described elsewhere (Tabeta et al., 2021). The raw data were collected, and GC-MS peak areas were calculated with GCMS software (Shimadzu). Suc content was quantified per etiolated seedling based on an internal standard.

Quantification of plant fresh weight (FW)

To measure FW, we used 12-day-old seedlings and 25-day-old plants grown on rockwool. Five 12-day-old seedlings were pooled, and their weight was measured (n = 10 biological replicates) with a precision balance (MS204S; Mettler Toledo). For 25-day-old plants, FW was measured (n = 20) with an electronic scale (TE1502S; Sartorius).

Statistical analysis

The data were subjected to statistical analyses by one-way ANOVA with Tukey's honestly significant difference (HSD) test (Kaleida Graph, v.4.1.1). The metabolome statistical analyses were conducted with MetaboAnalyst 4.0 and 5.0 (Chong et al., 2019; Pang et al., 2021[1]). The PCA plots were generated in MetaboAnalyst 5.0 (Pang et al., 2021). The selection of metabolites for the Venn diagram was based on Tukey's HSD test in MetaboAnalyst 4.0 (**Supplementary Tables 2, 4**), and the Venn diagram was generated with the R package VennDiagram (Chen, 2018; v.1.6.20; R v.3.6.3; R Core Team, 2020). Hierarchical cluster analyses (HCA) and heat maps were created with the R package pheatmap (Kolde, 2019; v.1.0.12; R v.3.5.1; R Core Team, 2018). The calculation of autoscaling sample data for HCA was performed in MetaboAnalyst 4.0 (Chong et al., 2019).

Results

Tissue-specific expression of IPP1 affect morphological and cellular phenotypes in the *fugu5* background

It is reported that $AVP1_{pro}$ is active throughout the plant body (Segami et al., 2014), and hence it is unsuitable for evaluating the inhibitory effects of PPi in the palisade or the epidermis or at a given developmental stage. Whereas CCE in *fugu5* is triggered by a lack of Suc, the developmental defects in the *fugu5* epidermis are assumed to be triggered by excess PPi. To formally test this hypothesis, we examined the effects of tissue-specific hydrolysis of PPi. We used the *PROTODERMAL FACTOR 1* ($PDF1_{pro}$) and *CLAVATA1*

1 https://www.metaboanalyst.ca

(*CLV1*$_{pro}$) promoters because they are active in the epidermis and in the subepidermal layer of palisade tissue, respectively (Abe et al., 2001; Kawade et al., 2013; Asaoka et al., 2021; **Figures 1A–D**). Moreover, *PDF1*$_{pro}$*::IPP1* and *CLV1*$_{pro}$*::IPP1* transgenic lines were constructed on the *fugu5-1* background and characterized in detail.

Although *fugu5* displayed a delayed post-germinative growth, expression of *PDF1*$_{pro}$*::IPP1* and *CLV1*$_{pro}$*::IPP1* on the *fugu5-1* background substantially improved overall plant growth (**Figure 1E**; **Supplementary Figures 1, 2A,B**). Whereas *PDF1*$_{pro}$*::IPP1* lines displayed round cotyledons, *CLV1*$_{pro}$*::IPP1* cotyledons were oblong, mimicking the *fugu5-1* single mutant (**Figure 1E**; **Supplementary Figure 2C**).

Next, to assess the epidermis phenotype, we conducted SEM observation of the cotyledon adaxial side. The SEM images revealed that the clusters of stomata had formed in *fugu5-1*, which proved to be consistent with our previous report (Asaoka et al., 2019; **Figure 1F**; **Supplementary Figure 3**). Moreover, PCs in *fugu5-1* and *CLV1*$_{pro}$*::IPP1* lines were smaller compared to the WT, *PDF1*$_{pro}$*::IPP1*, and *AVP1*$_{pro}$*::IPP1* lines (**Figures 1F,G**). Consistently, PCs in *fugu5-1* exhibited simpler shapes than the WT (Gunji et al., 2020; **Figures 1F,H**). The undulation index (UI) values revealed that the WT and *PDF1*$_{pro}$*::IPP1* were comparable (**Figure 1H**). By contrast, UI values in the *CLV1*$_{pro}$*::IPP1* independent lines were similar to those of *fugu5-1* (**Figure 1H**). Although the stomatal index (SI) value was higher in *fugu5-1* and *CLV1*$_{pro}$*::IPP1*, it was partially restored in *PDF1*$_{pro}$*::IPP1* (**Figure 1I**).

Compensation is only partially affected upon tissue-specific expression of IPP1

After seed imbibition, TAG of the oil bodies, which is the major seed storage lipid in Arabidopsis, is converted into Suc *via* a sequence of metabolic processes (Graham, 2008). In one study of *fugu5*, the failure to hydrolyze PPi led to a ∼2.5-fold increase in its level compared to the WT (Ferjani et al., 2011). The excess PPi compromises the gluconeogenic enzyme UGPase, reducing levels of UDP-Glc and Suc (Ferjani et al., 2011, 2018). By contrast, oil bodies accumulate in the epidermal and mesophyll tissue of embryonic cotyledons within mature seeds of Arabidopsis. Hence, what are the effects of tissue-specific expression of IPP1 on gluconeogenesis and thus CCE?

To address this question, we performed the quantitative and comparative analyses of the cell number and size of palisade tissue in the WT, *fugu5-1*, *AVP1*$_{pro}$*::IPP1*#8-3, three independent *PDF1*$_{pro}$*::IPP1* lines, and three independent *CLV1*$_{pro}$*::IPP1* lines (**Figure 2**). Consistent with our previous reports, *fugu5-1* cell number and size in cotyledons were totally recovered in *AVP1*$_{pro}$*::IPP1*#8-3 (Ferjani et al., 2011; **Figures 2B,C**). By contrast, the targeted expression of IPP1 in the epidermis or palisade tissue had a small effect on cell number and size (**Figures 2B,C**). Given the ubiquitous expression of *AVP1*$_{pro}$ (Segami et al., 2018) and the tissue-specific expression of *PDF1*$_{pro}$ and *CLV1*$_{pro}$, and the fact that compensation in *fugu5-1* is triggered exclusively by defective TAG-to-Suc conversion, it is plausible that in *PDF1*$_{pro}$*::IPP1* and *CLV1*$_{pro}$*::IPP1* Suc production did not fully recover.

To corroborate this hypothesis, we crossed *PDF1*$_{pro}$*::IPP1*#6-7 with *CLV1*$_{pro}$*::IPP1*#8-3 and evaluated the cellular phenotypes in F_1 progeny heterozygous for both transgenes (**Supplementary Figure 4**). We were interested to find that CCE was abolished in the double transgenic heterozygous lines (**Supplementary Figures 4A–D**).

Impact of tissue-specific expression of IPP1 on hypocotyl elongation, triacylglycerol (TAG) mobilization and gluconeogenesis

In darkness and in the absence of exogenous Suc, a hypocotyl elongation relies on TAG-to-Suc conversion as the sole source of energy (Eastmond et al., 2000; Cornah et al., 2004; Penfield et al., 2004; Katano et al., 2016; Takahashi et al., 2017). We examined expression of *PDF1*$_{pro}$ and *CLV1*$_{pro}$ using *PDF1*$_{pro}$*::GUS* and *CLV1*$_{pro}$*::GUS* reporter lines. GUS staining of etiolated seedlings at 4 DAI revealed that both *PDF1*$_{pro}$*::GUS* and *CLV1*$_{pro}$*::GUS* were strongly expressed in cotyledons (**Figure 3A**). By contrast, whereas *PDF1*$_{pro}$*::GUS* was evenly expressed in the hypocotyl, *CLV1*$_{pro}$*::GUS* was not detected in this organ (**Figure 3A**). Therefore, we hypothesized that the removal of PPi was affected in *PDF1*$_{pro}$*::IPP1* and *CLV1*$_{pro}$*::IPP1*, altering Suc availability and thus affecting etiolated seedling elongation. To evaluate this hypothesis, we sowed seeds on MS only or MS + 2% Suc medium and allowed them to grow in darkness for 4 DAI. Quantification of the length of the hypocotyl grown on MS only revealed that although *PDF1*$_{pro}$*::IPP1* tended to be longer than *fugu5-1*, the length of *CLV1*$_{pro}$*::IPP1* etiolated seedlings did not recover (**Figure 3B**). Next, the amount of TAG in dry seeds and in 1, 2, 3, and 4 DAI etiolated seedlings was quantified as reported previously (Arai et al., 2008; Ferjani et al., 2011; Takahashi et al., 2017). It is interesting that the TAG content in dry seeds and their degradation during etiolated seedling establishment were similar in all genotypes except *CLV1*$_{pro}$*::IPP1*, in which TAG degradation was slightly delayed, in particular, at 2 and 3 DAI (**Figure 3C**).

Finally, to evaluate the impact of tissue-specific expression of IPP1 on gluconeogenesis, we quantified Suc content by GC-MS/MS (Tabeta et al., 2021). The Suc level in *PDF1*$_{pro}$*::IPP1* tended to increase (**Figure 3D**), whereas that in *CLV1*$_{pro}$*::IPP1* was indistinguishable from *fugu5-1* (**Figure 3E**).

10.3389/fpls.2022.945225

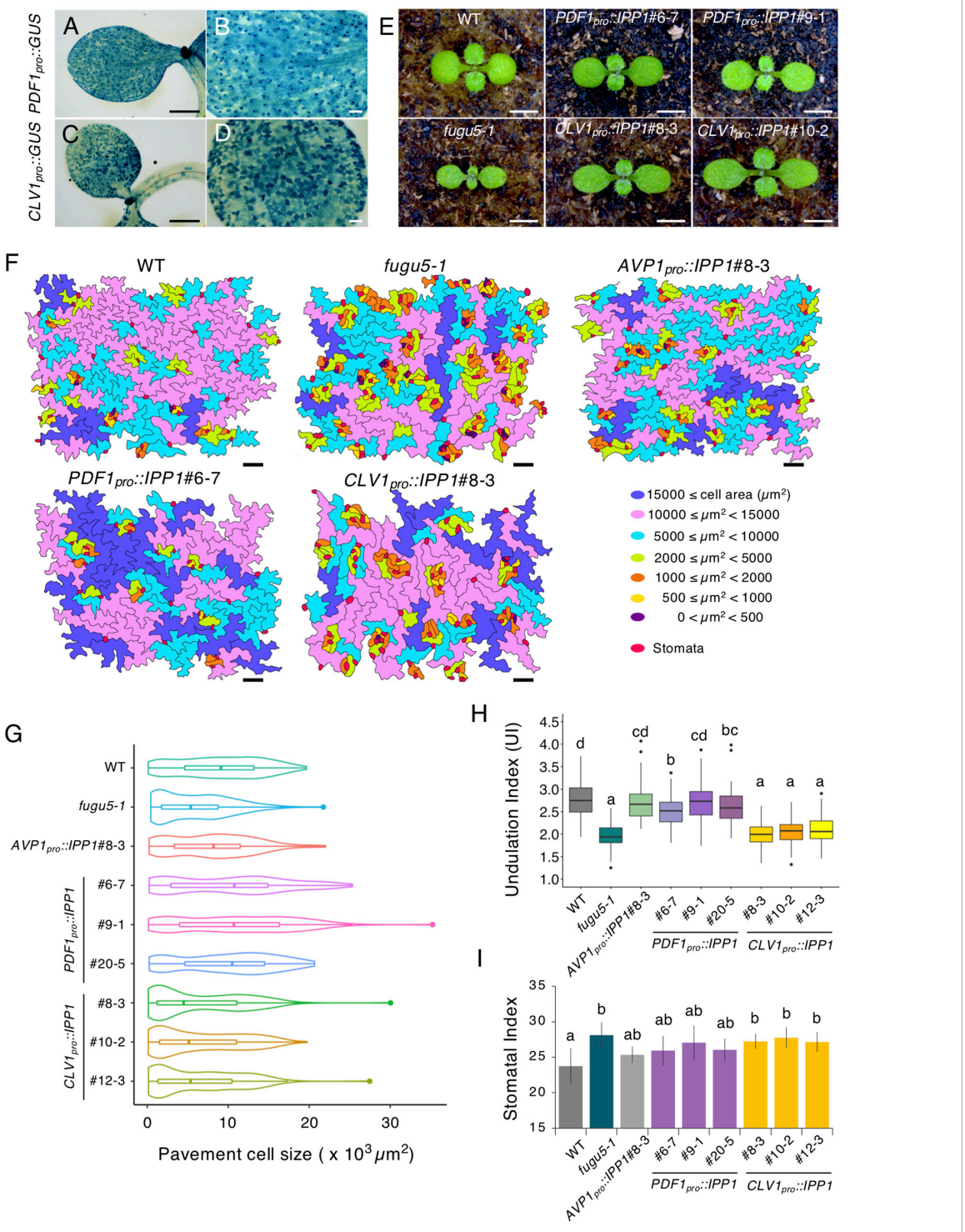

FIGURE 1

Phenotypes of transgenic plants expressing IPP1 in a tissue-specific manner. **(A–D)** The GUS staining of 5-day-old seedlings of *PDF1*$_{pro}$*::GUS* and *CLV1*$_{pro}$*::GUS* grown on MS medium. **(B,D)** are magnified images of **(A,C)**, respectively. Scale bar = 500 μm **(A,C)** and 100 μm **(B,D)**. **(E)** Gross morphology of representative transgenic lines grown on rockwool for 10 DAS. Scale bar = 2 mm. **(F)** Pavement cells (PCs) of the adaxial side on representative scanning electron microscopy (SEM) images were traced and color-coded based on cell size. Scale bar = 100 μm. **(G)** Violin plots of the size distribution of PCs, excluding stomata (n = 200 cells from four independent cotyledons). **(H)** Box-plot represents undulation index (UI) of PCs (n = 125 PCs from six cotyledons) at 25 DAS. The boxes of lower and upper are the first and third quantiles, the line in the boxes is the median and whiskers are maximum and minimum values. **(I)** The stomatal index was determined as the number of stomata per 100 PCs. Results are means ± SD (n = 6 cotyledons). Each character represents a significant difference at $p < 0.05$ (Tukey's HSD test). DAS, days after seed sowing.

10.3389/fpls.2022.945225

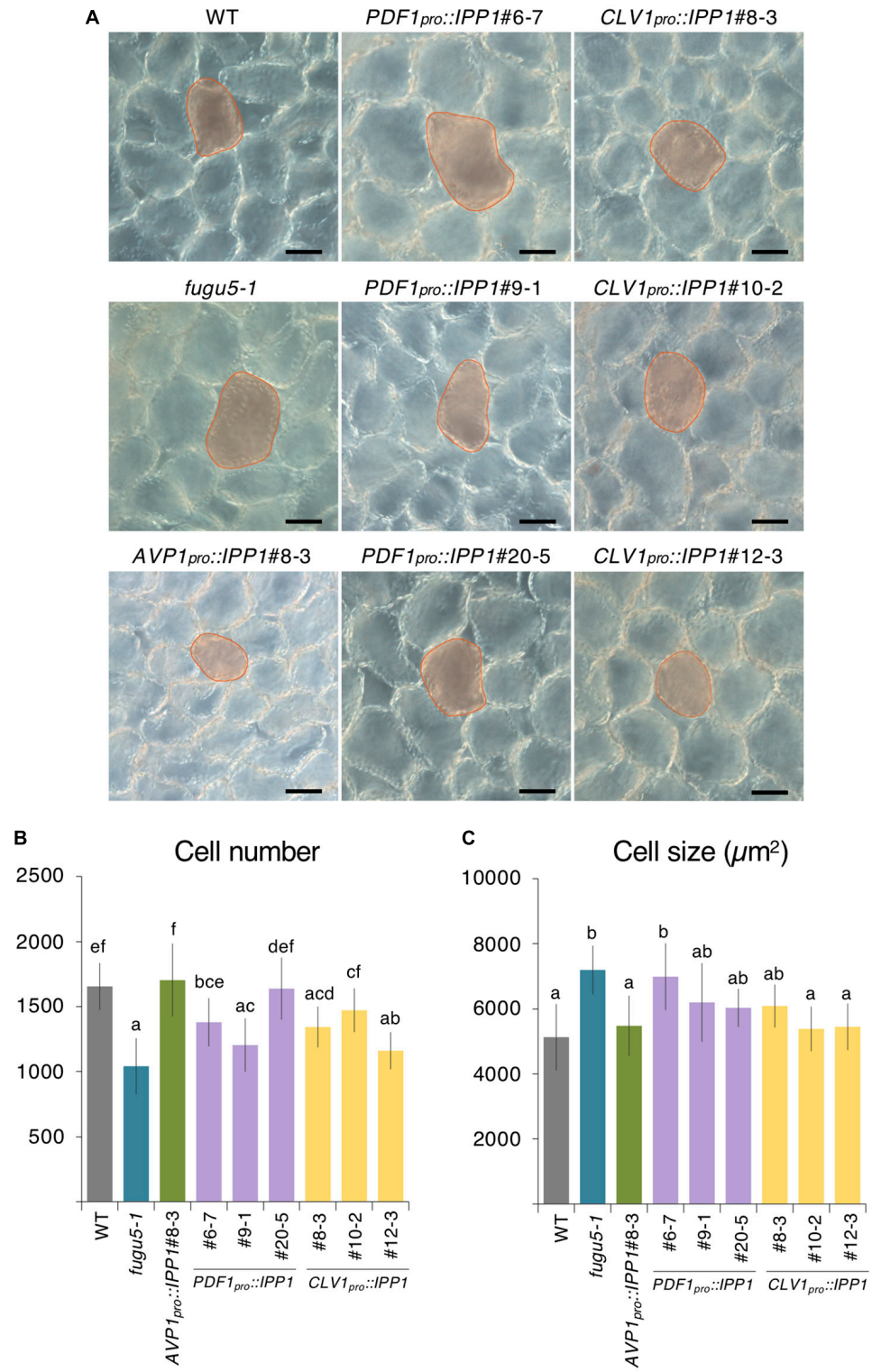

FIGURE 2
Palisade cellular phenotypes of mature cotyledons from the *PDF1*$_{pro}$*::IPP1* and *CLV1*$_{pro}$*::IPP1* transgenic lines. **(A)** Micrographs of palisade tissue cells from cleared cotyledons of the wildtype (WT), *fugu5-1*, *AVP1*$_{pro}$*::IPP1*#8-3, *PDF1*$_{pro}$*::IPP1*#6-7, *PDF1*$_{pro}$*::IPP1*#9-1, *PDF1*$_{pro}$*::IPP1*#20-5, *CLV1*$_{pro}$*::IPP1*#8-3, *CLV1*$_{pro}$*::IPP1*#10-2, and *CLV1*$_{pro}$*::IPP1*#12-3 lines at 25 DAS. Red contour and shadow highlight representative cell size in each genotype. Scale bar = 50 μm. **(B,C)** Numbers of subepidermal palisade tissue cells **(B)** and their average sizes **(C)**. Data are means ± SD ($n \geq 9$ cotyledons). Each character represents a significant difference at $p < 0.05$ (Tukey's HSD test). DAS, days after seed sowing.

10.3389/fpls.2022.945225

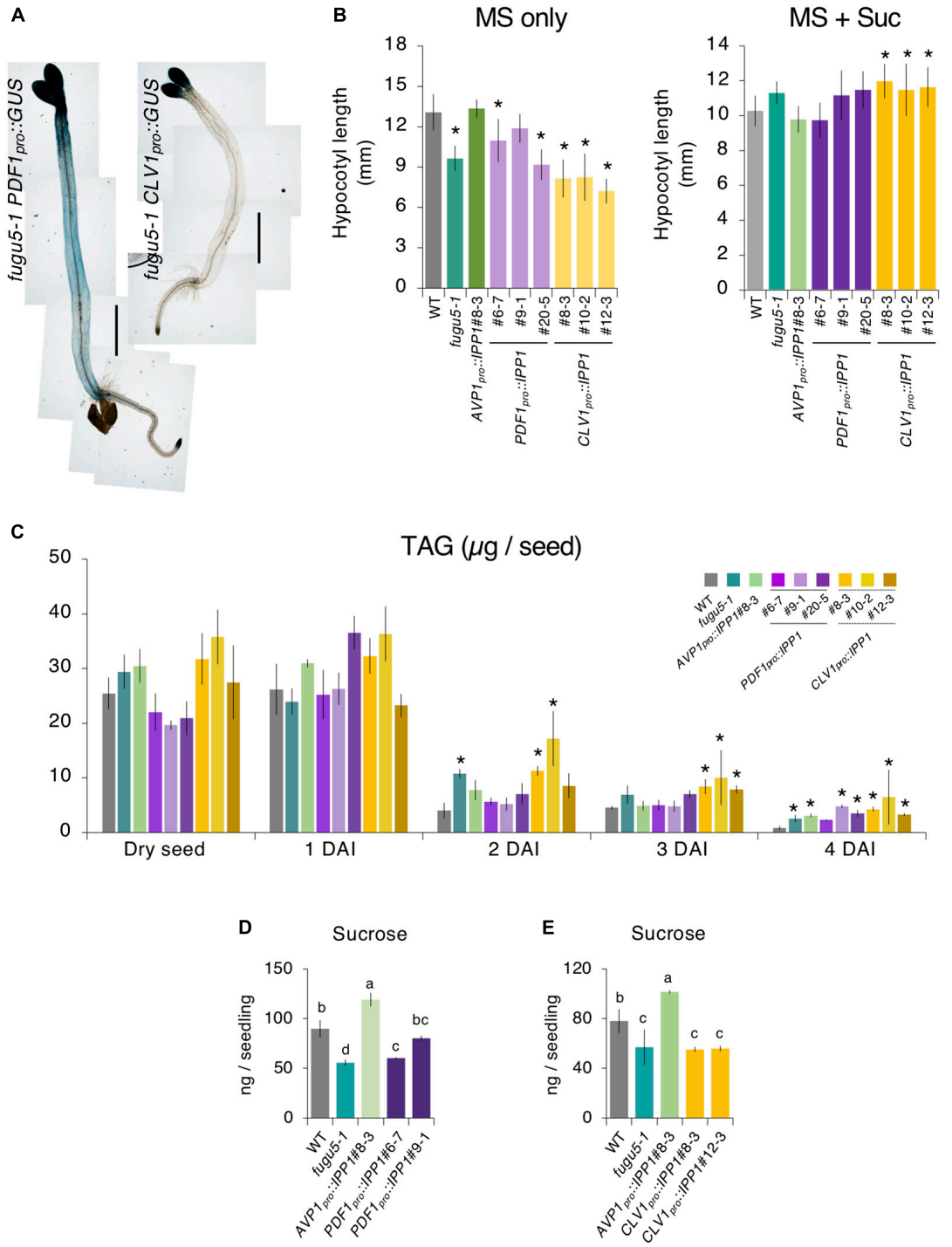

FIGURE 3

Etiolated seedling elongation and triacylglycerol (TAG) mobilization in transgenic plants expressing IPP1 in a tissue-specific manner. **(A)** Micrographs of GUS staining of etiolated seedlings of the *fugu5-1 PDF1*$_{pro}$*::GUS* and *fugu5-1 CLV1*$_{pro}$*::GUS* lines grown on MS medium in darkness for 4 DAI. Scale bar = 1 mm. **(B)** Length of hypocotyls of the wildtype (WT), *fugu5-1*, *AVP1*$_{pro}$*::IPP1*#8-3, *PDF1*$_{pro}$*::IPP1*, and *CLV1*$_{pro}$*::IPP1* lines grown on MS only and MS + Suc medium in the dark for 4 DAI. Data are means ± SD (n = 21). *Significant difference at $p < 0.05$ compared to the WT (Tukey's HSD test). **(C)** Mobilization of seed lipid reserves during post-germinative growth. The TAG content was quantified with 20 dry seeds or 20 etiolated seedlings at 1, 2, 3, and 4 DAI. Data are means ± SD (n = 3 independent experiments). *Significant difference at $p < 0.05$ compared to the WT (Tukey's HSD test). **(D,E)** Sucrose levels determined by GC-MS/MS of 100 etiolated seedlings at 3 DAI. Data are means ± SD (n = 3 independent experiments). Each character represents a significant difference at $p < 0.05$ (Tukey's HSD test). DAI, days after induction of seed germination.

Removal of inorganic pyrophosphate (PPi) immediately after seed imbibition promotes plant growth

The pleiotropic phenotype of the *fugu5* cotyledon is triggered by excess PPi produced following metabolic reactivation in the embryo upon seed imbibition. However, the post-germinative developmental stage susceptible to excess PPi is unclear.

Because *IPP1* was expressed constitutively in $AVP1_{pro}$::*IPP1*, $PDF1_{pro}$::*IPP1*, and $CLV1_{pro}$::*IPP1*, we assessed the contribution of PPi hydrolysis. To this end, the promoter of *ISOCITRATE LYASE* (*ICL*), a key enzyme in the peroxisomal glyoxylate cycle, was used because *ICL* transcription increased rapidly after seed imbibition, remained high for 3 days, and was negligible after 4 days (Eastmond et al., 2000). To investigate the inhibitory effects of PPi after seed imbibition on the *fugu5-1* background, we generated ICL_{pro}::*GUS* and ICL_{pro}::*IPP1* transgenic lines on the *fugu5-1* background.

ICL_{pro}::*GUS* expression in the cotyledon increased gradually following seed imbibition, peaked at 2 DAS, and decreased markedly at 3–4 DAS (**Figure 4A**). The post-germinative growth of ICL_{pro}::*IPP1* seedlings at 10 (**Figure 4B**), 14, and 23 (**Supplementary Figure 5A**) DAS was enhanced compared to *fugu5-1* and cotyledon size and aspect ratio were almost indistinguishable from the WT (**Figures 4C,D**). Indeed, ICL_{pro}::*IPP1* growth was markedly improved compared to *fugu5-1* in terms of FW, which increased 150–260% at 12 DAS and 140–180% at 25 DAS (**Supplementary Figure 5B,C**). Therefore, temporal removal of PPi upon seed imbibition and germination significantly promotes seedling growth at early stages, which enhances the subsequent growth of the plant.

Removal of inorganic pyrophosphate (PPi) immediately after seed imbibition partially rescues the epidermal developmental defects

To corroborate how the removal of PPi within 3,4 days of germination promotes plant growth, we quantified the shape and size of cotyledon PCs in the ICL_{pro}::*IPP1* transgenic line (**Figures 4E–G**; **Supplementary Figure 6**). The UI values of PCs in ICL_{pro}::*IPP1* were intermediate between the WT and *fugu5-1* single mutant (**Figure 4F**). PCs in *fugu5-1* are reportedly significantly smaller compared to the WT, in which cells less than 2,000 μm^2 account for more than or 30% of cotyledon PCs (Gunji et al., 2020). The number of cells less than 2,000 μm^2 was significantly decreased in ICL_{pro}::*IPP1*, and the proportion of cells > 15,000 μm^2 was increased (**Figures 4E,G**). Together, these findings indicate that the expression of IPP1 to a confined window of a few days following the seed germination is efficient but not enough to fully restore the PC jigsaw puzzle-like pattern that is generated by interdigitation of the cell wall during cotyledon development.

Triacylglycerol (TAG)-to-Suc conversion restores cell number and cancels compensated cell enlargement (CCE) in ICL_{pro}::*IPP1*

Excess PPi affects both the epidermis by altering PC shape (Gunji et al., 2020) and the palisade tissue cells in which CCE is triggered (Bertoni, 2011; Ferjani et al., 2011). The inhibitory mechanisms are different and independent for the two layers. To evaluate the phenotype of palisade tissue cells, namely, CCE, we quantified cell number and size in ICL_{pro}::*IPP1*. It is interesting that the cell number in the palisade tissue of the transgenic line recovered to the WT level, and CCE did not occur (**Figures 5A–C**). Provided that CCE in *fugu5-1* is triggered by a partial failure of TAG mobilization, transient expression of IPP1 under the control of ICL_{pro} is likely necessary and sufficient to provide the required amount of carbon for energy production to reactivate cell cycling in palisade tissue immediately after seed imbibition (Bertoni, 2011; Ferjani et al., 2011).

The seedlings kept in darkness adopt a skotomorphogenic developmental program, in which allocation of resources is typically directed toward a hypocotyl elongation at the expense of cotyledon and root development (Josse and Halliday, 2008). Indeed, the lack of Suc in *fugu5-1* compromises a hypocotyl elongation in darkness, resulting in ∼30% shorter hypocotyls compared to the WT (Ferjani et al., 2011; Katano et al., 2016). To evaluate the effects of ICL_{pro}::*IPP1* expression on the skotomorphogenic developmental program, we quantified the length of 4 DAI etiolated seedlings. Hypocotyl length in ICL_{pro}::*IPP1* significantly recovered to the WT level in the absence of exogenous Suc (**Figure 5D**). Indeed, ICL_{pro}::*IPP1* produced as much Suc as the WT (**Figure 5E**). The TAG mobilization was not affected in ICL_{pro}::*IPP1*, in agreement with our finding for the *fugu5-1* single mutant (Ferjani et al., 2011; Katano et al., 2016; Tabeta et al., 2021; **Figure 5F**). Taken together, these results indicate that PPi removal at the early stages of seed germination is critical for an efficient TAG-to-Suc conversion and re-establishment of normal palisade cell number and size.

Tissue-specific removal of inorganic pyrophosphate (PPi) in $PDF1_{pro}$:*IPP1* and $CLV1_{pro}$::*IPP1* affects metabolic profiles

The expression of $PDF1_{pro}$::*IPP1* and $CLV1_{pro}$::*IPP1* on the *fugu5-1* background had distinct effects on epidermis

10.3389/fpls.2022.945225

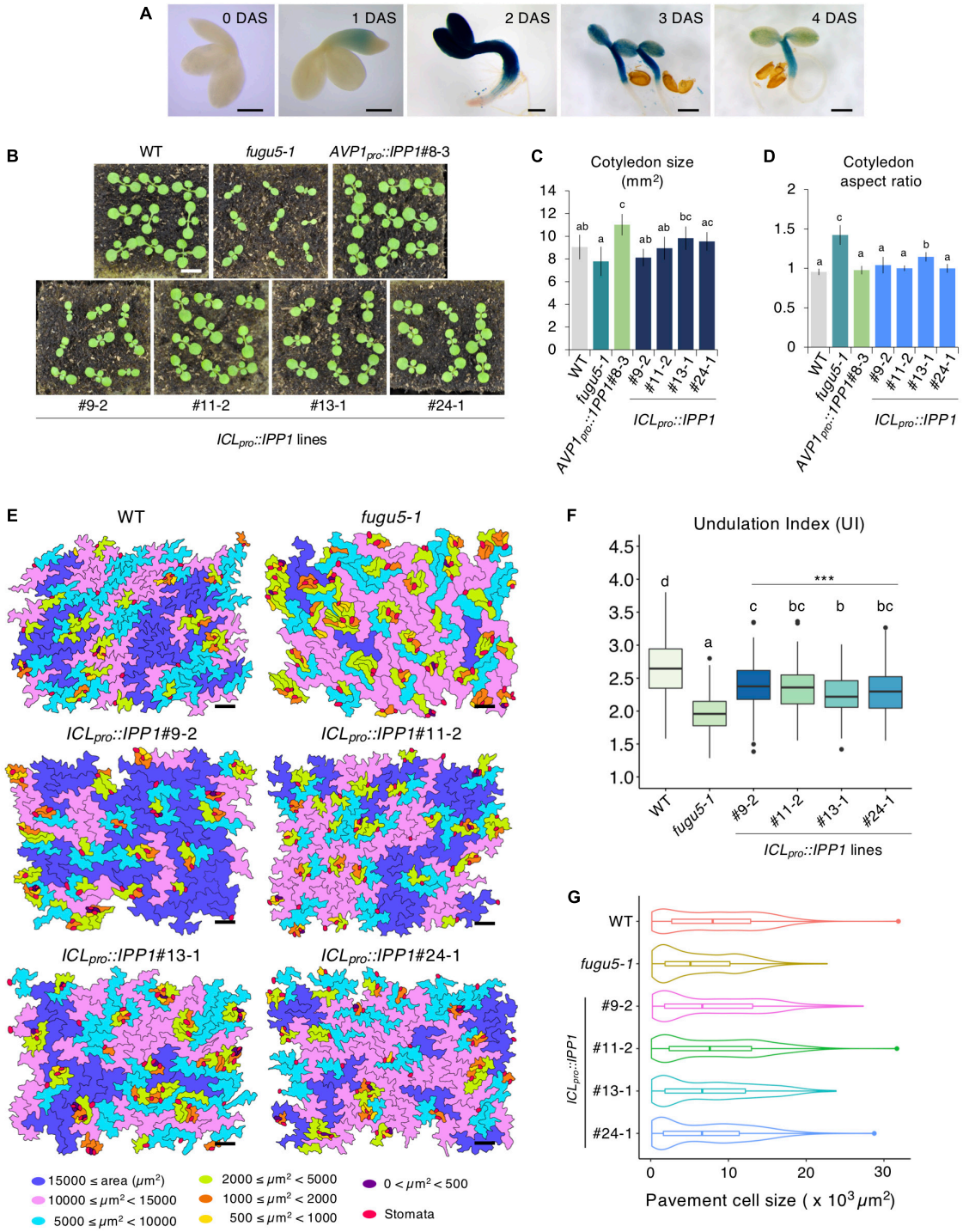

FIGURE 4

Effect of developmental stage-specific removal of inorganic pyrophosphate (PPi) on plant development. **(A)** Time course of GUS expression in *fugu5-1 ICL*$_{pro}$*::GUS*. Scale bar = 200 μm (at 0-, 1-, 2 DAS); Scale bar = 500 μm (at 3 and 4 DAS). **(B)** Gross morphology of the wildtype (WT), *fugu5-1*, *AVP1*$_{pro}$*::IPP1*#8-3, and *ICL*$_{pro}$*::IPP1* lines. Photographs of 10-day-old plants grown on rockwool. Scale bar = 5 mm. **(C)** Cotyledon size and **(D)** aspect ratio of six cotyledons at 25 DAS. Data are means ± SD. Each character represents a significant difference at $p < 0.05$ (Tukey's HSD test). **(E)** PCs in representative scanning electron microscopy (SEM) images of the WT, *fugu5-1*, *ICL*$_{pro}$*::IPP1*#9-2, *ICL*$_{pro}$*::IPP1*#11-2, *ICL*$_{pro}$*::IPP1*#13-1, and *ICL*$_{pro}$*::IPP1*#24-1 lines were traced and color-coded based on their size. Scale bar = 100 μm. **(F)** Box-plot represents undulation index (UI) of PCs (n = 180 PCs from six cotyledons) at 25 DAS. The boxes of lower and upper are the first and third quantiles, the line in the boxes is the median and whiskers are maximum and minimum values. Each character represents a significant difference at $p < 0.05$. ***Significant difference compared to *fugu5-1* at $p < 0.001$ (Tukey's HSD test). **(G)** Violin plots of the size distribution of PCs, excluding stomata (n = 480 cells from six cotyledons). DAS, days after seed sowing.

10.3389/fpls.2022.945225

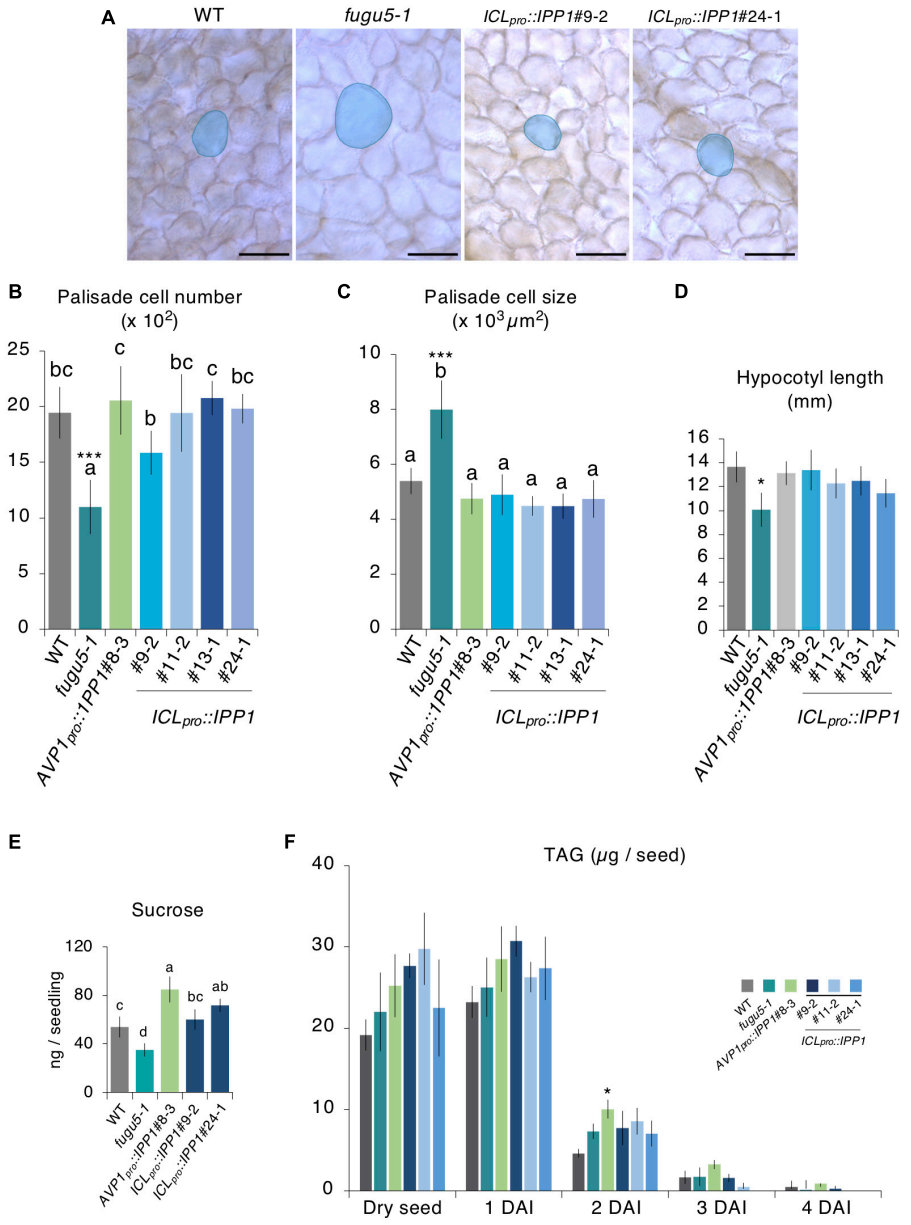

FIGURE 5
Effect of developmental stage-specific removal of inorganic pyrophosphate (PPi) on cotyledon cellular phenotype and etiolated seedling elongation. **(A)** Micrographs of cleared cotyledon palisade tissue cells from the wildtype (WT), *fugu5-1*, *ICL*$_{pro}$*::IPP1*#9-2, and *ICL*$_{pro}$*::IPP1*#24-1 at 25 DAS. Blue contour and shadow highlight representative cell size in each genotype. Scale bar = 100 μm. **(B)** Numbers and **(C)** sizes of cotyledon subepidermal palisade tissue cells; means ± SD (n = 6 cotyledons). Each character represents a significant difference at $p < 0.05$. ***Significant difference at $p < 0.0001$ compared to the WT (Tukey's HSD test). **(D)** Hypocotyl length at 4 DAI; means ± SD (n = 21 seedlings). *Significant difference at $p < 0.01$ compared to the WT (Tukey's HSD test). **(E)** Sucrose levels of 100 etiolated seedlings at 3 DAI by GC-MS/MS. Data are means ± SD (n = 4 independent experiments). Each character represents a significant difference at $p < 0.05$ (Tukey's HSD test). **(F)** Time course of the mobilization of triacylglycerol (TAG) during post-germinative growth. The TAG content was quantified with 20 dry seeds or 20 etiolated seedlings at 1, 2, 3, and 4 DAI. Data are means ± SD (n = 3 independent experiments). *Significant difference at $p < 0.05$ compared to the WT. DAS, days after seed sowing, DAI, days after induction of seed germination.

and palisade tissue morphogenesis. Specifically, although the removal of PPi from the epidermis by *PDF1*$_{pro}$*::IPP1* was sufficient to restore the PC phenotype, *CLV1*$_{pro}$*::IPP1* expression had only a partial effect (Figures 1F–I). Hence, the effects of PPi differ by leaf tissue, and we postulated that it would also have different impacts on the metabolic profiles of the transgenic lines. Because the conversion of glucose 1-phosphate (G1P) to UDP-Glc is inhibited by excess PPi on the *fugu5*

background (Ferjani et al., 2018), we used CE-TOF MS to evaluate metabolic changes in *PDF1*$_{pro}$*::IPP1* and *CLV1*$_{pro}$*::IPP1* compared to *fugu5-1*.

The CE-TOF MS analysis detected 136 metabolites (**Supplementary Table 1**), of which 115 were significantly altered (**Supplementary Table 2**). In *fugu5-1*, 52 and 5 metabolites were significantly increased and decreased, respectively, when compared to the WT (**Supplementary Table 2**). To gain insight into the metabolic changes correlated with tissue-specific removal of PPi, we performed principal component analysis (PCA) on the WT, *fugu5-1*, *AVP1*$_{pro}$*::IPP1*#8-3, *PDF1*$_{pro}$*::IPP1*#6-7, *PDF1*$_{pro}$*::IPP1*#9-1, *CLV1*$_{pro}$*::IPP1*#8-3, and *CLV1*$_{pro}$*::IPP1*#12-3; and *PDF1*$_{pro}$*::IPP1*#6-7$^{(+/-)}$ and *CLV1*$_{pro}$*::IPP1*#8-3$^{(+/-)}$ lines. The first (PC1) and second (PC2) components contributed 50.7% of the total variance (**Figure 6A**). A scores plot indicated that *fugu5-1 CLV1*$_{pro}$*::IPP1* was separable from the WT, *AVP1*$_{pro}$*::IPP1*, *PDF1*$_{pro}$*::IPP1*, and *fugu5-1*, yet *CLV1*$_{pro}$*::IPP1* lines and *fugu5-1* were closely aligned on the PC1 axis (**Figure 6A**). The *PDF1*$_{pro}$*::IPP1* and *PDF1*$_{pro}$*::IPP1*#6-7$^{(+/-)}$ and *CLV1*$_{pro}$*::IPP1*#8-3$^{(+/-)}$ were closer to the WT and *AVP1*$_{pro}$*::IPP1* (**Figure 6A**). In addition, a biplot of the PCA scores (**Supplementary Figure 7A**) showed the metabolites' contributions to PC1 and PC2 and identified 35 and 23 metabolites positively or negatively correlated with the PC1 and PC2 scores, respectively (**Supplementary Figure 7B**). Based on the factor loading scores, sugars, sugar phosphates, sugar amino acids, sugar nucleotides, and amino acids (Val, Ile, and Met) were significantly positively correlated with PC1 scores. By contrast, polyamines were negatively correlated with PC1.

The changes in the metabolic profile across the genotypes were recapitulated by visualization of the relative abundances of metabolites by means of Hierarchical Clustering Analysis (HCA) (**Figure 6B**). More specifically, HCA identified 10 clusters in total, among which metabolites that exhibited a positive correlation along PC1 axis were enriched in clusters 5 and 8 (**Figures 6A,B** and **Supplementary Figure 7**). On the contrary, metabolites that exhibited a positive correlation along PC2 axis were enriched in cluster 6 (**Figures 6A,B** and **Supplementary Figure 7**).

Effect of the removal of inorganic pyrophosphate (PPi) immediately after seed imbibition on the metabolic profile of *ICL*$_{pro}$*::IPP1*

Given that the expression of *ICL*$_{pro}$*::IPP1* on the *fugu5-1* background rescued developmental defects in palisade tissue, we assessed its effect on the metabolic profile immediately after seed germination.

The CE-TOF MS analysis detected 113 metabolites (**Supplementary Table 3**), of which 86 were significantly changed (**Supplementary Table 4**). The PCA of the metabolomics data showed that the global metabolic profile of *ICL*$_{pro}$*::IPP1* was similar to the WT and different from *fugu5-1* (**Figure 6C**). Furthermore, a biplot of the PCA scores (**Supplementary Figure 8A**) showed the metabolites' contributions to PC1 and PC2 and identified 22 and 12 metabolites positively or negatively correlated with the PC1 and PC2 scores, respectively (**Supplementary Figure 8B**). The factor loading scores indicated that the metabolites significantly positively correlated with PC1 scores in *ICL*$_{pro}$*::IPP1* overlapped with those in *PDF1*$_{pro}$*::IPP1* and *CLV1*$_{pro}$*::IPP1*. Finally, a HCA heat map of metabolite abundance confirmed the metabolic similarities between the WT and *ICL*$_{pro}$*::IPP1* (**Figure 6D**), whereby metabolites that exhibited a positive correlation along PC1 and PC2 axes were enriched in cluster 6 (**Figures 6C,D**; **Supplementary Figure 8**).

fugu5 central metabolism remarkably recover in *PDF1*$_{pro}$*::IPP1* and *ICL*$_{pro}$*::IPP1*

We summarized the number of metabolites whose accumulation was significantly changed on the *fugu5-1* background and recovered to the WT level by tissue-specific expression of *IPP1* on the *fugu5-1* background (**Figures 7A,B** and **Supplementary Tables 5,6**). *AVP1*$_{pro}$*::IPP1* expression had the highest recovery rate (∼79%), followed by *PDF1*$_{pro}$*::IPP1* and *CLV1*$_{pro}$*::IPP1* (70 and 48%, respectively), in two independent transgenic lines (**Figure 7A**). Although 18 metabolites were commonly affected in *AVP1*$_{pro}$*::IPP1* and *PDF1*$_{pro}$*::IPP1*, only 5 showed similar trends between *AVP1*$_{pro}$*::IPP1* and *CLV1*$_{pro}$*::IPP1* (**Figure 7A**). It is important to note that expression of *ICL*$_{pro}$*::IPP1* on the *fugu5-1* background yielded a recovery rate of ∼71%, which is roughly comparable to the 67% recovery rate in *AVP1*$_{pro}$*::IPP1* (**Figure 7B**).

Excess PPi *in planta* affected gluconeogenesis (**Figure 7C**) by inhibiting UDP-Glc production (Ferjani et al., 2018). The overaccumulation of glucose 6-phosphate (G6P), a precursor of UDP-Glc, in *fugu5-1* was largely recovered in *PDF1*$_{pro}$*::IPP1*, *CLV1*$_{pro}$*::IPP1*, and *ICL*$_{pro}$*::IPP1* (**Figures 7D,E**). The levels of G1P and (GlcNAc-6P; GalNAc-6P), whose accumulation increased in *fugu5-1*, were reduced in these transgenic lines (**Figures 7D,H,I**). It should be noted, however, that (UDP-GlcNAc; UDP-GalNAc) levels, which were expected to decrease in the *fugu5-1* background due to excess PPi (**Figure 7C**), were either slightly increased or unchanged (**Figures 7J,K**). This counter-intuitive result may indicate that the metabolic reaction converting GlcNAc-1P into (UDP-GlcNAc; UDP-GalNAc) is less susceptible to PPi-inhibition *in vivo*. For instance, PPi has relatively little effect on Arabidopsis PPDK activity *in vitro* (Chastain et al., 2011).

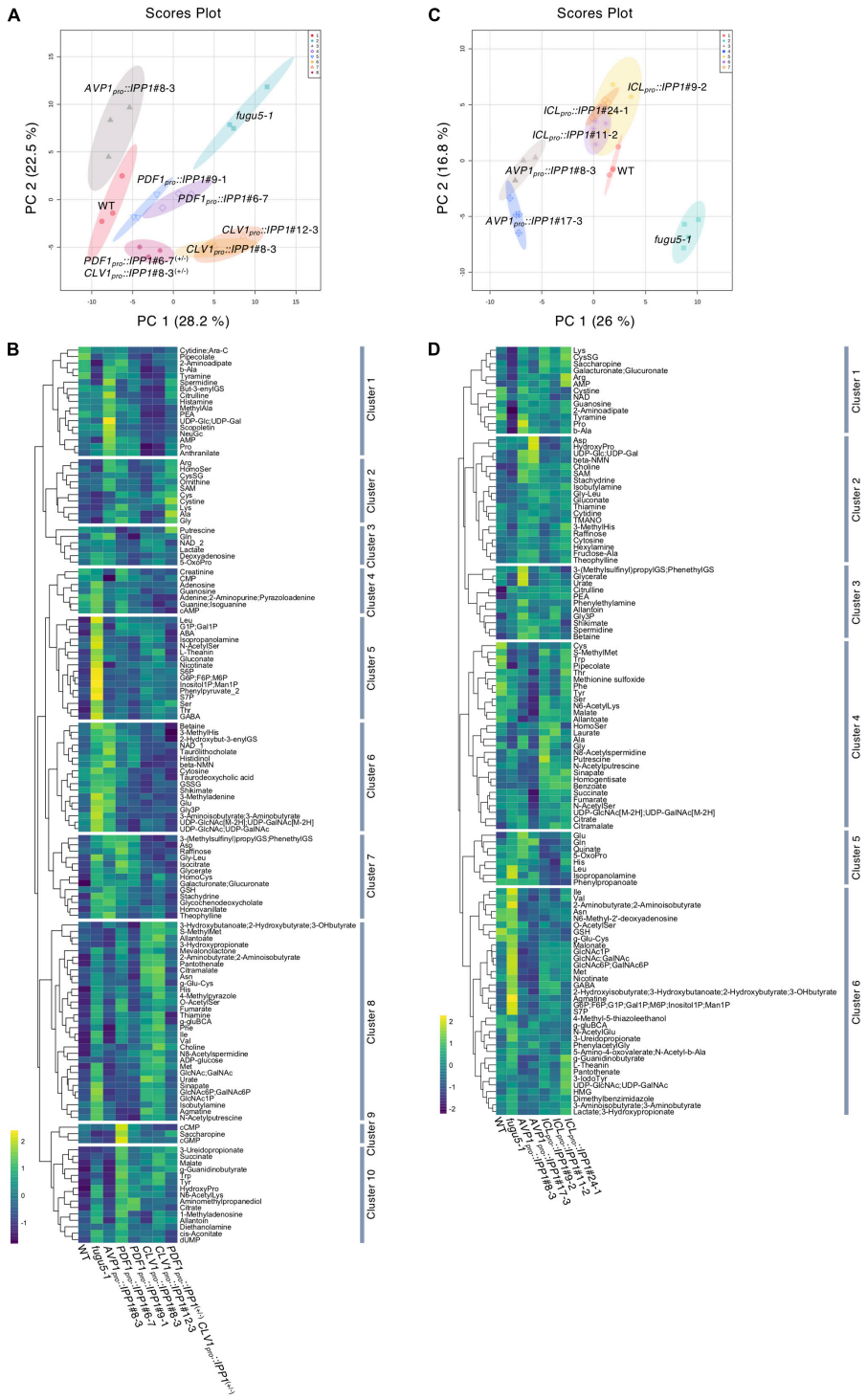

FIGURE 6
Effect of spatiotemporal expression of IPP1 on the *fugu5* background on the metabolic profiles of etiolated seedlings determined by capillary electrophoresis time-of-flight mass spectrometry (CE-TOF MS). The MetaboAnalyst (v.5.0) website was used to normalize the data and perform principal component analysis (PCA). The normalization procedures consisted of mean-centering and division by the standard deviation of each variable. **(A)** The PCA plot based on three independent experiments involving the wildtype (WT), *fugu5-1*, $AVP1_{pro}$::*IPP1*#8-3, $PDF1_{pro}$::*IPP1*#6-7, $PDF1_{pro}$::*IPP1*#9-1, $CLV1_{pro}$::*IPP1*#8-3, $CLV1_{pro}$::*IPP1*#12-3, and $PDF1_{pro}$::*IPP1*#6-$7^{(+/-)}$ $CLV1_{pro}$::*IPP1*#8-$3^{(+/-)}$ lines. **(B)** Hierarchical clustering heat map of the relative abundances of metabolites. Scale indicates the color code relative to normalized metabolite abundance. **(C)** PCA score plot from four independent experiments involving the WT, *fugu5-1*, $AVP1_{pro}$::*IPP1*#8-3, $AVP1_{pro}$::*IPP1*#17-3, ICL_{pro}::*IPP1*#9-2, ICL_{pro}::*IPP1*#11-2, and ICL_{pro}::*IPP1*#24-1 lines. **(D)** Hierarchical clustering heat map of the relative abundances of metabolites. Scale indicates the color code relative to normalized metabolite abundance.

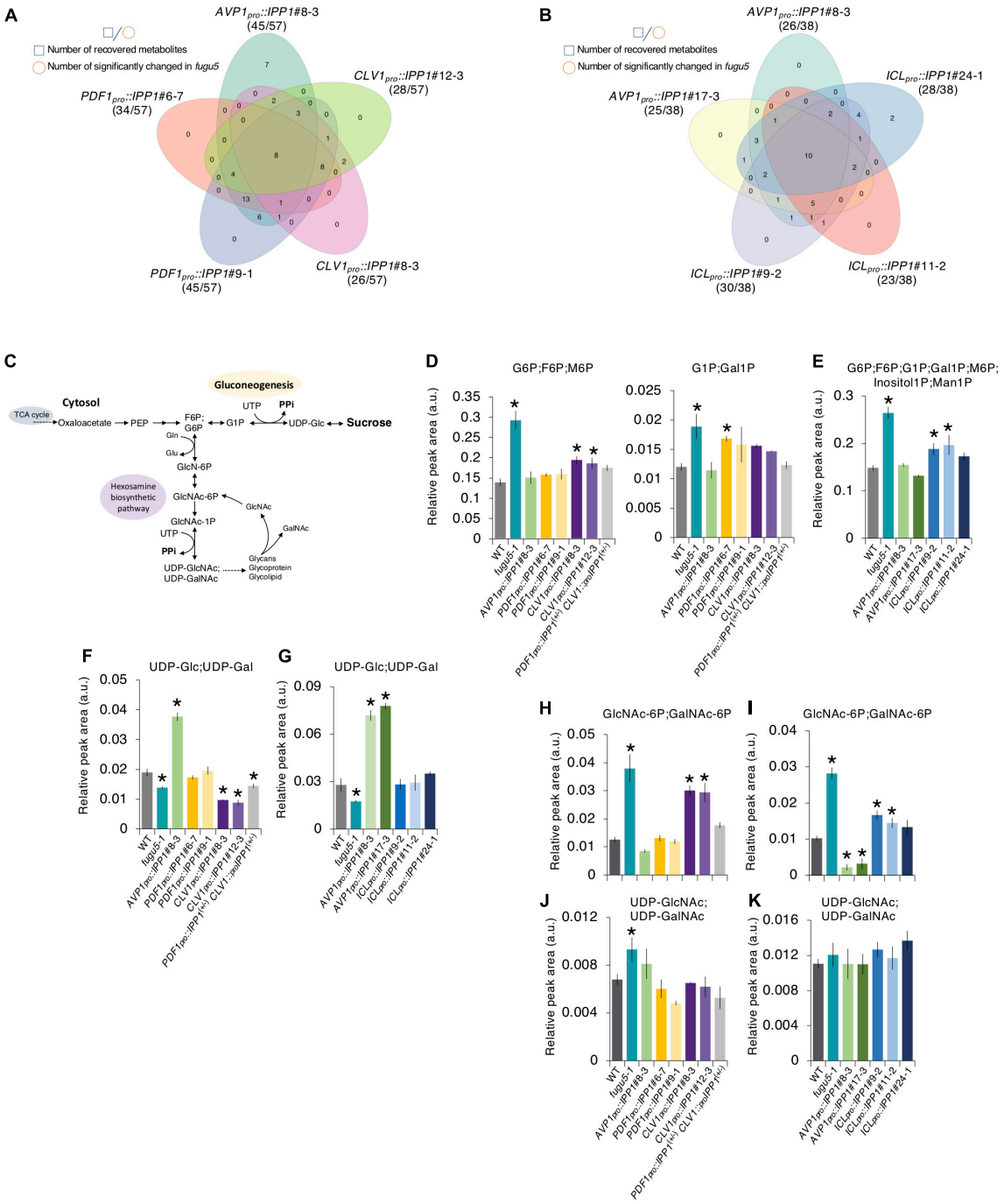

FIGURE 7
Effect on the metabolite profile of spatiotemporal expression of IPP1 on the *fugu5* background by capillary electrophoresis time-of-flight mass spectrometry (CE-TOF MS). **(A,B)** Venn diagram of metabolites that recovered to wildtype (WT) levels and those that exhibited opposite and significant fluctuations in *fugu5* vs. the indicated transgenic lines. **(C)** Schematic of the gluconeogenesis pathway targeted by inorganic pyrophosphate (PPi) overaccumulation in *fugu5-1* and the hexosamine biosynthetic pathway. **(D–K)** Fluctuations in major key metabolites in the indicated genotypes. Data are means ± SD (**E**, **F**, **H**, and **J:** $n = 3$; **E**, **G**, **I**, and **K:** $n = 4$). *Significant difference at $p < 0.05$ compared to the WT (Tukey's HSD test).

Finally, although UDP-Glc decreased in *fugu5-1*, it was comparable to the WT in *PDF1*$_{pro}$*::IPP1* and *ICL*$_{pro}$*::IPP1* (Figures 7F,G). This rescue of UDP-Glc was less in *CLV1*$_{pro}$*::IPP1*, likely because subepidermal mesophyll cell-specific removal of PPi had little impact on metabolism (Figures 6A, 7A).

Discussion

The concentration of PPi *in planta* is under the tight control of several PPases that make different contributions to PPi homeostasis and cooperate to prevent its accumulation to a toxic level (Ferjani et al., 2011, 2018; Segami et al., 2018). Proliferating cells generate large amounts of PPi owing to their active metabolism, which correlates with their high expression of PPases (Segami et al., 2018, and references therein). Excess PPi triggers a plethora of growth and developmental defects, but little is known about its effect on major growth stages and/or plant tissue.

Whereas most *fugu5* phenotypes, such as CCE and hypocotyl elongation defects, are attributable to reduced production of Suc from TAG (Ferjani et al., 2011), PC morphological defects are likely triggered by excess PPi (Gunji et al., 2020). Although phenotypic and functional analyses indicate different mechanisms for the palisade and the epidermal developmental defects, the possibility that both are triggered by PPi-related metabolic disorders cannot be ruled out. Hence, the CCE-Suc and PCs-PPi relationships suggest major differences in metabolic activity in the two leaf tissues. Therefore, the effects of excess PPi on metabolism in these tissues and its impact on organogenesis in plants, which is the major focus of this research, has been awaiting direct investigation.

Effect of excess inorganic pyrophosphate (PPi) on cotyledon development

Manipulating the PPi level in a plant tissue and/or cell type is technically challenging (Ferjani et al., 2011, 2014a,b; Hanchi et al., 2018; Segami et al., 2018) because of its broad contribution to metabolism. However, the genetic approach adopted in this study overcame these technical difficulties.

Our results revealed that the inhibitory effects of excess PPi were canceled in *IPP1*-expressing tissue only (**Figures 1**, **2**). Furthermore, the removal of excess PPi at early developmental stages was crucial for proper plant development (**Figures 4**, **5**). It is interesting that the inhibitory effects of PPi depended on the developmental stage of leaf tissue cells. Because hydrolysis of PPi by ICL_{pro}*::IPP1* abolished CCE, the intracellular metabolic state at early developmental stages resulting from excess PPi is likely the main trigger of CCE. However, PC developmental defects in ICL_{pro}*::IPP1* were only partially restored, which indicates that PC morphogenesis is mediated by a PPi-related mechanism that is likely different, at least in part, from post-germinative metabolism.

In this study, we constructed chimeric plants with respect to their ability to hydrolyze PPi by restricting IPP1 expression spatially or temporally using tissue- or developmental stage-specific promoters. Hence, PPi hydrolysis in a given tissue would reveal its impact on plant morphogenesis and metabolism. This would enable comparative analyses based on altered metabolic profiles and the identification of key metabolites in the CCE-Suc and PCs-PPi relationships.

Consistent with our previous report (Ferjani et al., 2018), the levels of gluconeogenesis-related metabolites and amino acids (e.g., Ile, Val, Met, and GABA) were altered in *fugu5* because of excess PPi (**Figure 6**). In addition, the levels of these metabolites were restored by PPi hydrolysis in the epidermis (**Figure 6**). By contrast, PPi hydrolysis by $CLV1_{pro}$*::IPP1* did not contribute to skotomorphogenesis because $CLV1_{pro}$*::IPP1* showed PPi-specific metabolic changes and the Suc level was as low as in *fugu5* (**Figures 3**, **7**). In fact, although $CLV1_{pro}$*::GUS* expression was confined to the single paradermal layer of the cotyledonary palisade tissue, it was patchy and lower compared to $PDF1_{pro}$*::GUS* (discussed further below). Hence, the partial repression of CCE in $CLV1_{pro}$*::IPP1* may reflect an amalgam of cellular behavior (i.e., CCE was solely repressed in *IPP1*-expressing cells in a tissue-autonomous manner). Such biased cellular behavior is likely supported by metabolic products synthesized after germination in tissue from which PPi has been removed.

Impact of excess inorganic pyrophosphate (PPi) on pavement cell (PC) morphogenesis

The PC formation has been proposed to involve local elongation of lobes, local restriction of dimples, or a combination of both (Fu et al., 2002, 2005, 2009; Xu et al., 2010; Zhang et al., 2011; Abley et al., 2013; Lin et al., 2013; Sampathkumar et al., 2014; Armour et al., 2015; Higaki et al., 2016; Majda et al., 2017; Sapala et al., 2018). In addition, although Roh of Plants (ROP) signaling and phytohormonal regulation of PC interdigitation play central roles in the determination of plant cell shape, the mechanical effects of the PC wall, and the mechanical interactions between the adjacent cells may be involved (Sampathkumar et al., 2014; Cosgrove, 2018; Sapala et al., 2018; Bidhendi et al., 2019; Cosgrove and Anderson, 2020; Haas et al., 2020; Liu et al., 2021).

Unlike palisade tissue cells, PCs lose their shape complexity because of excess PPi rather than compromised gluconeogenesis (Gunji et al., 2020). This is in agreement with the failure of exogenous Suc to restore PC shapes in the *fugu5* mutant and with the ability of *icl-2*, *mls-2*, and *pck1-2* mutants (which have defects in TAG-to-Suc conversion) to form typical jigsaw puzzle–shaped PCs (Gunji et al., 2020). Furthermore, PPi removal in $AVP1_{pro}$*::IPP1*, which ubiquitously expresses the yeast sPPase IPP1, restores PC developmental defects (Gunji et al., 2020). Consistently, exclusive expression of IPP1 in

the epidermis in *PDF1$_{pro}$::IPP1* confirms this hypothesis and suggests that PPi has its inhibitory effects *in planta* in a tissue- and cell-autonomous manner.

Despite the fact that IPP1 expression in *PDF1$_{pro}$::IPP1* was confined to the outermost layer, cell number and size in palisade tissue recovered partially compared to the *fugu5* single mutant (**Figure 2**). IPP1 transport from its target layer to neighboring layers is unlikely to underlie partial recovery of the compensation phenotype in transgenic lines expressing IPP1 in a tissue-specific manner. How can this discrepancy be explained?

First, if we assume that TAG in PCs of *PDF1$_{pro}$::IPP1* is fully converted into Suc, and provided that Suc is highly mobile, Suc may translocate from the epidermis to the palisade tissue, reactivating cell cycling and thereby inhibiting CCE. This partial recovery appears to be plausible provided that the *de novo* synthesis of Suc from TAG in *PDF1$_{pro}$::IPP1* is inferior to that in *AVP1$_{pro}$::IPP1*, because the former is epidermis specific and the latter is ubiquitously expressed. This is confirmed by the significantly lower Suc content in *PDF1$_{pro}$::IPP1* compared to *AVP1$_{pro}$::IPP1*#8-3 (**Figure 3**).

Second, upon the expression of *PDF1$_{pro}$::IPP1* on the *fugu5-1* background, a relaxed epidermis may allow proliferation and growth of mesophyll and other inner tissues in cotyledons. In this case, total or partial relief of the mechanical constraints exerted by the epidermis, the load-bearing layer (Asaoka et al., 2021), toward the inner tissues may stimulate their growth, resulting in partial recovery of their cellular phenotypes. Indeed, this may explain the recovered hypocotyl elongation in *PDF1$_{pro}$::IPP1* (**Figures 3A,B**).

Arabidopsis cotyledons are polarized with an adaxial side containing the palisade tissue and abaxial side containing the spongy parenchyma, all of them being wrapped by the single-layered epidermis on both sides. This has mechanical implications (e.g., see Onoda et al., 2015). More generally, the plant cells are enclosed by stiff cell walls, and the associated mechanical properties and signals should be integrated with genetic networks to fully understand their development (Autran et al., 2021; Trinh et al., 2021; Nakayama et al., 2022). Unlike cylindrical flowering stems with a relatively limited flexibility in growth direction, flat leaves where the stress patterns are relatively isotropic can grow with a higher degree of freedom (Zhang et al., 2011; Verger et al., 2018). Nonetheless, the computational modeling of stress patterns suggested that leaves are experiencing strongly anisotropic tensile stress across the organ thickness (Zhao et al., 2020), that if combined with CCE might further yield to stress. Importantly, excess PPi has recently been reported to cause morphological changes and weakening of cell walls (Segami et al., 2018), to reduce the polymerization velocity of cortical MTs, which appeared slightly fragmented and sparse (Gunji et al., 2020). Consistently, PPi delayed tubulin polymerization *in vitro* in a dose-dependent manner, thus supporting a link between PPi and MT dynamics (Gunji et al., 2020). Taking this into account, it seems that perturbation of cell wall stiffness and/or mechanosensing could also be amongst the most relevant factors, in addition to the above two possibilities, to explain the effect of excess PPi on PC growth and patterning.

Impact of excess inorganic pyrophosphate (PPi) on compensated cell enlargement (CCE)

Compensated cell enlargement in *CLV1$_{pro}$::IPP1* was not completely suppressed—the cell number and size of palisade tissue were only partially restored. Although the subepidermal cell-specific expression of *IPP1* against *fugu5-1* significantly altered the accumulation of key metabolites, including G6P, its impact was limited compared to the other transgenic lines (**Figures 3**, **6**, **7**). For instance, the decreased level of Suc in *fugu5-1* was rescued in *PDF1$_{pro}$::IPP1* and *ICL$_{pro}$::IPP1* but not in *CLV1$_{pro}$::IPP1*. These results are consistent with the fact that CCE induction is triggered by a decrease in cell number due to a reduced Suc content in *fugu5-1* (Tabeta et al., 2021).

The GUS staining of *CLV1$_{pro}$::GUS* showed low and patchy *CLV1* promoter activity; by contrast, the *PDF1* promoter was strongly and uniformly expressed. This suggests that PPi is less efficiently removed in the target tissue of *CLV1$_{pro}$::IPP1* compared to *PDF1$_{pro}$::IPP1*. In addition, the expression pattern may explain the discrepancy among the phenotypes of palisade tissue cells of the *CLV1$_{pro}$::IPP1*#8-3, #10-2, and #12-3 lines.

In one of our experiments, we checked whether PPi removal in the double transgenic heterozygous lines would contribute to suppressing CCE. Interestingly, while our data revealed that CCE was totally suppressed in *PDF1$_{pro}$::IPP1$^{(+/-)}$ CLV1$_{pro}$::IPP1$^{(+/-)}$* (**Supplementary Figure 4**), at the same time it raised the following question: Why did *PDF1$_{pro}$::IPP1* expression alone fail to restore normal cell division in palisade tissue cells, particularly when considering the highly mobile nature of sucrose? This question is open for future investigation to identify the critical factors behind this intriguing phenotype.

Inorganic pyrophosphate (PPi) removal from leaf tissue at different developmental stages reveals different cellular needs for proper morphogenesis

Furthermore, PPi homeostasis has been investigated in *fugu5* mutants (Ferjani et al., 2011; Kriegel et al., 2015; Asaoka et al., 2016, 2019; Fukuda et al., 2016; Wang et al., 2016; Segami et al., 2018; Gunji et al., 2020; Tabeta et al., 2021). The H^+-PPase is crucial for plant development, in particular, during the

mobilization of seed nutrient reserves, not as a proton pump but rather as a PPi-hydrolyzing enzyme (Ferjani et al., 2014a; Segami et al., 2018). It is intriguing that PPi accumulation may affect different leaf tissues or cell types by different mechanisms. For instance, the effects of a lack of Suc or its exogenous supply raise questions about the implication of PPi in any metabolic activity in the epidermis.

The reactivation of post-germinative cell division relies exclusively on energy produced by TAG mobilization (Bewley and Black, 1994; Graham, 2008). Nonetheless, whereas compensation was abolished, PC morphology did not fully recover in *ICL*$_{pro}$*::IPP1*. In *ICL*$_{pro}$*::IPP1*, PPi was hydrolyzed efficiently by the transgene, because cell number and size recovered to WT levels. This is in agreement with the fact that the *icl-2* mutant displays compensation and is classified with *mls-2* and *pck1-2* as showing class II CCE (Takahashi et al., 2017). Whereas PC morphology in all class II mutants was normal, *fugu5* had simpler PCs than the WT (Gunji et al., 2020). There could be many reasons for this. First, TAG-to-Suc conversion is immediately necessary for reactivation of cell division in palisade tissue after seed imbibition. Second, the lack of Suc is the main reason for class II CCE. Third, excess PPi on the *fugu5* background inhibits gluconeogenesis, but in *icl-2*, *mls-2*, and *pck1-2* the PPi level is canceled by their functional H^+-PPases. Finally, PCs in *icl-2*, *mls-2*, and *pck1-2* are normally shaped. This indicates that excess PPi, not lack of Suc, is related to PC development.

Taken together, these findings demonstrate that palisade tissue requires FUGU5 for a few days after seed imbibition, but prolonged H^+-PPase activity is required for PCs to adopt their typical jigsaw puzzle shape (Higaki et al., 2016). In other words, the decision to trigger CCE in cotyledons occurs early during postembryonic development and is followed by large-scale metabolic reprogramming involving IBA-to-IAA conversion as a key step in CCE induction (Tabeta et al., 2021). By contrast, PCs require more time than the palisade to mature and gradually adopt complex shapes (Fu et al., 2002, 2005; Armour et al., 2015; Higaki et al., 2016). Hence, the partial recovery in *ICL*$_{pro}$*::IPP1* indicates that PPi homeostasis must be maintained for a long period for the UI value to reach that of the WT. The complete recovery of palisade tissue cells and the partial recovery of PCs in the epidermis indicates that although PPi homeostasis is necessary for both tissues, leaf tissues have different cellular needs for proper morphogenesis.

Conclusions and future prospects

The H^+-PPase regulates both vacuolar acidification and cytosolic PPi concentration in living plant cells. Although various mechanisms have been proposed to explain its role in plant growth and development, a role in PPi homeostasis has been suggested. Hence, although the holistic contribution of H^+-PPase to plant growth has been investigated, its actions in different tissues and cell types throughout the plant life cycle with and without abiotic stresses are unclear (Schilling et al., 2017). This study provides a conceptual overview of how these questions should be approached. No direct measurement of PPi levels in major leaf tissues and/or cell types has been conducted because this is still technically challenging. Nonetheless, our previous works (Asaoka et al., 2019; Gunji et al., 2020; Tabeta et al., 2021), together with the spatiotemporal approach used in this study, unambiguously show that PPi has different effects on different plant tissues and cell types and at different developmental stages.

Data availability statement

The original contributions presented in the study are included in the article/**Supplementary material**, further inquiries can be directed to the corresponding author.

Author contributions

AF conceived the project, designed, supervised, and funded the study. SG performed the experiments, conducted the phenotyping analyses, and analyzed the data. SG, AF, and GH established the transgenic lines. KK and AO performed the CE-TOF MS metabolomic analyses. HTa performed Suc quantification. MA assisted metabolome data analyses. HTs and MH directed and funded the study. SG and AF wrote the manuscript with inputs from all co-authors. All authors read and approved the final manuscript.

Funding

This work was supported by Grant-in-Aid for Scientific Research (B) (JP16H04803 to AF); Grant-in-Aid for Scientific Research on Innovative Areas (JP25113002 and JP18H05487 to AF); and The Naito Foundation. HTa is a recipient of a Research Fellowship for Young Scientists (DC1).

Acknowledgments

The authors thank Ryosuke Sasaki for technical support with the CE-TOF MS analyses. The authors also thank Olivier Hamant (ENS de Lyon) and Kazuki Saito (RIKEN) for their critical reading of the manuscript.

Conflict of interest

The authors declare that the research was conducted in the absence of any commercial or financial relationships that could be construed as a potential conflict of interest.

Publisher's note

All claims expressed in this article are solely those of the authors and do not necessarily represent those of their affiliated organizations, or those of the publisher, the editors and the reviewers. Any product that may be evaluated in this article, or claim that may be made by its manufacturer, is not guaranteed or endorsed by the publisher.

Supplementary material

The Supplementary Material for this article can be found online at: https://www.frontiersin.org/articles/10.3389/fpls.2022.945225/full#supplementary-material

References

Abe, M., Takahashi, T., and Komeda, Y. (2001). Identification of a cis-regulatory element for L1 layer-specific gene expression, which is targeted by an L1-specific homeodomain protein. *Plant J.* 26, 487–494. doi: 10.1046/j.1365-313x.2001.01047.x

Abley, K., De Reuille, P. B., Strutt, D., Bangham, A., Prusinkiewicz, P., Marée, A. F., et al. (2013). An intracellular partitioning-based framework for tissue cell polarity in plants and animals. *Development* 140, 2061–2074. doi: 10.1242/dev.062984

Amano, R., Nakayama, H., Morohoshi, Y., Kawakatsu, Y., Ferjani, A., and Kimura, S. (2015). A decrease in ambient temperature induces post-mitotic enlargement of palisade cells in North American Lake Cress. *PLoS One* 10:e0141247. doi: 10.1371/journal.pone.0141247

Arai, Y., Hayashi, M., and Nishimura, M. (2008). Proteomic identification and characterization of a novel peroxisomal adenine nucleotide transporter supplying ATP for fatty acid beta-oxidation in soybean and *Arabidopsis*. *Plant Cell* 20, 3227–3240. doi: 10.1105/tpc.108.062877

Armour, W. J., Barton, D. A., Law, A. M., and Overall, R. L. (2015). Differential growth in periclinal and anticlinal walls during lobe formation in *Arabidopsis* cotyledon pavement cells. *Plant Cell* 27, 2484–2500. doi: 10.1105/tpc.114.126664

Asaoka, M., Inoue, S. I., Gunji, S., Kinoshita, T., Maeshima, M., Tsukaya, H., et al. (2019). Excess pyrophosphate within guard cells delays stomatal closure. *Plant Cell Physiol.* 60, 875–887. doi: 10.1093/pcp/pcz002

Asaoka, M., Ooe, M., Gunji, S., Milani, P., Runel, G., Horiguchi, G., et al. (2021). Stem integrity in *Arabidopsis thaliana* requires a load-bearing epidermis. *Development* 148:dev198028. doi: 10.1242/dev.198028

Asaoka, M., Segami, S., Ferjani, A., and Maeshima, M. (2016). Contribution of PPi-hydrolyzing function of vacuolar H^+-pyrophosphatase in vegetative growth of *Arabidopsis*: evidenced by expression of uncoupling mutated enzymes. *Front. Plant Sci.* 7:415. doi: 10.3389/fpls.2016.00415

Autran, D., Bassel, G., Chae, E., Ezer, D., Ferjani, A., Fleck, C., et al. (2021). What is quantitative plant biology? *Quant. Plant Biol.* 2:E10. doi: 10.1017/qpb.2021.8

Bertoni, G. (2011). A surprising role for vacuolar pyrophosphatase. *Plant Cell* 23:2808. doi: 10.1105/tpc.111.230813

Bewley, J. D., and Black, M. (1994). *Seeds Physiology of Development and Germination, Ed 2*. New York, NY: Plenum Press.

Bidhendi, A. J., Altartouri, B., Gosselin, F. P., and Geitmann, A. (2019). Mechanical stress initiates and sustains the morphogenesis of wavy leaf epidermal cells. *Cell Rep.* 28, 1237–1250. doi: 10.1016/j.celrep.2019.07.006

Chastain, C. J., Failing, C. J., Manandhar, L., Zimmerman, M. A., Lakner, M. M., and Nguyen, T. H. (2011). Functional evolution of C4 pyruvate, orthophosphate dikinase. *J. Exp. Bot.* 62, 3083–3091.

Chen, H. (2018). *VennDiagram: Generate High-Resolution Venn and Euler Plots. R Package Version 1.6.20.*

Chen, J., Brevet, A., Fromant, M., Lévêque, F., Schmitter, J. M., Blanquet, S., et al. (1990). Pyrophosphatase is essential for growth of *Escherichia coli*. *J. Bacteriol.* 172, 5686–5689.

Chong, J., Wishart, D. S., and Xia, J. (2019). Using metaboanalyst 4.0 for comprehensive and integrative metabolomics data analysis. *Curr. Protoc. Bioinform.* 68:e86.

Clough, S. J., and Bent, A. F. (1998). Floral dip: a simplified method for *Agrobacterium*-mediated transformation of *Arabidopsis thaliana*. *Plant J.* 16, 735–743.

Cornah, J. E., Germain, V., Ward, J. L., Beale, M. H., and Smith, S. M. (2004). Lipid utilization, gluconeogenesis, and seedling growth in *Arabidopsis* mutants lacking the glyoxylate cycle enzyme malate synthase. *J. Biol. Chem.* 279, 42916–42923. doi: 10.1074/jbc.M407380200

Cosgrove, D. J. (2018). Nanoscale structure, mechanics and growth of epidermal cell walls. *Curr. Opin. Plant Biol.* 46, 77–86.

Cosgrove, D. J., and Anderson, C. T. (2020). Plant cell growth: do pectins drive lobe formation in *Arabidopsis* pavement cells? *Curr. Biol.* 30, R660–R662. doi: 10.1016/j.cub.2020.04.007

Dennis, D. T., Huang, Y., and Negm, F. B. (1997). "Glycolysis, the pentose phosphate pathway and anaerobic respiration," in *Plant Metabolism*, eds D. T. Dennis, D. H. Turpin, D. D. Lefebvre, and D. B. Layzell (Harlow: Longman), 105–123.

Drozdowicz, Y. M., and Rea, P. A. (2001). Vacuolar H^+ pyrophosphatases: from the evolutionary backwaters into the mainstream. *Trends Plant Sci.* 6, 206–211. doi: 10.1016/s1360-1385(01)01923-9

Eastmond, P. J., Astley, H. M., Parsley, K., Aubry, S., Williams, B. P., Menard, G. N., et al. (2015). *Arabidopsis* uses two gluconeogenic gateways for organic acids to fuel seedling establishment. *Nat. Commun.* 6:6659. doi: 10.1038/ncomms7659

Eastmond, P. J., Germain, V., Lange, P. R., Bryce, J. H., Smith, S. M., and Graham, I. A. (2000). Postgerminative growth and lipid catabolism in oilseeds lacking the glyoxylate cycle. *Proc. Natl. Acad. Sci. U.S.A.* 97, 5669–5674. doi: 10.1073/pnas.97.10.5669

Ferjani, A., Horiguchi, G., and Tsukaya, H. (2010). Organ size control in Arabidopsis: Insights from compensation studies. *Plant Morphol.* 22, 65–71.

Ferjani, A., Horiguchi, G., Yano, S., and Tsukaya, H. (2007). Analysis of leaf development in fugu mutants of *Arabidopsis* reveals three compensation modes that modulate cell expansion in determinate organs. *Plant Physiol.* 144, 988–999. doi: 10.1104/pp.107.099325

Ferjani, A., Ishikawa, K., Asaoka, M., Ishida, M., Horiguchi, G., Maeshima, M., et al. (2013a). Enhanced cell expansion in a KRP2 overexpressor is mediated by increased V-ATPase activity. *Plant Cell Physiol.* 54, 1989–1998. doi: 10.1093/pcp/pct138

Ferjani, A., Ishikawa, K., Asaoka, M., Ishida, M., Horiguchi, G., Maeshima, M., et al. (2013b). Class III compensation, represented by KRP2 overexpression, depends on V-ATPase activity in proliferative cells. *Plant Signal. Behav.* 8:e27204. doi: 10.4161/psb.27204

Ferjani, A., Kawade, K., Asaoka, M., Oikawa, A., Okada, T., Mochizuki, A., et al. (2018). Pyrophosphate inhibits gluconeogenesis by restricting UDP-glucose formation in vivo. *Sci. Rep.* 8:14696.

Ferjani, A., Segami, S., Asaoka, M., and Maeshima, M. (2014a). "Regulation of PPi levels through the vacuolar membrane H^+-pyrophosphatase," in *Progress in Botany*, Vol. 75, eds U. Lüttge, W. Beyschlag, and J. Cushman (Berlin: Springer-Verlag), 145–165.

Ferjani, A., Segami, S., Horiguchi, G., Muto, Y., Maeshima, M., and Tsukaya, H. (2014b). Roles of the vacuolar H^+-PPase in seed storage oil mobilization and plant development. *Plant Morphol.* 26, 45–51.

Ferjani, A., Segami, S., Horiguchi, G., Muto, Y., Maeshima, M., and Tsukaya, H. (2011). Keep an eye on PPi: the vacuolar-type H^+-pyrophosphatase regulates postgerminative development in *Arabidopsis*. *Plant Cell* 23, 2895–2908. doi: 10.1105/tpc.111.085415

Ferjani, A., Yano, S., Horiguchi, G., and Tsukaya, H. (2008). "Control of leaf morphogenesis by long- and short-distance signaling: differentiation of leaves into sun or shade types and compensated cell enlargement," in *Plant Cell Monographs: Plant Growth Signaling*, eds L. Bögre and G. T. S. Beemster (Berlin: Springer Berlin Heidelberg), 47–62.

Fu, Y., Gu, Y., Zheng, Z., Wasteneys, G., and Yang, Z. (2005). *Arabidopsis* interdigitating cell growth requires two antagonistic pathways with opposing action on cell morphogenesis. *Cell* 120, 687–700. doi: 10.1016/j.cell.2004.12.026

Fu, Y., Li, H., and Yang, Z. (2002). The ROP2 GTPase controls the formation of cortical fine F-actin and the early phase of directional cell expansion during Arabidopsis organogenesis. *Plant Cell* 14, 777–794. doi: 10.1105/tpc.001537

Fu, Y., Xu, T., Zhu, L., Wen, M., and Yang, Z. (2009). A ROP GTPase signaling pathway controls cortical microtubule ordering and cell expansion in *Arabidopsis*. *Curr. Biol.* 19, 1827–1832. doi: 10.1016/j.cub.2009.08.052

Fukuda, M., Segami, S., Tomoyama, T., Asaoka, M., Nakanishi, Y., Gunji, S., et al. (2016). Lack of H^+-pyrophosphatase prompts developmental damage in *Arabidopsis* leaves on ammonia-free culture medium. *Front. Plant Sci.* 7:819. doi: 10.3389/fpls.2016.00819

Gibeaut, D. M. (2000). Nucleotide sugars and glucosyltransferases for synthesis of cell wall matrix polysaccharides. *Plant Physiol. Biochem.* 38, 69–80.

Graham, I. A. (2008). Seed storage oil mobilization. *Annu. Rev. Plant Biol.* 59, 115–142.

Gunji, S., Oda, Y., Takigawa-Imamura, H., Tsukaya, H., and Ferjani, A. (2020). Excess pyrophosphate restrains pavement cell morphogenesis and alters organ flatness in *Arabidopsis thaliana*. *Front. Plant Sci.* 11:31. doi: 10.3389/fpls.2020.00031

Gutiérrez-Luna, F. M., Navarro de la Sancha, E., Valencia-Turcotte, L. G., Vázquez-Santana, S., and Rodríguez-Sotres, R. (2016). Evidence for a non-overlapping subcellular localization of the family I isoforms of soluble inorganic pyrophosphatase in *Arabidopsis thaliana*. *Plant Sci.* 253, 229–242. doi: 10.1016/j.plantsci.2016.10.005

Haas, K. T., Wightman, R., Meyerowitz, E. M., and Peaucelle, A. (2020). Pectin homogalacturonan nanofilament expansion drives morphogenesis in plant epidermal cells. *Science* 28, 1003–1007.

Hanchi, M., Thibaud, M. C., Légeret, B., Kuwata, K., Pochon, N., Beisson, F., et al. (2018). The phosphate fast-responsive genes PECP1 and PPsPase1 affect phosphocholine and phosphoethanolamine content. *Plant Physiol.* 176, 2943–2962. doi: 10.1104/pp.17.01246

Heinonen, J. K. (2001). *Biological Role of Inorganic Pyrophosphate*. Boston: Kluwer Academic Publishers.

Higaki, T., Kutsuna, N., Akita, K., Takigawa-Imamura, H., Yoshimura, K., and Miura, T. (2016). A theoretical model of jigsaw-puzzle pattern formation by plant leaf epidermal cells. *PLoS Comput. Biol.* 12:e1004833. doi: 10.1371/journal.pcbi.1004833

Horiguchi, G., Ferjani, A., Fujikura, U., and Tsukaya, H. (2006a). Coordination of cell proliferation and cell expansion in the control of leaf size in *Arabidopsis thaliana*. *J. Plant Res.* 119, 37–42. doi: 10.1007/s10265-005-0232-4

Horiguchi, G., Fujikura, U., Ferjani, A., Ishikawa, N., and Tsukaya, H. (2006b). Large-scale histological analysis of leaf mutants using two simple leaf observation methods: identification of novel genetic pathways governing the size and shape of leaves. *Plant J.* 48, 638–644. doi: 10.1111/j.1365-313X.2006.02896.x

Horiguchi, G., Kim, G. T., and Tsukaya, H. (2005). The transcription factor AtGRF5 and the transcription coactivator AN3 regulate cell proliferation in leaf primordia of *Arabidopsis thaliana*. *Plant J.* 43, 68–78. doi: 10.1111/j.1365-313X.2005.02429.x

Johansson, H., Sterky, F., Amini, B., Lundeberg, J., and Kleczkowski, L. A. (2002). Molecular cloning and characterization of a cDNA encoding poplar UDP-glucose dehydrogenase, a key gene of hemicellulose/pectin formation. *Biochim. Biophys. Acta* 1576, 53–58. doi: 10.1016/s0167-4781(02)00292-0

Josse, E. M., and Halliday, K. J. (2008). Skotomorphogenesis: the dark side of light signalling. *Curr. Biol.* 18, R1144–R1146. doi: 10.1016/j.cub.2008.10.034

Katano, M., Takahashi, K., Hirano, T., Kazama, Y., Abe, T., Tsukaya, H., et al. (2016). Suppressor screen and phenotype analyses revealed an emerging role of the monofunctional peroxisomal enoyl-CoA hydratase 2 in compensated cell enlargement. *Front. Plant Sci.* 7:132. doi: 10.3389/fpls.2016.00132

Kawade, K., Horiguchi, G., Usami, T., Hirai, M. Y., and Tsukaya, H. (2013). ANGUSTIFOLIA3 signaling coordinates proliferation between clonally distinct cells in leaves. *Curr. Biol.* 23, 788–792. doi: 10.1016/j.cub.2013.03.044

Kleczkowski, L. A. (1994). Glucose activation and metabolism through UDP-glucose pyrophosphorylase in plants. *Phytochemistry* 37, 1507–1515.

Ko, K. M., Lee, W., Yu, J. R., and Ahnn, J. (2007). PYP-1, inorganic pyrophosphatase, is required for larval development and intestinal function in *C. elegans*. *FEBS Lett.* 581, 5445–5453. doi: 10.1016/j.febslet.2007.10.047

Kolde, O. (2019). *pheatmap: Pretty Heatmaps. R Package Version 1.0.12.*

Kriegel, A., Andrés, Z., Medzihradszky, A., Krüger, F., Scholl, S., Delang, S., et al. (2015). Job sharing in the endomembrane system: vacuolar acidification requires the combined activity of V-ATPase and V-PPase. *Plant Cell* 27, 3383–3396. doi: 10.1105/tpc.15.00733

Kürschner, W. M. (1997). The anatomical diversity of recent and fossil leaves of the durmast oak (*Quercus petraea* Lieblein/*Q. pseudocastanea* Goeppert) – implications for their use as biosensors of palaeoatmospheric CO2 levels. *Rev. Palaeobot. Palynol.* 96, 1–30.

Lin, D., Cao, L., Zhou, Z., Zhu, L., Ehrhardt, D., Yang, Z., et al. (2013). Rho GTPase signaling activates microtubule severing to promote microtubule ordering in *Arabidopsis*. *Curr. Biol.* 23, 290–297. doi: 10.1016/j.cub.2013.01.022

Liu, S., Jobert, F., Rahneshan, Z., Doyle, S. M., and Robert, S. (2021). Solving the puzzle of shape regulation in plant epidermal pavement cells. *Annu. Rev. Plant Biol.* 17, 525–550. doi: 10.1146/annurev-arplant-080720-081920

Lundin, M., Baltscheffsky, H., and Ronne, H. (1991). Yeast PPA2 gene encodes a mitochondrial inorganic pyrophosphatase that is essential for mitochondrial function. *J. Biol. Chem.* 266, 12168–12172.

Maeda, S., Gunji, S., Hanai, K., Hirano, T., Kazama, Y., Ohbayashi, I., et al. (2014). The conflict between cell proliferation and expansion primarily affects stem organogenesis in *Arabidopsis*. *Plant Cell Physiol.* 55, 1994–2007. doi: 10.1093/pcp/pcu131

Maeshima, M. (2000). Vacuolar H^+-pyrophosphatase. *Biochim. Biophys. Acta* 1465, 37–51.

Majda, M., Grones, P., Sintorn, I. M., Vain, T., Milani, P., Krupinski, P., et al. (2017). Mechanochemical polarization of contiguous cell walls shapes plant pavement cells. *Dev. Cell* 43, 290–304. doi: 10.1016/j.devcel.2017.10.017

Murashige, T., and Skoog, F. (1962). A revised medium for rapid growth and bioassays with tobacco tissue cultures. *Physiol. Plant* 15, 473–497.

Nakagawa, T., Nakamura, S., Tanaka, K., Kawamukai, M., Suzuki, T., Nakamura, K., et al. (2008). Development of R4 gateway binary vectors (R4pGWB) enabling high-throughput promoter swapping for plant research. *Biosci. Biotechnol. Biochem.* 72, 624–629. doi: 10.1271/bbb.70678

Nakayama, H., Koga, H., Long, Y., Hamant, O., and Ferjani, A. (2022). Looking beyond the gene network - metabolic and mechanical cell drivers of leaf morphogenesis. *J. Cell Sci.* 135:jcs259611. doi: 10.1242/jcs.259611

Oikawa, A., Otsuka, T., Jikumaru, Y., Yamaguchi, S., Matsuda, F., Nakabayashi, R., et al. (2011a). Effects of freeze-drying of samples on metabolite levels in metabolome analyses. *J. Sep. Sci.* 34, 3561–3567.

Oikawa, A., Fujita, N., Horie, R., Saito, K., and Tawaraya, K. (2011b). Solid-phase extraction for metabolomics analysis of high-salinity samples by capillary electrophoresis-mass spectrometry. *J. Sep. Sci.* 34, 1063–1068. doi: 10.1002/jssc.201000890

Onoda, Y., Schieving, F., and Anten, N. P. R. (2015). A novel method of measuring leaf epidermis and mesophyll stiffness shows the ubiquitous nature of the sandwich structure of leaf laminas in broad-leaved angiosperm species. *J. Exp. Bot.* 66, 2487–2499. doi: 10.1093/jxb/erv024

Öztürk, Z. N., Greiner, S., and Rausch, T. (2014). Subcellular localization and developmental regulation of cytosolic: soluble pyrophosphatase isoforms in *Arabidopsis thaliana*. *Turk. J. Bot.* 38, 1036–1049.

Pang, Z., Chong, J., Zhou, G., de Lima Morais, D. A., Chang, L., Barrette, M., et al. (2021). MetaboAnalyst 5.0: narrowing the gap between raw spectra and functional insights. *Nucleic Acids Res.* 49, W388–W396. doi: 10.1093/nar/gkab382

Parsley, K., and Hibberd, J. M. (2006). The *Arabidopsis* PPDK gene is transcribed from two promoters to produce differentially expressed transcripts responsible for cytosolic and plastidic proteins. *Plant Mol. Biol.* 62, 339–349. doi: 10.1007/s11103-006-9023-0

Penfield, S., Rylott, E. L., Gilday, A. D., Graham, S., Larson, T. R., and Graham, I. A. (2004). Reserve mobilization in the Arabidopsis endosperm fuels a hypocotyl elongation in the dark, is independent of abscisic acid, and requires *PHOSPHOENOLPYRUVATE CARBOXYKINASE1*. *Plant Cell* 16, 2705–2718. doi: 10.1105/tpc.104.024711

R Core Team (2018). *R: A Language and Environment for Statistical Computing*. Vienna: R Foundation for Statistical Computing.

R Core Team (2020). *R: A Language and Environment for Statistical Computing*. Vienna: R Foundation for Statistical Computing.

Rea, P. A., Kim, Y., Sarafian, V., Poole, R. J., Davies, J. M., and Sanders, D. (1992). Vacuolar H^+-translocating pyrophosphatases: a new category of ion translocase. *Trends Biochem. Sci.* 17, 348–353. doi: 10.1016/0968-0004(92)90313-x

Rea, P. A., and Poole, R. J. (1985). Proton-translocating inorganic pyrophosphatase in red beet (*Beta vulgaris* L.) tonoplast vesicles. *Plant Physiol.* 77, 46–52. doi: 10.1104/pp.77.1.46

Rea, P. A., and Poole, R. J. (1993). Vacuolar H^+-translocating pyrophosphatase. *Annu. Rev. Plant Physiol. Plant Mol. Biol.* 44, 157–180.

Sampathkumar, A., Krupinski, P., Wightman, R., Milani, P., Berquand, A., Boudaoud, A., et al. (2014). Subcellular and supracellular mechanical stress prescribes cytoskeleton behavior in *Arabidopsis* cotyledon pavement cells. *eLife* 3:e01967. doi: 10.7554/eLife.01967

Sapala, A., Runions, A., Routier-Kierzkowska, A. L., Das Gupta, M., Hong, L., Hofhuis, H., et al. (2018). Why plants make puzzle cells, and how their shape emerges. *eLife* 27:e32794. doi: 10.7554/eLife.32794

Sarafian, V., Kim, Y., Poole, R. J., and Rea, P. A. (1992). Molecular cloning and sequence of cDNA encoding the pyrophosphate-energized vacuolar membrane proton pump of *Arabidopsis thaliana*. *Proc. Natl. Acad. Sci. U.S.A.* 89, 1775–1779. doi: 10.1073/pnas.89.5.1775

Schilling, R. K., Tester, M., Marschner, P., Plett, D. C., and Roy, S. J. (2017). AVP1: one protein, many roles. *Trends Plant Sci.* 22, 154–162. doi: 10.1016/j.tplants.2016.11.012

Schulze, S., Mant, A., Kossmann, J., and Lloyd, J. R. (2004). Identification of an *Arabidopsis* inorganic pyrophosphatase capable of being imported into chloroplasts. *FEBS Lett.* 565, 101–105. doi: 10.1016/j.febslet.2004.03.080

Segami, S., Makino, S., Miyake, A., Asaoka, M., and Maeshima, M. (2014). Dynamics of vacuoles and H^+-pyrophosphatase visualized by monomeric green fluorescent protein in *Arabidopsis*: artifactual bulbs and native intravacuolar spherical structures. *Plant Cell* 26, 3416–3434. doi: 10.1105/tpc.114.127571

Segami, S., Tomoyama, T., Sakamoto, S., Gunji, S., Fukuda, M., Kinoshita, S., et al. (2018). Vacuolar H^+-pyrophosphatase and cytosolic soluble pyrophosphatases cooperatively regulate pyrophosphate levels in *Arabidopsis thaliana*. *Plant Cell* 30, 1040–1061. doi: 10.1105/tpc.17.00911

Stitt, M. (1990). Fructose-2,6-bisphosphate as a regulatory molecule in plants. *Annu. Rev. Plant Physiol. Plant Mol. Biol.* 41, 153–185.

Stitt, M. (1998). Pyrophosphate as an energy donor in the cytosol of plant cells: an enigmatic alternative to ATP. *Bot. Acta* 111, 167–175.

Sugimoto, M., Wong, D. T., Hirayama, A., Soga, T., and Tomita, M. (2010). Capillary electrophoresis mass spectrometry-based saliva metabolomics identified oral, breast and pancreatic cancer-specific profiles. *Metabolomics* 6, 78–95. doi: 10.1007/s11306-009-0178-y

Tabeta, H., Watanabe, S., Fukuda, K., Gunji, S., Asaoka, M., Hirai, M. Y., et al. (2021). An auxin signaling network translates low-sugar-state input into compensated cell enlargement in the *fugu5* cotyledon. *PLoS Genet.* 17:e1009674. doi: 10.1371/journal.pgen.1009674

Takahashi, K., Morimoto, R., Tabeta, H., Asaoka, M., Ishida, M., Maeshima, M., et al. (2017). Compensated cell enlargement in fugu5 is specifically triggered by lowered sucrose production from seed storage lipids. *Plant Cell Physiol.* 58, 668–678. doi: 10.1093/pcp/pcx021

Thomas, P. W., Woodward, F. I., and Quick, W. P. (2003). Systematic irradiance signalling in tobacco. *New Phytol.* 161, 193–198. doi: 10.1016/s1360-1385(01)02103-3

Trinh, D.-C., Alonso-Serra, J., Asaoka, M., Colin, L., Cortes, M., Malivert, A., et al. (2021). How mechanical forces shape plant organs. *Curr. Biol.* 31, R143–R159.

Tsuge, T., Tsukaya, H., and Uchimiya, H. (1996). Two independent and polarized processes of cell elongation regulate leaf blade expansion in *Arabidopsis thaliana* (L.) Heynh. *Development* 122, 1589–1600. doi: 10.1242/dev.122.5.1589

Tsukaya, H. (2002). Interpretation of mutants in leaf morphology: genetic evidence for a compensatory system in leaf morphogenesis that provides a new link between cell and organismal theories. *Int. Rev. Cytol.* 217, 1–39. doi: 10.1016/s0074-7696(02)17011-2

Tsukaya, H. (2008). Controlling size in multicellular organs: focus on the leaf. *PLoS Biol.* 6:e174. doi: 10.1371/journal.pbio.0060174

Verger, S., Long, Y., Boudaoud, A., and Hamant, O. (2018). A tension-adhesion feedback loop in plant epidermis. *eLife* 7:e34460.

Wang, X., Wang, H., Liu, S., Ferjani, A., Li, J., Yan, J., et al. (2016). Genetic variation in ZmVPP1 contributes to drought tolerance in maize seedlings. *Nat. Genet.* 48, 1233–1241. doi: 10.1038/ng.3636

Winter, H., and Huber, S. C. (2000). Regulation of sucrose metabolism in higher plants. Localization and regulation of activity of key enzymes. *Crit. Rev. Plant Sci.* 19, 31–67.

Xu, T., Wen, M., Nagawa, S., Fu, Y., Chen, J. G., Wu, M. J., et al. (2010). Cell surface- and rho GTPase-based auxin signaling controls cellular interdigitation in *Arabidopsis*. *Cell* 143, 99–110. doi: 10.1016/j.cell.2010.09.003

Zhang, C., Halsey, L. E., and Szymanski, D. B. (2011). The development and geometry of shape change in *Arabidopsis thaliana* cotyledon pavement cells. *BMC Plant Biol.* 11:27. doi: 10.1186/1471-2229-11-27

Zhao, F., Du, F., Oliveri, H., Zhou, L., Ali, O., Chen, W., et al. (2020). Microtubule-mediated wall anisotropy contributes to leaf blade flattening. *Curr. Biol.* 30, 3972–3985. doi: 10.1016/j.cub.2020.07.076

frontiers | Frontiers in Plant Science

TYPE Original Research
PUBLISHED 13 September 2022
DOI 10.3389/fpls.2022.1006735

OPEN ACCESS

EDITED BY
Binglian Zheng,
Fudan University, China

REVIEWED BY
Duarte D. Figueiredo,
Max Planck Institute of Molecular Plant Physiology, Germany
Caiji Gao,
South China Normal University, China

*CORRESPONDENCE
Wen-Hui Lin
whlin@sjtu.edu.cn

†These authors have contributed equally to this work and share first authorship

SPECIALTY SECTION
This article was submitted to Plant Physiology, a section of the journal Frontiers in Plant Science

RECEIVED 29 July 2022
ACCEPTED 26 August 2022
PUBLISHED 13 September 2022

CITATION
Jiang Y-T, Zheng J-X, Li R-H, Wang Y-C, Shi J, Ferjani A and Lin W-H (2022) Tonoplast proton pumps regulate nuclear spacing of female gametophytes *via* mediating polar auxin transport in *Arabidopsis*. *Front. Plant Sci.* 13:1006735. doi: 10.3389/fpls.2022.1006735

Tonoplast proton pumps regulate nuclear spacing of female gametophytes *via* mediating polar auxin transport in *Arabidopsis*

Yu-Tong Jiang[1†], Ji-Xuan Zheng[2†], Rong-Han Li[2], Yu-Chen Wang[2], Jianxin Shi[1], Ali Ferjani[3] and Wen-Hui Lin[1,4*]

[1]Laboratory of Metabolic and Developmental Sciences, School of Life Sciences and Biotechnology, The Joint International Research, Shanghai Jiao Tong University, Shanghai, China, [2]Zhiyuan College, Shanghai Jiao Tong University, Shanghai, China, [3]Department of Biology, Tokyo Gakugei University, Koganei, Japan, [4]Shanghai Collaborative Innovation Center of Agri-Seeds/Joint Center for Single Cell Biology, Shanghai Jiao Tong University, Shanghai, China

The vacuole is an important organelle with multiple functions in plants, and the tonoplast that wraps the vacuole also plays essential roles in intracellular trafficking and ion homeostasis. Previous studies found that tonoplast proton pumps regulate embryo development and morphogenesis through their effects on vacuole biogenesis and distribution, as well as polar auxin transport and concomitant auxin gradient. However, the precise roles of the tonoplast proton pumps in gametophyte development remain unclear. Here we demonstrated that the lack of two types of tonoplast proton pumps or the absence of V-ATPase alone leads to abnormal development and nuclear localization of female gametophyte (FG), and slowed endosperm nuclei division after fertilization of the central cell. We further revealed that V-ATPase regulates auxin levels in ovules through coordinating the content and localization of PIN-FORMED 1 (PIN1) protein, hence influencing nuclear spacing between centra cell and egg cell, and subsequent endosperm development. Collectively, our findings revealed a crucial role of V-ATPase in auxin-mediated FG development in *Arabidopsis* and expanded our understanding of the functions of tonoplast proton pumps in seed plants reproductive development.

KEYWORDS

plant vacuole, V-ATPase, female gametophyte, egg cell, central cell, endosperm

Introduction

The vacuole, as an organelle with a single membrane, forms compartments and is a sophisticated endomembrane system unique to plant cells (Marty, 1999). As an important barrier for material exchange into and out of the vacuole, the vacuolar membrane, also referred to as tonoplast, harbors a rich variety of transporters, among which the tonoplast proton pumps are the most fundamental proteins. There are two distinct proton pumps, namely the vacuolar H^+-pyrophosphatase (V-PPase, EC 3.6.1.1) and the vacuolar H^+-ATPase (V-ATPase, EC 3.6.4.10) (Hedrich et al., 1989), that have been reported in the literature, both exhibit completely different structural and functional properties. The V-PPase and V-ATPase catalyze the hydrolysis of Mg^{2+}-PPi and Mg^{2+}-ATP complex, respectively, and extract energy for pumping H^+ ions into the vacuolar lumen, thus maintaining a proton gradient (ΔpH) across the tonoplast (Maeshima, 2000; Martinoia et al., 2007).

Whereas V-PPase has a relatively simple structure and is encoded by *AVP1/FUGU5* in *Arabidopsis thaliana* (*Arabidopsis* hereafter) (Ferjani et al., 2011; Kriegel et al., 2015; Jiang et al., 2020), the V-ATPase is a versatile protein complex that broadly occurs in all cell types (Marshansky and Futai, 2008). It exhibits a unique differential targeting on endomembrane compartments, which is mediated by different isoforms of its subunit a (Lupanga et al., 2020). In *Arabidopsis*, V-ATPase complex containing VHA-a2 or VHA-a3 is localized at the tonoplast (Krebs et al., 2010; Jiang et al., 2020). According to previous studies, *fugu5-1*, a point mutation line of AVP1, lacks V-PPase activity and exhibits basically the same growth conditions as wild type (Kriegel et al., 2015; Jiang et al., 2020); *vha2* (*vha-a2 vha-a3*), T-DNA insertion line of VHA-a2 and VHA-a3, lacks V-ATPase activity at the tonoplast and exhibits overall impaired growth phenotypes (Krebs et al., 2010); and *fap3,* the triple mutant obtained by crossing *fugu5-1* with *vha2*, lacks both V-PPase and V-ATPase functions, and displays a hindered vegetative growth and an aberrant cotyledon boundary during embryogenesis due to blocked PIN-FORMED (PIN)1-mediated auxin transport (Kriegel et al., 2015; Jiang et al., 2020). Tonoplast proton pumps regulate embryo development through PIN1-mediated auxin transportation. However, tracking back along the reproductive developmental process, gametophyte development of plants lacking both tonoplast proton pumps remained poorly understood.

During the reproductive growth of angiosperms, male gametophytes are always produced in great redundancy, while female gametophytes (FGs) are produced in less abundance due to evolutionary specialization. Thus, FG development is indispensable for the generational alternation in higher plants. In most angiosperms with polygonum-type FGs, megaspore mother cell (MMC) undergoes meiosis to produce four megaspores and one of them becomes the functional megaspore, which gives rise to an FG. The development process of FGs can be divided into 8 stages from FG1 to FG8 (Christensen et al., 1997). At FG6 stage, with the fusion of polar nuclei, a fixed pattern of seven cells is formed: an egg cell and two synergid cells at the micropylar end, a central cell in the central area, and three antipodal cells at the chalazal end (Yang et al., 2010). The development of FGs determines the portion of fertile embryos and the number of seeds produced. Besides, FGs also influence many aspects of plant reproduction, including male-female crosstalk and maternal effects on seed development, highlighting the significance of untangling its developmental regulatory network.

Plant hormones, such as brassinosteroids (BRs), gibberellin (GA), cytokinin (CK), and auxin have been shown to play essential roles in FGs development (Pérez-España et al., 2011; Yuan et al., 2016; Gomez et al., 2020). BR, CK, and GA generally contribute indirectly to FG development through their effects on specific proteins that manipulate auxin levels among embryo sacs and change the FG fate (Pagnussat et al., 2009; Luca et al., 2013; Panoli et al., 2015). Auxin, due to its ubiquitous distribution and long-range mobility, has a crucial direct impact on FG development; as a signal molecule, auxin synthesis, transport, and dynamic concentration gradient are deeply involved in the whole process of female reproductive growth (Serbes et al., 2019). It is reported that auxin also acts as a positional cue for cell fate determination, and that the accurate positioning of FG nuclei is important for their identity (Sun et al., 2021). The build-up of auxin gradient relies on polar auxin transportation (PAT) through various organelles and the endomembrane transport system. Previously, we showed that tonoplast proton pumps regulate the intracellular trafficking of PIN1 protein, hence influencing auxin homeostasis during embryonic development in *Arabidopsis* (Jiang et al., 2020). Whether tonoplast proton pumps functions in FGs development, however, remains to be explored.

In this work, to fill knowledge gap about the precise function of tonoplast proton pumps in *Arabidopsis* FGs development, we conducted a multiscale phenotypic analysis of mutants lacking both V-PPase and V-ATPase activity, and found that these mutants exhibit an abnormal nuclear-spacing between FG nucleus and delayed endosperm division. We are also proposing a working model linking tonoplast proton pumps and PAT in FGs developmental process. Our results provide novel insights into roles of tonoplast proton pumps in the reproductive developmental process.

Abbreviations: DAG, days after seed germination; HAP, Hours after pollination; V-PPase, H^+-translocating pyrophosphatase; V-ATPase, vacuolar H^+-ATPase; PIC, picloram; MMC, megaspore mother cell; FM, functional megaspore.

Materials and methods

Plant material and growth conditions

All materials used in this study were generated in *Arabidopsis* ecotype Columbia 0 (Col-0) background. Seeds were soaked with sterile water for 1 min, surface sterilized with a 3% NaClO solution for 5 min, then rinsed 5 times in sterile distilled water. Sterile seeds were grown on agar plates containing 1/2 Murashige and Skoog (MS) medium [2.215 g L^{-1}, 0.75% agar (w/v), 1.5% sucrose (w/v), pH = 5.75]. Plates were incubated in the dark at 4°C for 2 days and cultured in a growth chamber with a photoperiod of 16 h/8 h, light/dark cycling, and a temperature of 22 ± 1°C. After 7 days, the plants on the dishes were transferred to a mixture of soil:vermiculite:perlite (10:10:1). In this paper, to make the mutant *vha2* grow better during vegetative stages, both *vha2* and its contemporaneous control plants were grown under 24-h long-day light.

Identification of the T-DNA insertion lines and construction of transgenic plants

For mutants of tonoplast proton pumps used in this study, *vha2* [crossing *vha-a2* (SALK_142642) with *vha-a3* (SALK_029786) from Salk Institute for Biological Studies] and *fap3* [obtained by crossing *fugu5-1* with *vha2*] were both described in detail in our previous work, as well as *ProPIN1:PIN1-YFP* and R2D2 marker line (Jiang et al., 2020; Yu et al., 2020). For quantification of fluorescent signals of R2D2, we used the DII-Venus relative to mDII-ntdTomato for the semi-quantitative analysis of auxin level in plants, which is represented by DII/mDII (Benková et al., 2003; Liao et al., 2015). The construction of *ProES1:H2B-GFP* were based on the previously published literature (Pagnussat et al., 2007). To generate the *ProVHA-a3:VHA-a3-GFP*, the promoter and genomic DNA sequences were amplified by PCR using genomic DNA of Col as templates, and then cloned into the pHB vectors (Biovector NTCC Inc.) digested by *Eco*RI and *Hin*dIII, respectively. The sequences of oligonucleotide primer sets used are listed in **Supplementary Table 1**.

RNA extraction and qRT-PCR assays

The materials used for total RNA extraction in this study were inflorescence apices of *Arabidopsis*, which were harvested with tweezers and quick-frozen in liquid nitrogen. Subsequent RNA extraction and reverse transcription were performed using the RNAprep Pure Plant Kit (TIANGEN) and ReverAid First Strand cDNA Synthesis Kit (Thermo Fisher Scientific) following the manufacturers' protocols. qRT-PCR assays were conducted for three technical replicates of three biological replicates, and the results are shown as the mean ± standard deviations. The details were carried out as described previously (Zhang et al., 2016). The sequences of oligonucleotide primer sets used are listed in **Supplementary Table 1**.

In vitro treatment assays

To analyze the development status of FG in different stages upon 1-naphthylacetic acid (NAA; Sigma-Aldrich 317918) and picloram (Sigma-Aldrich 1918021), vigorously growing inflorescence apices were used as experimental materials. Floral buds larger than stage 10 were removed and the remaining inflorescences apices were immersed in 0.01% (v/v) Silwet L-77 solutions containing 1 μM NAA, or 1 μM picloram. After 24 h, wash the inflorescences apices with distilled water to remove residual agent. The materials were collected after 2 days.

Confocal microscopy

Confocal laser-scanning microscopy (CLSM) observation of male and FG was strictly performed as described previously (Christensen et al., 1997), but with the modification that we used the Upright Laser Confocal Microscope (Nikon & Nikon Ni-E A1 HD25). For the collection of male and FGs, we took the vigorously growing buds from outside to inside of inflorescence apices. For the analysis of flowers containing GFP constructs, we first carefully peeled the pistils from the flowers in different periods and fixed them in 4% paraformaldehyde for 30 min and then immersed in Clearsee agent according to Clearsee method (Kurihara et al., 2015). Cell walls were stained with 0.02% Fluorescent Brightener 28 (FB28) in Clearsee agent for over 3 h, as described in our previous study (Zu et al., 2022). Before observation, materials were soaked in Clearsee reagent to wash away the cell wall stain for more than half an hour. For the ovule wrapped inside the pistils, we tapped the corresponding position of the coverslip with the tip of the tweezers to exposed the ovule. For CLSM, GFP was excited with an argon laser at a wavelength of 488 nm, and emission was detected between 500 and 530 nm. FB28 was excited with an argon laser at a wavelength of 395 nm, and emission was detected between 450 and 480 nm. Measurements of nuclear spacing and fluorescence intensity were obtained using the Image J software.

Male gametophyte observation assays

Male gametophyte analyses, including Alexander staining, scanning electron microscopy (SEM), *in vitro* culture of pollen grains, DAPI staining of pollen grains and aniline blue staining of pollen tube were performed as described previously (Johnson-Brousseau and McCormick, 2004; Li et al., 2013).

Quantification and statistical analysis

Data analysis and statistical graphs were carried out using GraphPad Prism 8 and Microsoft Office Excel software. For comparison between two groups, Two-tailed Student's *t*-test was used, and for more than two groups, Duncan's test was used. The specific statistical methods for each assay are described in figure legends. Quantification of the phenotypes were performed using the ImageJ software.[1]

Accession numbers

Arabidopsis genes mentioned in this article are as follows: *AVP1/FUGU5*, AT1G15690; *VHA-a2*, AT2G21410; *VHA-a3*, AT4G39080; *PIN1*, AT1G73590; *PIN3*, AT1G70940; *PIN4*, AT2G01420; *ARF1*, AT1G59750; *ARF2*, AT5G62000; *ARF3*, AT2G33860; *ARF4*, AT5G60450; *ARF5*, AT1G19850; *YUC2*, AT4G13260; *YUC5*, AT5G43890; *YUC8*, AT4G28720; *YUC9*, AT1G04180.

Results

Vacuolar H^+-ATPase deficiency results in ovule and seed abortion

To explore the role of the tonoplast proton pumps in gametophyte development of *Arabidopsis*, we focused on the reproductive development of *fap3* mutant lacking both V-PPase and V-ATPase activities. Most of mature flowers at stage 13 (72%, 112/156) obviously had morphological abnormalities (**Supplementary Figure 1A**) and 97% (118/121) ovules of *fap3* were aborted before fertilization (**Supplementary Figure 1B**). Further examinations with Alexander staining, CLSM, and SEM on pollen grains revealed that 72% (64/89) pollen grains of *fap3* are not fertile due to defective pollen development (**Supplementary Figures 1C–E**), indicating that loss-of-function of both V-PPase and V-ATPase activities severely affects male gametophyte development as well. Based on CLSM observation and statistics, only 2% (3/121) FGs of *fap3* could develop normally, and the rest prematurely aborted (**Supplementary Figure 1F**), confirming the roles of both V-PPase and V-ATPase in FG development. Collectively, the above results indicated that the lack of two tonoplast proton pumps can have extremely serious consequences for the entire process of plant reproduction. Therefore, *fap3* is unlikely an ideal material for studying the role of tonoplast proton pumps in plant FG development. Since the overall plant growth, male and female transmission of *fugu5-1* are comparable to those of the wild type Col-0 (Jiang et al., 2020; **Supplementary Table 1**), we next focused our study on V-ATPase mutant *vha2*.

As mentioned above, while VHA-a1 mediates TGN/EE targeting of V-ATPase, VHA-a2 and VHA-a3 mediate V-ATPase's tonoplastic localization (Krebs et al., 2010; Kriegel et al., 2015; Luo et al., 2015; Lupanga et al., 2020). Therefore, *vha2* was used to investigate its specific role in plant gametophyte development. Considering that an extended illumination time can improve vegetative growth of *vha2* (Krebs et al., 2010), *vha2* mutants were grown under continuous light conditions, which greatly improved inflorescence growth to a level almost indistinguishable from Col-0 (**Supplementary Figure 2**) and eased our analyses. Interestingly, most flowers of *vha2* displayed normal morphologies, as only 17% (19/112) of them were abnormal (**Figure 1A**). Correspondingly, most siliques elongated normally and bore seeds, and only 14% (21/150) of them were obviously shorter (**Figure 1B** and **Supplementary Figure 2**). Consistently, *vha2* abnormal siliques had a higher ovule abortion rate and developed only few seeds (**Figures 1B,C**). As the stigma was morphologically defective (**Supplementary Figure 3A**), when abnormal *vha2* pistils were hand-pollinated with the Col-0 pollen, ovules could develop till the FG7 stage and remained unfertilized as examined at 48 h after pollination (HAP) (**Supplementary Figure 3B**). Hence, it appears that the premature abortion prior to fertilization could be derived from abnormal growth of the pollen tube on the defective stigma (**Supplementary Figure 3C**). Based on the above observations, morphologically normal *vha2* flowers were mainly used in our following experiments.

Next, we examined the male and female transmission of *vha-a2* and *vha-a3* and found that transmission of the *vha-a2* and *vha-a3* mutant alleles is comparable to *VHA-A2* and *VHA-A3* in WT alleles (**Figure 1D**). For a more rigorous follow-up study, we need to demonstrate that *VHA-a2* and *VHA-a3* are expressed during gametophyte development. So we examined V-ATPase expression by constructing a transgenic line for *VHA-a3*, the predominant form of the a subunit on the tonoplast, which is fully redundant with VHA-a2. Fluorescence images of a *ProVHA-a3: VHA-a3-GFP* transgenic line confirmed the expression of V-ATPase during the whole process of *Arabidopsis* gametophyte development and early embryo development as well (**Figures 2A–I**).

Loss of vacuolar H^+-ATPase activity affects pollen development

vha2 normal siliques wrapped normal ovules, but the ratio of seed abortion in *vha2* normal siliques was higher than that of Col-0 (**Figures 1B,C**). To gain insights into the seed abortion in *vha2* normal siliques, we further examined male and FG development in *vha2*. For male fertility, *in vitro* pollen germination combined with alexander staining,

1 http://rsbweb.nih.gov/ij/download.html

10.3389/fpls.2022.1006735

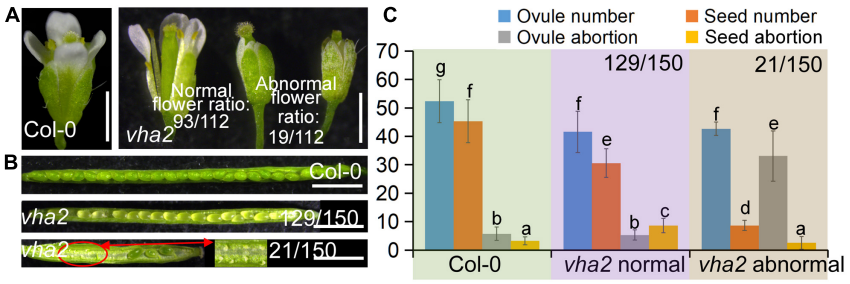

D

Parents	Genotype of Progenies								
	WT	*VHA-a2* *vha-a3/+*	*vha-a2/+* *VHA-a3*	*vha-a2/+* *vha-a3/+*	*vha-a2* *vha-a3/+*	*vha-a2/+* *vha-a3*	*vha-a2* *vha-a3*	Observed Ratio	Expected Ratio
♀ *vha-a2/+* *vha-a3/+* × ♂ **WT**	51	46	42	44	0	0	0	1:0.90 :0.82 :0.86[a]	1:1:1:1
♀ **WT** × ♂ *vha-a2/+* *vha-a3/+*	42	40	49	51	0	0	0	1:0.95 :1.17 :1.21[a]	1:1:1:1
♀ *vha-a2/+* *vha-a3/+* × ♂ *vha-a2/+* *vha-a3/+*	21	39	41	72	32	37	19	1:1.86 :1.95 :3.43 :1.52 :1.76 :0.90[b]	1:2:2 :4 :2:2:1

a Not significantly different from the expected segregation ratio 1:1:1:1 ($\chi 2$, $P > 0.05$).
b Not significantly different from the expected segregation ratio 1:2:2:4:2:2:1 ($\chi 2$, $P > 0.05$).

FIGURE 1
Lack of V-ATPase results in abnormal embryonic development. **(A)** Flower development at stage-13 in Col-0 and *vha2*. Statistics on the ratio of normal and abnormal microspores in *vha2* are shown in each image. Bar = 1 mm. **(B)** Seed development in Col-0 and *vha2*. Two types of siliques of *vha2* correspond to those in **(A)**. **(C)** Statistics analysis of ovule number, seed number, ovule abortion, and seed abortion in Col-0 and *vha2*. Bars represent the mean ± SD of three biological replicates (n =30). Lowercase letters indicate statistically significant differences between different stages ($P < 0.05$). Theoretically, ovule number = seed number + ovule abortion + seed abortion. **(D)** Both male and female transmission of *vha-a2*, and *vha-a3* are comparable to *VHA-a2* and *VHA-a3* of WT. Genotypes consistent with wild type are marked in red font, homozygous mutant genotypes are marked in blue font, and heterozygous mutant genotypes are marked in black font.

fluorescence microscopy and SEM were performed to examine the pollen viability. 77% (40/52) anthers from *vha2* were stained purplish red by Alexander dye that was consistent with Col-0 (Figure 3A), while only 23% (12/52) anthers showed light blue pollen coloration (Figure 3A), indicating that most pollen grains were vigorous. Further CLSM implied that pollen grains with large vacuoles in infertile anthers are arrested in pollen mitosis I (PMI) stage (Figure 3B). SEM images of *vha2* revealed that the majority of pollen grains (64%, 83/130) are oval-shaped similar to Col-0 (Figure 3C), and that the remaining portion of pollen grains are slightly wrinkled (Figure 3C). *In vitro* pollen germination demonstrated that there are no significant differences between *vha2* and Col-0 regarding pollen tube length and width (Figures 3D,E). Therefore, the slightly wrinkled pollens had similar fertility to Col-0 normal ones. Furthermore, DAPI staining further demonstrated that *vha2* mature pollen has a normal nuclear division (Figure 3F). The abovementioned results implied that even though a small portion of pollens are slightly wrinkled, the loss of V-ATPase function does not significantly affect pollen fertility.

When Col-0 and *vha2* pistils were pollinated with Col-0 and *vha2* pollen separately, most ovules in Col-0 and *vha2* pistils were targeted by the pollen tubes examined at 24 HAP (Figure 3G). This result indicated that *vha2* has a comparable pollen tube guidance and reception to that of the Col-0, therefore, we focused our study on the development of FGs to further explore the mechanism behind seed abortion in normal *vha2* siliques.

Vacuolar H^+-ATPase deficiency leads to aberrant nuclear spacing during female gametophyte development and affects endosperm nuclei division rate

To see if there are defects in *vha2* FGs, we examined *vha2* ovules at different developmental stages using CLSM. There was no detectable morphological difference between WT and *vha2* FGs until FG6 stage (Supplementary Figure 4 and Figure 4A). During the transition of late FG6 to early FG7, the distance between central cell and egg cell nuclei in more than half of *vha2* embryo sacs was remarkably larger than that of Col-0 (Figures 4A–C). In *Arabidopsis*, late FG6-to-FG7 transition is an important step for embryo sac cell-fate

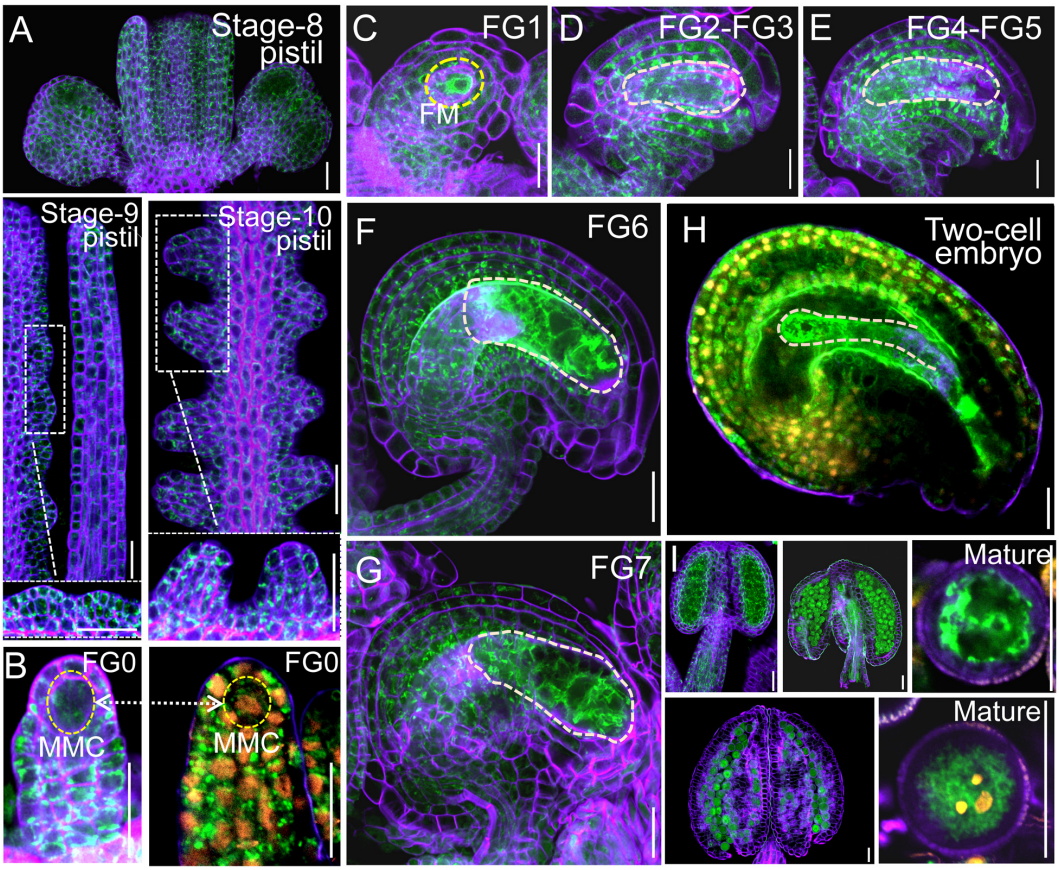

FIGURE 2
VHA-a3 is constitutively expressed in reproductive organs. Representative stage-8, stage-9, stage-10 pistil **(A)**, ovules during FG0 stage **(B)**, FG1 stage **(C)**, FG2-FG3 stage **(D)**, FG4-FG5 stage **(E)**, FG6 stage **(F)**, FG7 stage **(G)**, two-cell embryo **(H)**, anthers and mature pollen grain **(I)** from the *Pro VHA-a3: VHA-a3-GFP* plants. The nuclear staining with DAPI in FG0 stage **(B)** to demonstrate that MMC is present in this developmental stage. Yellow dotted circles in **(D–G)** indicate the embryo sac and in **(H)** indicate the two-cell embryo; Orange dots indicate the nucleus by DAPI staining of mature pollen grain. The purple part is the outline of pollen grains stained with FM4-64. Bars = 20 μm. MMC megaspore mother cell, FM functional megaspore.

decision and fertilization preparation. During this period, the pattern of eight nuclei and seven cells emerges, antipodal cells at chalaza end degenerates, and the distance between the central cell and egg cell nuclei is further shortened, preparing FGs for fertilization (Christensen et al., 1997; Sundaresan and Alandete-Saez, 2010).

Based on statistics of the distance in Col-0, we arbitrarily designated a distance less than 10 μm as normal spacing, and a distance larger than that as abnormal spacing, for convenient comparison and description. Under this criterion, the proportion of abnormal spacing in *vha2* was more than a half, while that in the wild type was about 10% (**Figures 4B,C**). Nuclear spacing abnormity was clearly associated with the failed movement of the central cell to the proper position at the micropyle end (**Figure 4D**). This increased nuclear spacing phenotype was also observed in abnormal embryo sacs in *fap3* (**Supplementary Figure 5**). Considering that *vha2* exhibited higher premature seed abortion rate compared with Col-0 (**Figure 1C**) and that the fusion of sperm and diploid central cell during double fertilization is essential for subsequent embryo, endosperm, and even seedling development (Portereiko et al., 2006; Wu et al., 2012), it is reasonable to assume that the distance between the nuclei of central cell and the egg cell that is affected by V-ATPase, may influence the fertilization process as well as the following division of endosperm nuclei.

To formally test this hypothesis, we compared the endosperm development of *vha2* to that of Col-0 at 18 HAP using CLSM. At 18 HAP, most egg cells and central cells were already fertilized, and endosperms consisted of four to eight nuclei in Col-0 (**Figures 5A,C**). In contrast, at the same stage, ∼80% egg cells and central cells remained unfertilized and ∼20% seeds had two endosperm nuclei in *vha2*. Until at 48 HAP, most *vha2* endosperms contained four to eight nuclei (**Figures 5B,C**),

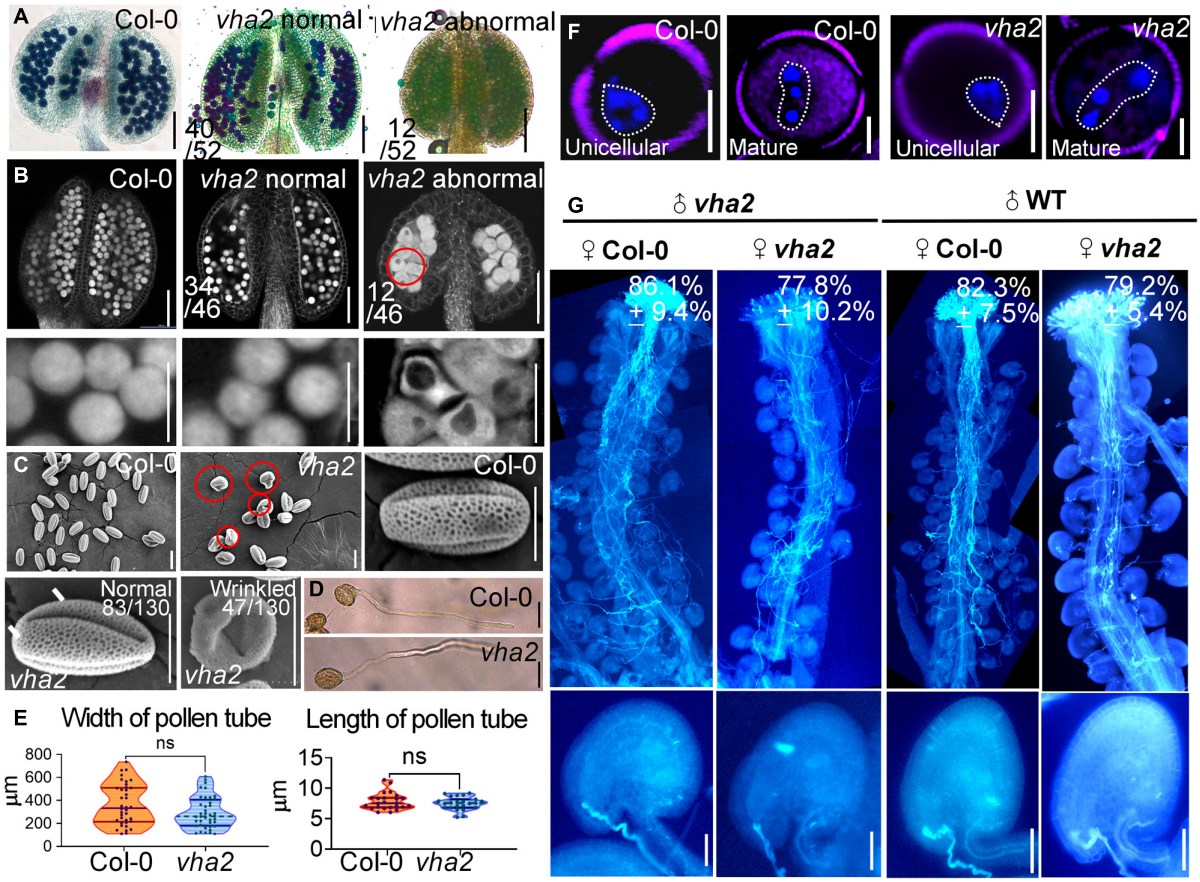

FIGURE 3
Lack of V-ATPase affects pollen development. **(A)** Alexander's staining of pollen from Col-0 and *vha2*. The purplish red color indicates viable pollen. Bar = 100 μm. **(B)** Anthers visualized by CLSM. Col-0 and *vha2* anthers at stage 12. Statistics on the ratio of normal and abnormal flowers in *vha2* are shown in each image. Scale bars represent 100 μm (main image) and 10 μm (partial enlargement). Red circle indicates the pollen grain that should have matured was stagnant at PMI stage with big vacuole. **(C)** SEMs observation on pollen grains from Col-0 and *vha2*. The scale bar is marked in each image. Bars = 10 μm. **(D)** A tetrad of mature pollen of Col-0 and *vha2* from in vitro pollen germination. Bars = 50 μm. **(E)** Quantitative analysis of pollen germination. Results shown are means ± standard errors (SE, *n* = 3). In total, 30 tetrads were examined for each genotype. **(F)** DAPI staining of unicellular and mature pollen grains from Col and *vha2*. The purple part is the outline of pollen grains stained with FM4-64. Bars = 5 μm. **(G)** Aniline blue staining of Col-0 and *vha2* pistils at 24 h after pollination (HAP) with Col-0 and *vha2* pollen. The whole pistil was overlaid by three overlapping images with Photoshop (Adobe). Numbers in **(G)** are quantification of targeted ovules out of total ovules. Results are means ± SD (*n* = 15). Bars = 20 μm.

while around 15% (23/158) nuclei of *vha2* endosperms did not divide, which was in line with the slightly increased ratio of seed abortion in *vha2* normal siliques (Figure 1C).

The above results indicated that V-ATPase deficiency leads to the increased nuclear spacing between the central and the egg cells in mature FGs, thus slowing down subsequent division of endosperm nuclei. These findings also demonstrated that nuclear spacing in mature FGs is essential for subsequent fertilization and seed development. Given that auxin acts as a positional cue for individual cell specification during FG6-to-FG7 stages (Sun et al., 2021), and that V-ATPase is a modulator of the polar transport and distribution of auxin in *Arabidopsis* embryos and seedlings (Jiang et al., 2020), we speculated that V-ATPase may affect *Arabidopsis* FG development *via* auxin-mediated functions.

Vacuolar H^+-ATPase regulates nuclear spacing between the egg and the central cells through PIN-FORMED 1-mediated auxin transport during female gametophyte development

At the late stages of FG development, auxin concentration in the embryo sac is relatively low and auxin transport in the sporophyte region surrounding the embryo sac mainly relies on the PIN1 protein (Luca et al., 2013; Panoli et al., 2015).

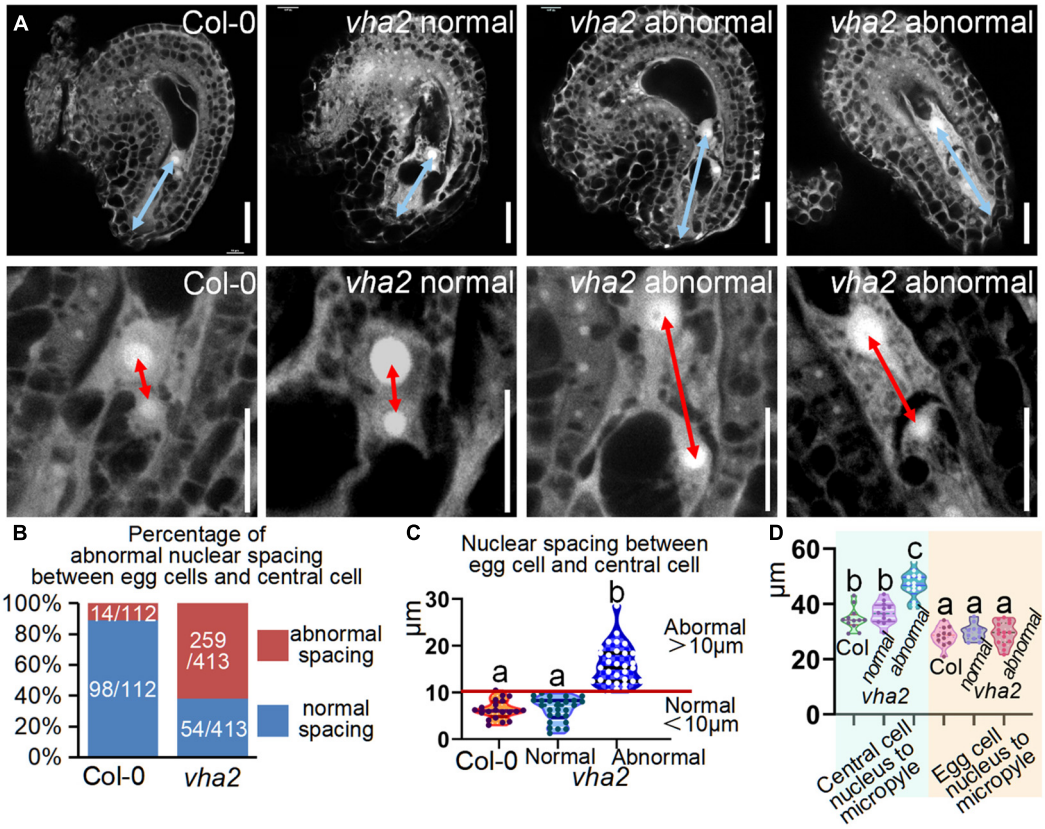

FIGURE 4
Lack of V-ATPase enlarges nuclear spacing of egg cells and central cells. **(A)** Embryo sac development of Col-0 and *vha2* at late-FG6 stage visualized by fluorescence microscopy. The picture below is an enlarged view of the nuclear spacing between the egg cell and central cell in the above image. The blue double arrows represent the distance from the central cell nucleus to the micropylar end, and the red double arrows in enlarged views represent nuclear spacing between egg cell and central cell. Bars = 20 μm. **(B)** Statistics analysis of the proportion of abnormal nuclear spacing between egg cell and central cell in Col-0 and *vha2*. The number of ovules counted and the actual ratio is marked in the image. **(C)** Statistics analysis of nuclear spacing between egg cell and central cell in Col-0 and *vha2*. Below the red line is defined as normal spacing if the nuclear spacing between egg cell and central cell is less than 10 μm, and it was considered abnormal spacing if spacing exceeds 10 μm. Lowercase letters indicate statistically significant differences between different stages ($P < 0.05$). 100 ovules shown in the statistical graph come from 20 different inflorescence apices. **(D)** Statistics analysis of the distance from the central cell nucleus or egg cell nucleus to the micropylar end in Col and *vha2*. Lowercase letters indicate statistically significant differences between different stages ($P < 0.05$). 30 ovules shown in the statistical graph come from 3 different inflorescence apices.

Since our previous studies found that tonoplast proton pumps activities affect auxin gradient by altering the expression level and polar localization of PIN1 during embryonic development (Jiang et al., 2020), we first quantified the expression level of *PIN1* gene as well as other genes associated with auxin biosynthesis and response in FGs, using qRT-PCR. We found that the expression level of *PIN* gene family members was generally lower in *vha2* inflorescence (**Figure 6A**), especially that of *PIN1*, so was the expression of genes associated with auxin biosynthesis and signaling (**Supplementary Figure 6**). This result indicated that the auxin concentrations in *vha2* inflorescence is generally low. We then detected fluorescent signals of PIN1-YFP in Col-0 and *vha2* ovules and found that, PIN1-YFP signal in *vha2* FG4 embryo sacs was indeed significantly weaker than that in Col-0 (**Figures 6B,C**). This reduced PIN1-YFP signal in *vha2* FG4 embryo sacs indicated that the transportation of auxin in ovules is impeded, and that the inferior auxin content in the *vha2* ovules might be a signal to affect the movement of the central cell to the proper position and increase the distance between the central cell and the egg cell.

To further validate our results, we treated Col-0 and *vha2* inflorescences *in vitro* with auxin analogs, picloram and NAA, respectively, and then examined the content of auxin using an auxin-level marker R2D2 (a semiquantitative and rapid auxin-input reporter with DII-Venus and mDII-tdTomato) after treatment, in which the absence of DII fluorescence marks auxin accumulation (Benková et al., 2003; Liao et al., 2015). Transport of picloram need the plasma membrane-bound carrier PIC30, rather than PIN family proteins that

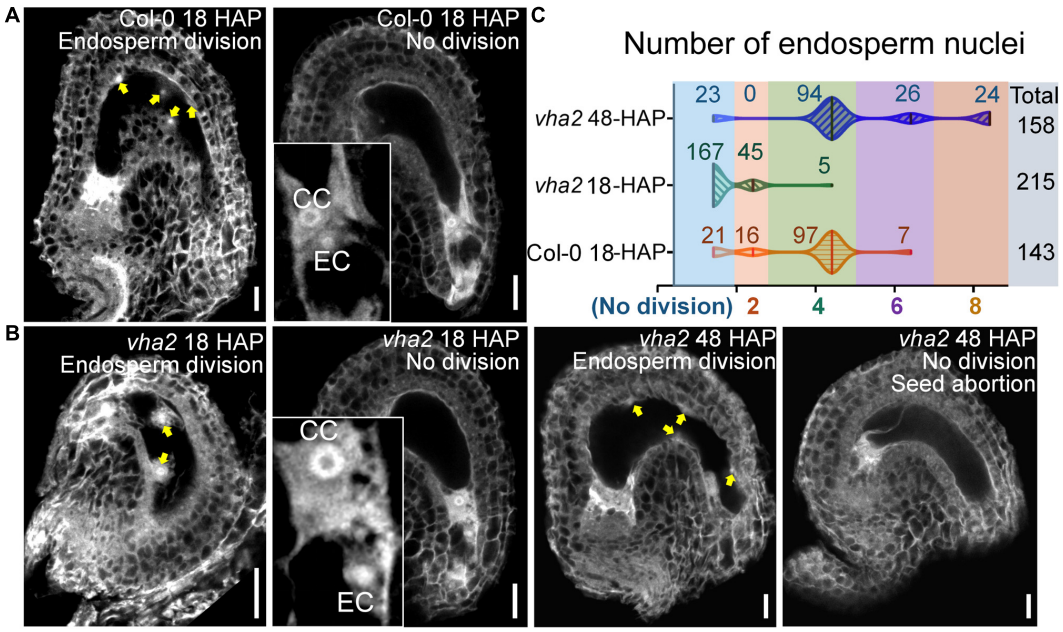

FIGURE 5
Lack of V-ATPase affects the division rate of endosperm nuclei. **(A)** Endosperm nuclei of Col-0 seeds at 18 h after pollination (HAP). **(B)** Endosperm nuclei of *vha2* seeds at 18 HAP and 48 HAP. Yellow arrows in **(A,B)** indicate the endosperm nuclei. EC egg cell, CC central cell, graphs represent typical phenotype of all samples. Bars = 20 μm. **(C)** Quantitative analysis of endosperm nuclei number in Col-0 and *vha2*. Seeds shown in the statistical graph come from 5 different inflorescence apices.

NAA transportations relies on. We found that the overall auxin level of *vha2* ovules along development is lower than that of Col-0 (Figures 6D,E). Auxin levels in *vha2* ovule were slightly and greatly restored by NAA or picloram treatment, respectively (Figures 6D,E). Notably, picloram treatment restored nuclear spacing in *vha2* embryo sacs to levels indistinguishable from Col-0 (Figures 7A,B), while NAA treatment hardly rescued the abnormal nuclear spacing albeit that a slight increase in normal proportions was observed (Figures 7A,B). These results indicated that, in *vha2*, PIN1 alone is not enough to transport sufficient NAA into ovules, resulting in the enlarged nuclear spacing. On the contrary, transportation of picloram does not require the participation of PIN1, so picloram could reach the ovules and to restore the abnormal nuclear distance between the egg cell and central cell.

In conclusion, V-ATPase regulates auxin levels in ovules through coordinating the content and localization of PIN-FORMED 1 (PIN1) protein, hence influencing nuclear spacing between centra cell and egg cell, and subsequent endosperm development (Figure 8).

Discussion

The life history of higher plants features an alternation between diploid sporophytes and haploid gametophytes. As model organism of angiosperms, *Arabidopsis* has been widely used to elucidate the underlying mechanisms of gametophyte developmental. In this study, we demonstrated that V-ATPase is essential for male and FG development, stigma patterning and early endosperm cell division. In this process, PIN1-mediated auxin transport is involved in the regulation of nuclear position downstream of the V-ATPase activity during FG development. These findings extend our understanding of the function of the tonoplast proton pump and auxin in the reproductive development of seed plants.

Vacuolar H^+-ATPase has multiple regulatory functions in male and female gametophytes and seed development

In this study, the triple mutant *fap3* lacking both tonoplast proton pumps was first used as the research material. Nevertheless, its severely impaired growth and uncompleted fertilizations in more than 90% gametophytes (Supplementary Figure 1) demonstrated that the lack of both tonoplast proton pumps severely affects the development of male and FGs, and that *fap3* is not suited to study the functions of the two tonoplast proton pumps during gametophyte development at the same time. Therefore, we

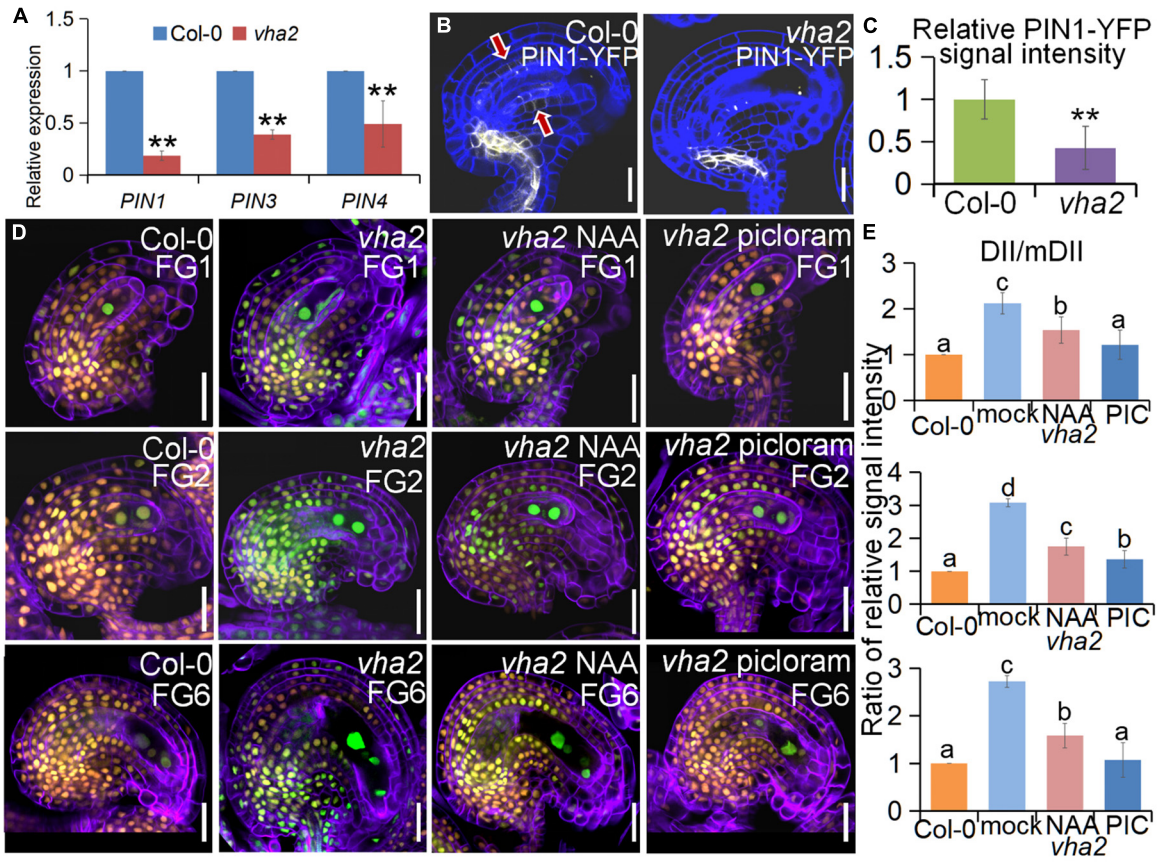

FIGURE 6
Lack of V-ATPase affects polar auxin transport and auxin distribution. **(A)** Relative transcript levels of *PIN1, PIN3,* and *PIN4* in inflorescence apices of Col-0 and *vha2*. Bars correspond to arithmetic means ± SE of three technical replicates of three biological replicates. Asterisks indicate significant difference (Studert's tw0-tailed *t*-test: $^{**}P < 0.01$). **(B)** PIN1-YFP express ion in Col-0 and *vha2* ovules. Bars = 20 μm. Graphs represent typical phenotype of all samples. **(C)** Quantitative analysis of PIN1-YFP fluorescence level in ovules. Bars correspond to relative YFP signal intensity. Relative fluorescence signal data were extracted from normalized mean gray levels in the above lines. Values correspond to arithmetic means ± SE of three biological replicates ($n = 20$). Asterisks indicate significant difference (Student's two-tailed *t*-test: $^{**}P < 0.01$). **(D)** R2D2 expression in Col-0 and *vha2* ovules under picloram and NAA treatment during FG development. (orange for mDII-tdTomato and green for DII-Venus). Cell walls were stained with FB28 (purple). Bars = 20 μm. Graphs represent the typical phenotype of all samples. **(E)** Quantification of fluorescent signals of R2D2 (DII/mDII). Relative fluorescence signal data were extracted from normalized mean gray levels in the above lines. Values correspond to arithmetic means ± SE of three biological replicates ($n = 20$). Lowercase letters indicate statistically significant differences between different stages ($P < 0.05$). 10 ovules shown in the statistical graph come from 3 different inflorescence apices.

decided to study two tonoplast proton pumps separately. Since the growth status, together with male and female transmission rate of *fugu5-1* mutant was comparable to that of Col-0, our work started to focus on V-ATPase instead of V-PPase.

After mutations of the a2 and a3 subunits that are responsible for tonoplast targeting of V-ATPase, male gametophytes in 26% (12/46) *Arabidopsis* anthers were arrested in PMI phase with large vacuoles (**Figure 3**). PMI is accompanied by vacuolar dynamics changes: a large central vacuole can be converted into several smaller vacuoles by convolution or fission (Yoko et al., 2003). It is well-known that endomembrane system proteins, including V-ATPases, are critical for the development of PMI (Whitley et al., 2009; Dettmer et al., 2010; Feng et al., 2017; Zhang et al., 2018). Our previous studies found that V-ATPase regulates the morphology and distribution of vacuoles during embryonic and seedling development, and that the loss of V-ATPase function in *vha2* male gametophytes results in the failure of 26% (12/46) large central vacuoles to transform into small ones.

During flower development of *vha2*, ovules in 17% (19/112) abnormal flowers could develop up to the FG7 stage but could not complete fertilization, because the lack of an active V-ATPase severely affected stigma morphology. The growth of pollen tube was seriously hindered, as most pollen tubes did not grow to the micropylar end to fertilize the ovule (**Supplementary Figure 3**). Consequently, *vha2* finally

10.3389/fpls.2022.1006735

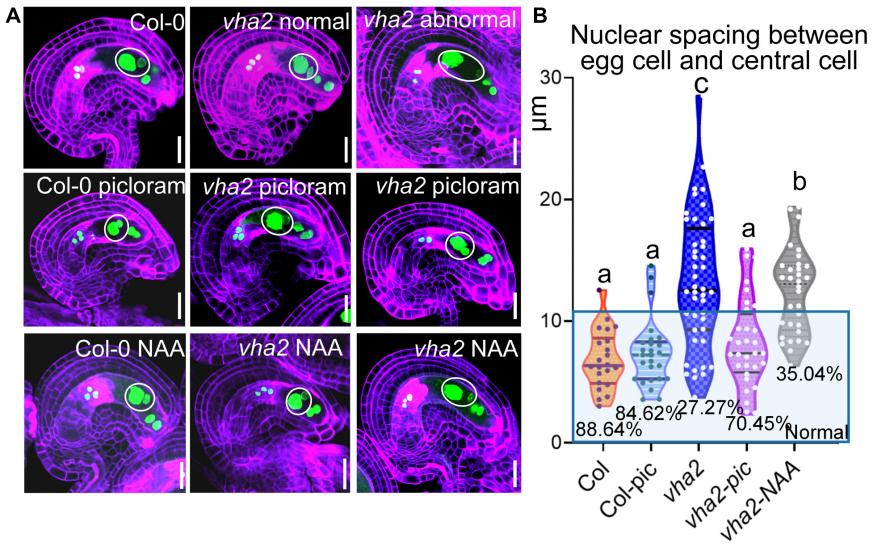

FIGURE 7
Picloram rescues the enlarged nuclear spacing of egg cells and central cells in *vha2* through PIN-independent pathway. **(A)** Nuclear spacing of Col-0 and *vha2* under picloram and NAA treatment at FG6 stage visualized using *ProES1:H2B-GFP* (green) by fluorescence microscopy. Cell walls were stained with FB28 (purple). Inflorescence apices grew for 2 days following 1 μM picloram or 1 μM NAA treatment for 24 h. In the white circles are nuclear of egg cells and central cells. Graphs represent the typical phenotype of all samples. Bars = 20 μm. **(B)** Statistics analysis of nuclear spacing between egg cell and central cell in Col and *vha2*. Dots in the blue box represent normal samples with nuclear spacing of egg cells and central cells less than 10 μm, and the proportions are shown in the chart. Lowercase letters indicate statistically significant differences between different stages ($P < 0.05$). 40 ovules shown in the statistical graph come from 10 different inflorescence apices.

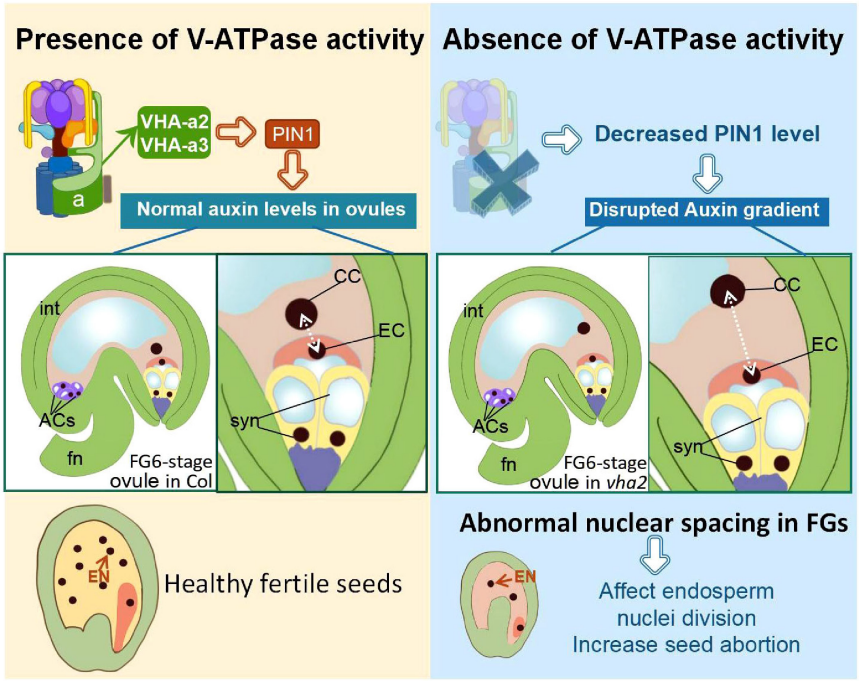

FIGURE 8
Schematic diagram of the role of V-ATPase on FGs and later endosperm development. Fn, funiculus; syn, synergid cell; EC, egg cell; CC, central cell; ACs, antipodal cells; int, integuments (inner and outer).

produced less than ten seeds. From FG development to double fertilization, the egg cell, as a female gamete, fuses with one sperm cell to give rise to the embryo. Meanwhile, the central cell, as the largest cell for nutrient storage, fuses with another sperm cell to form the endosperm. In *vha2* normal flowers, loss of V-ATPase resulted in a mis-localization of the central cell, and the subsequent division speed of endosperm cell was affected as well (**Figures 4**, **5**). This data indicates that the correct positioning of the nuclei of FG is essential for the double fertilization, and that V-ATPase plays a pivotal role in regulating the position of the nuclei.

The phytohormone auxin is involved in the regulation of vacuolar H^+-ATPase in the coordinated development of plant sporophyte and gametophyte

During ovule development, the spatiotemporal distribution of auxin is essential for coordinated development of sporophyte and gametophyte (Pagnussat et al., 2007; Bencivenga et al., 2011). However, mechanisms underlying the spatial and temporal distribution of auxin remain ill-known. Auxin is a long-distance transported phytohormone, and the gradient around FG relies on the polar auxin transporter PIN1 (Luca et al., 2013; Panoli et al., 2015). The intracellular localization of PIN1 depends on the coordination of the endomembrane trafficking system (Gälweiler et al., 1998; Steinmann et al., 1999; Huang et al., 2010; Dhonukshe et al., 2015). In this study, we demonstrated that tonoplast V-ATPase plays a crucial role in the fine regulation of auxin and its function in FG development in *Arabidopsis*.

The spatial and temporal distribution of auxin in ovules is under the tight control of PIN1 (Luca et al., 2013; Panoli et al., 2015). Long-term exposure to NPA or BFA treatment disrupts FG development, a phenotype that has been reported to occur in *pin1* mutants (Wang et al., 2021). In line with previous findings (Luca et al., 2013; Panoli et al., 2015), observation of the R2D2 auxin marker in *Arabidopsis* ovules confirmed that DII expression in FG is higher than that in the sporophyte (**Figure 6**), which implies that the auxin content in *Arabidopsis* FG is relatively low. Loss of V-ATPase decreased auxin content in ovules throughout the FG developmental stages (**Figure 6**), and this was mainly attributed to the abnormal localization of PIN1 (**Figure 6**). This result was also supported by the fact that picloram, but not NAA, was able to restore the position of the central cell nuclei (**Figure 7**).

Eukaryotic V-ATPase has gained a lot of unconventional cellular functions during evolution, such as the regulation of important intracellular proteins (Cross and Muller, 2004; Marshansky and Futai, 2008). In the current work, the epistatic regulation of V-ATPase exerted on PIN1-mediated auxin transport in ovules during FG development has been illustrated. Collectively, our findings revealed a crucial role of V-ATPase in auxin-related FG development in *Arabidopsis* and enhanced our understanding of the functions of tonoplast proton pumps in this vital process.

Data availability statement

The original contributions presented in this study are included in the article/**Supplementary material**, further inquiries can be directed to the corresponding author.

Author contributions

W-HL designed the study, supervised the project, analyzed the data, organized the results, modified the manuscript, and acquired the funding. Y-TJ and J-XZ performed the experiment, analyzed the data, organized the results, and wrote the manuscript. R-HL and Y-CW helped performed the experiments and conducted association analysis. JS helped modify the manuscript. AF offered the materials and helped organized the results and the manuscript. All authors agreed to be accountable for the content of this manuscript, reviewed, and approved of the final manuscript.

Funding

This research was supported by the National Natural Science Foundation of China (32070342 and 32000222), the National Basic Research Program of China (grant no. 2014CB943404), Shanghai Jiao Tong University JiRLMDS Joint Research Fund (Project MDS-JF-2020-8), the Agri-X Interdisciplinary Fund of Shanghai Jiao Tong University (Agri-X20200204 and Agri-X2017006), the Bio-X Interdisciplinary Fund of Shanghai Jiao Tong University (20CX-04), the Scientific and Technological Innovation Funds of Shanghai Jiao Tong University (19×160020009), Grant-in-Aid for Scientific Research (B) (JP16H04803), and Grant-in-Aid for Scientific Research on Innovative Areas (JP25113002 and JP18H05487).

Acknowledgments

We thank Jian Xu (NUS Centre for BioImaging Sciences) for donating marker lines *ProPIN1:PIN1-YFP*.

Conflict of interest

The authors declare that the research was conducted in the absence of any commercial or financial relationships that could be construed as a potential conflict of interest.

Publisher's note

All claims expressed in this article are solely those of the authors and do not necessarily represent those of their affiliated organizations, or those of the publisher, the editors and the reviewers. Any product that may be evaluated in this article, or claim that may be made by its manufacturer, is not guaranteed or endorsed by the publisher.

Supplementary material

The Supplementary Material for this article can be found online at: https://www.frontiersin.org/articles/10.3389/fpls.2022.1006735/full#supplementary-material

References

Bencivenga, S., Colombo, L., and Masiero, S. (2011). Cross talk between the sporophyte and the megagametophyte during ovule development. *Sex. Plant Reprod.* 24, 113–121. doi: 10.1007/s00497-011-0162-3

Benková, E., Michniewicz, M., Sauer, M., Teichmann, T., Seifertová, D., Jürgens, G., et al. (2003). Local, efflux-dependent auxin gradients as a common module for plant organ formation. *Cell* 115, 591–602. doi: 10.1016/S0092-8674(03)00924-3

Christensen, C. A., King, E. J., Jordan, J. R., and Drews, G. N. (1997). Megagametogenesis inArabidopsiswild type and the Gf mutant. *Sex. Plant Reprod.* 10, 49–64. doi: 10.1007/s004970050067

Cross, R. L., and Muller, V. (2004). The evolution of A-, F-, and V-type ATP synthases and ATPascs: Reversals in function and changes in the H+/ATP coupling ratio. *Febs Lett.* 576, 1–4. doi: 10.1016/j.febslet.2004.08.065

Dettmer, J., Schubert, D., Calvo-Weimar, O., Stierhof, Y. D., Schmidt, R., and Schumacher, K. (2010). Essential role of the V-ATPase in male gametophyte development. *Plant J. Cell Mol. Biol.* 41, 117–124. doi: 10.1111/j.1365-313X.2004.02282.x

Dhonukshe, P., Huang, F., Galvan-Ampudia, C. S., Mahonen, A. P., Kleine-Vehn, J., Xu, J., et al. (2015). Plasma membrane-bound AGC3 kinases phosphorylate PIN auxin carriers at TPRXS(N/S) motifs to direct apical PIN recycling. *Development* 142, 2386–2387. doi: 10.1242/dev.127415

Feng, Q. N., Zhang, Y., and Li, S. (2017). Tonoplast targeting of VHA-a3 relies on a Rab5-mediated but Rab7-independent vacuolar trafficking route. *J. Integr. Plant Biol.* 59:4. doi: 10.1111/jipb.12526

Ferjani, A., Segami, S., Horiguchi, G., Muto, Y., Maeshima, M., and Tsukaya, H. (2011). Keep an eye on PPi: The vacuolar-type H+-pyrophosphatase regulates postgerminative development in Arabidopsis. *Plant Cell* 23, 2895–2908. doi: 10.1105/tpc.111.085415

Gälweiler, L., Guan, C., Müller, A., Wisman, E., Mendgen, K., Yephremov, A., et al. (1998). Regulation of Polar Auxin Transport by AtPIN1 in Arabidopsis Vascular Tissue. *Science* 282, 2226–2230. doi: 10.1126/science.282.5397.2226

Gomez, M. D., Barro-Trastoy, D., Fuster-Almunia, C., Tornero, P., Alonso, J. M., and Perez-Amador, M. A. (2020). Gibberellin-mediated RGA-LIKE1 degradation regulates embryo sac development in Arabidopsis. *J. Exp. Bot.* 71, 7059–7072. doi: 10.1093/jxb/eraa395

Hedrich, R., Kurkdjian, A., Guern, J., and Flügge, U. I. (1989). Comparative studies on the electrical properties of the H+ translocating ATPase and pyrophosphatase of the vacuolar-lysosomal compartment. *EMBO J.* 8, 2835–2841. doi: 10.1002/j.1460-2075.1989.tb08430.x

Huang, F., Zago, M. K., Abas, L., Van Marion, A., Galvan-Ampudia, C. S., and Offringa, R. (2010). Phosphorylation of conserved PIN motifs directs Arabidopsis PIN1 polarity and auxin transport. *Plant Cell* 22, 1129–1142. doi: 10.1105/tpc.109.072678

Jiang, Y. T., Tang, R. J., Zhang, Y. J., Xue, H. W., Ferjani, A., Luan, S., et al. (2020). Two tonoplast proton pumps function in Arabidopsis embryo development. *New Phytol.* 225, 1606–1617. doi: 10.1111/nph.16231

Johnson-Brousseau, S. A., and McCormick, S. (2004). A compendium of methods useful for characterizing Arabidopsis pollen mutants and gametophytically-expressed genes. *Plant J.* 39, 761–775. doi: 10.1111/j.1365-313X.2004.02147.x

Krebs, M., Beyhl, D., Gorlich, E., Al-Rasheid, K. A., Marten, I., Stierhof, Y. D., et al. (2010). Arabidopsis V-ATPase activity at the tonoplast is required for efficient nutrient storage but not for sodium accumulation. *Proc. Natl. Acad. Sci. U.S.A.* 107, 3251–3256. doi: 10.1073/pnas.0913035107

Kriegel, A., Andres, Z., Medzihradszky, A., Kruger, F., Scholl, S., and Delang, S. (2015). Job Sharing in the Endomembrane System: Vacuolar Acidification Requires the Combined Activity of V-ATPase and V-PPase. *Plant Cell* 27, 3383–3396. doi: 10.1105/tpc.15.00733

Kurihara, D., Mizuta, Y., Sato, Y., and Higashiyama, T. (2015). ClearSee: A rapid optical clearing reagent for whole-plant fluorescence imaging. *Development* 142, 4168–4179. doi: 10.1242/dev.127613

Li, S., Ge, F. R., Xu, M., Zhao, X. Y., Huang, G. Q., Zhou, L. Z., et al. (2013). Arabidopsis COBRA-LIKE 10, a GPI-anchored protein, mediates directional growth of pollen tubes. *Plant J.* 74, 486–497. doi: 10.1111/tpj.12139

Liao, C. Y., Smet, W., Brunoud, G., Yoshida, S., Vernoux, T., and Weijers, D. (2015). Reporters for sensitive and quantitative measurement of auxin response. *Nat. Methods* 12, 207–210. doi: 10.1038/nmeth.3279

Luca, C., Simona, M., Dola, S. R., Stefano, B., Irma, R. V., Anicet, D. F., et al. (2013). Maternal Control of PIN1 Is Required for Female Gametophyte Development in Arabidopsis. *PLoS One* 8:e66148. doi: 10.1371/journal.pone.0066148

Luo, Y., Scholl, S., Doering, A., Zhang, Y., Irani, N. G., Rubbo, S. D., et al. (2015). V-ATPase activity in the TGN/EE is required for exocytosis and recycling in Arabidopsis. *Nat. Plants* 1, 15094–15094. doi: 10.1038/nplants.2015.94

Lupanga, U., Röhrich, R., Askani, J., Hilmer, S., Kiefer, C., Krebs, M., et al. (2020). The Arabidopsis V-ATPase is localized to the TGN/EE via a seed plant-specific motif. *eLife* 9:e60568. doi: 10.7554/eLife.60568

Maeshima, M. (2000). Vacuolar H+-pyrophosphatase. *Biochim. Biophys. Acta Biomembranes* 1465, 37–51. doi: 10.1016/S0005-2736(00)00130-9

Marshansky, V., and Futai, M. (2008). The V-type H+-ATPase in vesicular trafficking: Targeting, regulation and function. *Curr. Opin Cell Biol.* 20, 415–426. doi: 10.1016/j.ceb.2008.03.015

Martinoia, E., Maeshima, M., and Neuhaus, H. E. (2007). Vacuolar transporters and their essential role in plant metabolism. *J. Exp. Bot.* 58, 83–102. doi: 10.1093/jxb/erl183

Marty, F. (1999). Plant Vacuoles. *Plant Cell* 11, 587–600. doi: 10.1105/tpc.11.4.587

Pagnussat, G. C., Alandete-Saez, M., Bowman, J. L., and Sundaresan, V. (2009). Auxin-Dependent Patterning and Gamete Specification in the Arabidopsis Female Gametophyte. *Science* 324, 1684–1689. doi: 10.1126/science.1167324

Pagnussat, G. C., Yu, H.-J., and Sundaresan, V. (2007). Cell-Fate Switch of Synergid to Egg Cell in Arabidopsis eostre Mutant Embryo Sacs Arises from Misexpression of the BEL1-Like Homeodomain Gene BLH1. *Plant Cell* 19, 3578–3592. doi: 10.1105/tpc.107.054890

Panoli, A., Martin, M. V., Alandete-Saez, M., Simon, M., and Sundaresan, V. (2015). Auxin Import nd Local Auxin Biosynthesis Are Required for Mitotic Divisions, Cell Expansion and Cell Specification during Female Gametophyte Development in Arabidopsis thaliana. *PLoS One* 10:e0126164. doi: 10.1371/journal.pone.0126164

Pérez-España, V. H., Sánchez-León, N., and Vielle-Calzada, J.-P. (2011). CYP85A1 is required for the initiation of female gametogenesis in Arabidopsis thaliana. *Plant Signaling Behav.* 6, 321–326. doi: 10.4161/psb.6.3.13206

Portereiko, M. F., Lloyd, A., Steffen, J. G., Punwani, J. A., Otsuga, D., and Drews, G. N. (2006). AGL80 Is Required for Central Cell and Endosperm Development in Arabidopsis. *Plant Cell* 18, 1862–1872. doi: 10.1105/tpc.106.040824

Serbes, I. E., Palovaara, J., and Groß-Hardt, R. (2019). "Chapter Fifteen - Development and function of the flowering plant female gametophyte," in *Current Topics in Developmental Biology*, ed. U. GROSSNIKLAUS (Cambridge, MA: Academic Press), 401–434. doi: 10.1016/bs.ctdb.2018.11.016

Steinmann, T., Geldner, N., Grebe, M., Mangold, S., Jackson, C. L., Paris, S., et al. (1999). Coordinated Polar Localization of Auxin Efflux Carrier PIN1 by GNOM ARF GEF. *Science* 286, 316–318. doi: 10.1126/science.286.5438.316

Sun, Y., Wang, X., Pan, L., Xie, F., Dai, B., Sun, M., et al. (2021). Plant egg cell fate determination depends on its exact position in female gametophyte. *Proc. Natl. Acad. Sci. U.S. A.* 118:e2017488118. doi: 10.1073/pnas.2017488118

Sundaresan, V., and Alandete-Saez, M. (2010). Pattern formation in miniature: The female gametophyte of flowering plants. *Development* 137, 179–189. doi: 10.1242/dev.030346

Wang, J., Guo, X., Xiao, Q., Zhu, J., Cheung, A. Y., Yuan, L., et al. (2021). Auxin efflux controls orderly nucellar degeneration and expansion of the female gametophyte in Arabidopsis. *New Phytol.* 230, 2261–2274. doi: 10.1111/nph.17152

Zhang, W. T., Li, E., Guo, Y. K., Yu, S. X., Wan, Z. Y., Ma, T., et al. (2018). Arabidopsis VAC14 is critical for pollen development through mediating vacuolar organization. *Plant Physiol.* 177, 1529–1538. doi: 10.1104/pp.18.00495

Whitley, P., Hinz, S., and Doughty, J. (2009). Arabidopsis FAB1/PIKfyve proteins are essential for development of viable pollen. *Plant Physiol.* 151, 1812–1822. doi: 10.1104/pp.109.146159

Wu, J.-J., Peng, X.-B., Li, W.-W., He, R., Xin, H.-P., and Sun, M.-X. (2012). Mitochondrial GCD1 Dysfunction Reveals Reciprocal Cell-to-Cell Signaling during the Maturation of Arabidopsis Female Gametes. *Dev. Cell* 23, 1043–1058. doi: 10.1016/j.devcel.2012.09.011

Yang, W. C., Shi, D. Q., and Chen, Y. H. (2010). Female gametophyte development in flowering plants. *Annu. Rev. Plant Biol.* 61, 89–108. doi: 10.1146/annurev-arplant-042809-112203

Yoko, Y., Mikio, N., Ikuko, H. N., and Tetsuko, N. (2003). Behavior of Vacuoles during Microspore and Pollen Development in Arabidopsis thaliana. *Plant Cell Physiol.* 44, 1192–1201. doi: 10.1093/pcp/pcg147

Yu, S. X., Zhou, L. W., Hu, L. Q., Jiang, Y. T., Zhang, Y. J., Feng, S. L., et al. (2020). Asynchrony of ovule primordia initiation in Arabidopsis. *Development* 147:dev196618. doi: 10.1242/dev.196618

Yuan, L., Liu, Z., Song, X., Johnson, C., Yu, X., and Sundaresan, V. (2016). The CKI1 Histidine Kinase Specifies the Female Gametic Precursor of the Endosperm. *Dev. Cell* 37, 34–46. doi: 10.1016/j.devcel.2016.03.009

Zhang, Y., Zhang, Y. J., Yang, B. J., Yu, X. X., Wang, D., Zu, S. H., et al. (2016). Functional characterization of GmBZL2 (AtBZR1 like gene) reveals the conserved BR signaling regulation in Glycine max. *Sci. Rep.* 6:31134. doi: 10.1038/srep31134

Zu, S. H., Jiang, Y. T., Chang, J. H., Zhang, Y. J., Xue, H. W., and Lin, W. H. (2022). Interaction of brassinosteroid and cytokinin promotes ovule initiation and increases seed number per silique in Arabidopsis. *J. Integr. Plant Biol.* 64, 702–716. doi: 10.1111/jipb.13197

frontiers | Frontiers in Plant Science

TYPE Correction
PUBLISHED 10 February 2023
DOI 10.3389/fpls.2023.1152598

OPEN ACCESS

APPROVED BY
Frontiers Editorial Office,
Frontiers Media SA, Switzerland

*CORRESPONDENCE
Wen-Hui Lin
whlin@sjtu.edu.cn

†These authors have contributed equally to this work and share first authorship

SPECIALTY SECTION
This article was submitted to Plant Physiology, a section of the journal Frontiers in Plant Science

RECEIVED 28 January 2023
ACCEPTED 31 January 2023
PUBLISHED 10 February 2023

CITATION
Jiang Y-T, Zheng J-X, Li R-H, Wang Y-C, Shi J, Ferjani A and Lin W-H (2023) Corrigendum: Tonoplast proton pumps regulate nuclear spacing of female gametophytes *via* mediating polar auxin transport in arabidopsis. *Front. Plant Sci.* 14:1152598. doi: 10.3389/fpls.2023.1152598

Corrigendum: Tonoplast proton pumps regulate nuclear spacing of female gametophytes *via* mediating polar auxin transport in arabidopsis

Yu-Tong Jiang[1†], Ji-Xuan Zheng[2†], Rong-Han Li[2], Yu-Chen Wang[2], Jianxin Shi[1], Ali Ferjani[3] and Wen-Hui Lin[1,4*]

[1]Laboratory of Metabolic and Developmental Sciences, School of Life Sciences and Biotechnology, The Joint International Research, Shanghai Jiao Tong University, Shanghai, China, [2]Zhiyuan College, Shanghai Jiao Tong University, Shanghai, China, [3]Department of Biology, Tokyo Gakugei University, Koganei, Japan, [4]Shanghai Collaborative Innovation Center of Agri-Seeds/Joint Center for Single Cell Biology, Shanghai Jiao Tong University, Shanghai, China

KEYWORDS

plant vacuole, V-ATPase, female gametophyte, egg cell, central cell, endosperm

A Corrigendum on

Tonoplast proton pumps regulate nuclear spacing of female gametophytes *via* mediating polar auxin transport in arabidopsis.

By Jiang Y-T, Zheng J-X, Li R-H, Wang Y-C, Shi J, Ferjani A and Lin W-H (2022) *Front. Plant Sci.* 13:1006735. doi: 10.3389/fpls.2022.1006735

In the published article, there was a writing mistake in the schematic diagram of Figure 8. The cell abbreviations “EC” and “CC” were marked in the wrong place. The corrected Figure 8 and its caption appear below:

The authors apologize for this error and state that this does not change the scientific conclusions of the article in any way. The original article has been updated.

10.3389/fpls.2023.1152598

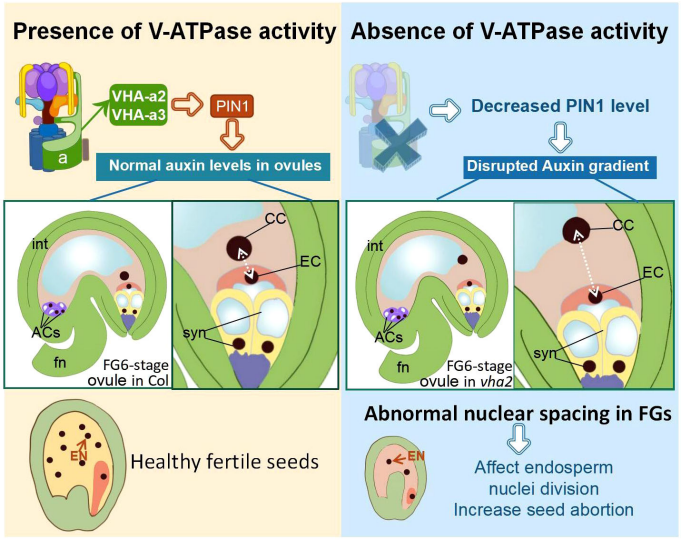

FIGURE 8
Schematic diagram of the role of V-ATPase on FGs and later endosperm development. fn funiculus, syn synergid cell, EC egg cell, CC central cell, ACs antipodal cells, int integuments (inner and outer).

Publisher's note

frontiers | Frontiers in Plant Science

TYPE Original Research
PUBLISHED 14 September 2022
DOI 10.3389/fpls.2022.953225

OPEN ACCESS

EDITED BY
Valya N. Vassileva,
Bulgarian Academy of Sciences, Bulgaria

REVIEWED BY
Irina Ivanova Vaseva,
Bulgarian Academy of Sciences, Bulgaria
Jiejie Li,
Beijing Normal University,
China

*CORRESPONDENCE
Geupil Jang
yk3@jnu.ac.kr

SPECIALTY SECTION
This article was submitted to Plant Development and EvoDevo, a section of the journal Frontiers in Plant Science

RECEIVED 25 May 2022
ACCEPTED 06 July 2022
PUBLISHED 14 September 2022

CITATION
Kim H, Jang J, Seomun S, Yoon Y and Jang G (2022) Division of cortical cells is regulated by auxin in *Arabidopsis* roots. *Front. Plant Sci.* 13:953225. doi: 10.3389/fpls.2022.953225

Division of cortical cells is regulated by auxin in *Arabidopsis* roots

Huijin Kim[1], Jinwoo Jang[1], Subhin Seomun[1], Youngdae Yoon[2] and Geupil Jang[1]*

[1]School of Biological Sciences and Technology, Chonnam National University, Gwangju, South Korea, [2]Department of Environmental Health Science, Konkuk University, Seoul, South Korea

The root cortex transports water and nutrients absorbed by the root epidermis into the vasculature and stores substances such as starch, resins, and essential oils. The cortical cells are also deeply involved in determining epidermal cell fate. In *Arabidopsis thaliana* roots, the cortex is composed of a single cell layer generated by a single round of periclinal division of the cortex/endodermis initials. To further explore cortex development, we traced the development of the cortex by counting cortical cells. Unlike vascular cells, whose number increased during the development of root apical meristem (RAM), the number of cortical cells did not change, indicating that cortical cells do not divide during RAM development. However, auxin-induced cortical cell division, and this finding was confirmed by treatment with the auxin transport inhibitor *N*-1-naphthylphthalamic acid (NPA) and examining transgenic plants harboring *CO2::ΔARF5*, in which cortical expression of truncated AUXIN RESPONSE FACTOR5 (*ΔARF5*) induces auxin responses. NPA-induced cortical auxin accumulation and *CO2::ΔARF5*-mediated cortical auxin response induced anticlinal and periclinal cell divisions, thus increasing the number of cortical cells. These findings reveal a tight link between auxin and cortical cell division, suggesting that auxin is a key player in determining root cortical cell division.

KEYWORDS

auxin, cortex, cortical cell division, polar auxin transport, epidermal cell fate, *Arabidopsis*

Introduction

The plant root contains a variety of tissues with specialized functions. The root cortex, which is located between the root epidermis and endodermis, mediates the transport of water and nutrients absorbed by the epidermis into the central vascular tissue *via* apoplastic and symplastic routes. The root cortex is also responsible for storing photoassimilates in the form of starch, which is imported from the shoot through the phloem, and a variety of secondary metabolites including resins, latex, essential oils, and tannins (Von Fircks and Sennerby-Forsse, 1998; Lux et al., 2004; Azhar et al., 2019).

In *Arabidopsis thaliana* roots, the cortex is part of the ground tissues and originates from the cortex/endodermis initial (CEI) in the stem cell niche. The CEI produces two types of cells *via* a single round of periclinal division; the resulting cells develop into cortical and endodermal cells. Consequently, this developmental process forms double layers of ground

tissues, which contain a single layer of cortex and endodermis (Benfey et al., 1993; Dolan et al., 1993; Scheres et al., 1994). Several key genes have been identified that are related to the asymmetric periclinal division of the CEI and the formation of the cortex initial cell, such as *SHORT-ROOT* (*SHR*) and *SCARECROW* (*SCR*). SHR is a key regulator of root growth and development. The movement of stele-expressed SHR proteins to the CEI activates the expression of *SCR* and triggers the asymmetric periclinal division of the CEI (Nakajima et al., 2001; Gallagher et al., 2004). The essential roles of SHR and SCR in this process are supported by the phenotypes of *SHR* and *SCR* knock-out plants. In *shr* and *scr* mutants, the asymmetric periclinal division of the CEI does not occur, and only a single layer of ground tissue called the mutant layer is formed (Benfey et al., 1993; Scheres et al., 1995; Di Laurenzio et al., 1996; Helariutta et al., 2000). Although these findings explain the initial formation of cortical cells in the stem cell niche, the subsequent steps of cortical cell development remain largely unknown.

Auxin is a key phytohormone that regulates all aspects of plant development and growth. Auxin induces an auxin response in cells *via* an auxin-specific signaling pathway involving AUXIN RESPONSE FACTORs (ARFs). These key transcription factors, which are responsible for the mass transcription of auxin-responsive genes, typically consist of four domains: a DNA-binding domain, an activation domain, and domains III and IV (Ulmasov et al., 1999; Tiwari et al., 2003; Li et al., 2016). Domains III and IV mediate the interactions between the ARFs and the auxin signaling repressor proteins Aux/IAAs. These interactions suppress the cellular auxin response by inactivating the transcriptional activities of ARFs. In response to cellular auxin, the interaction between ARFs and Aux/IAAs is abolished by SCF^{TIR1} E3 ligase-mediated proteolysis of the Aux/IAAs, leading to release of the ARFs and the activation of the auxin response (Gray et al., 2001; Weijers et al., 2005; Mockaitis and Estelle, 2008).

The essential role of ARFs in auxin responses has been confirmed *via* many genetic and molecular biological studies. For example, gain-of-function *axr3-1* mutants produce a mutant version of Aux/IAA17 with a single amino acid change, and have severely compromised auxin responses. Because the mutant Aux/IAA17 protein is resistant to SCF^{TIR1} E3 ligase-mediated degradation, the interaction between this protein and ARFs is maintained and ARFs are inactivated, regardless of cellular auxin levels (Leyser et al., 1996; Rouse et al., 1998; Bishopp et al., 2011). Also, a knock-out mutation of *ARF5* suppresses the auxin response, whereas overexpression of a truncated form of ARF5 that is unable to interact with Aux/IAAs is sufficient to activate the auxin response (Hardtke and Berleth, 1998; Liscum and Reed, 2002; Krogan et al., 2012).

The auxin response in roots is position-dependent. This position-dependent auxin response regulates root cell and tissue development by providing key information required for cell fate determination, cell division and differentiation, and polar auxin transport, representing a key mechanism governing position-dependent auxin accumulation and auxin-dependent development (Friml et al., 2002; Teale et al., 2006; Vanneste and Friml, 2009). Polar auxin transport also mediates the establishment of directional auxin flow, including acropetal (toward the root tip through the central vasculature) and basipetal (toward the root base through the epidermis) flow (Rashotte et al., 2000; Muday and DeLong, 2001; Friml et al., 2002; Friml, 2003; Blilou et al., 2005; Michniewicz et al., 2007; van Berkel et al., 2013). Acropetal and basipetal auxin flow are thought to be linked to centripetal auxin flow, which transports auxin from the epidermis to the central vasculature (Kepinski and Leyser, 2005; Lewis et al., 2007; Baluška et al., 2010).

In this study, we investigated the development of the cortex in *Arabidopsis* roots. Unlike vascular cells, the number of cortical cells did not change during root development, indicating that root cortical cells that initially form by the asymmetric periclinal division of the CEI do not further divide. However, cortical auxin accumulation *via* the treatment of an auxin transport inhibitor strongly activated the division of cortical cells, suggesting that auxin induces cortical cell division. This notion was supported by the finding that cortical cell division was promoted in *CO2::ΔARF5* transgenic plants whose cortical auxin response was activated by the cortical-specific expression of truncated *ARF5* (*ΔARF5*). Collectively, these results suggest that auxin is a key regulator of the division of cortical cells in *Arabidopsis* roots.

Materials and methods

Plant materials and growth condition

Arabidopsis thaliana ecotype Columbia-0 was used as the wild-type control. The *DR5::VENUS* line was described previously (Brunoud et al., 2012; Seo et al., 2021). Seeds were obtained from the Nottingham Arabidopsis Stock Centre. Seeds were sterilized for 15 min in 70% ethanol and then for 15 min in 100% ethanol, and sown on 1/2 Murashige and Skoog (MS) solid medium. After vernalization at 4°C for 4 days in the dark, plants were grown vertically at 23°C under a 16/8 h (light/dark) cycle. For auxin and *N*-1-naphthylphthalamic acid (NPA) treatment, plants were grown on 1/2 MS solid medium supplied with 500 nM indole-3-acetic acid (IAA) and 3 μM NPA for 7 days.

Construction of *CO2::ΔARF5* and *IAA2::GFP* plasmids and plant transformation

To construct the *CO2::ΔARF5* plasmid, a DNA fragment containing the *CO2* promoter, which exhibits cortex-specific expression (Heidstra et al., 2004), was amplified by PCR. The DNA fragments were inserted into the HindIII/KpnI-digested pMDC plant binary vector using the Gibson Assembly Cloning system

Abbreviations: RAM, Root apical meristem; NPA, *N*-1-naphthylphthalamic acid; ΔARF5, truncated AUXIN RESPONSE FACTOR 5; WT, Wild-type; CEI, Cortex/endodermis initial; IAA, Indole-3-acetic acid; CO2, Cortex-specific transcript 2; PCR, Polymerase chain reaction; RT, Reverse transcription; SD, Standard deviation; H cells, Hair cells; N cells, Non-hair cells.

(New England BioLabs). To generate ΔARF5 cDNA, total RNA was extracted from 7-day-old *Arabidopsis* plants grown on 1/2 MS solid medium using RNeasy Plant Mini-prep kits (Qiagen). Reverse transcription was performed using 1 μg of total RNA, oligo dT primers, and Superscript III reverse transcriptase (Invitrogen). The ΔARF5 cDNA was amplified by PCR. The ΔARF5 cDNA fragment was introduced into the pDONR221 vector by BP reaction using the GATEWAY system (Invitrogen). The ΔARF5 cDNA fragment in the pDONR vector was inserted into the *CO2* promoter-carrying pMDC plant binary vector using LR Clonase (Invitrogen). For the construction of *IAA2::GFP* plasmid, *IAA2* promoter which induces xylem-specific transcription (Bishopp et al., 2011) was amplified by PCR, and then inserted into pDONR P4-P1R *via* a BP reaction. The IAA2 promoter was inserted into the GFP-carrying dpGreen binary vector using MULTISITE GATEWAY LR recombination system (Invitrogen). To generate transgenic *Arabidopsis* expressing *CO2::ΔARF5* or *IAA2::GFP*, the recombinant plasmids were introduced into Col-0 wild-type using the floral dip method, as described previously (Clough and Bent, 1998). Primer sequence information for the construction is available in Supplementary Table 1.

Embedding, sectioning, and staining

To visualize the internal anatomy of *Arabidopsis* roots, physical sectioning was performed using the Technovit 8100 system (Heraeus Kulzer, Hanau). To embed the *Arabidopsis* roots, the samples were fixed in 4% paraformaldehyde for 1 h, washed five times with ddH_2O, and incubated overnight at room temperature. The roots were realigned on a 1 mm layer of solid 1.2% agarose and covered with 1.2% molten agarose. After solidification, the samples were cut into small blocks, washed three times in ddH_2O for 30 min, and dehydrated in a graded ethanol series (25, 50, 75, and 100% [v/v] in ddH_2O), 1 h per step. The dehydrated samples were incubated in a Technovit 8100 series (25, 50, 75, and 100% [v/v] in EtOH) for 1 h per step, incubated in 100% Technovit 8100 solution for 1 day, and placed in molds. To solidify the samples, a mixture of Technovit 8100 and hardener solution (15:1 [v/v]) was added to the molds, and the samples were incubated at room temperature for 2 days. Sections (3–3.5 μm) were taken from the apical meristem and maturation regions of the roots using a Leica RM 2145 sectioning machine. The sections were stained with 0.05% toluidine blue solution for 1.5 min and washed with ddH_2O.

RT-qPCR analysis

RT-qPCR analyses were performed using total RNA extracted from the NPA-untreated and treated roots. To synthesize the first-strand cDNA, reverse transcription was performed using 1 μg of total RNA and Superscript III reverse transcriptase (Invitrogen). For qPCR, a master mix was prepared using a LightCycler 480 SYBR GREEN I Master (Roche). PCR reactions and fluorescence detection were performed using a LightCycler NANO Real-Time PCR machine (Roche). PCR conditions were programmed according to the manufacturer's instructions (initial denaturation at 95°C for 5 min, denaturation at 95°C for 10 s, annealing at 60°C for 10 s, and extension at 72°C for 10 s for 45 cycles). Three technical replicates of the qRT-qPCR were performed using three biological replicates. *ACTIN2* (*ACT2*) was used as an internal control. Primer sequence information is available in Supplementary Table 1.

Microscopic observations

To visualize fluorescent signals in wild-type Col-0, *CO2::ΔARF5*, and *DR5::VENUS*, whole roots of the indicated plants grown in 1/2 MS medium for 1 week were dipped in propidium iodide (PI) solution (10 μg/ml) for 2 min. After staining, the roots were mounted on glass slides in ddH_2O. For excitation, 561 nm light for PI fluorescence and 488 nm light for VENUS fluorescence were used. Fluorescence was visualized at wavelengths of 591–635 nm for PI and 505–530 nm for VENUS. The fluorescent signals were visualized and captured under a Leica HCS A confocal microscope (Leica HCS A), and Z-stack images were obtained using Leica LAS X software. To visualize cortex development and quantify anticlinal and periclinal division of cortical cells in the indicated plants, root sections were examined with Leica DM 2500 light microscope, and images were captured with a Leica DFC450 C camera mounted on the light microscope. The frequency of anticlinal and periclinal division of cortical cells was obtained by dividing the number of plants with anticlinal and periclinal division by the total number of plants we tested ($n > 15$). To visualize root hair patterning and quantify root hair abnormality, the samples were examined with Zeiss Discovery.V12 stereo microscope, and images were captured with Axiocam 105 color camera mounted on the stereo microscope. The root hair abnormality was obtained by dividing the number of plants with the double H cell file phenotype by the total number of plants we tested ($n > 20$).

Statistical analysis

Data were presented as mean values, and the number of samples is indicated in the figure legends. The statistical difference between the samples and their control was determined using a two-tailed Student's *t*-test with a $p < 0.01$.

Results

Cortical cell division is not coordinated with root apical meristem cell division

In *Arabidopsis* roots, the development of the cortex, a single cell layer between the epidermis and endodermis, begins with the

asymmetric division of the daughter cell of the cortex/endodermis initial in the root apical meristem (RAM). To further explore cortex development, we tracked changes in the number of cortical cells along the RAM, where cells divide and produce daughter cells that give rise to differentiated cells with specialized functions (Figures 1A, B). As expected, vascular cells divided in conjunction with RAM growth. The number of vascular cells was higher in the distal versus proximal region of the RAM. However, unlike vascular cells, no change was observed in the number of cortical cells: exactly eight cortical cells were present in both the proximal and distal regions of the RAM (Figure 1C). This result indicates that cortical cells do not divide in the RAM, as confirmed by the finding that the number of cortical cells in the root maturation region is identical to that of the RAM (eight cells; Supplementary Figure 1).

Cortical auxin accumulation by NPA promotes cortical cell division

Auxin provides the key positional information required for cell division and differentiation, which strongly affects root cell and tissue development. To explore the possible role of auxin in cortex development, we counted the number of cortical cells in wild-type roots supplemented with auxin. Whereas untreated wild-type roots contained exactly eight cortical cells, wild-type roots treated with auxin showed a significant increase in the number of cortical cells (Figures 2A,B; Supplementary Figure 2). This result suggests that auxin is involved in the division of cortical cells.

To further investigate this notion, we analyzed changes in the auxin response and cortical cell division in response to the auxin transport inhibitor NPA using the auxin-responsive *DR5::VENUS* reporter system (Figure 2C). Previous studies suggested that auxin moves centripetally from the epidermis to the central vasculature and mediates the establishment of an auxin reflux loop (Kepinski and Leyser, 2005; Lewis et al., 2007; Baluška et al., 2010). If auxin moves centripetally, we expected that treatment with NPA would suppress centripetal auxin movement and cause auxin to accumulate in the cortex, provoking the cortical auxin response. To test this hypothesis, we visualized VENUS fluorescent signals in the roots of *DR5::VENUS* plants treated with the auxin transport inhibitor NPA. When *DR5::VENUS* plants were treated with NPA for 6 and 24 h, the VENUS fluorescent signals in the central xylem were shown to decrease gradually with increasing incubation time (Supplementary Figure 3). In addition, the number of cortical cells slightly increased in the *DR5::VENUS* plants treated with NPA for 24 h. The effect of NPA on the auxin response change and cortical cell division was more evident in the *DR5::VENUS* plants grown in NPA-treated conditions for 7 days (Figure 2C; Supplementary Figure 4). In the NPA-treated plants, the xylem-specific VENUS fluorescent signals were absent, whereas tissues surrounding the vascular tissue (including the cortex) showed VENUS signals. More importantly, the optical visualization showed that NPA induces the formation of extra cortical cells in a cortical cell file. These suggest that cortical cells divide in response to an NPA-induced

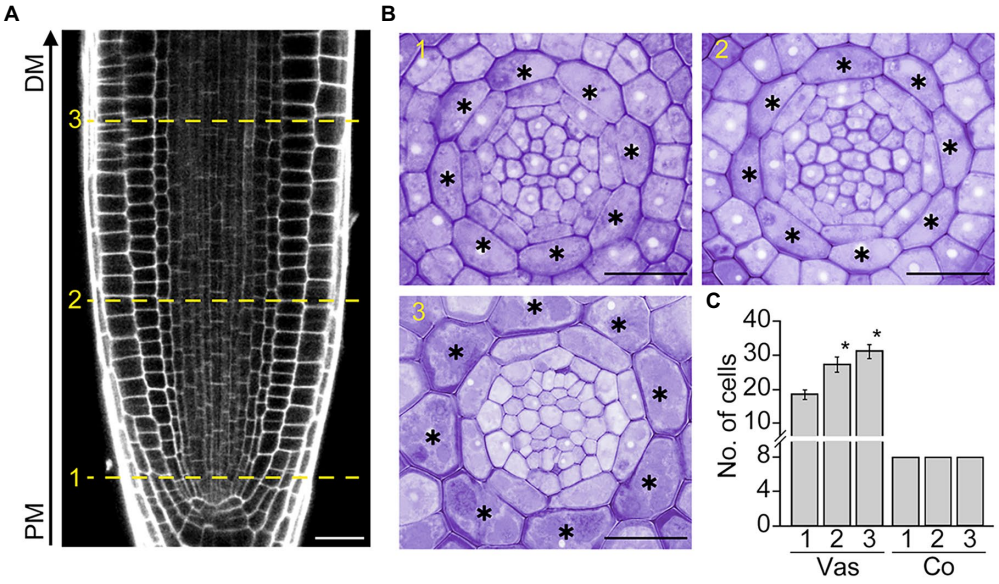

FIGURE 1
Cortex development in *Arabidopsis* roots. Longitudinal **(A)** and transverse sections **(B)** of the root apical meristem (RAM) of Col-0 wild-type plants grown in half-strength Murashige and Skoog (1/2 MS) medium for 7days. The numbers 1, 2, and 3 indicate the positions where transverse sectioning was performed, and asterisks indicate cortical cells. PM, proximal region of the RAM; DM, distal region of the RAM. Scale bars=20μm. **(C)** Quantification of vascular (Vas) and cortical cells (Co) in these plants (n >15). Error bars represent SD. Asterisks indicate statistically significant differences between the corresponding samples and the control (PM1; p <0.01, two-tailed t-test).

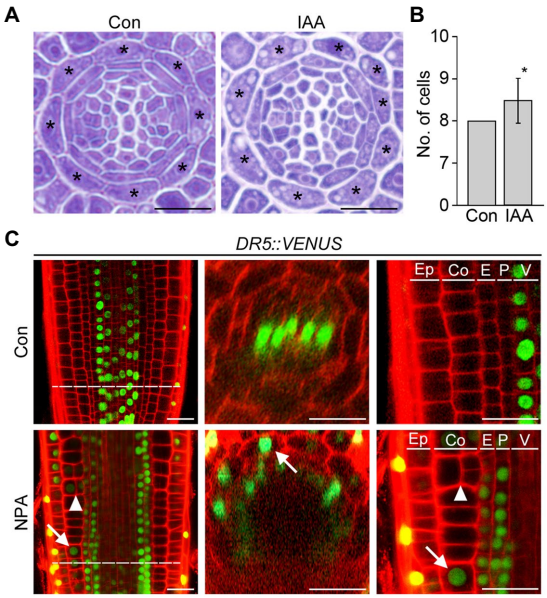

FIGURE 2
Auxin affects cortical cell division. Transverse sections **(A)** and quantification of the number of cortical cells **(B)** in the roots of wild-type plants grown under control conditions (Con) and plants treated with auxin (IAA, 500nM) for 7days (*n* >15). Asterisks in the images indicate cortical cells. Error bar represents SD, and the asterisk in the graph indicates a statistically significant difference between the corresponding samples and the control (Con; p <0.01, two-tailed t-test). **(C)** Fluorescence images of *DR5::VENUS* roots grown under control (Con, top) and 3μM NPA-treated conditions (NPA, bottom) for 7days (left, longitudinal sections; middle, cross-sections; right, high-magnification images of longitudinal sections). Green and red fluorescence correspond to VENUS and propidium iodide (PI) signals, respectively. Dotted lines indicate the position where cross-sectioning was performed. White arrows and triangles indicate the auxin response in cortical cells and cortical cell division, respectively. Ep, epidermis; Co, cortex; E, endodermis; P, pericycle; V, vasculature. Scale bars=20μm.

cortical auxin response, and they partially support the existence of centripetal auxin movement.

IAA2 and *RSL4* are specifically expressed in the xylem and epidermis, and their expression is positively regulated by auxin (Yi et al., 2010; Bishopp et al., 2011). RT-qPCR assays showed that the NPA treatment reduces expression of the xylem-specific *IAA2*, but does not affect the expression of epidermis-specific *RSL4* (Supplementary Figure 5). To verify the change in the *IAA2* expression, we visualized GFP fluorescent signals in the roots of *IAA2::GFP* plants grown in NPA-untreated and treated conditions. NPA treatment strongly decreased the intensity of GFP fluorescent signals in xylem cells, but increased the number of cortical cells, supporting the visualization result of *DR5::VENUS* plants (Figure 3A). To further characterize and quantify the effect of NPA on cortical cell division, we prepared root sections from NPA-treated and untreated wild-type plants and counted the number of cortical cells by physical sectioning (Figures 3B,C). In response to NPA, wild-type plants formed approximately 13 root cortical cells due to increases in both anticlinal and periclinal divisions of cortical cells. When we quantified cell divisions in root sections, anticlinal divisions were more frequently detected than periclinal divisions (Supplementary Figure 6). In addition, we found that the cortical cell division is dependent on the concentration of NPA; the number of cortical cells increased as the NPA concentration increased (Supplementary Figure 7). Collectively, these findings indicate that the NPA-induced cortical auxin response activates divisions of cortical cells.

Division of cortical cells in *CO2::ΔARF5* transgenic plants

If auxin positively regulates cortical cell division, we expected that the activation of the cortical-specific auxin response might be sufficient to provoke the division of cortical cells. To test this idea, we generated *CO2::ΔARF5* transgenic plants in which the cortical-specific *CO2* promoter drives the expression of the truncated *ARF5/MONOPTEROS* (*ΔARF5*) gene (Supplementary Figure 8). Although no obvious difference in root length and thickness was not observed between wild-type and the *CO2::ΔARF5* transgenic plants (Supplementary Figure 9), we found that *CO2* promoter-driven expression of *ΔARF5* activated cortical cell division (Figure 4). Similar to the NPA-treated wild-type plants, *CO2::ΔARF5* plants produced increased numbers of cortical cells (approximately 10 cells) due to both anticlinal and periclinal division of cortical cells, and a lower ratio of periclinal division versus anticlinal division was observed. The periclinal division of cortical cells in the *CO2::ΔARF5* plants was further observed by propidium iodide staining and optical sectioning. Unlike wild-type plants, *CO2::ΔARF5* plants displayed double cortical cell phenotype, as the NPA-treated wild-type plants did. This finding was partially supported by additional sectioning results of the root apical meristem and maturation regions in the *CO2::ΔARF5* plants (Supplementary Figure 10). Furthermore, when we visualized the auxin response in *CO2::ΔARF5* plants using the *DR5::VENUS* reporter system, *CO2::ΔARF5* plants exhibited VENUS fluorescent signals in cortical cells as well as central xylem cells (Figure 5). Collectively, these results indicate that the *CO2* promoter-mediated expression of *ΔARF5* promotes cortical cell division by inducing cortical auxin response. Taken together, these findings indicate that auxin is a key signal that determines the division of cortical cells.

Abnormal root hair patterning in *CO2::ΔARF5* plants

As described above, there was no obvious difference in root length between wild-type and *CO2::ΔARF5* transgenic plants. However, when we examined root hair development in *CO2::ΔARF5* plants, the root hair pattern in these *CO2::ΔARF5* plants differed from that in wild-type plants (Figures 6A,B). In wild-type roots, hair (H) and non-hair (N) cells were regularly arranged in alternating files, with each H cell file next to N cell

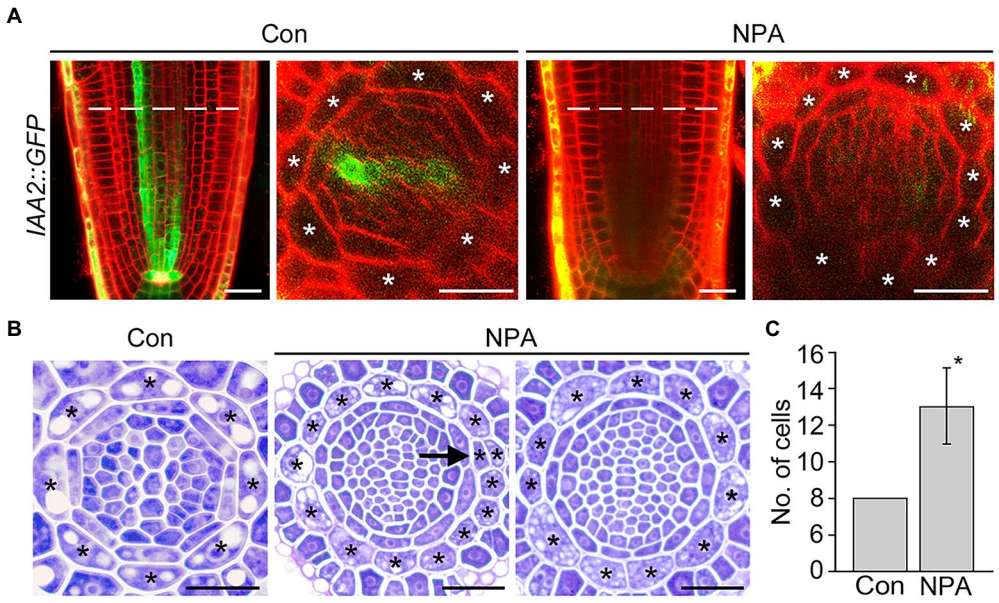

FIGURE 3
NPA strongly induces the division of cortical cells. **(A)** Fluorescence images of *IAA2::GFP* plants grown under control (Con) and 3μM NPA-treated conditions (NPA) for 7days (left, longitudinal sections; right, cross-sections). Dotted lines indicate the position where cross-sectioning was performed. **(B)** Transverse sections of wild-type roots were grown under control (Con) and NPA-treated conditions (NPA, 3μM) for 7days. Asterisks in the images indicate cortical cells, and arrow indicates periclinal division of cortical cells. Scale bars=20μm. **(C)** Quantification of cortical cells in these plants (n >15). Error bar represents SD. The asterisk indicates statistically significant differences between the corresponding samples and the controls (p <0.01, two-tailed t-test).

files. Unlike wild-type roots, *CO2::ΔARF5* roots exhibited double H cell files, in which a single H cell file was next to another H cell files. We compared the number of plants with abnormal root hair patterns, finding that the double H cell file phenotype was present in approximately 5% of wild-type plants but in 80–90% of *CO2::ΔARF5* plants (n >30; Figure 6C). Similar to the *CO2::ΔARF5* plants, wild-type plants grown in NPA-treated conditions displayed the double H cell file phenotype (Supplementary Figure 11). Therefore, these findings indicate that the cortical auxin response is involved in root hair development, supporting the idea that cortical cells provide key positional information required for the determination of epidermal cell identity and patterning.

Discussion

In this study, we revealed that cortical cells do not divide during RAM development. Instead, exogenous auxin provoked the division of cortical cells. The auxin-responsive transcription factor ARF5 contains four distinct domains: domains III and IV are responsible for interacting with Aux/IAA repressors (Weijers et al., 2006; Krogan et al., 2012). Since ΔARF5 lacks these domains, it provokes the auxin response more strongly than intact ARF5 (Krogan et al., 2012; Zhang et al., 2014). We also showed that cortical auxin response and cortical cell division are activated, when *ΔARF5* was expressed under the control of the cortex-specific *CO2* promoter. These findings indicate that auxin is a key regulator of cortical cell division.

Polar auxin transport is deeply involved in cell and tissue-specific auxin accumulation, providing key positional information required for cell division and differentiation (Friml, 2003). Polar auxin transport, which is mediated by auxin influx and efflux carrier proteins, forms directional auxin flows, such as an acropetal flow toward the root tip through the central xylem and a basipetal flow toward the root base through the epidermis (Rashotte et al., 2000; Muday and DeLong, 2001; Friml et al., 2002; Friml, 2003; Blilou et al., 2005; Michniewicz et al., 2007; van Berkel et al., 2013). Previous studies proposed that centripetal auxin flow from the epidermis to the central xylem vasculature connects acropetal and basipetal auxin flow and establishes an auxin reflux loop in the RAM (Kepinski and Leyser, 2005; Lewis et al., 2007; Baluška et al., 2010). In this study, we showed that *DR5::VENUS* plants treated with the polar auxin transport inhibitor NPA exhibit severely reduced auxin response in central xylem cells. Instead, the NPA treatment induced a cortical auxin response and cortical cell division. These NPA-induced spatial changes in the auxin response point to the existence of centripetal auxin flow and support the pivotal role of auxin in inducing cortical cell division.

In plants, the correct orientation of cell division is essential for proper embryogenesis and post-embryonic development by determining cell and tissue patterning and function; altering the orientation of cell division leads to severe defects in plant growth and development (Pietra et al., 2013; Van Norman, 2016;

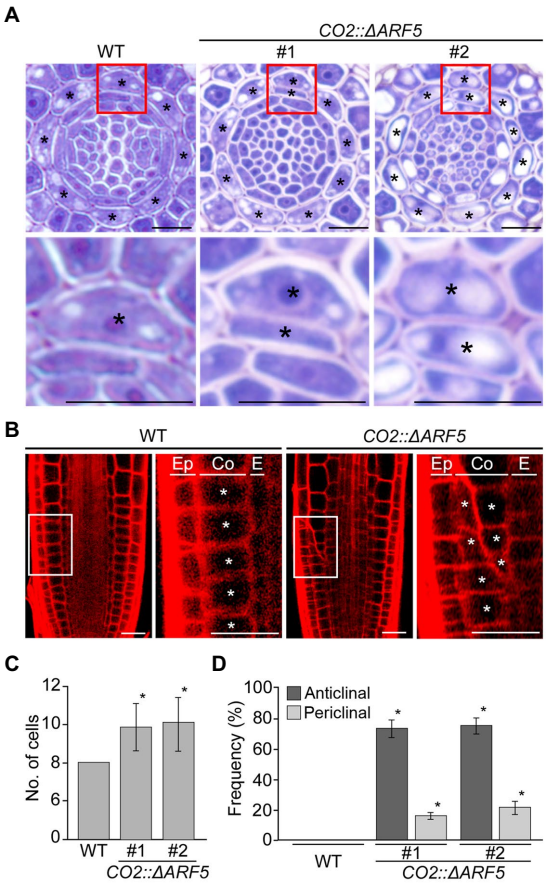

FIGURE 4
Division of cortical cells in *CO2::ΔARF5* plants. **(A)** Transverse sections of the root meristem regions of wild-type and *CO2::ΔARF5* plants grown in 1/2 MS solid medium for 7days (top), and high-magnification images of the regions in boxes showing the periclinal division of cortical cells (bottom). #1 and 2 indicate two independent lines of *CO2::ΔARF5* transgenic plants. **(B)** Fluorescence images of propidium iodide (PI)-stained wild-type and *CO2::ΔARF5* plants (#1), and high-magnification images of the sections shown in white boxes. Ep, epidermis; Co, cortex; E, endodermis. Asterisks in **(A)** and **(B)** indicate cortical cells. Scale bars=20μm. **(C,D)** Quantification of cortical cells **(C)**, and the frequency of anticlinal and periclinal divisions of cortical cells **(D)** in wild-type and *CO2::ΔARF5* plants (n >15). Error bars represent SD, and asterisks in the graphs indicate statistically significant differences between the corresponding samples and wild-type controls (p <0.01, two-tailed t-test).

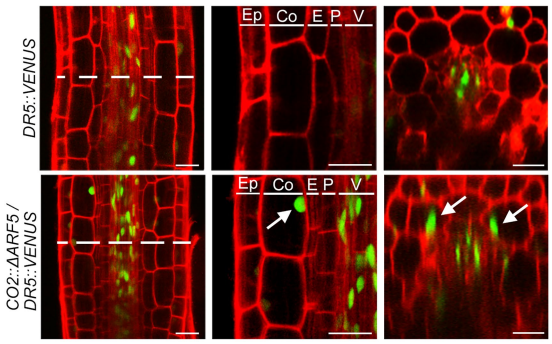

FIGURE 5
Cortical-specific auxin response in *CO2::ΔARF5* plants. Visualization of the auxin response in the roots of *DR5::VENUS* (top) and *CO2::ΔARF5*/*DR5::VENUS* plants (bottom) grown in 1/2 MS solid medium for 7days (left, longitudinal sections; middle, high-magnification images of the longitudinal sections; right, cross-sections). White arrows indicate VENUS fluorescent signals in the cortical cells of *CO2::ΔARF5* plants. Green and red fluorescence correspond to VENUS and PI signals, respectively. Ep, epidermis; Co, cortex; E, endodermis; P, pericycle; V, vasculature. Scale bars=20μm.

Luptovčiak et al., 2017; Ovečka et al., 2020). Little is known about the molecular mechanism underlying this process, but recent studies suggested that auxin is deeply involved in determining cell division patterning (Yamaguchi et al., 2013; Marhavý et al., 2016; Huang et al., 2019; Vaddepalli et al., 2021). Huang et al. (2019) demonstrated that auxin signaling regulates cell division patterning during lateral root development (Huang et al., 2019). A recent study by Vaddepalli et al. (2021) showed that the orientations of cell shape and division are tightly coupled and that auxin-dependent control of the cytoskeleton and cell shape regulates cell division orientation during embryogenesis (Vaddepalli et al., 2021). These findings suggest that auxin regulates cell division patterning, as supported by the finding that auxin is involved in the rearrangement of actin filaments and actin-dependent transport (Waller et al., 2002; Nick et al., 2009; Kovaleva et al., 2015; Zhu and Geisler, 2015).

In the current study, we demonstrated that auxin increases the number of cortical cells by promoting the anticlinal and periclinal division of cortical cells. Analysis of the frequency of anticlinal and periclinal divisions in wild-type plants treated with IAA or NPA and transgenic plants expressing *CO2::ΔARF5* showed that anticlinal division is more frequent than periclinal division in these plants (Supplementary Figure 12). Exogenous auxin treatment slightly but significantly increased the number of cortical cells due only to increased anticlinal divisions. The expression of *CO2::ΔARF5* and exogenous NPA treatment strongly increased the number of cortical cells (by approximately 2–5) by inducing both anticlinal and periclinal divisions; the frequency of anticlinal divisions was approximately 2.5-fold higher than that of periclinal divisions. When considering the tight link between the cortical auxin response and cortical cell division, these results support the previous finding that auxin plays an essential role in determining cell division patterning, and suggest that cell division orientation in the cortex is regulated by auxin.

Root hairs are formed by the differentiation of root epidermal cells (Dolan et al., 1993; Galway et al., 1994; Yi et al., 2010). In *Arabidopsis*, the epidermal cells that contact two neighboring cortical cells differentiate into root hair cells (H cells), whereas epidermal cells that contact a single cortical cell differentiate into non-hair cells (N cells). Therefore, the patterning of root hair formation in *Arabidopsis* is characterized by alternating H cell and N cell files (Dolan and Roberts, 1995; Lee and Schiefelbein, 1999). Previous many studies have suggested that cortical cells are deeply involved in determining root hair cell identity and patterning

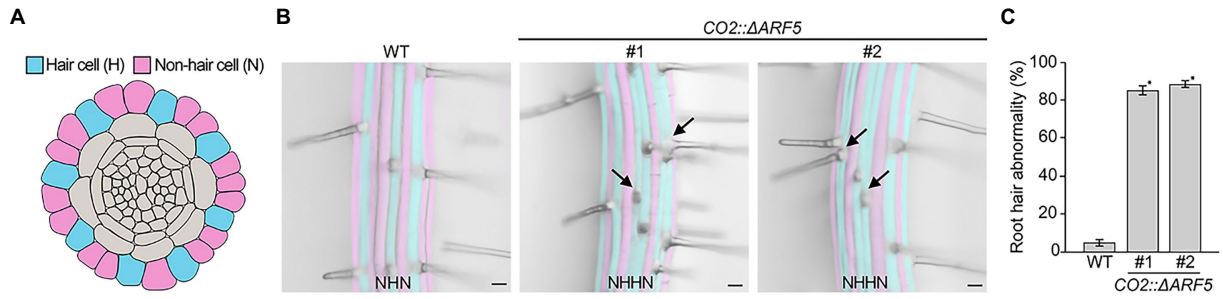

FIGURE 6
Abnormal root hair patterning in *CO2::ΔARF5* plants. **(A)** Schematic diagram of root hair patterning in *Arabidopsis* roots. Blue and pink indicate hair cells (H) and non-hair cells (N), respectively. **(B)** Root hair patterning in wild-type and *CO2::ΔARF5* transgenic plants grown in 1/2 MS solid medium for 7days. #1 and 2 indicate two independent lines of *CO2::ΔARF5* plants. Black arrows point to the formation of double H files in *CO2::ΔARF5* plants. Scale bars=20μm. **(C)** Quantification of abnormal root hair patterning in these plants (n >30). Error bars represent SD, and asterisks indicate a significant difference from the wild-type control (p <0.01, two-tailed t-test).

(Kwak et al., 2005; Schiefelbein et al., 2009; Hassan et al., 2010; Grebe, 2012; Song et al., 2019). In this study, we observed that *CO2::ΔARF5* plants displayed abnormal root hair patterning. Unlike the root hair patterning in wild-type plants, the alternation between H and N cell files was perturbed in *CO2::ΔARF5* plants, and the double H cell file phenotype was frequently detected. This finding suggests that the cortical auxin response and cortical cell division might be involved in epidermal cell fate. The determination of cell fate is a pivotal process in multicellular organisms. Cell-to-cell communication is one of the key processes underlying cell fate determination. Communication between cortical cells and epidermal cells mediates the determination of epidermal cell fate, and several genes involved in this process have been identified, such as *SCRAMBLED* (*SCM*), *QUIRKY* (*QKY*), and *JACKDAW* (*JKD*; Kwak et al., 2005; Hassan et al., 2010; Song et al., 2019). Although the relationship between the cortical auxin response and *SCM*, *QKY*, and *JKD* expression is largely unknown, our findings support the idea that cortical cells play a crucial role in providing information required for determining epidermal cell fate and that the cortical auxin response might be involved in this process. Further molecular and genetic analyses will expand our understanding of the mechanisms underlying this process.

Data availability statement

The original contributions presented in the study are included in the article/Supplementary material; further inquiries can be directed to the corresponding author.

Author contributions

GJ conceived the original screening and research plans, and agreed to serve as the author responsible for contact and ensures communication. HK, JJ, and SS performed the experiments and analyzed the data. YY and GJ wrote the article with contributions from all authors. All authors contributed to the article and approved the submitted version.

Funding

This work was carried out with the support of the BioGreen21 Agri-Tech Innovation Program (Project No. PJ01567301) and the New Breeding Technologies Development Program (Project No. PJ01653503), Rural Development Administration, Republic of Korea. This work was also supported by the Korea Institute of Planning and Evaluation for Technology in Food, Agriculture, and Forestry through Agricultural Machinery/Equipment Localization Technology Development Program, funded by the Ministry of Agriculture, Food, and Rural Affairs (122022-03-1-HD020), and the National Research Foundation of Korea Grant funded by the Korean Government (NRF-2022R1A2C1003615).

Acknowledgments

We thank Deok Hyun Seo and Haewon Jeong (Chonnam National University), for their valuable technical support in the physical sectioning and the microscopic analysis.

Conflict of interest

The authors declare that the research was conducted in the absence of any commercial or financial relationships that could be construed as a potential conflict of interest.

Publisher's note

All claims expressed in this article are solely those of the authors and do not necessarily represent those

of their affiliated organizations, or those of the publisher, the editors and the reviewers. Any product that may be evaluated in this article, or claim that may be made by its manufacturer, is not guaranteed or endorsed by the publisher.

Supplementary materials

The Supplementary materials for this article can be found online at: https://www.frontiersin.org/articles/10.3389/fpls.2022.953225/full#supplementary-material

References

Azhar, S. Z. A., Ghani, K. A., and Yusuf, N. A. (2019). Histological observations of adventitious root derived from in vitro plantlet and shoot bud of *Boesenbergia rotunda* (Zingiberaceae). *Pertanika J. Trop. Agric. Sci.* 42, 699–707.

Baluška, F., Mancuso, S., Volkmann, D., and Barlow, P. W. (2010). Root apex transition zone: a signalling–response nexus in the root. *Trends Plant Sci.* 15, 402–408. doi: 10.1016/j.tplants.2010.04.007

Benfey, P. N., Linstead, P. J., Roberts, K., Schiefelbein, J. W., Hauser, M.-T., and Aeschbacher, R. A. (1993). Root development in Arabidopsis: four mutants with dramatically altered root morphogenesis. *Development* 119, 57–70. doi: 10.1242/dev.119.1.57

Bishopp, A., Help, H., El-Showk, S., Weijers, D., Scheres, B., Friml, J., et al. (2011). A mutually inhibitory interaction between auxin and cytokinin specifies vascular pattern in roots. *Curr. Biol.* 21, 917–926. doi: 10.1016/j.cub.2011.04.017

Blilou, I., Xu, J., Wildwater, M., Willemsen, V., Paponov, I., Friml, J., et al. (2005). The PIN auxin efflux facilitator network controls growth and patterning in Arabidopsis roots. *Nature* 433, 39–44. doi: 10.1038/nature03184

Brunoud, G., Wells, D. M., Oliva, M., Larrieu, A., Mirabet, V., Burrow, A. H., et al. (2012). A novel sensor to map auxin response and distribution at high spatio-temporal resolution. *Nature* 482, 103–106. doi: 10.1038/nature10791

Clough, S. J., and Bent, A. F. (1998). Floral dip: a simplified method for Agrobacterium-mediated transformation of *Arabidopsis thaliana*. *Plant J.* 16, 735–743. doi: 10.1046/j.1365-313x.1998.00343.x

Di Laurenzio, L., Wysocka-Diller, J., Malamy, J. E., Pysh, L., Helariutta, Y., Freshour, G., et al. (1996). The SCARECROW gene regulates an asymmetric cell division that is essential for generating the radial organization of the Arabidopsis root. *Cell* 86, 423–433. doi: 10.1016/S0092-8674(00)80115-4

Dolan, L., Janmaat, K., Willemsen, V., Linstead, P., Poethig, S., Roberts, K., et al. (1993). Cellular organisation of the *Arabidopsis thaliana* root. *Development* 119, 71–84. doi: 10.1242/dev.119.1.71

Dolan, L., and Roberts, K. (1995). The development of cell pattern in the root epidermis. *Philos. Trans. R. Soc. Lond. B Biol. Sci.* 350, 95–99.

Friml, J. (2003). Auxin transport—shaping the plant. *Curr. Opin. Plant Biol.* 6, 7–12. doi: 10.1016/S1369526602000031

Friml, J., Benková, E., Blilou, I., Wisniewska, J., Hamann, T., Ljung, K., et al. (2002). AtPIN4 mediates sink-driven auxin gradients and root patterning in Arabidopsis. *Cell* 108, 661–673. doi: 10.1016/S0092-8674(02)00656-6

Gallagher, K. L., Paquette, A. J., Nakajima, K., and Benfey, P. N. (2004). Mechanisms regulating SHORT-ROOT intercellular movement. *Curr. Biol.* 14, 1847–1851. doi: 10.1016/j.cub.2004.09.081

Galway, M. E., Masucci, J. D., Lloyd, A. M., Walbot, V., Davis, R. W., and Schiefelbein, J. W. (1994). The TTG gene is required to specify epidermal cell fate and cell patterning in the Arabidopsis root. *Dev. Biol.* 166, 740–754. doi: 10.1006/dbio.1994.1352

Gray, W. M., Kepinski, S., Rouse, D., Leyser, O., and Estelle, M. (2001). Auxin regulates SCFTIR1-dependent degradation of AUX/IAA proteins. *Nature* 414, 271–276. doi: 10.1038/35104500

Grebe, M. (2012). The patterning of epidermal hairs in Arabidopsis—updated. *Curr. Opin. Plant Biol.* 15, 31–37. doi: 10.1016/j.pbi.2011.10.010

Hardtke, C. S., and Berleth, T. (1998). The Arabidopsis gene MONOPTEROS encodes a transcription factor mediating embryo axis formation and vascular development. *EMBO J.* 17, 1405–1411. doi: 10.1093/emboj/17.5.1405

Hassan, H., Scheres, B., and Blilou, I. (2010). JACKDAW controls epidermal patterning in the Arabidopsis root meristem through a non-cell-autonomous mechanism. *Development* 137, 1523–1529. doi: 10.1242/dev.048777

Heidstra, R., Welch, D., and Scheres, B. (2004). Mosaic analyses using marked activation and deletion clones dissect Arabidopsis SCARECROW action in asymmetric cell division. *Genes Dev.* 18, 1964–1969. doi: 10.1101/gad.305504

Helariutta, Y., Fukaki, H., Wysocka-Diller, J., Nakajima, K., Jung, J., Sena, G., et al. (2000). The SHORT-ROOT gene controls radial patterning of the Arabidopsis root through radial signaling. *Cell* 101, 555–567. doi: 10.1016/S0092-8674(00)80865-X

Huang, R., Zheng, R., He, J., Zhou, Z., Wang, J., Xiong, Y., et al. (2019). Noncanonical auxin signaling regulates cell division pattern during lateral root development. *Proc. Natl. Acad. Sci. U. S. A.* 116, 21285–21290. doi: 10.1073/pnas.1910916116

Kepinski, S., and Leyser, O. (2005). Plant development: auxin in loops. *Curr. Biol.* 15, R208–R210. doi: 10.1016/j.cub.2005.03.012

Kovaleva, L., Voronkov, A., and Zakharova, E. (2015). Role of auxin and cytokinin in the regulation of the actin cytoskeleton in the in vitro germinating male gametophyte of petunia. *Russ. J. Plant Physiol.* 62, 179–186. doi: 10.1134/S1021443715020107

Krogan, N. T., Ckurshumova, W., Marcos, D., Caragea, A. E., and Berleth, T. (2012). Deletion of MP/ARF5 domains III and IV reveals a requirement for Aux/IAA regulation in Arabidopsis leaf vascular patterning. *New Phytol.* 194, 391–401. doi: 10.1111/j.1469-8137.2012.04064.x

Kwak, S.-H., Shen, R., and Schiefelbein, J. (2005). Positional signaling mediated by a receptor-like kinase in Arabidopsis. *Science* 307, 1111–1113. doi: 10.1126/science.1105373

Lee, M. M., and Schiefelbein, J. (1999). WEREWOLF, a MYB-related protein in Arabidopsis, is a position-dependent regulator of epidermal cell patterning. *Cell* 99, 473–483. doi: 10.1016/S0092-8674(00)81536-6

Lewis, D. R., Miller, N. D., Splitt, B. L., Wu, G., and Spalding, E. P. (2007). Separating the roles of acropetal and basipetal auxin transport on gravitropism with mutations in two Arabidopsis multidrug resistance-like ABC transporter genes. *Plant Cell* 19, 1838–1850. doi: 10.1105/tpc.107.051599

Leyser, H. O., Pickett, F. B., Dharmasiri, S., and Estelle, M. (1996). Mutations in the AXR3 gene of Arabidopsis result in altered auxin response including ectopic expression from the SAUR-AC1 promoter. *Plant J.* 10, 403–413. doi: 10.1046/j.1365-313x.1996.10030403.x

Li, S.-B., Xie, Z.-Z., Hu, C.-G., and Zhang, J.-Z. (2016). A review of auxin response factors (ARFs) in plants. *Front. Plant Sci.* 7, 47. doi: 10.3389/fpls.2016.00047

Liscum, E., and Reed, J. (2002). Genetics of Aux/IAA and ARF action in plant growth and development. *Plant Mol. Biol.* 49, 387–400. doi: 10.1023/A:1015255030047

Luptovčiak, I., Komis, G., Takáč, T., Ovečka, M., and Šamaj, J. (2017). Katanin: a sword cutting microtubules for cellular, developmental, and physiological purposes. *Front. Plant Sci.* 8, 1982. doi: 10.3389/fpls.2017.01982

Lux, A., Luxová, M., Abe, J., and Morita, S. (2004). Root cortex: structural and functional variability and responses to environmental stress. *Root Res.* 13, 117–131. doi: 10.3117/rootres.13.117

Marhavý, P., Montesinos, J. C., Abuzeineh, A., Van Damme, D., Vermeer, J. E., Duclercq, J., et al. (2016). Targeted cell elimination reveals an auxin-guided biphasic mode of lateral root initiation. *Genes Dev.* 30, 471–483. doi: 10.1101/gad.276964.115

Michniewicz, M., Brewer, P. B., and Friml, J. (2007). Polar auxin transport and asymmetric auxin distribution. *Arabidopsis Book* 5:e0108. doi: 10.1199/tab.0108

Mockaitis, K., and Estelle, M. (2008). Auxin receptors and plant development: a new signaling paradigm. *Annu. Rev. Cell Dev. Biol.* 24, 55–80. doi: 10.1146/annurev.cellbio.23.090506.123214

Muday, G. K., and DeLong, A. (2001). Polar auxin transport: controlling where and how much. *Trends Plant Sci.* 6, 535–542. doi: 10.1016/S1360-1385(01)02101-X

Nakajima, K., Sena, G., Nawy, T., and Benfey, P. N. (2001). Intercellular movement of the putative transcription factor SHR in root patterning. *Nature* 413, 307–311. doi: 10.1038/35095061

Nick, P., Han, M.-J., and An, G. (2009). Auxin stimulates its own transport by shaping actin filaments. *Plant Physiol.* 151, 155–167. doi: 10.1104/pp.109.140111

Ovečka, M., Luptovčiak, I., Komis, G., Šamajová, O., Samakovli, D., and Šamaj, J. (2020). Spatiotemporal pattern of ectopic cell divisions contribute to mis-shaped phenotype of primary and lateral roots of katanin1 mutant. *Front. Plant Sci.* 11, 734. doi: 10.3389/fpls.2020.00734

Pietra, S., Gustavsson, A., Kiefer, C., Kalmbach, L., Hörstedt, P., Ikeda, Y., et al. (2013). Arabidopsis SABRE and CLASP interact to stabilize cell division plane orientation and planar polarity. *Nat. Commun.* 4, 1–15. doi: 10.1038/ncomms3779

Rashotte, A. M., Brady, S. R., Reed, R. C., Ante, S. J., and Muday, G. K. (2000). Basipetal auxin transport is required for gravitropism in roots of Arabidopsis. *Plant Physiol.* 122, 481–490. doi: 10.1104/pp.122.2.481

Rouse, D., Mackay, P., Stirnberg, P., Estelle, M., and Leyser, O. (1998). Changes in auxin response from mutations in an AUX/IAA gene. *Science* 279, 1371–1373. doi: 10.1126/science.279.5355.1371

Scheres, B., Di Laurenzio, L., Willemsen, V., Hauser, M.-T., Janmaat, K., Weisbeek, P., et al. (1995). Mutations affecting the radial organisation of the Arabidopsis root display specific defects throughout the embryonic axis. *Development* 121, 53–62. doi: 10.1242/dev.121.1.53

Scheres, B., Wolkenfelt, H., Willemsen, V., Terlouw, M., Lawson, E., Dean, C., et al. (1994). Embryonic origin of the Arabidopsis primary root and root meristem initials. *Development* 120, 2475–2487. doi: 10.1242/dev.120.9.2475

Schiefelbein, J., Kwak, S.-H., Wieckowski, Y., Barron, C., and Bruex, A. (2009). The gene regulatory network for root epidermal cell-type pattern formation in Arabidopsis. *J. Exp. Bot.* 60, 1515–1521. doi: 10.1093/jxb/ern339

Seo, D. H., Jeong, H., Choi, Y. D., and Jang, G. (2021). Auxin controls the division of root endodermal cells. *Plant Physiol.* 187, 1577–1586. doi: 10.1093/plphys/kiab341

Song, J. H., Kwak, S.-H., Nam, K. H., Schiefelbein, J., and Lee, M. M. (2019). QUIRKY regulates root epidermal cell patterning through stabilizing SCRAMBLED to control CAPRICE movement in Arabidopsis. *Nat. Commun.* 10, 1–12. doi: 10.1038/s41467-019-09715-8

Teale, W. D., Paponov, I. A., and Palme, K. (2006). Auxin in action: signalling, transport and the control of plant growth and development. *Nat. Rev. Mol. Cell Biol.* 7, 847–859. doi: 10.1038/nrm2020

Tiwari, S. B., Hagen, G., and Guilfoyle, T. (2003). The roles of auxin response factor domains in auxin-responsive transcription. *Plant Cell* 15, 533–543. doi: 10.1105/tpc.008417

Ulmasov, T., Hagen, G., and Guilfoyle, T. J. (1999). Dimerization and DNA binding of auxin response factors. *Plant J.* 19, 309–319. doi: 10.1046/j.1365-313X.1999.00538.x

Vaddepalli, P., de Zeeuw, T., Strauss, S., Bürstenbinder, K., Liao, C.-Y., Ramalho, J. J., et al. (2021). Auxin-dependent control of cytoskeleton and cell shape regulates division orientation in the Arabidopsis embryo. *Curr. Biol.* 31:e4944, 4946–4955.e4. doi: 10.1016/j.cub.2021.09.019

van Berkel, K., de Boer, R. J., Scheres, B., and ten Tusscher, K. (2013). Polar auxin transport: models and mechanisms. *Development* 140, 2253–2268. doi: 10.1242/dev.079111

Van Norman, J. M. (2016). Asymmetry and cell polarity in root development. *Dev. Biol.* 419, 165–174. doi: 10.1016/j.ydbio.2016.07.009

Vanneste, S., and Friml, J. (2009). Auxin: a trigger for change in plant development. *Cell* 136, 1005–1016. doi: 10.1016/j.cell.2009.03.001

Von Fircks, Y., and Sennerby-Forsse, L. (1998). Seasonal fluctuations of starch in root and stem tissues of coppiced *Salix viminalis* plants grown under two nitrogen regimes. *Tree Physiol.* 18, 243–249. doi: 10.1093/treephys/18.4.243

Waller, F., Riemann, M., and Nick, P. (2002). A role for actin-driven secretion in auxin-induced growth. *Protoplasma* 219, 0072–0081. doi: 10.1007/s007090200007

Weijers, D., Benkova, E., Jäger, K. E., Schlereth, A., Hamann, T., Kientz, M., et al. (2005). Developmental specificity of auxin response by pairs of ARF and Aux/IAA transcriptional regulators. *EMBO J.* 24, 1874–1885. doi: 10.1038/sj.emboj.7600659

Weijers, D., Schlereth, A., Ehrismann, J. S., Schwank, G., Kientz, M., and Jürgens, G. (2006). Auxin triggers transient local signaling for cell specification in Arabidopsis embryogenesis. *Dev. Cell* 10, 265–270. doi: 10.1016/j.devcel.2005.12.001

Yamaguchi, N., Wu, M.-F., Winter, C. M., Berns, M. C., Nole-Wilson, S., Yamaguchi, A., et al. (2013). A molecular framework for auxin-mediated initiation of flower primordia. *Dev. Cell* 24, 271–282. doi: 10.1016/j.devcel.2012.12.017

Yi, K., Menand, B., Bell, E., and Dolan, L. (2010). A basic helix-loop-helix transcription factor controls cell growth and size in root hairs. *Nat. Genet.* 42, 264–267. doi: 10.1038/ng.529

Zhang, J.-Y., He, S.-B., Li, L., and Yang, H.-Q. (2014). Auxin inhibits stomatal development through MONOPTEROS repression of a mobile peptide gene STOMAGEN in mesophyll. *Proc. Natl. Acad. Sci. U. S. A.* 111, E3015–E3023. doi: 10.1073/pnas.1400542111

Zhu, J., and Geisler, M. (2015). Keeping it all together: auxin–actin crosstalk in plant development. *J. Exp. Bot.* 66, 4983–4998. doi: 10.1093/jxb/erv308

frontiers | Frontiers in Plant Science

TYPE Original Research
PUBLISHED 28 November 2022
DOI 10.3389/fpls.2022.1011360

OPEN ACCESS

EDITED BY
Valya N. Vassileva,
Bulgarian Academy of Sciences,
Bulgaria

REVIEWED BY
Denise Scuffi,
Consejo Nacional de Investigaciones Científicas y Técnicas, Argentina
Takayuki Shimizu,
The University of Tokyo, Japan

*CORRESPONDENCE
Toshinori Kinoshita
kinoshita@bio.nagoya-u.ac.jp

†These authors share first authorship

SPECIALTY SECTION
This article was submitted to Plant Physiology, a section of the journal Frontiers in Plant Science

RECEIVED 04 August 2022
ACCEPTED 11 November 2022
PUBLISHED 28 November 2022

CITATION
Soda MN, Hayashi Y, Takahashi K and Kinoshita T (2022) Tryptophan synthase ß subunit 1 affects stomatal phenotypes in *Arabidopsis thaliana*. *Front. Plant Sci.* 13:1011360. doi: 10.3389/fpls.2022.1011360

Tryptophan synthase ß subunit 1 affects stomatal phenotypes in *Arabidopsis thaliana*

Midori N. Soda[1†], Yuki Hayashi[1†], Koji Takahashi[1] and Toshinori Kinoshita[1,2*]

[1]Division of Biological Science, Graduate School of Science, Nagoya University, Chikusa, Nagoya, Japan, [2]Institute of Transformative Bio-Molecules (WPI-ITbM), Nagoya University, Chikusa, Nagoya, Japan

Stomata open in response to several environmental stimuli, such as light and low CO_2. Plasma membrane (PM) H^+-ATPase in guard cells plays a pivotal role for light-induced stomatal opening. In contrast, stomata close in response to the dark or plant hormone abscisic acid (ABA). However, molecular mechanisms of stomatal movements remain unclear. To elucidate the molecular mechanism of stomatal movements, we performed a genetic screen based on stomatal aperture-dependent weight decrease of detached leaves from EMS-treated *Arabidopsis thaliana* and isolated a *rapid transpiration in detached leaves 2* (*rtl2*). The *rtl2* mutant showed constitutive open-stomata phenotype with lower leaf temperature. ABA had no effect on stomatal aperture in *rtl2*. The *rtl2* mutant also showed increased stomatal density, severe dwarf phenotype with pale green leaves and dark veins. Map-based analysis of the *RTL2* locus revealed that the *rtl2* mutant possesses a single nucleotide substitution, which induces amino acid substitution Gly162 to Glu in the tryptophan synthase ß subunit 1 (TSB1). The *TSB1* encodes an enzyme in tryptophan (Trp) biosynthetic pathway. Amount of TSB1 protein was drastically reduced in *rtl2* mutant. A different allele of *tsb1* mutant (*tsb1-1*) also showed constitutive open-stomata phenotype with reduced TSB1 protein as in *rtl2*. Analyses of test-crossed plants of *rtl2* and *tsb1-1* showed open-stomata and dwarf phenotypes. These results indicate that a responsible gene for *rtl2* is *TSB1*. We further investigated stomatal phenotype in mutants from Trp biosynthetic pathway, such as *wei2-1 wei7-1*, *trp3-1*, and *tsb2-1*. The *trp3-1* mutant showed significant wider stomatal aperture as well as *tsb1-1*. Trp biosynthetic pathway closely relates to auxin biosynthesis. Then, we investigated auxin responsible genes and found that an expression of *AUR3* was up in *rtl2*. In contrast, auxin had no effect on stomatal aperture in Arabidopsis and the phosphorylation status of PM H^+-ATPase in guard cell protoplasts from *Vicia faba*. In addition, auxin antagonist had no effect on stomatal aperture. Interestingly, *tsb1-1* grown under hydroponic culture system showed normal stomatal aperture by exogenously application of Trp. These results suggest that open stomata phenotype in *tsb1-1* is due to Trp deficiency but not auxin.

KEYWORDS

stomata, guard cell, water loss, tryptophan biosynthetic pathway, tryptophan synthase ß subunit 1, PM H^+-ATPase

Introduction

Stomata in the plant epidermis, surrounded by a pair of guard cells, control gas exchange between the plants and the atmosphere. Opening of the stomata induces both transpiration and CO_2 uptake for photosynthesis. Under drought condition, stomata close in response to the plant hormone abscisic acid (ABA) to prevent water loss (Schroeder et al., 2001; Shimazaki et al., 2007). Diverse external and internal stimuli, such as blue light (BL), red light (RL), the phytotoxin fusicoccin (FC), CO_2, ABA, and microbial elicitors, regulate stomatal aperture (Munemasa et al., 2015; Inoue and Kinoshita, 2017; Ye et al., 2020). It has been demonstrated that stomatal opening contributes photosynthesis, plant growth, and yield (Wang et al., 2014; Toh et al., 2021; Zhang et al., 2021). In the BL-induced stomatal opening, BL photoreceptor phototropins activate plasma membrane (PM) H^+-ATPase through the phosphorylation of C-terminal penultimate residue, threonine (Thr) (Kinoshita and Shimazaki, 1999; Kinoshita et al., 2001). BL-activated PM H^+-ATPase creates an electrochemical gradient of H^+ across the PM and an inside-negative electrical potential of PM that activate inward-rectifying voltage-gated K^+ channels for K^+ influx into guard cells (Schroeder et al., 1987). The K^+ accumulation induces elevation of turgor pressure and opening of stomata (Schroeder et al., 2001; Shimazaki et al., 2007). Several signalling components, a protein kinase BLUE LIGHT SIGNALING1 (BLUS1) (Takemiya et al., 2013), a Raf-like protein kinase BLUE LIGHT-DEPENDENT H^+-ATPASE PHOSPHORYLATION (BHP) (Hayashi et al., 2017), and a Type 1 protein phosphatase (PP1) (Takemiya et al., 2006), mediate the BL signalling pathway in guard cells. RL also induces stomatal opening through the phosphorylation of PM H^+-ATPase penultimate residue, Thr, and activation of PM H^+-ATPase in intact leaves (Ando and Kinoshita, 2018). However, the molecular mechanism of signalling pathway for light-induced stomatal opening remains incompletely understood (Inoue and Kinoshita, 2017).

Tryptophan (Trp) is an essential amino acid for all living organisms, but Trp is not synthesized in animals and some eubacteria. All catalytic enzymes and their encoding genes for Trp biosynthetic pathway have been identified in plants (Radwanski and Last, 1995; Tzin and Galili, 2010). The Trp biosynthesis includes six reaction steps from chorismate to Trp. In the first step, anthranilate synthase (AS) (CE 4.1.3.27) catalyzes a transfer of an amino group of glutamine to chorismate to generate anthranilate and pyruvate. In the second step, anthranilate phosphoribosylanthranilate transferase (PAT) (CE 2.4.2.1) catalyzes conversion of anthranilate and phosphoribosylpyrophosphate into phosphoribosylanthranilate and pyrophosphate. In the third step, phosphoribosylanthranilate isomerase (PAI) (CE 5.3.1.24) catalyzes conversion of phosphoribosylanthranilate into l-(O-carboxyphenylamino)-l-deoxyribulose-5-phosphate (CDRP). In the fourth step, indole-3-glycerol phosphate synthase (IGPS) (EC 4.1.1.48) catalyzes conversion of 1-(O-carboxyphenylamino)-1-deoxyribulose-5-phosphate to indole-3-glycerol phosphate. Trp synthase (TS) (CE 4.2.1.20), α (TSA) and ß (TSB) subunits, is involved in the last two steps. TSA cleaves indole-3-glycerol phosphate to indole and glyceraldehyde-3-phosphate. Finally, TSB catalyzes condensation of indole and serine to produce Trp. Trp biosynthetic pathway closely relates to auxin biosynthesis (Ouyang et al., 2000; Stepanova et al., 2008; Tao et al., 2008; Mashiguchi et al., 2011; Zhao, 2012; Tivendale et al., 2014).

Among them, Trp synthase ß subunit 1 (TSB1) is essential for Trp synthesis in plants; thus, it affects several developmental and physiological responses in plants (Last et al., 1991). Jing et al. (2009) reported that *smo1/trp2-301*, a mutant of *TSB1*, exhibits a reduction of the size of its aerial organs because of the retardation of growth by cell expansion, and that these phenotypes are rescued by addition of Trp. The *trp2* mutants also showed higher endogenous IAA content and increased expression of auxin responsive genes, such as *IAA1*, *IAA5* and *IAA6*. Ursache et al. (2014) reported that *trp2-12* and *trp2-13*, mutants of *TSB1*, showed incomplete vascular tissue development, and found that the expression of most of the HD-ZIPIII genes, which play a crucial role in xylem specification, is down regulated in the *trp2-1*. Wang et al. (2015) showed that *trp2-1*, a mutant of *TSB1*, has higher level of IAA than the wild type probably through the Trp-independent auxin biosynthetic pathway. Liu et al. (2022) reported that TSB1 interacts with ABA metabolism enzyme, ß-glucosidase 1 and mediates regulation of plant growth and abiotic stress responses.

In the previous study, we performed a screen focused on stomatal aperture-dependent of weight decrease of the detached leaves from ethyl methanesulfonate (EMS)-treated *Arabidopsis thaliana* and identifed a *rapid transpiration in detached leaves 1* (*rtl1*) mutant. The *rtl1* mutant showed ABA-insensitive stomatal phenotype and possesses a novel missense mutantion in the Mg-chelatase H subunit (CHLH). It is worthy of note that CHLH affects ABA-induced stomatal closure and inhibition of stomatal opening, but does not act as an ABA receptor (Tsuzuki et al., 2011). In this study, we isolated *rtl2* mutant, which shows open-stomata phenotype. Map-based analysis and genetic analysis strongly indicated that a responsible gene for *rtl2* is *TSB1* involved in Trp biosynthetic pathway. Based on phenotypic and genetic analyzes, we propose that the Trp synthesis pathway has a significant effect on stomatal phenotypes, control of stomatal aperture and density.

Materials and methods

Plant materials and growth conditions

For plant growth on soil, plants were grown under 16-h fluorescent light (50 μmol m^{-2} s^{-1})/8-h dark cycle at 24°C in 55-70% humidity in a growth room. For plant growth on plate followed by on soil, seeds were surface-sterilized and sown on Murashige and Skoog-agar plate supplied with 1% (w/v) sucrose under 16-h fluorescent light (50 μmol m^{-2} s^{-1})/8-h dark cycle. Four-week-old

plants were transferred to soil and grown under 16-h fluorescent light (50 μmol m^{-2} s^{-1})/8-h dark cycle at 24°C in 55-70% humidity in a growth room. *gl1* [Columbia (Col-0), carrying *gl1* mutation] is the background ecotype of an *rtl2* mutant and used as the wild type (WT). We backcrossed *rtl2* with *gl1* three times. The mutants used in this study, *tsb1-1* (SAIL_886_A01), *tsb2-1* (SAIL_598_H05), *trp3-1* (CS8331; Radwanski et al., 1996), *wei2-1 wei7-1* (CS16399; Stepanova et al., 2005) were obtained from the Arabidopsis Biological Resource Center (ABRC) (Ohio State University, Columbus, OH, USA). Col-0 is the background ecotype of these mutants. For plant growth in hydroponic culture, seeds were surface-sterilized and sown on Murashige and Skoog-agar plate as described above. Ten-day-old seedlings were transferred to hydroponic culture system with a nutrient solution (Gibeaut et al., 1997). The solution was constantly replaced every 1 week.

Isolation of the *rtl2* mutant and identification of the *RTL2* locus

Mutant screening based on stomatal aperture-dependent water loss was performed as previously described (Tsuzuki et al., 2011). Briefly, ethyl methanesulfonate (EMS)-treated *gl1* M_2 seeds were germinated and grown on soil. We measured the fresh weight of a detached rosette leaf at 0 and 90 min from each 4-week-old M_2 plant and isolated some *rapid transpiration in detached leaves* (*rtl*) mutants (Tsuzuki et al., 2011). In this study, we investigated an *rtl2* mutant, which shows rapid weight change compared to WT plants. Mapping populations were generated by crossing the *rtl2* mutant with the Landsberg *erecta* (L*er*) accession of *Arabidopsis thaliana*. *RTL2* locus was identified by mapping using simple-sequence length polymorphism (SSLP) and cleaved amplified polymorphism (CAPS) markers from 910 F_2 plants showing dwarf phenotype with pale green leaves and dark veins.

Measurement of stomatal aperture

Stomatal apertures in the isolated epidermis were measured according to the previous method (Inoue et al., 2008) with modifications. The epidermal fragments isolated from overnight dark-adapted 4- to 6-week-old plants or 4- to 6-week-old plants from illuminated growth condition at zeitgeber time (ZT) 4 to 7 were incubated in basal buffer (5 mM MES-BTP, pH 6.5, 50 mM KCl, and 0.1 mM $CaCl_2$). For investigations of light-induced stomatal opening and effect of ABA or auxinole, the epidermal fragments were incubated under light [blue light (Stick-B-32; EYELA, Tokyo, Japan) at 10 μmol m^{-2} s^{-1} superimposed on background red light (LED-R; EYELA, Tokyo, Japan) at 50 μmol m^{-2} s^{-1}] at 24°C in the presence or absence of 20 μM ABA or 10 μM auxinole for 2.5 hr or kept in the dark at 24°C for 2.5 hr. For investigation of the effect of auxin, the epidermal tissues were incubated in the basal buffer for 1.5 hr in darkness to deplete endogenous auxin. Then, the pre-incubated epidermal tissues were treated with 10 μM IAA in the dark for 3 hr. Stomatal apertures were measured microscopically by focusing on the inner lips of stomata in the abaxial epidermis.

For determination of stomatal aperture from test-crossed plants under illuminated growth condition, we used intact leaves for measurements according to the previous method (Toh et al., 2018). Rosette leaves were detached from the plants at ZT 4 to 7. We cut out central areas of the leaves without the midrib were cut out and mounted leaf disc on microscope slides with the abaxial side attached to the cover glass. We obtained Images using an optical microscope (BX43; Olympus) with a charge-coupled device (CCD) camera (DP27; Olympus) with a x20 objective lens (UPlanFL N; Olympus). For getting extended focus imaging, we used cellSens standard software (Olympus) to maximize the number of analyzable focused stomata within each image. Stomatal apertures in the abaxial side were measured on the inner lips of stomata using ImageJ software (http://imagej.nih.gov/ij/).

Determination of leaf temperature using the infrared thermography

Plants were grown on MS plate for 4 weeks and transferred to soil in each pot for 1 week. We measured leaf temperatures using a TVS-500EX infrared thermography instrument (NEC Avio Infrared Technologies Co., Ltd.) and analyzed images using the Avio Thermography Studio software.

Determination of stomatal size and density

Stomatal size and density were determined according to a previous method (Wang et al., 2011).

RT-PCR and quantitative RT-PCR

We purified total RNA from rosette leaves of 4- to 6-week-old plants using an RNeasy Plant Mini Kit (Qiagen). We synthesized 1st-strand cDNAs using a Takara PrimeScript II First Strand cDNA Synthesis Kit (Takara) with oligo$(dT)_{12–18}$ primer. For RT-PCR, we amplified cDNA fragments by PCR using specific primers (Supplementary Table S2). Quantitative RT-PCR (qRT-PCR) was performed as previously described (Kinoshita et al., 2011) using specific primers (Supplementary Table S2). We used *TUB2* (AT5G62690) as an internal standard for PCRs.

Anti-TSB1 antibody

Anti-TSB1 antibody was raised against the recombinant TSB1ΔN, TSB1 protein without chloroplast targeting signal peptide in its N-terminus, as an antigen in a rabbit (Medical & Biological Laboratories). We amplified the *TSB1* DNA fragment from 1st-strand Arabidopsis cDNA by PCR using the specific primers 5′-CGGGATCCGACCCGGCCCTGTGGCAAC-3′ and 5′-CGGGATCCTCAAACATCAAGATATTTAGCCACTGTCTG AAC-3′. We cloned the *TSB1* CDS of 202–1413 bp containing *Bam*HI site at both ends into the *Bam*HI site of the pGEX-2T vector (GE Healthcare) to express as a fusion protein with glutathione S-transferase (GST). The pGEX-2T-TSB1 was transformed into the *E. coli* BL21 strain. The fusion protein (GST-TSB1ΔN) was purified using the glutathione-Sepharose 4B (GE Healthcare). The TSB1ΔN protein was obtained by digestion with thrombin to cut off the GST and used for the immunization as antigen.

Immunoblots

Immunoblot analysis was performed according to the methods described in Hayashi et al. (2010) with modifications. We grinded leaves from 5- to 6-week-old plants using a mortar and pestle in extraction buffer (50 mM MOPS–KOH, pH 7.5, 2.5 mM EDTA, 100 mM NaCl, 1 mM phenylmethylsulfonyl fluoride, 20 μM leupeptin, and 2 mM DTT). Proteins (20 μg) were loaded and separated by SDS-PAGE. We detected TSB1 protein using the polyclonal antibody raised against recombinant TSB1ΔN protein (Anti-TSB1 antibody) in rabbits. We detected the 14-3-3 proteins with the anti-14-3-3 protein (GF14 ø) antibody (Kinoshita and Shimazaki, 1999) as a control. We used the antibodies at a 3,000-fold dilution.

Detections of PM H^+-ATPase protein and phosphorylation status of the penultimate residue, Thr, of PM H^+-ATPase in guard cell protoplasts (GCPs) from *Vicia faba* were performed using anti-H^+-ATPase antibody and anti-pThr antibody, respectively (Hayashi et al., 2010).

Measurement of Tryptophan synthase ß subunit activity

TSB activity was determined according to Greenberg and Galston (1959) with modifications. For measurement in leaf extracts, leaves from 5- to 6-week-old plants were ground in phosphate buffer (0.1 M Potassium phosphate-KOH, pH 8.2, 30% [w/v] Insoluble-Polyvinylpolypyrrolidone [Sigma-Aldrich]) with 212-300 μm glass beads (Sigma-Aldrich) using a mortar and pestle. Then the extract was sonicated and centrifuged at 4 °C (12,000 *g* for 15 min). The supernatant was used as the enzyme source. The supernatant (150–250 μg of protein) was suspended in reaction buffer (50 μl; 80 mM Potassium phosphate-KOH, pH 8.2, 60 mM L-Serine, 200 μM indole, 10 μg/ml pyridoxal phosphate) and reacted at 30 °C for 90 min. The reaction was stopped by the addition of 5 μl of 0.2 M NaOH. To assay for residual unreacted indole, 200 μl of toluene was added to the reaction mixture and then shaken and centrifuged at 1,500 *g* for 15 min. The resulting toluene layer was transferred and mixed with 4 times the volume of Ethanol and twice the volume of Ehrlich's reagent (36 mg/ml *p*-dimethylaminobenzaldehyde, 2.13 M HCl dissolved in Ethanol). After incubation at 25 °C for 30 min, the absorbance at 540 nm was measured and differences of absorbance between before and after the reaction was converted to the disappearance of indole using the standard curve generated with dilution series of indole. For expression of recombinant TSB1ΔN protein, the *TSB1* DNA fragments derived from WT and *rtl2* were cloned into the vector as described above. The recombinant TSB1ΔN proteins were purified using the glutathione-Sepharose 4B (GE Healthcare) and used for measurement of TSB activity.

Isolation of GCPs from *Vicia faba* and auxin treatments

We isolated guard cell protoplasts (GCPs) enzymatically from lower epidermis of leaves from 4- to 6-week-old *Vicia faba* according to a previous method (Hayashi et al., 2021). GCPs in suspension buffer (5mM MES-NaOH [pH 6.0], 10mM KCl, 0.4 M mannitol and 1mM $CaCl_2$) were treated with auxins (IAA, 1-NAA, 2,4-D) and fusicoccin (FC) at 10 μM in the dark for 30 min. Proteins (20 μg) were loaded and separated by SDS-PAGE.

Accession number

ASA1; AT5G05730, ASB1; AT1G25220, AUR3; AT4G37390, IAA1; AT4G14560, IAA24; AT4G14560, SAUR9; AT4G36110, TSA1; AT3G54640, TSB1; AT5G54810, TSB2; AT4G27070, TUB2; AT5G62690.

Results

An *rtl2* mutant exhibited widely opened stomatal phenotype

To elucidate the mechanism of stomatal movement, we have performed a mutant screening based on stomatal aperture-dependent weight loss of detached leaves *via* transpiration using a microbalance (Tsuzuki et al., 2011). In addition to a *rapid transpiration in detached leaves 1* (*rtl1*) mutant (Tsuzuki et al., 2011), we isolated an *rtl2* mutant. The *rtl2* showed rapid weight loss of detached leaves under growth condition. The WT (Col-*gl1*; background plant of the screening) leaf weight decreased to 59% of initial weight for 90 min, whereas the *rtl2*

leaf weight decreased to 2% (Figure 1A). In addition, *rtl2* mutant showed severe dwarf phenotype with pale green leaves and dark veins under soil grown condition (Figure 1B). It is worthy of note that stomatal size and index in *rtl2* and *tsb1-1* were almost comparable to those in background strains. In contrast, stomatal density in *rtl2* and *tsb1-1* were ~30-46% increase compared to that in background strains (Table 1). Furthermore, color of dry seeds from *rtl2* and *tsb1-1* showed a lighter color than background strain seeds (Supplementary Figure 1) (Last et al., 1991).

As shown in Figure 1C, stomata of *rtl2* opened widely compared to WT under illuminated growth condition. We further examined stomatal responses of *rtl2* in detail. The stomata in WT closed in the dark and opened in response to light, and ABA (20 μM) suppressed light-induced stomatal opening (Figure 1D). By contrast, the stomata in *rtl2* opened widely even in the dark and 20 μM ABA had no effect on stomatal aperture. In accord with open-stomata phenotype in *rlt2* mutant, *rtl2* mutant exhibited clear low leaf temperature phenotype under illuminated growth condition (Figure 1E). Average leaf temperature of the *rtl2* mutant was reduced over 3.0°C relative to WT.

Open stomata phenotype is caused by a missense mutation in *TSB1*

To identify the *RTL2* locus, we performed a map-based analysis and found strong linkage the CAPS marker K5F14-1-1 and MBG8-1 in *rtl2* (Figure 2A). According to the Arabidopsis Information

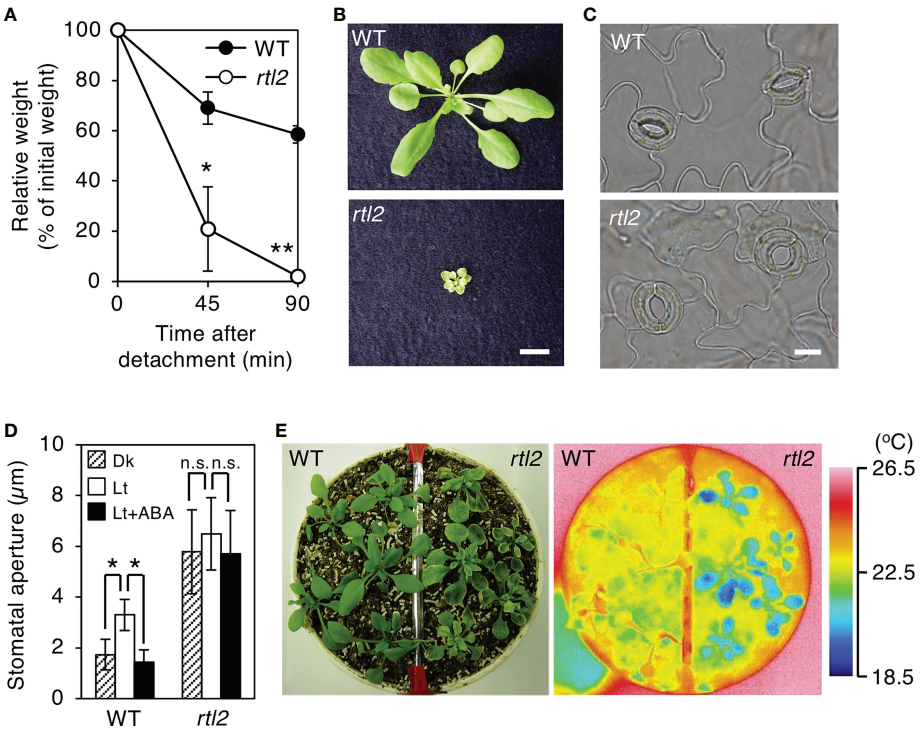

FIGURE 1
Characterization of the *rtl2* mutant. **(A)** Kinetics of the fresh weight change in the detached rosette leaves from 4-week-old WT (closed circles) and *rtl2* (open circles) plants. The relative weights of leaves are presented as a percentage of the initial weight, which was the weight of each rosette leaf immediately after detachment from the plants. Values are means of three independent experiments with SDs. Asterisks indicate a significant difference in leaf weight change relative to WT by Student *t* test; $*P < 0.05$, $**P < 0.01$. **(B)** Four-week-old WT and *rtl2* plants grown on soil. Scale bar = 1 cm. **(C)** Typical stomata in the epidermis of WT and *rtl2* plants under illuminated growth conditions. Scale bar = 10 μm. **(D)** Stomatal aperture of 5-week-old WT and *rtl2* plants. Plants were grown on MS plate for 4 weeks and transferred to soil for 1 week. Epidermal tissues from dark-adapted plants were incubated under light (blue light at 10 μmol m^{-2} s^{-1} superimposed on red light at 50 μmol m^{-2} s^{-1}) with (black; Lt+ABA) or without (white; Lt) 20 μM ABA or kept in the dark (hatched; Dk) for 2.5 hr. Values represent mean ± SD (n = 3); measurement of > 25 stomata in each experiment. Asterisks indicate a significant difference by Student *t* test; $*P < 0.05$. n.s., not significant. **(E)** Thermal image (right) and the corresponding bright-field image (left) of WT and *rtl2* plants. The images of the 5-week-old plants were grown on MS plate for 4 weeks and transferred to soil for 1 week.

TABLE 1 Stomatal size, index and density in plants.

	Stomatal size (μm)	Stomatal index	Stomatal density (mm^{-2})
WT	22.7 ± 0.81	0.267 ± 0.036	94.8 ± 24.2
rtl2	21.9 ± 1.38*	0.254 + 0.057	123 ± 24.8**
Col-0	22.5 ± 1.09	0.243 + 0.033	107 ± 24.3
tsb1-1	22.2 ± 1.13	0.210 + 0.033*	156 ± 54.4**

Stomatal size, index, and density were calculated according to a previous method (Wang et al., 2011). Asterisks indicate a significant statistical difference relative to background plants by Student t test (*P < 0.05, **P < 0.01).

Resource (TAIR) database, *Tryptophan synthase beta-subunit 1* (*TSB1*; AT5G54810) is a candidate gene. Because there is a *TSB1* locus between K5F14-1-1 and MBG8-1 and known *TSB1* mutants showed dwarf phenotype with pale green leaves and dark veins same as in *rtl2* (Figures 1B, 2B) (Jing et al., 2009). Sequence analysis of *TSB1* cDNA from *rtl2* revealed a single nucleotide substitution from G485 to A, which induces a novel missense mutation from Gly162 to Glu (Figure 2B). Next, we investigated the*TSB1* transcript level and protein amount of TSB1 in rosette leaves. As shown in Figure 2C, 2D, the level of *TSB1* transcript was similar to that of the

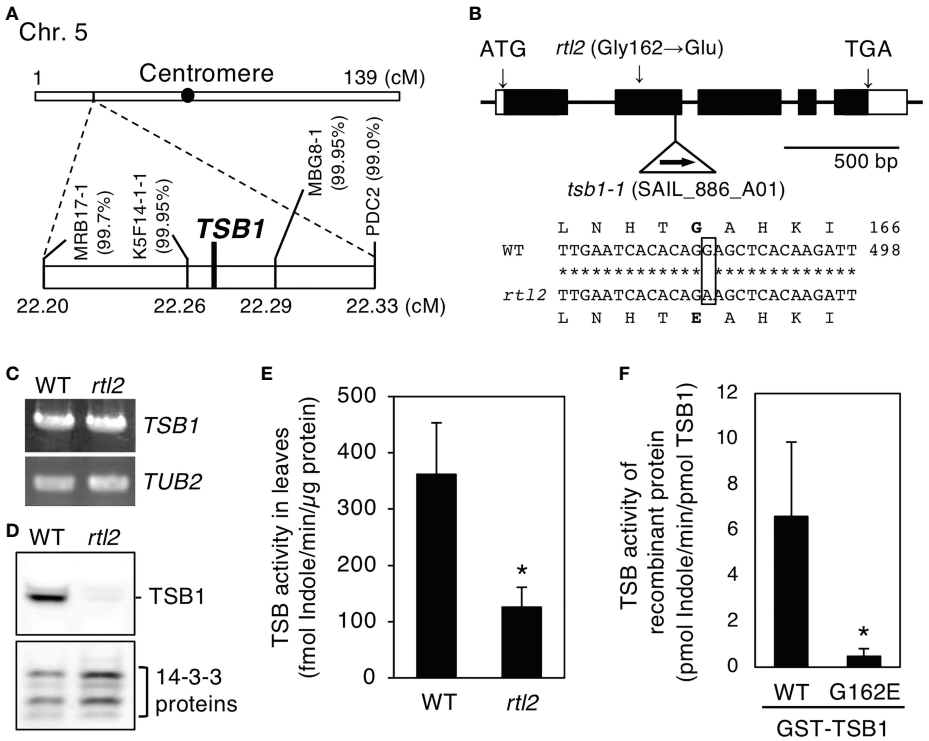

FIGURE 2
Determination of the mutation in the *rtl2* mutant. **(A)** Mapping analysis of the *RTL2* locus. Numbers in parentheses indicate percentages of no recombination in 1820 chromosomes. The *RTL2* locus was close to CAPS marker K5F14-1-1, MBG8-1 and *Tryptophan synthase ß subunit 1* (*TSB1*). **(B)** Schematic representation of the structure of the *TSB1* gene and the position of T-DNA insertion in the *tsb1-1* mutant (upper). Boxes and lines represent exons and introns respectively. The T-DNA insertion was located in 2nd exon of the *TSB1* gene. The position of the amino acid substitution (Gly162 to Glu) in *rtl2* is indicated. The partial sequences of *TSB1* cDNA and the deduced amino acid in WT and *rtl2* are shown (lower). A single nucleotide substitution (G485 to A) is shown by a box. Nucleotide and amino acid numbers are indicated in the right. Asterisks indicate the same nucleotide of the *TSB1* gene in WT and *rtl2*. **(C)** *TSB1* expression analyzed by RT-PCR in WT and *rtl2*. Total RNA was extracted from rosette leaves of 5-week-old plants grown on MS plate for 4 weeks and transferred to soil for 1 week. *TUB2* was amplified as a control. PCRs were performed with 30 cycles for *TSB1* and with 25 cycles for *TUB2*, respectively. **(D)** Immunoblot analysis of TSB1 protein in WT and *rtl2*. Twenty micrograms of protein extracted from rosette leaves of 5-week-old plants was loaded on each lane. The 14-3-3 proteins were detected using anti-14-3-3 antibody as a control. **(E)** TSB activity in rosette leaves of 5-week-old WT and *rtl2*. Values are means of three independent experiments with SDs. Asterisk indicates a significant difference in TSB activity relative to WT by Student *t* test (*$P < 0.05$). **(F)** TSB activity of recombinant TSB1 (WT) and TSB1-G162E. Values are means of three independent experiments with SDs. Asterisk indicates a significant difference in TSB activity relative to WT by Student *t* test (*$P < 0.05$).

WT, whereas the amount of TSB1 protein was significantly decreased in *rtl2*. We further determined the TSB activity in leaf extracts by measuring disappearance of indole. The results showed that *rtl2* has ~35% TSB catalytic activity compared to that of WT (Figure 2E). Reduction of TSB activity in *rtl2* may be caused by not only lower amount of TSB1 protein but also less activity of *rtl2* mutation (Gly162 to Glu in TSB1), because the recombinant TSB1-G162E has only ~7.2% TSB activity compared to that of WT-TSB1 (Figure 2F).

To determine whether *rtl2* is an allele of *tsb1*, a T-DNA insertion mutant *tsb1-1* (SAIL_886_A01) was obtained from ABRC (Figure 2B). The *tsb1-1* showed *rtl2*-like dwarf phenotype with pale green leaves and dark veins (Figure 3A). RT-PCR analysis revealed that *tsb1-1* is a knockout mutant, which results in significant decrease of protein amount in rosette leaves of *tsb1-1* (Figures 3B, C). Stomata of *tsb1-1* also opened widely even in the dark and could not close in response to ABA, suggesting that *TSB1* is responsible for the *rtl2* phenotype (Figure 3D). To confirm this, we have tried to complement the WT *TSB1* genome to *rtl2*, however, we could not obtain the transgenic *rtl2* plants carrying the WT *TSB1* gene under its own promoter, probably due to growth defect of *rtl2* plants. Therefore, we performed test-cross of *rtl2* and *tsb1-1* to show that these are allelic gene. As shown in Figure 4A, F_1-generation plants showed dwarf phenotype with pale green leaves and dark veins same as in *rtl2* and *tsb1-1*, indicating that these are allelic gene. In addition, stomata of F_1-generation plants widely opened under illuminated growth condition (Figure 4B). From these results, we concluded that *TSB1* is responsible for the *rtl2* phenotype.

Mutant of another tryptophan synthetic enzyme *TSA1* also had open stomata phenotype

TSB1 encodes a predominantly expressed Trp synthase ß subunit in Trp biosynthetic pathway, in which Trp is synthesized from chorismate *via* six reaction steps as shown in Figure 5A (Radwanski and Last, 1995; Tzin and Galili, 2010). To investigate whether other Trp biosynthesis enzymes affect stomatal opening, we measured the stomatal aperture of the double mutant of AS, *wei2-1 wei7-1*, single substitution mutant of TSA1, *trp3-1*, and a T-DNA insertion knockout mutant of TSB1 paralog, TSB2 (*tsb2-1*; Supplementary Figure S2). Among the mutants, *trp3-1* showed open stomata phenotype similar to *tsb1-1*, but not in *wei2-1 wei7-1* and *tsb2-1* (Figure 5B).

Auxin treatment did not affect stomatal aperture

Indole-2-glycerol phosphate and Indole are substrates of TSA and TSB respectively. These are thought to be converted to indole-3-acetic-acid (IAA) *via* Trp-independent pathway (Ouyang et al., 2000). Jing et al. (2009) reported that free IAA levels in two *tsb1* alleles, *trp2-1* and *trp2-8*, were elevated and auxin responsive genes were up-regulated in these mutants. To clarify whether IAA contents in *rtl2* is also elevated, we investigated the expression level of some auxin responsive genes, *AUXIN UP REGULATED 3* (*AUR3*), *SMALL AUXIN*

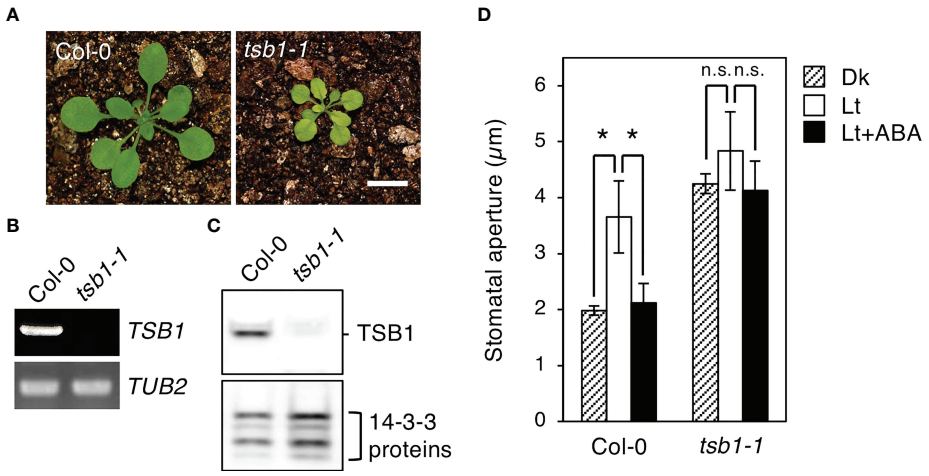

FIGURE 3
Phenotypic analysis of a *TSB1* knockout mutant, *tsb1-1*. **(A)** Five-week-old Col-0 and *tsb1-1* plants. Plants were grown on MS plate for 4 weeks and transferred to soil for 1 week. Scale bar = 1 cm. **(B)** *TSB1* expression analyzed by RT-PCR in Col-0 and *tsb1-1*. Other details are the same as in Figure 2C. **(C)** Immunoblot analysis of TSB1 protein in Col-0 and *tsb1-1*. Other details are the same as in Figure 2D. **(D)** Stomatal aperture of Col-0 and *tsb1-1* plants. Other details are the same as in Figure 1D. Values represent mean ± SD (n = 3); measurement of 35 stomata in each experiment. Asterisks indicate a significant difference by Student *t* test; $^*P < 0.05$. n.s., not significant.

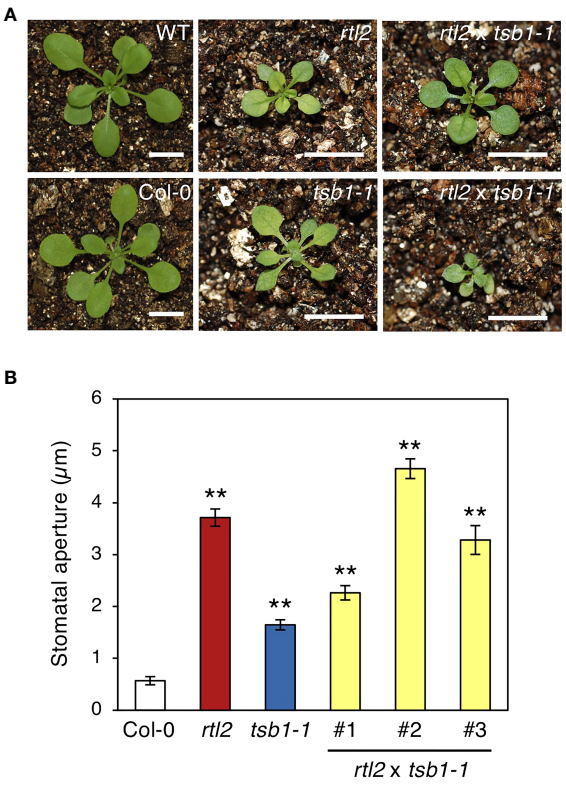

FIGURE 4
Phenotypes of test-crossed plants. **(A)** Five-week-old WT, Col-0, *rtl2*, *tsb1-1* and test-crossed F_1 plants (*rtl2* x *tsb1-1*). Plants were grown on MS plate for 4 weeks and transferred to soil for 1 week. The scale bar represents 1 cm. **(B)** Stomatal aperture of 5-week-old Col-0, *rtl2*, *tsb1-1* and test-crossed F_1 plants (*rtl2* x *tsb1-1*) under illuminated growth condition. Rosette leaves were detached from the plants at ZT4-7 and immediately subjected to measurement of stomatal aperture. Values are means of > 25 stomata with SDs. Asterisks indicate a significant statistical difference relative to Col-0 by Student *t* test (**$P < 0.01$).

UPREGULATED RNA 9 (*SAUR9*), *INDOLE-3-ACETIC ACID INDUCIBLE 1* (*IAA1*) and *INDOLE-3-ACETIC ACID INDUCIBLE 24* (*IAA24*). As shown in Figure 6A, *AUR3* was significantly up-regulated in both *rtl2* and *tsb1-1*, though other auxin responsive genes were not. Given that up-regulation of *AUR3* expression in *tsb1* alleles, we speculated that open stomata phenotype in *rtl2* is caused by elevated levels of auxin. To address the possibility, we first investigated the effect of auxin on stomatal aperture. Incubation of the epidermal tissues with 10 μM IAA in the dark for 3 hr had no effect on stomatal aperture (Figure 6B). Next, we investigated effect of auxins, IAA and synthetic auxins, 1-naphthylacetic acid (1-NAA) and 2,4-dichlorophenoxyacetic acid (2.4-D), on phosphorylation status of the penultimate residue, Thr, of PM H^+-ATPase in guard cell protoplasts (GCPs) from *Vicia faba*, because auxin activates PM H^+-ATPase *via* phosphorylation during auxin-induced hypocotyl elongation (Takahashi et al., 2012; Uchida et al., 2018). However, consistent with a recent report that IAA did not induce phosphorylation of PM H^+-ATPase in guard cells of *Arabidopsis thaliana* (Akiyama et al., 2022), all auxins had no effect on phosphorylation status of PM H^+-ATPase for 30 min, although a fungal toxin fusicoccin (FC) induced phosphorylation of PM H^+-ATPase (Figure 6C). These results suggest that short term treatment of auxin (within 3 hr) has no effect on both stomatal aperture and phosphorylation status of PM H^+-ATPase in guard cells. Furthermore, we found that auxin antagonist, auxinole (Hayashi et al., 2012), did not change the stomatal aperture in *rtl2* and *tsb1-1* (Figure 6D).

Exogenous Trp rescued the phenotypes of *tsb1-1*

To verify whether the open stomata phenotype in *tsb1* mutants is caused by Trp deficiency, L-Tryptophan (L-Trp) was exogenously supplied to *tsb1-1*. We used only *tsb1-1* mutant in this experiment due to less growth of *rtl2* in hydroponic culture. Ten-day-old *tsb1-1* seedlings grown on MS plate were transferred to hydroponic system supplemented with/without 0.25 mM L-Trp for 2-4 weeks. Similar to the previous report (Jing et al., 2009), dwarf and pale green phenotype in *tsb1-1* were partially rescued by exogenous application of L-Trp (Figure 7A). Interestingly, *tsb1-1* showed normal stomatal aperture by application of L-Trp (Figure 7B), suggesting that open stomata phenotype in *tsb1-1* is due to Trp deficiency. On the other hand, under hydroponic culture condition, stomatal density in *tsb1-1* did not show significant differences compared to that in Col-0 and L-Trp application did not change the stomatal density in both Col-0 and *tsb1-1* (Supplementary Table S1). Therefore, Trp deficiency may have no effect on the stomatal density.

Discussion

In this study, we isolated *rapid transpiration in detached leaves 2* (*rtl2*), that exhibited a higher rate of water loss *via* transpiration and clear low leaf temperature phenotype (Figures 1A, E). Detailed analysis of stomatal phenotypes of *rtl2* revealed that constitutive open-stomata phenotype and higher stomatal density contribute rapid transpiration in *rtl2* (Figure 1D, Table 1). Map-based analysis and test-cross with *tsb1-1* revealed that *Tryptophan synthase ß subunit 1* (*TSB1*) is responsible for *RTL2* locus (Figures 2, 3, 4). The missense mutation of TSB1 Gly162 to Glu found in *rtl2* resulted in significantly reduction of TSB activity (Figure 2F). Even though the transcript level of *TSB1* in *rtl2* were comparative to that in WT, amount of TSB1 protein in *rtl2* was significantly reduced (Figures 2C, D). This could be due to active degradation

10.3389/fpls.2022.1011360

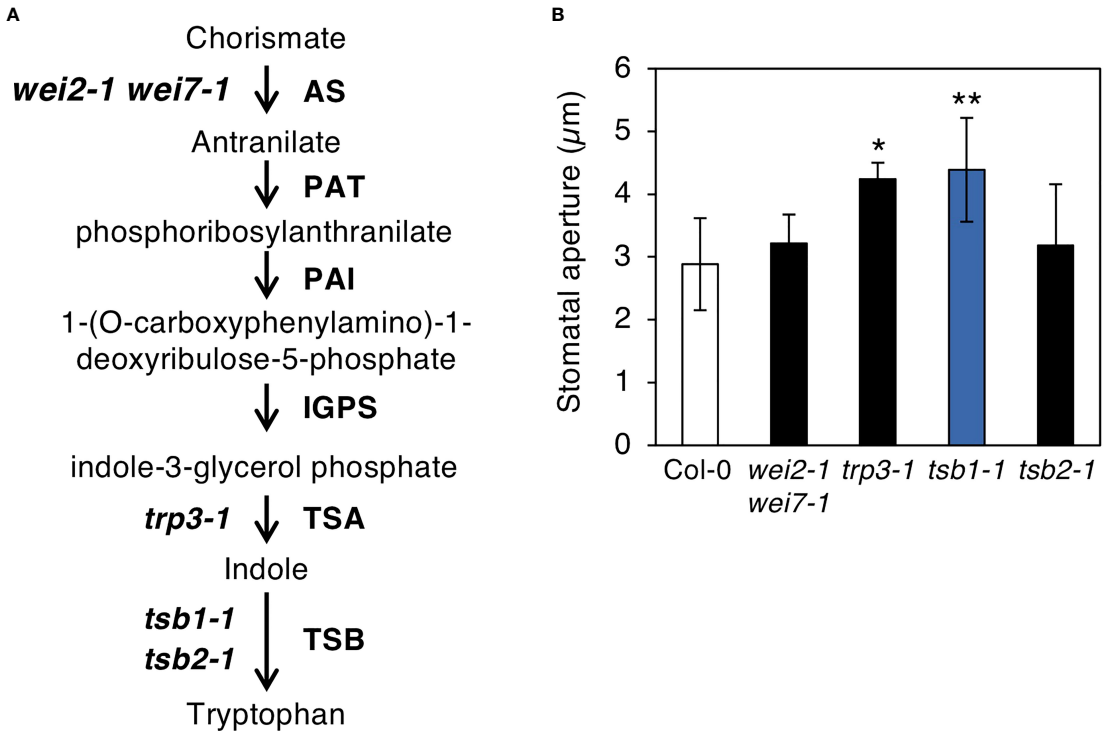

FIGURE 5
Characterization of the mutants related to Tryptophan biosynthetic pathway. **(A)** Tryptophan biosynthetic pathway in *Arabidopsis thaliana*. Tryptophan biosynthetic pathway starting from chorismate are shown with the enzymes of each step (right) and the mutants used in this study (left). AS, anthranilate synthase; PAT, anthranilate phosphoribosylanthranilate transferase; PAI, phosphorybosylanthranilate isomerase; IGPS, indole-3-glycerol phosphate synthase; TSA, tryptophan synthase α subunit; TSB, tryptophan synthase ß subunit. **(B)** Stomatal aperture of Tryptophan biosynthetic mutants under illuminated growth condition. Epidermal tissues were isolated from 5-week-old plants grown on MS plate for 4 weeks and transferred to soil for 1 week at ZT4-7 and immediately subjected to measurement of stomatal aperture. Values represent mean ± SD (n = 3); measurement of > 25 stomata in each experiment Asterisks indicate a significant statistical difference relative to Col-0 by Student *t* test (*$P < 0.05$, **$P < 0.01$).

of mutated TSB1 in *rtl2*. The residual TSB activity in *rtl2*, ~35% of WT, may come from *TSB2*, a paralog of *TSB1* (Figure 2E).

Very recently, Liu et al. (2022) reported that *amiR*-TSB1 lines, which have reduced expression of *TSB1* to 64-73% of wild-type plants, exhibited lower water loss rate from detached leaves and higher survival rate under salt and drought stress compared with wild-type plants. They also found that TSB1 interacts with and inhibits *ß*-glucosidase (BG1), catalyzing the conversion of glucose-conjugated ABA into active ABA. In consistent with this, the ABA contents in *amiR*-TSB1 lines were significantly higher than those in the wild-type. They concluded that TSB1 regulates stress tolerance and the accumulation of ABA *via* repression of BG1 activity. In contrast, we found that stomata in two *tsb1* mutants, *rtl2* and *tsb1-1*, significantly opened even in the dark condition and in the presence of ABA (Figures 1, 3). Thus, since the phenotype related to stomatal aperture is considered to be greatly different between *amiR*-TSB1 lines and *rtl2* and *tsb1-1*, it is possible that *amiR*-TSB1 lines induce salt and drought resistance regardless of stomatal phenotype. Therefore, *rtl2* and *tsb1-1* may exhibit such salt and drought tolerance, it is necessary to investigate the tolerance in *rtl2* and *tsb1-1*. As a point of concern, the amount of protein in *amiR*-TSB1 lines have decreased to 64-73%, while *tsb1-1* used in this study is a complete knockout. In this study, we found that not only *tsb1* mutants but also *trp3-1*, single substitution mutant of *TSA1*, exhibited open-stomata phenotype, whereas Liu et al. (2022) showed stress sensitivities in terms of chlorophyll content in *trp3-1* was similar to those in wild type. In addition, TSA1 did not interact with BG1 in yeast cells. These results suggest that TSB1 may affect stomatal aperture as well as TSA1 without affecting BG1.

Why does the *rtl2* mutant show an open-stomata phenotype compared to WT (Figure 1)? Jing et al. (2009) indicated that the *trp2* mutants showed higher auxin contents in plants. Ouyang et al. (2000) found that IAA contents in *TSA1* mutant, *trp3-1*, was also elevated and proposed Trp-independent IAA biosynthetic pathway, in which IAA is synthesized from IGP and indole. In this study, both *trp3-1* and *tsb1* mutants showed open-stomata phenotype (Figure 5). Stomatal phenotype in *trp3-1* and *tsb1* mutants

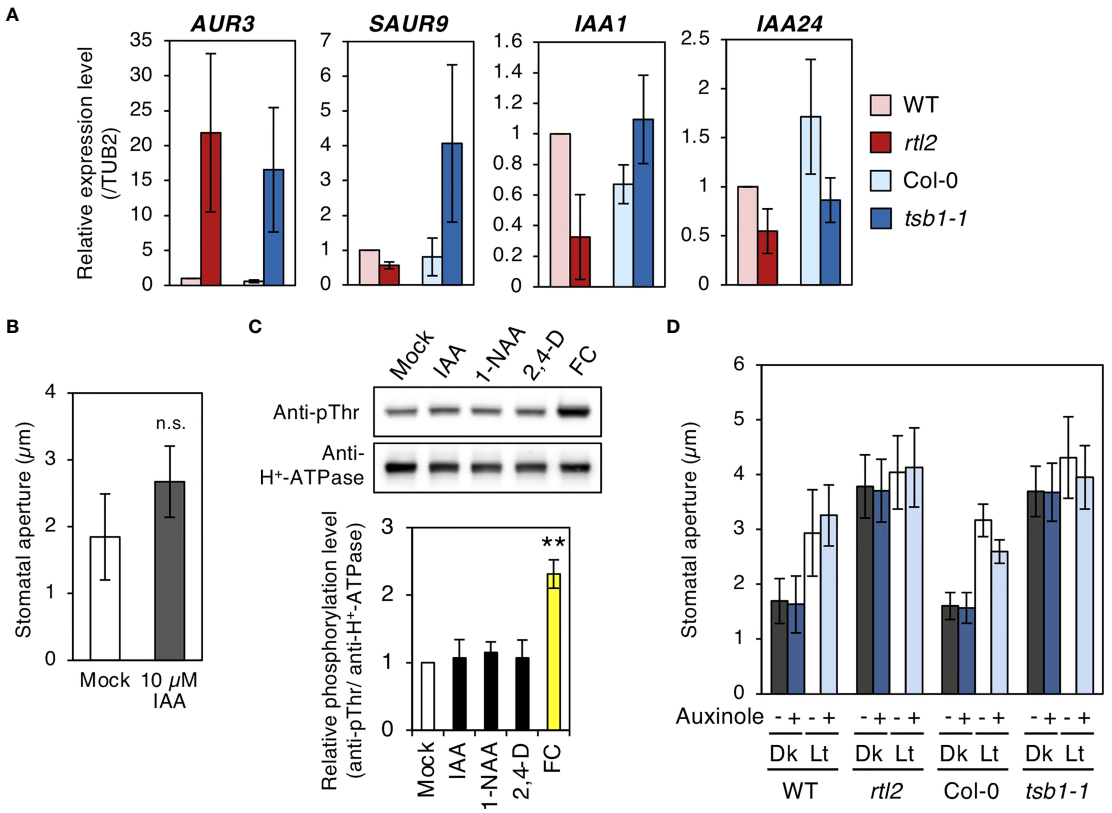

FIGURE 6
Characterizations of *rtl2* and *tsb1-1* mutants and auxin responses in stomata. **(A)** Expression of auxin responsive genes analyzed by qRT-PCR in WT, *rtl2*, Col-0 and *tsb1-1*. Total RNA was extracted from rosette leaves of 5-week-old plants grown on MS plate for 4 weeks and transferred to soil for 1 week. *TUB2* was amplified as a control. **(B)** Effect of exogenous auxin on stomatal aperture in Col-0. Epidermal tissues from dark-adapted 4-week-old plants grown on soil were incubated with 0.25% (v/v) DMSO (Mock) and10 μM IAA in the dark for 3 hr. Values represent mean ± SD (n = 4); measurement of 45 stomata in each experiment n.s. not significant. **(C)** Effect of auxins to the phosphorylation status of the penultimate residue, Thr, of PM H^+-ATPase in guard cell protoplasts (GCPs) from *Vicia faba*. GCPs were incubated with IAA and synthetic auxins (1-NAA, 2,4-D) and fusicoccin (FC) at 10 μM in the dark for 30 min. DMSO was used as a solvent control (Mock). Immunoblots of the phosphorylated PM H^+-ATPase and total PM H^+-ATPase were performed using anti-pThr antibody and anti-H^+-ATPase antibody, respectively. The graph below the blot shows the relative phosphorylation level of PM H^+-ATPase, defined as the ratio of the phosphorylated PM H^+-ATPase to the total quantity of the protein, set as 1 for Mock. The bars represent the means ± SD for three independent experiments. Asterisks indicate a significant statistical difference relative to Col-0 by Student *t* test (**$P < 0.01$). **(D)** Effect of auxin antagonist, auxinole, on light-induced stomatal opening in WT, *rtl2*, Col-0 and *tsb1-1*. Plants were grown on MS plate for 4 weeks and transferred to soil for 1 week. Epidermal tissues from dark-adapted plants were incubated under light (Lt) or kept in the dark (Dk) in the presence or absence of auxinole for 2.5 hr. Other details are the same as in Figure 1D.

showed correlation with IAA contents in these mutants. It has been demonstrated that auxin induces phosphorylation of the penultimate residue, Thr, of PM H^+-ATPase and activation of PM H^+-ATPase in the etiolated seedlings (Takahashi et al., 2012). To confirm the possibility that auxin mediates open-stomata phenotype in *rtl2*, we examined the effect of auxin on stomatal phenotypes. However, short-term treatment of auxin (within 3 hr) had no effect on stomatal aperture and phosphorylation status of PM H^+-ATPase in guard cells (Figure 6B, C). Moreover, auxin antagonist auxinole did not affect the stomatal aperture in *tsb1* mutants (Figure 6D). Further investigations will be needed to investigate effect of long-term treatment of auxin (e.g., for several days) on stomatal opening and the phosphorylation level of PM H^+-ATPase in guard cells. Exogenous application of Trp to *tsb1-1* resulted in suppression of open stomata phenotype in *tsb1-1* (Figure 7B). Although molecular mechanisms are still unclear, but to our knowledge, this is the first report that Trp biosynthetic pathway has significant effect on stomatal aperture in plants.

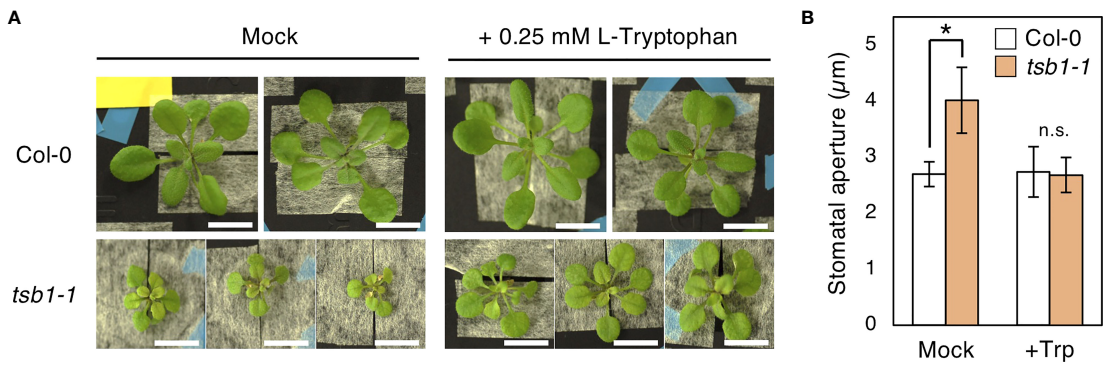

FIGURE 7
Effect of exogenous L-Trp on the phenotypes of *tsb1-1*. **(A)** Four-week-old Col-0 and *tsb1-1* plants grown with or without L-Trp. Plants were grown on MS plate for 10days and transferred to hydroponic system with or without 0.25 mM L-Trp for 2 weeks. Scale bar = 1 cm. **(B)** Stomatal aperture of Col-0 and *tsb1-1* plants grown with or without L-Trp under illuminated growth condition. 10-day-old seedlings germinated on MS plate were transferred to hydroponic system with or without 0.25 mM L-Trp, and were grown for a further 3 to 4 weeks. Epidermal tissues were isolated at ZT4-7 and immediately subjected to measurement of stomatal aperture. Values represent mean ± SD (n = 3); measurement of > 25 stomata in each experiment. Asterisk indicates a significant statistical difference relative to Col-0 by Student *t* test (*$P < 0.05$; n.s., not significant).

Data availability statement

The original contributions presented in the study are included in the article/Supplementary Materials. Further inquiries can be directed to the corresponding author.

Author contributions

MNS, YH and TK designed the experiments. MNS, YH, KT and TK performed experiments. MNS, YH and TK wrote the manuscript. All authors contributed to the article and approved the submitted version.

Funding

This work was supported by Grants-in-Aid for Scientific Research from MEXT (nos. 20H05687 and 20H05910 to T.K.).

Acknowledgments

We are grateful to Mami Uchida (Nagoya University) for technical support.

Conflict of interest

The authors declare that the research was conducted in the absence of any commercial or financial relationships that could be construed as a potential conflict of interest.

Publisher's note

Supplementary material

The Supplementary Material for this article can be found online at: https://www.frontiersin.org/articles/10.3389/fpls.2022.1011360/full#supplementary-material

References

Akiyama, M., Sugimoto, H., Inoue, S. I., Takahashi, Y., Hayashi, M., Hayashi, Y., et al. (2022). Type 2C protein phosphatase clade D family members dephosphorylate guard cell plasma membrane H^+-ATPase. *Plant Physiol.* 188, 2228–2240. doi: 10.1093/plphys/kiab571

Ando, E., and Kinoshita, T. (2018). Red light-induced phosphorylation of plasma membrane H^+-ATPase in stomatal guard cells. *Plant Physiol.* 178, 838–849. doi: 10.1104/pp.18.00544

Gibeaut, D. M., Hulett, J., Cramer, R., and Seemann, J. R. (1997). Maximal biomass of arabidopsis fha/iana using a simple, low-maintenance hydroponic method and favorable environmental conditions. *Plant Physiol.* 115, 317–319. doi: 10.1104/pp.115.2.317

Greenberg, J. B., and Galston, A. W. (1959). Tryptophan synthetase activity in pea seedling extracts. *Plant Physiol.* 34, 489–494. doi: 10.1104/pp.34.5.489

Hayashi, M., Inoue, S. I., Ueno, Y., and Kinoshita, T. (2017). A raf-like protein kinase BHP mediates blue light-dependent stomatal opening. *Sci. Rep.* 7, 1–12. doi: 10.1038/srep45586

Hayashi, Y., Nakamura, S., Takemiya, A., Takahashi, Y., Shimazaki, K. I., and Kinoshita, T. (2010). Biochemical characterization of *in vitro* phosphorylation and dephosphorylation of the plasma membrane H^+-ATPase. *Plant Cell Physiol.* 51, 1186–1196. doi: 10.1093/pcp/pcq078

Hayashi, K. I., Neve, J., Hirose, M., Kuboki, A., Shimada, Y., Kepinski, S., et al. (2012). Rational design of an auxin antagonist of the SCF TIR1 auxin receptor complex. *ACS Chem. Biol.* 7, 590–598. doi: 10.1021/cb200404c

Hayashi, Y., Takahashi, Y., Fukatsu, K., Tada, Y., Takahashi, K., Kuwata, K., et al. (2021). Identification of abscisic acid-dependent phosphorylated basic helix-Loop-Helix transcription factors in guard cells of *Vicia faba* by mass spectrometry. *Front. Plant Sci.* 12. doi: 10.3389/fpls.2021.735271

Inoue, S. I., and Kinoshita, T. (2017). Blue light regulation of stomatal opening and the plasma membrane H^+-ATPase. *Plant Physiol.* 174, 531–538. doi: 10.1104/pp.17.00166

Inoue, S. I., Kinoshita, T., Matsumoto, M., Nakayama, K. I., Doi, M., and Shimazaki, K. I. (2008). Blue light-induced autophosphorylation of phototropin is a primary step for signaling. *Proc. Natl. Acad. Sci. U. S. A.* 105, 5626–5631. doi: 10.1073/pnas.0709189105

Jing, Y., Cui, D., Bao, F., Hu, Z., Qin, Z., and Hu, Y. (2009). Tryptophan deficiency affects organ growth by retarding cell expansion in arabidopsis. *Plant J.* 57, 511–521. doi: 10.1111/j.1365-313X.2008.03706.x

Kinoshita, T., Doi, M., Suetsugu, N., Kagawa, T., Wada, M., and Shimazaki, K. (2001). phot1 and phot2 mediate blue light regulation of stomatal opening. *Nature* 414, 656–660. doi: 10.1038/414656a

Kinoshita, T., Ono, N., Hayashi, Y., Morimoto, S., Nakamura, S., Soda, M., et al. (2011). *FLOWERING LOCUS T* regulates stomatal opening. *Curr. Biol.* 21, 1232–1238. doi: 10.1016/j.cub.2011.06.025

Kinoshita, T., and Shimazaki, K. I. (1999). Blue light activates the plasma membrane H^+-ATPase by phosphorylation of the C-terminus in stomatal guard cells. *EMBO J.* 18, 5548–5558. doi: 10.1093/emboj/18.20.5548

Last, R. L., Bissinger, P. H., Mahoney, D. J., Radwanski, E. R., and Fink, G. R. (1991). Tryptophan mutants in arabidopsis: The consequences of duplicated tryptophan synthase β genes. *Plant Cell* 3, 345–358. doi: 10.1105/tpc.3.4.345

Liu, W.-C., Song, R.-F., Zheng, S.-Q., Li, T.-T., Zhang, B.-L., Gao, X., et al. (2022). Coordination of plant growth and abiotic stress responses by tryptophan synthase β subunit 1 through modulation of tryptophan and ABA homeostasis in arabidopsis. *Mol. Plant* 15, 973–990. doi: 10.1016/j.molp.2022.04.009

Mashiguchi, K., Tanaka, K., Sakai, T., Sugawara, S., Kawaide, H., Natsume, M., et al. (2011). The main auxin biosynthesis pathway in arabidopsis. *Proc. Natl. Acad. Sci. U. S. A.* 108, 18512–18517. doi: 10.1073/pnas.1108434108

Munemasa, S., Hauser, F., Park, J., Waadt, R., Brandt, B., and Schroeder, J. I. (2015). Mechanisms of abscisic acid-mediated control of stomatal aperture. *Curr. Opin. Plant Biol.* 28, 154–162. doi: 10.1016/j.pbi.2015.10.010

Ouyang, J., Shao, X., and Li, J. (2000). Indole-3-glycerol phosphate, a branchpoint of indole-3-acetic acid biosynthesis from the tryptophan biosynthetic pathway in *Arabidopsis thaliana*. *Plant J.* 24, 327–333. doi: 10.1046/j.1365-313X.2000.00883.x

Radwanski, E. R., Barczak, A. J., and Last, R. L. (1996). Characterization of tryptophan synthase alpha subunit mutants of *Arabidopsis thaliana*. *Mol. Gen. Genet.* 253, 353–361. doi: 10.1007/s004380050331

Radwanski, E. R., and Last, R. L. (1995). Tryptophan biosynthesis and metabolism: Biochemical and molecular genetics. *Plant Cell* 7, 921–934. doi: 10.2307/3870047

Schroeder, J. I., Allen, G. J., Hugouvieux, V., Kwak, J. M., and Waner, D. (2001). Guard cell signal transduction. *Annu. Rev. Plant Biol.* 52, 627–658. doi: 10.1146/annurev.arplant.52.1.627

Schroeder, J. I., Raschke, K., and Neher, E. (1987). Voltage dependence of k^+ channels in guard-cell protoplasts. *Proc. Natl. Acad. Sci. U. S. A.* 84, 4108–4112. doi: 10.1073/pnas.84.12.4108

Shimazaki, K. I., Doi, M., Assmann, S. M., and Kinoshita, T. (2007). Light regulation of stomatal movement. *Annu. Rev. Plant Biol.* 58, 219–247. doi: 10.1146/annurev.arplant.57.032905.105434

Stepanova, A. N., Hoyt, J. M., Hamilton, A. A., and Alonso, J. M. (2005). A link between ethylene and auxin uncovered by the characterization of two root-specific ethylene-insensitive mutants in arabidopsis. *Plant Cell* 17, 2230–2242. doi: 10.1105/tpc.105.033365

Stepanova, A. N., Robertson-Hoyt, J., Yun, J., Benavente, L. M., Xie, D. Y., Doležal, K., et al. (2008). TAA1-mediated auxin biosynthesis is essential for hormone crosstalk and plant development. *Cell* 133, 177–191. doi: 10.1016/j.cell.2008.01.047

Takahashi, K., Hayashi, K. I., and Kinoshita, T. (2012). Auxin activates the plasma membrane H^+-ATPase by phosphorylation during hypocotyl elongation in arabidopsis. *Plant Physiol.* 159, 632–641. doi: 10.1104/pp.112.196428

Takemiya, A., Kinoshita, T., Asanuma, M., and Shimazaki, K. I. (2006). Protein phosphatase 1 positively regulates stomatal opening in response to blue light in *Vicia faba*. *Proc. Natl. Acad. Sci. U. S. A.* 103, 13549–13554. doi: 10.1073/pnas.0602503103

Takemiya, A., Sugiyama, N., Fujimoto, H., Tsutsumi, T., Yamauchi, S., Hiyama, A., et al. (2013). Phosphorylation of BLUS1 kinase by phototropins is a primary step in stomatal opening. *Nat. Commun.* 4, 2094. doi: 10.1038/ncomms3094

Tao, Y., Ferrer, J.-L., Ljung, K., Pojer, F., Hong, F., Long, J. A., et al. (2008). Rapid synthesis of auxin *via* a new tryptophan-dependent pathway is required for shade avoidance in plants. *Cell* 133, 164–176. doi: 10.1016/j.cell.2008.01.049

Tivendale, N. D., Ross, J. J., and Cohen, J. D. (2014). The shifting paradigms of auxin biosynthesis. *Trends Plant Sci.* 19, 44–51. doi: 10.1016/j.tplants.2013.09.012

Toh, S., Inoue, S., Toda, Y., Yuki, T., Suzuki, K., Hamamoto, S., et al. (2018). Identification and characterization of compounds that affect stomatal movements. *Plant Cell Physiol.* 59, 1568–1580. doi: 10.1093/pcp/pcy061

Toh, S., Takata, N., Ando, E., Toda, Y., Wang, Y., Hayashi, Y., et al. (2021). Overexpression of plasma membrane H^+-ATPase in guard cells enhances light-induced stomatal opening, photosynthesis, and plant growth in hybrid aspen. *Front. Plant Sci.* 12. doi: 10.3389/fpls.2021.766037

Tsuzuki, T., Takahashi, K., Inoue, S.i., Okigaki, Y., Tomiyama, M., Hossain, M. A., et al. (2011). Mg-chelatase H subunit affects ABA signaling in stomatal guard cells, but is not an ABA receptor in *Arabidopsis thaliana*. *J. Plant Res.* 124, 527–538. doi: 10.1007/s10265-011-0426-x

Tzin, V., and Galili, G. (2010). The biosynthetic pathways for shikimate and aromatic amino acids in *Arabidopsis thaliana*. *Arab. B.* 8, e0132. doi: 10.1199/tab.0132

Uchida, N., Takahashi, K., Iwasaki, R., Yamada, R., Yoshimura, M., Endo, T. A., et al. (2018). Chemical hijacking of auxin signaling with an engineered auxin-TIR1 pair. *Nat. Chem. Biol.* 14, 299–305. doi: 10.1038/nchembio.2555

Ursache, R., Miyashima, S., Chen, Q., Vatén, A., Nakajima, K., Carlsbecker, A., et al. (2014). Tryptophan-dependent auxin biosynthesis is required for HD-ZIP III-mediated xylem patterning. *Dev.* 141, 1250–1259. doi: 10.1242/dev.103473

Wang, B., Chu, J., Yu, T., Xu, Q., Sun, X., Yuan, J., et al. (2015). Tryptophan-independent auxin biosynthesis contributes to early embryogenesis in arabidopsis. *Proc. Natl. Acad. Sci. U. S. A.* 112, 4821–4826. doi: 10.1073/pnas.1503998112

Wang, Y., Noguchi, K., Ono, N., Inoue, S. I., Terashima, I., and Kinoshita, T. (2014). Overexpression of plasma membrane H^+-ATPase in guard cells promotes light-induced stomatal opening and enhances plant growth. *Proc. Natl. Acad. Sci. U. S. A.* 111, 533–538. doi: 10.1073/pnas.1305438111

Wang, Y., Noguchi, K., and Terashima, I. (2011). Photosynthesis-dependent and -independent responses of stomata to blue, red and green monochromatic light: Differences between the normally oriented and inverted leaves of sunflower. *Plant Cell Physiol.* 52, 479–489. doi: 10.1093/pcp/pcr005

Ye, W., Munemasa, S., Shinya, T., Wu, W., Ma, T., Lu, J., et al. (2020). Stomatal immunity against fungal invasion comprises not only chitin-induced stomatal closure but also chitosan-induced guard cell death. *Proc. Natl. Acad. Sci. U. S. A.* 117, 20932–20942. doi: 10.1073/pnas.1922319117

Zhang, M., Wang, Y., Chen, X., Xu, F., Ding, M., Ye, W., et al. (2021). Plasma membrane H^+-ATPase overexpression increases rice yield *via* simultaneous enhancement of nutrient uptake and photosynthesis. *Nat. Commun.* 12. doi: 10.1038/s41467-021-20964-4

Zhao, Y. (2012). Auxin biosynthesis: A simple two-step pathway converts tryptophan to indole-3-Acetic acid in plants. *Mol. Plant* 5, 334–338. doi: 10.1093/mp/ssr104

frontiers | Frontiers in Plant Science

TYPE Mini Review
PUBLISHED 01 December 2022
DOI 10.3389/fpls.2022.1060018

OPEN ACCESS

EDITED BY
Valya N. Vassileva,
Bulgarian Academy of Sciences,
Bulgaria

REVIEWED BY
Mateusz Majda,
Université de Lausanne, Switzerland

*CORRESPONDENCE
Feng Zhao
feng.zhao@nwpu.edu.cn
Yuchen Long
yuchen.long@nus.edu.sg

SPECIALTY SECTION
This article was submitted to Plant Development and EvoDevo, a section of the journal Frontiers in Plant Science

RECEIVED 02 October 2022
ACCEPTED 21 November 2022
PUBLISHED 01 December 2022

CITATION
Zhao F and Long Y (2022) Mechanosensing, from forces to structures.
Front. Plant Sci. 13:1060018.
doi: 10.3389/fpls.2022.1060018

Mechanosensing, from forces to structures

Feng Zhao[1,2]* and Yuchen Long[3,4]*

[1]Collaborative Innovation Center of Northwestern Polytechnical University, Shanghai, China,
[2]School of Ecology and Environment, Northwestern Polytechnical University, Xi'an, Shaanxi, China,
[3]Department of Biological Sciences, The National University of Singapore, Singapore, Singapore,
[4]Mechanobiology Institute, The National University of Singapore, Singapore, Singapore

Sessile plants evolve diverse structures in response to complex environmental cues. These factors, in essence, involve mechanical stimuli, which must be sensed and coordinated properly by the plants to ensure effective growth and development. While we have accumulated substantial knowledge on plant mechanobiology, how plants translate mechanical information into three-dimensional structures is still an open question. In this review, we summarize our current understanding of plant mechanosensing at different levels, particularly using Arabidopsis as a model plant system. We also attempt to abstract the mechanosensing process and link the gaps from mechanical cues to the generation of complex plant structures. Here we review the recent advancements on mechanical response and transduction in plant morphogenesis, and we also raise several questions that interest us in different sections.

KEYWORDS

morphogenesis, mechano-sensation, mechano-heterogeneity, mechano-transduction, arabidopsis

Introduction

Plants, like other living organisms, are constantly exposed to various stimuli from their environments, including mechanical stimuli. Being relatively sessile compared to animals, plants have evolved different strategies in response to these stimuli. The mechanical stimuli that affect plants could be classified into two types: contact (e.g. rain, wind, touch by another organism, etc.), and non-contact (e.g. gravity, electromagnetic force, etc.) forces. Whatever the source of stimuli, plants do not only passively adapt to the outside 'risks', but rather actively respond to these stimuli by incorporating their intrinsic machinery to reproducibly shape themselves, and in turn sculpt the ecosphere.

Morphogenesis is a multiscale process, involving complex feedback between genetic, biochemical and biomechanical regulations. Plant cells cannot move as they are constrained by rigid extracellular matrices or "cell walls". Thus, plant morphogenesis

mainly depends on growth regulations, specifically in growth rates and directions. The force that drives growth is ultimately generated by turgor pressure, which is borne and harnessed by the cell wall. The plant primary cell wall is a complex amalgamation of various polysaccharides, glycoproteins, and water, and is known for its remarkable properties to both withstand mechanical forces and being pliable to grow. The design principle behind such property has recently been intensively reviewed by Cosgrove (2022).

During growth, the walls yield to the mechanical stresses caused by turgor pressure, allowing the cells to change their shape. Cell wall extensibility and stiffness are found to be associated with growth rates, and growth direction is often found regulated by wall anisotropy. Good examples are the largely anisotropic cell wall stiffness patterns in the elongating *Arabidopsis* hypocotyl (Peaucelle et al., 2015) versus the largely isotropic cell walls of the organ primordia in the *Arabidopsis* shoot apical meristem (SAM) (Sassi et al., 2014). Specific cell shapes in turn prescribe specific stress patterns, which could be sensed by cells. This "mechanical feedback" between force and shape has been well-known to channel several morphological events (Hamant et al., 2008; Hervieux et al., 2016; Zhao et al., 2020; Trinh et al., 2021). Additionally, thanks to the heterogeneous property of cell wall mechanics, the stress intensity and direction appear very noisy at the tissue or even larger scale. Given the plant cells are connected by the cell-cell adhesion and plasmodesmata, the local mechano-heterogeneity could be sometimes buffered or oppositely amplified (Uyttewaal et al., 2012; Hong et al., 2018). How do plants coordinate the fluctuations coming from external and internal mechanical stimuli and reproduce robust structures? To discuss this complex issue, we will first look at how plants sense external cues.

Mechanical sensation– from external to internal signals

Touch

Touch is a contact force. In theory, wind, rain, hail, tides, and touch by other organisms should all trigger touch responses. Hence, the reaction to touching is very general and complex in plants. In some plants, the touch response could be very fast (within 1 second), and it is usually associated with specialized structures. For example, the trigger hairs on the Venus Flytrap's leaves and the motor cells of *Mimosa pudica* are well-known structures for sensing and conducting fast responses. Similarly, the Arabidopsis leaf trichomes are also reported as fast touch signal transduction sensors (Matsumura et al., 2022).

How do plants sense touch? Often, the site of force sensing can be less defined, as demonstrated by experiments of brushing (Jensen et al., 2017), wounding (Hamant et al., 2008), stretching and compressing (Robinson and Kuhlemeier, 2018). Other touch responses may involve specialized structures mentioned above. For example, hair-like structures have high aspect ratios (length: diameter) and are easy to bend, the causal longitudinal strain perception is known critical for touch sensitivity (Seale et al., 2018). At the molecular level, several mechanisms have been proposed. One hypothesis suggests squeeze-generated cytosolic stream is essential for the perception of touch, evidenced by the moving of organelles upon stimulations (Chehab et al., 2009). A second hypothesis suggests stretch-activated channels are responsible for triggering touch sensing, where touch-induced bending may trigger asymmetric stretching on the outside and the inside of the bend. This idea is further supported by a recent study showing the expression of mechanosensitive ion channels in the Venus flytrap trigger hairs (Procko et al., 2021). The third possibility suggests that touch results in the perturbation of the cell wall-plasma membrane-cytoskeleton continuum (Chehab et al., 2009).

Touch simultaneously induces a deformation of the plant, or strain, and a stress pattern associated to it. At the cellular level, how strain and stress are sensed upon touching is still poorly understood (Fruleux et al., 2019). Periodic touch stimuli could lead to altered plant growth, like reduced elongation, excess lateral expansion of stems, and delayed flowering. This phenomenon was first coined by Mark Jaffe (Jaffe, 1973) as thigmomorphogenesis, which is a relatively slow process over days to weeks. It has been known for a long time that, many touch-inducible genes were associated with intrinsic mechanical responses, such as Ca^{2+} signaling (like calmodulin-like, CML genes), hormones (like ethylene), and cell wall metabolism (like xyloglucan endotransglucosylase/hydrolase, XTH genes) (Braam, 2005). Recent research nicely presents a link from external touching to internal signaling pathway, showing plants incorporate ethylene-dependent pectin degradations to tune their own shape (Wu et al., 2020).

Gravity

Compared to touch, gravity is a non-contact force. How plants react to gravity is a long-standing biological question. When we talk about gravity response, we usually discuss growth directionality relative to the gravity vector, alias gravitropism. Gravitropism is a complex process, which could be simplified into three stages: perception, signaling transduction, and bending. Gravity is believed to be mainly sensed within specific cell types: columella in the root, and endodermis in the shoot (Kawamoto and Morita, 2022). In the classical starch-statolith hypothesis (Sack, 1997), the direction of gravity is proposed to be sensed by the sedimentation of statoliths (starch-filled amyloplasts) in columella and endodermal cells, where the weight of statolith is either sensed by the cell edge or cytoskeleton (e.g. Perbal and Driss-Ecole, 2003; Leitz et al., 2009). Recent studies have revealed

the complexity of statolith movement, showing that the statoliths behave more like an active liquid than a granular material (Bérut et al., 2018), and that shoot bending is insensitive to a range of gravity intensities artificially applied by centrifugation but to the inclination angles between the shoot and the gravitational vector (Chauvet et al., 2016). Contrarily, another series of hypotheses (including the gravitational pressure hypothesis (Staves, 1997); tensegrity hypothesis (Ingber, 1997), etc.) suggested that gravity is sensed generally by all cell types, and the cell wall-plasma membrane-cytoskeleton continuum can act as a force-transmission scaffold to transduce mechanical signals into biochemical response.

Upon gravity sensing, several biochemical signal transductions are activated. Among these signals auxin is prominent in modulating differential growth and organ bending (Takahashi et al., 2021). Gravitropic bending is actually a biphasic process: the first phase is curving towards gravity axis, the second phase is a straightening process called autotropism (Bastien et al., 2013). Intriguingly, the second decurving process is gravity-independent. Recent research shows that actin cables in stem fiber cells perform as plant posture sensors. This intrinsic geometric sensing is essential for gravitropism (Okamoto et al., 2015; Moulia et al., 2021).

Mechano-heterogeneity

In multicellular plants, cells are glued together to form a continuity (Atakhani et al., 2022). However, the mechanical response for each cell is not necessarily homogeneous. Heterogeneity is an intrinsic property of the biological system, spanning all aspects from molecular to organism levels. Therefore, how a robust order is built up during plant morphogenesis is a fascinating question.

Cell wall heterogeneity

Being a fiber-enforced complex structure, the plant cell wall is far from homogenous. Several key compounds and structures in the cell wall have been proposed to mediate its physical properties during morphogenesis. For example, the stiff cellulose microfibrils can be randomly arranged or aligned into directional arrays. Microfibril anisotropy is thought to be laid down primarily during synthesis by the cellulose synthase complex (CSC) tracing along existing microfibrils or the underlying cortical microtubule (CMT), which were shown to align to the direction of the principal tensile stress (Hamant et al., 2008; Chan and Coen, 2020). Anisotropic microfibril arrays can then fortify cell walls in the same direction to restrict growth, biasing growth anisotropy in the perpendicular direction (Jonsson et al., 2022). Pectin forms matrices in the cell wall, and its methylesterification state and binding to Ca^{2+} can modulate the matrix stiffness to modulate cellular growth (Du et al., 2022). Recently, it was proposed that pectin can form nanofilaments, which are local heterogeneities of methylated/demethylated pectin foci, and their unequal swelling may contribute to the undulated shape of Arabidopsis pavement cells (Haas et al., 2020).

Cell wall synthesis and modifications are highly local during development (Dauphin et al., 2022), which implies that cell wall mechanical properties can vary spatiotemporally. Indeed, direct mechanical measurements revealed that cell wall moduli, a measure of material stiffness, is highly patchy from subcellular to tissue levels (reviewed by Hong et al. (2018)). One may expect such "noisy" cell wall patterns should introduce growth heterogeneity and reduce organ shape reproducibility. Surprisingly, however, plants may alternate the stiff and soft patches over time by "spatiotemporal averaging", as proposed in the Arabidopsis sepal (Hong et al., 2016). Long-range coordination between patches dampens local variability, but counterintuitively reduces the effect of the "spatiotemporal averaging, thereby reducing organ shape reproducibility (Hong et al., 2016). This example demonstrates how local mechanical heterogeneity may contribute to global shape robustness.

The biochemical reactions between wall polymers are proposed to account for cell wall's macroscopic mechanical properties (Zhang et al., 2021; Dumais, 2021). These reactions also occur over time, and together with the laminar deposition of new cell wall materials, may create gradients of stress and strain on top of the patchiness along the thickness of the wall (Lipowczan et al., 2018). One may picture this as a "fractal of heterogeneity": existing patchy cell wall expands differentially and gets larger, and a new layer of cell wall with smaller patches is added underneath the previous layer, and repeats. Over time, this temporal accumulation can lead to heterogeneity on many lengthscales, which may contribute to the different levels of local growth variability and long-range coordination in plant tissues (Fruleux and Boudaoud, 2021).

Heterogeneity arising from cell-cell interaction

Arabidopsis pavement cells acquire interlocked jigsaw shapes, generated by coordinated, heterogeneous growths within and between the cells (Elsner et al., 2018). Besides the well-established molecular pathways involving auxin and Rho GTPases, biomechanical heterogeneity has been considered as another candidate for shape generation [reviewed by Liu et al. (2021)]. The aforementioned mechanical feedback theory can explain shape acquisition for single pavement cells (Sampathkumar et al., 2014; Sapala et al., 2018), particularly in reinforcing and amplifying initial minor undulations of the cell. However, pavement cells are not isolated, and one cell's lobe must match its neighbor's neck. It was found that anticlinal cell

walls between two neighboring pavement cells can have asymmetric pectin deposition and different moduli, which precedes lobe-neck formation and would lead to bending either under tension or when pectin expands upon demethylation (Majda et al., 2017; Haas et al., 2020). Another study proposes that mechanical asymmetry in anticlinal walls is not sufficient for pavement cell shape, and stress pattern in the outer periclinal wall is further required to generate the matching puzzle shapes of the pavement cells: by including periclinal walls in mechanical simulations, turgor pressure may cause the cell edge to buckle. The resulting stress heterogeneity may initiate local cytoskeleton reorganization, which will promote lobe-neck formation (Bidhendi and Geitmann, 2019). The attractive part of this model is that, the regular wavelength of the buckling may emerge from cell geometry and mechanical properties like bending stiffness, potentially giving rise to predictable heterogeneity that contributes to complex cell shape formation without initial prepatterning. All these, coupled with local growth heterogeneity and the microtubule-CSC-mediated mechanical feedback, likely underlie the generation of the convoluted pavement cell geometry (Belteton et al., 2021). In a more complex three-dimensional context, a recent model suggested that different mechanical feedback activity in inner and outer cell walls of laminar organ primordia ensures the cortical microtuble-mediated growth anisotropy for organ flattening (Zhao et al., 2020).

Other kinds of mechanical heterogeneity can also emerge from tissue arrangements. For example, cell arrangements can contribute to heterogeneity in apparent stiffness on both cell and tissue levels (Mosca et al., 2017; Majda et al., 2022). Turgor pressure, which was often believed to be homogenous between plant cells connected by plasmodesmata, was recently demonstrated to be heterogeneous in the epidermis of Arabidopsis shoot apical meristem (SAM). Unlike the heterogeneity of cell wall moduli, which appears random, turgor pressure level anticorrelates with cell size and cell neighbor number in the epidermis (Long et al., 2020). This pressure pattern is reminiscent of the pressure distribution in soap bubbles (Weaire and Hutzler, 2001), which emerges from cell geometry and topology. This, and the buckling theory above, hint that biomechanical variability may not always be random; the pattern may be predictable, and they may serve as the symmetry-breaking event for subsequent growth patterning. For further discussion on variability versus stochasticity, see Long and Boudaoud (2019).

Mechanical signaling transduction

Considering all challenges posed above, how is stress or strain being sensed by plants, and what's the molecular mechanism behind? In the last decades, we accumulated substantial knowledge about mechanical signaling transductions. Exploring the underlying mechanism may help us to get a better understanding of how plants react to forces.

Mechano-sensors

A plant cell could be conceptually described as a plasma membrane (PM) wrapped water balloon constrained by the rigid cell wall. As mentioned above, cell wall is the main load-bearing component in a plant cell, and the trigger for cell wall mechanical responses could be stress, strain, or both (Fruleux et al., 2019). At the molecular level, a large protein family–receptor-like kinase (RLK) is generally thought to be important for cell wall mechano-sensing. The most well-studied RLKs in mechano-transduction are FERONIA (FER) and THESEUS1 (THE1). FER is multifunctional. For instance, FER is a negative regulator in touch response (Darwish et al., 2022), whereas actively regulates the F-actin mediated PIN polar localization in gravity response (Dong et al., 2019). Interestingly, FER could interact with pectin to activate ROP GTPase and thus regulates pavement cell morphogenesis (Tang et al., 2022; Lin et al., 2022), and also contributes to the mechanical sensing in shoot morphogenesis in a microtubule-independent manner (Malivert et al., 2021). By contrast, THE1 is first identified as a wall integrity sensor by pharmacological screen, and recently reported to be responsible for coordinating changes in turgor pressure and cell wall stiffness (Bacete et al., 2022).

In normal conditions, the rigid cell wall resists the internal turgor pressure and reaches an equilibrium. In definition, turgor is the force within the cell that pushes the plasma membrane against the cell wall. The turgor thus must be surveilled constantly in order to keep the wall and membrane integrity. Indeed, a class of proteins named mechanosensitive (MS) ion channels is important for membrane tension perception. For example, Ca^{2+} channels like OSCA relies on tension sensing and mediates osmosensing in Arabidopsis (Yuan et al., 2014), and intrinsically disordered region (IDR) proteins like AtLEA4 are important for the response to increased osmolarity (Cuevas-Velazquez et al., 2021). For a detailed review on osmotic sensing, referred to Gorgues et al. (2022).

Whereas the importance of cell wall and PM in mechano-sensing is obvious, more and more evidence supports the rational existence of a physical continuum from cell wall to PM, cytoskeletons, and even internal organelles (Lang et al., 2004; Fal et al., 2017; Hamant et al., 2019; Lee et al., 2019; Yoneda et al., 2020; Goswami et al., 2020a; Goswami et al., 2020b; Fal et al., 2021; Schneider et al., 2021; Codjoe et al., 2022; Radin et al., 2022). Once the force transmission chain is a continuum at the cellular level, where are the hotspots for the connection among different compartments is still an open question.

In theory, the propagation of force is very fast in stiff tissues. Thus, mechanical forces could reasonably act as long-distance signals to cooperate plant growth and morphogenesis at tissue or

even organ level. On such a larger scale, cells are connected *via* plasmodesmata and cell-cell adhesions. Interestingly, plasmodesmata and cell adhesions are recently reported as important components for the coordination of tensile stress and tissue patterning at the supracellular level (Verger et al., 2018; Hernández-Hernández et al., 2020). While supracellular mechanical signaling has been shown to be important for plant growth and morphogenesis (Zhao et al., 2018; Long et al., 2020; Moulia et al., 2021; Trinh et al., 2021), how the cellular mechano-sensing is coordinated at a larger scale is still poorly understood.

Signaling transduction

Force transduction must include the interaction with chemical signals. Recently, some nexuses of force and chemical signaling transduction are emerging. Ca^{2+}-mediated signaling, hormones (such as auxin, ethylene, JA, GA), ROS, and immune response are all involved for example in touch response (Li et al., 2019; Wu et al., 2020; Darwish et al., 2022; Matsumura et al., 2022). A clear picture emerges: once the machinal signals arrive, there must be a very fast response (like electric and Ca^{2+} signaling) to the stimuli, (e.g., Nguyen et al., 2018; Hagihara et al., 2022), after that, the components related to energy, material production, and modifications are mobilized to support the whole system. The feedback is thus essential.

Discussion

In this review, we take touch and gravity perception as two examples, representing contact and non-contact environmental forces respectively, to glimpse how these forces shape plant organs, and how plants in turn feed back to these physical stimuli. In addition, we also discussed how mechanical heterogeneity may arise from stochasticity or emerge from tissue geometrical arrangements. It is likely that tissue mechanical heterogeneity may introduce further complexity and refinement to the local and global perceptions of external mechanical stimuli, which may then trigger different morphological responses, forming yet another feedback that integrates information across various scales. Lastly, and in response to this proposition, we try to find the nexus point of extrinsic and intrinsic mechanical responsive pathways.

There are many outstanding questions. First, how do plants distinguish different mechanical cues? One apparent strategy/solution is to form specific tissues or organs. This raises another connected question: do mechanical cues contribute to the specification of these cells? Recently, several studies indicated how mechanical forces are upstream of cell fates specification (Landrein et al., 2015; Fal et al., 2016; Hernandez-Lagana et al., 2021), although there are still large spaces for further exploration; Second, how do plants embrace the seemingly contradictory heterogeneity and robustness? Regarding this intriguing topic, readers could refer to Hong et al. (2018); Third, where and how are the mechano-chemical hotpots formed? This is relevant to cell and organ polarity, which is also a kind of heterogeneity. For polarity and mechanics, readers could refer to Gorelova et al. (2021); The last, on a large scale, how the plant shapes are evolutionally preserved and finally fixed under environmental force pressure is also not fully understood.

Author contributions

FZ and YL contributed equally. All authors contributed to the article and approved the submitted version.

Funding

This work was supported by the Basic Research Field Project "Science and Technology Innovation Action Plan" of the Shanghai Science and Technology Commission (22JC1402800) and the Fundamental Research Founds for the Central University (D5000220167) to FZ, and a Ministry of Education Academic Research Fund Tier 1 grant (MOE AcRF 21-0065) to YL.

Acknowledgments

We thank Ali Ferjani for the invitation to write this review. We apologized to those authors whose excellent work was not included in this review due to the word limit.

Conflict of interest

The authors declare that the research was conducted in the absence of any commercial or financial relationships that could be construed as a potential conflict of interest.

Publisher's note

References

Atakhani, A., Bogdziewiez, L., and Verger, S. (2022).). characterising the mechanics of cell–cell adhesion in plants. *Quantitative Plant Biol.* 3, 1–13. doi: 10.1017/qpb.2021.16

Bacete, L., Schulz, J., Engelsdorf, T., Bartosova, Z., Vaahtera, L., Yan, G., et al. (2022). THESEUS1 modulates cell wall stiffness and abscisic acid production in *Arabidopsis thaliana*. *Proc. Natl. Acad. Sci. U.S.A.* 119, e2119258119. doi: 10.1073/pnas.2119258119

Bastien, R., Bohr, T., Moulia, B., and Douady, S. (2013). Unifying model of shoot gravitropism reveals proprioception as a central feature of posture control in plants. *Proc. Natl. Acad. Sci. U.S.A.* 110, 755–760. doi: 10.1073/pnas.1214301109

Belteton, S. A., Li, W., Yanagisawa, M., Hatam, F. A., Quinn, M. I., Szymanski, M. K., et al. (2021). Real-time conversion of tissue-scale mechanical forces into an interdigitated growth pattern. *Nat. Plants* 7, 826–841. doi: 10.1038/s41477-021-00931-z

Bérut, A., Chauvet, H., Legué, V., Moulia, B., Pouliquen, O., and Forterre, Y. (2018). Gravisensors in plant cells behave like an active granular liquid. *Proc. Natl. Acad. Sci. U.S.A.* 115, 5123–5128. doi: 10.1073/pnas.1801895115

Bidhendi, A. J., and Geitmann, A. (2019). Geometrical details matter for mechanical modeling of cell morphogenesis. *Dev. Cell* 50, 117–125.e2. doi: 10.1016/j.devcel.2019.05.001

Braam, J. (2005). In touch: plant responses to mechanical stimuli. *New Phytol.* 165, 373–389. doi: 10.1111/j.1469-8137.2004.01263.x

Chan, J., and Coen, E. (2020). Interaction between autonomous and microtubule guidance systems controls cellulose synthase trajectories. *Curr. Biol.* 30, 941–947.e2. doi: 10.1016/j.cub.2019.12.066

Chauvet, H., Pouliquen, O., Forterre, Y., Legué, V., and Moulia, B. (2016). Inclination not force is sensed by plants during shoot gravitropism. *Sci. Rep.* 6, 35431. doi: 10.1038/srep35431

Chehab, E. W., Eich, E., and Braam, J. (2009). Thigmomorphogenesis: a complex plant response to mechano-stimulation. *J. Exp. Bot.* 60, 43–56. doi: 10.1093/jxb/ern315

Codjoe, J. M., Miller, K., and Haswell, E. S. (2022). Plant cell mechanobiology: Greater than the sum of its parts. *Plant Cell* 34, 129–145. doi: 10.1093/plcell/koab230

Cosgrove, D. J. (2022). Building an extensible cell wall. *Plant Physiol.* 189, 1246–1277. doi: 10.1093/plphys/kiac184

Cuevas-Velazquez, C. L., Vellosillo, T., Guadalupe, K., Schmidt, H. B., Yu, F., Moses, D., et al. (2021). Intrinsically disordered protein biosensor tracks the physical-chemical effects of osmotic stress on cells. *Nat. Commun.* 12, 5438. doi: 10.1038/s41467-021-25736-8

Darwish, E., Ghosh, R., Ontiveros-Cisneros, A., Tran, H. C., Petersson, M., De Milde, L., et al. (2022). Touch signaling and thigmomorphogenesis are regulated by complementary CAMTA3- and JA-dependent pathways. *Sci. Adv.* 8, eabm2091. doi: 10.1126/sciadv.abm2091

Dauphin, B. G., Ranocha, P., Dunand, C., and Burlat, V. (2022). Cell-wall microdomain remodeling controls crucial developmental processes. *Trends Plant Sci.* 27, 1033–1048. doi: 10.1016/j.tplants.2022.05.010

Dong, Q., Zhang, Z., Liu, Y., Tao, L.-Z., and Liu, H. (2019). FERONIA regulates auxin-mediated lateral root development and primary root gravitropism. *FEBS Lett.* 593, 97–106. doi: 10.1002/1873-3468.13292

Du, J., Anderson, C. T., and Xiao, C. (2022). Dynamics of pectic homogalacturonan in cellular morphogenesis and adhesion, wall integrity sensing and plant development. *Nat. Plants* 8, 332–340. doi: 10.1038/s41477-022-01120-2

Dumais, J. (2021). Mechanics and hydraulics of pollen tube growth. *New Phytol.* 232, 1549–1565. doi: 10.1111/nph.17722

Elsner, J., Lipowczan, M., and Kwiatkowska, D. (2018). Differential growth of pavement cells of arabidopsis thaliana leaf epidermis as revealed by microbead labeling. *Am. J. Bot.* 105, 257–265. doi: 10.1002/ajb2.1021

Fal, K., Asnacios, A., Chabouté, M.-E., and Hamant, O. (2017). Nuclear envelope: a new frontier in plant mechanosensing? *Biophys. Rev.* 9, 389–403. doi: 10.1007/s12551-017-0302-6

Fal, K., Korsbo, N., Alonso-Serra, J., Teles, J., Liu, M., Refahi, Y., et al. (2021). Tissue folding at the organ-meristem boundary results in nuclear compression and chromatin compaction. *Proc. Natl. Acad. Sci. U.S.A.* 118, e2017859118. doi: 10.1073/pnas.2017859118

Fal, K., Landrein, B., and Hamant, O. (2016). Interplay between miRNA regulation and mechanical stress for CUC gene expression at the shoot apical meristem. *Plant Signal. Behav.* 11, e1127497. doi: 10.1080/15592324.2015.1127497

Fruleux, A., and Boudaoud, A. (2021). Cellular Fourier analysis for geometrically disordered materials. *Phys. Rev. Res.* 3, 23036. doi: 10.1103/PhysRevResearch.3.023036

Fruleux, A., Verger, S., and Boudaoud, A. (2019). Feeling stressed or strained? a biophysical model for cell wall mechanosensing in plants. *Front. Plant Sci.* 10. doi: 10.3389/fpls.2019.00757

Gorelova, V., Sprakel, J., and Weijers, D. (2021). Plant cell polarity as the nexus of tissue mechanics and morphogenesis. *Nat. Plants* 7, 1548–1559. doi: 10.1038/s41477-021-01021-w

Gorgues, L., Li, X., Maurel, C., Martinière, A., and Nacry, P. (2022). Root osmotic sensing from local perception to systemic responses. *Stress Biol.* 2, 36. doi: 10.1007/s44154-022-00054-1

Goswami, R., Asnacios, A., Hamant, O., and Chabouté, M.-E. (2020a). Is the plant nucleus a mechanical rheostat? *Curr. Opin. Plant Biol.* 57, 155–163. doi: 10.1016/j.pbi.2020.09.001

Goswami, R., Asnacios, A., Milani, P., Graindorge, S., Houlné, G., Mutterer, J., et al. (2020b). Mechanical shielding in plant nuclei. *Curr. Biol.* 30, 2013–2025.e3. doi: 10.1016/j.cub.2020.03.059

Haas, K. T., Wightman, R., Meyerowitz, E. M., and Peaucelle, A. (2020). Pectin homogalacturonan nanofilament expansion drives morphogenesis in plant epidermal cells. *Science* 367, 1003–1007. doi: 10.1126/science.aaz5103

Hagihara, T., Mano, H., Miura, T., Hasebe, M., and Toyota, M. (2022). Calcium-mediated rapid movements defend against herbivorous insects in mimosa pudica. *Nat. Commun.* 13, 6412. doi: 10.1038/s41467-022-34106-x

Hamant, O., Heisler, M. G., Jönsson, H., Krupinski, P., Uyttewaal, M., Bokov, P., et al. (2008). Developmental patterning by mechanical signals in arabidopsis. *Science* 322, 1650–1655. doi: 10.1126/science.1165594

Hamant, O., Inoue, D., Bouchez, D., Dumais, J., and Mjolsness, E. (2019). Are microtubules tension sensors? *Nat. Commun.* 10, 2360. doi: 10.1038/s41467-019-10207-y

Hernández-Hernández, V., Benítez, M., and Boudaoud, A. (2020). Interplay between turgor pressure and plasmodesmata during plant development. *J. Exp. Bot.* 71, 768–777. doi: 10.1093/jxb/erz434

Hernandez-Lagana, E., Mosca, G., Mendocilla-Sato, E., Pires, N., Frey, A., Giraldo-Fonseca, A., et al. (2021). Organ geometry channels reproductive cell fate in the arabidopsis ovule primordium. *eLife* 10, e66031. doi: 10.7554/eLife.66031

Hervieux, N., Dumond, M., Sapala, A., Routier-Kierzkowska, A.-L., Kierzkowski, D., Roeder, A. H. K., et al. (2016). A mechanical feedback restricts sepal growth and shape in *Arabidopsis*. *Curr. Biol.* 26, 1019–1028. doi: 10.1016/j.cub.2016.03.004

Hong, L., Dumond, M., Tsugawa, S., Sapala, A., Routier-Kierzkowska, A.-L., Zhou, Y., et al. (2016). Variable cell growth yields reproducible OrganDevelopment through spatiotemporal averaging. *Dev. Cell* 38, 15–32. doi: 10.1016/j.devcel.2016.06.016

Hong, L., Dumond, M., Zhu, M., Tsugawa, S., Li, C.-B., Boudaoud, A., et al. (2018). Heterogeneity and robustness in plant morphogenesis: from cells to organs. *Annu. Rev. Plant Biol.* 69, 469–495. doi: 10.1146/annurev-arplant-042817-040517

Ingber, D. E. (1997). Tensegrity: the architectural basis of cellular mechanotransduction. *Annu. Rev. Physiol.* 59, 575–599. doi: 10.1146/annurev.physiol.59.1.575

Jaffe, M. J. (1973). Thigmomorphogenesis: The response of plant growth and development to mechanical stimulation: With special reference to bryonia dioica. *Planta* 114, 143–157. doi: 10.1007/BF00387472

Jensen, G. S., Fal, K., Hamant, O., and Haswell, E. S. (2017). The RNA polymerase-associated factor 1 complex is required for plant touch responses. *J. Exp. Bot.* 68, 499–511. doi: 10.1093/jxb/erw439

Jonsson, K., Hamant, O., and Bhalerao, R. P. (2022). Plant cell walls as mechanical signaling hubs for morphogenesis. *Curr. Biol.* 32, R334–R340. doi: 10.1016/j.cub.2022.02.036

Kawamoto, N., and Morita, M. T. (2022). Gravity sensing and responses in the coordination of the shoot gravitropic setpoint angle. *New Phytol.* 236, 1637–1654. doi: 10.1111/nph.18474

Landrein, B., Kiss, A., Sassi, M., Chauvet, A., Das, P., Cortizo, M., et al. (2015). Mechanical stress contributes to the expression of the STM homeobox gene in arabidopsis shoot meristems. *eLife* 4, e07811. doi: 10.7554/eLife.07811

Lang, I., Barton, D. A., and Overall, R. L. (2004). Membrane-wall attachments in plasmolysed plant cells. *Protoplasma* 224, 231–243. doi: 10.1007/s00709-004-0062-6

Lee, J. S., Wilson, M. E., Richardson, R. A., and Haswell, E. S. (2019). Genetic and physical interactions between the organellar mechanosensitive ion channel homologs MSL1, MSL2, and MSL3 reveal a role for inter-organellar

communication in plant development. *Plant Direct* 3, e00124. doi: 10.1002/pld3.124

Leitz, G., Kang, B.-H., Schoenwaelder, M. E. A., and Staehelin, L. A. (2009). Statolith sedimentation kinetics and force transduction to the cortical endoplasmic reticulum in gravity-sensing arabidopsis columella cells. *Plant Cell* 21, 843–860. doi: 10.1105/tpc.108.065052

Lin, W., Tang, W., Pan, X., Huang, A., Gao, X., Anderson, C. T., et al. (2022). Arabidopsis pavement cell morphogenesis requires FERONIA binding to pectin for activation of ROP GTPase signaling. *Curr. Biol.* 32, 497–507.e4. doi: 10.1016/j.cub.2021.11.030

Lipowczan, M., Borowska-Wykret, D., Natonik-Bialon, S., and Kwiatkowska, D. (2018). Growing cell walls show a gradient of elastic strain across their layers. *J. Exp. Bot.* 69, 4349–4362. doi: 10.1093/jxb/ery237

Liu, S., Jobert, F., Rahneshan, Z., Doyle, S. M., and Robert, S. (2021). Solving the puzzle of shape regulation in plant epidermal pavement cells. *Annu. Rev. Plant Biol.* 72, 525–550. doi: 10.1146/annurev-arplant-080720-081920

Li, T., Yan, A., Bhatia, N., Altinok, A., Afik, E., Durand-Smet, P., et al. (2019). Calcium signals are necessary to establish auxin transporter polarity in a plant stem cell niche. *Nat. Commun.* 10, 726. doi: 10.1038/s41467-019-08575-6

Long, Y., and Boudaoud, A. (2019). Emergence of robust patterns from local rules during plant development. *Curr. Opin. Plant Biol.* 47, 127–137. doi: 10.1016/j.pbi.2018.11.002

Long, Y., Cheddadi, I., Mosca, G., Mirabet, V., Dumond, M., Kiss, A., et al. (2020). Cellular heterogeneity in pressure and growth emerges from tissue topology and geometry. *Curr. Biol.* 30, 1504–1516.e8. doi: 10.1016/j.cub.2020.02.027

Majda, M., Grones, P., Sintorn, I.-M., Vain, T., Milani, P., Krupinski, P., et al. (2017). Mechanochemical polarization of contiguous cell walls shapes plant pavement cells. *Dev. Cell* 43, 290–304.e4. doi: 10.1016/j.devcel.2017.10.017

Majda, M., Trozzi, N., Mosca, G., and Smith, R. S. (2022). How cell geometry and cellular patterning influence tissue stiffness. *Int. J. Mol. Sci.* 23:5651. doi: 10.3390/ijms23105651

Malivert, A., Erguvan, Ö., Chevallier, A., Dehem, A., Friaud, R., Liu, M., et al. (2021). FERONIA and microtubules independently contribute to mechanical integrity in the arabidopsis shoot. *PloS Biol.* 19, e3001454. doi: 10.1371/journal.pbio.3001454

Matsumura, M., Nomoto, M., Itaya, T., Aratani, Y., Iwamoto, M., Matsuura, T., et al. (2022). Mechanosensory trichome cells evoke a mechanical stimuli-induced immune response in arabidopsis thaliana. *Nat. Commun.* 13, 1216. doi: 10.1038/s41467-022-28813-8

Mosca, G., Sapala, A., Strauss, S., Routier-Kierzkowska, A.-L., and Smith, R. S. (2017). On the micro-indentation of plant cells in a tissue context. *Phys. Biol.* 14, 015003. doi: 10.1088/1478-3975/aa5698

Moulia, B., Douady, S., and Hamant, O. (2021). Fluctuations shape plants through proprioception. *Science* 372:eabc6868. doi: 10.1126/science.abc6868

Nguyen, C. T., Kurenda, A., Stolz, S., Chételat, A., and Farmer, E. E. (2018). Identification of cell populations necessary for leaf-to-leaf electrical signaling in a wounded plant. *Proc. Natl. Acad. Sci. U.S.A.* 115, 10178–10183. doi: 10.1073/pnas.1807049115

Okamoto, K., Ueda, H., Shimada, T., Tamura, K., Kato, T., Tasaka, M., et al. (2015). Regulation of organ straightening and plant posture by an actin-myosin XI cytoskeleton. *Nat. Plants* 1, 15031. doi: 10.1038/nplants.2015.31

Peaucelle, A., Wightman, R., and Höfte, H. (2015). The control of growth symmetry breaking in the arabidopsis hypocotyl. *Curr. Biol.* 25 (13), 1746–1752. doi: 10.1016/j.cub.2015.05.022

Perbal, G., and Driss-Ecole, D. (2003). Mechanotransduction in gravisensing cells. *Trends Plant Sci.* 8, 498–504. doi: 10.1016/j.tplants.2003.09.005

Procko, C., Murthy, S., Keenan, W. T., Mousavi, S. A. R., Dabi, T., Coombs, A., et al. (2021). Stretch-activated ion channels identified in the touch-sensitive structures of carnivorous droseraceae plants. *eLife* 10, e64250. doi: 10.7554/eLife.64250

Radin, I., Richardson, R. A., and Haswell, E. S. (2022). Moss PIEZO homologs have a conserved structure, are ubiquitously expressed, and do not affect general vacuole function. *Plant Signal. Behav.* 17, 2015893. doi: 10.1080/15592324.2021.2015893

Robinson, S., and Kuhlemeier, C. (2018). Global compression reorients cortical microtubules in arabidopsis hypocotyl epidermis and promotes growth. *Curr. Biol.* 28, 1794–1802.e2. doi: 10.1016/j.cub.2018.04.028

Sack, F. D. (1997). Plastids and gravitropic sensing. *Planta* 203, S63–S68. doi: 10.1007/pl00008116

Sampathkumar, A., Krupinski, P., Wightman, R., Milani, P., Berquand, A., Boudaoud, A., et al. (2014). Subcellular and supracellular mechanical stress prescribes cytoskeleton behavior in arabidopsis cotyledon pavement cells. *eLife* 3, e01967. doi: 10.7554/eLife.01967

Sapala, A., Runions, A., Routier-Kierzkowska, A.-L., Das Gupta, M., Hong, L., Hofhuis, H., et al. (2018). Why plants make puzzle cells, and how their shape emerges. *eLife* 7, e32794. doi: 10.7554/eLife.32794

Sassi, M., Ali, O., Boudon, F., Cloarec, G., Abad, U., Cellier, C., et al. (2014). An auxin-mediated shift toward growth isotropy promotes organ formation at the shoot meristem in arabidopsis. *Curr. Biol.* 24 (19), 2335–2342. doi: 10.1016/j.cub.2014.08.036

Schneider, R., Ehrhardt, D. W., Meyerowitz, E. M., and Sampathkumar, A. (2021). Tethering of cellulose synthase to microtubules dampens mechano-induced cytoskeletal organization in arabidopsis pavement cells. *Nat. Plants* 8, 1064–1073. doi: 10.1038/s41477-022-01218-7

Seale, M., Cummins, C., Viola, I. M., Mastropaolo, E., and Nakayama, N. (2018). Design principles of hair-like structures as biological machines. *J. R. Soc Interface* 15, 20180206. doi: 10.1098/rsif.2018.0206

Staves, M. P. (1997). Cytoplasmic streaming and gravity sensing in chara internodal cells. *Planta* 203, S79–S84. doi: 10.1007/pl00008119

Takahashi, K., Takahashi, H., Furuichi, T., Toyota, M., Furutani-Seiki, M., Kobayashi, T., et al. (2021). Gravity sensing in plant and animal cells. *NPJ Microgravity* 7, 2. doi: 10.1038/s41526-020-00130-8

Tang, W., Lin, W., Zhou, X., Guo, J., Dang, X., Li, B., et al. (2022). Mechano-transduction *via* the pectin-FERONIA complex activates ROP6 GTPase signaling in arabidopsis pavement cell morphogenesis. *Curr. Biol.* 32, 508–517.e3. doi: 10.1016/j.cub.2021.11.031

Trinh, D.-C., Alonso-Serra, J., Asaoka, M., Colin, L., Cortes, M., Malivert, A., et al. (2021). How mechanical forces shape plant organs. *Curr. Biol.* 31, R143–R159. doi: 10.1016/j.cub.2020.12.001

Uyttewaal, M., Burian, A., Alim, K., Landrein, B., Borowska-Wykręt, D., Dedieu, A., et al. (2012). Mechanical stress acts *via* katanin to amplify differences in growth rate between adjacent cells in arabidopsis. *Cell* 149, 439–451. doi: 10.1016/j.cell.2012.02.048

Verger, S., Long, Y., Boudaoud, A., and Hamant, O. (2018). A tension-adhesion feedback loop in plant epidermis. *eLife* 7, e34460. doi: 10.7554/eLife.34460

Weaire, D. L., and Hutzler, S. (2001). *The physics of foams* (Oxford: Oxford University Press).

Wu, Q., Li, Y., Lyu, M., Luo, Y., Shi, H., and Zhong, S. (2020). Touch-induced seedling morphological changes are determined by ethylene-regulated pectin degradation. *Sci. Adv.* 6, eabc9294. doi: 10.1126/sciadv.abc9294

Yoneda, A., Ohtani, M., Katagiri, D., Hosokawa, Y., and Demura, T. (2020). Hechtian strands transmit cell wall integrity signals in plant cells. *Plants* 9, 604. doi: 10.3390/plants9050604

Yuan, F., Yang, H., Xue, Y., Kong, D., Ye, R., Li, C., et al. (2014). OSCA1 mediates osmotic-stress-evoked Ca2+ increases vital for osmosensing in arabidopsis. *Nature* 514, 367–371. doi: 10.1038/nature13593

Zhang, Y., Yu, J., Wang, X., Durachko, D. M., Zhang, S., and Cosgrove, D. J. (2021). Molecular insights into the complex mechanics of plant epidermal cell walls. *Science* 372, 706–711. doi: 10.1126/science.abf2824

Zhao, F., Chen, W., and Traas, J. (2018). Mechanical signaling in plant morphogenesis. *Curr. Opin. Genet. Dev.* 51, 26–30. doi: 10.1016/j.gde.2018.04.001

Zhao, F., Du, F., Oliveri, H., Zhou, L., Ali, O., Chen, W., et al. (2020). Microtubule-mediated wall anisotropy contributes to leaf blade flattening. *Curr. Biol.* 30, 3972–3985.e6. doi: 10.1016/j.cub.2020.07.076

frontiers | Frontiers in Plant Science

TYPE Review
PUBLISHED 23 January 2023
DOI 10.3389/fpls.2022.1024945

OPEN ACCESS

EDITED BY
Mary Byrne,
The University of Sydney, Australia

REVIEWED BY
Aashish Ranjan,
National Institute of Plant Genome Research (NIPGR), India
John Paul Alvarez,
Monash University, Australia
Chihiro Furumizu,
Hiroshima University, Japan, in collaboration with reviewer JPA

*CORRESPONDENCE
Ali Ferjani
ferjani@u-gakugei.ac.jp

†These authors have contributed equally to this work and share first authorship

SPECIALTY SECTION
This article was submitted to Plant Development and EvoDevo, a section of the journal Frontiers in Plant Science

RECEIVED 22 August 2022
ACCEPTED 28 December 2022
PUBLISHED 23 January 2023

CITATION
Tabeta H, Gunji S, Kawade K and Ferjani A (2023) Leaf-size control beyond transcription factors: Compensatory mechanisms. *Front. Plant Sci.* 13:1024945. doi: 10.3389/fpls.2022.1024945

Leaf-size control beyond transcription factors: Compensatory mechanisms

Hiromitsu Tabeta[1,2,3†], Shizuka Gunji[2†], Kensuke Kawade[3,4,5†] and Ali Ferjani[2*]

[1]Department of Life Sciences, Graduate School of Arts and Sciences, The University of Tokyo, Tokyo, Japan, [2]Department of Biology, Tokyo Gakugei University, Tokyo, Japan, [3]RIKEN Center for Sustainable Resource Science, Yokohama, Japan, [4]National Institute for Basic Biology, Okazaki, Japan, [5]Department of Basic Biology, School of Life Science, Graduate University for Advanced Studies (SOKENDAI), Okazaki, Japan

Plant leaves display abundant morphological richness yet grow to characteristic sizes and shapes. Beginning with a small number of undifferentiated founder cells, leaves evolve *via* a complex interplay of regulatory factors that ultimately influence cell proliferation and subsequent post-mitotic cell enlargement. During their development, a sequence of key events that shape leaves is both robustly executed spatiotemporally following a genomic molecular network and flexibly tuned by a variety of environmental stimuli. Decades of work on *Arabidopsis thaliana* have revisited the compensatory phenomena that might reflect a general and primary size-regulatory mechanism in leaves. This review focuses on key molecular and cellular events behind the organ-wide scale regulation of compensatory mechanisms. Lastly, emerging novel mechanisms of metabolic and hormonal regulation are discussed, based on recent advances in the field that have provided insights into, among other phenomena, leaf-size regulation.

KEYWORDS

***Arabidopsis thaliana*, leaf morphogenesis, cell proliferation, post-mitotic cell expansion, compensation, cell-autonomous, non-cell-autonomous**

1 Introduction

Pioneering studies on Arabidopsis unveiled the basis of genetic control of major plant organs, such as leaves, flowers, and roots (Irish, 2010; Petricka et al., 2012; González et al., 2012; Kalve et al., 2014). Although most developmental events and concomitant cellular processes have been described thoroughly, it is only during the past few decades that we have

Abbreviations: *an3*, *angustifolia3*; ARF, AUXIN RESPONSE FACTOR; CCE, Compensated cell enlargement; CCX4, CATION CALCIUM EXCHANGER 4; H^+-PPase, H^+-translocating inorganic pyrophosphatase; IAA, Indole-3-acetic acid; IBA, Indole-3-butyric acid; IBR, INDOLE-3-BUTYRIC ACID RESPONSE; *KRP, INHIBITOR/INTERACTOR OF CYCLIN-DEPENDENT KINASE /KIP-RELATED PROTEIN*; ECH2, ENOYL-COA HYDRATASE 2; PPi, Pyrophosphate; SAM, Shoot apical meristem; TAG, Triacylglycerol; ROS, Reactive oxygen species; SA, Salicylic acid; Suc, Sucrose; V-ATPases, Vacuolar-type H^+-ATPases; *xs, extra-small sisters*.

integrated the molecular pathways (i.e. relating key genes, receptors, sensors, etc.) behind plant morphogenesis.

Leaf emergence and polarity acquisition and the differentiation of the various cell types and tissues have been described in detail (Asnacios and Hamant, 2012; Lau and Bergmann, 2012; Du et al., 2018; Ali et al., 2020; Vercruysse et al., 2020; Gorelova et al., 2021; Liu et al., 2021). Yet, the core molecular framework behind leaf-size regulation remains unclear. We argue that this relates to a conserved feature of growing organs in seed plants: compensation, a phenomenon whereby cell size compensates for cell division in the establishment of organ size. This is what this review focuses on, taking the leaf as a model system.

2 Compensation: One phenotype, several means

Leaves are typically flat. They capture sunlight, and convert carbon dioxide into carbohydrates by photosynthesis to sustain the plant autotrophic lifestyle. Also, plant leaves are polarized, possessing two structurally different sides, the adaxial and abaxial sides, which are specialized for light capture/photosynthesis and gas exchange, respectively (Bowman et al., 2002; Dkhar and Pareek, 2014; Dow and Bergmann, 2014; and the references therein). Hence, plant leaves can be viewed as expandible structural units, which emerge and grow to highly reproducible predetermined sizes and shapes, which are often used as traits in taxonomy (Tsukaya, 2003). Plant leaves, in general, lack a self-renewing meristem and thus cannot grow indefinitely. Leaf development usually proceeds *via* initiation, growth, and maturation stages (Tsukaya, 2002a; Kalve et al., 2014; Tsukaya, 2014; Tsukaya, 2018).

Leaf cells can divide only for a fixed period of time, which is crucial to determine the number of cells within the leaf. Then, their proliferative ability is gradually lost, as they enter a second stage of post-mitotic cell differentiation marked by a considerable increase in cell size accompanied by increased vacuole volume and cell wall synthesis (Johnson and Lenhard, 2011; González et al., 2012; Powell and Lenhard, 2012). Leaf size is reproducible under controlled light, temperature, and nutritional regimes. In addition, size increase in plants is an irreversible process. That is because morphogenesis in the plant kingdom, unlike the animal kingdom, does not rely on cell contractility, cell migration and cell death. Therefore, leaves are also a simpler model system to decipher what makes organs stop growing upon reaching an appropriate size (Beemster et al., 2006; Micol, 2009; Tsukaya, 2018).

Molecular genetics have identified a plethora of genes contributing to leaf-size control (González et al., 2012; Hepworth and Lenhard, 2014). This has led to draw an overall picture of the gene regulatory network operating during leaf development (González and Inzé, 2015; Wang et al., 2021). The dynamic interactions among key genetic components have recently been uncovered. For instance, DELLA proteins repress gibberellin signaling to modulate cell proliferation and expansion (Sun and Gubler, 2004; de Lucas et al., 2008; Achard et al., 2009). Such DELLA-mediated growth suppression is executed by GROWTH REGULATORY FACTOR (GRF) transcriptional factors at least in cold stress response (Lantzouni et al., 2020). GRFs act within a core module to primarily orchestrate cell proliferation together with GRF INTERACTING FACTOR (GIF) transcriptional co-activators including GIF1/ANGUSTIFOLIA3 (AN3) (Kim and Kende, 2004; Horiguchi et al., 2005; Kim and Tsukaya, 2015; Liebsch and Palatnik, 2020). This module is also connected downstream of TCP transcriptional factors and their targeting microRNA miR319 (Rodriguez et al., 2010; Schommer et al., 2014), which are recognized as important components of leaf lamina growth (Nath et al., 2003; Efroni et al., 2013; Das Gupta and Nath, 2015; Challa et al., 2021; Rath et al., 2022). Although the above findings delineate the hierarchical organization and interconnections among the genetic network governing leaf-size control, this topic has already been covered with an increasing pace. A more exhaustive synthesis of our current knowledge can be found elsewhere (Vercruysse et al., 2020).

In the simplest scenario, leaf size would be defined as the linear function of cell number and cell size. However, in leaf primordia, failure in the proliferative stage to produce sufficient cells triggers excessive cell expansion, the so-called compensation (Tsukaya, 2002b; Beemster et al., 2003; Beemster et al., 2006; Tsukaya, 2008). Because cell division precedes cell differentiation (which also involves cell expansion) in a region confined to the leaf primordia basal part, the proliferative stage likely generates intrinsic signals that affect the final cell size during the following differentiation stage. This poses a question of how the above cellular processes, which occur in distinct regions of leaf primordia, are coordinated during development. Given the importance of cell division and expansion in leaf-size control, compensation has emerged as a key phenomenon to uncover how the interconnection between cell division and expansion is achieved. However the molecular basis behind compensation remains unclear.

Large scale genetic screening has uncovered some of the compensatory mechanisms through the identification of a large number of mutants and transgenics displaying compensation (Table 1; Horiguchi et al., 2005; Horiguchi et al., 2006a; Horiguchi et al., 2006b; Fujikura et al., 2007a, Fujikura et al., 2007b, Fujikura et al., 2009). For instance, kinematic analyses of cell size dynamism unveiled the presence of three classes of compensation, based on cell expansion mode (Ferjani et al., 2007). More specifically, while class I has an enhanced post-mitotic cell expansion rate (seen in *angustifolia* [*an*]*3-4*, *fugu2-1*/*fasciata* [*fas*]*1-6*, and *erecta*[*er*]*-102*); class II has an extended post-mitotic cell expansion period (seen in *fugu5-1*, *icl-2*, *mls-2*, *pck1-2*, and *ibr10*), and class III has an increased size of dividing cells (seen in *KIP-RELATED PROTEIN 2* [*KRP2*] overexpressing plants) (De Veylder et al., 2001; Ferjani et al., 2007; Ferjani et al., 2008; Ferjani et al., 2010; Ferjani et al., 2013a; Ferjani et al., 2013b; Ferjani et al., 2014a; Ferjani et al., 2014b; Katano et al., 2016; Takahashi et al., 2017; Tabeta et al., 2021).

Taking the above into account, compensation-exhibiting mutants have altered coordination between cell division and expansion (Ferjani et al., 2008; Nakayama et al., 2022). Furthermore, cell-autonomous and non-cell-autonomous pathways have been demonstrated to be implicated in compensation (Ferjani et al., 2008; Kawade et al., 2010; Ferjani et al., 2013a; Ferjani et al., 2014a; Nozaki et al., 2020). Finally, the fact that compensation occurs in a wide range of plant species other than Arabidopsis—including tobacco, rice, snapdragon, and North American lake cress—suggests

TABLE 1 List of compensation-exhibiting mutants, transgenic plants and their related suppressors.

ORF number	Gene name	Type of mutation	Reference	Compensation category	Suprossor of CCE
AT1G68310	*AE7*	Loss-of-function	Yuan et al. (2010)		
AT5G28640	*AN3/ GIF1*	Loss-of-function	Kim and Kende (2004) Horiguchi et al. (2005)	Class I	*XS2/CCX4* (Fujikura et al., 2020)
AT4G37750	*ANT*	Loss-of-function	Mizukami and Fischer (2000)		
AT3G48750	*CDKA;1*	Dominant negative	Hemerly et al. (1995)		
AT4G34160 AT5G67260 AT3G50070	*CYCD3*	Loss-of-function of *CYCD3;1 CYCD3;2 CYCD3;3*	Dewitte et al. (2007)		
AT2G26330	*ER*	Loss-of-function	Horiguchi et al. (2006b) Ferjani et al. (2007)	Class I	
AT2G40550	*ETG1*	Loss-of-function	Takahashi et al. (2008)		
AT5G64630	*FAS2*	Loss-of-function	Exner et al. (2006)		
*	*FUGU1*	Recessive mutation	Ferjani et al. (2007)		
AT1G65470	*FUGU2/ FAS1*	Loss-of-function	Exner et al. (2006); Ferjani et al. (2007); Ramirez-Parra and Gutierrez (2007); Hisanaga et al. (2013)	Class I	
*	*FUGU3*	Dominant mutation	Ferjani et al. (2007)		
*	*FUGU4*	Dominant mutation	Ferjani et al. (2007)		
AT1G15690	*FUGU5*	Loss-of-function	Ferjani et al. (2007); Ferjani et al. (2011)	Class II	*ECH2*; *IBR1,3,10*; *VHA-a2* and *VHA-a3* (Katano et al., 2016; Takahashi et al., 2017; Tabeta et al., 2021; Nakayama et al., 2022)
AT2G26300	*GPA1*	Loss-of-function	Ullah et al. (2001)		
AT4G14430	*IBR10*	Recessive mutation	Tabeta et al. (2021)	Class II	*ECH2* (Katano et al., 2016; Tabeta et al., 2021)
AT3G21720	*ICL*	Loss-of-function	Takahashi et al. (2017)	Class II	*ECH2* (Katano et al., 2016; Takahashi et al., 2017)
AT2G23430	*KRP1/ ICK1*	Over-expression	Wang et al. (2000)		
AT3G50630	*KRP2*	Over-expression	De Veylder et al. (2001); Ferjani et al. (2007)	Class III	*DET3* (Ferjani et al., 2013a; Ferjani et al., 2013b)
AT5G48820	*KRP3*	Over-expression	Jun et al. (2013)		
AT2G42620	MAX2	Loss-of-function	Horiguchi et al. (2006b)		
AT5G03860	*MLS*	Loss-of-function	Takahashi et al. (2017)	Class II	*ECH2* (Katano et al., 2016; Takahashi et al., 2017)
AT2G10606 AT5G35407	*miR396*	Over-expression of *miR396A* or *miR396B*	Liu et al. (2009); Rodriguex et al. (2010)		
AT5G55920 AT3G25520 AT5G39740	*OLI*	Loss-of-function of *OLI2* and *OLI5* or *OLI2* and *OLI7*	Fujikura et al. (2009)		
AT4G37870	*PEPCK*	Loss-of-function	Takahashi et al. (2017)	Class II	*ECH2* (Katano et al., 2016; Takahashi et al., 2017)
AT4G00100	*PFL2*	Loss-of-function	Ito et al. (2000)		
AT4G31700	*RPS6A*	Loss-of-function	Horiguchi et al. (2011)		
AT3G53890	*RPS21B*	Loss-of-function	Horiguchi et al. (2011)		
AT5G64140	*RPS28B*	Loss-of-function	Horiguchi et al. (2011)		
AT1G65660	*SMP*	Epimutation	Clay and Nelson (2005)		
AT3G04740	*SWP*	Loss-of-function	Autran et al. (2002)		
AT2G42260	*UVI4/ PYM*	Loss-of-function	Hase et al. (2006)		

* Indicates unpublished and/or unidentified gene.

that the developmental mechanisms that trigger compensation are widely conserved at least in seed plants (Hemerly et al., 1995; Barrôco et al., 2006; Delgado-Benarroch et al., 2009; Horiguchi and Tsukaya, 2011; Amano et al., 2015). However, despite their similar cellular phenotypes, compensation refers to a group of heterogeneous processes driven by different mechanisms (Ferjani et al., 2007; Ferjani et al., 2008; Hisanaga et al., 2015).

3 Underpinnings of compensatory coordination between cell division and expansion

Cell-to-cell communication is an effective way to coordinate cellular processes in time and space and hence to realize stereotyped leaf size. Besides classical anatomy (Szymkowiak and Sussex, 1996), a series of works on the model plant Arabidopsis identified signaling pathways that facilitate cell-to-cell communication (Sieburth et al., 1998; Kim et al., 2003; Serralbo et al., 2006; Savaldi-Goldstein et al., 2007; Eriksson et al., 2010). However, the compensatory interplay between cell proliferation and post-mitotic cell expansion during the induction of compensatory cell enlargement (CCE) is ill-known. Because this knowledge on cellular dynamics is instrumental in determining future directions aiming to delineate the holistic mechanisms of compensation, it has been recently investigated using leaves chimeric for the key elements of class I, II, or III compensation (Kawade et al., 2010; Gunji et al., 2022) (Figure 1). The above investigations revealed that both cell-autonomous and non-cell autonomous mechanisms are involved in CCE. In the following sections, we summarize the major outcome of these studies.

3.1 *an3*-mediated class I compensation: contribution of plasmodesmata

The Cre/*lox*-P system enables heat shock-dependent induction or suppression of *AN3* expression in an *an3* or wild-type genetic background, respectively (Kawade et al., 2010). When the expression of *AN3* is induced in *an3* subepidermal cells in very-early-stage leaf primordia, an *AN3*-expressing sector forms among the *an3* cell population during leaf development. This leaf chimera exhibited CCE irrespective of cellular genotype (*i.e.*, *an3* and *AN3*-expressing cells). Similar results were obtained when leaf chimeras were generated by patchy deletion of the expression of *AN3* in the wild-type genetic background. These observations indicated that the *an3*-mediated induction of CCE occurs *via* cell-to-cell communication in leaf mesophyll tissue. Although the ability to stimulate CCE propagates in a non-cell-autonomous manner, the signaling range is confined to one half of the leaf partitioned by the midrib (Kawade et al., 2010). In contrast to mesophyll tissue, cell-autonomous behavior to stimulate CCE was observed in epidermal tissue of AN3 leaf chimeras generated using the Cre/*lox*-P system or a tissue-specific expression system (Nozaki et al., 2020). In summary, the cell-to-cell communication that induces CCE in *an3* is cell-type dependent (Figure 1A).

It is plausible that this property is attributable to the plasmodesmata aperture size, which varies in time and space to control symplasmic connections (Crawford and Zambryski, 2001; Roberts et al., 2001; Burch-Smith and Zambryski, 2010; Fitzgibbon et al., 2013). Several chaperones and RNA exosomes mediate selective symplasmic transport of signaling molecules, including proteins and mRNAs (Xu et al., 2011; Kitagawa et al., 2022). Apoplastic transport is an alternative pathway for the exchange of signaling molecules between cells. This machinery has been characterized in the context of plant defense, in which bursts of reactive oxygen species (ROS) upon pathogen infection elicit phytohormone signaling (Wendehenne et al., 2014; Noctor et al., 2018). ROS-mediated signaling contributes to the balance between cell proliferation and post-mitotic cell expansion in growing sepals and roots (Tsukagoshi et al., 2010; Tsukagoshi, 2012; Hong et al., 2016; Mabuchi et al., 2018).

In leaf development, the salicylic acid (SA) response is involved in CCE in *an3*. The *extra-small sisters* (*xs*) mutants isolated from a large leaf-size and -shape mutant collection (Horiguchi et al., 2006b) showed normal cell proliferation but compromised post-mitotic cell expansion (Fujikura et al., 2007a). Among them, the *xs2* mutant, which harbors a mutation in a gene encoding the putative endomembrane H^+-dependent K^+ transporter CATION CALCIUM EXCHANGER 4 (CCX4), showed ROS overproduction and an elevated SA response (Fujikura et al., 2020). Importantly, eliminating XS2/CCX4 function in the *an3* mutant fully suppressed CCE (Fujikura et al., 2020), indicating crosstalk between CCE and the SA response. This finding provides insight into the mechanism by which cell proliferation and post-mitotic cell expansion are coordinated beyond the cellular level.

Whereas the AN3 protein is capable of moving between cells to promote cell proliferation (Kawade et al., 2013; Kawade et al., 2017), the aforementioned cell-to-cell communication for CCE is observed in the *an3* genetic background. The non-cell-autonomous signaling that activates CCE in *an3*, in addition to the non-cell-autonomous signaling downstream of AN3 protein movement to promote cell proliferation, are both largely unclear. Enhanced knowledge of AN3-related genetic regulatory networks will be instrumental in resolving these issues at the molecular level (Vercruyssen et al., 2014; Nelissen et al., 2015; Zhang et al., 2018; Jun et al., 2019; Fujikura et al., 2020; Hussain et al., 2022).

3.2 *fugu5*-mediated class II compensation: contribution of metabolic regulation

Although a factor(s) produced in the mesophyll has been proposed as a signal that coordinates leaf size *via* cell-to-cell communication (class I), compensation is likely mediated by large-scale metabolic reprogramming in class II. Therefore, from the perspective of cell number and size dynamism, a key task is to identify which metabolic changes contribute to class II-mediated compensation.

For instance, class II is observed in the *fugu5* Arabidopsis mutant, which has lost H^+-PPase activity, the ability to hydrolyze pyrophosphate (PPi), and concomitant vacuolar acidification (Ferjani et al., 2007; Ferjani et al., 2011; Bertoni, 2011; Kriegel et al., 2015; Segami et al., 2018). This mutation leads to excessive accumulation of PPi in the cytosol, partial

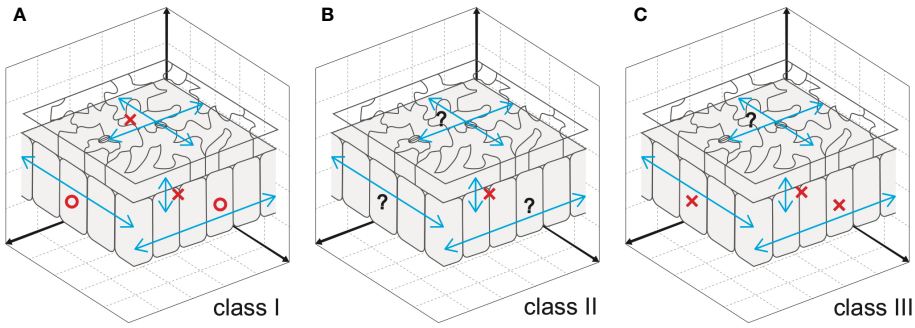

FIGURE 1
Cellular spatial relationships during induction of CCE. **(A)** Mesophyll cells exploit cell-to-cell communication to stimulate CCE in response to deficient cell proliferation in *an3*, which has class I compensation (Kawade et al., 2010). By contrast, epidermal cells trigger CCE in a cell-autonomous manner, preventing cell-to-cell communication across tissue layers (Nozaki et al., 2020). **(B)** Cell-to-cell communication between epidermal and mesophyll cells is absent in *fugu5*, which has class II compensation (Gunji et al., 2022). Given that excess PPi inhibits metabolic reactions, *fugu5*-mediated induction of CCE is likely controlled in a cell-autonomous manner. **(C)** Direct inhibition of cell cycle progression by KRP overexpression, a representative of class III compensation, induces CCE in a cell- and tissue-autonomous manner. This was determined using chimeric KRP2-overexpressing leaves generated using the Cre/*lox*-P system (Kawade et al., 2010) and KRP1-overexpressing leaves with a tissue-specific expression system (Bemis and Torii, 2007). Epidermal cell-to-cell communication remains to be explored. Circles and crosses indicate, respectively, the presence and absence of cell-to-cell communication that stimulates CCE. Question marks are added when cell-to-cell communication is still untested.

inhibition of gluconeogenesis, and a reduction in the content of sucrose (Suc) produced from triacylglycerol (TAG), the major seed storage lipid in Arabidopsis (Ferjani et al., 2011). Consequently, Suc deficiency significantly reduced the cell number in *fugu5* cotyledons and triggered CCE (Ferjani et al., 2007; Ferjani et al., 2008; Ferjani et al., 2011; Ferjani et al., 2014a; Ferjani et al., 2018). Also, excess PPi triggered major developmental (reduced pavement cell shape complexity) and patterning (stomatal distribution and functioning) defects (Asaoka et al., 2019; Gunji et al., 2020). The above indicates that the impact of PPi is broad but specific. TAG-to-Suc conversion is a major metabolic process that fuels seedling establishment (Bewley and Black, 1994; Graham, 2008). Whereas most studies described a role of Suc in hypocotyl elongation in the dark, its impact on aboveground organ development (in light) was described only recently (Henninger et al., 2022).

PPi may trigger several specific cellular responses (Chen et al., 1990; Lundin et al., 1991; Stitt, 1998; Maeshima, 2000; Heinonen, 2001; Ko et al., 2007; Wang et al., 2016). For example, although excess PPi-related phenotypes in palisade tissue were suppressed by an external supply of carbon (such as Suc) or the removal of PPi in the *fugu5* background, Suc supply had no effect on epidermal cell developmental defects (Asaoka et al., 2019; Gunji et al., 2020). Together, the above reports are in line with the assumption that PPi indeed exerts different effects on different plant tissues and cell types and at different developmental stages.

Because PPi is a strong inhibitor of anabolic reactions, several PPases are dedicated to its hydrolysis, preventing accumulation of toxic levels (Segami et al., 2018). H^+-PPase (*FUGU5*) is a master regulator of cytosolic PPi homeostasis (Ferjani et al., 2011; Kriegel et al., 2015; Asaoka et al., 2016; Fukuda et al., 2016; Ferjani et al., 2018; Asaoka et al., 2019). *fugu5* provided insight into the effect of PPi metabolism on leaf development and their potential crosstalk. In other words, phenotypic dissection of *fugu5* suggested a pivotal role for balanced metabolism during the heterotrophic growth stage, indicating that leaf size is controlled by metabolic networks, with a relatively long-lasting effect. The mechanism is discussed in Section 4.

Genetic studies of the TAG-to-Suc pathway identified several key enzymes whose loss-of-function affected seedling establishment with varying levels of penetrance (Hayashi et al., 1998; Hooks et al., 1999; Froman et al., 2000; Eastmond et al., 2000; Germain et al., 2001; Footitt et al., 2002; Rylott et al., 2003; Fulda et al., 2004). To evaluate the link between TAG-to-Suc conversion and CCE, we phenotypically characterized *icl-2*, *mls-2*, *pck1-2* (Takahashi et al., 2017), and *ibr10* mutants (Tabeta et al., 2021; Tabeta et al., 2022), all of which displayed class II CCE (Katano et al., 2016; Takahashi et al., 2017; Tabeta et al., 2021). Hence, producing Suc from TAG during seed germination is crucial for proper cotyledon development. Yet, based on the high mobility of Suc between leaf cells and tissues, as well as its vital role in plant cells, it is technically challenging to pursue the molecular mechanism of class II CCE by simply restricting Suc production and or tracking its dynamic flux.

H^+-PPases are implicated in plant growth, development, and PPi homeostasis (Ferjani et al., 2011; Segami et al., 2018). Nonetheless, although the contribution of PPi homeostasis to plant growth and development has been investigated, its effect on different tissues and cell types during the plant lifecycle is unclear (Schilling et al., 2017). Does altered PPi homeostasis act cell-autonomously or non-cell-autonomously to modulate critical cell fates *via* specific metabolic processes?

The above hypothesis has been formally tested using a spatiotemporal approach by constructing and analyzing transgenic lines in which PPi has been removed from the epidermis, from palisade tissue cells, or during the 4 days following seed imbibition (Gunji et al., 2022). When the yeast PPase IPP1 was expressed in the epidermis or palisade tissue alone, *fugu5* phenotypes were independently restored (Gunji et al., 2022) (Figure 1B). Furthermore, the immediate removal of excess PPi after seed imbibition suppressed CCE of palisade cells but failed to totally rescue the epidermal development defects (Gunji et al., 2022). Next, the impacts of spatial and temporal removal of PPi were investigated by capillary electrophoresis time-of-flight mass spectrometry. This analysis revealed that metabolic profiles are differentially affected

among transgenic lines, consistent with an axial role in the central metabolism of gluconeogenesis in CCE (Gunji et al., 2022). These findings not only provide a conceptual framework to unveil metabolic fluctuations within leaf tissues with high spatiotemporal resolution, but also suggest that excess PPi exerts its inhibitory effect *in planta* during the early stages of seedling establishment in a tissue- and cell-autonomous manner. In other words, leaf size is a highly complex trait governed by multiple regulatory layers, in which metabolic regulation represents another fundamental side.

3.3 *KRP2* overexpression-mediated class III compensation: contribution of cell cycle regulation

INHIBITOR/INTERACTOR OF CYCLIN-DEPENDENT KINASES/KIP-RELATED PROTEINS (*KRPs*) encode cyclin-dependent kinase inhibitors, which block cell cycle progression (Wang et al., 1998; Lui et al., 2000; De Veylder et al., 2001). Constitutive overexpression of individual proteins in this family prematurely arrests the mitotic cell cycle and triggers CCE (De Veylder et al., 2001; Verkest et al., 2005; Ferjani et al., 2007; Jun et al., 2013). The activity that stimulates CCE acts in a cell-autonomous manner, because KRP2 overexpressor cells did not stimulate CCE in the adjacent wild-type cells in leaf chimeras for KRP2 overexpression (Kawade et al., 2010). Notably, epidermis-specific expression of *KRP1* induced a similar phenomenon (*i.e.*, CCE was detected in pavement cells without affecting the subepidermal cells of palisade tissue) (Bemis and Torii, 2007) (Figure 1C).

The endogenous KRP2 protein is more abundant in post-mitotic cells than in proliferating cells (Ormenese, 2004; Verkest et al., 2005). Strong *KRP2*-overexpressing lines exhibited a more obvious CCE phenotype compared with their weak-expressing counterparts (Verkest et al., 2005; Ferjani et al., 2013a; Ferjani et al., 2013b). Therefore, KRP2 may enhance post-mitotic cell expansion; however, this was refuted by clonal analysis using the Cre/*lox*-P system. In brief, CCE is undetectable when *KRP2* overexpression is induced after exiting the mitotic cell cycle (Kawade et al., 2010). As mitotic cell size in *KRP2* overexpressers is twice that in the wild type (De Veylder et al., 2001; Ferjani et al., 2007; Ferjani et al., 2013a; Ferjani et al., 2013b), the mechanism by which cells sense their default size to set the timing of mitotic entry is likely perturbed. Given that cell-size homeostasis is generally explained by a sizer, timer, or adder model (Roeder et al., 2012; Wood and Nurse, 2015; Pavelescu et al., 2018; D'Ario et al., 2021), it would be of interest to investigate the involvement of the components of these models in CCE. To corroborate this, we need to quantify leaf cellular dynamics, taking into account the contribution of nutritional resource allocation from seeds, which affects seedling growth in particular (Sizani et al., 2019). Future work aims to clarify how mitotic cells integrate information on cell-size homeostasis, and hence cell proliferation, into cell-autonomous stimulation of CCE.

Clonal analyses enabled the dissection of cellular dynamics, *i.e.*, cell-autonomous or non-cell-autonomous, in class I, II, and III compensation. The results suggest that cell-to-cell communication coordinates cell proliferation and post-mitotic cell expansion in class I but is not a prerequisite in classes II and III. How then does deficient cell proliferation trigger post-mitotic cell expansion within a cell or cell population? The molecular mechanism underlying *fugu5*-mediated compensation is in good agreement with the cell-autonomous nature of cellular metabolic disorders.

4 Hormonal regulation of class II response phase: contribution of the phytohormone auxin

To elucidate the molecular mechanisms of compensation, it is important to understand the molecular framework of the cell-autonomous induction and response phases for which the *fugu5* mutant (class II compensation) has been used as a prototype. Although the reduced cell number in the induction phase in *fugu5* was attributed to reduced Suc synthesis, CCE in *fugu5* is also controlled metabolically and hormonally (Figure 2). In this section, we describe how forward and reverse genetics-based approaches have provided insight into class II CCE (Katano et al., 2016; Tabeta et al., 2021; Nakayama et al., 2022).

By mutagenizing *fugu5* dry seeds using $^{12}C^{6+}$ heavy-ion irradiation, Katano and colleagues performed a large-scale screening using forward genetics to identify key genes in CCE. This phenotypic screening identified ENOYL-CoA HYDRATASE 2 (ECH2) activity as a prerequisite for CCE to occur in the *fugu5* background. Because ECH2 has dual functions (β-oxidation of TAG-to-Suc conversion (Graham, 2008; Li et al., 2019) and conversion of indole-3-butyric acid (IBA) to the auxin 3-indole acetic acid (IAA) (Strader et al., 2011)), these metabolic processes have been postulated to play a major role in CCE. IAA levels are tightly regulated by *de novo* biosynthesis, transportation, and inactive conversion, and IBA has been implicated in cotyledon and root development (Strader et al., 2010; Frick and Strader, 2018). Hence, the suppression of CCE in *fugu5 ech2* was a result of defective IAA biosynthesis from IBA caused by loss of ECH2 activity.

Reverse genetics in the *fugu5* background showed that CCE in the *ibr1 ibr3 ibr10 fugu5* quadruple mutant, which is defective in IBA-to-IAA conversion (Strader et al., 2010; Strader et al., 2011), was totally suppressed (Tabeta et al., 2021). In contrast, *pen3 fugu5* and *pdr9 fugu5*, in which IBA efflux is compromised, exhibited a high-IAA phenotype (Strader and Bartel, 2009; Ruzicka et al., 2010; Aryal et al., 2019) and enhanced CCE (Tabeta et al., 2021). Consistently, endogenous IAA levels were twofold higher in *fugu5* (in 8-10-day-old seedlings). These findings indicate that IAA converted from IBA is essential for CCE, in agreement with the finding that the degree of CCE reflects the intracellular IAA level (Tabeta et al., 2021). How is high auxin sensed, interpreted, and transduced into CCE in *fugu5*?

AUXIN RESPONSE FACTORS (ARF) 7 and 19 and V-ATPase activity are essential for CCE in *fugu5*. More specifically, *arf7-1 arf19-1 fugu5-1* and *vha-a2 vha-a3 fugu5-1* triple mutants did not exhibit CCE, despite having a significantly reduced number of cells (Tabeta et al., 2021). The vacuole accounts for the majority of the cell volume and is essential for cell enlargement, in class II CCE, proton translocation *via* V-ATPase contributes to vacuole enlargement and promotes cell-size control *via* the ARF7 ARF19 module. The above findings are valid for all other mutants with class II CCE, namely *isocitrate lyase* (*icl*;

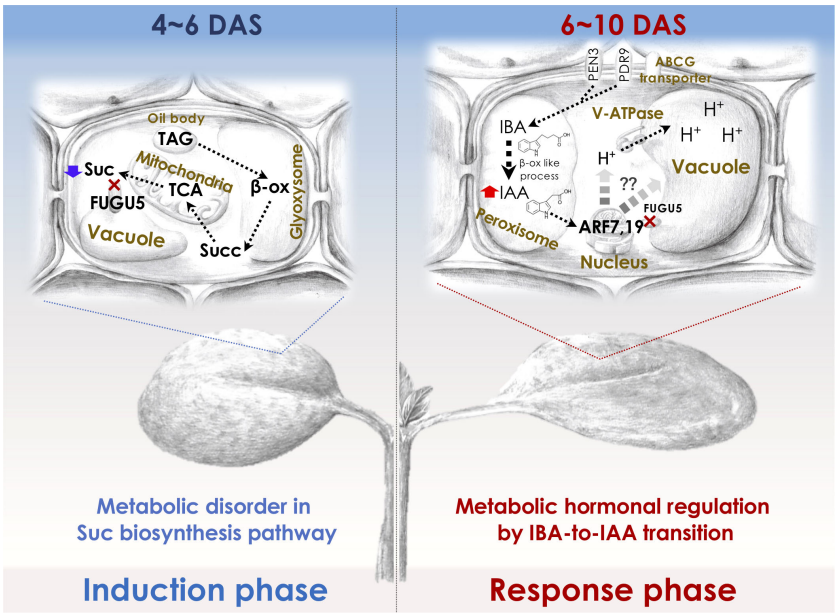

FIGURE 2
Molecular machinery of the induction and response phases in class II CCE. The decreased cell number (induction phase) in Arabidopsis *fugu5*-mutant cotyledons has been shown to be exclusively due to a decreased level of TAG-derived Suc, and IBA-derived IAA (Katano et al., 2016; Takahashi et al., 2017) has been suggested to mediate CCE (response phase) as follows: First, upon seed imbibition, excess cytosolic PPi in *fugu5* leads to the inhibition of *de novo* Suc synthesis from TAG, a major seed-storage lipid and substrate for the conversion of fatty acids to acetyl-CoA for glyoxylate bypass that takes place in the glyoxysome (Ferjani et al., 2011). This is owing to inhibition of gluconeogenesis (Ferjani et al., 2018). Second, during seedling establishment, metabolic disorder associated with the reduced Suc content (4-6 DAS; left panel) is converted into an 'output instructive signal' (6-10 DAS; right panel) that promotes the conversion of IBA, an auxin precursor, to IAA, the natural phytohormone auxin, leading to an increase in endogenous IAA concentration, which is crucial for CCE (Tabeta et al., 2021). Third, increased endogenous IAA (IAA concentration peaks at 8-10 DAS) triggers the TIR/AFB-dependent auxin signaling pathway through the AUXIN RESPONSE FACTORs ARF7 and ARF19, transcriptional activators of early auxin-response genes. This subsequently activates the vacuolar type V-ATPase, leading to an increase in turgor pressure, which ultimately drives an increase in cell size and CCE (Tabeta et al., 2021; Nakayama et al., 2022). β-ox, β-oxidation; Succ, succinate. Glyoxysome, the single membrane-bound organelles that house most of the biochemical machinery required to convert fatty acids derived from TAG to 4-carbon compounds. TCA, the tricarboxylic acid cycle. PEN3, PENETRATION (PEN) 3 is a membrane-localized ATP-binding cassette (ABC) transporter. PDR9, is a member of the pleiotropic drug resistance (PDR) family of ATP-binding cassette transporters. ABCG transporter, G-type ATP-binding cassette (ABCG) transporter. DAS, days after seed sowing.

Eastmond et al., 2000), *malate synthase* (*mls*; Cornah et al., 2004), *phosphoenolpyruvate carboxykinase1* (*pck1*; Penfield et al., 2004), and *ibr10* (Zolman et al., 2008), but not *an3* and *fas1* (class I compensation) (Katano et al., 2016; Takahashi et al., 2017; Tabeta et al., 2021). Therefore, IBA-related hormonal signaling is likely activated in response to metabolic disorders of the central metabolism. If so, one major question arises: Could this rather indicate that auxin integrates more signals (metabolism, cell cycle, vacuole volume, cell wall remodeling etc.) and thus is at the same hierarchical level as compensation (i.e., integrating heterogeneous pathways)?

Finally, although auxin signaling plays a major role in class II, the phytohormone SA has been proposed to relate to class I CCE in the *an3-4* mutant (Fujikura et al., 2020). These findings indicate that the response phase in classes I and II is under phytohormonal control. Importantly, hormonal cross-talk controlling leaf development has also been discussed. As mentioned above, gibberellins together with DELLA proteins, which are downstream of the IAA response, modulate cell proliferation and expansion (Sun and Gubler, 2004; de Lucas et al., 2008; Achard et al., 2009). Also, some TCPs have been reported to regulate auxin homeostasis and cytokinin by altering the expression of auxin biosynthetic enzymes (Lucero et al., 2015). Since IBA-derived IAA provides NO signaling and promotes other hormonal responses (Fattorini et al., 2017), hormonal cross-talk regulation might also have a role in leaf size regulation in compensation-exhibiting mutant background. To this end, compensation-mediated leaf size control may represent a good starting point for further studies aiming to unveil the broader picture of phytohormonal regulation.

5 Environmentally-induced compensation

Growth and development of plants are greatly affected by environmental changes. Because plants cannot move, altering their own tissue structure and concomitant organ size and/or shape to adapt to the ambient environment is critical for their survival. For instance, heterophylly, which is defined as a leaf-form alteration triggered by the surrounding environment, is commonly observed in aquatic and amphibious plants (Li et al., 2019). *Rorippa aquatica* is an amphibious plant found in riparian environments, such as the bank of a natural watercourse including lakes, ponds, and streams, in North America. *R. aquatica* shows a remarkable heterophylly, and develops deeply dissected narrow leaves under submerged conditions whereas it develops simple shaped leaves on terrestrial conditions. The leaf shape changes also in response to varying ambient temperature, in which lower temperature induces dissected narrow leaves. Recently, it was shown that both submergence (Sakamoto et al., 2022) and low-temperature (Amano et al., 2015) treatments

caused an increase in cell size in the sub-epidermal palisade tissue layer in mature leaves, along with a decrease in leaf blade area. This phenotype in which cell size increase occurs in the background of tissue-size reduction resembles compensation. Indeed, the expression of some of the compensation-related genes is altered under low-temperature or submergence in *R. aquatica*.

Because phytohormones usually reflect the environmental status, in some ways they represent the secondary messengers of environmental cues. Therefore, it is not surprising to see compensation being dependent on the environment. In other words, in the case of *R. aquatica*, environmental cues may have triggered compensation *via* a yet unidentified hormonal regulatory pathway. These observations also indicate that compensation could be induced not only in mutants, transgenics, and γ-ray–treated plants, but also as an adaptive response to a wide range of environmental stimuli. Together, these findings provide evidence that compensation is a universal phenomenon that is also seen in nature, whereby hormones are acting as downstream instructive signal of the environmental status.

6 Outstanding questions and future prospects

Large-scale genetic screening identified a number of genes whose loss- or gain-of-function alters final leaf size. For decades, this prompted work on the morphogenesis of Arabidopsis. Subsequent functional analyses of the above genetic factors revealed the molecular events governing leaf development. Furthermore, bioinformatics techniques identified several key transcription factors (TFs) relevant to core genetic modules (Ichihashi et al., 2014; Sinha et al., 2016). However, our understanding of leaf-size control is incomplete.

Most developmental events are interpreted based on TFs (Kaufmann and Airoldi, 2018; and references therein). Although TFs are crucial in orchestrating organogenesis, other regulatory factors with more indirect effects have been overlooked. This is a result of the inherent bias of most genetic screening approaches, which identify major non-redundant players, overlooking more indirect and diffuse properties that build on more complex interactions (Nakayama et al., 2022). This includes understudied players (e.g., metabolic molecules) and understudied systemic interactions (e.g., feedback loops). Thus, the compensatory mechanism of leaf-size control cannot be explained by transcriptional regulation processes only (Ferjani et al., 2008; Ferjani et al., 2014a; Ferjani et al., 2018). Multi-omics enables identification of novel small molecules (including metabolic components and regulators) critical in major developmental transitions during plant growth (Omidbakhshfard et al., 2021) and leaf development (Tabeta et al., 2021). Systems biology may also help to identify, in the topology of the molecular network, key events and interactions, to explain how compensation emerges.

Beyond molecule identity and interactions, the mechanical properties of plant cells and tissues should be regarded as an integral part of developmental signaling pathways. Advances in quantitative plant biology have allowed experimentation and modeling using plants (Autran et al., 2021). Hence, the regulatory mechanisms at the crossroads of metabolism, morphogenesis, and mechanics should be integrated with genetic mechanisms to understand the multimodal drivers of leaf-size control (Trinh et al., 2021; Nakayama et al., 2022).

Finally, if compensation is a general and primary size-regulatory mechanism in plant leaves, does it involve, by default, a proprioceptive sensing step? Does CCE generate an additional instructive mechanical signal? If so, how is such a signal perceived, resolved, integrated, and executed to guarantee proper size? To address these questions, leaf development should be reexamined from the perspectives of biomechanics and metabolism.

Author contributions

HT, SG, KK and AF drafted and wrote the paper. All authors contributed to the article and approved the submitted version.

Funding

This work was supported by Grant-in-Aid for Scientific Research (B) (JP16H04803 to AF); Grant-in-Aid for Scientific Research on Innovative Areas (JP25113002 and JP18H05487 to AF); The Naito Foundation. HT is a recipient of a Research Fellowship for Young Scientists (20J20901).

Acknowledgments

We thank Prof. Olivier Hamant (ENS de Lyon) and Prof. Seisuke Kimura (Kyoto Sangyo University) for their critical reading of the manuscript. AF along with co-authors wrote this review in celebration of the 20th anniversary of compensation, and dedicates this article to Prof. Hirokazu Tsukaya (The University of Tokyo) and Prof. Gorou Horiguchi (Rikkyo University), the ones who helped to make amazing discoveries, and brought attention to crucial issues in leaf development.

Conflict of interest

The authors declare that the research was conducted in the absence of any commercial or financial relationships that could be construed as a potential conflict of interest.

Publisher's note

References

Achard, P., Gusti, A., Cheminant, S., Alioua, M., Dhondt, S., Coppens, F., et al. (2009). Gibberellin signaling controls cell proliferation rate in Arabidopsis. *Curr. Biol.* 19, 1188–1193. doi: 10.1016/j.cub.2009.05.059

Ali, S., Khan, N., and Xie, L. (2020). Molecular and hormonal regulation of leaf morphogenesis in *Arabidopsis*. *Int. J. Mol. Sci.* 21, 5132. doi: 10.3390/ijms21145132

Amano, R., Nakayamam, H., Morohoshim, Y., Kawakatsu, Y., Ferjani, A., and Kimura, S. (2015). A decrease in ambient temperature induces post-mitotic enlargement of palisade cells in north american lake cress. *PloS One* 10, e0141247. doi: 10.1371/journal.pone.0141247

Aryal, B., Huynh, J., Schneuwly, J., Siffert, A., Liu, J., Alejandro, S., et al. (2019). ABCG36/PEN3/PDR8 is an exporter of the auxin precursor, indole-3-Butyric acid, and involved in auxin-controlled development. *Front. Plant Sci.* 10, 899. doi: 10.3389/fpls.2019.00899

Asaoka, M., Inoue, S. I., Gunji, S., Kinoshita, T., Maeshima, M., Tsukaya, H., et al. (2019). Excess pyrophosphate within guard cells delays stomatal closure. *Plant Cell Physiol.* 60, 875–887. doi: 10.1093/pcp/pcz002

Asaoka, M., Segami, S., Ferjani, A., and Maeshima, M. (2016). Contribution of PPi-hydrolyzing function of vacuolar H^+-pyrophosphatase in vegetative growth of Arabidopsis: evidenced by expression of uncoupling mutated enzymes. *Front. Plant Sci.* 7, 415. doi: 10.3389/fpls.2016.00415

Asnacios, A., and Hamant, O. (2012). The mechanics behind cell polarity. *Trends Cell Biol.* 11, 584–591. doi: 10.1016/j.tcb.2012.08.005

Autran, D., Bassel, G. W., Chae, E., Ezer, D., Ferjani, A., Fleck, C., et al. (2021). What is quantitative plant biology? *Quantitative Plant Biol.* 2, e10. doi: 10.1017/qpb.2021.8

Autran, D., Jonak, C., Belcram, K., Beemster, G. T., Kronenberger, J., Grandjean, O., et al. (2002). Cell numbers and leaf development in *Arabidopsis*: A functional analysis of the *STRUWWELPETER* gene. *EMBO J.* 21, 6036–6049. doi: 10.1093/emboj/cdf614

Barrôco, R. M., Peres, A., Droual, A. M., De Veylder, L., Nguyen le, S. L., De Wolf, J., et al. (2006). The cyclin-dependent kinase inhibitor Orysa;KRP1 plays an important role in seed development of rice. *Plant Physiol.* 142, 1053–1064. doi: 10.1104/pp.106.087056

Beemster, G. T., Fiorani, F., and Inzé, D. (2003). Cell cycle: the key to plant growth control? *Trends Plant Sci.* 8, 154–158. doi: 10.1016/S1360-1385(03)00046-3

Beemster, G. T., Vercruysse, S., De Veylder, L., Kuiper, M., and Inzé, D. (2006). The Arabidopsis leaf as a model system for investigating the role of cell cycle regulation in organ growth. *J. Plant Res.* 119, 43–50. doi: 10.1007/s10265-005-0234-2

Bemis, S. M., and Torii, K. U. (2007). Autonomy of cell proliferation and developmental programs during Arabidopsis aboveground organ morphogenesis. *Dev. Biol.* 304, 367–381. doi: 10.1016/j.ydbio.2006.12.049

Bertoni, G. (2011). A surprising role for vacuolar pyrophosphatase. *Plant Cell* 23, 2808. doi: 10.1105/tpc.111.230813

Bewley, J. D., and Black, M. (1994). Seeds: in *Physiology of development and germination*, *Ed. 2* (New York: Plenum Press).

Bowman, J. L., Eshed, Y., and Baum, S. F. (2002). Establishment of polarity in angiosperm lateral organs. *Trends Genet.* 18, 134–141. doi: 10.1016/S0168-9525(01)02601-4

Burch-Smith, T. M., and Zambryski, P. C. (2010). Loss of INCREASED SIZE EXCLUSION LIMIT (ISE)1 or ISE2 increases the formation of secondary plasmodesmata. *Curr. Biol.* 20, 989–993. doi: 10.1016/j.cub.2010.03.064

Challa, K. R., Rath, M., Sharma, A. N., Bajpai, A. K., Davuluri, S., Acharya, K. K., et al. (2021). Active suppression of leaflet emergence as a mechanism of simple leaf development. *Nat. Plants* 7, 1264–1275. doi: 10.1038/s41477-021-00965-3

Chen, J., Brevet, A., Fromant, M., Lévêque, F., Schmitter, J. M., Blanquet, S., et al. (1990). Pyrophosphatase is essential for growth of *Escherichia coli*. *J. Bacteriol.* 172, 5686–5689. doi: 10.1128/jb.172.10.5686-5689.1990

Clay, N. K., and Nelson, T. (2005). The recessive epigenetic *swellmap* mutation affects the expression of two step II splicing factors required for the transcription of the cell proliferation gene *STRUWWELPETER* and for the timing of cell cycle arrest in the *Arabidopsis* leaf. *Plant Cell* 17, 1994–2008. doi: 10.1105/tpc.105.032771

Cornah, J. E., Germain, V., Ward, J. L., Beale, M. H., and Smith, S. M. (2004). Lipid utilization, gluconeogenesis, and seedling growth in Arabidopsis mutants lacking the glyoxylate cycle enzyme malate synthase. *J. Biol. Chem.* 279, 42916–42923. doi: 10.1074/jbc.M407380200

Crawford, K. M., and Zambryski, P. C. (2001). Non-targeted and targeted protein movement through plasmodesmata in leaves in different developmental and physiological states. *Plant Physiol.* 125, 1802–1812. doi: 10.1104/pp.125.4.1802

D'Ario, M., Tavares, R., Schiessl, K., Desvoyes, B., Gutierrez, C., Howard, M., et al. (2021). Cell size controlled in plants using DNA content as an internal scale. *Science* 372, 1176–1181. doi: 10.1126/science.abb4348

Das Gupta, M., and Nath, U. (2015). Divergence in patterns of leaf growth polarity is associated with the expression divergence of miR396. *Plant Cell* 27, 2785–2799. doi: 10.1105/tpc.15.00196

Delgado-Benarroch, L., Weiss, J., and Egea-Cortines, M. (2009). The mutants compacta ähnlich, nitida and grandiflora define developmental compartments and a compensation mechanism in floral development in *Antirrhinum majus*. *J. Plant Res.* 122, 559–569. doi: 10.1007/s10265-009-0236-6

Dewitte, W., Scofield, S., Alcasabas, A. A., Maughan, S. C., Menges, M., Braun, N., et al. (2007). *Arabidopsis* CYCD3 d-type cyclins link cell proliferation and endocycles and are rate-limiting for cytokinin responses. *Proc. Natl. Acad. Sci. U. S. A.* 104, 14537–14542. doi: 10.1073/pnas.0704166104

de Lucas, M., Davière, J. M., Rodríguez-Falcón, M., Pontin, M., Iglesias-Pedraz, J. M., Lorrain, S., et al. (2008). A molecular framework for light and gibberellin control of cell elongation. *Nature* 451, 480–484. doi: 10.1038/nature06520

De Veylder, L., Beeckman, T., Beemster, G. T., Krols, L., Terras, F., Landrieu, I., et al. (2001). Functional analysis of cyclin-dependent kinase inhibitors of Arabidopsis. *Plant Cell* 13, 1653–1668. doi: 10.1105/TPC.010087

Dkhar, J., and Pareek, A. (2014). What determines a leaf's shape? *EvoDevo* 5, 47. doi: 10.1186/2041-9139-5-47

Dow, G. J., and Bergmann, D. C. (2014). Patterning and processes: how stomatal development defines physiological potential. *Curr. Opin. Plant Biol.* 21, 67–74. doi: 10.1016/j.pbi.2014.06.007

Du, F., Guan, C., and Jiao, Y. (2018). Molecular mechanisms of leaf morphogenesis. *Mol. Plant* 11, 1117–1134. doi: 10.1016/j.molp.2018.06.006

Eastmond, P. J., Germain, V., Lange, P. R., Bryce, J. H., Smith, S. M., and Graham, I. A. (2000). Postgerminative growth and lipid catabolism in oilseeds lacking the glyoxylate cycle. *Proc. Natl. Acad. Sci. U.S.A.* 97, 5669–5674. doi: 10.1073/pnas.97.10.5669

Efroni, I., Han, S. K., Kim, H. J., Wu, M. F., Steiner, E., Birnbaum, K. D., et al. (2013). Regulation of leaf maturation by chromatin-mediated modulation of cytokinin responses. *Dev. Cell* 24, 438–445. doi: 10.1016/j.devcel.2013.01.019

Eriksson, S., Stransfeld, L., Adamski, N. M., Breuninger, H., and Lenhard, M. (2010). *KLUH/CYP78A5*-dependent growth signaling coordinates floral organ growth in *Arabidopsis*. *Curr. Biol.* 20, 527–532. doi: 10.1016/j.cub.2010.01.039

Exner, V., Taranto, P., Schönrock, N., Gruissem, W., and Hennig, L. (2006). Chromatin assembly factor CAF-1 is required for cellular differentiation during plant development. *Development* 133, 4163–4172. doi: 10.1242/dev.02599

Fattorini, L., Veloccia, A., Della Rovere, F., D'Angeli, S., Falasca, G., and Altamura, M. M. (2017). Indole-3-butyric acid promotes adventitious rooting in *Arabidopsis thaliana* thin cell layers by conversion into indole-3-acetic acid and stimulation of anthranilate synthase activity. *BMC Plant Biol.* 17, 121. doi: 10.1186/s12870-017-1071-x

Ferjani, A., Horiguchi, G., and Tsukaya, H. (2010). Organ size control in Arabidopsis: Insights from compensation studies. *Plant Morphol.* 22, 65–71. doi: 10.5685/plmorphol.22.65

Ferjani, A., Horiguchi, G., Yano, S., and Tsukaya, H. (2007). Analysis of leaf development in *fugu* mutants of Arabidopsis reveals three compensation modes that modulate cell expansion in determinate organs. *Plant Physiol.* 144, 988–999. doi: 10.1104/pp.107.099325

Ferjani, A., Ishikawa, K., Asaoka, M., Ishida, M., Horiguchi, G., Maeshima, M., et al. (2013a). Enhanced cell expansion in a *KRP2* overexpressor is mediated by increased V-ATPase activity. *Plant Cell Physiol.* 54, 1989–1998. doi: 10.1093/pcp/pct138

Ferjani, A., Ishikawa, K., Asaoka, M., Ishida, M., Horiguchi, G., Maeshima, M., et al. (2013b). Class III compensation, represented by *KRP2* overexpression, depends on V-ATPase activity in proliferative cells. *Plant Signal. Behav.* 8, e27204. doi: 10.4161/psb.27204

Ferjani, A., Kawade, K., Asaoka, M., Oikawa, A., Okada, T., Mochizuki, A., et al. (2018). Pyrophosphate inhibits gluconeogenesis by restricting UDP-glucose formation *in vivo*. *Sci. Rep.* 8, 14696. doi: 10.1038/s41598-018-32894-1

Ferjani, A., Segami, S., Asaoka, M., and Maeshima, M. (2014a). Regulation of PPi levels through the vacuolar membrane H^+-pyrophosphatase. in *Progress in botany*, vol. 75 . Eds. U. Lüttge, W. Beyschlag and J. Cushman (Berlin: Springer-Verlag), 145–165. doi: 10.1007/978-3-642-38797-5_5

Ferjani, A., Segami, S., Horiguchi, G., Muto, Y., Maeshima, M., and Tsukaya, H. (2011). Keep an eye on PPi: the vacuolar-type H^+-pyrophosphatase regulates postgerminative development in *Arabidopsis*. *Plant Cell* 23, 2895–2908. doi: 10.1105/tpc.111.085415

Ferjani, A., Segami, S., Horiguchi, G., Muto, Y., Maeshima, M., and Tsukaya, H. (2014b). Roles of the vacuolar H^+-PPase in seed storage oil mobilization and plant development. *Plant Morphol.* 26, 45–51. doi: 10.5685/plmorphol.26.45

Ferjani, A., Yano, S., Horiguchi, G., and Tsukaya, H. (2008). Control of leaf morphogenesis by long- and short-distance signaling: Differentiation of leaves into sun or shade types and compensated cell enlargement. in *Plant cell monographs: Plant growth signaling*. Eds. L. Bögre and G. T. S. Beemster (Berlin, Heidelberg, Germany: Springer Berlin Heidelberg), 47–62. doi: 10.1007/7089_2007_148

Fitzgibbon, J., Beck, M., Zhou, J., Faulkner, C., Robatzek, S., and Oparka, K. (2013). A developmental framework for complex plasmodesmata formation revealed by large-scale imaging of the *Arabidopsis* leaf epidermis. *Plant Cell* 25, 57–70. doi: 10.1105/tpc.112.105890

Footitt, S., Slocombe, S. P., Larner, V., Kurup, S., Wu, Y., Larson, T., et al. (2002). Control of germination and lipid mobilization by COMATOSE, the *Arabidopsis* homologue of human ALDP. *EMBO J.* 21, 2912–2922. doi: 10.1093/emboj/cdf300

Frick, E. M., and Strader, L. C. (2018). Roles for IBA-derived auxin in plant development. *J. Exp. Bot.* 69, 169–177. doi: 10.1093/jxb/erx298

Froman, B. E., Edwards, P. C., Bursch, A. G., and Dehesh, K. (2000). ACX3, a novel medium-chain acyl-coenzyme a oxidase from *Arabidopsis*. *Plant Physiol.* 123, 733–742. doi: 10.1104/pp.123.2.733

Fujikura, U., Ezaki, K., Horiguchi, G., Seo, M., Kanno, Y., Kamiya, Y., et al. (2020). Suppression of class I compensated cell enlargement by *xs2* mutation is mediated by salicylic acid signaling. *PloS Genet.* 16, e1008873. doi: 10.1371/journal.pgen.1008873

Fujikura, U., Horiguchi, G., Ponce, M. R., Micol, J. L., and Tsukaya, H. (2009). Coordination of cell proliferation and cell expansion mediated by ribosome-related processes in the leaves of *Arabidopsis thaliana*. *Plant J.* 59, 499–508. doi: 10.1111/j.1365-313X.2009.03886.x

Fujikura, U, Horiguchi, G, and Tsukaya, H (2007a). Dissection of enhanced cell expansion processes in leaves triggered by a defect in cell proliferation, with reference to roles of endoreduplication. *Plant Cell Physiol.* 48, 278–286. doi: 10.1093/pcp/pcm002

Fujikura, U, Horiguchi, G, and Tsukaya, H (2007b). Genetic relationship between *angustifolia3* and *extra-small sisters* highlights novel mechanisms controlling leaf size. *Plant Signal. Behav* 2, 378–380. doi: 10.4161/psb.2.5.4525

Fukuda, M., Segami, S., Tomoyama, T., Asaoka, M., Nakanishi, Y., Gunji, S., et al. (2016). Lack of H^+-pyrophosphatase prompts developmental damage in Arabidopsis leaves on ammonia-free culture medium. *Front. Plant Sci.* 7, 819. doi: 10.3389/fpls.2016.00819

Fulda, M., Schnurr, J., Abbadi, A., Heinz, E., and Browse, J. (2004). Peroxisomal acyl-CoA synthetase activity is essential for seedling development in *Arabidopsis thaliana*. *Plant Cell* 16, 394–405. doi: 10.1105/tpc.019646

Germain, V., Rylott, E. L., Larson, T. R., Sherson, S. M., Bechtold, N., Carde, J. P., et al. (2001). Requirement for 3-ketoacyl-CoA thiolase-2 in peroxisome development, fatty acid beta-oxidation and breakdown of triacylglycerol in lipid bodies of *Arabidopsis* seedlings. *Plant J.* 28, 1–12. doi: 10.1046/j.1365-313X.2001.01095.x

González, N., and Inzé, D. (2015). Molecular systems governing leaf growth: from genes to networks. *J. Exp. Bot.* 66, 1045–1054. doi: 10.1093/jxb/eru541

González, N., Vanhaeren, H., and Inzé, D. (2012). Leaf size control: complex coordination of cell division and expansion. *Trends Plant Sci.* 6, 332–340. doi: 10.1016/j.tplants.2012.02.003

Gorelova, V., Sprakel, J., and Weijers, D. (2021). Plant cell polarity as the nexus of tissue mechanics and morphogenesis. *Nat. Plants* 12, 1548–1559. doi: 10.1038/s41477-021-01021-w

Graham, I. A. (2008). Seed storage oil mobilization. *Annu. Rev. Plant Biol.* 59, 115–142. doi: 10.1146/annurev.arplant.59.032607.092938

Gunji, S., Kawade, K., Tabeta, H., Horiguchi, G., Oikawa, A., Asaoka, M., et al. (2022). Tissue-targeted inorganic pyrophosphate hydrolysis in a *fugu5* mutant reveals that excess inorganic pyrophosphate triggers developmental defects in a cell-autonomous manner. *Front. Plant Sci.* 13, 945225. doi: 10.3389/fpls.2022.945225

Gunji, S., Oda, Y., Takigawa-Imamura, H., Tsukaya, H., and Ferjani, A. (2020). Excess pyrophosphate restrains pavement cell morphogenesis and alters organ flatness in *Arabidopsis thaliana*. *Front. Plant Sci.* 11, 31. doi: 10.3389/fpls.2020.00031

Hase, Y., Trung, K. H., Matsunaga, T., and Tanaka, A. (2006). A mutation in the *uvi4* gene promotes progression of endo-reduplication and confers increased tolerance towards ultraviolet b light. *Plant J.* 46, 317–326. doi: 10.1111/j.1365-313X.2006.02696.x

Hayashi, M., Toriyama, K., Kondo, M., and Nishimura, M. (1998). 2,4-dichlorophenoxybutyric acid-resistant mutants of Arabidopsis have defects in glyoxysomal fatty acid beta-oxidation. *Plant Cell* 10, 183–195. doi: 10.1105/tpc.10.2.183

Heinonen, J. K. (2001). *Biological role of inorganic pyrophosphate* (Boston/Dordrecht/London: Kluwer Academic Publishers).

Hemerly, A., Engler, J. A., Bergounioux, C., Van Montagu, M., Engler, G., Inzé, D., et al. (1995). Dominant negative mutants of the Cdc2 kinase uncouple cell division from iterative plant development. *EMBO J.* 14, 3925–3936. doi: 10.1002/j.1460-2075.1995.tb00064.x

Henninger, M., Pedrotti, L., Krischke, M., Draken, J., Wildenhain, T., Fekete, A., et al. (2022). The evolutionarily conserved kinase SnRK1 orchestrates resource mobilization during Arabidopsis seedling establishment. *Plant Cell* 34, 616–632. doi: 10.1093/plcell/koab270

Hepworth, J., and Lenhard, M. (2014). Regulation of plant lateral-organ growth by modulating cell number and size. *Curr. Opin. Plant Biol.* 17, 36–42. doi: 10.1016/j.pbi.2013.11.005

Hisanaga, T., Kawade, K., and Tsukaya, H. (2015). Compensation: a key to clarifying the organ-level regulation of lateral organ size in plants. *J. Exp. Bot.* 66, 1055–1063. doi: 10.1093/jxb/erv028

Hisanaga, T., Ferjani, A., Horiguchi, G., Ishikawa, N., Fujikura, U., Kubo, M., et al. (2013). The ATM-dependent DNA damage response acts as an upstream trigger for compensation in the *fas1* mutation during Arabidopsis leaf development. *Plant Physiol.* 162, 831–841. doi: 10.1104/pp.113.216796

Hong, L., Dumond, M., Tsugawa, S., Sapala, A., Routier-Kierzkowska, A. L., Zhou, Y., et al. (2016). Variable cell growth yields reproducible organ development through spatiotemporal averaging. *Dev. Cell* 38, 15–32. doi: 10.1016/j.devcel.2016.06.016

Hooks, M. A., Kellas, F., and Graham, I. A. (1999). Long-chain acyl-CoA oxidases of *Arabidopsis*. *Plant J.* 20, 1–13. doi: 10.1046/j.1365-313X.1999.00559.x

Horiguchi, G., Ferjani, A., Fujikura, U., and Tsukaya, H. (2006a). Coordination of cell proliferation and cell expansion in the control of leaf size in *Arabidopsis thaliana*. *J. Plant Res.* 119, 37–42. doi: 10.1007/s10265-005-0232-4

Horiguchi, G., Fujikura, U., Ferjani, A., Ishikawa, N., and Tsukaya, H. (2006b). Large-Scale histological analysis of leaf mutants using two simple leaf observation methods: Identification of novel genetic pathways governing the size and shape of leaves. *Plant J.* 48, 638–644. doi: 10.1111/j.1365-313X.2006.02896.x

Horiguchi, G., Kim, G. T., and Tsukaya, H. (2005). The transcription factor AtGRF5 and the transcription coactivator AN3 regulate cell proliferation in leaf primordia of *Arabidopsis thaliana*. *Plant J.* 43, 68–78. doi: 10.1111/j.1365-313X.2005.02429.x

Horiguchi, G., and Tsukaya, H. (2011). Organ size regulation in plants: insights from compensation. *Front. Plant Sci.* 2, 24. doi: 10.3389/fpls.2011.00024

Hussain, E., Romanowski, A., and Halliday, K. J. (2022). PIF7 controls leaf cell proliferation through an AN3 substitution repression mechanism. *Proc. Natl. Acad. Sci. U.S.A.* 119, e2115682119. doi: 10.1073/pnas.2115682119

Ichihashi, Y., Aguilar-Martínez, J. A., Farhi, M., Chitwood, D. H., Kumar, R., Millon, L. V., et al. (2014). Evolutionary developmental transcriptomics reveals a gene network module regulating interspecific diversity in plant leaf shape. *Proc. Natl. Acad. Sci. U.S.A.* 111, E2616–21. doi: 10.1073/pnas.1402835111

Irish, V. F. (2010). The flowering of Arabidopsis flower development. *Plant J.* 61, 1014–1028. doi: 10.1111/j.1365-313X.2009.04065.x

Ito, T., Kim, G. T., and Shinozaki, K. (2000). Disruption of an *Arabidopsis* cytoplasmic ribosomal protein S13-homologous gene by transposon-mediated mutagenesis causes aberrant growth and development. *Plant J.* 22, 257–264. doi: 10.1046/j.1365-313x.2000.00728.x

Johnson, K., and Lenhard, M. (2011). Genetic control of plant organ growth. *New Phytol.* 191, 319–333. doi: 10.1111/j.1469-8137.2011.03737.x

Jun, S. E., Kim, J. H., Hwang, J. Y., Huynh Le, T. T., and Kim, G. T. (2019). ORESARA15 acts synergistically with ANGUSTIFOLIA3 and separately from AINTEGUMENTA to promote cell proliferation during leaf growth. *Int. J. Mol. Sci.* 21, 241. doi: 10.3390/ijms21010241

Jun, S. E., Okushima, Y., Nam, J., Umeda, M., and Kim, G. T. (2013). Kip-related protein 3 is required for control of endoreduplication in the shoot apical meristem and leaves of Arabidopsis. *Mol. Cells* 35, 47–53. doi: 10.1007/s10059-013-2270-4

Kalve, S., De Vos, D., and Beemster, G. T. (2014). Leaf development: a cellular perspective. *Front. Plant Sci.* 5, 362. doi: 10.3389/fpls.2014.00362

Katano, M., Takahashi, K., Hirano, T., Kazama, Y., Abe, T., Tsukaya, H., et al. (2016). Suppressor screen and phenotype analyses revealed an emerging role of the monofunctional peroxisomal enoyl-CoA hydratase 2 in compensated cell enlargement. *Front. Plant Sci.* 7, 132. doi: 10.3389/fpls.2016.00132

Kaufmann, K., and Airoldi, C. A. (2018). Master regulatory transcription factors in plant development: a blooming perspective. *Methods Mol. Biol.* 1830, 3–22. doi: 10.1007/978-1-4939-8657-6_1

Kawade, K., Horiguchi, G., and Tsukaya, H. (2010). Non-cell-autonomously coordinated organ size regulation in leaf development. *Development* 137, 4221–4227. doi: 10.1242/dev.057117

Kawade, K., Horiguchi, G., Usami, T., Hirai, M. Y., and Tsukaya, H. (2013). ANGUSTIFOLIA3 signaling coordinates proliferation between clonally distinct cells in leaves. *Curr. Biol.* 23, 788–792. doi: 10.1016/j.cub.2013.03.044

Kawade, K., Tanimoto, H., Horiguchi, G., and Tsukaya, H. (2017). Spatially different tissue-scale diffusivity shapes ANGUSTIFOLIA3 gradient in growing leaves. *Biophys. J.* 113, 1109–1120. doi: 10.1016/j.bpj.2017.06.072

Kim, J. H., and Kende, H. (2004). A transcriptional coactivator, AtGIF1, is involved in regulating leaf growth and morphology in Arabidopsis. *Proc. Natl. Acad. Sci. U. S. A.* 101, 13374–13379. doi: 10.1073/pnas.0405450101

Kim, J. H., and Tsukaya, H. (2015). Regulation of plant growth and development by the GROWTH-REGULATING FACTOR and GRF-INTERACTING FACTOR duo. *J. Exp. Bot.* 66, 6093–6107. doi: 10.1093/jxb/erv349

Kim, J. Y., Yuan, Z., and Jackson, D. (2003). Developmental regulation and significance of KNOX protein trafficking in *Arabidopsis*. *Development* 130, 4351–4362. doi: 10.1242/dev.00618

Kitagawa, M., Wu, P., Balkunde, R., Cunniff, P., and Jackson, D. (2022). An RNA exosome subunit mediates cell-to-cell trafficking of a homeobox mRNA *via* plasmodesmata. *Science* 375, 177–182. doi: 10.1126/science.abm0840

Ko, K. M., Lee, W., Yu, J. R., and Ahnn, J. (2007). PYP-1, inorganic pyrophosphatase, is required for larval development and intestinal function in *C. elegans*. *FEBS Lett.* 581, 5445–5453. doi: 10.1016/j.febslet.2007.10.047

Kriegel, A., Andrés, Z., Medzihradszky, A., Krüger, F., Scholl, S., Delang, S., et al. (2015). Job sharing in the endomembrane system: Vacuolar acidification requires the combined activity of V-ATPase and V-PPase. *Plant Cell* 27, 3383–3396. doi: 10.1105/tpc.15.00733

Lantzouni, O., Alkofer, A., Falter-Braun, P., and Schwechheimer, C. (2020). GROWTH-REGULATING FACTORS interact with DELLAs and regulate growth in cold stress. *Plant Cell* 32, 1018–1034. doi: 10.1105/tpc.19.00784

Lau, O. S., and Bergmann, D. C. (2012). Stomatal development: a plant's perspective on cell polarity, cell fate transitions and intercellular communication. *Development* 139, 3683–3692. doi: 10.1242/dev.080523

Liebsch, D., and Palatnik, J. F. (2020). MicroRNA miR396, GRF transcription factors and GIF co-regulators: a conserved plant growth regulatory module with potential for breeding and biotechnology. *Curr. Opin. Plant Biol.* 53, 31–42. doi: 10.1016/j.pbi.2019.09.008

Li, G., Hu, S., Hou, H., and Kimura, S. (2019). Heterophylly: Phenotypic plasticity of leaf shape in aquatic and amphibious plants. *Plants* 8, 420–1–13. doi: 10.3390/plants8100420

Li, Y., Liu, Y., and Zolman, B. K. (2019). Metabolic alterations in the enoyl-CoA hydratase 2 mutant disrupt peroxisomal pathways in seedlings. *Plant Physiol.* 180, 1860–1876. doi: 10.1104/pp.19.00300

Liu, S., Jobert, F., Rahneshan, Z., Doyle, S. M., and Robert, S. (2021). Solving the puzzle of shape regulation in plant epidermal pavement cells. *Annu. Rev. Plant Biol.* 72, 525–550. doi: 10.1146/annurev-arplant-080720-081920

Liu, D., Song, Y., Chen, Z., and Yu, D. (2009). Ectopic expression of miR396 suppresses *GRF* target gene expression and alters leaf growth in *Arabidopsis*. *Physiol. Plant* 136, 223–236. doi: 10.1111/j.1399-3054.2009.01229.x

Lucero, L. E., Uberti-Manassero, N. G., Arce, A. L., Colombatti, F., Alemano, S. G., and Gonzalez, D. H. (2015). TCP15 modulates cytokinin and auxin responses during gynoecium development in Arabidopsis. *Plant J.* 8, 267–282. doi: 10.1111/tpj.12992

Lui, H., Wang, H., Delong, C., Fowke, L. C., Crosby, W. L., and Fobert, P. R. (2000). The Arabidopsis Cdc2a-interacting protein ICK2 is structurally related to ICK1 and is a potent inhibitor of cyclin-dependent kinase activity *in vitro*. *Plant J.* 21, 379–385. doi: 10.1046/j.1365-313x.2000.00688.x

Lundin, M., Baltscheffsky, H., and Ronne, H. (1991). Yeast PPA2 gene encodes a mitochondrial inorganic pyrophosphatase that is essential for mitochondrial function. *J. Biol. Chem.* 266, 12168–12172. doi: 10.1016/S0021-9258(18)98875-7

Mabuchi, K., Maki, H., Itaya, T., Suzuki, T., Nomoto, M., Sakaoka, S., et al. (2018). MYB30 links ROS signaling, root cell elongation, and plant immune responses. *Proc. Natl. Acad. Sci. U.S.A.* 115, E4710–E4719. doi: 10.1073/pnas.1804233115

Maeshima, M. (2000). Vacuolar H^+-pyrophosphatase. *Biochim. Biophys. Acta* 1465, 37–51. doi: 10.1016/S0005-2736(00)00130-9

Micol, J. L. (2009). Leaf development: time to turn over a new leaf? *Curr. Opin. Plant Biol.* 12, 9–16. doi: 10.1016/j.pbi.2008.11.001

Mizukami, Y., and Fischer, R. L. (2000). Plant organ size control: *AINTEGUMENTA* regulates growth and cell numbers during organogenesis. *Proc. Natl. Acad. Sci. U. S. A.* 97, 942–947. doi: 10.1073/pnas.97.2.942

Nakayama, H., Koga, H., Long, Y., Hamant, O., and Ferjani, A. (2022). Looking beyond the gene network - metabolic and mechanical cell drivers of leaf morphogenesis. *J. Cell Sci.* 135, jcs259611. doi: 10.1242/jcs.259611

Nath, U., Crawford, B. C. W., Carpenter, R., and Coen, E. (2003). Genetic control of surface curvature. *Science* 299, 1404–1407. doi: 10.1126/science.1079354

Nelissen, H., Eeckhout, D., Demuynck, K., Persiau, G., Walton, A., van Bel, M., et al. (2015). Dynamic changes in ANGUSTIFOLIA3 complex composition reveal a growth regulatory mechanism in the maize leaf. *Plant Cell* 27, 1605–1619. doi: 10.1105/tpc.15.00269

Noctor, G., Reichheld, J.-P., and Foyer, C. H. (2018). ROS-related redox regulation and signaling in plants. *Semin. Cell Dev. Biol.* 80, 3–12. doi: 10.1016/j.semcdb.2017.07.013

Nozaki, M., Kawade, K., Horiguchi, G., and Tsukaya, H. (2020). *an3*-mediated compensation is dependent on a cell-autonomous mechanism in leaf epidermal tissue. *Plant Cell Physiol.* 61, 1181–1190. doi: 10.1093/pcp/pcaa048

Omidbakhshfard, M. A., Sokolowska, E. M., Di Vittori, V., Perez de Souza, L., Kuhalskaya, A., Brotman, Y., et al. (2021). Multi-omics analysis of early leaf development in *Arabidopsis thaliana*. *Patterns (N Y).* 2, 100235. doi: 10.1016/j.patter.2021.100235

Ormenese, S. (2004). Analysis of the spatial expression pattern of seven kip related proteins (KRPs) in the shoot apex of *Arabidopsis thaliana*. *Ann. Bot.* 93, 575–580. doi: 10.1093/aob/mch077

Pavelescu, I., Vilarrasa-Blasi, J., Planas-Riverola, A., González-García, M., Caño-Delgado, A. I., and Ibañes, M. (2018). A sizer model for cell differentiation in *Arabidopsis thaliana* root growth. *Mol. Syst. Biol.* 14, e7687. doi: 10.15252/msb.20177687

Penfield, S., Rylott, E. L., Gilday, A. D., Graham, S., Larson, T. R., and Graham, I. A. (2004). Reserve mobilization in the Arabidopsis endosperm fuels hypocotyl elongation in the dark, is independent of abscisic acid, and requires PHOSPHOENOLPYRUVATE CARBOXYKINASE1. *Plant Cell* 16, 2705–2718. doi: 10.1105/tpc.104.024711

Petricka, J. J., Winter, C. M., and Benfey, P. N. (2012). Control of Arabidopsis root development. *Annu. Rev. Plant Biol.* 63, 563–590. doi: 10.1146/annurev-arplant-042811-105501

Powell, A. E., and Lenhard, M. (2012). Control of organ size in plants. *Curr. Biol.* 22, 360–367. doi: 10.1016/j.cub.2012.02.010

Ramirez-Parra, E., and Gutierrez, C. (2007). E2F regulates *FASCIATA1*, a chromatin assembly gene whose loss switches on the endocycle and activates gene expression by changing the epigenetic status. *Plant Physiol.* 144, 105–120. doi: 10.1104/pp.106.094979

Rath, M., Challa, K. R., Sarvepalli, K., and Nath, U. (2022). CINCINNATA-like TCP transcription factors in cell growth - an expanding portfolio. *Front. Plant Sci.* 13, 825341. doi: 10.3389/fpls.2022.825341

Roberts, I. M., Boevink, P., Roberts, A. G., Sauer, N., Reichel, C., and Oparka, K. J. (2001). Dynamic changes in the frequency and architecture of plasmodesmata during the sink-source transition in tobacco leaves. *Protoplasma* 218, 31–44. doi: 10.1007/BF01288358

Rodriguez, R. E., Mecchia, M. A., Debernardi, J. M., Schommer, C., Weigel, D., and Palatnik, J. F. (2010). Control of cell proliferation in *Arabidopsis thaliana* by microRNA miR396. *Development* 137, 103–112. doi: 10.1242/dev.043067

Roeder, A. H. K., Cunha, A., Ohno, C. K., and Meyerowitz, E. M. (2012). Cell cycle regulates cell type in the *Arabidopsis* sepal. *Development* 139, 4416–4427. doi: 10.1242/dev.082925

Ruzicka, K., Strader, L. C., Bailly, A., Yang, H., Blakeslee, J., Langowski, L., et al. (2010). Arabidopsis PIS1 encodes the ABCG37 transporter of auxinic compounds including the auxin precursor indole-3-butyric acid. *Proc. Natl. Acad. Sci. U.S.A.* 107, 10749–10753. doi: 10.1073/pnas.1005878107

Rylott, E. L., Gilday, A. D., and Graham, I. A. (2003). The gluconeogenic enzyme phosphoenolpyruvate carboxykinase in *Arabidopsis* is essential for seedling establishment. *Plant Physiol.* 131, 1834–1842. doi: 10.1104/pp.102.019174

Sakamoto, T., Ikematsu, S., Namie, K., Hou, H., Li, G., and Kimura, S. (2022). Leaf cell morphology alternation in response to environmental signals in *Rorippa aquatica*. *Int. J. Mol. Sci.* 23, 10401–1–10. doi: 10.3390/ijms231810401

Savaldi-Goldstein, S., Peto, C., and Chory, J. (2007). The epidermis both drives and restricts plant shoot growth. *Nature* 446, 199–202. doi: 10.1038/nature05618

Schilling, R. K., Tester, M., Marschner, P., Plett, D. C., and Roy, S. J. (2017). AVP1: One protein, many roles. *Trends Plant Sci.* 22, 154–162. doi: 10.1016/j.tplants.2016.11.012

Schommer, C., Debernardi, J. M., Bresso, E. G., Rodriguez, R. E., and Palatnik, J. F. (2014). Repression of cell proliferation by miR319-regulated TCP4. *Mol. Plant* 7, 1533–1544. doi: 10.1093/mp/ssu084

Segami, S., Tomoyama, T., Sakamoto, S., Gunji, S., Fukuda, M., Kinoshita, S., et al. (2018). Vacuolar H^+-pyrophosphatase and cytosolic soluble pyrophosphatases cooperatively regulate pyrophosphate levels in *Arabidopsis thaliana*. *Plant Cell* 30, 1040–1061. doi: 10.1105/tpc.17.00911

Serralbo, O., Pérez-Pérez, J. M., Heidstra, R., and Scheres, B. (2006). Non-cell-autonomous rescue of anaphase-promoting complex function revealed by mosaic analysis of HOBBIT, an Arabidopsis CDC27 homolog. *Proc. Natl. Acad. Sci. U.S.A.* 103, 13250–13255. doi: 10.1073/pnas.0602410103

Sieburth, L. E., Drews, G. N., and Meyerowitz, E. M. (1998). Non-autonomy of AGAMOUS function in flower development: use of a Cre/loxP method for mosaic analysis in Arabidopsis. *Development* 125, 4303–4312. doi: 10.1242/dev.125.21.4303

Sinha, N. R., Rowland, S. D., and Ichihashi, Y. (2016). Using gene networks in EvoDevo analyses. *Curr. Opin. Plant Biol.* 33, 133–139. doi: 10.1016/j.pbi.2016.06.016

Sizani, B. L., Kalve, S., Markakis, M. N., Domagalska, M. A., Stelmaszewska, J., AbdElgawad, H., et al. (2019). Multiple mechanisms explain how reduced *KRP* expression increases leaf size of *Arabidopsis thaliana*. *New Phytol.* 221, 1345–1358. doi: 10.1111/nph.15458

Stitt, M. (1998). Pyrophosphate as an energy donor in the cytosol of plant cells: an enigmatic alternative to ATP. *Bot. Acta* 111, 167–175. doi: 10.1111/j.1438-8677.1998.tb00692.x

Strader, L. C., and Bartel, B. (2009). The Arabidopsis PLEIOTROPIC DRUG RESISTANCE8/ABCG36 ATP binding cassette transporter modulates sensitivity to the auxin precursor indole-3-butyric acid. *Plant Cell* 21, 1992–2007. doi: 10.1105/tpc.109.065821

Strader, L. C., Culler, A. H., Cohen, J. D., and Bartel, B. (2010). Conversion of endogenous indole-3-butyric acid to indole-3-acetic acid drives cell expansion in Arabidopsis seedlings. *Plant Physiol.* 153, 1577–1586. doi: 10.1104/pp.110.157461

Strader, L. C., Wheeler, D. L., Christensen, S. E., Berens, J. C., Cohen, J. D., Rampey, R. A., et al. (2011). Multiple facets of Arabidopsis seedling development require indole-3-butyric acid-derived auxin. *Plant Cell* 23, 984–999. doi: 10.1105/tpc.111.083071

Sun, T., and Gubler, F. (2004). Molecular mechanism of gibberellin signaling in plants. *Annu. Rev. Plant Biol.* 55, 197–223. doi: 10.1146/annurev.arplant.55.031903.141753

Szymkowiak, E. J., and Sussex, I. M. (1996). What chimeras can tell us about plant development. *Annu. Rev. Plant Physiol. Plant Mol. Biol.* 47, 351–376. doi: 10.1146/annurev.arplant.47.1.351

Tabeta, H., Higashi, Y., Okazaki, Y., Toyooka, K., Wakazaki, M., Sato, M., et al. (2022). Skotomorphogenesis exploits threonine to promote hypocotyl elongation. *Quantitative Plant Biol.* 3, E26. doi: 10.1017/qpb.2022.19

Tabeta, H., Watanabe, S., Fukuda, K., Gunji, S., Asaoka, M., Hirai, M. Y., et al. (2021). An auxin signaling network translates low-sugar-state input into compensated cell enlargement in the *fugu5* cotyledon. *PloS Genet.* 17, e1009674. doi: 10.1371/journal.pgen.1009674

Takahashi, K., Morimoto, R., Tabeta, H., Asaoka, M., Ishida, M., Maeshima, M., et al. (2017). Compensated cell enlargement in *fugu5* is specifically triggered by lowered sucrose production from seed storage lipids. *Plant Cell Physiol.* 58, 668–678. doi: 10.1093/pcp/pcx021

Takahashi, N., Lammens, T., Boudolf, V., Maes, S., Yoshizumi, T., De Jaeger, G., et al. (2008). The DNA replication checkpoint aids survival of plants deficient in the novel replisome factor ETG1. *EMBO J.* 27, 1840–1851. doi: 10.1038/emboj.2008.107

Trinh, D. C., Alonso-Serra, J., Asaoka, M., Colin, L., Cortes, M., Malivert, A., et al. (2021). How mechanical forces shape plant organs. *Curr. Biol.* 31, R143–R159. doi: 10.1016/j.cub.2020.12.001

Tsukagoshi, H. (2012). Defective root growth triggered by oxidative stress is controlled through the expression of cell cycle-related genes. *Plant Sci.* 197, 30–39. doi: 10.1016/j.plantsci.2012.08.011

Tsukagoshi, H., Busch, W., and Benfey, P. N. (2010). Transcriptional regulation of ROS controls transition from proliferation to differentiation in the root. *Cell* 143, 606–616. doi: 10.1016/j.cell.2010.10.020

Tsukaya, H. (2002a). Interpretation of mutants in leaf morphology: Genetic evidence for a compensatory system in leaf morphogenesis that provides a new link between cell and organismal theories. *Int. Rev. Cytol.* 217, 1–39. doi: 10.1016/S0074-7696(02)17011-2

Tsukaya, H. (2002b). The leaf index : Heteroblasty, natural variation, and the genetic control of polar processes of leaf expansion. *Plant Cell Physiol.* 43, 372–378. doi: 10.1093/pcp/pcf051

Tsukaya, H. (2003). Organ shape and size : A lesson from studies of leaf morphogenesis. *Curr. Opi. Plant Biol.* 6, 57–62. doi: 10.1016/S1369526602000055

Tsukaya, H. (2008). Controlling size in multicellular organs: focus on the leaf. *PloS Biol.* 6, e174. doi: 10.1371/journal.pbio.0060174

Tsukaya, H. (2014). Comparative leaf development in angiosperms. *Curr. Opin. Plant Biol.* 17, 103–109. doi: 10.1016/j.pbi.2013.11.012

Tsukaya, H. (2018). Leaf shape diversity with an emphasis on leaf contour variation, developmental background, and adaptation. *Semin. Cell Dev. Biol.* 79, 48–57. doi: 10.1016/j.semcdb.2017.11.035

Ullah, H., Chen, J. G., Young, J. C., Im, K. H., Sussman, M. R., and Jones, A. M. (2001). Modulation of cell proliferation by heterotrimeric g protein in *Arabidopsis*. *Science* 292, 2066–2069. doi: 10.1126/science.1059040

Vercruysse, J., Baekelandt, A., Gonzalez, N., and Inzé, D. (2020). Molecular networks regulating cell division during Arabidopsis leaf growth. *J. Exp. Bot.* 71, 2365–2378. doi: 10.1093/jxb/erz522

Vercruyssen, L., Verkest, A., Gonzalez, N., Heyndrickx, K. S., Eeckhout, D., Han, S. K., et al. (2014). ANGUSTIFOLIA3 binds to SWI/SNF chromatin remodeling complexes to regulate transcription during *Arabidopsis* leaf development. *Plant Cell* 26, 210–229. doi: 10.1105/tpc.113.115907

Verkest, A., Manes, C. L., de, O., Vercruysse, S., Maes, S., van der Schueren, E., et al. (2005). The cyclin-dependent kinase inhibitor KRP2 controls the onset of the endoreduplication cycle during Arabidopsis leaf development through inhibition of mitotic CDKA;1 kinase complexes. *Plant Cell* 17, 1723–1736. doi: 10.1105/tpc.105.032383

Wang, H., Kong, F., and Zhou, C. (2021). From genes to networks: The genetic control of leaf development. *J. Integr. Plant Biol.* 63, 1181–1196. doi: 10.1111/jipb.13084

Wang, H., Qi, Q., Schorr, P., Cutler, A. J., Crosby, W. L., and Fowke, L. C. (1998). ICK1, a cyclin-dependent protein kinase inhibitor from Arabidopsis thaliana interacts with both Cdc2a and CycD3, and its expression is induced by abscisic acid. *Plant J.* 15, 501–510. doi: 10.1046/j.1365-313X.1998.00231.x

Wang, X., Wang, H., Liu, S., Ferjani, A., Li, J., Yan, J., et al. (2016). Genetic variation in *ZmVPP1* contributes to drought tolerance in maize seedlings. *Nat. Genet.* 48, 1233–1241. doi: 10.1038/ng.3636

Wang, H., Zhou, Y., Gilmer, S., Whitwill, S., and Fowke, L. C. (2000). Expression of the plant cyclin-dependent kinase inhibitor ICK1 affects cell division, plant growth and morphology. *Plant J.* 24, 613–623. doi: 10.1046/j.1365-313x.2000.00899.x

Wendehenne, D., Gao, Q., Kachroo, A., and Kachroo, P. (2014). Free radical-mediated systemic immunity in plants. *Curr. Opin. Plant Biol.* 20, 127–134. doi: 10.1016/j.pbi.2014.05.012

Wood, E., and Nurse, P. (2015). Sizing up to divide: Mitotic cell-size control in fission yeast. *Annu. Rev. Cell Dev. Biol.* 31, 11–29. doi: 10.1146/annurev-cellbio-100814-125601

Xu, X. M., Wang, J., Xuan, Z., Goldshmidt, A., Borrill, P. G. M., Hariharan, N., et al. (2011). Chaperonins facilitate KNOTTED1 cell-to-Cell trafficking and stem cell function. *Science* 333, 1141–1144. doi: 10.1126/science.1205727

Yuan, Z., Luo, D., Li, G., Yao, X., Wang, H., Zeng, M., et al. (2010). Characterization of the *AE7* gene in Arabidopsis suggests that normal cell proliferation is essential for leaf polarity establishment. *Plant J.* 64, 331–342. doi: 10.1111/j.1365-313X.2010.04326.x

Zhang, D., Sun, W., Singh, R., Zheng, Y., Cao, Z., Li, M., et al. (2018). *GRF-interacting factor1* regulates shoot achitecture and meristem determinacy in maize. *Plant Cell* 30, 360–374. doi: 10.1105/tpc.17.00791

Zolman, B. K., Martinez, N., Millius, A., Adham, A. R., and Bartel, B. (2008). Identification and characterization of Arabidopsis indole-3-butyric acid response mutants defective in novel peroxisomal enzymes. *Genetics* 180, 237–251. doi: 10.1534/genetics.108.090399

frontiers | Frontiers in Plant Science

TYPE Original Research
PUBLISHED 27 January 2023
DOI 10.3389/fpls.2023.1031426

OPEN ACCESS

EDITED BY
Taku Takahashi,
Okayama University, Japan

REVIEWED BY
Jianmin Wan,
Institute of Crop Sciences (CAAS), China
Hiroyasu Motose,
Okayama University, Japan

*CORRESPONDENCE
Hélène Javot
helene.javot@cea.fr
Ali Ferjani
ferjani@u-gakugei.ac.jp

SPECIALTY SECTION
This article was submitted to Plant Physiology, a section of the journal Frontiers in Plant Science

RECEIVED 30 August 2022
ACCEPTED 09 January 2023
PUBLISHED 27 January 2023

CITATION
Tojo H, Tabeta H, Gunji S, Hirai MY, David P, Javot H and Ferjani A (2023) Roles of type II H^+-PPases and PPsPase1/PECP2 in early developmental stages and PPi homeostasis of *Arabidopsis thaliana*. *Front. Plant Sci.* 14:1031426. doi: 10.3389/fpls.2023.1031426

Roles of type II H^+-PPases and PPsPase1/PECP2 in early developmental stages and PPi homeostasis of *Arabidopsis thaliana*

Hiroshi Tojo[1,2], Hiromitsu Tabeta[1,2,3], Shizuka Gunji[2], Masami Y. Hirai[3], Pascale David[4], Hélène Javot[4,5]* and Ali Ferjani[2]*

[1]Department of Life Sciences, Graduate School of Arts and Sciences, The University of Tokyo, Tokyo, Japan, [2]Department of Biology, Tokyo Gakugei University, Koganei, Tokyo, Japan, [3]RIKEN Center for Sustainable Resource Science, Yokohama, Japan, [4]Aix Marseille Univ, CEA, CNRS, BIAM, Saint Paul-Lez-Durance, France, [5]Aix Marseille Univ, CEA, CNRS, BIAM, Marseille, France

The regulation of intracellular pyrophosphate (PPi) level is crucial for proper morphogenesis across all taxonomic kingdoms. PPi is released as a byproduct from ~200 metabolic reactions, then hydrolyzed by either membrane-bound (H^+-PPase) or soluble pyrophosphatases (PPases). In Arabidopsis, the loss of the vacuolar H^+-PPase/FUGU5, a key enzyme in PPi homeostasis, results in delayed growth and a number of developmental defects, pointing to the importance of PPi homeostasis in plant morphogenesis. The Arabidopsis genome encodes several PPases in addition to FUGU5, such as PPsPase1/PECP2, VHP2;1 and VHP2;2, although their significance regarding PPi homeostasis remains elusive. Here, to assess their contribution, phenotypic analyses of cotyledon aspect ratio, palisade tissue cellular phenotypes, adaxial side pavement cell complexity, stomatal distribution, and etiolated seedling length were performed, provided that they were altered due to excess PPi in a *fugu5* mutant background. Overall, our analyses revealed that the above five traits were unaffected in *ppspase1/pecp2*, *vhp2;1* and *vhp2;2* loss-of-function mutants, as well as in *fugu5* mutant lines constitutively overexpressing *PPsPase1/PECP2*. Furthermore, metabolomics revealed that *ppspase1/pecp2*, *vhp2;1* and *vhp2;2* etiolated seedlings exhibited metabolic profiles comparable to the wild type. Together, these results indicate that the contribution of PPsPase1/PECP2, VHP2;1 and VHP2;2 to PPi levels is negligible in comparison to FUGU5 in the early stages of seedling development.

KEYWORDS

***Arabidopsis thaliana*, pyrophosphate homeostasis, vacuolar type-I H^+-PPase, vacuolar type-II H^+-PPases, PPsPase1/PECP2, metabolism**

Abbreviations: H^+-PPase, H^+-translocating pyrophosphatase; sPPase, soluble pyrophosphatase; PPi, inorganic pyrophosphate; PCho, phosphocholine; PEtn, phosphoethanolamine; ThMP, thiamine monophosphatase; PC, pavement cell; UI, undulation index; SI, stomatal index; DAS, days after seed sowing; DAI, days after induction of seed germination.

Introduction

Pyrophosphate (PPi) is produced from nearly 200 different metabolic reactions, as a byproduct of macromolecule synthesis (Heinonen, 2001). It is released during the production of DNA, RNA, proteins and polysaccharides, and can reciprocally be used as a phosphate donor or an energy donor in conditions where ATP levels are limited, although this dogma was challenged recently (Wimmer et al., 2021). Due to the reversibility of many enzymatic reactions, PPi overaccumulation is strictly avoided in the plant cytoplasm, in order to prevent retroinhibition of metabolic pathways (Stitt, 1998; Wimmer et al., 2021). PPi-degrading enzymes (i.e. pyrophosphatases) are key players in the maintenance of the PPi cell concentration, and belong to very distinct families of soluble or membrane-bound proteins (Heinonen, 2001).

The vacuolar (type-I) V-PPases are 16 TM-domain proteins, and are the most well-described category of pyrophosphatases. The crystal structure of the V-PPase from *Vigna radiata* (*Vr*H$^+$-PPase) has been resolved (Figure 1A; Supplemental Movie 1), revealing residues involved in PPi hydrolysis (Figure 1B; Supplemental Movie 1) and proton transport (Figure 1C; Supplemental Movie 1; Lin et al., 2012; Tsai et al., 2019). In Arabidopsis, this family is represented by a single gene (*FUGU5*/*VHP1*;*1*/*AVP1*/AT1G15690; Figures 1A–C). The study of V-PPase loss-of-function *fugu5* mutants has revealed the importance of this enzyme, as they display a range of mild phenotypic defects that are particularly clear in tissues showing intense gluconeogenesis activity (growing tissues and etiolated seedlings in particular). FUGU5 is a bifunctional protein that also combines proton pumping and PPase activities (Figures 1B, C), and is capable of translocating protons from the cytosol into the vacuole lumen by PPi hydrolysis (Maeshima, 2000). The consequences of altering PPase activity in *fugu5* mutants are particularly clear for germinating seedlings, and this phenotype is independent from FUGU5 proton pumping activity (Bertoni, 2011; Ferjani et al., 2011; Asaoka et al., 2016; Takahashi et al., 2017). Increased PPi levels in *fugu5* are associated with inhibited hypocotyl elongation in etiolated seedlings (Ferjani et al., 2011). Seedlings grown in the light also display an altered cotyledon shape, as well as modifications of their palisade tissues, adaxial-side pavement cell complexity and stomatal distribution (Ferjani et al., 2007; Ferjani et al., 2011; Asaoka et al., 2019; Fukuda et al., 2020; Gunji et al., 2020; Gunji et al., 2022). These characteristics can be rescued by expressing IPP1, a soluble yeast pyrophosphatase (Ferjani et al., 2011; Segami et al., 2018; Gunji et al., 2020; Gunji et al., 2022). The proton pumping activity of FUGU5 is important in conditions where ATP levels are limiting, allowing the cells to sustain a proton gradient between the vacuole and the cytosol even when the primary vacuolar proton pumps (V-ATPases) display limiting activities, such as during anoxia (Maeshima, 2000; Kriegel et al., 2015). The remarkable abundance of these two categories of proton pumps (V-PPases and V-ATPases) within the vacuolar membrane highlights the importance of maintaining an active proton gradient (ΔpH) in a wide range of conditions (Gaxiola et al., 2007; Schumacher, 2014; Kriegel et al., 2015).

Other proteins are capable of degrading PPi in plant cells, which explains why *fugu5* mutants only show phenotypic defects in

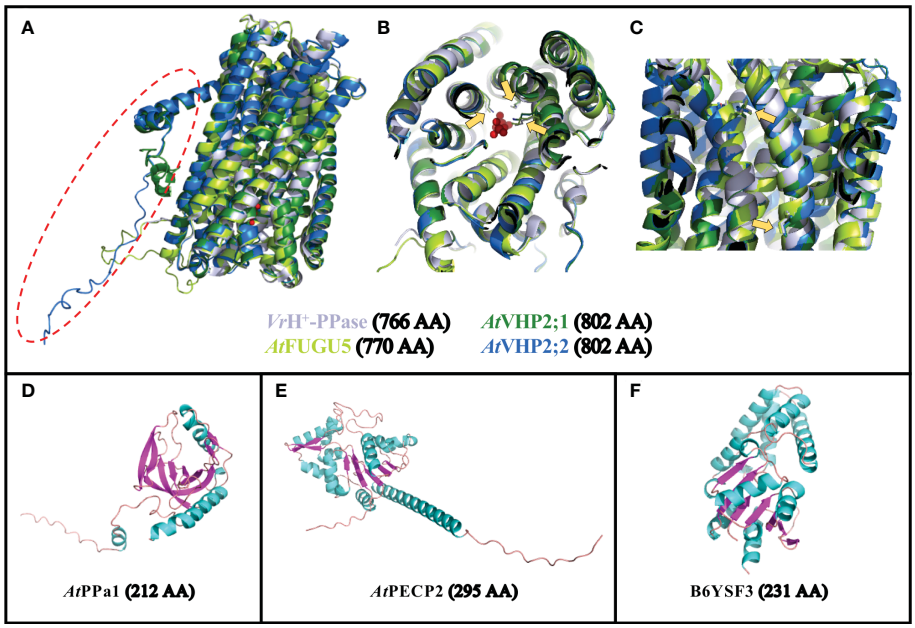

FIGURE 1
Predicted structures of selected PPases. **(A–C)** Overlay of the predicted structures for FUGU5 (UniProt P31414; in bright green),VHP2;1 (UniProt Q56ZN6; in dark green) and VHP2;2 (UniProt Q9FWR2; in blue) onto the crystal structure of *Vr*H$^+$-PPase (PDB reference 4A01, Chain A; in light gray). **(A)** General overview of the 4 structures showing the strong conservation of these 16-TM proteins, with the exception of an additional N-terminal domain in VHP2;1 and 2;2 (surrounded by a red dotted circle). **(B)** Rotated view showing the positions of 3 AA (yellow arrows) involved in PPi binding in *Vr*H$^+$-PPase, overlapping with the corresponding positions within the 3 predicted structures of FUGU5, VHP2;1 and VHP2;2. **(C)** Side view showing the positions of 2 AA (yellow arrows) involved in proton pumping in *Vr*H$^+$-PPase, overlapping with the corresponding positions within the 3 predicted structures of FUGU5, VHP2;1 and VHP2;2. **(D)** Predicted structure for PPa1 (UniProt Q93V56). **(E)** Predicted structure for PECP2 (UniProt Q67YC0). **(F)** Predicted structure for *T. onnurineus* TON_0002 PPase (UniProt B6YSF3). The number of AA for the full-length proteins is indicated between brackets. AA, amino acid.

conditions where PPi production is particularly intense (Ferjani et al., 2011; Ferjani et al., 2014). A number of proteins use PPi as a cofactor to empower metabolic reactions, such as the enzyme pyrophosphate fructose-6-phosphate 1-phosphotransferase (PFP or PPi-PFK; EC 2.7.1.90), which is responsible for the reversible conversion of fructose-6-phosphate into fructose-1,6-biphosphate (Lim et al., 2009; Lim et al., 2014; Duan et al., 2016). In addition, UDP-glucose pyrophosphorylase (UGPase; EC 2.7.7.9) catalyzes the reversible production of UDP-Glu and PPi from a range of substrates (Kleczkowski et al., 2004; Liu et al., 2021). Clearly, their enzymatic activities are not centered on PPi homeostasis, although their ability to use PPi as a substrate and their sensitivity to PPi levels does explain why impairing PPi homeostasis has such a strong impact on carbohydrate metabolism.

In contrast to these enzymes, soluble pyrophosphatases (sPPases; Figure 1D) are dedicated to the degradation of PPi into two Pi molecules (Öztürk et al., 2014; Gutiérrez-Luna et al., 2016; Segami et al., 2018). The crystal structure of soluble AtPPa1 was recently determined, and its strong similarity to yeast IPP1 sPPase was confirmed (Grzechowiak et al., 2019). Their comparison highlighted the highly conserved active sites and their organization, but also revealed that PPa1 is even closer to prokaryotic PPases (Grzechowiak et al., 2019). PPa1 enzyme is composed of nine β-strands and two α-helices, with a compact core containing five anti-parallel β-barrels (Figure 1D; Grzechowiak et al., 2019). In Arabidopsis, sPPases are mostly targeted to the cytosol (AtPPa1 through 5), whereas only one is targeted to the plastids (AtPPa6; Öztürk et al., 2014; Schulze et al., 2004). Previous work has shown that mutations in these enzymes could have strong developmental defects (hypocotyl elongation, cell wall composition, starch content, etc.), particularly when combined with *fugu5* mutations (Segami et al., 2018). The severity of the phenotype was then correlated with the level of PPi increase in the cell. The large set of sPPase genes, together with the abundance of V-PPase in the vacuolar membrane, is another indication of the tight control exerted by plant cells on PPi cytoplasmic levels (Kriegel et al., 2015; Segami et al., 2018).

In addition to these different categories of PPases, several other plant pyrophosphatases are associated with subcellular compartments. Type-II H^+-PPases (VHP2/AVP2 or AVPL1-like) have a dual function of PPi hydrolysis and H^+-translocation (Drozdowicz and Rea, 2001), like the vacuolar FUGU5, however they are localized in the Golgi (Drozdowicz and Rea, 2001; Mitsuda et al., 2001; Segami et al., 2010). This family contains two genes in Arabidopsis, *AtVHP2;1* (At1g78920) and *AtVHP2;2* (At1g16780), in which *VHP2;1* expression levels are much higher than *VHP2;2* levels (Segami et al., 2010). *VHP2;1* is particularly expressed in the cotyledons and roots of young seedlings, as well as in the trichomes of rosette leaves, and the stamina (Mitsuda et al., 2001). Type-I and type-II H^+-PPases show highly conserved structures, with the exception of an additional N-terminal domain for type-II PPases (Figures 1A–C; Supplemental Movie 1); however, type-II H^+-PPases are expressed at much lower levels than type-I H^+-PPases (Segami et al., 2010). Although the properties and expression patterns of these PPases have been well-studied (Drozdowicz and Rea, 2001; Segami et al., 2010), their *in vivo* significance regarding their physiological role remains to be characterized. The precise overlap of their structures with type-I H^+-PPase (Figure 1) reflects their dual function in PPi hydrolysis and proton pumping, driving Golgi acidification. However, the importance of this protein in terms of overall cytosolic PPi homeostasis within the cell, and in terms of Golgi acidification, still remains to be discovered.

The endoplasmic reticulum compartment might be associated with a final PPase category: Arabidopsis HAD-type protein PPsPase1/PECP2 (encoded by At1g73010; Figure 1E). This protein was identified based on its fast responsiveness to phosphate starvation (May et al., 2011; Hanchi et al., 2018; Angkawijaya et al., 2019). Phosphate is an essential macronutrient for plant growth and development, and its deficiency triggers striking morphological changes in plant roots, such as reduced primary root length and increased lateral root length, as well as root hair length and density (Williamson et al., 2001; Linkohr et al., 2002; Al-Ghazi et al., 2003; Reymond et al., 2006). From a structural point of view, PPsPase1/PECP2 is completely different from sPPases (Figures 1D, E), as it possesses the typical structure of HAD hydrolases, composed of a Rossmann-like fold (a set of about 6 parallel β-strands surrounded by additional helices on each side), completed by an additional "cap domain" (Kuznetsova et al., 2015). The enzymatic characterization of the recombinant protein PPsPase1/PECP2 in *Escherichia coli* revealed an efficient cleavage of PPi by this enzyme, making it one of the rare pyrophosphatases from the HAD superfamily, along with others including the first-identified member (B6YSF3; Figure 1F) from *Thermococcus onnurineus* (Lee et al., 2009; May et al., 2011). Another enzyme among the rare HAD family members with pyrophosphatase activity is BT2127 from *Bacteroides thetaiotaomicron*, which has been crystallized (Huang et al., 2011). The His23 and Lys79 residues of BT2127 are thought to be responsible for the efficient PPi catalysis of this protein, whereas most of the other HAD members show a phosphomonoesterase activity (Zhang et al., 2022). As these two residues do not seem to be conserved in B6YSF3 (data not shown), it appears that this mechanisms might not be a universal feature of PPases belonging to the HAD family. In the case of PECP2, the sequences are even more divergent from the above two reference HAD-type PPases. Experiments with *ppspase1/pecp2* mutants, especially when combined with mutations in the homolog gene *pecp1*, revealed that the most obvious phenotype was related to altered phosphocholine (PCho) and phosphoethanolamine (PEtn) content (Hanchi et al., 2018; Tannert et al., 2018; Angkawijaya and Nakamura, 2017; Angkawijaya et al., 2019). Since PECP1 exhibits an affinity for PCho and PEtn when expressed in *E. coli* (May et al., 2012), it was suggested that PPsPase1/PECP2 might actually favor this substrate *in vivo* rather than PPi. Indeed, KO mutants of *PPsPase1/PECP2* did not display any phenotypes that are classically associated with PPi defects (Hanchi et al., 2018). In addition, the combination of *fugu5* with *ppspase1/pecp2* and *pecp1* mutations did not accentuate *fugu5* phenotypes. However, it remains to be demonstrated if *ppspase1/pecp2* has any detectable impact on PPase homeostasis *in planta*. A third and final homolog named *ThMPase1/PECP3* (encoded by At4g29530) is expressed in plants at low levels, and does not respond to Pi availability (Hanchi et al., 2018; Tannert et al., 2021). Based on heterologous expression in yeast, this homolog was initially shown to dephosphorylate thiamine monophosphate with a high

efficiency (Hasnain et al., 2016). PEtn was later revealed to be the favored substrate of this enzyme *in planta*, instead of thiamine monophosphate (Tannert et al., 2021).

Clearly, there is a need to further characterize *VHP2;1, VHP2;2* and *PPsPase1/PECP2* in relation to their physiological functions; moreover, the unambiguous demonstration of a substantial impact on overall PPi content *in planta* is lacking. Although the quantification of PPi levels in KO lines might be a useful strategy, PPi is notoriously difficult to extract from plant cells for quantification due to its labile nature (Heinonen, 2001). Analysis of cell contents by ion-exchange chromatography (Yoza et al., 1991; Ruiz-Calero and Galceran, 2005) was instrumental in demonstrating the altered PPi content of several PPi homeostasis mutants (Ferjani et al., 2011; Segami et al., 2018), but PPi quantification from plant extracts remains rare. Nevertheless, there is an active field of research focused on developing methods for *in vivo* PPi measurements based on fluorescent probes. Although recent progress in this domain seems promising (Wang et al., 2021), no probe has yet been established as a standard.

As a proxy for direct PPi quantification, one powerful substitute consists in revealing alterations of PPi homeostasis based on plant phenotypic changes (Ferjani et al., 2011; Segami et al., 2018; Asaoka et al., 2019; Fukuda et al., 2020; Gunji et al., 2020; Tabeta et al., 2021). Thanks to the in-depth characterization of Arabidopsis mutants showing altered PPi homeostasis, specific plant anatomical parameters can be quantified to reveal subtle alterations in parameters linked to PPi concentration.

The *fugu5* mutants were initially characterized on the basis of the alteration of their cotyledon shape (Ferjani et al., 2007). Later, it was revealed that altered PPi levels were also responsible for hypocotyl elongation defects in etiolated seedlings (Ferjani et al., 2011). This parameter, more easily quantifiable than the determination of cotyledon rotundity, is inversely correlated with PPi accumulation in germinating seedlings grown in the absence of sucrose (Segami et al., 2018). This phenotype is strongly aggravated when combined with a mutation in the cytosolic sPPase *PPa1* gene, whereas combination with *ppa2* through 5 did not enhance the *fugu5* phenotype. Using *fugu5 ppa1* double mutants was necessary to validate the *in vivo* PPase activity of PPa1, since the effects of a single *ppa1* mutation can be masked by the activity of the vacuolar (type-I) FUGU5 V-PPase (Segami et al., 2018; Fukuda et al., 2020). Combinations of *fugu5* and candidate PPases are therefore capable of revealing the importance of genes in relation to PPi homeostasis, in a highly quantifiable manner. Other parameters such as cell complexity or cell wall composition were subsequently identified as also altered in the *fugu5* mutant in response to PPi levels (Segami et al., 2018; Fukuda et al., 2020; Gunji et al., 2020; Gunji et al., 2022). Altogether, the quantification of these parameters makes it possible to unambiguously predict a PPi homeostasis defect for novel mutants.

Reciprocally, it is also possible to demonstrate the PPase activity of enzymes by overexpressing candidate genes in a *fugu5* mutant background, as shown with the heterologous expression of the soluble yeast pyrophosphatase IPP1 in Arabidopsis, which rescued the *fugu5* phenotype (Ferjani et al., 2011; Asaoka et al., 2019; Gunji et al., 2020; Gunji et al., 2022). This complementation also demonstrated that the developmental alterations of *fugu5* were due to the loss of pyrophosphatase function, rather than its proton translocation activity. This approach is similar to the complementation of the growth defect of yeast deficient in the endogenous cytosolic PPase (IPP1), which can be complemented by overexpression of *IPP1* or other PPases, as previously demonstrated for Arabidopsis sPPases (Schulze et al., 2004; Segami et al., 2018). Altogether, the use of *fugu5* as a standard instead of WT plants, combined with the scoring of anatomical properties, makes it possible to detect increases in cytosolic PPi levels even beyond the ones in *fugu5* (as reported in Segami et al., 2018), or a range of intermediate levels between those in WT and *fugu5* (as reported in Ferjani et al., 2011).

Here, to assess the contribution of type-II H^+-PPases (VHP2;1, VHP2;2) and PPsPase1/PECP2 to PPi homeostasis, we opted for an in-depth phenotypical characterization of single and combined mutants, as well as a set of overexpressing lines. As we show that no obvious alteration of the overall PPi levels is associated with PPsPase1/PECP2, we use the name PECP2 throughout the manuscript. In addition, our study presents metabolomics data that provide a complete overview of the mutant characterizations, focusing on the early stages of seedling development.

Materials and methods

Comparison of protein structures

The structures of the full length proteins corresponding to FUGU5 (UniProt Accession P31414), VHP2;1 (UniProt Q56ZN6), VHP2;2 (UniProt Q9FWR2), PPa1 (UniProt Q93V56), PECP2 (UniProt Q67YC0) and *Thermococcus onnurineus* TON_0002 PPase (UniProt B6YSF3) were predicted using AlphaFold (Jumper et al., 2021; Varadi et al., 2022). The crystal structure from *Vr*H^+-PPase (UniProt 21616) was obtained from the Protein Data Bank (PDB reference 4A01, Chain A; Lin et al., 2012). Overlays and visualization of structures were performed using The PyMOL Molecular Graphics System, Version 2.5 Schrödinger, LLC.

Plant materials and growth conditions

Mutants and all transgenic plants were in the Columbia-0 (Col-0) background, and *Arabidopsis thaliana* Col-0 was used as the wild type (WT). *fugu5-1* and *fugu5-3* were isolated and characterized as the loss-of-function mutant of the vacuolar type-I H^+-PPase (Horiguchi et al., 2006b; Ferjani et al., 2007; Ferjani et al., 2011; Fukuda et al., 2016; Segami et al., 2018; Fukuda et al., 2020; Gunji et al., 2020; Gunji et al., 2022). *pecp2-1* and *pecp2-3* (previously described as *ppspase1-1* or *ps2-1*, and *ppspase1-3*, respectively), *pecp1-1*, the *fugu5-1 pecp2-1 pecp1-1* triple homozygous mutant (Hanchi et al., 2018), and the *vhp2;1* and *vhp2;2-2* (Segami et al., 2010) loss-of-function mutants were previously reported.

Seeds were sown on rockwool (Nippon Rockwool Corp.), watered daily with 0.5 g L^{-1} Hyponex solution and grown under a 16/8-h

light/dark cycle with white light from fluorescent lamps at approximately 50 µmol m^{-2} s^{-1} and 22°C.

Sterilized seeds were sown on sucrose-free Murashige and Skoog (MS) medium (Wako Pure Chemical). 0.1% (w/v) 2-(N-morpholino) ethanesulfonic acid (MES) was added, the pH was adjusted to 5.8 with KOH, and then the medium was solidified using 0.2% to 0.5% (w/v) gellan gum (Murashige and Skoog, 1962). The seeds were sown on the MS plates, which were then stored at 4°C in the dark for 3 days of cold treatment. After cold treatment, the seedlings were grown either in the light (as indicated above) or in the dark for the indicated periods of time.

Generation of transgenic plants and gene overexpression quantification by RT-qPCR

To overexpress *PECP2* under *35S* promoter control, *fugu5-1* and *fugu5-3* mutants (Ferjani et al., 2011) were transformed with the previously described *Prom35S::PECP2* plasmids (Hanchi et al., 2018). Plant transformation was performed using *Agrobacterium tumefaciens* C58C1 with a simplified version of the floral dip method (Clough and Bent, 1998; Logemann et al., 2006).

After transformation, T_1 transformants were selected on soil using Basta, and a preliminary selection of overexpressing lines was performed by RT-qPCR. Only overexpressing lines showing a 3:1 segregation of PPT resistance in T_2 (suggesting a single T-DNA insertion event) were re-amplified to obtain homozygous plants in T_3. Quantification of the overexpression level was performed by RT-qPCR in the T_3 generation as in Hanchi et al. (2018), using *ROC3* and *GAPC1* as reference genes. RNA was extracted from two independent biological replicates (9-12 plants; 50–90 mg of frozen plant tissue per sample). Data were analyzed using the Relative Expression Software Tool REST2009 running 5,000 iterations of the randomized test (Pfaffl et al., 2002).

Morphological observations and cellular phenotypic analyses

Photographs of gross plant phenotypes at 10 days after seed sowing (DAS) and 3 days after induction of seed germination (DAI) were obtained using a stereoscopic microscope (M165FC; Leica Microsystems) connected to a charge-coupled device (CCD) camera (DFC300FX; Leica Microsystems). Cotyledons were fixed in formalin–acetic acid–alcohol (FAA; 4% formalin, 5% acetic acid, and 50% ethanol) and cleared with chloral solution (200 g of chloral hydrate, 20 g of glycerol, and 50 mL of deionized water) to measure cotyledon area and cell number, as previously described (Tsuge et al., 1996). Whole cotyledons were observed using a stereoscopic microscope equipped with a CCD camera. Cotyledon palisade tissue cells were observed and photographed under a light microscope (DM-2500; Leica Microsystems) equipped with Nomarski differential interference contrast optics and a CCD camera. Cell size was determined as mean palisade cell area, determined from a paradermal view, as previously described (Ferjani et al., 2011). The cotyledon aspect ratio was calculated as the ratio of the cotyledon blade length to its width.

Electron microscopy observation and quantitative analysis of epidermal cells

For scanning electron microscopy (SEM), cotyledons were dissected from plants at the indicated growth stages. Samples were fixed overnight in FAA at room temperature. The fixed specimens were dehydrated in an ethanol series (50, 60, 70, 80, 90, 95, 99.5, and 100% [v/v]; 60 min per step) and stored overnight in 100% (v/v) ethanol at room temperature. The ethanol was replaced with 3-methylbutyl acetate and the samples were dried in a critical-point dryer (JCPD-5; JEOL), sputter-coated with gold–palladium using an anion sputter (JFC-1100; JEOL), and examined under an S-3400N SEM (Hitachi), as previously described (Maeda et al., 2014; Gunji et al., 2020; Gunji et al., 2022). SEM images of the adaxial side of cotyledons were used to quantify pavement cell complexity. The area and perimeter of individual pavement cells (25 cells from one cotyledon; six cotyledons in total) were measured using ImageJ (version 1.63), and their complexity was quantified by calculating the undulation index (UI; Thomas et al., 2003) using the following equation (Kürschner, 1997):

$$UI = \frac{Ce}{2\pi\sqrt{Ae/\pi}}$$

where UI (dimensionless) is the undulation index, *Ce* (µm) is the cell perimeter, and *Ae* (µm^2) is the cell area. Note that an increased undulation index means increased pavement cell complexity, and *vice versa*. The stomatal index (SI) is the percentage of the number of stomata to the total number of epidermal cells. The SI was calculated using the following equation:

$$SI = (Stx100)/(E + St)$$

where St is the number of stomata per unit area, and E is the number of epidermal cells within the same unit area.

Wide-target metabolome analysis of GC-QqQ-MS

A total of 100 etiolated seedlings at 3 DAI were collected in one tube in liquid nitrogen and freeze-dried. Subsequently, the samples were extracted using a bead shocker in a 2-mL tube with 5-mm zirconia beads and 80% MeOH for 2 min at 1,000 rpm (Shake Master NEO, Biomedical Sciences). The extracted solutions were centrifuged at 1,000 rpm for 1 min, and 100 µL of centrifuged solution and 10 µL of 0.2 mg/mL Adonitol (Internal Standard; I.S.) were dispensed into 1.5-mL tubes. After drying the solution using a centrifuge evaporator (SpeedVac, Thermo), 100 µL Mox reagent (2% methoxyamine in pyridine, Thermo) was added to the 1.5-mL tubes, and the metabolites were methoxylated at 30°C and 1,200 rpm for approximately 6 h using a Thermo shaker (BSR-MSC100, Biomedical Sciences). After methoxylation, 50 µL (1% v/v) of trimethylchlorosilane (TMS, Thermo) were added to the 1.5-mL tubes. For TMS derivatization, the mixture was incubated for 30 min at 1,200 rpm and 37°C, as stated above. Finally, 50 µL of the derivatized samples were dispensed in vials for wide-target metabolome analyses of GC-QqQ-MS (AOC-5000 Plus with

GCMS-TQ8040, Shimadzu Corporation). Raw data collection was performed using the GCMSsolution software (Shimadzu Corporation). Calculation of the peak area values was conducted using MRMPROBS (Tsugawa et al., 2013; Tsugawa et al., 2014a; Tsugawa et al., 2014b). Peak areas were normalized using a quality control sample and the LOWESS/Spline normalization tool (Tsugawa et al., 2014a). Detailed GC-QqQ-MS parameters and MRM transitions for wide-target analysis were previously described (Tabeta et al., 2021; Tabeta et al., 2022).

Statistical analyses

Statistical analyses were performed using Tukey's HSD test (R ver. 4.0.2.; R Core Team, 2020). Multiple comparisons were performed using the multcomp package (Hothorn et al., 2008). PCA plots were calculated and constructed using Statistics in Microsoft Excel (URL http://prime.psc.riken.jp/compms/others/main.html#Statistics) (Tsugawa et al., 2015; Matsuo et al., 2017). RT-qPCR data were analyzed using the randomization method from the Relative Expression Software Tool REST2009 (Pfaffl et al., 2002) as in Hanchi et al. (2018).

Results

Effect of the *pecp2* and *vhp2;1 vhp2;2* mutations on cotyledon gross morphology and cellular phenotypes

The loss of H^+-PPase activity in *fugu5* resulted in excess PPi and diminished sucrose production from seed storage lipids (Ferjani et al., 2011). Careful examination revealed that postgerminative reactivation of cell cycling, particularly in the mediolateral axis of cotyledons, was compromised in the *fugu5* mutants, which apparently led to their typical oblong shape (Ferjani et al., 2007; Ferjani et al., 2011; Figure 2A). To examine this more closely, cotyledon morphology was assessed by quantification of their aspect ratio at maturity, namely at 25 DAS. These findings confirmed our previous results, as the *fugu5-1* aspect ratio was ~1.5; in comparison, the WT aspect ratio was around 1.0 (Figure 2B). In addition, whereas the *pecp2-1*, *vhp2;1*, *vhp2;2-2*, and *vhp2;1 vhp2;2-2* aspect ratios were comparable to the WT, *fugu5-1 vhp2;1* cotyledons were reminiscent of *fugu5-1* (Figure 2B). Together, these results indicate that the *pecp2-1*, *vhp2;1*, *vhp2;2-2*, and *vhp2;1 vhp2;2-2* mutations do not affect cotyledon shape, and that cotyledons are oblong only in the *fugu5* background.

fugu5 mutants were originally characterized as having cotyledons that contain fewer but larger cells, a phenotype that we have named compensation (Ferjani et al., 2007; Ferjani et al., 2008). Although cotyledons of the *pecp2-1*, *vhp2;1*, *vhp2;2-2*, and *vhp2;1 vhp2;2-2* mutations did not differ morphologically, they may have differences at the cellular level, despite their apparent similarities. Quantitative analysis of cotyledon area, palisade cell number and cell size in cotyledons of the WT and the above genotypes revealed that only *fugu5-1* and *fugu5-1 vhp2;1* exhibited compensation, whereas the other mutant lines were indistinguishable from the WT (Figures 2C–E). Note that the mutants and the transgenic lines did not show any remarkable phenotypes in later developmental stages.

Effect of the *pecp2* and *vhp2;1 vhp2;2* mutations on pavement cell shape and stomata distribution

The cotyledon epidermis in Arabidopsis is composed of two types of cells: the pavement cells (PCs) and the stomata. In the *fugu5* mutant backgrounds, excess PPi reduced PC complexity and altered stomatal distribution (Gunji et al., 2020). It is worth noting that while externally supplied sucrose suppressed compensation in the palisade tissue, the above epidermal developmental defects did not recover (Gunji et al., 2020). Hence, the above key phenotypes can be used as indicators of excess PPi in the epidermis of a given Arabidopsis plant, irrespective of its genotype.

Scanning electron microscope (SEM) images including the WT as a control indicated that whereas *fugu5-1* and *fugu5-1 vhp2;1* had simply-shaped PCs and abnormal stomatal distribution, PCs and stomatal distribution were apparently unaffected by the *pecp2-1*, *vhp2;1*, *vhp2;2-2*, or *vhp2;1 vhp2;2-2* mutations (Figure 3A). Subsequent quantification revealed that PC complexity and stomatal density, evaluated by the Undulation Index (UI) and the Stomatal Index (SI), respectively, were significantly different from the WT only in the *fugu5-1* background (Figures 3B, C).

Impact of *PECP2* overexpression in the *fugu5* background on cotyledon morphological and cellular phenotypes

In our hands, the *pecp2* loss-of-function mutant did not display any of the excess PPi-related phenotypes previously recognized in the *fugu5* mutant, the master enzyme of PPi homeostasis (Ferjani et al., 2011; Ferjani et al., 2014; Segami et al., 2018). Therefore, to fully understand the impact of PECP2 regarding overall PPi levels *in planta*, we constructed transgenic lines constitutively overexpressing *PECP2* in the *fugu5-1* and *fugu5-3* mutant backgrounds. For convenience, lines constitutively overexpressing *PECP2* in the *fugu5-1* and *fugu5-3* backgrounds will be respectively referred to as *fugu5-1 35S::PECP2* A~C and *fugu5-3 35S::PECP2* A~C.

qRT-PCR quantification of *PECP2* mRNA level in *fugu5-1 35S::PECP2* lines A, B, and C indicated fold changes of 500, 900 and 5,000 in transcript level, respectively, in comparison to their *fugu5-1* controls (Figure 4A). *PECP2* mRNA was even more overexpressed in the *fugu5-3 35S::PECP2* lines in comparison to their *fugu5-3* controls (with fold changes of 1,100 for *line* A and ~1,200 for lines B and C (Figure 4B). If PECP2 shows a significant pyrophosphatase activity *in planta*, its constitutive overexpression in the above transgenic lines should restore excess PPi content to either normal or lower levels, and restore the developmental defects stated above. To formally check this, we assessed the cotyledon aspect ratio and palisade tissue cellular phenotypes in the WT, *fugu5-1*, and *fugu5-3* lines, as well as the above transgenic lines (Figure 5). Overall, the constitutive overexpression of *PECP2* in both *fugu5-1* and *fugu5-3* had no remarkable effect on morphological or cellular phenotypes.

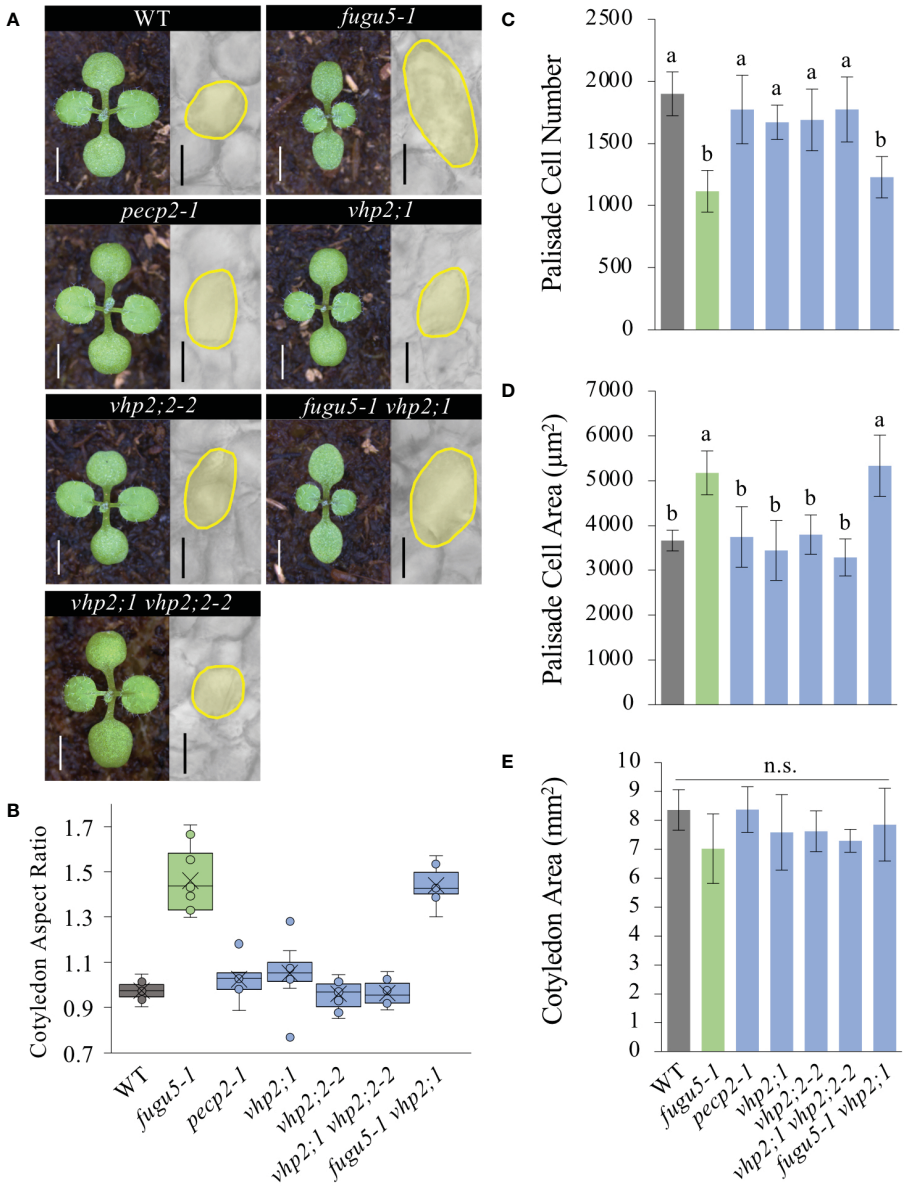

FIGURE 2
Quantification of cotyledon morphological and cellular phenotypes. **(A)** Gross morphology of the indicated genotypes (left), grown on rockwool for 10 DAS. Scale bar = 2 mm. Micrographs of palisade tissue cells from cleared cotyledons of WT, *fugu5-1*, *pecp2-1*, *vhp2;1*, *vhp2;2-2*, *vhp2;1 vhp2;2-2* and *fugu5-1 vhp2;1* lines (right), at 25 DAS. Scale bar = 50 μm. **(B)** Box plots of cotyledon aspect ratio at 25 DAS (n = 8). The lower and upper portions of the boxes are the first and third quartiles, respectively, and the dividing line is the median. Dots represent each value. **(C–E)** Numbers of subepidermal palisade tissue cells **(C)**, their average sizes **(D)**, and the average sizes of each cotyledon **(E)** at 25 DAS. Data are means ± SD (n = 160 cells from eight different cotyledons). Each character represents a significant difference at P< 0.05 (Tukey's HSD test). n.s., not significant. DAS, days after seed sowing.

More specifically, neither cotyledon shape (Figures 5A, B) nor compensation (Figures 5C–E) phenotypes were restored in spite of the extremely high expression level of *PECP2*. Taken together, these results imply that PECP2 is unlikely to act as an efficient PPi-scavenging enzyme *in planta*, and that the findings of May et al. (2011) might be reflecting particular *in vitro* conditions.

Next, the transgenic lines were used to evaluate the consequences of the constitutive overexpression of *PECP2* on PC shape, stomatal density and distribution. We found that while the WT PCs were complex (UI ≈ 2.5), UI values in *fugu5-1*, *fugu5-3*, and all transgenic lines were significantly reduced (UI ≈ 2.0) as compared to the WT (Figures 6A, B). In addition, SI values clearly indicated that stomata number was consistently higher in the *fugu5* background, including the transgenic lines, and SEM images indicated that stomata density was also affected, mimicking *fugu5* single mutant phenotypes (Figure 6C; Gunji et al., 2020). Together, the above results demonstrate that constitutive overexpression of *PECP2* failed to rescue the epidermal developmental defects in the *fugu5* background. If we assume that the anatomical phenotypes are PPi-specific (Gunji et al., 2020; Gunji et al., 2022), the above data also suggest that constitutive overexpression of *PECP2* failed to restore PPi levels.

10.3389/fpls.2023.1031426

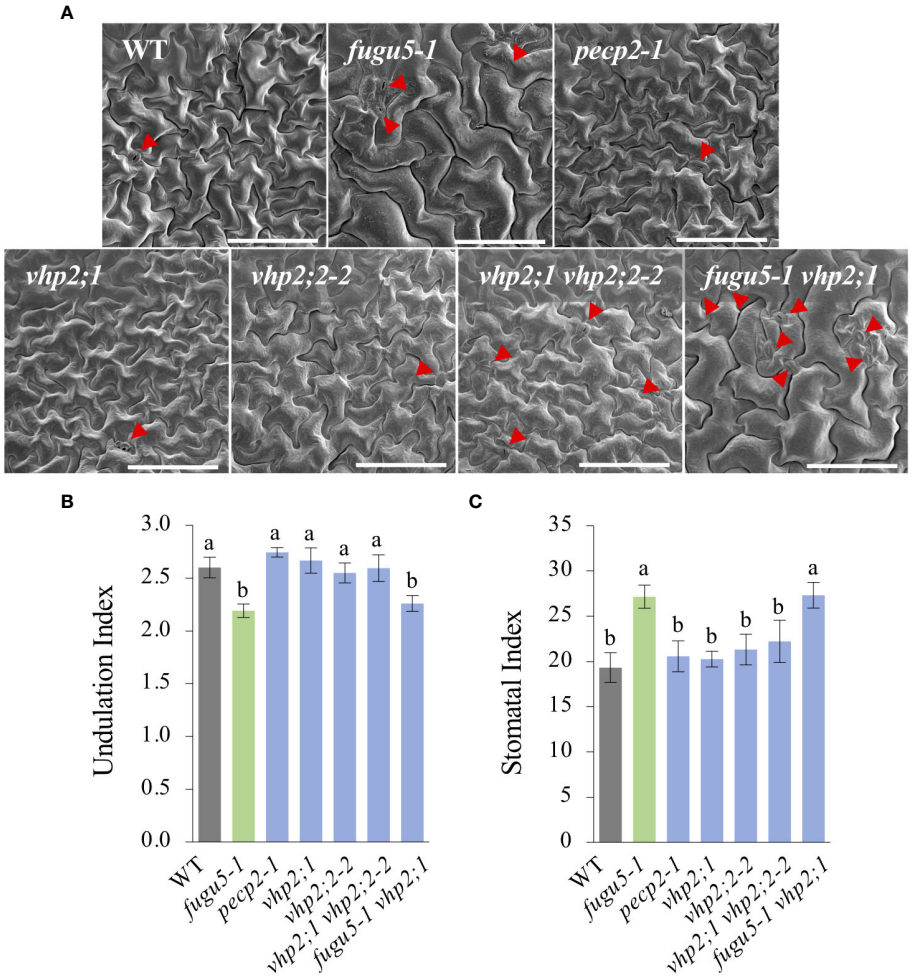

FIGURE 3
Quantification of pavement cell complexity and stomata distribution on the cotyledon adaxial side. **(A)** Representative SEM images of pavement cells (PCs) from the cotyledon adaxial side of WT, *fugu5-1*, *pecp2-1*, *vhp2;1*, *vhp2;2-2*, *vhp2;1 vhp2;2-2* and *fugu5-1 vhp2;1* lines at 25 DAS. Red arrowheads indicate stomata. Scale bar = 150 µm. **(B)** Undulation index (UI) of PCs. Data are means ± SD (*n* = 5 cotyledons). **(C)** Stomatal index (SI) determined as the number of stomata per 100 PCs. Data are means ± SD (*n* = 5 cotyledons). Each character represents a significant difference at $P < 0.05$ (Tukey's HSD test). DAS, days after seed sowing.

Impact of *PECP2* overexpression in the *fugu5* background on the skotomorphogenic developmental program

Arabidopsis seedlings grown in the dark follow a skotomorphogenic developmental program, whereby seed reserve resources are allocated toward hypocotyl elongation at the expense of other organs, namely cotyledons and roots (Josse and Halliday, 2008). Upon seed imbibition, dark-grown seedling establishment depends on oilseed mobilization as the sole source of energy, until photosynthesis begins. It is worth mentioning that the lack of sucrose in *fugu5-1* etiolated seedlings, due to the inhibitory effect of PPi on gluconeogenesis, reduced hypocotyl length by ~30% as compared to the WT (Ferjani et al., 2011; Katano et al., 2016). Therefore, to evaluate the role of PECP2, VHP2;1 and VHP2;2 in this process, hypocotyl length was determined by using all genotypes indicated in Figure 7.

Our measurements clearly indicated no impact on the hypocotyl length of either single mutants (i.e. *pecp2-1*, *vhp2;1*, and *vhp2;2-2*) or double mutants (*vhp2;1 vhp2;2-2*; Figures 7A, B). Moreover, while *fugu5-1* and *fugu5-3* hypocotyls were significantly shorter (Figures 7A, B) in comparison to the WT, constitutive overexpression of *PECP2* did not rescue hypocotyl elongation defects (Figures 7A–C). Altogether, these findings are in line with our aforementioned conclusions that the PECP2, VHP2;1 and VHP2;2 enzymes do not strongly influence overall PPi levels in plant cells *in vivo*.

Gluconeogenesis from seed storage lipids is not affected in the *pecp2-1*, *vhp2;1*, or *vhp2;2-2* mutant backgrounds

In Arabidopsis, defects in V-PPase activity lead to a net increase in PPi content (up to ~2.5-fold), partial inhibition of the gluconeogenic enzyme UGPase (Ferjani et al., 2018), and a 50% reduction in sucrose concentration (Ferjani et al., 2011). These reports indicate that PPi homeostasis is important during

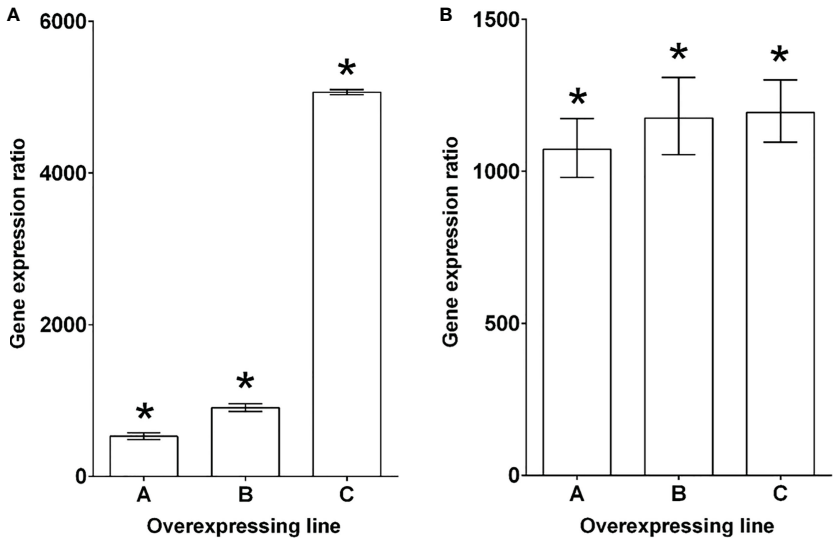

FIGURE 4
Characterization of *PECP2* overexpressing lines in *fugu5* mutant backgrounds. Lines that overexpress *PECP2* in the *fugu5-1* **(A)** and *fugu5-3* **(B)** backgrounds show very high transcript levels for these phosphatases, even in the high Pi condition. The results are expressed as gene induction level in overexpressing lines (#A to #C) in comparison to their respective *fugu5* controls grown under the same conditions. *fugu5* control values were arbitrarily set to one. The results are presented as the median ± 95% confidence interval. Asterisks indicate a statistically significant difference between overexpressing lines and *fugu5* (REST randomization test, $P < 0.05$). The reference genes used for the individual panels were *ROC3* and *GAPC1*.

postgerminative development, and that UGPase is rate-limiting (Park et al., 2010). Although PECP2 has been reported as being one of the rare PPase enzymes belonging to the HAD superfamily (Lee et al., 2009; May et al., 2011), the quantification of morphological traits has failed to support its role as an enzyme able to efficiently hydrolyze PPi once in the cell context.

In order to assess the role of PECP2 and VHPs in PPi homeostasis, we performed a comparative metabolomic analysis at 3 DAI by using GC-MS-MS to detect any subtle metabolic perturbation in these mutant lines. First, metabolomic data were subjected to Principal Component Analysis (PCA), which provides a more comprehensive view of patterns in metabolic profiles among genotypes (Ferjani et al., 2018; Gunji et al., 2022). The PCA (Figure 8A) first component (PC1) explained 46.6% of the metabolic variation, and the second component (PC2) explained 18.6%. Collectively, PC1 and PC2 depicted 65.2% of the total variance among genotypes. PC1 showed scattered plots and identified several differences in metabolic profiles. Whereas the WT, *pecp2-1*, *pecp2-3*, *vhp2;1* and *vhp2;2-2* lines belonged to the same group, *fugu5-1* showed a remarkable difference along PC2 (Figure 8A).

In contrast, the overexpression of *PECP2* in the *fugu5-1* or *fugu5-3* background had a negligible effect on their metabolic profiles in comparison to the parental lines, which showed a clear separation between the WT and *fugu5 35S::PECP2* lines along PC1 (Figure 8B). Finally, pathway analysis focusing on gluconeogenesis revealed that the contents of major metabolites of the central metabolism, previously recognized to be up- or down-regulated in *fugu5* due to excess PPi, were unaffected (Figure 8C). Taken together, our comparative metabolomic analysis, performed using highly sensitive GC-MS-MS, confirms that PECP2 and VHPs show no signs of cytosolic PPi homeostasis defects *in planta*.

Discussion

In this study, our careful in-depth phenotypic characterization led us to the conclusion that PECP2, VHP2;1 and VHP2;2 have a negligible impact on the overall cytosolic PPi levels *in vivo*. In the process, we established a set of different parameters that can be used as references for the identification of PPi homeostasis defects at different developmental stages of the plants. By quantifying the cotyledon aspect ratio, palisade tissue cellular phenotypes, adaxial side pavement cell complexity, stomatal distribution, and etiolated seedling length, especially when used in combination with *fugu5* reference mutants, we were able to reveal subtle alterations of cytosolic PPi levels using anatomical alterations as a proxy for PPi quantification. This strategy is reminiscent of the successful screens for mutants impaired in Pi homeostasis that were based on observed defects in root hair elongation or density, primary root growth, or anthocyanin development (Williamson et al., 2001; Reymond et al., 2006). Considering the difficulties of direct PPi quantification, which is considerably more complex than Pi quantification, the possibility to use PPi-related anatomical defects at different developmental stages could be instrumental in identifying new genes involved in the regulation of this important metabolite.

In the case of the VHP2;1 and VHP2;2 proteins, their lack of a general impact on PPi homeostasis might be due to their overall low expression levels, since protein quantification of these type-II H^+-PPases revealed that they amount to only ~0.2% of type-I H^+-PPase levels (Segami et al., 2010). Low expression levels might actually be linked with their presence within the Golgi membrane, as opposed to the tonoplastic type-I H^+-PPases: the cells maintain a sharp pH gradient of about Δ2 pH units between the cytoplasm and the acidic vacuole, while a Δ0.5-1 pH unit is sufficient to maintain the slightly more acidic cis-Golgi and TGN compartments when

10.3389/fpls.2023.1031426

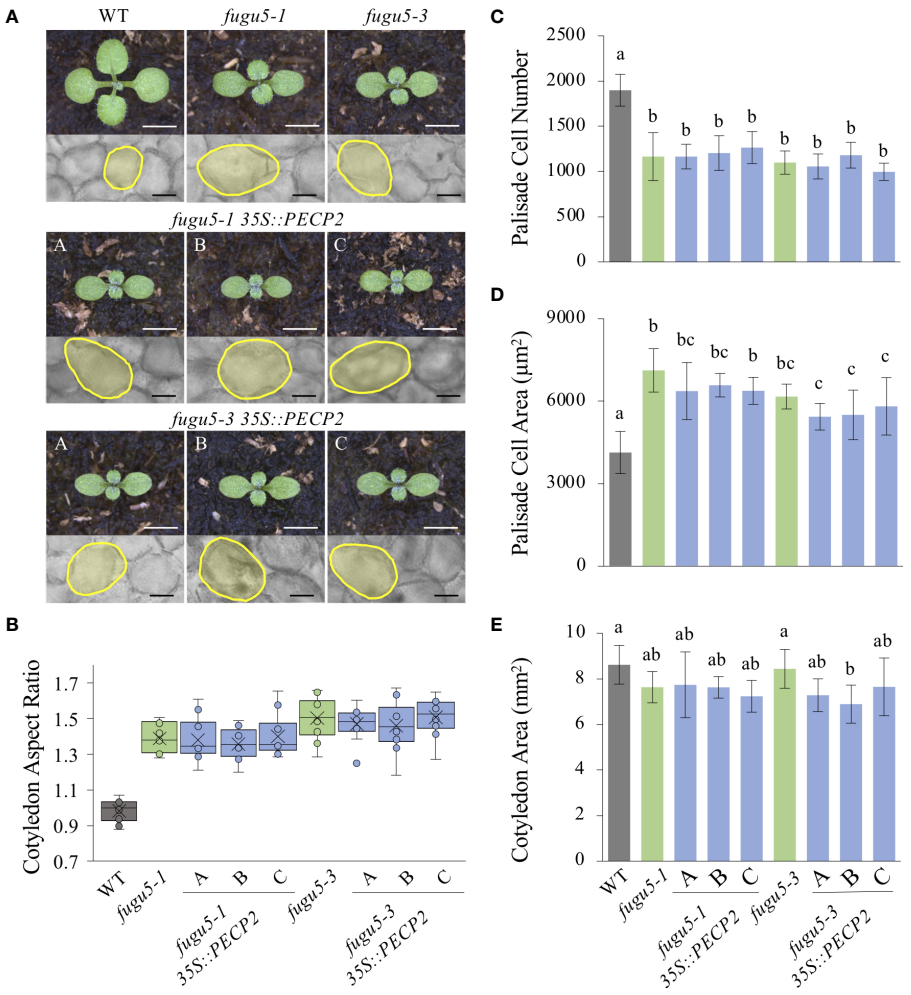

FIGURE 5
Quantification of cotyledon morphological and cellular phenotypes of *PECP2* overexpressing lines in the *fugu5* background. **(A)** Gross morphology of the indicated genotypes (above), grown on rockwool for 10 DAS. Scale bar = 2 mm. Micrographs of palisade tissue cells from cleared cotyledons of the WT, *fugu5-1*, *fugu5-3*, *fugu5-1 35S::PECP2*, and *fugu5-3 35S::PECP2* lines (below), at 25 DAS. Scale bar = 50 µm. **(B)** Box plots of cotyledon aspect ratio at 25 DAS (*n* = 8 cotyledons). The lower and upper portions of the boxes are the first and third quartiles, respectively, and the dividing line is the median. Dots represent each value. **(C–E)** Numbers of subepidermal palisade tissue cells **(C)**, their average sizes **(D)**, and the average sizes of each cotyledon **(E)** at 25 DAS. Data are means ± SD (*n* = 160 cells from eight different cotyledons). Each character represents a significant difference at $P < 0.05$ (Tukey's HSD test). DAS, days after seed sowing.

compared to the cytosol (Shen et al., 2013; Tsai and Schmidt, 2021). For this reason, the lack of *fugu5*-type phenotypes in *vhp2* mutants might not be a reflection of a lesser role for type-II versus type-I H^+-PPases, but simply the consequence of a more limited proton pump activity required to maintain Golgi acidification. Generating overexpressing lines in a *fugu5* background, as we did here with *PECP2* overexpressers, might be used to validate this hypothesis. Type-II H^+-PPases remain a very intriguing area of study, due to their specific Golgi targeting (as opposed to the vacuolar location of FUGU5/type-I H^+-PPases; Drozdowicz and Rea, 2001; Mitsuda et al., 2001; Segami et al., 2010). Nevertheless, the respective importance of their combined functions (PPi hydrolysis coupled to proton pumping) still awaits demonstration of their impact on biological functions. As deletion of these transporters has no overall impact on PPi homeostasis, it will be important to characterize the impact of *vhp2* mutations on Golgi pH maintenance, likely in combination with mutations of other known membrane-bound pH regulators present in the endomembrane network (McKay et al., 2022). Overall, a careful analysis of these mutants, particularly under stress conditions where PPi could be limiting, and where pH maintenance within the Golgi might be affected, is necessary to understand under which conditions the dual activity of these proteins (pyrophosphatase/proton pump) could become limiting.

For PECP2, we provided a more complete demonstration that this enzyme, although initially shown to be a pyrophosphatase based on *in vitro* data (May et al., 2011), actually does not significantly impact PPi homeostasis *in planta*. This was already suggested following the characterization of hypocotyl elongation in *pecp1/2/3* triple mutants and *fugu5 pecp1/2* triple mutants (Hanchi et al., 2018), but we performed a more in-depth characterization of these mutants, along with the demonstration that *fugu5* PPi homeostasis defects cannot be complemented by *pecp2* overexpression. The initial *in vitro* characterization of PECP2 (May et al., 2011), completed later on by characterizing PECP1 and PECP3 (May et al., 2011; Hasnain et al., 2016; Tannert et al., 2021), remains fundamental for the study of the PECP family, as it clearly demonstrates that each of these enzymes

10.3389/fpls.2023.1031426

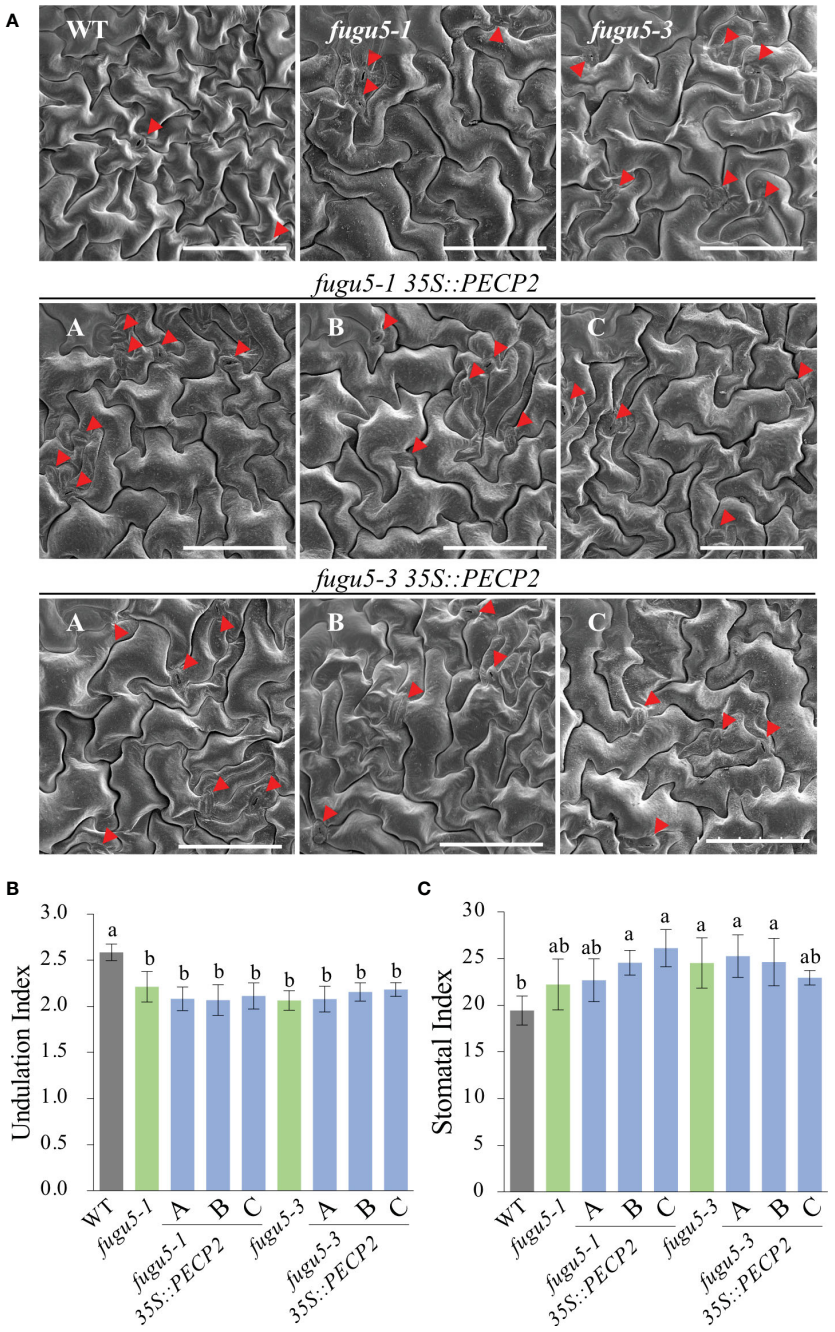

FIGURE 6
Quantification of pavement cell complexity and stomata distribution on the cotyledon adaxial side in *PECP2* overexpressing lines in the *fugu5* background. **(A)** Representative SEM images of pavement cells (PCs) from the cotyledon adaxial side of the WT, *fugu5-1*, *fugu5-3*, *fugu5-1 35S::PECP2*, and *fugu5-3 35S::PECP2* lines at 25 DAS. Red arrowheads indicate stomata. Scale bar = 150 µm. **(B)** Undulation index (UI) of PCs. Data are means ± SD (n = 5 cotyledons). **(C)** Stomatal index (SI) determined as the number of stomata per 100 PCs. Data are means ± SD (n = 5 cotyledons). Each character represents a significant difference at $P< 0.05$ (Tukey's HSD test). DAS, days after seed sowing.

can dephosphorylate a range of different substrates with different affinities. For instance, each PECP protein demonstrates some ability to cleave PPi, even if only marginally. In fact, the pyrophosphatase activity measured *in vitro* for PECP2 was quite low (<1 nmol Pi min^{-1} mg $protein^{-1}$; May et al., 2011) in comparison to the one associated with PECP3 (177 nmol Pi min^{-1} mg $protein^{-1}$; Tannert et al., 2021), although another study only revealed a very marginal pyrophosphatase activity for PECP3 (Hasnain et al., 2016). Interestingly, their *in vitro* specific activities also suggested that each of these three enzymes metabolizes PEtn more efficiently than PCho *in vitro* (PECP1: 3,665 (PEtn) versus 475 (PCho) nmol Pi min^{-1} mg $protein^{-1}$ (May et al., 2012); PECP2: 0.02 (PEtn) versus<0.001 (PCho) nmol Pi min^{-1} mg $protein^{-1}$ (May et al., 2011); PECP3: 1,379 (PEtn) versus 315 (Pcho) nmol Pi min^{-1} mg $protein^{-1}$ (Tannert et al., 2021). Furthermore, PECP3 was initially described as being a thiamine monophosphatase (ThMP) *in vitro* (Hasnain et al., 2016),

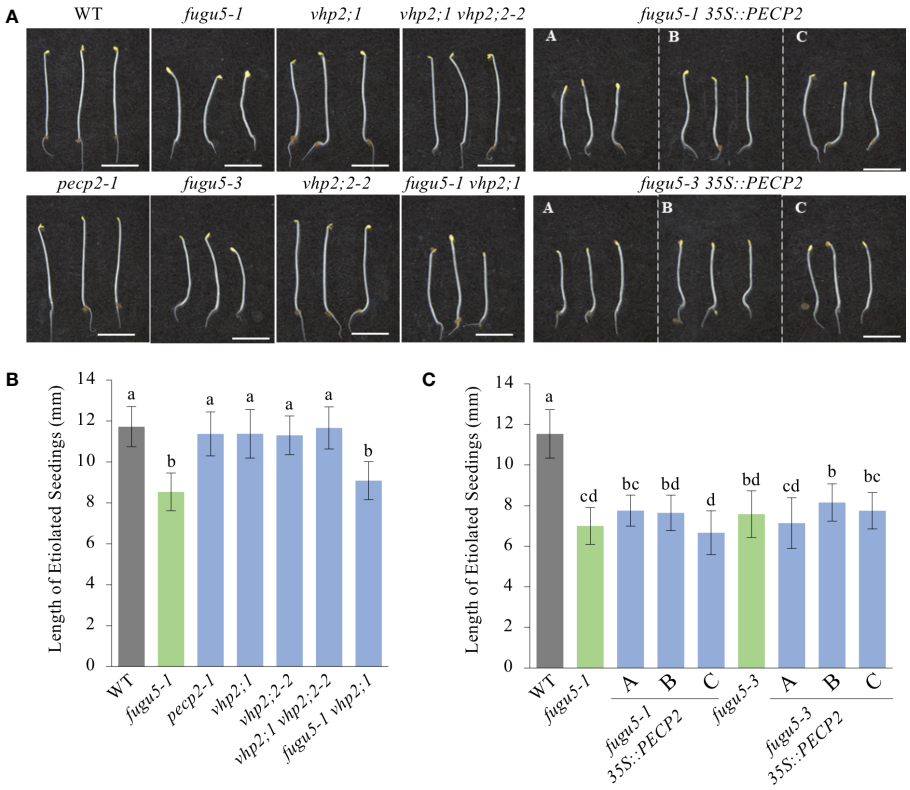

FIGURE 7
Quantification of hypocotyl length of etiolated seedlings. **(A)** Photographs of etiolated seedlings of the indicated genotypes grown on MS-only medium (without sucrose) in the dark for 4 DAI. Scale bar = 5 mm. **(B)** Hypocotyl length of etiolated seedlings of the WT, *fugu5-1*, *pecp2-1*, *vhp2;1*, *vhp2;2-2*, *vhp2;1 vhp2;2-2* and *fugu5-1 vhp2;1* lines grown on MS-only medium in the dark for 4 DAI. Data are means ± SD (*n* = 20 seedlings). **(C)** Hypocotyl length of etiolated seedlings of the WT, *fugu5-1*, *fugu5-3*, *fugu5-1 35S::PECP2* and *fugu5-3 35S::PECP2* lines grown on MS-only medium in the dark for 4 DAI. Data are means ± SD (*n* = 20 etiolated seedlings). Each character represents a significant difference at *P*< 0.05 (Tukey's HSD test). DAI, days after induction of seed germination.

but direct comparison with PEtn and PCho revealed that its specific activity towards ThMP is actually intermediate (895 nmol Pi min^{-1} mg $protein^{-1}$; Tannert et al., 2021).

Substrate affinities and expected substrate concentrations must also be taken into account before predicting *in vivo* functions, even though the comparison of enzyme-specific activities already provides an interesting quantification of the enzymatic dephosphorylation capabilities. Nevertheless, characterization of mutants and overexpressing lines constitute a necessary step for the effective determination of the *in vivo* substrates of HAD-type proteins such as Arabidopsis PECP1/2 and 3. Although a whole range of molecules have been described as potential substrates for these enzymes, including primarily PEtn and PCho for PECP1, PPi for PECP2, and ThMP for PECP3 (May et al., 2011; Hasnain et al., 2016), only PEtn and PCho homeostasis were *de facto* altered in mutant and overexpressing lines (Hasnain et al., 2016; Mimura et al., 2016; Hanchi et al., 2018; Tannert et al., 2018; Angkawijaya et al., 2019; Tannert et al., 2021). Even though there is some discrepancy regarding whether PEtn or PCho could be considered as a favored substrate of these enzymes, all *in planta* data (including this study) point to a role for this enzyme family in PEtn and PCho dephosphorylation. PECP2 is therefore unlikely to play a major role in cytosolic PPi homeostasis *in vivo*.

The impact of this protein could possibly be limited to its subcellular compartment, and indeed it has been suggested that PECP1 and 2 associate with ER structures through GFP-tagging (Angkawijaya et al., 2019). It might be relevant to refine and confirm this localization through complementary methods to eliminate the risk of artefacts associated with GFP-tagging strategies, or to identify the enzyme action site. Even so, considering that changes in the expression level of *PECP2* had a very a strong impact on PEtn and PCho content at the whole-cell level, it is unlikely that the observed lack of a PPi defect might be caused by PECP2 association with the ER.

Discrepancies between the *in vitro* and *in vivo* data should certainly not discourage further *in vitro* characterization of HAD-type proteins. However, these gaps are a reminder that the range of substrates assayed *in vitro* must be as large as possible and that ultimately, the cell environment can strongly affect the enzyme activities. *In vitro* assays on purified PECP2 proteins (May et al., 2011) were performed using substrate concentrations that could occur *in vivo*, as candidate substrates were added at a concentration of 500 µM. The PPi concentration is estimated to be within that range *in vivo*, as it is maintained around 0.2-0.3 mM in the cytosol (Weiner et al., 1987). Using PCho at 500 µM is also reasonable *in vitro*, since PCho and PPi contents in plants are within the same range (around 50 nmol/g FW; Heinonen, 2001; Kraner et al., 2017).

However, it is rarely possible to test a mix of candidate substrates to evaluate their possible competition, since the enzyme activity assays are often based on the measurement of

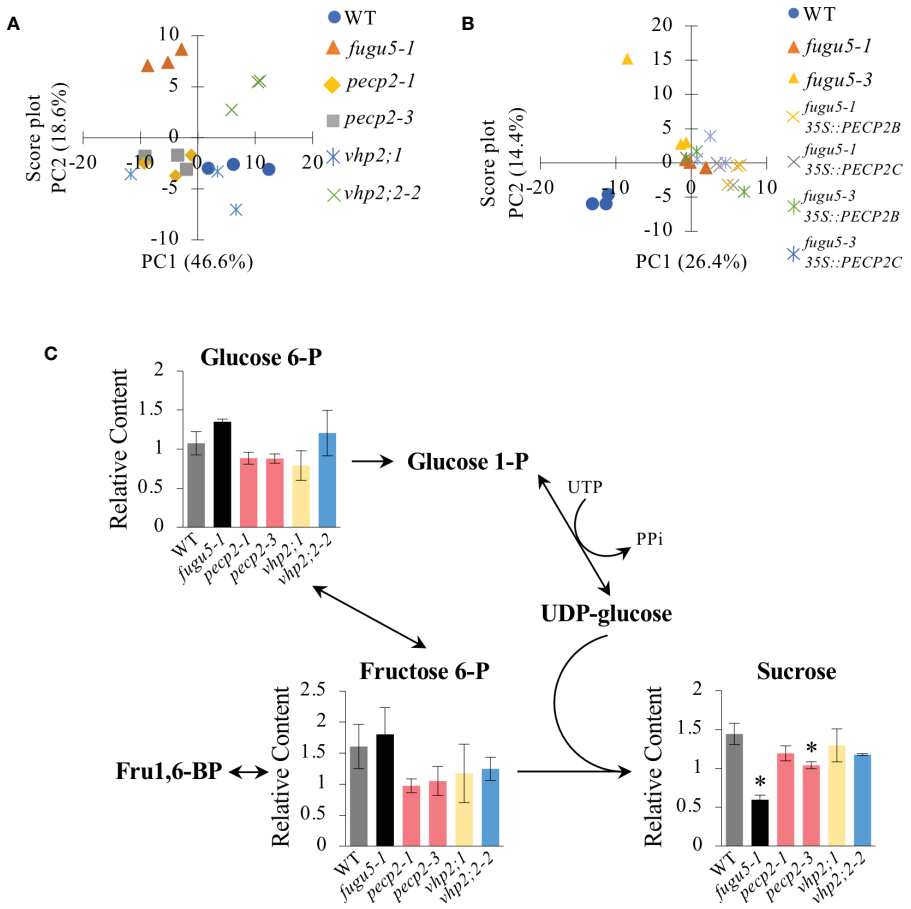

FIGURE 8
Comparative metabolomic analysis of etiolated seedlings. Metabolomic analysis of etiolated seedlings was performed by GC-MS/MS (n = 3 biological replicates; 100 etiolated seedlings per sample). Etiolated seedlings were grown on MS-only medium in the dark for 3 DAI. **(A)** Principal Component Analysis (PCA) score plot of the WT, *fugu5-1*, *pecp2-1*, *vhp2;1*, *vhp2;2-2*, *vhp2;1 vhp2;2-2* and *fugu5-1 vhp2;1* lines. **(B)** PCA score plot of the WT, *fugu5-1*, *fugu5-3*, *fugu5-1 35S::PECP2* and *fugu5-3 35S::PECP2* transgenic lines. Color plots refer to the genotype in the legend. **(C)** Pathway analysis focusing on gluconeogenesis-related metabolites. Metabolite contents relative to the quality control sample are plotted on the corresponding pathway. Data are means ± SD (n = 3 biological replicates; 100 etiolated seedlings per sample). Asterisks indicate mutants with significant differences as compared to the WT (Dunnett's test at P< 0.05). DAI, days after induction of seed germination.

phosphate release (typically quantified by ammonium molybdate or malachite-based assays). As the output (i.e. phosphate release) is common to all cleaved substrates, this method is not applicable to the study of substrate competition. In addition, the activity of all PPases (membrane-bound as well as soluble and HAD-like proteins) is strongly dependent on the nature and quantity of metal ions available to the purified protein (May et al., 2011; Kuznetsova et al., 2015; Grzechowiak et al., 2019; Tsai et al., 2019). As such, assay conditions might not correspond to *in vivo* metal content.

Altogether, *in vitro* properties will only reflect the behavior of enzymes within the limits of the artificial conditions selected for the assays. This might only be remotely related to *in vivo* conditions, once the mix of ion metals and substrates competing for the candidate protein in the cytoplasm of plant cells is taken into account. These knowledge gaps also demonstrate the limits of our understanding of the key determinants of HAD-type protein-substrate recognition specificities, promoting active research in this field (Tian et al., 2022).

Data availability statement

The original contributions presented in the study are included in the article/Supplementary Material. Further inquiries can be directed to the corresponding authors.

Author contributions

AF conceived the project and designed, supervised, and funded the study. HTo performed the experiments, conducted the phenotyping analysis, and analyzed the data. HTa performed wide-target metabolomics, data collection and analyzed data. HTo and SG performed SEM observations and the quantification of all epidermis phenotypes. HJ generated the overexpressing lines and analyzed the predicted protein structures. PD performed the qPCR experiments. MH supervised and funded the study. HJ and AF wrote the paper with input from the coauthors. All authors contributed to the article and approved the submitted version.

Funding

This work was supported by Grant-in-Aid for Scientific Research (B) (JP16H04803 to AF), Grant-in-Aid for Scientific Research on Innovative Areas (JP25113002 and JP18H05487 to AF), and The Naito Foundation. HTa is a recipient of a Research Fellowship for Young Scientists (DC1) (20J20901).

Acknowledgments

We thank Mohamed Hanchi, Sarah Salomon, Marie-Christine Thibaud and members of the GRAP team (CEA) for their help during the generation of *PECP2* overexpressing lines. We thank Dr. Brandon Loveall from IMPROVENCE for professional English editing of the manuscript, and Laurence Blanchard for her introduction to PyMol capabilities.

Conflict of interest

The authors declare that the research was conducted in the absence of any commercial or financial relationships that could be construed as a potential conflict of interest.

Publisher's note

Supplementary material

The Supplementary Material for this article can be found online at: https://www.frontiersin.org/articles/10.3389/fpls.2023.1031426/full#supplementary-material

SUPPLEMENTAL MOVIE 1

Animation showing the overlay of selected type II H^+-PPases. The overlay compares the predicted structures for FUGU5 (UniProt P31414; in bright green),VHP2;1 (UniProt Q56ZN6; in dark green) and VHP2;2 (UniProt Q9FWR2; in blue) to the crystal structure of *Vr*H^+-PPase (PDB reference 4A01, Chain A; in light gray). A general overview of the 4 structures shows the strong conservation of these 16-TM proteins, with the exception of an additional N-terminal domain in VHP2;1 and 2;2, briefly shown in black. Subsequently, a rotated view zooms to compare the positions of 3 AA involved in PPi binding in *Vr*H^+-PPase, with the corresponding positions within the 3 predicted structures of FUGU5, VHP2;1 and VHP2;2. Finally, a side view highlights the positions of 2 AA involved in proton pumping in *Vr*H^+-PPase, overlapping with the corresponding positions within the 3 predicted structures of FUGU5, VHP2;1 and VHP2;2. AA: amino acid.

References

Al-Ghazi, Y., Muller, B., Pinloche, S., Tranbarger, T. J., Nacry, P., Rossignol, M., et al. (2003). Temporal responses of Arabidopsis root architecture to phosphate starvation: Evidence for the involvement of auxin signalling. *Plant Cell Environ.* 26, 1053–1066. doi: 10.1046/j.1365-3040.2003.01030.x

Angkawijaya, A. E., and Nakamura, Y. (2017). Arabidopsis PECP1 and PS2 are phosphate starvation-inducible phosphocholine phosphatases. *Biochem. Biophys. Res. Commun.* 494, 397–401. doi: 10.1016/j.bbrc.2017.09.094

Angkawijaya, A. E., Ngo, A. H., Nguyen, V. C., Gunawan, F., and Nakamura, Y. (2019). Expression profiles of 2 phosphate starvation-inducible phosphocholine/phosphoethanolamine phosphatases, PECP1 and PS2, in Arabidopsis. *Front. Plant Sci.* 10, 662. doi: 10.3389/fpls.2019.00662

Asaoka, M., Inoue, S. I., Gunji, S., Kinoshita, T., Maeshima, M., Tsukaya, H., et al. (2019). Excess pyrophosphate within guard cells delays stomatal closure. *Plant Cell Physiol.* 60, 875–887. doi: 10.1093/pcp/pcz002

Asaoka, M., Segami, S., Ferjani, A., and Maeshima, M. (2016). Contribution of PPi-hydrolyzing function of vacuolar H^+-pyrophosphatase in vegetative growth of Arabidopsis: Evidenced by expression of uncoupling mutated enzymes. *Front. Plant Sci.* 7, 415. doi: 10.3389/fpls.2016.00415

Bertoni, G. (2011). A surprising role for vacuolar pyrophosphatase. *Plant Cell* 23, 2808. doi: 10.1105/tpc.111.230813

Clough, S. J., and Bent, A. F. (1998). Floral dip: a simplified method for agrobacterium-mediated transformation of *Arabidopsis thaliana*. *Plant J.* 16, 735–743. doi: 10.1046/j.1365-313x.1998.00343.x

Drozdowicz, Y. M., and Rea, P. A. (2001). Vacuolar H+- pyrophosphatases: from the evolutionary backwaters into the mainstream. *Trends Plant Sci.* 6, 206–211. doi: 10.1016/S1360-1385(01)01923-9

Duan, E., Wang, Y., Liu, L., Zhu, J., Zhong, M., Zhang, H., et al. (2016). Pyrophosphate: fructose-6-phosphate 1-phosphotransferase (PFP) regulates carbon metabolism during grain filling in rice. *Plant Cell Rep.* 35, 1321–1331. doi: 10.1007/s00299-016-1964-4

Ferjani, A., Horiguchi, G., Yano, S., and Tsukaya, H. (2007). Analysis of leaf development in *fugu* mutants of Arabidopsis reveals three compensation modes that modulate cell expansion in determinate organs. *Plant Physiol.* 144, 988–999. doi: 10.1104/pp.107.099325

Ferjani, A., Kawade, K., Asaoka, M., Oikawa, A., Okada, T., Mochizuki, A., et al. (2018). Pyrophosphate inhibits gluconeogenesis by restricting UDP-glucose formation *in vivo*. *Sci. Rep.* 8, 14696. doi: 10.1038/s41598-018-32894-1

Ferjani, A., Segami, S., Asaoka, M., and Maeshima, M. (2014). Regulation of PPi levels through the vacuolar membrane H^+-pyrophosphatase. in *Progress in botany*, vol. 75 . Eds. U. Lüttge, W. Beyschlag and J. Cushman (Berlin: Springer-Verlag), 145–165.

Ferjani, A., Segami, S., Horiguchi, G., Muto, Y., Maeshima, M., and Tsukaya, H. (2011). Keep an eye on PPi: the vacuolar-type H^+-pyrophosphatase regulates postgerminative development in *Arabidopsis*. *Plant Cell* 23, 2895–2908. doi: 10.1105/tpc.111.085415

Ferjani, A., Yano, S., Horiguchi, G., and Tsukaya, H. (2008). Control of leaf morphogenesis by long- and short-distance signaling: Differentiation of leaves into sun or shade types and compensated cell enlargement. in *Plant cell monographs: Plant growth signaling*. Eds. L. Bögre and G. T. S. Beemster (Berlin, Heidelberg, Germany: Springer Berlin Heidelberg), 47–62.

Fukuda, M., Mieda, M., Sato, R., Kinoshita, S., Tomoyama, T., Ferjani, A., et al. (2020). Lack of vacuolar H^+-pyrophosphatase and cytosolic pyrophosphatases causes fatal developmental defects in *Arabidopsis thaliana*. *Front. Plant Sci.* 11, 655. doi: 10.3389/fpls.2020.00655

Fukuda, M., Segami, S., Tomoyama, T., Asaoka, M., Nakanishi, Y., Gunji, S., et al. (2016). Lack of H^+-pyrophosphatase prompts developmental damage in Arabidopsis leaves on ammonia-free culture medium. *Front. Plant Sci.* 7, 819. doi: 10.3389/fpls.2016.00819

Gaxiola, R. A., Palmgren, M. G., and Schumacher, K. (2007). Plant proton pumps. *FEBS Lett.* 581, 2204–2214. doi: 10.1016/j.febslet.2007.03.050

Grzechowiak, M., Ruszkowski, M., Sliwiak, J., Szpotkowski, K., Sikorski, M., and Jaskolski, M. (2019). Crystal structures of plant inorganic pyrophosphatase, an enzyme with a moonlighting autoproteolytic activity. *Biochem. J.* 476, 2297–2319. doi: 10.1042/BCJ20190427

Gunji, S., Kawade, K., Tabeta, H., Horiguchi, G., Oikawa, A., Asaoka, M., et al. (2022). Tissue-targeted inorganic pyrophosphate hydrolysis in a *fugu5* mutant reveals that excess inorganic pyrophosphate triggers developmental defects in a cell-autonomous manner. *Front. Plant Sci.* 13, 945225. doi: 10.3389/fpls.2022.945225

Gunji, S., Oda, Y., Takigawa-Imamura, H., Tsukaya, H., and Ferjani, A. (2020). Excess pyrophosphate restrains pavement cell morphogenesis and alters organ flatness in *Arabidopsis thaliana*. *Front. Plant Sci.* 11, 31. doi: 10.3389/fpls.2020.00031

Gutiérrez-Luna, F. M., Navarro de la Sancha, E., Valencia-Turcotte, L. G., Vázquez-Santana, S., and Rodríguez-Sotres, R. (2016). Evidence for a non-overlapping subcellular localization of the family I isoforms of soluble inorganic pyrophosphatase in *Arabidopsis thaliana*. *Plant Sci.* 253, 229–242. doi: 10.1016/j.plantsci.2016.10.005

Hanchi, M., Thibaud, M. C., Légeret, B., Kuwata, K., Pochon, N., Beisson, F., et al. (2018). The phosphate fast-responsive genes *PECP1* and *PPsPase1* affect phosphocholine and phosphoethanolamine content. *Plant Physiol.* 176, 2943–2962. doi: 10.1104/pp.17.01246

Hasnain, G., Roje, S., Sa, N., Zallot, R., Ziemak, M. J., de Crécy-Lagard, V., et al. (2016). Bacterial and plant HAD enzymes catalyse a missing phosphatase step in thiamin diphosphate biosynthesis. *Biochem. J.* 473, 157–166. doi: 10.1042/BJ20150805

Heinonen, J. K. (2001). Biological role of inorganic pyrophosphate (Boston/Dordrecht/London: Kluwer Academic Publishers).

Horiguchi, G., Fujikura, U., Ferjani, A., Ishikawa, N., and Tsukaya, H. (2006b). Large-Scale histological analysis of leaf mutants using two simple leaf observation methods: Identification of novel genetic pathways governing the size and shape of leaves. *Plant J.* 48, 638–644. doi: 10.1111/j.1365-313X.2006.02896.x

Hothorn, T., Bretz, F., and Westfall, P. (2008). Simultaneous inference in general parametric models. *Biom. J.* 50, 346–363. doi: 10.1002/bimj.200810425

Huang, H., Patskovsky, Y., Toro, R., Farelli, J. D., Pandya, C., Almo, S. C., et al. (2011). Divergence of Structure and Function in the Haloacid Dehalogenase Enzyme Superfamily: *Bacteroides thetaiotaomicron* BT2127 Is an Inorganic Pyrophosphatase. *Biochemistry* 50, 8937–8949. doi: 10.1021/bi201181q

Josse, E. M., and Halliday, K. J. (2008). Skotomorphogenesis: The dark side of light signalling. *Curr. Biol.* 18, R1144–R1146. doi: 10.1016/j.cub.2008.10.034

Jumper, J., Evans, R., Pritzel, A., Green, T., Figurnov, M., Ronneberger, O., et al. (2021). Highly accurate protein structure prediction with AlphaFold. *Nature* 596, 583–589. doi: 10.1038/s41586-021-03819-2

Katano, M., Takahashi, K., Hirano, T., Kazama, Y., Abe, T., Tsukaya, H., et al. (2016). Suppressor screen and phenotype analyses revealed an emerging role of the monofunctional peroxisomal enoyl-CoA hydratase 2 in compensated cell enlargement. *Front. Plant Sci.* 7, 132. doi: 10.3389/fpls.2016.00132

Kleczkowski, L. A., Geisler, M., Ciereszko, I., and Johansson, H. (2004). UDP-Glucose pyrophosphorylase. an old protein with new tricks. *Plant Physiol.* 134, 912–918. doi: 10.1104/pp.103.036053

Kraner, M. E., Link, K., Melzer, M., Ekici, A. B., Uebe, S., Tarazona, P., et al. (2017). Choline transporter-like1 (CHER1) is crucial for plasmodesmata maturation in *Arabidopsis thaliana*. *Plant J.* 89, 394–406. doi: 10.1111/tpj.13393

Kriegel, A., Andrés, Z., Medzihradszky, A., Krüger, F., Scholl, S., Delang, S., et al. (2015). Job sharing in the endomembrane system: Vacuolar acidification requires the combined activity of V-ATPase and V-PPase. *Plant Cell* 27, 3383–3396. doi: 10.1105/tpc.15.00733

Kürschner, W. M. (1997). The anatomical diversity of recent and fossil leaves of the durmast oak (*Quercus petraea* Lieblein/*Q. pseudocastanea* Goeppert) – implications for their use as biosensors of palaeoatmospheric CO_2 levels. *Rev. Palaeobot. Palynol.* 96, 1–30. doi: 10.1016/S0034-6667(96)00051-6

Kuznetsova, E., Nocek, B., Brown, G., Makarova, K. S., Flick, R., Wolf, Y. I., et al. (2015). Functional diversity of haloacid dehalogenase superfamily phosphatases from *Saccharomyces cerevisiae*: BIOCHEMICAL, STRUCTURAL, AND EVOLUTIONARY INSIGHTS. *Biol. Chem.* 290 (30), 18678–18698. doi: 10.1074/jbc.M115.657916

Lee, H. S., Cho, Y., Kim, Y. J., Lho, T. O., Cha, S. S., Lee, J. H., et al. (2009). A novel inorganic pyrophosphatase in *Thermococcus onnurineus* NA1. *FEMS Microbiol. Lett.* 300, 68–74. doi: 10.1111/j.1574-6968.2009.01766.x

Lim, H., Cho, M. H., Jeon, J.S., Bhoo, S. H., Kwon, Y. K., and Hahn, T. R. (2009). Altered expression of pyrophosphate: Fructose-6-phosphate 1-phosphotransferase affects the growth of transgenic Arabidopsis plants. M*olecules and Cells* 27, 641–649. doi: 10.1007/s10059-009-0085-0

Lim, H., Cho, M. H., Bhoo, S. H., and Hahn, T. R. (2014). Pyrophosphate: Fructose-6-phosphate 1-phosphotransferase is involved in the tolerance of Arabidopsis seedlings to salt and osmotic stresses. *In Vitro Cellular & Developmental Biology - Plant* 50, 84–91. doi: 10.1007/s11627-013-9578-9

Linkohr, B. I., Williamson, L. C., Fitter, A. H., and Leyser, H. M. (2002). Nitrate and phosphate availability and distribution have different effects on root system architecture of Arabidopsis. *Plant J.* 29, 751–760. doi: 10.1046/j.1365-313X.2002.01251.x

Lin, S. M., Tsai, J. Y., Hsiao, C. D., Huang, Y. T., Chiu, C. L., Liu, M. H., et al. (2012). Crystal structure of a membrane-embedded H^+-translocating pyrophosphatase. *Nature* 484, 399–403. doi: 10.1038/nature10963

Liu, S., Zhong, H., Wang, Q., Liu, C., Li, T., Peng, Z., et al. (2021). Global analysis of UDP glucose pyrophosphorylase (UDPGP) gene family in plants: Conserved evolution involved in cell death. *Front. Plant Sci.* 12, 681719. doi: 10.3389/fpls.2021.681719

Logemann, E., Birkenbihl, R. P., Ulker, B., and Somssich, I. E. (2006). An improved method for preparing agrobacterium cells that simplifies the Arabidopsis transformation protocol. *Plant Methods* 2, 16. doi: 10.1186/1746-4811-2-16

Maeda, S., Gunji, S., Hanai, K., Hirano, T., Kazama, Y., Ohbayashi, I., et al. (2014). The conflict between cell proliferation and expansion primarily affects stem organogenesis in Arabidopsis. *Plant Cell Physiol.* 55, 1994–2007. doi: 10.1093/pcp/pcu131

Maeshima, M. (2000). Vacuolar H^+-pyrophosphatase. *Biochim. Biophys. Acta* 1465, 37–51. doi: 10.1016/S0005-2736(00)00130-9

Matsuo, T., Tsugawa, H., Miyagawa, H., and Fukusaki, E. (2017). Integrated strategy for unknown EI-MS identification using quality control calibration curve, multivariate analysis, EI-MS spectral database, and retention index prediction. *Anal. Chem.* 89, 6766–6773. doi: 10.1021/acs.analchem.7b01010

May, A., Berger, S., Hertel, T., and Köck, M. (2011). The *Arabidopsis thaliana* phosphate starvation responsive gene *AtPPsPase1* encodes a novel type of inorganic pyrophosphatase. *Biochim. Biophys. Acta* 1810, 178–185. doi: 10.1016/j.bbagen.2010.11.006

May, A., Spinka, M., and Köck, M. (2012). *Arabidopsis thaliana* PECP1: enzymatic characterization and structural organization of the first plant phosphoethanolamine/phosphocholine phosphatase. *Biochim. Biophys. Acta* 1824, 319–325. doi: 10.1016/j.bbapap.2011.10.003

McKay, D. W., McFarlane, H. E., Qu, Y., Situmorang, A., Gilliham, M., and Wege, S. (2022). Plant trans-golgi Network/Early endosome pH regulation requires cation chloride cotransporter (CCC1). *Elife* 11, e70701. doi: 10.7554/eLife.70701

Mimura, M., Zallot, R., Niehaus, T. D., Hasnain, G., Gidda, S. K., Nguyen, T. N. D., et al. (2016). Arabidopsis *TH2* encodes the orphan enzyme thiamin monophosphate phosphatase. *Plant Cell* 28, 2683–2696. doi: 10.1105/tpc.16.00600

Mitsuda, N., Enami, K., Nakata, M., Takeyasu, K., and Sato, M. H. (2001). Novel type *Arabidopsis thaliana* H^+-PPase is localized to the golgi apparatus. *FEBS Lett.* 488, 29–33. doi: 10.1016/S0014-5793(00)02400-5

Murashige, T., and Skoog, F. (1962). A revised medium for rapid growth and bioassays with tobacco tissue cultures. *Physiol. Plant* 15, 473–497. doi: 10.1111/j.1399-3054.1962.tb08052.x

Oüztürk, Z. N., Greiner, S., and Rausch, T. (2014). Subcellular localization and developmental regulation of cytosolic: soluble pyrophosphatase isoforms in *Arabidopsis thaliana*. *Turk. J. Bot.* 38, 1036–1049. doi: 10.3906/bot-1403-67

Park, J. I., Ishimizu, T., Suwabe, K., Sudo, K., Masuko, H., Hakozaki, H., et al. (2010). UDP-Glucose pyrophosphorylase is rate limiting in vegetative and reproductive phases in *Arabidopsis thaliana*. *Plant Cell Physiol.* 51, 981–996. doi: 10.1093/pcp/pcq057

Pfaffl, M. W., Horgan, G. W., and Dempfle, L. (2002). Relative expression software tool (REST©) for group-wise comparison and statistical analysis of relative expression results in real-time PCR. *Nucleic Acids Res.* 30, e36. doi: 10.1093/nar/30.9.e36

R Core Team (2020). *R: A language and environment for statistical computing* (Vienna, Austria: R Foundation for Statistical Computing). Available at: https://www.R-project.org/.

Reymond, M., Svistoonoff, S., Loudet, O., Nussaume, L., and Desnos, T. (2006). Identification of QTL controlling root growth response to phosphate starvation in *Arabidopsis thaliana*. *Plant Cell Environ.* 29, 115–125. doi: 10.1111/j.1365-3040.2005.01405.x

Ruiz-Calero, V., and Galceran, M. T. (2005). Ion chromatographic separations of phosphorus species: a review. *Talanta* 66, 376–410. doi: 10.1016/j.talanta.2005.01.027

Schulze, S., Mant, A., Kossmann, J., and Lloyd, J. R. (2004). Identification of an Arabidopsis inorganic pyrophosphatase capable of being imported into chloroplasts. *FEBS Lett.* 565, 101–105. doi: 10.1016/j.febslet.2004.03.080

Schumacher, K. (2014). pH in the plant endomembrane system-an import and export business. *Curr. Opin. Plant Biol.* 22, 71–76. doi: 10.1016/j.pbi.2014.09.005

Segami, S., Nakanishi, Y., Sato, H. M., and Maeshima, M. (2010). Quantification, organ-specific accumulation and intracellular localization of type II H^+-pyrophosphatase in. *Arabidopsis thaliana. Plant Cell Physiol.* 51, 1350–1360. doi: 10.1093/pcp/pcq096

Segami, S., Tomoyama, T., Sakamoto, S., Gunji, S., Fukuda, M., Kinoshita, S., et al. (2018). Vacuolar H^+-pyrophosphatase and cytosolic soluble pyrophosphatases cooperatively regulate pyrophosphate levels in *Arabidopsis thaliana*. *Plant Cell* 30, 1040–1061. doi: 10.1105/tpc.17.00911

Shen, J., Zeng, Y., Zhuang, X., Sun, L., Yao, X., Pimpl, P., et al. (2013). Organelle pH in the Arabidopsis endomembrane system. *Mol. Plant* 6, 1419–1437. doi: 10.1093/mp/sst079

Stitt, M. (1998). Pyrophosphate as an energy donor in the cytosol of plant cells: an enigmatic alternative to ATP. *Bot. Acta* 111, 167–175. doi: 10.1111/j.1438-8677.1998.tb00692.x

Tabeta, H., Higashi, Y., Okazaki, Y., Toyooka, K., Wakazaki, M., Sato, M., et al. (2022). Skotomorphogenesis exploits threonine to promote hypocotyl elongation. *Quant. Plant Biol.* 3, E26. doi: 10.1017/qpb.2022.19

Tabeta, H., Watanabe, S., Fukuda, K., Gunji, S., Asaoka, M., Hirai, M. Y., et al. (2021). An auxin signaling network translates low-sugar-state input into compensated cell enlargement in the *fugu5* cotyledon. *PLoS Genet.* 17, e1009674. doi: 10.1371/journal.pgen.1009674

Takahashi, K., Morimoto, R., Tabeta, H., Asaoka, M., Ishida, M., Maeshima, M., et al. (2017). Compensated cell enlargement in *fugu5* is specifically triggered by lowered sucrose production from seed storage lipids. *Plant Cell Physiol.* 58, 668–678. doi: 10.1093/pcp/pcx021

Tannert, M., Balcke, G. U., Tissier, A., and Köck, M. (2021). At4g29530 is a phosphoethanolamine phosphatase homologous to PECP1 with a role in flowering time regulation. *Plant J.* 107, 1072–1083. doi: 10.1111/tpj.15367

Tannert, M., May, A., Ditfe, D., Berger, S., Balcke, G. U., Tissier, A., et al. (2018). Pi starvation-dependent regulation of ethanolamine metabolism by phosphoethanolamine phosphatase PECP1 in Arabidopsis roots. *J. Exp. Bot.* 69, 467–481. doi: 10.1093/jxb/erx408

Thomas, P. W., Woodward, F. I., and Quick, W. P. (2003). Systematic irradiance signalling in tobacco. *New Phytol.* 161, 193–198. doi: 10.1046/j.1469-8137.2003.00954.x

Tian, C., Yang, J., Liu, C., Chen, P., Zhang, T., Men, Y., et al. (2022). Engineering substrate specificity of HAD phosphatases and multienzyme systems development for the

thermodynamic-driven manufacturing sugars. *Nat. Commun.* 13, 3582. doi: 10.1038/s41467-022-31371-8

Tsai, H. H., and Schmidt, W. (2021). The enigma of environmental pH sensing in plants. *Nat. Plants* 7, 106–115. doi: 10.1038/s41477-020-00831-8

Tsai, J. Y., Tang, K. Z., Li, K. M., Hsu, B. L., Chiang, Y. W., Goldman, A., et al. (2019). Roles of the hydrophobic gate and exit channel in *Vigna radiata* pyrophosphatase ion translocation. *J. Mol. Biol.* 431, 1619–1632. doi: 10.1016/j.jmb.2019.03.009

Tsugawa, H., Arita, M., Kanazawa, M., Ogiwara, A., Bamba, T., and Fukusaki, E. (2013). MRMPROBS: a data assessment and metabolite identification tool for large-scale multiple reaction monitoring based widely targeted metabolomics. *Anal. Chem.* 85, 5191–5199. doi: 10.1021/ac400515s

Tsugawa, H., Cajka, T., Kind, T., Ma, Y., Higgins, B., Ikeda, K., et al. (2015). MS-DIAL: data-independent MS/MS deconvolution for comprehensive metabolome analysis. *Nat. Methods* 12, 523–526. doi: 10.1038/nmeth.3393

Tsugawa, H., Kanazawa, M., Ogiwara, A., and Arita, M. (2014a). MRMPROBS suite for metabolomics using large-scale MRM assays. *Bioinformatics* 30, 2379–2380. doi: 10.1093/bioinformatics/btu203

Tsugawa, H., Ohta, E., Izumi, Y., Ogiwara, A., Yukihira, D., Bamba, T., et al. (2014b). MRM-DIFF: data processing strategy for differential analysis in large scale MRM-based lipidomics studies. *Front. Genet.* 5, 471. doi: 10.3389/fgene.2014.00471

Tsuge, T., Tsukaya, H., and Uchimiya, H. (1996). Two independent and polarized processes of cell elongation regulate leaf blade expansion in *Arabidopsis thaliana* (L.) heynh. *Development* 122, 1589–1600. doi: 10.1242/dev.122.5.1589

Varadi, M., Anyango, S., Deshpande, M., Nair, S., Natassia, C., Yordanova, G., et al. (2022). AlphaFold protein structure database: Massively expanding the structural coverage of protein-sequence space with high-accuracy models. *Nucleic Acids Res.* 50 (D1), D439–D444. doi: 10.1093/nar/gkab1061

Wang, W., Zhao, H., Zhao, B., Liu, H., Liu, Q., and Gao, Y. (2021). Highly selective recognition of pyrophosphate by a novel coumarin-iron (III) complex and the application in living cells. *Chemosensors* 9, 48. doi: 10.3390/chemosensors9030048

Weiner, H., Stitt, M., and Heldt, H. W. (1987). Subcellular compartmentation of pyrophosphate and alkaline pyrophosphatase in leaves. *Biochim. Biophys. Acta* 893, 13–21. doi: 10.1016/0005-2728(87)90143-5

Williamson, L. C., Ribrioux, S. P., Fitter, A. H., and Leyser, H. M. (2001). Phosphate availability regulates root system architecture in Arabidopsis. *Plant Physiol.* 126, 875–882. doi: 10.1104/pp.126.2.875

Wimmer, J. L. E., Kleinermanns, K., and Martin, W. F. (2021). Pyrophosphate and irreversibility in evolution, or why PPi is not an energy currency and why nature chose triphosphates. *Front. Microbiol.* 12, 759359. doi: 10.3389/fmicb.2021.759359

Yoza, N., Akazaki, I., Nakazato, T., Ueda, N., Kodama, H., and Tateda, A. (1991). High-performance liquid chromatographic determination of pyrophosphate in the presence of a 20,000-fold excess of orthophosphate. *Anal. Biochem.* 199, 279–285. doi: 10.1016/0003-2697(91)90102-Y

Zhang, M., Yang, L., Ding, W., and Zhang, H. (2022). The His23 and Lys79 pair determines the high catalytic efficiency of the inorganic pyrophosphatase of the haloacid dehalogenase superfamily. *Biochim. Biophys. Acta* 1866, 130128. doi: 10.1016/j.bbagen.2022.130128

frontiers | Frontiers in Plant Science

TYPE Original Research
PUBLISHED 29 March 2023
DOI 10.3389/fpls.2023.1138563

OPEN ACCESS

EDITED BY
Ali Ferjani,
Tokyo Gakugei University, Japan

REVIEWED BY
Rachapudi V. Sreeharsha,
Indian Institute of Chemical Technology (CSIR), India
Muhammad Ahsan Asghar,
Centre for Agricultural Research, Hungary

*CORRESPONDENCE
Ya-Qi An
1120180343@mail.nankai.edu.cn
Zhen Xi
zhenxi@nankai.edu.cn

SPECIALTY SECTION
This article was submitted to Plant Physiology, a section of the journal Frontiers in Plant Science

RECEIVED 05 January 2023
ACCEPTED 13 March 2023
PUBLISHED 29 March 2023

CITATION
An Y-Q, Qin Z-T, Li D-D, Zhao R-Q, Bi B-S, Wang D-W, Ma D-J and Xi Z (2023) The combined formulation of brassinolide and pyraclostrobin increases biomass and seed yield by improving photosynthetic capacity in *Arabidopsis thaliana*. *Front. Plant Sci.* 14:1138563. doi: 10.3389/fpls.2023.1138563

The combined formulation of brassinolide and pyraclostrobin increases biomass and seed yield by improving photosynthetic capacity in *Arabidopsis thaliana*

Ya-Qi An*, Zi-Ting Qin, Dan-Dan Li, Rui-Qi Zhao, Bo-Shi Bi, Da-Wei Wang, De-Jun Ma and Zhen Xi*

State Key Laboratory of Elemento-Organic Chemistry, and Department of Chemical Biology, National Pesticide Engineering Research Center, Collaborative Innovation Center of Chemical Science and Engineering, College of Chemistry, Nankai University, Tianjin, China

In the context of global food crisis, applying the phytohormone-brassinosteroids (BRs) in combination with the fungicide-pyraclostrobin (Pyr) was beneficial for plant quality and productivity in several field trials. However, in addition to the benefits of disease control due to the innate fungicidal activity of Pyr, it remains to be understood whether the coapplication of BL+ Pyr exerts additional growth-promoting effects. For this purpose, the effects of BL treatment, Pyr treatment, and BL+ Pyr treatment in *Arabidopsis thaliana* were compared. The results showed that the yield increased at a rate of 25.6% in the BL+Pyr group and 9.7% in the BL group, but no significant change was observed in the Pyr group. Furthermore, the BL+Pyr treatment increased the fresh weight of both the leaves and the inflorescences. In contrast, the Pyr and BL treatments only increased the fresh weight of leaves and inflorescences, respectively. Additionally, the BL + Pyr treatment increased the P_n, G_s, T_r, $V_{c,\ max}$, J_{max}, V_{TPU}, ETR, F_v'/F_m', ΦPSII, Rd, AYE and Rubisco enzyme activity by 26%, 38%, 40%, 16%, 19%, 15%, 9%, 10%, 17%, 179%, 18% and 32%, respectively. While, these paraments did not change significantly by the BL or Pyr treatments. Treatment with BL + Pyr and Pyr, rather than BL, improved the chlorophyll a and chlorophyll b contents by upregulating genes related to chlorophyll biosynthesis and downregulating genes related to chlorophyll degradation. Additionally, according to transcriptomic and metabolomic analysis, the BL+ Pyr treatment outperformed the individual BL or Pyr treatments in activating the transcription of genes involved in photosynthesis and increasing sugar accumulation. Our results first validated that the combined usage of BL and Pyr exerted striking synergistic effects on enhancing plant biomass and yield by increasing photosynthetic efficiency. These results might provide new understanding for the agricultural effects by the co-application of BL and Pyr, and it might stimulate the efforts to develop new environment-friendly replacement for Pyr to minimize the ecotoxicology of Pyr.

KEYWORDS

brassinosteroids, pyraclostrobin, photosynthesis, transcriptomics, metabolomics, yield, *Arabidopsis thaliana*

1 Introduction

Food security is a long-term and urgent issue (Godfray et al., 2010). Over the past decades, agricultural yields have risen, which is primarily due to the greater and more consistent crop production achieved by genetic engineering strategies (Bailey-Serres et al., 2019). However, the year-on-year increase in yields of major crops has plateaued in many parts of the world (Simkin et al., 2019). Additionally, the potential contribution of genetic modification engineering to yield increases were restricted, as the development of a new genetically engineered crop is a challenging, long-term, and expensive enterprise, and the application of genetically modified crops is severely limited in many countries (Prado et al., 2014). Currently, more than 800 million people are suffering from a food crisis globally (Wei et al., 2022). Moreover, the current crop yield increases are insufficient to feed nearly 10 billion people by 2050, which is even more concerning when the expected adverse effects of climate changes and the reduced availability of arable land are considered (Tilman et al., 2011; Araus et al., 2021).

Oxygenic photosynthesis initiates with light absorption, followed by excitation energy transfer to the reaction center, primary photochemistry, transport of electrons and protons, NADPH, and ATP synthesis, preceded by CO_2 fixation through the Calvin–Benson cycle (Stirbet et al., 2020). Photosynthesis is regulated by various factors, such as the process of gas exchange, the content of photosynthetic pigments, the activity of photosynthesis-related enzymes, the transcription of photosynthesis-related genes, and the allocation of photosynthetic intermediates, *etc.* (Foyer and Noctor, 2000; Colombo et al., 2016; Heyneke and Fernie, 2018; Mu and Chen, 2021; Zahra et al., 2022). As photosynthetic products can either serve as carbon skeletons to assemble the whole plant or produce ATP through the re-oxidation by mitochondrial respiration to fuel metabolic or transport processes, optimization of photosynthesis has been demonstrated to be a practical approach for improving crop yield (Ruan, 2014; Nuccio et al., 2015). Numerous genes and enzymes involved in photosynthetic processes have been proven to be targeted for enhancing photosynthetic efficiency and thus yield (Long et al., 2015; Simkin et al., 2019; Araus et al., 2021).

Brassinosteroids (BRs), as the sixth class of plant hormones, regulate a broad spectrum of physiological functions in plants, such as cell division and elongation, xylem differentiation, photosynthesis, photomorphogenesis, senescence, and reproduction (Nolan et al., 2020). Furthermore, the physiological effects of BRs are more noticeable when the plant suffers from adverse environmental stress, leading BRs to protect against the pressures that plants may eventually experience (Sharma et al., 2018; Ahammed et al., 2020; Wang et al., 2020b). As reported, BRs and their analogs have been widely used as regulators of plant growth in agriculture to improve quality and yield (Vriet et al., 2012; Ali, 2017; Tong and Chu, 2018; Padhiary et al., 2020). However, the regulation of growth by endogenous BRs is temporally and spatially specific, and the effectiveness of exogenous BRs is susceptible to the time of application, treatment frequency, dose, and complex field conditions (Zu et al., 2019; Lin, 2020; Hwang et al., 2021). Therefore, the effects of exogenous BR application are not always as satisfactory as expected under field conditions due to the feedback inhibition or ineffectiveness of BR signaling, which has discouraged the usage of exogenous BRs in agriculture and horticulture (Khripach et al., 2000; Vriet et al., 2012).

Pyraclostrobin (Pyr), a strobilurin fungicide, is widely used in agriculture (Bartlett et al., 2002). Pyr not only shows fungicidal activity but also displays benefits for plant growth, including increasing net photosynthesis, improving the efficiency of water utilization, activating nitrate reductase, strengthening stress tolerance, and delaying senescence (Amaro et al., 2019). However, Pyr is more likely to improve plant biomass than grain yield due to the compensatory efforts of plants in adjusting yield components (Swoboda and Pedersen, 2009; Factor et al., 2010). Albeit with the beneficial regulatory functions, Pyr also exerts adverse effects on plants; for example, Pyr can partially inhibit electron transport in the cytochrome *bc1* complex of mitochondria, which leads to reduced ATP production in plants (Nason et al., 2007; Pedersen et al., 2017). Furthermore, Pyr also impaired the photosynthetic process due to the blockage of electron transport between photosystem II (PSII) and photosystem I (PSI) by binding to the Q_i site of the chloroplast cytochrome *bf* complex (Nason et al., 2007; Debona et al., 2016).

To alleviate the side effects of Pyr, Pyr in combination with BRs has gradually been used in the field. Interestingly, the combined use of BL and Pyr not only provided better protection in terms of reducing the phytotoxicity of Pyr but also produced unexpected beneficial improvements in plant growth in several field trials (Li et al., 2018; Li et al., 2020; Zhang, 2020; Li et al., 2021; Zhao et al., 2021). However, the abovementioned discovery of the benefits of BL and Pyr coapplication is still largely restricted to a few in-field applications. Since the threat of pests and pathogens is unavoidable in fields, it is quite difficult to distinguish the plant protective effect exerted by the intrinsic fungicidal activity of Pyr from the additional physiological benefits of the BR plus Pyr treatment on plants. Hence, the actual growth-promoting activity of BR plus Pyr coapplication through the preclusion of the fungicidal effect of Pyr, as well as the corresponding underlying mechanisms, remain to be experimentally verified in the laboratory.

For this purpose, the effects of different applications, including BL, Pyr, and BL+ Pyr, in *A. thaliana* were compared under pathogen-free environmental conditions. The results showed that, in addition to the benefits of disease control due to the fungicidal activity of Pyr, the coapplication of BL and Pyr exerted a synergistic effect on simultaneously enhancing the biomass and yield of *A. thaliana*. Based on the physiological, biochemical, transcriptomic and metabolomic analyses, we found that the synergistic enhancement of biomass and yield of BL+Pyr was related to the improved photosynthetic performance and the increased sugar accumulation. Our study indicated that applying a group of chemical compounds might be a simple but efficient way to promote plant productivity through the regulation of photosynthesis. Given that many reports indicated the adverse effects of Pyr on terrestrial and aquatic life forms (Liu et al., 2018; Zhang et al., 2020; Wang et al., 2020a), we hope that the identification of candidate genes and compounds based on transcriptome and metabolome analyses would be

helpful to search and design new environmentally friendly yield-promoting agrochemicals.

2 Materials and methods

2.1 Plant material and experimental design

The surfaces of A. *thaliana* plant seeds (ecotype Col-0) were sterilized in ethanol-water (70:30, v/v) for 10 minutes, washed with distilled water and then plated on 0.5 × MS medium (Duchefa, Haarlem, the Netherlands) supplemented with 1% sucrose (Macklin, Shanghai) and 0.8% agar (Macklin, Shanghai). After being pretreated at 4°C for 2 days, the plates were placed horizontally in the artificial climate chamber under long-day conditions (22°C, 30% humidity, and approximately 120 photons μmol m^{-2} s^{-1} on a 16 h day/night cycle) until the seedlings were transplanted into the soil after 7 days.

The seedlings were grown for 14 days in soil, and then the seedlings with similar size were picked out for subsequent experiments. To determine the optimal concentration of BL+Pyr for promoting plant growth, seedlings were divided into 12 groups and each group included 10 biological replicates. Then the seedlings were sprayed with 1‰ DMSO (Sigma-Aldrich), 0.03, 0.3, 3 or 30 μM of pyraclostrobin (Pyr, Shanghai Lvze Bio-Tech Co. 99%), 0.1, 1 or 10 μM of brassinolide (BL, Sigma-Aldrich), 0.1, 1 or 10 μM of BL in combination with 0.03, 0.3, 3 or 30 μM of Pyr at each concentration, respectively. In the subsequent comprehensive study of the effects of BL (1 μM) and Pyr (3 μM) on plant growth, seedlings were divided into 4 groups and 60 biological replicates were used for each treatment. Then the seedings were separately foliar spray with 1‰ DMSO, BL (1 μM), Pyr (3 μM), or a mixture of BL (1 μM) and Pyr (3 μM). A total of 3 foliar sprays were applied to 20-day-old seedlings (vegetable growth stage), 35-day-old seedlings (floral development stage) and 55-day-old seedlings (silique development stage). The seedings treated with 1‰ DMSO was considered as untreated control group. The leaves of 31-day-old seedlings were harvested for further physiological, biochemical, transcriptomic and metabolomic analyses.

2.2 Phenotypic index measurement

To determine optimal concentration of BL+Pyr for promoting plant growth, the major axis and the fresh weight of the rosette leaves in each treatment were measured on 35-day-old seedlings with 10 biological replicates. 3 independent experiments were performed from October 2018 to December 2018.

In the comprehensive study of the effects of the coapplication of BL (1 μM) and Pyr (3 μM) on plant growth, the major axis and the fresh weight of the rosette leaves were measured on 27-day-old seedlings and 31-day-old seedlings with 20 biological replicates in each treatment. Similarly, 20 biological replicates in each treatment were measured for obtaining the fresh weights of rosette leaves and inflorescences of 39-day-old seedlings, 51-day-old seedlings, and 69-day-old seedlings or to count the inflorescence height, number of rosette branches, and number of branches with two or more seed-bearing siliques of 69-day-old seedlings. And the time of the first bud appearing and the first flower opening was recorded at 12-hour intervals with 60 biological replicates in each treatment. Also, 20 biological replicates in each treatment were used to collect the seeds every 5 days after the first silique shattered until senescence complete. Then the collected seeds were dried in an oven at 28°C for 48 hours before being weighed on a 1/10,000 scale to obtain the seed yield. Thousand kernel weight were weighed with 4 biological replicates in each treatment and calculated according to the following formula: Thousand kernel weight (mg) = weight (mg)/ seed number × 1000. All the images were captured using a digital camera (Canon DS126201, Japan). Phenotypic and yield traits were assessed in the artificial climate chamber and 4 independent experiments were performed in Tianjin to obtain the results (March 2019 to July 2019, April 2019 to August 2019, June 2019 to October 2019, September 2019 to January 2020).

2.3 Measurement of rubisco activity

The *in-vitro* activity of ribulose-1,5-bisphosphate carboxylase/ oxygenase (Rubisco; EC 4.1.1.39) was determined by monitoring NADH oxidation at 30°C at 340 nm, accompanied by the conversion of glycerol 3-phosphate to glycerol 3-phosphate upon the addition of an enzyme extract to the reaction mixture. Rubisco enzyme activity was measured by Rubisco Activity Assay Kit (Solarbio, China) according to the manufacturer's instructions. Each independent experiment consisted of 3 biological replicates and 3 independent experiments were performed.

2.4 Measurement of chlorophyll content

Fresh leaf tissue (0.5 g) was homogenized on ice, extracted repeatedly with 80% acetone (v/v) until no visible pigment remained. The combined extracts were then centrifuged at 4500 g at 4 °C. The absorbance values of the solution at 646 and 663 nm were recorded to calculate the chlorophyll (Chl a and Chl b) contents (μg/g FW) according to a previous report (Lichtenthaler, 1987). Each independent experiment consisted of 3 biological replicates and 3 independent experiments were performed.

$$C_a = \frac{12.21 \times A_{663} - 2.81 \times A_{646}}{M_{plant}} \quad (1)$$

$$C_b = \frac{20.13 \times A_{646} - 5.03 \times A_{663}}{M_{plant}} \quad (2)$$

2.5 Measurement of photosynthesis-related indicators

Gas exchange parameters were measured on the 7th leaf using an infrared gas analyzer (IRGA) portable photosynthesis system LI-6800 (Li-COR, USA) with a 2 cm^2 fluorescent leaf chamber. The gas

exchange constants, including net photosynthetic rate (P_n), transpiration rate (T_r), stomatal conductance (G_s), and intercellular CO_2 concentrations (C_i), were measured under the settings of 750 μmol s^{-1} flow rate, 600 μmol m^{-2} s^{-1} photosynthetic photon flux density (PPFD), and 400 ppm ambient CO_2 (C_a). During the measurement, leaf temperature and relative humidity were maintained at 22°C and at 55-65%, respectively. The stomatal restriction value (L_s) and apparent mesophyll conductance (AMC) were calculated following the formulations L_s=1-C_i/C_a and AMC=P_n/C_i. Each independent experiment consisted of 10 biological replicates and 3 independent experiments were performed.

The light response curves and the CO_2 response curves were also measured on the 7th leaf according to the standard settings of the Li-COR 6800's automatic procedure. Saturated light intensity (PARsat) were calculated with a modified model of the light reaction curve for plant photosynthesis (Ye and Kang, 2012). The dark respiration rate (Rd) and the apparent quantum efficiency (AYE) were calculated according to the previous reports (Sekhar et al., 2014; Sekhar et al., 2015). The V_{cmax}, V_{TPU} and J_{max} were calculated according to Farquhar, von Caemmerer and Berry model using PCE Calculator(version 2.0) (Long and Bernacchi, 2003). Each independent experiment consisted of 2 biological replicates and 3 independent experiments were performed.

Chlorophyll fluorescence parameters were measured on the 7th leaf. Plants were dark treated for 1 hour prior to the measurement of the minimal fluorescence (F_o), after which the maximum fluorescence (F_m) was measured by irradiating a polyphasic saturating flash (4000 μmol m^{-2} s^{-1}). Subsequently, the steady-state fluorescence under light (F_s), the maximum fluorescence under light (F_m') and the minimum fluorescence under light (F_o') were recorded on the leaves being adequately light-adapted for 1 hour. The quantum yield of PSII (ΦPSII), maximum quantum yield of PSII (F_v/F_m), efficiency of energy capture by open PSII (F_v'/F_m'), electron transfer rates (ETR) were calculated as previously described (Maxwell and Johnson, 2000; Sreeharsha et al., 2015). Each independent experiment consisted of 10 biological replicates and 3 independent experiments were performed.

2.6 Extraction of mRNA and real-time fluorescence PCR (qRT-PCR)

Leaf samples (0.1 g) were ground in liquid nitrogen, and total RNA was extracted using an RNA extraction kit (TransGen, China) according to the instructions. The extracted RNAs were then converted to cDNA using a PrimScript RT kit (Takara, Kyoto, Japan). 10 genes (*PSAB*, *PSAA*, *PSAF*, *PSBA*, *ATPD*, *CPN60A1*, *RBCL*, *RCA*, *SBPASE*, *CFBP*) were selected for the validation of Seq-analysis. The expression levels of the target genes were analyzed by qRT-PCR using *Actin 2* as the internal reference gene and using SYBR Premix Ex TaqTM (Takara, Kyoto, Japan) as the fluorescent dye. The primers for the target genes were listed in Table S1. The relative expression of the target genes was calculated according to the $2^{-\Delta\Delta CT}$ formula. Each independent experiment consisted of 3 biological replicates and 3 independent experiments were performed to obtain the results.

2.7 RNA-seq analysis

RNA-Seq analysis was conducted using the UMI-mRNA sequencing method by Novogene Bioinformatics Technology Co., Ltd. (Tianjin, China). The mRNA libraries were prepared and sequenced on an Illumina Nova Seq 6000 platform with 3 biological replicates. After filtering the raw data, clean data with high quality were subjected to subsequent analysis. Then, FPKM (expected number of fragments per kilobase of transcript sequence per million base pairs sequenced) values were used to estimate gene expression levels. Differential expression analysis was performed using the DESeq R package (1.10.1), and hypothesis test probability (p-value) was corrected using the Benjamin–Hochberg method. Genes with an FDR (false discovery rate)<0.05 were considered differentially expressed. GO and KEGG enrichment analyses of differentially expressed genes were conducted using the Gene Ontology (http://geneontology.org/) and KEGG PATHWAY (https://www.kegg.jp/kegg/pathway.html) databases, respectively. All raw sequence data from this study have been deposited into the NCBI's SRA database with the link of https://www.ncbi.nlm.nih.gov/sra/PRJNA930055, under the accession number SAMN32982539 to SAMN32982550, the temporary Submission ID SUB12691837 and the BioProject ID PRJNA930055.

2.8 Metabolite profiling

Metabolite profiling was carried out using the Quasi-Targeted Metabolomics method by Novogene Bioinformatics Technology Co., Ltd. (Tianjin, China) with 3 biological replicates. Metabolites were extracted according to an available protocol(Want et al., 2013), and untargeted metabolites were screened by LC-MS/MS analyses were performed using an ExionLC™ AD system (SCIEX) coupled with a TRAP® 6500+ mass spectrometer (SCIEX). After metabolites were detected using MRM (multiple reaction monitoring) based on the Novogene in-house database, metabolite quantification and identification were performed using Q3 and Q1, Q3, RT (retention time), DP (depolymerization potential) and CE (collision energy). The integration and correction of peaks in data files generated by HPLC–MS/MS were performed using SCIEX OS version 1.4. The statistical significance (P-value) was calculated based on univariate analysis (T-test), and the metabolites with variable importance in projection (VIP) ≥ 1, fold change (FC) ≤ 0.8 or ≥1.2, and P-value< 0.05 were identified as DAMs (differential accumulation metabolites). These metabolites were annotated using the online KEGG (http://www.kegg.jp/), HMDB (http://www.hmdb.ca/) and Lipidmaps (http://www.lipidmaps.org/) databases.

2.9 Statistical analysis

To compare the differences among different treatment groups, statistical analysis was performed with one-way ANOVA followed by Tukey's HSD test (P< 0.05) using SPSS software (Ver 26.0, Chicago, IL, USA). The data are presented as the means ± standard deviations (SD).

3 Results

3.1 The increase in plant biomass and seed yield of *A. thaliana* seedlings by the coapplication of brassinolide and pyraclostrobin

To explore the optimal concentration of BL + Pyr for promoting plant growth, the main axis and fresh weight of rosette leaves of *A. thaliana* treated with different concentrations of BL, Pyr and BL + Pyr were measured separately. As shown in Figure S1, no significant changes in leaf growth were observed at BL concentrations of 0.1 or 1 μM, while abnormal elongation of the rosette with an increased major axis but reduced fresh weight was observed for plants treated with 10 μM BL (Figure S1A, B). Similarly, Pyr promoted leaf growth at low concentrations (0.3 μM) and inhibited leaf growth at high concentrations (30 μM) (Figures S1C, D). There was no significant effect when the applied concentration of Pyr was 0.03 or 3 μM (Figures S1C, D). When different concentrations of BL (0.1 μM, 1 μM, 10 μM) or Pyr (0.03 μM, 0.3 μM, 3 μM, 30 μM) were coapplied, the coapplication of BL (1 μM) plus Pyr (3 μM) outperformed all other treatments in terms of simultaneously increasing the major axis and fresh weight of the rosette (Table S2, S3). In contrast, 1 μM BL or 3 μM Pyr induced no significant effect on the major axis and fresh weight of the rosette (Table S2, S3).

To comprehensively study the synergistic effect of BL and Pyr on plant growth, BL (1 μM), Pyr (3 μM) and BL (1 μM) + Pyr (3 μM) were chosen, and the phenotypic traits were assessed throughout the vegetative stage and reproductive stage. In the vegetative stage, a significant effect on leaf growth of 27-day-old seedlings was observed only in the BL + Pyr group rather than the BL or Pyr group, with the major axis and the fresh weight of rosette leaves increasing by 21% and 41.5% compared with the untreated group, respectively (Table 1, Figure 1A). Similarly, only the BL + Pyr treatment increased the major axis and the fresh weight of rosette leaves of 31-day-old seedlings by 20.3% and 30.3% compared with the untreated group, respectively. In contrast, treatment with BL alone decreased the fresh weight of leaves by 17.8% compared to the untreated group (Table 1, Figures 1B-D).

In addition to comparing the traits of leaf growth in the vegetative stage, the phenotypic traits of four groups (untreated, BL+Pyr-treated, BL-treated or Pyr-treated) were further compared during the reproductive development stage. In the early stage of reproductive development (39-day-old seedlings), the fresh weight of rosette leaves increased by 51% and 42% when treated with BL +Pyr and Pyr, respectively, and decreased by 11% when treated with BL compared to the untreated group. Conversely, the fresh weight of inflorescences decreased by 43% and 74% when treated with BL +Pyr and Pyr, respectively, and increased by 18% when treated with BL compared to the untreated group (Table 2, Figures 2A, 2B). Furthermore, the budding time and the corresponding flowering time were accelerated by the BL treatment and delayed by both the BL+Pyr and Pyr treatments compared with the untreated group (Figures 2A, 3A-B).

In the mid-stage of reproductive development (51-day-old seedlings), the fresh weight of rosette leaves and inflorescence in the group treated with BL+Pyr were increased by 25% and 40%, respectively, compared to the untreated group (Table 2 and Figures 2C, D). The fresh weight of rosette leaves was increased by 21% in the group treated with Pyr and decreased by 22% in the group treated with BL. Conversely, the fresh weight of inflorescence was decreased by 28% in the group treated with Pyr and increased by 25% in the group treated with BL compared to the untreated group (Table 2, Figures 2C, D). This change was also observed in the late stage of reproductive development (69-day-old seedlings). Compared to the untreated group, the fresh weight of rosette leaves and inflorescence was significantly increased by 181% and 46% in the BL+Pyr group, while Pyr treatment increased the fresh weight of rosette leaves by 293% without any obvious influence on the fresh weight of the inflorescence. In contrast, BL treatment increased the fresh weight of inflorescence by 24% and showed no detectable effect on the fresh weight of rosette leaves (Table 2, Figure 2E).

To explore the reasons for the variation in the fresh weight of inflorescences among the four groups, measurements were subsequently performed on the height of inflorescence, the number of rosette branches and effective branches in the late stage of reproductive development. No significant difference in inflorescence height was observed among the four groups (Table 3). Consistent with the fresh weight of inflorescence, the seedlings treated with BL+Pyr generated the most rosette branches and effective branches (branches with two or more seed-bearing siliques), followed by the seedlings treated with BL, then the untreated seedlings, and finally, the seedlings treated with Pyr (Figures 2D-E, Table 3).

Finally, the seed yield per plant and thousand-kernel weight of the 4 groups (untreated, BL+Pyr, BL and Pyr) were further compared.

TABLE 1 The major axis (cm) and fresh weight (mg) of rosette leaves during vegetative development stage.

Paraments	Age (days)	Pesticide Applied strategy			
		CK	Pyr	BL+Pyr	BL
Major axis(cm)	27	8.21 ± 0.55b	8.28 ± 0.63b	9.96 ± 0.53a	8.59 ± 0.67b
	31	9.5 ± 0.68b	9.74 ± 0.64b	11.49 ± 0.93a	10.02 ± 0.58b
Fresh weight(mg)	27	373 ± 26b	396 ± 22b	529 ± 42a	382 ± 29b
	31	800 ± 75b	828 ± 65b	1048 ± 95a	668 ± 51c

Data was measured on the 7th day after the first-round application (27-day-old seedlings) and 11th day after the first-round application (31-day-old seedlings). Data were presented as the mean ± SD of four independent replicate experiments. In a line, different letters indicate significant differences ($p < 0.05$) according to ANOVA followed by Tukey's test. CK, untreated seedlings; Pyr, Treated with 3 μM pyraclostrobin; BL+Pyr, Treated with 1 μM BL in combination with 3 μM pyraclostrobin; BL, Treated with 1 μM BL.

10.3389/fpls.2023.1138563

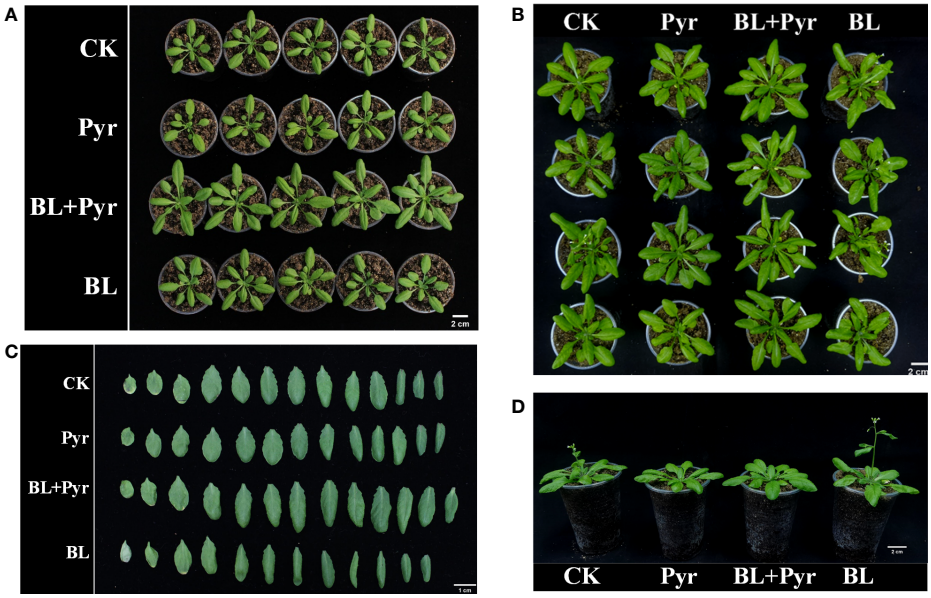

FIGURE 1
BL+Pyr increased the major axis and the fresh weight of rosette leaves during the vegetative growth period. Photos were taken on the 7th day after the first-round application (**A**, 27-day-old seedlings) and 11th day after the first-round application (**B–D**, 31-day-old seedlings). CK, untreated seedlings; Pyr, seedlings treated with 3 μM pyraclostrobin; BL+Pyr, seedlings treated with 1 μM BL and 3 μM pyraclostrobin; BL, seedlings treated with 1 μM BL.

Compared to the untreated group, the seed yield was increased by 25.6% in the BL+Pyr group, which was much higher than that (9.7%) in the BL group. In contrast, Pyr did not show a significant increase in seed yield (Table 3). Additionally, there was no significant difference in thousand-kernel weight among the four groups (Table 3).

3.2 Synergistic enhancement of photosynthetic efficiency by the coapplication of brassinolide and pyraclostrobin

To investigate whether the mechanism by which the BL + Pyr treatment synergistically enhanced the biomass and yield was related to photosynthesis, the influence of the four treatments (untreated, BL+Pyr, BL and Pyr) on photosynthetic traits was analyzed. The results of the gas exchange constant measurements indicated that BL+Pyr treatment significantly increased the net photosynthetic rate (P_n), the stomatal conductance (G_s), the transpiration rate (T_r), and the apparent mesophyll conductance (AMC) by 26%, 38%, 40% and 25%, respectively, while decreased the stomatal restriction value (L_s) by 20%, compared to the untreated group (Figures 3A-E). While, no statistically significant differences were observed between the untreated group and individual BL or Pyr treatments regarding these above gas exchange parameters (Figure 3). However, the enhanced gas exchange process in the BL + Pyr treatment did not result in a corresponding increase in intercellular CO_2 concentration (C_i), as

TABLE 2 The fresh weight (mg) of rosette leaves and inflorescence during the reproductive development stage.

Paraments	Age (days)	Pesticide Applied strategy			
		CK	Pyr	BL+Pyr	BL
Fresh weight of leaves	39	1513 ± 108b	2147 ± 187a	2286 ± 175a	1336 ± 144c
	51	2776 ± 432b	3377 ± 579a	3490 ± 636a	2179 ± 264c
	69	285 ± 29c	1122 ± 118a	803 ± 114b	231 ± 23d
Fresh weight of inflorescence	39	1121 ± 109b	291 ± 138d	633 ± 34c	1326 ± 187a
	51	2941 ± 323b	2107 ± 507c	4123 ± 579a	3685 ± 495a
	69	3988 ± 833c	4147 ± 609c	5828 ± 1026a	4946 ± 724b

Data was measured on the 4th day after the second-round application (39-day-old seedlings), the 16th day after the second-round application (51-day-old seedlings), and the 14th day of the third-round application (69-day-old seedlings). Data were presented as the mean ± SD of four independent replicate experiments. In a line, different letters indicate significant differences ($p< 0.05$) according to ANOVA followed by Tukey's test. CK, untreated; Pyr, Treated with 3 μM pyraclostrobin; BL+Pyr, Treated with 1 μM BL in combination with 3 μM pyraclostrobin; BL, Treated with 1 μM BL.

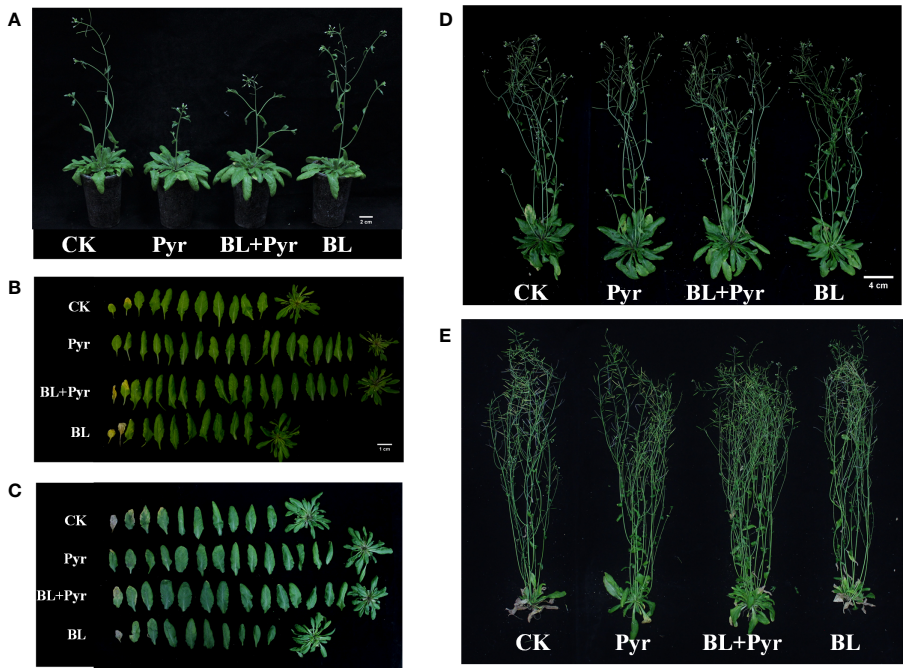

FIGURE 2
BL+Pyr increased the major axis and the fresh weight of rosette leaves and inflorescence during the reproductive growth period. Photos were taken on the 4th day after the second-round application (**A, B**, 39-day-old seedlings), 16th day after the second-round application (**C**, **D**, 51-day-old seedlings), and 14th day after the third-round application (**E**, 69-day-old seedlings). CK, untreated seedlings; Pyr, seedlings treated with 3 μM pyraclostrobin; BL+Pyr, seedlings treated with 1 μM BL and 3 μM pyraclostrobin; BL, seedlings treated with 1 μM BL.

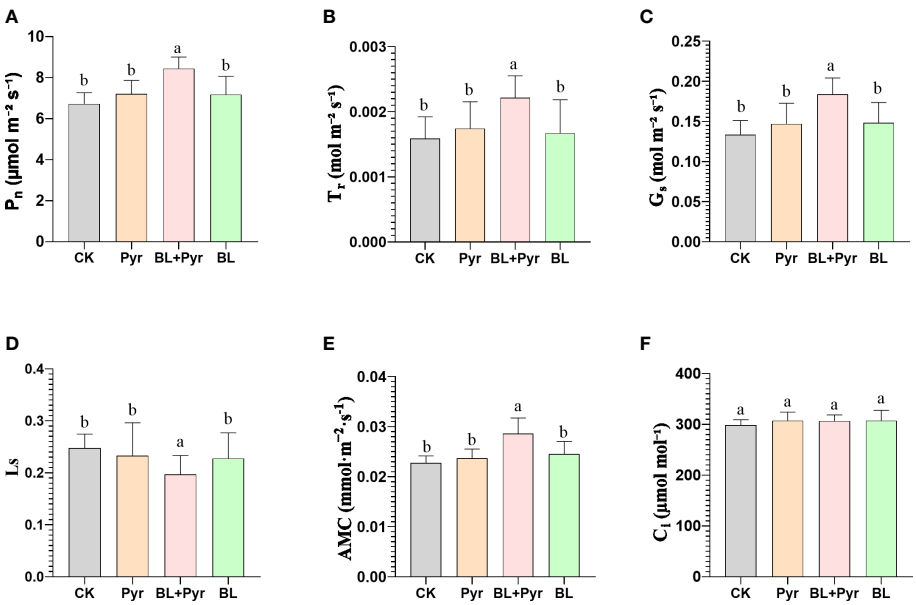

FIGURE 3
BL+Pyr showed a synergistic effect on increasing the photosynthetic efficiency by enhancing the gas exchange process. **(A)** Net photosynthetic rate (P_n); **(B)** Transpiration rate (T_r); **(C)** Stomatal conductance (G_s); **(D)** Stomatal restriction value (L_s); **(E)** Apparent mesophyll conductance (AMC); **(F)** Intercellular CO_2 concentrations (C_i). Data are presented as the mean ± SD of three independent replicate experiments. Different letters indicate significant differences ($p < 0.05$) according to ANOVA followed by Tukey's test. 31-day-old seedlings (the 11th day after the first-round application) were used. CK, untreated seedlings; Pyr, seedlings treated with 3 μM pyraclostrobin; BL+Pyr, seedlings treated with 1 μM BL and 3 μM pyraclostrobin; BL, seedlings treated with 1 μM BL.

10.3389/fpls.2023.1138563

TABLE 3 The floral development, inflorescence architecture, and seed yield parameters.

	Pesticide Applied strategy			
Parament	CK	Pyr	BL+Pyr	BL
The first bud appearing time (day)	30.37 ± 1.30c	32.60 ± 1.34a	31.43 ± 1.13b	29.23 ± 1.25d
The first flower opening time (day)	33.16 ± 1.56c	34.83 ± 1.64a	33.94 ± 1.29b	31.8 ± 1.36d
Number of Rosette Branches	5.03 ± 0.91b	4.55 ± 0.82c	6.12 ± 0.92a	5.42 ± 1.05b
Number of Effective Branches	23.5 ± 3.5c	22.3 ± 3.9c	30.8 ± 4.5a	26.2 ± 3.2b
Length of branch (cm)	32.21 ± 2.48	31.79 ± 2.50	31.02 ± 2.68	32.66 ± 3.06
Seeds weight per plant (mg)	239.6 ± 32.5c	252.6 ± 30.2bc	301.2 ± 51.0a	263.1 ± 31.1b
Thousand kernel weight (mg)	19.03 ± 0.62	19.28 ± 1.40	19.12 ± 1.08	19.29 ± 0.74

The first bud appearing time (n=60)and the first flower opening time (n=60) was counted at 12 hourly intervals during the floral transition and opening stage; The height of inflorescence(cm, n=60), number of rosette branches (n=60) and number of branches with two or more seeds-bearing siliques (n=60) were measured on 14th day after the third-round application (69-day-old seedings); Seeds weight per plant (n=60, mg) and thousand kernel weight (n=12, mg) were measured after dried in an oven at 28°C for 48 hours. Data are presented as the mean ± SD of four independent replicate experiments. Different letters indicate significant differences ($p< 0.05$) according to ANOVA followed by Tukey's test. CK, untreated; Pyr, Treated with 3 μM pyraclostrobin; BL+Pyr, Treated with 1 μM BL in combination with 3 μM pyraclostrobin; BL, Treated with 1 μM BL.

C_i showed almost no change between the four treatments (untreated, BL + Pyr, BL and Pyr) (Figure 3F).

To compare CO_2 assimilation efficiency among the four groups, CO_2 response curves were measured. As shown in Figure 4, the ribulose-1,5-bisphosphate (RuBP) carboxylase/oxygenase (Rubisco) carboxylation (V_{cmax}), the maximum rate of the electron transport driving regeneration of RuBP (J_{max}) and the triose-phosphate utilization (V_{TPU}) were improved by 16%, 19% and 15%, respectively, in the group treated with BL + Pyr, while they were not significantly changed in the groups treated with BL or Pyr alone compared to the untreated group (Figure 4).

As the increase in CO_2 assimilation efficiency was largely correlated with Rubisco enzyme activity, Rubisco enzyme activity was then compared. Consistent with the increase in CO_2 assimilation efficiency, ribulose-1,5-bisphosphate carboxylase/oxygenase (Rubisco) enzyme activity was also increased by 32%

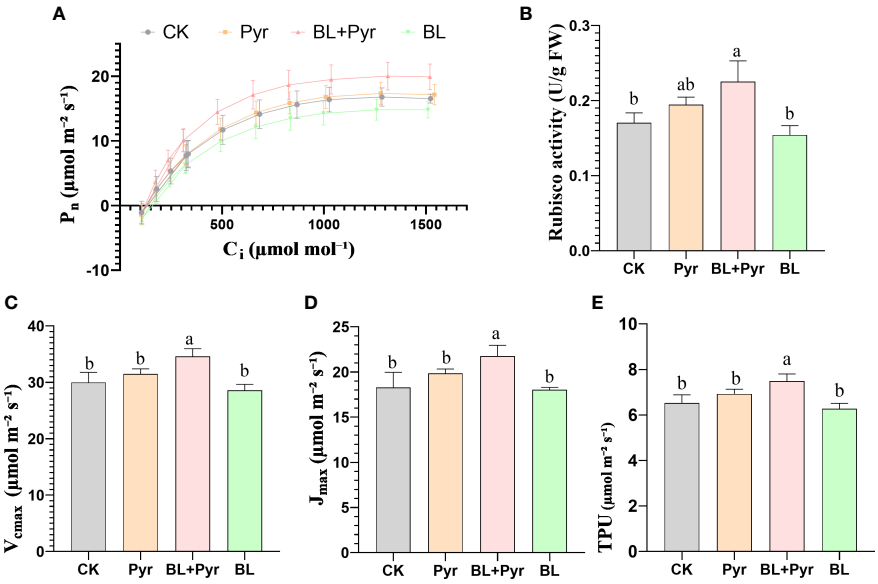

FIGURE 4
BL+Pyr showed a synergistic effect on increasing CO_2 assimilation efficiency. **(A)** Net photosynthetic rate (P_n) at different CO_2 concentration (400, 300, 200, 100, 400, 400, 600, 800, 1000, 1200, 1500, 1800 μmol mol^{-1}) under saturated light intensity (600 μmol m^{-2} s^{-1}); **(B)** Rubisco enzyme activity (U/g FW); **(C)** Maximum *in-vivo* Rubisco carboxylation rates ($V_{c,max}$); **(D)** the maximum rate of electron transport driving regeneration of RuBP (J_{max}); **(E)** Maximum rate of photosynthetic product triose-phosphate utilization (V_{TPU}. Data are presented as the mean ± SD (n=3, measured at random in 3 separate replicate experiments). Data are presented as the mean ± SD of three independent replicate experiments. Different letters indicate significant differences ($p< 0.05$) according to ANOVA followed by Tukey's test. 31-day-old seedlings (the 11th day after the first-round application) were used. CK, untreated seedlings; Pyr, seedlings treated with 3 μM pyraclostrobin; BL+Pyr, seedlings treated with 1 μM BL and 3 μM pyraclostrobin; BL, seedlings treated with 1 μM BL.

in the BL+Pyr group, while no significant increase was identified in the BL or Pyr-treated groups in comparison with the untreated group (Figure 4B).

To verify that the differences in photosynthetic characteristics were not associated with the changes in individual saturation light intensity between the four groups, light response curves were generated. The results verified that saturated light intensity (L_{sat}) did not greatly vary among the four groups (Figure S2). Furthermore, the BL+Pyr treatment improved the dark respiration rate (Rd) and the apparent quantum efficiency (AYE) by 179% and 18%, respectively, when compared to the untreated group (Figure S3). While, no significant increase of Rd and AYE was identified in the BL or Pyr-treated groups in comparison with the untreated group (Figure S3).

To better understand the light absorption, electron transfer, and energy partitioning in photosynthetic apparatus in the four groups, chlorophyll fluorescence parameters were further measured. As shown in Figure S4, the efficiency of excitation energy capture by open PSII (F_v'/F_m'), the actual quantum yield of PSII (ΦPSII) and the electron transfer rates (ETR) increased by 10%, 9% and 17% in the group treated with BL+Pyr, while did not significantly varied in the BL or Pyr-treated groups, when compared to the untreated group (Figure S4). Meanwhile, there was no significant difference in the maximum quantum yield of PSII (F_v/F_m) among the four groups (Figure S4).

3.3 The positive regulation of chlorophyll synthesis by the coapplication of brassinolide and pyraclostrobin

To determine the unique role of chlorophyll content in the improvement of photosynthetic performance by the BL + Pyr treatment, the contents of chlorophyll a and chlorophyll b in the 4 groups were further compared. Compared with the untreated group, the contents of chlorophyll a and chlorophyll b were substantially increased by 16% and 26% in the BL+Pyr group, respectively, which was similar to the percentage of increase in the Pyr group (Figure 5A). However, there was no obvious change between the BL treatment and untreated groups (Figure 5A).

To explore the mechanisms underlying the variation in chlorophyll content among the four groups, the differentially expressed genes (DEGs) involved in the chlorophyll metabolic pathway were further analyzed according to the transcriptome analysis. As shown in Figure 5B, the majority of genes associated with chlorophyll biosynthesis, such as the genes encoding protoporphyrinogen oxidase (*PPO*), tetrapyrrole (corrin/porphyrin) methylases (*UMP1*), Mg chelatase (*CHLD, CHLI1, CHLI2*), magnesium-protoporphyrin IX methyltransferase (*CHLM*), 3,8-divinyl protochlorophyllide a 8-vinyl reductase (*DVR*), protochlorophyllide oxidoreductase (*PORA, PORB, PORC*), and Chl synthase (*CHLG*), were upregulated in both the

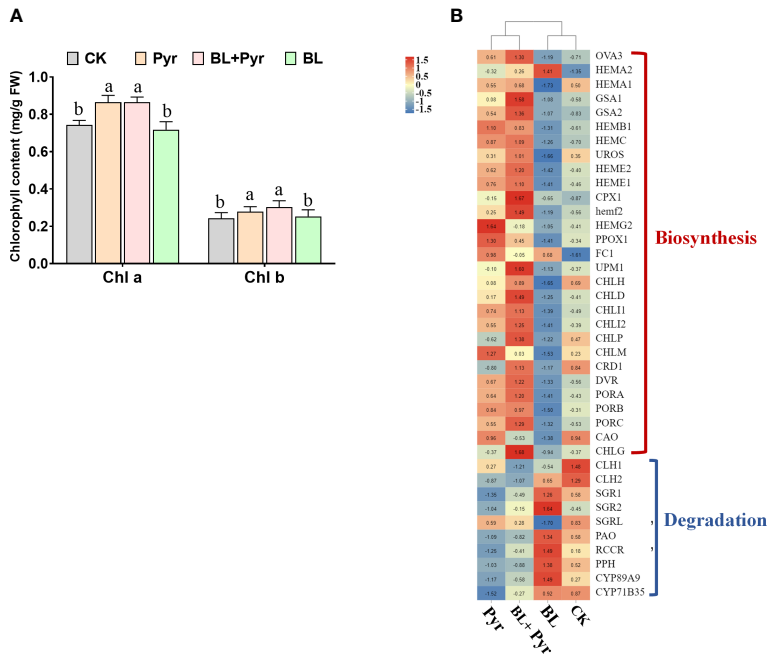

FIGURE 5
BL+Pyr and Pyr increased chlorophyll contents by regulating the transcript levels of genes in the chlorophyll metabolism pathway. **(A)** The chlorophyll a and chlorophyll b contents (mg/g FW); **(B)** Hierarchical cluster analysis of the differentially expressed genes (DEGs) associated with chlorophyll biosynthesis and degradation, and FPKM was Z-scole normalised prior to analysis. Data are presented as the mean ± SD of three independent biological replicates. Different letters indicated significant differences ($p< 0.05$) according to ANOVA followed by Tukey's test. The red line represents positive correlation and the blue line represents negative correlation. 31-day-old seedlings (the 11th day after the first-round application) were used. CK, untreated seedlings; Pyr, seedlings treated with 3 μM pyraclostrobin; BL+Pyr, seedlings treated with 1 μM BL and 3 μM pyraclostrobin; BL, seedlings treated with 1 μM BL.

BL+Pyr and Pyr groups. Conversely, the majority of genes associated with chlorophyll degradation, such as the genes encoding chlorophyllase (*CLH1* and *CLH2*), pheophorbide a oxygenase (*PAO*), chlorophyll b reductase (*NYC1*), RCC reductase (*RCCR*), pheophytinase (*PPH*), and Mendel's Stay-green gene (*SGR1*), which encodes Mg-dechelatase, were downregulated in both the BL+Pyr and Pyr groups. In contrast to these two treatments, the transcript levels of several chlorophyll biosynthesis-related genes were downregulated and several chlorophyll degradation-related genes were upregulated by BL treatment.

3.4 RNA-Seq reveals the improved transcription levels of photosynthesis-related genes by the coapplication of brassinolide and pyraclostrobin

To gain a deeper understanding of the transcriptional mechanisms by which the BL+Pyr treatment specifically enhances photosynthetic performance, the photosynthesis-related DEGs were analyzed based on the transcriptome analysis of the four treatment groups (untreated, BL+Pyr, BL and Pyr). The results showed that BL+Pyr treatment (51 downregulated and 115 upregulated) and Pyr treatment (111 downregulated and 67 upregulated) both greatly altered the expression levels of genes involved in photosynthesis, followed by BL treatment (37 downregulated and 13 upregulated), which had a relatively weak effect on those genes, compared with the untreated group (Figures 6A, B). In addition, the BL+Pyr treatment also resulted in remarkable differences in the expression levels of photosynthesis-related genes relative to the BL or Pyr treatment, with 124 upregulated and 19 downregulated DEGs relative to the Pyr treatment and 108 upregulated and 30 downregulated DEGs relative to the BL treatment (Figures 6A, B). To validate the RNA-seq data, 10 photosynthesis-related DEGs were selected for qRT–PCR validation. The differential expression of these genes according to qRT–PCR was highly correlated with the RNA-seq data, confirming the transcriptome data (Figure S5).

Further analysis of the expression profiles differentially expressed gene in the photosynthetic and carbon fixation pathways was performed. The results showed that the transcription levels of the key proteins involved in the photosynthesis pathway, such as PSII (*PSBA*, *PSBB*, *PSBC*, *etc.*), PSI (*PSAA* and *PSAB, etc.*), ferredoxin (*FD2* and *FdC1*), plastocyanin (*DRT112*), Cyt b_6f (*PETB*), and ATP synthase (*ATPA*, *ATPC* and *ATPD*), were increased by the BL+Pyr treatment (Figures 7A, Table S4). Additionally, the transcription levels of the majority of enzymes in the Calvin cycle, including

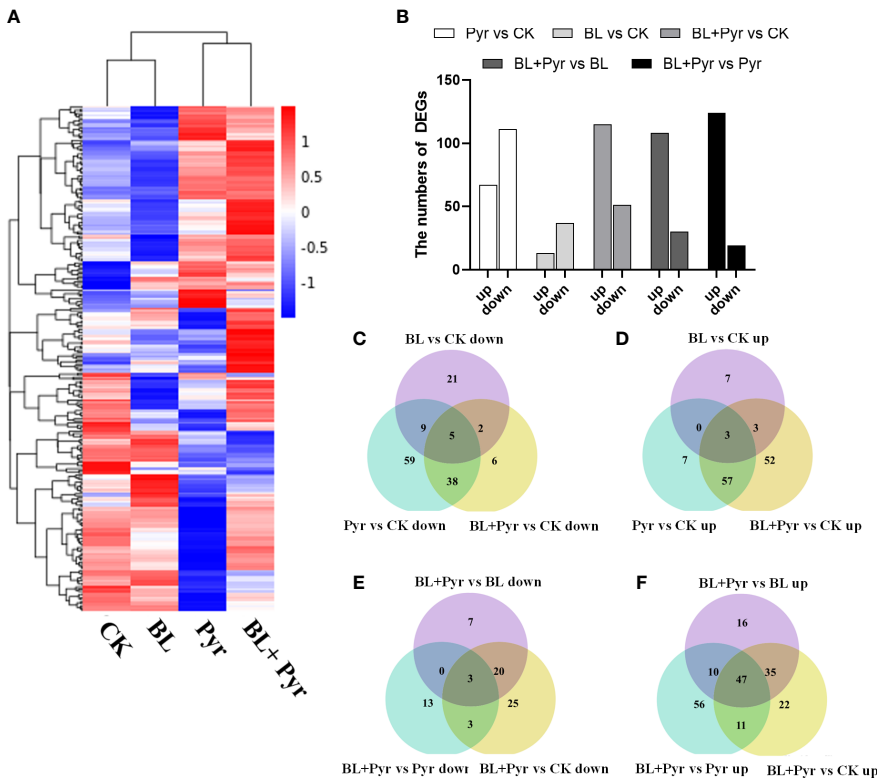

FIGURE 6
BL+Pyr activated the transcription of genes related to photosynthesis. **(A)** Hierarchical cluster analysis of the differentially expressed genes (DEGs) involved in photosynthesis according to the average FPKM (expected number of Fragments Per Kilobase of transcript sequence per Millions base pairs sequenced) of 3 biological repeats; **(B)** The number of photosynthesis-related DEGs among the comparisons. 'up' represented up-regulated and 'down' represented down-regulated. **(C-F)** Venn diagrams showing the overlapping and non-overlapping (DEGs) related to photosynthesis among the comparisons. The genes with an FDR (the false discovery rate)<0.05 were assigned as DEG. CK, untreated; Pyr, Treated with 3 μM pyraclostrobin; BL+Pyr, Treated with 1 μM BL in combinations with 3 μM pyraclostrobin; BL, Treated with 1 μM BL.

Rubisco, sedoheptulose-1,7-bisphosphatase (SBPase), fructose-1,6-bisphosphate aldolase (FBPA), fructose-1,6-bisphosphatases (FBPase), transketolase (TK), ribulose-phosphate 3-epimerase (RPE), triosephosphate isomerase (TPI), glyceraldehyde 3-phosphate dehydrogenase (GAPDH), phosphoglycerate kinase (PGK), and ribose 5-phosphate isomerase A (RPI), were also increased by the BL+Pyr treatment (Figure 7B, Table S4). In contrast, Pyr treatment and BL treatment showed opposite effects in regulating the transcript levels of genes in the photosynthetic light reaction pathway and carbon fixation pathway. Pyr treatment upregulated the transcript levels of the reaction center proteins PSII and PSI and downregulated the transcript levels of the majority of enzymes in the Calvin cycle (Figures S6A-B). Conversely, BL treatment downregulated the transcript levels of several PSII and PSI subunit proteins and upregulated the transcript levels of major enzymes in the Calvin cycle (Figures S6C-D).

To discriminate hub genes related to photosynthesis whose expression was induced by the BL+Pyr treatment, the photosynthesis-related DEGs uniquely regulated by the BL+Pyr treatment were further analyzed, including the nonoverlapping photosynthesis-related DEGs between the BL+Pyr treatment and BL or Pyr treatments versus the untreated group and the overlapping photosynthesis-related DEGs between the BL+Pyr group and the other 3 groups (untreated, BL and Pyr groups) (Figures 6C-F). A total of 79 DEGs fit the above criteria, including 10 downregulated and 69 upregulated DEGs (Figure S7 and Table S5). To investigate the specific functions and pathways of photosynthesis that were uniquely transcriptionally regulated by BL+Pyr treatment, GO and KEGG enrichment analyses were performed on those 79 DEGs. The significantly enriched GO terms were photosynthesis, generation of precursor metabolites and energy, photosynthesis-light reaction, carbon fixation, hexose biosynthetic process, and photosynthetic electron transport chain, and more related DEGs were upregulated than downregulated (Figure S8). Similarly, the significantly enriched KEGG pathways were photosynthesis and carbon fixation in photosynthetic

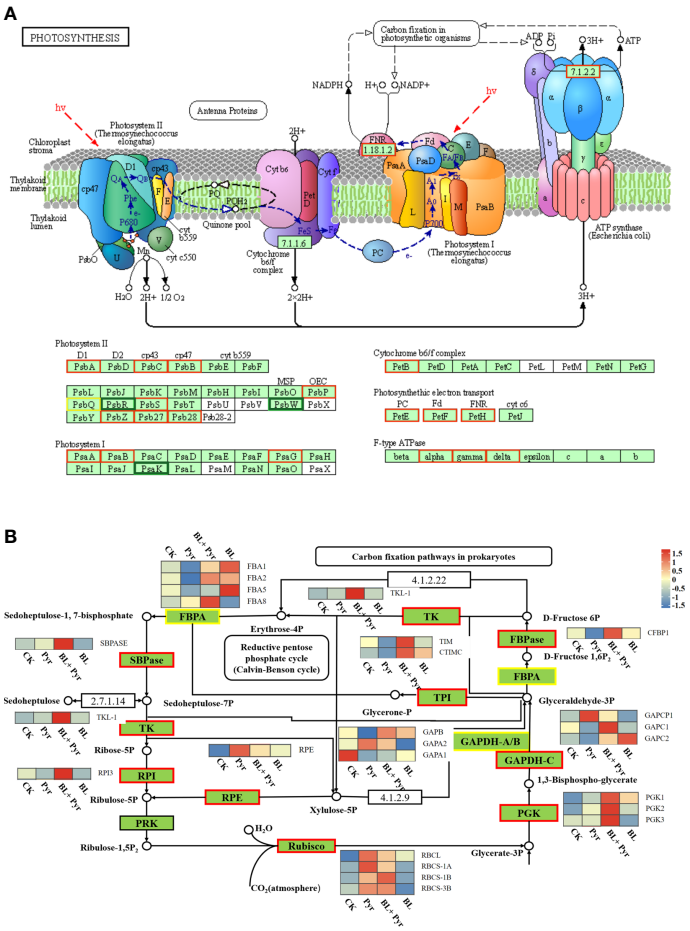

FIGURE 7
BL+Pyr treatment activated transcription of genes in photosynthesis and carbon fixation pathway. **(A)** Photosynthesis pathway tagged with DEGs of BL+Pyr-treated group versus untreated group; **(B)** Carbon fixation pathway tagged with DEGs of BL+Pyr-treated group versus untreated group. The heat map close to the enzyme showed the expression level of the gene encoding the corresponding enzyme. The different colored boxes on the protein names indicate that the gene encoding the protein is either up- or down-regulated by the BL+Pyr-treated group versus the untreated group. CK, untreated; Pyr, Treated with 3 μM pyraclostrobin; BL+Pyr, Treated with 1 μM BL in combinations with 3 μM pyraclostrobin; BL, Treated with 1 μM BL. SBPase, Sedoheptulose-1,7-bisphosphatase; FBPA, Fructose-1,6-bisphosphate aldolase; FBPase, Fructose-1,6-bisphosphatases; TK, Transketolase; RPE, Ribulose-phosphate 3-epimerase; TPI, Triosephosphate isomerase; GAPDH, Glyceraldehyde 3-phosphate dehydrogenase; PGK, Phosphoglycerate kinase; RPI, Ribose 5-phosphate isomerase A; PRK, Phosphoribulokinase.

organisms, and all of the related DEGs were upregulated (Figure S8B). In addition, the in-depth analysis of these 79 genes showed that the majority of the genes that were specifically upregulated by BL+Pyr were associated with the assembly factors of PSII and PSI, photosynthetic electron transport and the key enzyme of the Calvin cycle (Table S5).

3.5 The metabolome analysis validates the increased accumulation of photosynthates by the coapplication of brassinolide and pyraclostrobin

Since the co-application of BL and Pyr promoted photosynthesis efficiency by regulating multiple genes, we then used metabolome analysis to identify the variations in the accumulation of photosynthates in the four groups. As shown in Figure 8A, a total of 35 DAMs in the CO_2 fixation pathway and belonging to sugars were identified in the three groups (BL + Pyr, BL and Pyr) versus the untreated group, including 8 DAMs in the BL-treated group (8 upregulated), 27 DAMs in the BL+Pyr-treated group (21 upregulated and 6 downregulated), and 21 DAMs in the Pyr-treated group (16 upregulated and 5 downregulated).

Based on the hierarchical cluster analysis of DAMs belonging to sugars and the synthetic precursors for sugars, the accumulation of these compounds exhibited a significantly increasing trend in the BL+Pyr group compared to the other three groups (untreated, BL and Pyr) (Figure 8B). Sucrose was highly accumulated in the BL +Pyr group (2.4-fold), followed by the Pyr group (1.9-fold), and the BL group, which showed no significant increase, compared with the untreated group (Figure S9). In addition, the highest accumulation of other sugars, including maltose, trehalose, lactose, arabitol, isomaltulose, melibiose, turanose and cellobiose, was also achieved by the BL+Pyr treatment (Figure 8B).

Furthermore, hierarchical clustering analysis of DAMs in the CO_2 fixation pathway showed that the accumulation of regenerative precursors of RuBP, including Xu5P (xylulose 5-phosphate) and R5P (ribose 5-phosphate), exhibited a decreasing trend in the BL +Pyr and Pyr groups (Figure 8C). Similarly, the accumulation of 3-PGA (3-phosphoglyceric acid), a key intermediate in the Calvin cycle for initiating sugar synthesis, also showed a decreasing trend in the BL+Pyr and Pyr groups (Figure 9C).

The contents of several photosynthates were only significantly increased in the BL+Pyr treatment group, rather than the BL or Pyr treatment groups, compared with the untreated group. The majority of these compounds are synthetic precursors of sugars, including D-glucose 6-phosphate (G1P), D-glucose 1-phosphate (G6P), GDP-D-glucose (GDPG), sorbitol 6-phosphate, galactose 1-phosphate and erythrose-4-phosphate (E4P) (Figure 8B). Additionally, only BL+Pyr treatment significantly increased the contents of ADP (adenosine 5'-diphosphate), which is the precursor for ATP biosynthesis *via* photosynthetic oxidative phosphorylation (Figure 8C).

Pearson correlation analysis of the content of the photosynthesis-related DAMs further indicated that ADP, E4P, G1P, G6P, GDPG, sorbitol 6-phosphate and galactose 1-phosphate were all positively correlated with sugars, with correlation coefficients ranging from 0.96 to 1, from 0.78 to 0.90, from 0.66 to 0.84, from 0.57 to 0.75, from 0.72 to 0.88, from 0.63 to 0.81, and from 0.56 to 0.76, respectively (Figure S10). Among these sugars, sucrose was the most highly correlated with these synthesis precursors of sugars, and the correlation coefficients between sucrose and ADP, E4P, G1P, G6P, GDPG, sorbitol 6-phosphate and galactose 1-phosphate were 0.99, 0.90, 0.84, 0.75, 0.88, 0.81 and 0.76, respectively (Figure S10). In addition, the contents of 3-PGA, Xu5P and R5P were all significantly positively correlated with the contents of those sugars, with correlation coefficients ranging from 0.92 to 0.98, from 0.83 to 0.95, and from 0.94 to 0.99, respectively (Figure S10).

3.6 Integration analysis of the transcriptome and metabolome profiles related to photosynthesis

To explore the association between the differences in the accumulation of photosynthates and the differences in the transcriptional regulation of photosynthesis among the four groups, correlation analysis between the expression level of photosynthesis-related DEGs and the accumulation of photosynthesis-related DAMs in the four groups was performed. The results showed that 160 of 243 photosynthesis-related DEGs were significantly correlated with photosynthesis-related metabolites, with a correlation coefficient >0.95 and p-value<0.05. A total of 650 significantly related pairs were identified, including 423 positively correlated pairs and 227 negatively correlated pairs (Figure S11). In addition, 90 of 243 photosynthesis-related DEGs and 150 significantly related pairs (90 positively correlated and 60 negatively correlated) met the correlation thresholds of Pearson's correlation coefficient >0.99 and p-value<0.01 (Figure 9A). Furthermore, more DEGs were significantly correlated with the synthetic precursors of sugars than with the sugars (Figure S11, Figure 9A).

To clarify the relevance of the unique transcriptional regulation of photosynthesis to sugar accumulation in the BL+Pyr group, further correlation analysis was performed on the photosynthesis-related genes and photosynthates that were differentially regulated by the BL+Pyr treatment rather than the BL or Pyr treatments. As shown in Figure 9B, 36 of 79 unique photosynthesis-related DEGs in the BL+Pyr group were significantly correlated with all 7 unique photosynthesis-related DAMs in the BL+Pyr group. A total of 121 significantly related pairs were identified, including 86 positively correlated pairs and 35 negatively correlated pairs with correlation coefficients >0.95 and p-values<0.05 (Figure 9B). In addition, 27 of 79 photosynthesis-related DEGs and 37 significant related pairs (29 positively correlated and 8 negatively correlated) met the correlation thresholds of Pearson's correlation coefficient >0.99 and p-value<0.01 (Figure 9C). Additionally, the 36 DEGs significantly associated with unique photosynthesis-related DAMs in the BL+Pyr group were involved in multiple levels of photosynthesis, such as *1-Sep, PPL1, PSBTN, PSBS, PNSL3, PPD7, PSB28, PAM68* and *STN7*, which are involved in the light reaction;

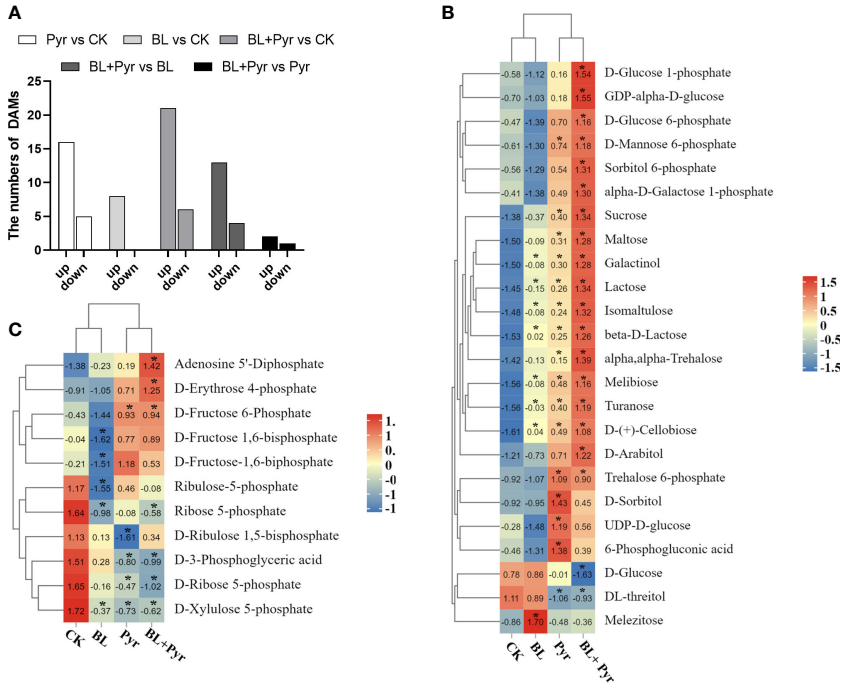

FIGURE 8
BL+Pyr showed a synergistic effect on increasing the accumulation of photosynthates. **(A)** Number of DAMs in the CO_2 fixation pathway and belonging to sugars of the three treatments (BL + Pyr, BL and Pyr) versus the untreated group; **(B)** Hierarchical cluster analysis of the sugars content of the three treatments (BL + Pyr, BL and Pyr) versus the untreated group; **(C)** Hierarchical cluster analysis of the content of DAMs in the CO_2 fixation pathway of the three treatments (BL + Pyr, BL and Pyr) versus the untreated group. The Metabolites with variable importance in projection (VIP) ≥ 1, fold change (FC) ≤ 0.8 or ≥1.2, and P-value< 0.05 were classified as DAMs (differential accumulation metabolites). Values shown in **(B, C)** are Z-scores normalized to concentrations, and '*' represent significant differences versus the untreated group.

FD2, GLUTRBP, PIF1 and *NDHS*, which are involved in photosynthetic electron transport; *RBCS-1B, ATNOS1, RAF1.1, CPN60A1* and *RBCX1*, which are associated with Rubisco; and *PGK3, FBA8, SBPASE* and *RPI2*, which are associated with key enzymes in the Calvin cycle (Figure 9B).

To identify the photosynthesis-related core genes and metabolites specifically induced by BL+Pyr treatment, 37 highly significant correlation pairs with Pearson's correlation coefficient >0.99 and p-value<0.01 were further selected for correlation network analysis. As shown in Figure 9C, more DAMs were significantly associated with *AT4G09040, CPFTSY, PPD7, PSB28, RAF1.1, RLSB* and *TIC62* (Figure 9C). More DEGs were significantly associated with sorbitol 6-phosphate, D-glucose 1-phosphate, GDP-alpha-D-glucose and D-glucose 6-phosphate (Figure 9C), indicating that these DEGs and DAMs might be core genes and metabolites for BL+Pyr treatment in synergistically improving biomass and yield.

4 Discussion

In this study, we comprehensively compared the effects of BL, Pyr and BL + Pyr on the biomass, yield and photosynthesis *of A. thaliana*. Exogenous application of BRs or Pyr has been reported to improve plant growth in some cases (Amaro et al., 2019; Lin, 2020; Padhiary et al., 2020). However, the growth-promoting effects of BRs are not always apparent, and Pyr inevitably causes phytotoxicity (Khripach et al., 2000; Nason et al., 2007; Vriet et al., 2012; Debona et al., 2016; Pedersen et al., 2017). Similar to previous studies, BL did not influence leaf growth when the applied dosage did not exceed 1 μM, while BL at concentrations up to 10 μM impaired leaf growth due to a disruption in the balance of the plant hormone network (Figures S1A, B). Additionally, Pyr affected leaf growth in a concentration-dependent manner, promoting plant growth at low concentrations and inhibiting plant growth at high concentrations due to its phytotoxicity (Figures S1C, D). According to Tables S2, S3, treatment with BL (1 μM) + Pyr (3 μM) showed the most striking leaf growth-promoting activity among all treatments, so BL (1 μM), Pyr (3 μM) and BL (1 μM) + Pyr (3 μM) were chosen for the following test to further verify the synergistic regulatory effects of BL + Pyr on promoting leaf growth. Although applying Pyr in combination with BRs has been observed to benefit plant growth in several field trials (Li et al., 2018; Li et al., 2020; Zhang, 2020; Li et al., 2021; Zhao et al., 2021), this was the first study to validate the striking synergistic effect of BL + Pyr on enhancing plant growth by precluding the benefits of disease control from Pyr.

Although BL and Pyr did not improve leaf growth during the vegetative growth period, and BL even inhibited leaf growth due to earlier bud emergence during the floral transition period (Table 1 and Figure 1), BL or Pyr alone affected the growth of leaves and inflorescences in opposite ways during the reproductive development stage (Table 2, 3 and Figure 2).Pyr treatment

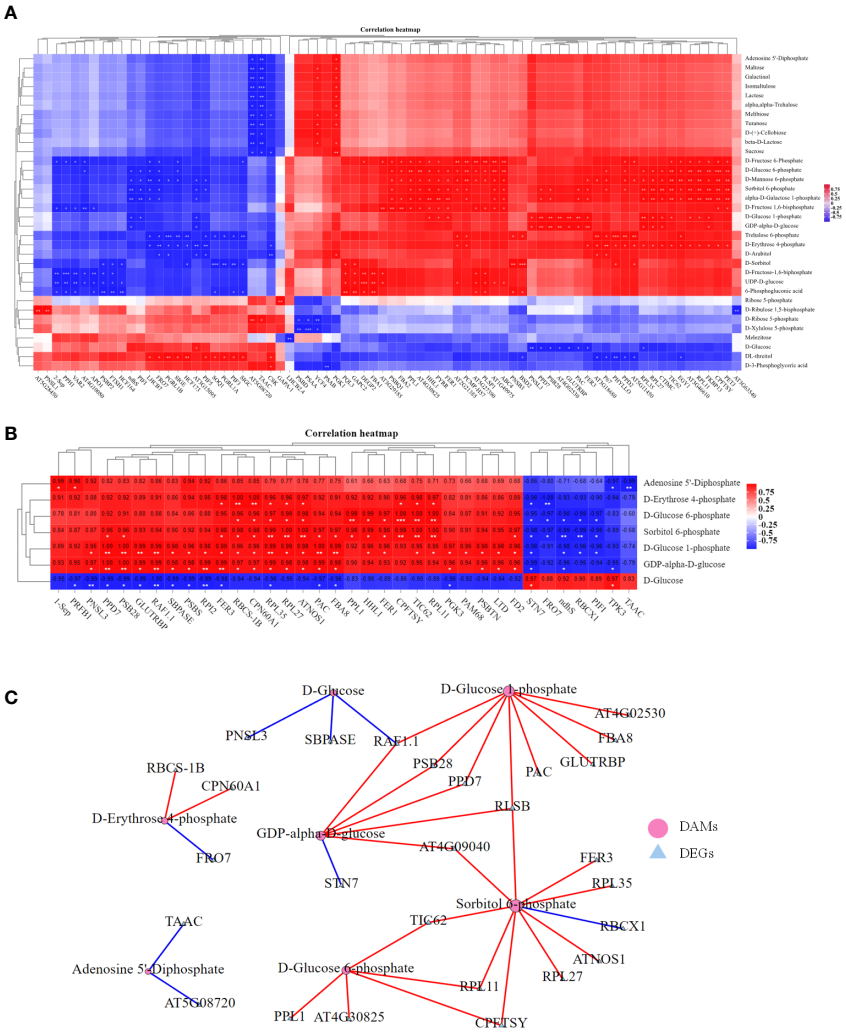

FIGURE 9
Correlation analysis of the transcriptome and metabolome profiles related to photosynthesis. **(A)** Pearson correlation analysis between photosynthesis-related DAMs and DEGs of the three treatments (BL + Pyr, BL and Pyr) versus the untreated group with correlation coefficient >0.99 and p-value<0.01. **(B)** Pearson correlation analysis between the unique photosynthesis-related DEGs and unique photosynthesis-related DAMs of the BL+Pyr group with correlation coefficient >0.95 and p-value<0.05. **(C)** The correlation network plot displaying the highly significant correlation pairs between the unique photosynthesis-related DEGs and unique photosynthesis-related DAMs of the BL+Pyr group with Pearson's correlation coefficient >0.99 and p-value<0.01. Metabolite and transcriptome data were log2-transformed prior to correlation analysis. "*" represented 0.01< p-value<0.05, "**" represented 0.001< p-value<0.01 and "***" represented p-value ≤ 0.001.

increased the fresh weight of leaves, while BL treatment increased the number of rosette branches and effective branches and thus the fresh weight of inflorescences during the reproductive stage (Tables 2, 3 and Figure 2). Similarly, the floral transition process was delayed by Pyr and accelerated by BL according to the budding time and the flowering time (Figures 1D, 2A and Table 3). These results suggested that Pyr benefited plants primarily by promoting the growth of vegetative organs and prolonging the vegetative growth phase, while BL benefited plants primarily by promoting the growth of reproductive organs and prolonging the reproductive growth phase. These results were consistent with previous research, as BL is extensively involved in regulating the reproductive development of plants and Pyr improves plant vegetative growth (Amaro et al., 2019; Zu et al., 2019; Li and He, 2020). Furthermore, the process of leaf senescence was delayed by Pyr, as shown by the strikingly increased fresh weight of leaves in the Pyr group at the late stage of reproductive development (Table 2 and Figure 2E). This result was also consistent with the previously reported green effect of Pyr in delaying senescence (Jabs et al., 2002; Ruske et al., 2003). Yield measurements showed that yield was significantly increased by BL rather than by Pyr (Table 3). This result was also consistent with previous reports that Pyr benefited plants mainly by increasing biomass rather than yield in soybean (Swoboda and Pedersen, 2009), while exogenous BR could increase seed production (Tong and Chu, 2018).

Surprisingly, the yield increases achieved by BL + Pyr were almost double the total yield gain of BL or Pyr treatment alone with no accompanying variation in thousand grain weight (Table 3). Similarly, BL + Pyr outperformed Pyr in increasing the fresh weight of leaves in the vegetative and reproductive growth stages, apart from late

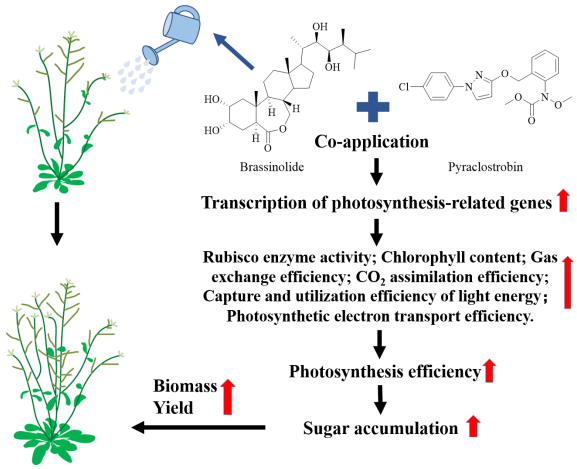

FIGURE 10
A potential model for the combined application of BL+Pyr in synergistically increasing biomass and yield through improving photosynthetic efficiency.

reproductive development (Tables 1, 2 and Figures 1, 2). BL + Pyr also outperformed BL in increasing the number of rosette branches and effective branches and thus the fresh weight of inflorescences (Table 3 and Figure 2). Furthermore, BL + Pyr delayed the floral transition process and senescence, and these processes were delayed compared with the untreated group but accelerated compared with the Pyr group (Table 3 and Figure 1, 2). All these results suggested that the combined usage of BL + Pyr not only integrated the beneficial effects of Pyr on leaves with the beneficial effects of BL on inflorescences but also exerted a synergistic effect in enhancing biomass and yield. The increased biomass and prolonged duration of photosynthetic activity by Pyr benefited the prestorage of nutrients and BL regulated harvested organ development to reinforce the partitioning of nutrients from source to sink, which might contribute to the synergistic yield increase of BL + Pyr (Patrick and Colyvas, 2014; Mathan et al., 2016).

Improving biomass production and yield by enhancing photosynthetic capacity has been widely reported (Parry et al., 2011; Faralli and Lawson, 2020). In this study, the P_n was increased by the BL + Pyr treatment rather than by the BL or Pyr treatment, suggesting that the synergistic yield increase achieved by BL + Pyr was associated with improved photosynthetic capacity (Figures 3A-B). The corresponding increase in G_s, T_r, and AMC, together with deceased L_s, in the BL + Pyr group rather than in the BL or Pyr group revealed that the enhanced photosynthesis efficiency of the BL + Pyr group was related to enhanced gas and water exchange between the photosynthetic apparatus interior and the external environment (Figure 3) (Kimura et al., 2020).

Furthermore, the enhanced gas exchange process in the BL + Pyr treatment did not result in a corresponding increase in intercellular CO_2 concentration (C_i), implying that the increased P_n in the BL + Pyr group might also be associated with improved CO_2 assimilation efficiency (Figure 3E) (Araus et al., 2021). This assumption was further validated by the increased V_{cmax}, J_{max}, and V_{TPU} in the BL + Pyr group rather than in the BL or Pyr group according to CO_2 response curves (Figure 4). These results demonstrated that BL + Pyr treatment enhanced the CO_2 assimilation efficiency by increasing carboxylation efficiency, the effect of electron transport on driving the regeneration of RuBP, and triose-phosphate utilization efficiency, which contributed to the unique increase in photosynthetic efficiency induced by BL + Pyr treatment (Simkin et al., 2015; Raines, 2022).

Rubisco is the rate-limiting enzyme in the CO_2 assimilation process and thus largely determines photosynthesis efficiency (Parry et al., 2013). Abundant studies have reported successful improvement in plant productivity and yield through overproducing Rubisco (Salesse-Smith et al., 2018; Suganami et al., 2021). So, the increased enzyme activity of Rubisco in the BL + Pyr group compared with the BL or Pyr group further supported the benefits of the BL + Pyr treatment in enhancing CO_2 assimilation efficiency and thereby increasing the biomass and yield by enhancing photosynthetic efficiency, which were not achieved by the BL or Pyr treatments (Figure 4B). Meanwhile, the increased apparent quantum efficiency (AQE) by the BL+Pyr treatment rather than by the BL or Pyr treatments (Figure S3), further suggested that the unique benefits of the BL + Pyr treatment for photosynthesis might be related to the reduced photorespiration from increased CO_2 concentration at the Rubisco active site(Sekhar et al., 2014). While, the corresponding increased dark respiration rate (Rd) in the BL+Pyr group might be associated with the increased availability of carbohydrates (Figure S3 and Figure 8B), just as previous reported in tomato (Li et al., 2013). Additionally, this result also indicated that the increased net photosynthetic rate by the BL+Pyr treatment was not dependent on the reduction in photosynthates consumption during dark respiration.

Furthermore, compare to the untreated group, the BL+Pyr treatment, rather than the BL or Pyr treatments, improved the F_v'/F_m', ΦPSII and ETR, which are positively correlated with the light harvesting and energy transduction (Figure S4) (Sreeharsha et al., 2015). This result supported the unique advantage of BL+Pyr treatment over the individual BL or Pyr treatments on enhancing the energy capture and utilization efficiencies by PSII and amplifying the photosynthetic electron transport efficiency. This

might contribute to the production of reducing power (ATP and NADPH) for the carbon fixation process and result in the increased photosynthetic efficiency in the BL+Pyr group (Baker, 2008).

Chlorophyll a and chlorophyll b are the prime photosynthetic pigments, and they are crucial for harvesting light energy by photosynthetic antenna systems and for charge separation and electron transport within light reaction centers (Simkin et al., 2022). Many studies have proven that photosynthetic efficiency is positively correlated with chlorophyll content (Mu and Chen, 2021). However, in this study, the BL + Pyr treatment was consistent with the Pyr treatment in improving the chlorophyll a and chlorophyll b contents by upregulating genes associated with chlorophyll biosynthesis and downregulating genes associated with chlorophyll degradation (Figure 5). These results were not quite consistent with the overwhelming advantage of the BL + Pyr treatment over the Pyr treatment in enhancing photosynthesis, implying that the improvement in photosynthetic efficiency achieved by the BL + Pyr treatment was only partially dependent on the increase in photosynthetic pigment content.

Although exogenous BRs have been reported to positively regulate photosynthesis and alleviate the photosynthetic inhibition of plants growing under stress (Xia et al., 2009; Jiang et al., 2012; Siddiqui et al., 2018), there were no observable benefits of BL alone to the photosynthetic phenotype in this study. This contradictory result might be due to the differences in species, time of observation, application concentration, *etc.* (Zu et al., 2019; Lin, 2020; Hwang et al., 2021). In contrast, Pyr has been reported to block electron transport in photosynthesis by binding the Q_i site of the chloroplast cytochrome *bf* complex, thereby exerting a negative effect on photosynthesis in plants (Nason et al., 2007; Debona et al., 2016; Amaro et al., 2019). A reasonable speculation might be that Pyr only slightly inhibited photosynthesis in the plants, which was not sufficient to cause a change in the photosynthetic phenotype. However, this slight inhibitory effect of Pyr stimulated the regulatory effect of BL on photosynthesis to a greater extent, resulting in a striking increase in photosynthetic efficiency in the BL+Pyr group.

The expression profile of photosynthesis-related genes based on transcriptome analysis suggested a more significant activation of photosynthetic gene transcription by the BL+Pyr treatment than by the BL or Pyr treatment according to the following evidence. First, the BL+Pyr group had far more upregulated genes than downregulated genes compared with the other 3 groups (BL, Pyr and untreated) (Figure 6). Similarly, the majority of photosynthesis-related DEGs that were differentially regulated in the BL+Pyr treatment group rather than in the BL and Pyr treatment groups were also upregulated (Figure S7). Second, Pyr treatment and BL treatment upregulated the transcript levels of genes in the photosynthetic light reaction pathway and carbon fixation pathway, respectively (Figure S6). The BL+Pyr treatment not only integrated the advantages of the BL and Pyr alone in upregulating the transcription of genes in the photosynthetic pathway and the carbon fixation pathway but also was more effective than either BL or Pyr alone in upregulating the transcription of genes related to both the photosynthetic and carbon fixation pathways (Figure 7). Third, the GO and KEGG enrichment analysis of the photosynthesis-related genes that were differentially regulated by the BL+Pyr treatment, rather than by the BL and Pyr treatments, further indicated that BL+Pyr treatment resulted in unique transcriptional activation at multiple levels of photosynthesis, particularly in photosystem assembly, electron transport and CO_2 assimilation (Figure S8).

It has been proven that photosynthetic performance can be improved by enhancing the expression of key genes involved in photosynthesis to increase the yield potential of diverse crops (Simkin et al., 2015; Simkin et al., 2019; Theeuwen et al., 2022). Therefore, the BL+Pyr treatment increases photosynthesis, and thus, the effects on biomass and yield might stem from its transcriptional activation of photosynthesis (Figure 6, S7). Photosynthesis comprises a light reaction and carbon reduction reaction (Mu and Chen, 2021). Light reactions are catalyzed by four major protein complexes, namely, PSI, PSII, cytochrome *b6f* complex (*Cyt* b_6f), and adenosine triphosphate (ATP) synthase, which provide the reducing power (ATP and NADPH) for the carbon fixation process (Stirbet et al., 2020). The carbon fixation pathway is responsible for carbon assimilation by a series of enzymatic reactions, which are responsible for converting light energy to biomass and yield (Michelet et al., 2013). Thus, the synergistic effect of the BL+Pyr treatment on increasing photosynthesis might be associated with its transcriptional activation of the light and dark reaction of photosynthesis (Figure 7, Figure S8).

The positive contribution of improved photosynthetic efficiency to yield is achieved through the increased production of sugars, as carbohydrates derived from sugars account for more than 90% of plant biomass, making them a key determinant of yield (Ruan, 2014; Nuccio et al., 2015). Based on the metabolomic analysis, the BL+Pyr treatment was better than the BL or Pyr treatment in promoting the accumulation of sugar metabolites, including sucrose (Figure 8 and S9). This result bridged the link between the synergistic enhancement of photosynthetic efficiency and synergistic increase in yield with improved sugar accumulation in the BL+Pyr group. The decreased accumulation of intermediates in the CBC cycle did not contradict the increased sugar content after BL+Pyr treatment, as the contents of 3-PGA, Xu5P and R5P were all significantly positively correlated with the contents of those sugars (Figure 8C and S10). This result consistent with previous reports that the appropriately reduced contents of CBC cycle intermediates were beneficial for improving carbon fixation efficiency and sugar synthesis (Sharkey et al., 1986; Borghi et al., 2019; Stitt et al., 2021).

The integration analysis of the transcriptome and metabolome profiles related to photosynthesis suggested that the transcription levels of photosynthesis-related DEGs were highly correlated with the accumulation of carbohydrates (Figure S11 and Figure 9A). Additionally, according to the correlation analysis of the photosynthesis-related genes and the photosynthates that were differentially regulated by the BL+Pyr treatment rather than the BL or Pyr treatment, the advantage of BL+Pyr treatment in promoting photosynthate accumulation was highly correlated with the unique trans-regulation of photosynthesis at multiple levels (Figures 9B-C). Based on correlation analysis of sugar metabolite content, the unique advantage of the BL+Pyr treatment in enhancing sugar accumulation, particularly sucrose accumulation, might be related to the higher levels of sugar and ATP synthesis precursor accumulation than those observed in the other three groups (Figure S10). Furthermore, more DEGs were significantly correlated with synthetic precursors of sugars

than with sugars in the integration analysis of the photosynthesis-related transcriptome and metabolome profiles (Figure S11 and Figure 9A). These results implied that BL+Pyr mainly increased the production of the synthetic precursors of sugars through transcriptional regulation of photosynthesis, leading to improved accumulation of sugars.

Among the core DEGs that participate in the synergistic increase in biomass and yield after the BL+ Pyr treatment, most DAMs were associated with *RLSB* and *RAF1.1*, which are important photosynthetic regulatory proteins that regulate the translation and assembly of Rubisco, respectively (Figure 9C) (Yerramsetty et al., 2016; Xia et al., 2020). This result was consistent with the increased rubisco enzyme activity that was uniquely observed in the BL+ Pyr group, implying that the core genes and metabolites identified by the integration analysis of the photosynthesis-related transcriptome and metabolome profiles might contribute to exploring candidate target genes and compounds for increasing yields (Figure 9C).

5 Conclusion

In summary, we first demonstrated the synergistic effect of the BL + Pyr treatment on increasing the biomass and yield by a range of phenotypic analyses throughout the full growth cycle in *A. thaliana*, and this effect occurs independently of the intrinsic fungicidal effect of Pyr and outperformed the additive effect of individual BL or Pyr treatments. The potential mechanism underlying this synergistic enhancement effect of the coapplication of BL + Pyr was shown to be closely associated with the increased photosynthesis efficiency (Figure 10). The BL + Pyr treatment showed an overwhelming advantage over the individual BL or Pyr treatments in enhancing the gas exchange process, CO_2 assimilation efficiency, capture and utilization efficiency of light energy, and photosynthetic electron transport efficiency. Additionally, both BL + Pyr and Pyr treatments improved the chlorophyll a and chlorophyll b contents by upregulating genes related to chlorophyll biosynthesis and downregulating genes related to chlorophyll degradation. Based on the transcriptomic analysis, the potential mechanism by which the BL+Pyr treatment regulates photosynthesis was further revealed, and it was related to the upregulation of the transcription levels of key genes involved in multiple levels of photosynthesis. Furthermore, the BL+Pyr treatment was superior to the individual BL or Pyr treatments in increasing sugar accumulation, according to the metabolomic analysis. This result formed a bridge between the synergistic increase in photosynthetic efficiency and the synergistic increase in yield achieved by the BL+Pyr treatment. The integrated analysis of photosynthesis-related DEGs and DAMs validated the correlation between transcriptional regulation of photosynthesis at multiple levels and increased accumulation of sugars achieved by the BL+Pyr treatment. All these results potentially revealed the synergistic mechanisms by which the BL + Pyr treatment boosted the photosynthetic efficiency by increasing the transcripts of photosynthesis-related key genes, which resulted in increased carbohydrate accumulation and thus improved biomass and yield. Despite the ecotoxicology of Pyr, the revelation of the synergistic action and the potential mechanisms of the BL+Pyr treatment verified that simultaneous application of specific compounds with different targets could generate a synergistic effect in increasing plant productivity. This further provided a rational guideline for designing new eco-friendly productivity-enhancing agents. Furthermore, the identification of photosynthesis-related core genes and metabolites uniquely induced by the BL+Pyr treatment might contribute to exploring potential candidate genes and compounds for increasing yield through regulating photosynthesis.

Data availability statement

The data presented in the study are deposited in into the NCBI's SRA database with the link of https://www.ncbi.nlm.nih.gov/sra/PRJNA930055, under the accession number SAMN32982539 to SAMN32982550.

Author contributions

Y-QA and ZX contributed to the conception and design of the study. Y-QA and Z-TQ performed the experiments and collected the data. D-DL, R-QZ and B-SB organized the database and performed the statistical analysis. Y-QA prepared the manuscript. D-JM, D-WW and ZX contribute to revising the manuscript. All authors contributed to the article and approved the submitted version.

Funding

This work was funded by the National Key Research and Development Program of China (2021YFD1700101) and National Science Foundation of China (21332004, 21472101, 21672118).

Conflict of interest

The authors declare that the research was conducted in the absence of any commercial or financial relationships that could be construed as a potential conflict of interest.

Publisher's note

Supplementary material

The Supplementary Material for this article can be found online at: https://www.frontiersin.org/articles/10.3389/fpls.2023.1138563/full#supplementary-material

References

Ahammed, G. J., Li, X., Liu, A., and Chen, S. (2020). Brassinosteroids in plant tolerance to abiotic stress. *J. Plant Growth Regul.* 39, 1451–1464. doi: 10.1007/s00344-020-10098-0

Ali, B. (2017). Practical applications of brassinosteroids in horticulture-some field perspectives. *Sci. Hortic. (Amsterdam Neth.)* 225, 15–21. doi: 10.1016/j.scienta.2017.06.051

Amaro, A. C. E., Baron, D., Ono, E. O., and Rodrigues, J. D. (2019). Physiological effects of strobilurin and carboxamides on plants: An overview. *Acta Physiol. Plant* 42, 1–10. doi: 10.1007/s11738-019-2991-x

Araus, J. L., Sanchez-Bragado, R., and Vicente, R. (2021). Improving crop yield and resilience through optimization o photosynthesis: Panacea or pipe dream? *J. Exp. Bot.* 72, 3936–3955. doi: 10.1093/jxb/erab097

Bailey-Serres, J., Parker, J. E., Ainsworth, E. A., Oldroyd, G. E. D., and Schroeder, J. I. (2019). Genetic strategies for improving crop yields. *Nature* 575, 109–118. doi: 10.1038/s41586-019-1679-0

Baker, N. R. (2008). Chlorophyll fluorescence: A probe of photosynthesis *in vivo*. *Annu. Rev. Plant Biol.* 59, 89–113. doi: 10.1146/annurev.arplant.59.032607.092759

Bartlett, D. W., Clough, J. M., Godwin, J. R., Hall, A. A., Hamer, M., and Parr-Dobrzanski, B. (2002). The strobilurin fungicides. *Pest Manage. Sci.* 58, 649–662. doi: 10.1002/ps.520

Borghi, G. L., Moraes, T. A., Guenther, M., Feil, R., Mengin, V., Lunn, J. E., et al. (2019). Relationship between irradiance and levels of Calvin-Benson cycle and other intermediates in the model eudicot arabidopsis and the model monocot rice. *J. Exp. Bot.* 70, 5809–5825. doi: 10.1093/jxb/erz346

Colombo, M., Suorsa, M., Rossi, F., Ferrari, R., Tadini, L., Barbato, R., et al. (2016). Photosynthesis control: An underrated short-term regulatory mechanism essential for plant viability. *Plant Signaling Behav.* 11, 1165382. doi: 10.1080/15592324.2016.1165382

Debona, D., Nascimento, K. J. T., Gomes, J. G. O., Aucique-Perez, C. E., and Rodrigues, F. A. (2016). Physiological changes promoted by a strobilurin fungicide in the rice-bipolaris oryzae interaction. *Pestic. Biochem. Physiol.* 130, 8–16. doi: 10.1016/j.pestbp.2015.12.006

Factor, T. L., Junior, S. L., Purquerio, L. F. V., and Calori, A. H. (2010). *Secondary effects of fungicides in tomato seedlings production* (Lisbon, PORTUGAL: XXVIII International Horticultural Congress on Science and Horticulture for People).

Faralli, M., and Lawson, T. (2020). Natural genetic variation in photosynthesis: an untapped resource to increase crop yield potential? *Plant J.* 101, 518–528. doi: 10.1111/tpj.14568

Foyer, C. H., and Noctor, G. (2000). Oxygen processing in photosynthesis: regulation and signalling. *New Phytol.* 146, 359–388. doi: 10.1046/j.1469-8137.2000.00667.x

Godfray, H. C. J., Beddington, J. R., Crute, I. R., Haddad, L., Lawrence, D., Muir, J. F., et al. (2010). Food security: The challenge of feeding 9 billion people. *Science* 327, 812–818. doi: 10.1126/science.1185383

Heyneke, E., and Fernie, A. R. (2018). Metabolic regulation of photosynthesis. *Biochem. Soc Trans.* 46, 321–328. doi: 10.1042/BST20170296

Hwang, H., Ryu, H., and Cho, H. (2021). Brassinosteroid signaling pathways interplaying with diverse signaling cues for crop enhancement. *Agronomy* 11, 556. doi: 10.3390/agronomy11030556

Jabs, T., Pfirrmann, J., Schafer, S., Wu, Y. X., Von Tiedemann, A.Bcpc (2002). *Anti-oxidative and anti-senescence effects of the strobilurin pyraclostrobin in plants: A new strategy to cope with environmental stress in cereals* (Brighton, UK: The BCPC Conference: Pests and diseases).

Jiang, Y. P., Cheng, F., Zhou, Y. H., Xia, X. J., Mao, W. H., Shi, K., et al. (2012). Brassinosteroid-induced CO_2 assimilation is associated with increased stability of redox-sensitive photosynthetic enzymes in the chloroplasts in cucumber plants. *Biochem. Biophys. Res. Commun.* 426, 390–394. doi: 10.1016/j.bbrc.2012.08.100

Khripach, V., Zhabinskii, V., and De Groot, A. (2000). Twenty years of brassinosteroids: Steroidal plant hormones warrant better crops for the XXI century. *Ann. Bot.* 86, 441–447. doi: 10.1006/anbo.2000.1227

Kimura, H., Hashimoto-Sugimoto, M., Iba, K., Terashima, I., and Yamori, W. (2020). Improved stomatal opening enhances photosynthetic rate and biomass production in fluctuating light. *J. Exp. Bot.* 71, 2339–2350. doi: 10.1093/jxb/eraa090

Li, Z., and He, Y. (2020). Roles of brassinosteroids in plant reproduction. *Int. J. Mol. Sci.* 21, 872. doi: 10.3390/ijms21030872

Li, X., Li, J., Shen, X. Q., Jin, Y. Q., Song, Y. F., Guo, H. F., et al. (2020). Effect of brassinolide combined with pyraclostrobin on wheat yield. *Agric. Tech. Equip.* 367, 135–136. doi: 10.3969/j.issn.1673-887X.2020.07.062

Li, W. W., Zhang, W. Y., Cao, H., Q., S. X., He, C. J., Liu, F., et al. (2021). Effect of brassinolide combined with pyraclostrobin on growth and development of apple trees. *J. Shanxi Agric. Sci.* 49, 50–51. doi: 10.3969/j.issn.1002-2481.2021.01.11

Li, X., Zhang, G., Sun, B., Zhang, S., Zhang, Y., Liao, Y., et al. (2013). Stimulated leaf dark respiration in tomato in an elevated carbon dioxide atmosphere. *Sci. Rep.* 3, 3433. doi: 10.1038/srep03433

Li, H., Zhao, B. M., Wu, W. Z., Huang, Y. H., and Wu, B. S. (2018). Yunleshou on cotton yield resistance. *China Cott.* 45, 23–25. doi: 10.11963/1000-632X.lhwwz.20180516

Lichtenthaler, H. K. (1987). Chlorophylls and carotenoids: Pigments of photosynthetic biomembranes. *Methods Enzymol.* 148, 350–382. doi: 10.1016/0076-6879(87)48036-1

Lin, W. H. (2020). Designed manipulation of the brassinosteroid signal to enhance crop yield. *Front. Plant Sci.* 11, 854. doi: 10.3389/fpls.2020.00854

Liu, X., Wang, Y., Chen, H., Zhang, J., Wang, C., Li, X., et al. (2018). Acute toxicity and associated mechanisms of four strobilurins in algae. *Environ. Toxicol. Pharmacol.* 60, 12–16. doi: 10.1016/j.etap.2018.03.021

Long, S. P., and Bernacchi, C. J. (2003). Gas exchange measurements, what can they tell us about the underlying limitations to photosynthesis? procedures and sources of error. *J. Exp. Bot.* 54, 2393–2401. doi: 10.1093/jxb/erg262

Long, S. P., Marshall-Colon, A., and Zhu, X.-G. (2015). Meeting the global food demand of the future by engineering crop photosynthesis and yield potential. *Cell* 161, 56–66. doi: 10.1016/j.cell.2015.03.019

Mathan, J., Bhattacharya, J., and Ranjan, A. (2016). Enhancing crop yield by optimizing plant developmental features. *Development* 143, 3283–3294. doi: 10.1242/dev.134072

Maxwell, K., and Johnson, G. N. (2000). Chlorophyll fluorescence - a practical guide. *J. Exp. Bot.* 51, 659–668. doi: 10.1093/jexbot/51.345.659

Michelet, L., Zaffagnini, M., Morisse, S., Sparla, F., Perez-Perez, M. E. , Francia, F., et al. (2013). Redox regulation of the Calvin-Benson cycle: something old, something new. *Front. Plant Sci.* 4, 470. doi: 10.3389/fpls.2013.00470

Mu, X., and Chen, Y. (2021). The physiological response of photosynthesis to nitrogen deficiency. *Plant Physiol. Biochem.* 158, 76–82. doi: 10.1016/j.plaphy.2020.11.019

Nason, M. A., Farrar, J., and Bartlett, D. (2007). Strobilurin fungicides induce changes in photosynthetic gas exchange that do not improve water use efficiency of plants grown under conditions of water stress. *Pest Manage. Sci.* 63, 1191–1200. doi: 10.1002/ps.1443

Nolan, T. M., Yin, Y., Vukasinovic, N., Liu, D., Russinova, E., Vukasinovic, N., et al. (2020). Brassinosteroids: Multidimensional regulators of plant growth, development, and stress responses. *Plant Cell* 32, 295–318. doi: 10.1105/tpc.19.00335

Nuccio, M. L., Wu, J., Mowers, R., Zhou, H.-P., Meghji, M., Primavesi, L. F., et al. (2015). Expression of trehalose-6-phosphate phosphatase in maize ears improves yield in well-watered and drought conditions. *Nat. Biotechnol.* 33, 862–86+. doi: 10.1038/nbt.3277

Padhiary, A. K., Mishra, S. P., Nandi, A., Pattanaik, A., and Nayak, B. R. (2020). Role of brassinosteroids in horticultural crops (reviews). *Int. J. Chem. Stud.* 8, 18–22. doi: 10.22271/chemi.2020.v8.i3a.9458

Parry, M., Andralojc, P. J., Scales, J. C., Salvucci, M. E., Carmo-Silva, A. E., Alonso, H., et al. (2013). Rubisco activity and regulation as targets for crop improvement. *J. Exp. Bot.* 64, 717–730. doi: 10.1093/jxb/ers336

Parry, M., Reynolds, M., Salvucci, M. E., Raines, C., Andralojc, P. J., Zhu, X.-G., et al. (2011). Raising yield potential of wheat. II. increasing photosynthetic capacity and efficiency. *J. Exp. Bot.* 62, 453–467. doi: 10.1093/jxb/erq304

Patrick, J. W., and Colyvas, K. (2014). Crop yield components - photoassimilate supply- or utilisation limited-organ development? *Funct. Plant Biol.* 41, 893–913. doi: 10.1071/fp14048

Pedersen, M., Wegner, C., Phansak, P., Sarath, G., Gaussoin, R., and Schlegel, V. (2017). Monitoring wheat mitochondrial compositional and respiratory changes using Fourier transform mid-infrared spectroscopy in response to agrochemical treatments. *Spectrochim. Acta Part A* 173, 727–732. doi: 10.1016/j.saa.2016.10.025

Prado, J. R., Segers, G., Voelker, T., Carson, D., Dobert, R., Phillips, J., et al. (2014). Genetically engineered crops: From idea to product. *Annu. Rev. Plant Biol.* 65, 769–790. doi: 10.1146/annurev-arplant-050213-040039

Raines, C. A. (2022). Improving plant productivity by re-tuning the regeneration of RuBP in the Calvin-Benson-Bassham cycle. *New Phytol.* 236, 350–356. doi: 10.1111/nph.18394

Ruan, Y.-L. (2014). Sucrose metabolism: Gateway to diverse carbon use and sugar signaling. *Annu. Rev. Plant Biol.* 65, 33–67. doi: 10.1146/annurev-arplant-050213-040251

Ruske, R. E., Gooding, M. J., and Jones, S. A. (2003). The effects of triazole and strobilurin fungicide programmes on nitrogen uptake, partitioning, remobilization and grain n accumulation in winter wheat cultivars. *J. Agric. Sci.* 140, 395–407. doi: 10.1017/S0021859603003228

Salesse-Smith, C. E., Sharwood, R. E., Busch, F. A., Kromdijk, J., Bardal, V., and Stern, D. B. (2018). Overexpression of rubisco subunits with RAF1 increases rubisco content in maize. *Nat. Plants* 4, 802–810. doi: 10.1038/s41477-018-0252-4

Sekhar, K. M., Rachapudi, V. S., Mudalkar, S., and Reddy, A. R. (2014). Persistent stimulation of photosynthesis in short rotation coppice mulberry under elevated CO_2 atmosphere. *J. Photochem. Photobiol. B* 137, 21–30. doi: 10.1016/j.jphotobiol.2014.05.001

Sekhar, K. M., Sreeharsha, R. V., and Reddy, A. R. (2015). Differential responses in photosynthesis, growth and biomass yields in two mulberry genotypes grown under elevated CO_2 atmosphere. *J. Photochem. Photobiol. B* 151, 172–179. doi: 10.1016/j.jphotobiol.2015.08.008

Sharkey, T. D., Stitt, M., Heineke, D., Gerhardt, R., Raschke, K., and Heldt, H. W. (1986). Limitation of photosynthesis by carbon metabolism : II. O_2-insensitive CO_2 uptake results from limitation of triose phosphate utilization. *Plant Physiol.* 81, 1123–1129. doi: 10.1104/pp.81.4.1123

Sharma, A., Kumar, V., Kumar, R., Shahzad, B., Thukral, A. K., and Bhardwaj, R. (2018). Brassinosteroid-mediated pesticide detoxification in plants: A mini-review. *Cogent Food Agric.* 4, 1436212. doi: 10.1080/23311932.2018.1436212

Siddiqui, H., Hayat, S., and Bajguz, A. (2018). Regulation of photosynthesis by brassinosteroids in plants. *Acta Physiol. Plant* 40, 1–15. doi: 10.1007/s11738-018-2639-2

Simkin, A. J., Kapoor, L., Doss, C. G. P., Hofmann, T. A., Lawson, T., and Ramamoorthy, S. (2022). The role of photosynthesis related pigments in light harvesting, photoprotection and enhancement of photosynthetic yield in planta. *Photosynth. Res.* 152, 23–42. doi: 10.1007/s11120-021-00892-6

Simkin, A. J., Lopez-Calcagno, P. E., and Raines, C. A. (2019). Feeding the world: improving photosynthetic efficiency for sustainable crop production. *J. Exp. Bot.* 70, 1119–1140. doi: 10.1093/jxb/ery445

Simkin, A. J., Mcausland, L., Headland, L. R., Lawson, T., and Raines, C. A. (2015). Multigene manipulation of photosynthetic carbon assimilation increases CO_2 fixation and biomass yield in tobacco. *J. Exp. Bot.* 66, 4075–4090. doi: 10.1093/jxb/erv204

Sreeharsha, R. V., Sekhar, K. M., and Reddy, A. R. (2015). Delayed flowering is associated with lack of photosynthetic acclimation in pigeon pea (Cajanus cajan l.) grown under elevated CO_2. *Plant Sci. (Amsterdam Neth.)* 231, 82–93. doi: 10.1016/j.plantsci.2014.11.012

Stirbet, A., Lazar, D., Guo, Y., and Govindjee, G. (2020). Photosynthesis: basics, history and modelling. *Ann. Bot.* 126, 511–537. doi: 10.1093/aob/mcz171

Stitt, M., Borghi, G. L., and Arrivault, S. (2021). Targeted metabolite profiling as a top-down approach to uncover interspecies diversity and identify key conserved operational features in the Calvin-Benson cycle. *J. Exp. Bot.* 72, 5961–5986. doi: 10.1093/jxb/erab291

Suganami, M., Suzuki, Y., Tazoe, Y., Yamori, W., and Makino, A. (2021). Co-Overproducing rubisco and rubisco activase enhances photosynthesis in the optimal temperature range in rice. *Plant Physiol.* 185, 108–119. doi: 10.1093/plphys/kiaa026

Swoboda, C., and Pedersen, P. (2009). Effect of fungicide on soybean growth and yield. *Agron. J.* 101, 352–356. doi: 10.2134/agronj2008.0150

Theeuwen, T. P. J. M., Logie, L. L., Harbinson, J., and Aarts, M. G. M. (2022). Genetics as a key to improving crop photosynthesis. *J. Exp. Bot.* 73, 3122–3137. doi: 10.1093/jxb/erac076

Tilman, D., Balzer, C., Hill, J., and Befort, B. L. (2011). Global food demand and the sustainable intensification of agriculture. *Proc. Natl. Acad. Sci. U. S. A.* 108, 20260–20264. doi: 10.1073/pnas.1116437108

Tong, H. N., and Chu, C. C. (2018). Functional specificities of brassinosteroid and potential utilization for crop improvement. *Trends Plant Sci.* 23, 1016–1028. doi: 10.1016/j.tplants.2018.08.007

Vriet, C., Russinova, E., and Reuzeau, C. (2012). Boosting crop yields with plant steroids. *Plant Cell* 24, 842–857. doi: 10.1105/tpc.111.094912

Wang, K., Sun, Z., Yang, L., He, L., Li, X., and Wang, G. (2020a). Respiratory toxicity of azoxystrobin, pyraclostrobin and coumoxystrobin on chlorella vulgaris. *Bull. Environ. Contam. Toxicol* 104, 799-803. doi: 10.1007/s00128-020-02869-y

Wang, S.-Q., Zhao, H.-H., Zhao, L.-M., Gu, C.-M., Na, Y.-G., Xie, B., et al. (2020b). Application of brassinolide alleviates cold stress at the booting stage of rice. *J. Integr. Agric.* 19, 975–987. doi: 10.1016/S2095-3119(19)62639-0

Want, E. J., Masson, P., Michopoulos, F., Wilson, I. D., Theodoridis, G., Plumb, R. S., et al. (2013). Global metabolic profiling of animal and human tissues *via* UPLC-MS. *Nat. Protoc.* 8, 17–32. doi: 10.1038/nprot.2012.135

Wei, S. B., Li, X., Lu, Z. F., Zhang, H., Ye, X. Y., Zhou, Y. J., et al. (2022). A transcriptional regulator that boosts grain yields and shortens the growth duration of rice. *Science* 377, 8455. doi: 10.1126/science.abi8455

Xia, X.-J., Huang, L.-F., Zhou, Y.-H., Mao, W.-H., Shi, K., Wu, J.-X., et al. (2009). Brassinosteroids promote photosynthesis and growth by enhancing activation of rubisco and expression of photosynthetic genes in cucumis sativus. *Planta* 230, 1185–1196. doi: 10.1007/s00425-009-1016-1

Xia, L.-Y., Jiang, Y.-L., Kong, W.-W., Sun, H., Li, W.-F., Chen, Y., et al. (2020). Molecular basis for the assembly of RuBisCO assisted by the chaperone Raf1. *Nat. Plants* 6, 708–70+. doi: 10.1038/s41477-020-0665-8

Ye, Z.-P., and Kang, H.-J. (2012). Effects of CO_2 concentration on the quantum yield in the vicinity of plant light compensation point. *Chin. J. Ecol.* 31, 1949–1953. doi: 10.13292/j.1000-4890.2012.0264

Yerramsetty, P., Stata, M., Siford, R., Sage, T. L., Sage, R. F., Wong, G. K. S., et al. (2016). Evolution of RLSB, a nuclear-encoded S1 domain RNA binding protein associated with post-transcriptional regulation of plastid-encoded rbcL mRNA in vascular plants. *BMC Evol. Biol.* 16, 1–15. doi: 10.1186/s12862-016-0713-1

Zahra, N., Al Hinai, M. S., Hafeez, M. B., Rehman, A., Wahid, A., Siddique, K. H. M., et al. (2022). Regulation of photosynthesis under salt stress and associated tolerance mechanisms. *Plant Physiol. Biochem.* 178, 55–69. doi: 10.1016/j.plaphy.2022.03.003

Zhang, C.-H. (2020). Spray of "Yunleshou" in different period on rice production. *Fujian Sci. Tech. Rice Wheat.* 38, 29–30.

Zhang, C., Zhou, T., Xu, Y., Du, Z., Li, B., Wang, J., et al. (2020). Ecotoxicology of strobilurin fungicides. *Sci. Total Environ.* 742, 140611. doi: 10.1016/j.scitotenv.2020.140611

Zhao, J.-T. Y., X., -H., and Fu, Z.-B. (2021). Effect of plant growth regulator yunleshou on main agronomic characters and yield of barley. *J. Anhui Agric. Sci.* 49, 150–152. doi: 10.3969/ j.issn.0517-6611.2021.13.036

Zu, S.-H., Jiang, Y.-T., Hu, L.-Q., Zhang, Y.-J., Chang, J.-H. , Xue, H.-W., et al. (2019). Effective modulating brassinosteroids signal to study their specific regulation of reproductive development and enhance yield. *Front. Plant Sci.* 10, 980. doi: 10.3389/fpls.2019.00980

frontiers | Frontiers in Plant Science

TYPE Original Research
PUBLISHED 29 March 2023
DOI 10.3389/fpls.2023.1099816

OPEN ACCESS

EDITED BY
Hironaka Tsukagoshi,
Meijo University, Japan

REVIEWED BY
Luis Bolaños,
Autonomous University of Madrid, Spain
Kaoru Okamoto Yoshiyama,
Tohoku University, Japan

*CORRESPONDENCE
Naoyuki Sotta
nsotta@gmail.com
Toru Fujiwara
atorufu@g.ecc.u-tokyo.ac.jp

SPECIALTY SECTION
This article was submitted to Plant Physiology, a section of the journal Frontiers in Plant Science

RECEIVED 16 November 2022
ACCEPTED 28 February 2023
PUBLISHED 29 March 2023

CITATION
Sotta N, Sakamoto T, Kamiya T, Tabata R, Yamaguchi K, Shigenobu S, Yamada M, Hasebe M, Sawa S and Fujiwara T (2023) *NAC103* mutation alleviates DNA damage in an *Arabidopsis thaliana* mutant sensitive to excess boron.
Front. Plant Sci. 14:1099816.
doi: 10.3389/fpls.2023.1099816

NAC103 mutation alleviates DNA damage in an *Arabidopsis thaliana* mutant sensitive to excess boron

Naoyuki Sotta[1]*, Takuya Sakamoto[2], Takehiro Kamiya[1], Ryo Tabata[3,4], Katsushi Yamaguchi[5], Shuji Shigenobu[5,6], Masashi Yamada[7,8], Mitsuyasu Hasebe[5,6], Shinichiro Sawa[3,9] and Toru Fujiwara[1]*

[1]Department of Applied Biological Chemistry, Graduate School of Agricultural and Life Sciences, The University of Tokyo, Tokyo, Japan, [2]Department of Applied Biological Science, Faculty of Science and Technology, Tokyo University of Science, Tokyo, Japan, [3]Graduate School of Science and Technology, Kumamoto University, Kumamoto, Japan, [4]Graduate School of Bioagricultural Sciences, Nagoya University, Nagoya, Japan, [5]National Institutes for Basic Biology, National Institutes of Natural Sciences, Okazaki, Japan, [6]School of Life Science, Graduate University for Advanced Studies, Okazaki, Japan, [7]Agricultural Biotechnology Research Center, Academia Sinica, Taipei, Taiwan, [8]Biotechnology Center in Southern Taiwan, Academia Sinica, Tainan, Taiwan, [9]International Research Center for Agricultural & Environmental Biology, Kumamoto University, Kumamoto, Japan

Excess boron (B) is toxic to plants and thereby causes DNA damage and cell death in root meristems. However, the underlying mechanisms which link boron and DNA damage remain unclear. It has been reported that the *rpt5a-6* mutant of the 26S proteasome is sensitive to excess boron, resulting in more frequent cell death in root meristem and reduced root elongation. In this study, we showed that a reduction in root growth in the *rpt5a* mutant in the presence of high boron levels is repressed by a mutation in NAC domain containing transcription factor NAC103, a substrate of the proteasome, which functions in the unfolded protein response pathway. The mutation in NAC103 alleviated excess-B-induced DNA damage and cell death in root meristems of the *rpt5a* mutant. Superoxide (O_2^-) staining with nitroblue tetrazolium revealed that boron stress causes O_2^- accumulation in root tips, which was higher in the *rpt5a-6* mutant, whereas the accumulation was lower in the *rpt5a-6 nac103-3* double mutant. Our work demonstrates the overall involvement of *NAC103* in maintaining healthy root meristem under excess boron conditions in the absence of *RPT5A* proteasome subunit.

KEYWORDS

abiotic stress, *Arabidopsis thaliana*, DNA repair, meristems, reactive oxygen species, root, stress response

1 Introduction

Boron is an essential element for plants but is also toxic to them at high concentrations (Warington, 1923; Nable et al., 1997). Excess boron causes reduced root and shoot growth (Reid et al., 2004), and deformities in fruit growth (Dye et al., 1983; Sinha et al., 2006). Because excess boron can cause such defects in crops, the issue has become a significant

agricultural problem. Thus, it is important to understand the mechanisms of plant tolerance to boron toxicity. In *Arabidopsis thaliana* roots, excess boron inhibits cell division and causes cell death, resulting in a reduced root meristem size and a slower root elongation (Aquea et al., 2012). Excess boron induces DNA damage within the root tip, and this phenomenon has been suggested to be a mechanism for the growth defects in the presence of excess boron (Sakamoto et al., 2011). The molecular mechanisms involved in DNA damage caused by boron stress are relatively unknown; however, recently we reported that the 26S proteasome is crucial for excess boron tolerance and that several 26S proteasome component genes are essential for ameliorating excess boron-induced DNA damage (Sakamoto et al., 2018).

26S proteasome is a protein complex which has a key function in selective proteolysis carried out by the ubiquitin (Ub)–proteasome pathway (Smalle and Vierstra, 2004). The Ub–proteasome pathway is a core mechanism for protein breakdown and is conserved in eukaryote species. In the pathway, target proteins were tagged with Ub, a highly conserved 76-amino acid protein (Smalle and Vierstra, 2004). The tagging is catalyzed by an ATP-dependent cascade involving the Ub-activating enzyme (E1), Ub-conjugating enzyme (E2), and Ub-protein ligase (E3) (Vierstra, 2003). The fact that *A. thaliana* genome encodes approximately 1200 E3 components suggests the involvement of the Ub-proteasome pathway in a wide range of biological processes and having different specificities. In fact, the Ub-proteasome pathway has been found to be important in a wide variety of physiological processes including cell division, differentiation, and development; stress response and extracellular modulation; morphogenesis of neuronal networks; cell surface receptor modulation; ion channeling and secretion pathways; DNA repair; regulation of the immune and inflammatory response; and, organelle biogenesis and apoptosis (Ciechanover, 1998).

The 26S proteasome consists of two subunits, the 20S proteasome [core particle (CP)] and the 19S complex [regulatory particle (RP)] (Kurepa and Smalle, 2008). Typically, the CP consists of two pairs of α and β subunits that form a barrel-like structure containing three sites for protease activity. The RP is located at the end of the CP barrel and forms a gate- cap structure through which the substrate proteins enter the CP. The RP consists of a base and lid. The base contains three RP non-ATPases (RPNs), namely RPN1, RPN2, and RPN10 and six RP AAA-ATPases (RPTs), i.e., RPT1–RPT6) (Fu et al., 2001). RPTs have an ATP-dependent function in the unfolding of substrate proteins and opening of the gate in order to allow the substrate to enter the CP (Wolf and Hilt, 2004).

RPT2A, RPT5A, RPN2A, and RPN8a have been identified as essential subunits playing a role in excess boron tolerance (Sakamoto et al., 2018). Mutants of the abovementioned subunits exhibit a significantly reduced root growth, stunned root meristems, increase in the number of root hairs, and frequent death of root meristematic cells under excess boron conditions. In the *rpt5a-4* mutant, a reduction in Ub–proteasome pathway activity and an overaccumulation of *BRAHMA* (*BRM*), a substrate of the Ub–proteasome pathway, were observed (Sakamoto et al., 2018). Because *BRM* is an SWI/SNF chromatin remodeling ATPase, sensitivity of the *rpt5a-4* mutant to excess boron was partially explained by a failure in BRM protein degradation, which resulted in over-loosening of chromatin and made the DNA more susceptible to damage. However, introducing the *brm* mutation only partially increased the tolerance of the *rpt5a-4* mutant to excess boron. This suggests that the *RPT5A* is required for excess boron tolerance and is also part of a pathway different to that used to degrade the BRM protein. To further the limited knowledge on molecular mechanisms underlying plant tolerance to excess boron, we screened for suppressor mutants of the *rpt5a* mutation in *A. thaliana*. In this work, we report characterization of several *rpt5a* suppressor lines and identification of a transcription factor which is involved in excess boron sensitivity in plant root growth.

2 Materials and methods

2.1 Plant materials and growth conditions

For screening *rpt5a* suppressor mutants, approximately 20,000 *rpt5a-4* and *rpt5a-6* seeds were treated with 0.2% ethyl methanesulfonate (EMS) for 16 h; then, those seeds were sown and grown on rockwool. The harvested seeds were cultured to produce M_2 seeds that were subsequently harvested. Approximately 20,000 M_2 seedlings were grown for 10 days in a 3 mM B MGRL media (Fujiwara et al., 1992) supplemented with 1.0% sucrose and solidified using 1.5% gellan gum (Wako, Japan). Plants that exhibited longer roots than those of the parental mutant were selected and transferred to 30 μM B plates for incubation. After 2–3 days of incubation, the selected plants were transferred to a rockwool, and the M_3 seeds were eventually harvested. The phenotypes of the selected suppressor lines were confirmed with the seedlings of the M_3 generation.

To obtain the *nac103-3* single mutant, the *rpt5a-6 nac103-3* mutant was backcrossed with the wild type to create a selfed-F_2 population. The *nac103-3* mutation was detected by a CAPS marker after performing amplification of the genome using the primers nac103-3_F and nac103-3_R followed by digestion using *Hin*fI; the resultant band sizes were as follows: wild type: 234; *nac103-3*: 66, 168 bp. The *rpt5a-6* mutation was detected by a dCAPS marker after performing amplification using the primers rpt5a-6_BfuAI_F and rpt5a-6_R followed by digestion using *Bfu*IA; the resultant band sizes were as follows: wild type: 254, 297, 401; *rpt5a-6*: 254, 698 bp.

To obtain mutant combination of *rpt5a-6*, *nac103-3*, and *sog1-101*, *rpt5a-6 nac103-3* double mutant was crossed with *sog1-101* mutant, and homozygous lines for the genotype of interests were established from their F_2 generation. *sog1-101* mutation was detected by PCR using the specific primers as described previously (Ogita et al., 2018).

For the growth tests, seeds were surface sterilized using 70% ethanol aq. For 5 min followed by 99.5% ethanol aq. For 1 min. After rinsing off the ethanol, the seeds were sown on a sterile MGRL medium supplemented with 1.0% sucrose and solidified using gellan gum (Wako). Boric acid concentrations in the medium were modified from the original concentration for each specific

test. After vernalization at 4°C for 2 days, the medium-containing plates were placed vertically in incubators at 22°C under a 16-h light (fluorescent lamps, 100–160 μmol photons m^{-2} s^{-1}) and 8-h dark cycle.

2.2 Positional identification of the causal mutation gene

The positional identification of the causal mutation gene was conducted by utilizing the polymorphism between the two ecotypes, Col-0 and L*er*. To obtain the F_2-segregating generation, *rpt5a-6 sup1* (Col-0 background) mutant was crossed with L*er*. The F_1 was self-pollinated, and the obtained F_2 seeds were used for mapping of the gene responsible for the altered phenotype in root growth under excess boron condition. The F_2 seedlings were grown under excess boron conditions (3 mM boric acid), and seedlings with short hairy roots similar to the *rpt5a-6* phenotype were selected for genotyping. The presence of *rpt5a-6* mutations in the mapping population was confirmed by the CAPS marker, as described above. For genotyping, a single-sequence length polymorphism (SSLP) marker between Col-0 and L*er* was used. A list of genetic markers near the candidate region used for mapping is shown in Table S1.

2.3 Plasmid construction and transformation of plants

For the genetic complementation tests, the *NAC103* genomic sequence without the termination codon was cloned from the Col-0 genomic DNA using the primers NAC103ATG-2k_F and NAC103CDS-TAA_R with a PrimeSTAR® GXL DNA Polymerase (Takara). The amplified fragment contained an upstream region of 1,589 bp in size beginning at the annotated transcription start sites. The fragment was cloned into pENTR D-TOPO (Invitrogen) according to the instructions in the manufacturer's manual. The obtained entry vector was designated as pSOT1. The entire insert sequences in the entry vector were verified by sequencing analysis. Sequences of primers are listed in Table S1. The vector for GFP fusion protein expression in plants was obtained by LR reaction between pSOT1 and pMDC107 (Curtis and Grossniklaus, 2003) using the gateway LR clonase enzyme mix (Invitrogen). The resultant expression vector carrying *proNAC103-NAC103-GFP* construct was designated as pSOT2. In a similar way, for NAC103 overexpression, the coding sequence of *NAC103* was cloned from the cDNA derived mRNA isolated from Col-0 roots into pENTR D-TOPO using the primers NAC103_CDS_F and NAC103_CDS_R and then transferred into the expression vector, pMDC32 (Curtis and Grossniklaus, 2003). The resultant expression vector carrying the *pro35S-NAC103* construct was designated as pSOT3.

For the stable transformation of the experimental plants, the binary vectors were introduced into the *Agrobacterium tumefaciens* strain GV3101(Bechtold and Pelletier, 1998), and the target plants were transformed with this culture using the floral dipping method (Clough and Bent, 1998). The transformed plants were selected on a half-strength MS medium containing 20 μg/mL hygromycin B (Wako) and 250 μg/mL Claforan (Sanofi), which was solidified using 0.5% agarose. Expression of the transgene was confirmed by qRT-PCR.

2.4 ROS staining

The superoxide was visualized by nitroblue tetrazolium (NBT) staining. Roots were incubated with an NBT staining solution (2 mM NBT in 20 mM MES, pH 6.1) for 5 min at room temperature in the dark. The roots were washed with water after staining and then mounted in chloral hydrate solution (a mixture of 4-g chloral hydrate, 1-mL glycerol, and 2-mL water). These roots were observed under a bright field microscope.

2.5 qRT-PCR analysis

For RNA extraction, 6-day-old wild-type seedlings were grown under control conditions (30 μM boric acid) and were either subsequently subjected to excess boron conditions (3 mM boric acid) or maintained under control conditions for an additional 3 days. The whole roots were harvested and subjected to RNA extraction using a RNeasy Plant Mini Kit (Qiagen). For qRT-PCR analysis, approximately 500 ng of total RNA was reverse transcribed using a Takara Prime Script RT Master Mix according to the manufacturer's instructions at a 10-μL scale. Real-time PCR was performed using a Takara Thermal Cycler Dice TP800 and Takara SYBR® Premix Ex Taq™ II (Tli RNaseH Plus) according to the manufacturer's instructions. For amplification, the PCR cycle was set at 95°C for 30 s, 40 cycles of (95°C for 5s, 60°C for 30s*) for amplification, and then 95°C for 15s, 60°C for 30s, and 95°C for 15s* for dissociation curve analysis. The fluorescence intensity was recorded at the steps marked with asterisks, and the primers used are shown in Table S1.

2.6 Confocal microscopy

For observation of the root meristems, approximately 5-mm regions from the root tips were excised and mounted in 10-μg/mL propidium iodide (PI) aq. For visualizing cell walls. The prepared slides were immediately observed under a confocal microscope (FV1000, OLYMPUS), which is equipped with a 40x objective lens, and subjected to excitation at 556 nm; the resulting signal intensity was detected between 570–670 nm.

2.7 Root growth measurement

Root images were captured using a digital camera, and root length was measured using the "Segmented Line" function in FIJI software (Schindelin et al., 2012).

2.8 DNA damage quantification

For the comet assay, nuclei were extracted from 100 primary root tips (1 cm from the tip) for every single replicate. Roots were chopped in 300 µL of nuclei extraction buffer (50 mM EDTA in PBS) using a razor. The buffer was collected and passed through a 30-µm membrane filter (CellTrics®, Sysmex Partec) to remove large cellular structures. Comet assay was performed using CometAssay® Kit (25 x 2-well slides; Trevigen) by following the instructions in the kit's manual and performing slight modifications: electrophoresis was performed at 1 V/cm for 6 min in an ice-cooled TBE buffer. For DNA staining, SYBR® Gold Nucleic Acid Gel Stain (10,000x Concentrate in DMSO; Thermo Fisher) was used after diluting it by 30,000 times using TE buffer (pH 8.0). The prepared slides were observed under a fluorescent microscope (BX50WI, OLYMPUS), which was equipped with a U-MWIBA3 mirror unit (460–495 nm excitation, 510–550 nm absorbance, and a 505-nm dichroic mirror). Image quantification was performed by using default settings of CASP software (Końca et al., 2003).

2.9 Statistical analysis

For root length and elongation measurements, primary roots of 9-24 individuals were measured. For qRT-PCR, roots of 10 seedlings were sampled as one biological replicate, and three biological replicates were analyzed. For comet assay, nuclei were extracted from 100 seedlings as one sample, and 125 nuclei were measured for each sample. Dunnett's test was applied for multiple comparison against control or wild-type. Tukey-Kramer's test was applied for multiple comparison among all groups.

3 Results

3.1 Isolation of *rpt5a-6* suppressor mutants

It has been reported that mutants of a subunit of the 26S proteasome, the *RPT5A* gene, are sensitive to excess boron (Sakamoto et al., 2018). Under excess boron conditions, mutants exhibit a severely inhibited root elongation phenotype, which is restored under normal boron conditions. To obtain insights into the role of the *RPT5A* gene with regard to excess boron tolerance, we screened for its suppressor mutants from M_2 population of mutagenized *rpt5a-6*, a non-sense mutant, and *rpt5a-4*, a knock-out mutant. From the M_2 *rpt5a-6* population, we isolated a suppressor line, *rpt5a-6 sup1*, the root elongation of which under conditions of boron stress (3 mM boric acid) was greater than that of the original mutant *rpt5a-6* (Figure 1A). Under normal conditions, roots of *rpt5a-6 sup1* was significantly longer than that of *rpt5a-6*, but shorter than the wild type, suggesting that *sup1* mutation suppresses not all the growth defects in *rpt5a-6* (Figure 1B). To evaluate excess boron sensitivity, apart from basic growth defects, we compared relative root growth (excess boron/control) among the genotypes. Relative root growth of *rpt5a-6 sup1* was higher than *rpt5a-6* and comparable to the wild type, suggesting that *sup1* mutation suppresses the excess boron sensitivity of *rpt5a-6* to the same levels as the wild type.

Previously, *rpt5a-6* had been found to exhibit an altered root morphology with short and squeezed root apical meristems and frequent cell death in the meristem even under normal boron conditions; these features become more evident by excess boron stress (Sakamoto et al., 2018). In *rpt5a-6 sup1*, the abnormal root meristem shape under excess boron stress was recovered and indistinguishable from the wild type (Figure 1C). Visualization of cell walls and dead cells using propidium iodide (PI) stain revealed that cell death is evident in stele cells in the meristem of *rpt5a* mutants after 40 h of excess boron treatment, and that the cell death was suppressed in *rpt5a-6 sup1* (Figure 1D and Supplementary Figure 1). From these results, we concluded that *rpt5a-6 sup1* completely suppresses the root growth sensitivity observed in *rpt5a-6* mutants to excess boron.

3.2 *NAC103* gene responsible for suppressing excess boron sensitivity in *rpt5a* mutants

Crossing between the *rpt5a-6 sup1* and *rpt5a-4* mutants suggested that the *rpt5a-6 sup1* mutation is semi-dominant because the F1-progeny exhibited intermediate root growth between *rpt5a-6 sup1* and *rpt5a-4* (Supplementary Figure 2). Map-based cloning revealed that the causal gene for the suppression of excess boron sensitivity in *rpt5a-6 sup1* is located on chromosome 5, between 25.4 Mb and 25.8 Mb (Figure 2A). Within the chromosomal region, whole genome sequencing identified only a single homozygous mutation. The mutation was in the NAC transcription factor family, *NAC103* (AT5G64060), and is predicted to produce a premature stop codon in its coding region. We designated the mutation as *nac103-3* (Figure 2B). In addition, we isolated other 11 independent suppressor lines from the M_2 *rpt5a-4* population (Supplementary Figure 3). These lines exhibited phenotypes similar to those exhibited by *rpt5a-6 nac103-3*. We determined the *NAC103* genomic sequence in the 11 *rpt5a-4* mutant suppressor lines and found that seven lines harbored a distinct mutation in the *NAC103* coding sequence, designated as *nac103-4, 5, 6, 7, 8, 9, and 10* (Figures 2B, S2). The presence of several alleles exhibiting similar phenotypes strongly suggests that *NAC103* is the gene responsible for the suppression. Because the phenotype was comparable among the abovementioned alleles, we focused on *rpt5a-6 nac103-3* for further analysis.

To further confirm that the mutation in *NAC103* is responsible for the suppression of the *rpt5a-6* phenotype, we conducted complementation tests. A construct carrying *proNAC103-NAC103-GFP* was introduced into *rpt5a-6 nac103-3*, and two independent homozygous transgenic lines were established. A qRT-PCR analysis confirmed that those lines accumulated higher or comparable *NAC103* mRNA compared to *rpt5a-6*. Under both normal boron concentration (control) and excess boron concentration, root elongation of these transformants was found to be significantly reduced in comparison with that of *rpt5a-6 nac103-3* (Figure 2C). To examine the effect of expressing the

10.3389/fpls.2023.1099816

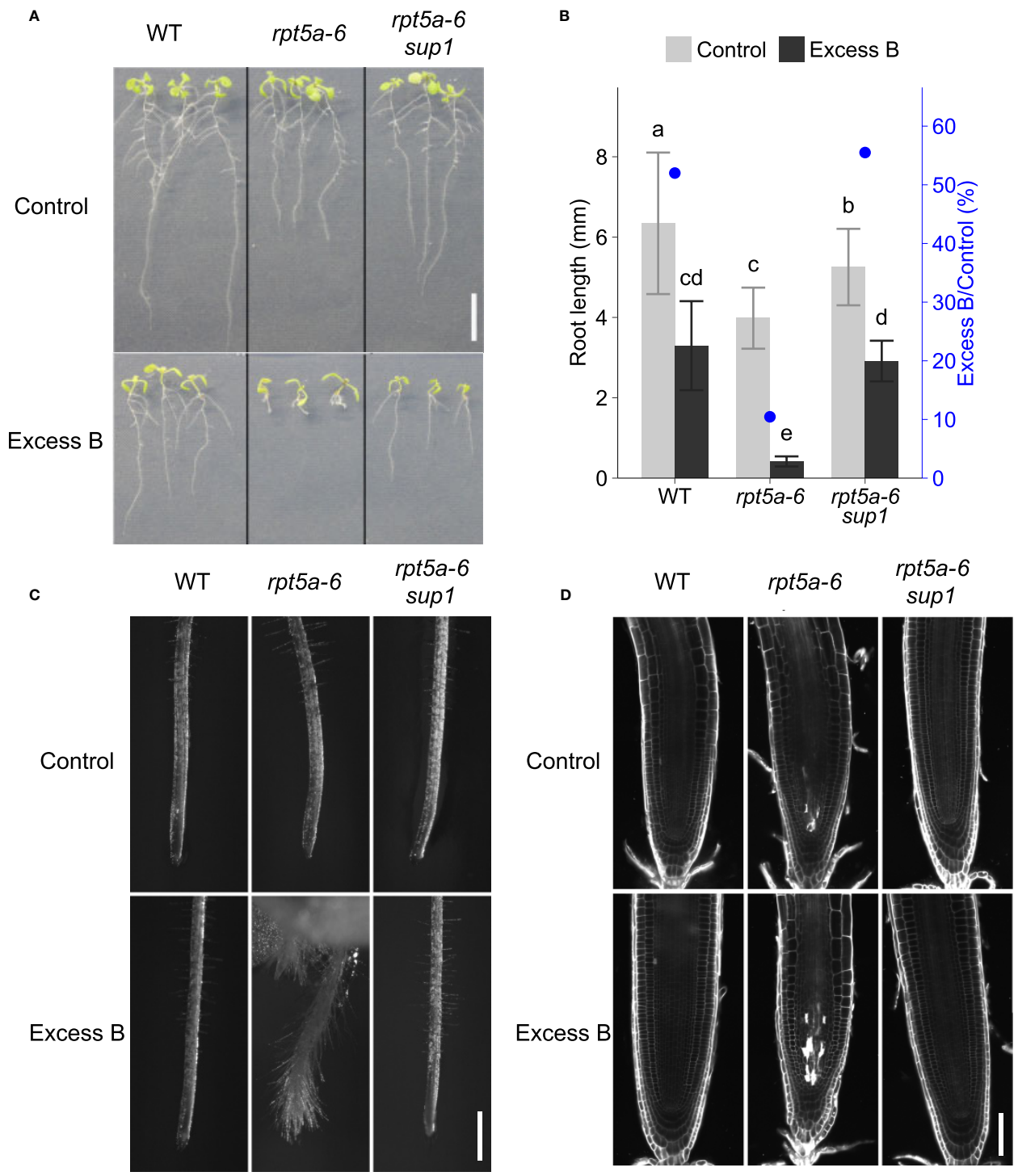

FIGURE 1
Phenotypes of the mutant in which excess boron sensitivity of *rpt5a-6* is suppressed. Wild type, *rpt5a-6* and its suppressor mutant *rpt5a-6 sup1* were grown under excess boron (3 mM boric acid) or control (30 μM boric acid) conditions. **(A)** Ten-day-old seedlings. Bar, 1cm. **(B)** Primary root length of ten-day-old seedlings. Values are mean ± standard deviation of 12-23 individuals. Blue dots represent relative root length. Groups sharing the same letters are not significantly different at $p < 0.05$ by Tukey-Kramer's test. **(C)** Primary root tip morphology of 11-day-old seedlings by stereomicroscopy. Bar, 500 μm. **(D)** Confocal microscopy of root meristems. Six-day-old seedlings grown under the control condition were treated with control or excess boron conditions for 40 hours. Cell walls and dead cells were visualized with propidium iodide. Bar, 50 μm.

NAC103 gene without *rpt5a-6* mutation, we also introduced the same construct into the *nac103-3* single mutant. The *nac103-3* single mutant was generated by backcrossing *rpt5a-6 nac103-3* with the wild type. The root elongation phenotype of the established *nac103-3* single mutant was indistinguishable from that of the wild type (Figure 2C). In contrast to the *rpt5a-6 nac103-3 proNAC103-NAC103-GFP* lines, the three transformant lines of *nac103-3 proNAC103-NAC103-GFP* exhibited root growth indistinguishable

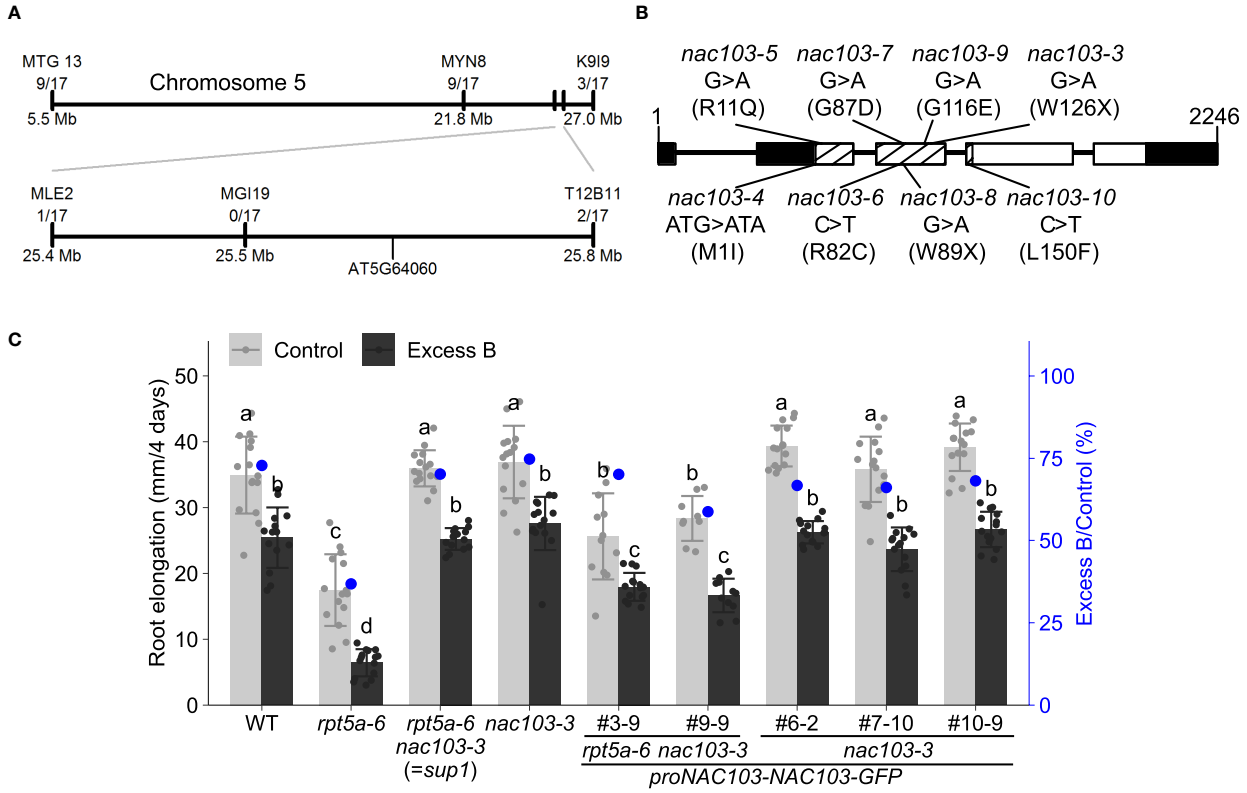

FIGURE 2
Positional identification of the mutation responsible for suppression of excess boron sensitivity in *rpt5a-6 sup1*. **(A)** Schematic diagram for candidate region in chromosome 5. Molecular markers and the number of recombinant plants found in the mapping population are shown. **(B)** Schematic diagram of *NAC103* gene and point mutations in suppressor lines. For each suppressor line, the line names, nucleotide changes and amino acid changes (parenthesis) are shown. Lines and boxes represent introns and exons respectively. White and black boxes represent cording regions and untranslated regions, respectively. NAC domain is shown by meshing. **(C)** Root elongation of the complementation lines. Constructs carrying *proNAC103-NAC103-GFP* was introduced into *rpt5a-6 nac103-3* or *nac103-3*. Seedlings were grown under normal conditions (30 μM boric acid) for eight days and then transferred to excess boron (3 mM boric acid) or control conditions. Root elongation during for four days after the transfer was measured. Numbering with # indicates transformant lines isolated independently. Values are mean ± standard deviation of 9-15 measurements. Groups sharing the same letters are not significantly different at $p < 0.05$ by Tukey's test.

to that of *nac103-3*, thereby indicating that growth defects caused by the introduction of *NAC103* is specific to an *rpt5a-6* background. Given that the expression of *NAC103-GFP* in the *rpt5a-6 nac103-3* mutant resulted in the inhibition of root elongation in the *rpt5a-6* mutant, we concluded that *NAC103* is at least partly responsible for the phenotype of the *rpt5a-6* suppressor mutant.

3.3 Expression of *NAC103* gene induced by boron stress

To investigate the reaction of the *NAC103* gene to boron stress, we examined the accumulation of *NAC103* mRNA in the *rpt5a-6* mutant in response to conditions of excess boron. RNA was extracted from whole roots of seedlings treated with excess boron (3 mM boric acid) and from those of seedlings grown under control conditions (30 μM boric acid) for 3 days. In the wild type, excess boron significantly induced the *NAC103* mRNA level by more than 10-fold (Figure 3A). mRNA accumulation was much higher in *rpt5a-6* plants grown under both conditions, having more than 50-fold increase in comparison with that in the wild-type plants grown under control condition. These results suggest the possibility that the overaccumulation of *NAC103* mRNA is responsible for root growth inhibition under conditions of excess boron in the *rpt5a-6* mutant.

3.4 *NAC103* overexpression in the wild type background did not induce root growth inhibition under excess boron condition

We hypothesized that an over accumulation of *NAC103* mRNA is responsible for root growth inhibition under excess boron stress. To test the hypothesis, we generated *NAC103* overexpression lines to observe their phenotypes under excess boron stress. For the *NAC103* overexpression lines, the coding sequence of *NAC103* was cloned from cDNA and introduced into the wild type under the control of the cauliflower mosaic virus 35S RNA promoter. Three independent transformant lines were established. A qRT-PCR analysis confirmed that those lines accumulated higher *NAC103* mRNA than the wild type as well

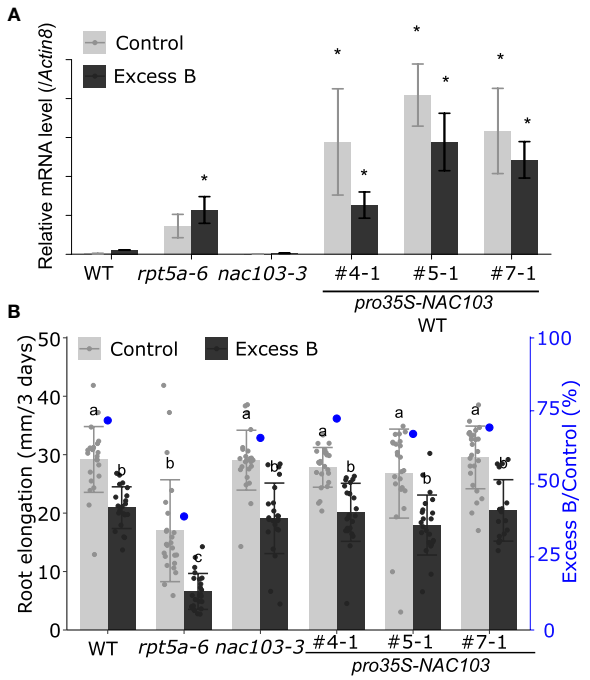

FIGURE 3
Effect of *NAC103* expression on excess boron sensitivity in root growth. **(A)** *NAC103* mRNA accumulation in *rpt5a-6* mutant and *NAC103* overexpression lines. Seedlings were grown for six days under control or excess boron conditions. Total RNA was extracted from whole root and *NAC103* mRNA accumulation was quantified by qRT-PCR. Expression levels were normalized by *Actin8*. Values represent mean ± standard deviation of three biological replicates. Asterisk indicate significant difference from the wild type in the same condition at $p < 0.05$ by Dunnett's test. **(B)** Root elongation of *NAC103* overexpression lines. Seedlings were precultured in normal conditions (30 μM boric acid) for six days and then transferred to excess boron (3 mM boric acid) or control conditions. Root elongation during three days after the transfer was measured. Numbering with # indicates transformant lines isolated independently. Values are mean ± standard deviation of 18-24 measurements. Groups sharing the same letters are not significantly different at $p < 0.05$ by Tukey-Kramer's test.

as the *rpt5a-6* mutant, with a tendency to reduce under excess boron conditions for unknown reasons (Figure 3A). However, root growth in the overexpressing lines was indistinguishable from that in the wild type under both the excess boron and control conditions (Figure 3B). These results suggest that growth defects caused by excess boron are not explained by *NAC103* mRNA over accumulation alone.

3.5 No significant difference was observed between *rpt5a-6* and *rpt5a-6 nac103-3* mutants regarding the expression of already known NAC103-downstream genes

The *NAC103* gene has been reported to play a role in the transcriptional regulatory cascade of the unfolded protein response (UPR) (Sun et al., 2013). They have reported that *NAC103* expression is induced by endoplasmic reticulum (ER) stress, which is caused by an accumulation of unfolded proteins *via* direct transcriptional activation by an ER stress signaling regulator bZIP60, and transmits the signal by upregulating the downstream UPR genes. To examine the effects of the *nac103-3* mutation on tolerance to unfolded protein accumulation and root growth, we treated *rpt5a-6* and *rpt5a-6 nac103-3* mutant seedlings with the reagent L-canavanine, which induces protein unfolding *via* its incorporation into the protein; L-canavanine is an analog of arginine and induces protein misfolding (Kurepa et al., 2003). Treatment with 0.5 μM L-canavanine reduced root elongation in the *rpt5a-6* single mutant but not in the *rpt5a-6 nac103-3* double mutant (Figure 4A), suggesting that the *nac103-3* mutation suppressed the sensitivity of *rpt5a-6* to the accumulated unfolded proteins.

To assess the involvement of the downstream UPR pathway in excess boron sensitivity with regard to the *rpt5a-6* mutant, we examined the expression levels of the already known NAC103-downstream UPR-related genes: *calnexin* (*CNX*), *calreticulin* (*CRT*), protein disulfide-isomerase 5 (PDI5), and ubiquitin conjugase 32 (UBC32) (Sun et al., 2013). A qRT-PCR analysis detected no significant difference in the expression of the four abovementioned genes and proteins between the *rpt5a-6* and *rpt5a-6 nac103-3* mutants (Figure 4B), suggesting that the transcriptional regulation of these genes by *NAC103* is not responsible for excess boron sensitivity of the *rpt5a-6* mutant.

3.6 *nac103-3* mutation reduces DNA damage accumulation caused by excess boron stress in the *rpt5a-6* mutant

It has been reported that excess boron stress induces DNA damage in *Arabidopsis* root meristem (Sakamoto et al, 2011), and that the extent of the DNA damage is more severe in the *rpt5a-6* mutant than that in the wild-type plant (Sakamoto et al., 2018). In addition, treatment of *rpt5a-6* with zeocin, a reagent that causes DNA damage, results in a development of a phenotype similar to that of the wild type under excess boron stress conditions (Sakamoto et al., 2018). These results suggest that the susceptibility to DNA damage is a critical factor for excess boron sensitivity in *rpt5a-6*.

To investigate the role of *NAC103* in this context, we examined the extent of DNA damage in the *rpt5a-6 nac103-3* mutant under the excess boron stress. To estimate the accumulation of DNA damage in roots, the expression levels of genes known to respond to DNA damage, namely *RAD51*, *BRCA1*, and *PARP2*(AT4G02390), were quantified by qRT-PCR analysis (Figures 5A–C). Among all genotypes, expression of these genes tended to be higher under excess boron conditions compared to the control condition. Under excess boron conditions, expression of *BRCA1* and *PARP2* was significantly higher in *rpt5a-6* than in wild type, but in *rpt5a-6 nac103-3* it was comparable to wild type. These results suggest that the *nac103-3* mutation suppresses DNA damage accumulation in the *rpt5a-6* mutant. To obtain direct evidence for this, we assessed the extent of DNA damage in root tips using a comet assay

10.3389/fpls.2023.1099816

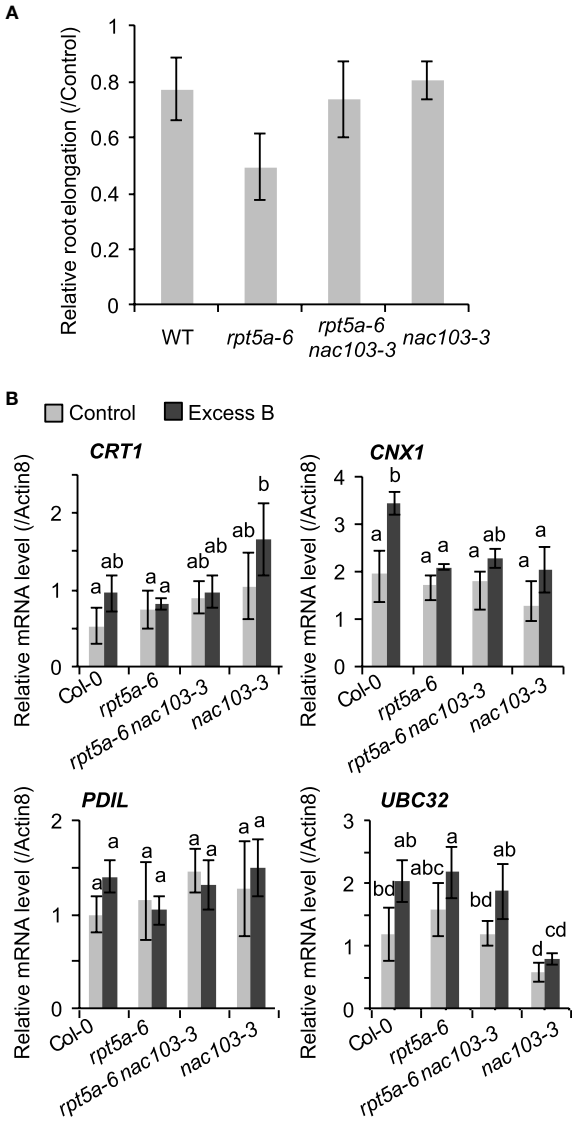

FIGURE 4
Effect of *nac103-3* mutation on unfolded stress response **(A)** Sensitivity to unfolded protein inducible reagent L-canavanine. Seedlings were precultured in normal conditions (30 µM boric acid) for six days and then transferred to 0.5 µM L-canavanine or control conditions. Root elongation during three days after the transfer was measured and normalized by the average elongation under control conditions. Values represent mean ± standard deviation of measurements of 11-15 seedlings. An asterisk indicates significant difference from the wild type at $p < 0.05$ by Dunnett's test. **(B)** mRNA accumulation of *NAC103*-downstream unfolded protein response related genes, *CRT1, CNX1, PDIL1* and *UBC32*. Seedlings were grown for 6 days under control conditions (30 µM boric acid) and further 3 days on control or excess boron conditions (3 mM boric acid). Total RNA was extracted from whole root of 10 seedlings and mRNA accumulation was quantified by qRT-PCR. Expression levels were normalized by *Actin8*. Values represent mean ± standard deviation of three biological replicates. Groups sharing the same letters are not significantly different at $p < 0.05$ by Tukey's test.

(Figure 5D). The comet assay revealed that DNA damage accumulation was significantly lower in the *rpt5a-6 nac103-3* mutant than in the *rpt5a-6* mutant, regardless of boron concentration. These results also reveal that the *nac103-3* mutation ameliorated the extent of DNA damage in *rpt5a-6* mutant plants.

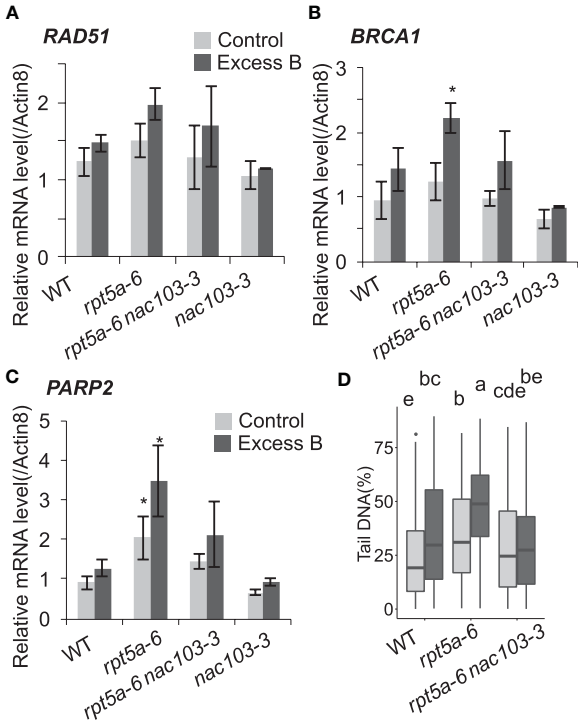

FIGURE 5
nac103-3 mutation suppressed DNA damage accumulation in *rpt5a-6* Seedlings were grown for six days under control conditions (30 µM boric acid) and further three days on control or excess boron conditions (3 mM boric acid). **(A–C)** mRNA accumulation of DNA damage maker genes. Total RNA was extracted from whole root of 10 seedlings and mRNA accumulation was quantified by qRT-PCR. Expression levels were normalized by *Actin8*. Values represent mean ± standard deviation of three biological replicates. Asterisks indicate significant difference from the wild type in each condition at $p < 0.05$ by Dunnett's test. **(D)** Accumulation of DNA damage (double strand break) was quantified with comet assay neutral method. Seedlings were grown for 6 days under control conditions (30 µM boric acid) and further 3 days on control or excess boron conditions (3 mM boric acid). Nuclei were extracted from 1 cm of root tips of approximately 100 seedlings per each condition. The ratios of DNA in tail were calculated by CASP software. For each condition, 125 nuclei were measured. Groups sharing same letters were not significantly different by Steel-Dwass test at $p < 0.05$.

3.7 *nac103-3* mutation ameliorates DNA damage-induced growth defects in *rpt5a-6* mutant

The *rpt5a-6* mutant has been reported to be more susceptible to DNA damage and, more specifically, that caused by radiation or chemical reagents (Sakamoto et al., 2018). To investigate the involvement of *NAC103* in sensitivity to DNA damage, we assessed the root growth of the *rpt5a-6 nac103-3* mutant after treatment with zeocin (Figure 6). Treatment with zeocin reduced root elongation in a dose-dependent manner among all tested genotypes (Figure 6A). Consistent with previous results, the *rpt5a-6* mutant was more sensitive to zeocin than the wild type, with the former showing a higher root elongation inhibition rate and a more severe morphological alteration, including cell death in root meristems (Figure 6C). However, none of these defects were evident in the *rpt5a-6 nac103* double mutant, suggesting that the

10.3389/fpls.2023.1099816

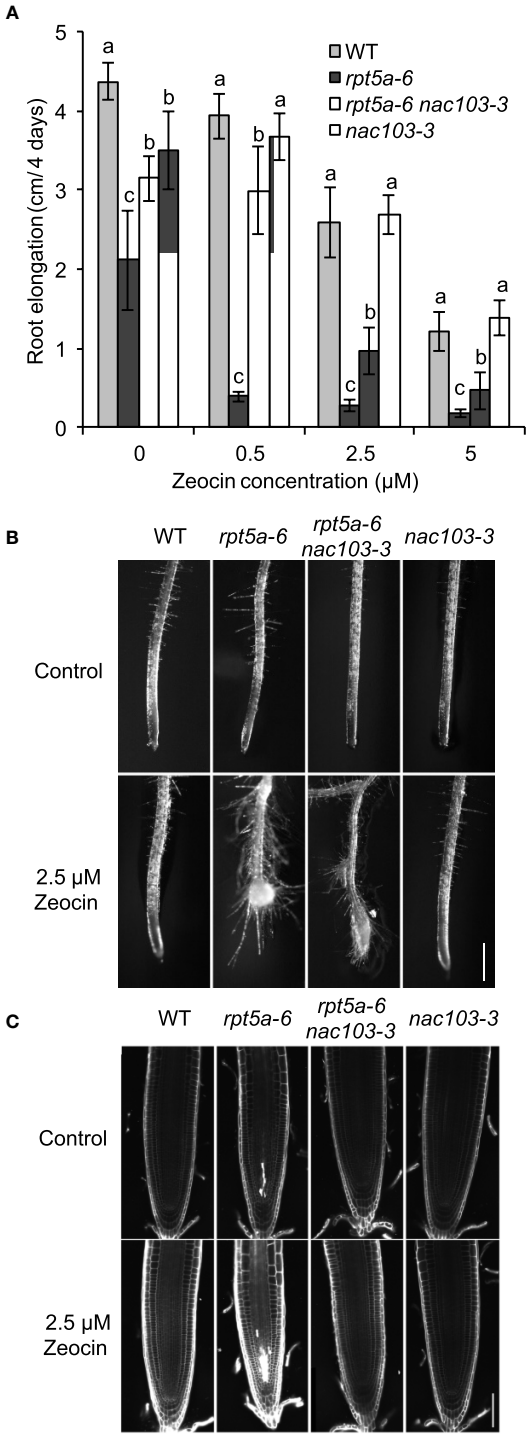

FIGURE 6
DNA damage sensitivity of *rpt5a-6* is suppressed in *rpt5a-6 nac103-3*. Sensitivity to DNA damage causing regent Zeocin. **(A)** Root elongation under various Zeocin concentrations. Seedlings were precultured the control condition for six days and for further four days with or without Zeocin. Primary root elongation during last four days were measured. Values represent mean ± standard deviation of ten seedlings. For each condition, groups sharing same letters were not significantly different by Tukey-Kramer's test at $p < 0.05$. **(B)** Primary root tip morphology of 11-day-old seedlings under control or 2.5 μM Zeocin conditions. Bar, 500 μm. **(C)** Confocal microscopy of root meristems. Six-day-old seedlings grown under the control condition were treated with control or 2.5 μM Zeocin conditions for 16 hours. Cell walls and dead cells were visualized with propidium iodide. Bar, 50 μm.

NAC103 gene is responsible for the growth defects caused by DNA damage in the *rpt5a-6* mutant.

3.8 *nac103-3* mutation alleviates ROS accumulation under excess boron stress in root tips

The accumulation of DNA damage motivated us to focus on reactive oxygen species (ROS) because oxidation by ROS is known to be a cause of DNA damage (Amor et al., 1998). To observe ROS accumulation in the mutants, we stained control and excess boron-treated roots with nitroblue tetrazolium (NBT), rendering a purple stain to the superoxide (Figure 7). Under excess boron conditions, the stain was more intense in *rpt5a-6* mutant roots than that in the wild-type roots. However, *rpt5a-6 nac103-3* showed lesser staining intensity than both the *rpt5a-6* and the *rpt5a-6 nac103-3* mutants, but it was comparable to that associated with the wild type. These results suggest that NAC103 is responsible for ROS accumulation in *rpt5a-6* under excess boron stress.

3.9 *SOG1* is not involved in excess boron sensitivity in *rpt5a* mutants

As *NAC103* has been suggested to function downstream of *SOG1* transcription factor, a master regulator of DNA damage response genes (Ryu et al., 2019), we examined whether the suppression of excess boron sensitivity by *nac103* mutation is related to SOG1 pathway. Examination of root elongation revealed that excess boron sensitivity of *rpt5a-6 sog1-101* was not significantly different from *rpt5a-6*, suggesting that *sog1-101* mutation does not alleviate excess boron sensitivity of *rpt5a-6* (Figure 8A). In addition, excess boron sensitivity of *rpt5a-6 nac103 sog1-101* triple mutant was similar to that of *rpt5a-6 nac103* double mutant. To examine whether induction of *NAC103* by excess boron stress depends on *SOG1*, we examined *NAC103* mRNA abundance in *sog1-101* mutant. Compared to *rpt5a-6* mutant, *rpt5a-6 sog1-101* exhibited even higher *NAC103* mRNA abundance under excess boron conditions, indicating that upregulation of NAC103 under excess B condition does not require *SOG1* (Figure 8B). Taken together, these results suggest that contribution of *NAC103* to excess boron sensitivity is likely due to its involvement in pathways other than the SOG1 pathway.

4 Discussion

4.1 Identification of causal genes as *rpt5a* suppressor mutants

We were able to limit the positional identification of the suppressor mutation in *rpt5a-6 sup1* to the chromosomal region of 353 kb (Figure 2A). Whole-genome sequencing revealed DNA sequences in this region; within that region, we found only a single homozygous mutation in the *NAC103* gene. Through independent experiments, we identified 11 mutants exhibiting phenotype similar

10.3389/fpls.2023.1099816

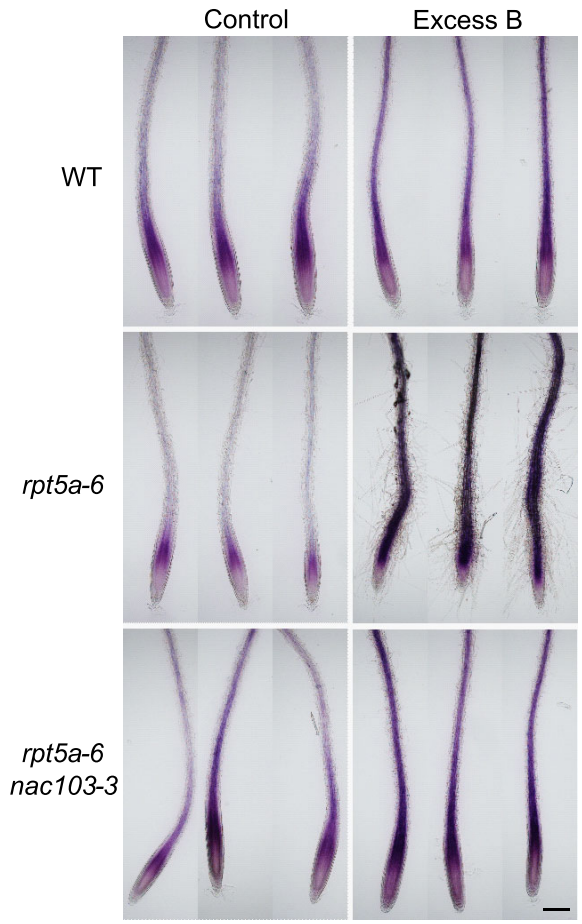

FIGURE 7
Superoxide accumulation in root tips of *rpt5a-6* and *rpt5a-6 nac103-3*. Seedlings were grown for six days under control conditions (30 μM boric acid) and further three days on control or excess boron conditions (3 mM boric acid). Superoxide was observed as purple stain by nitroblue tetrazolium (NBT) staining. Images from three biological replicates are shown. Bar, 200 μm.

to that of *rpt5a-6 sup1*. Examination of the *NAC103* sequences revealed that 7 alleles out of the 11 *rpt5a-4* lines carried distinct mutations in *NAC103* (Figure 2B). These results suggest that *NAC103* is the gene responsible for the suppression of the *rpt5a* mutant phenotype, but it is fair to consider the possibility that NAC103 is located on so-called hot spot of mutagenesis by EMS. In other projects apart from boron toxicity, we also sequenced other eight mutants, which were also mutagenized in a manner similar to the *rpr5a-6 sup1* mutant. As none of the eight mutants carried a mutation in *NAC103*, the mutations in *NAC103* in *rpt5a* suppressor mutants should not be attributed to a mutagenesis hot spot. In addition, all the *NAC103* mutations in the *rpt5a* suppressor mutants were located within the N-terminus half of the gene, which was annotated as the NAC domain, a conserved DNA binding domain (Figure 2). Thus, we suggest that the mutations can be attributed to the functionality of the proteins rather than chromosomal location. In the complementation tests, the introduction of the *proNAC103-NAC103-GFP* construct partially reversed the phenotype of the *rpt5a-6 sup1* mutant to that of the *rpt5a-6*. The incomplete recovery could be attributed to possible effects GFP-tag fused to C-terminus of NAC103, rather than low expression levels of the transgene, because *NAC103* mRNA levels in the transgenic lines were comparable or higher than in *rpt5a-6* (Supplementary Figure 4). However, given that the changes in phenotype were observed, the transgene is at least partially functional, and *NAC103* gene is likely to be involved in the root growth defects in the *rpt5a-6* mutant under boron stress. Taken together, we conclude that the mutation in NAC103 is responsible for the suppression of the excess boron-sensitive phenotype of *rpt5a* mutant.

4.2 Involvement of *NAC103* in excess boron sensitivity

The NAC family is one of the largest families of plant-specific transcription factors (Ooka et al., 2003). *NAC103* has been characterized in the context of its expression in response to unfolded proteins levels (Sun et al., 2013). They showed that the NAC103 protein is a substrate of the 26S proteasome, and that it is maintained at a low concentration under normal conditions; furthermore, it is stabilized under unfolded protein stress.

The upregulation of NAC103 in turn activates the transcription of downstream unfolded protein response genes such as molecular chaperones [namely, *calnexin* (*CNX*), *calreticulin* (*CRT*), and *protein disulfide-isomerase 5* (*PDI5*), and *ubiquitin conjugase 32* (*UBC32*)]. In our study, mRNA accumulation of those *NAC103* downstream genes was not significantly different between the *rpt5a-6* and *rpt5a-6 nac103-3* mutants (Figure 4B), suggesting that these genes were not responsible for the suppression of the *rpt5a-6* phenotype in *rpt5a-6 nac103-3* mutant plants. In addition, our previous study demonstrated that excess boron treatment does not affect accumulation of poly-ubiquitinated proteins, which include unfolded proteins to be degraded by proteasome (Sakamoto et al., 2018) Thus we can deduce that excess boron treatment does not induce unfolded protein significantly. These together suggest that it is not unfolded protein response pathway that is critical for excess boron response.

It has been reported that NAC103 interacts with VND, a master regulator of xylem vessel differentiation that functions as a transcription activator (Yamaguchi et al., 2015). According to their yeast two-hybrid assay, NAC103 can form hetero-complexes with various other NAC transcription factors, such as VND1, VND2, VND3, VND7, NAC1, CUC2, and VNI1. This suggests that *NAC103* can play multiple roles in different cellular processes through its interaction with different counterparts. They also indicated that *NAC103* may regulate cellular stress response by binding with other NAC domain proteins. This point of view provides possible explanation for our observation that overexpressing *NAC103* alone did not affect root growth under excess B conditions. If NAC103 requires counterpart(s) to be functional under excess B conditions, overexpressing NAC103 could affect the phenotype only when enough number of counterpart proteins are available. Identification of the potential counterpart in future study would clarify this point.

Assuming that the mutations in NAC103 are loss of function, our results suggest that accumulation of NAC103 has negative effects on root growth, because *nac103* mutations suppressed the growth defects

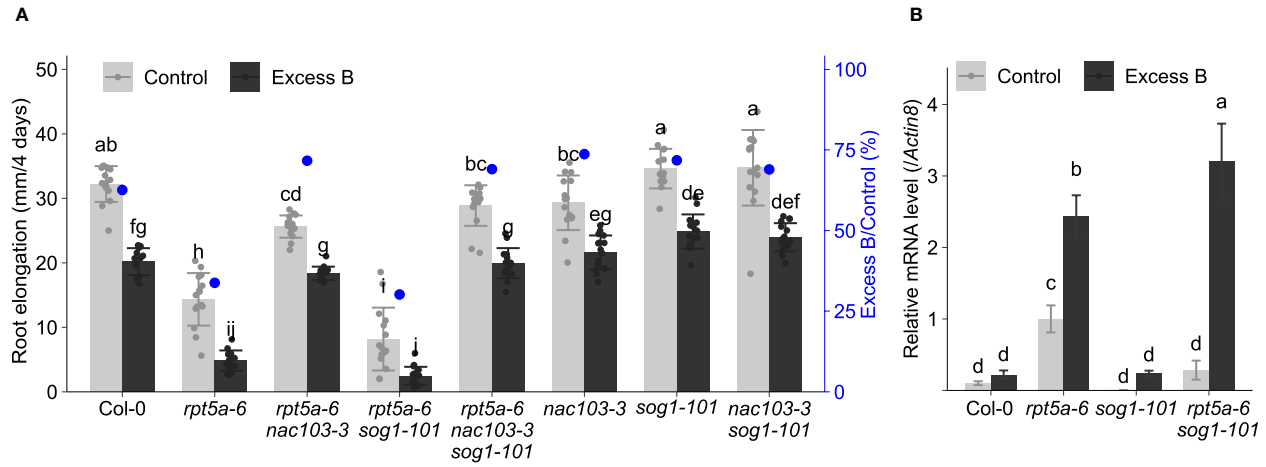

FIGURE 8
Effect of *sog1* mutation on excess boron sensitivity in root growth. **(A)** Root elongation of rpt5a-6, *nac103-3, sog1-101*, and their double and triple mutants. Seedlings were precultured in normal conditions (30 μM boric acid) for six days and then transferred to excess boron (3 mM boric acid) or control conditions. Root elongation during four days after the transfer was measured. Values are mean ± standard deviation of 15-16 measurements. Groups sharing the same letters are not significantly different at $p < 0.05$ by Tukey-Kramer's test. **(B)** *NAC103*m RNA accumulation in *sog1-101* mutant. Plants were grown under the same condition as **(A)** and mRNA accumulation was quantified by qRT-PCR. Expression levels were normalized by *Actin8*. Values represent mean ± standard deviation of four biological replicates. Groups sharing the same letters are not significantly different at $p < 0.05$ by Tukey's test.

of *rpt5a* mutants. Considering that *NAC103* is a substrate of the 26S proteasome and that *RPT5A* is suggested its involvement in recognition of poly-ubiquitinated proteins in the Ub–proteasome pathway (Lam et al., 2002), it can be speculated that control of NAC103 protein accumulation was altered in *rpt5a* mutants. This should be confirmed by observation of NAC103-GFP in *rpt5a-6 nac103-3*. However, under our experimental conditions, we could not detect GFP fluorescence in transgenic plants introduced with the *proNAC103-NAC103-GFP* construct, even after treatment with MG132, which stabilizes the NAC103 protein (Sun et al., 2013). Could be because we did not have enough expression to observe fluorescence as the construct was driven by *NAC103* own promoter, not by a strong constitutive promoter.

4.3 Possible mechanisms of excess boron sensitivity in roots

In *Brassica napus*, homologue of *NAC103*, *BnaNAC103* was identified with 75.4% identity and 76.5% similarity at the nucleotide level (Niu et al., 2014). Furthermore, they revealed that in *Nicotiana benthamiana* leaves, overexpression of *BnaNAC103* causes ROS accumulation and induces cell death. They mentioned in the report that whether *NAC103 in A. thaliana* (*AtNAC103*) regulates cell death is unknown yet. However, it is likely that *AtNAC103* has a similar negative function considering that ROS accumulation and cell death in the *rpt5a-6* mutant under excess boron stress was suppressed in *rpt5a-6 nac103-3* (Figure 7). Although how *NAC103* could induce ROS remains unclear, the simplest hypothesis should be that *NAC103* may upregulate ROS producing enzyme, or negative regulator of ROS scavenger, considering that NAC103 is a transcription factor.

The observed ROS accumulation and cell death under excess boron conditions can be interpreted in two ways: ROS induces cell death, or, cell death releases ROS from cells. Although further careful investigation is needed to dissect this cause-effect relationship, our results allow us to infer it. After three days of excess boron treatment, strong NBT staining was observed throughout most of the root area in *rpt5a* mutant, suggesting that ROS is accumulated in whole root (Figure 7). On the other hand, under the same treatment condition, cell death was observed only in stele cells in the meristem (Supplementary Figure 1). This suggests that, at least in most of the root tissue, ROS accumulation does not require preceding cell death. Thus, we deduce that it is more likely that ROS is the cause of cell death, rather than ROS accumulation is the result of cell death.

Several independent microarray analyses have revealed that *NAC103* expression is induced during conditions of DNA damage caused by γ-ray exposure or treatment with hydroxyurea or bleomycin (Culligan et al., 2006; Yoshiyama et al., 2009; Cools et al., 2011; Yi et al., 2014). Ryu et al. (2019) reported that *NAC103* is induced by SOG1, a NAC transcription factor known to regulate DNA damage response gene, and is partially responsible for DNA damage response phenotypes. They revealed that *NAC103* interacts with the putative promoter regions of *Rad51, PARP2* (AT4G02390, which is referred to as *PARP1* in Ryu et al., 2018), *RPA1E, BRCA1* and *At4g22960*, suggesting that *NAC103* is a putative *SOG1*-dependent DNA damage response regulator. However, our results indicate that *NAC103* has some functions in *SOG1*-independent pathway, because *NAC103* induction under excess boron condition was *SOG1*-independent and *sog1* mutation did not suppress excess boron sensitivity of *rpt5a* mutant (Figure 8). In our study, the *nac103-3* mutation suppressed both DNA damage and ROS accumulation in the root tips of *rpt5a-6* mutant plants in the presence of excess boron. This indicates that irregular accumulation of *NAC103* in the proteasome mutant *rpt5a-6* induces DNA damage and ROS accumulation under excess boron stress, suggesting the role of

NAC103 in DNA damage induction or suppression of DNA repair and/or ROS production or radical scavenging activity.

In summary, our study sheds light on the mechanisms underlying excess boron-induced DNA damage accumulation and growth reduction (Figure 9). Our previous study revealed that excess boron causes histone acetylation and BRM-dependent chromatin opening (Sakamoto et al., 2018). This is thought to increase the susceptibility to DNA damaging factors. On the other hand, our study suggested that NAC103 is involved in a downstream pathway, which is likely responsible for the accumulation of a DNA damaging factor, ROS. Excess boron stress induces NAC103 mRNA in *SOG1*-independent manner. In the wild type, NAC103 protein level is likely maintained at low level by the 26S proteasome, which would ameliorate excessive ROS accumulation. However, an alteration in the 26S proteasome of the *rpt5a-6* mutant can lose this maintenance, which may in turn result in accelerated ROS accumulation. This would result in increased DNA damage, which could be the direct cause for root growth inhibition. *rpt5a-6* mutation also induced *NAC103* mRNA, but considering that the induction was observed even under control conditions, this mRNA induction itself is likely due to a boron-independent mechanism.

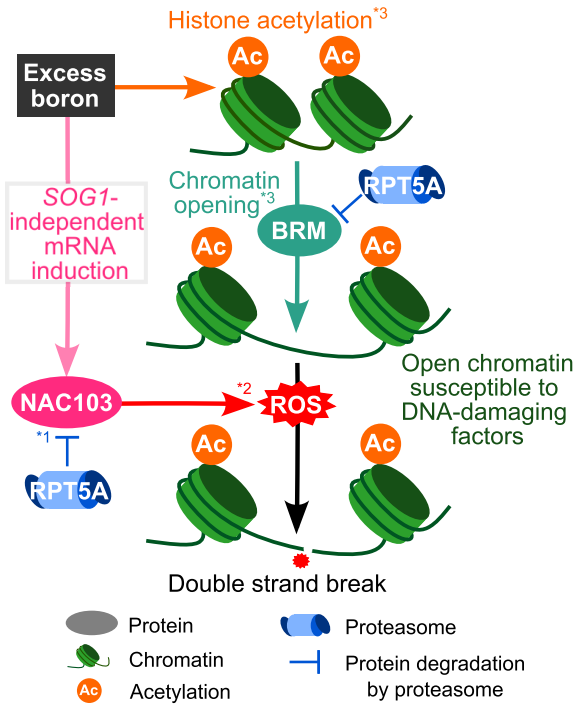

FIGURE 9
Suggested mechanisms for DNA damage caused by excess boron stress in wild type plants. Excess boron stress induces *NAC103* mRNA in *SOG1*-independent manner. As NAC103 protein is degraded *via* proteasome pathway (*[1] Sun et al., 2013), mutation in proteasome (RPT5A) should result in over-accumulation of NAC103 protein. Over-accumulation of *NAC103* is likely to induce ROS accumulation (*[2] Niu et al., 2014). ROS is a major cause of DNA damage. Together with the known BRAHMA(BRM)-dependent pathway in which excess boron stress induces histone acetylation to loosen chromatin, making DNA susceptible to DNA-damaging factors (*[3]Sakamoto et al., 2018), the NAC103 dependent pathway plays a crucial role in growth defects under excess boron conditions.

Data availability statement

The original contributions presented in the study are included in the article/Supplementary Material. Further inquiries can be directed to the corresponding authors.

Author contributions

NS: Conceptualization, investigation, resources, writing – original draft, visualization, funding acquisition. TS: Conceptualization, investigation, resources, writing – review and editing, visualization, funding acquisition. TK: Investigation, resources. RT: Investigation, writing – review and editing. KY: Formal analysis. SSh: Formal analysis. MY: Investigation. MH: Investigation, resources. SSa: Investigation, resources, funding acquisition. TF: Conceptualization, resources, writing – review and editing, supervision, funding acquisition. All authors contributed to the article and approved the submitted version.

Funding

This work was supported in part by a grant from the Japan Society for the Promotion of Science (No. 15J11021 and 21H05653 to NS, No. 25221202 and 18H05490 to TF), Kato Memorial Bioscience Foundation to TS, and NIBB Collaborative Research Program (12-103 to SS).

Acknowledgments

We would like to thank Yuko Kawara and Sayoko Mibu for their excellent technical assistance, and the Nottingham Arabidopsis Stock Centre (NASC) (http://arabidopsis.info) for *sog1-101* (GABI_602B10).

Conflict of interest

The authors declare that the research was conducted in the absence of any commercial or financial relationships that could be construed as a potential conflict of interest.

Publisher's note

Supplementary material

The Supplementary Material for this article can be found online at: https://www.frontiersin.org/articles/10.3389/fpls.2023.1099816/full#supplementary-material

References

Amor, Y., Babiychuk, E., Inzé, D., and Levine, A. (1998). The involvement of poly (ADP-ribose) polymerase in the oxidative stress responses in plants. *FEBS Lett.* 440, 1–7. doi: 10.1016/S0014-5793(98)01408-2

Aquea, F., Federici, F., Moscoso, C., Vega, A., Jullian, P., Haseloff, J., et al. (2012). A molecular framework for the inhibition of arabidopsis root growth in response to boron toxicity. *Plant Cell Environ.* 35, 719–734. doi: 10.1111/j.1365-3040.2011.02446.x

Bechtold, N., and Pelletier, G. (1998). "In planta agrobacteriummediated transformation of adult arabidopsis thaliana plants by vacuum infiltration," in *Arabidopsis protocolsAnonymous* (Totowa, NJ: Humana Press Springer), 259–266. doi: 10.1385/0-89603-391-0:259

Ciechanover, A. (1998). The ubiquitin-proteasome pathway: on protein death and cell life. *EMBO J.* 17, 7151–7160. doi: 10.1093/emboj/17.24.7151

Clough, S. J., and Bent, A. F. (1998). Floral dip: A simplified method forAgrobacterium-mediated transformation ofArabidopsis thaliana. *Plant J.* 16, 735–743. doi: 10.1046/j.1365-313x.1998.00343.x

Cools, T., Iantcheva, A., Weimer, A. K., Boens, S., Takahashi, N., Maes, S., et al. (2011). The arabidopsis thaliana checkpoint kinase WEE1 protects against premature vascular differentiation during replication stress. *Plant Cell* 23, 1435–1448. doi: 10.1105/tpc.110.082768

Culligan, K. M., Robertson, C. E., Foreman, J., Doerner, P., and Britt, A. B. (2006). ATR and ATM play both distinct and additive roles in response to ionizing radiation. *Plant J.* 48, 947–961. doi: 10.1111/j.1365-313X.2006.02931.x

Curtis, M. D., and Grossniklaus, U. (2003). A gateway cloning vector set for high-throughput functional analysis of genes in planta. *Plant Physiol.* 133, 462–469. doi: 10.1104/pp.103.027979

Dye, M., Buchanan, L., Dorofaeff, F., and Beecroft, F. (1983). Die-back of apricot trees following soil application of boron. *New Z. J. Exp. Agric.* 11, 331–342. doi: 10.1080/03015521.1983.10427778

Fu, H., Reis, N., Lee, Y., Glickman, M. H., and Vierstra, R. D. (2001). Subunit interaction maps for the regulatory particle of the 26S proteasome and the COP9 signalosome. *EMBO J.* 20, 7096–7107. doi: 10.1093/emboj/20.24.7096

Fujiwara, T., Hirai, M. Y., Chino, M., Komeda, Y., and Naito, S. (1992). Effects of sulfur nutrition on expression of the soybean seed storage protein genes in transgenic petunia. *Plant Physiol.* 99, 263–268. doi: 10.1104/pp.99.1.263

Końca, K., Lankoff, A., Banasik, A., Lisowska, H., Kuszewski, T., Góźdź, S., et al. (2003). A cross-platform public domain PC image-analysis program for the comet assay. *Mutat. Research/Genetic Toxicol. Environ. Mutagenesis* 534, 15–20. doi: 10.1016/s1383-5718(02)00251-6

Kurepa, J., and Smalle, J. A. (2008). Structure, function and regulation of plant proteasomes. *Biochimie* 90, 324–335. doi: 10.1016/j.biochi.2007.07.019

Kurepa, J., Walker, J. M., Smalle, J., Gosink, M. M., Davis, S. J., Durham, T. L., et al. (2003). The small ubiquitin-like modifier (SUMO) protein modification system in arabidopsis. accumulation of SUMO1 and -2 conjugates is increased by stress. *J. Biol. Chem.* 278, 6862–6872. doi: 10.1074/jbc.M209694200

Lam, Y. A., Lawson, T. G., Velayutham, M., Zweier, J. L., and Pickart, C. M. (2002). A proteasomal ATPase subunit recognizes the polyubiquitin degradation signal. *Nature* 416, 763–767. doi: 10.1038/416763a

Nable, R. O., Bañuelos, G. S., and Paull, J. G. (1997). Boron toxicity. *Plant Soil* 193, 181–198. doi: 10.1023/A:1004272227886

Niu, F., Wang, B., Wu, F., Yan, J., Li, L., Wang, C., et al. (2014). Canola (Brassica napus l.) NAC103 transcription factor gene is a novel player inducing reactive oxygen species accumulation and cell death in plants. *Biochem. Biophys. Res. Commun.* 454, 30–35. doi: 10.1016/j.bbrc.2014.10.057

Ogita, N., Okushima, Y., Tokizawa, M., Yamamoto, Y. Y., Tanaka, M., Seki, M., et al. (2018). Identifying the target genes of SUPPRESSOR OF GAMMA RESPONSE 1, a master transcription factor controlling DNA damage response in arabidopsis. *Plant J.* 94, 439–453. doi: 10.1111/tpj.13866

Ooka, H., Satoh, K., Doi, K., Nagata, T., Otomo, Y., Murakami, K., et al. (2003). Comprehensive analysis of NAC family genes in oryza sativa and arabidopsis thaliana. *DNA Res.* 10, 239–247. doi: 10.1093/dnares/10.6.239

Reid, R. J., Hayes, J. E., Post, A., Stangoulis, J. C. R., and Graham, R. D. (2004). A critical analysis of the causes of boron toxicity in plants. *Plant Cell Environ.* 27, 1405–1414. doi: 10.1111/j.1365-3040.2004.01243.x

Ryu, T. H., Go, Y. S., Choi, S. H., Kim, J., Chung, B. Y., and Kim, J. (2019). SOG 1-dependent NAC 103 modulates the DNA damage response as a transcriptional regulator in arabidopsis. *Plant J.* 98, 83–96. doi: 10.1111/tpj.14201

Sakamoto, T., Inui, Y. T., Uraguchi, S., Yoshizumi, T., Matsunaga, S., Mastui, M., et al. (2011). Condensin II alleviates DNA damage and is essential for tolerance of boron overload stress in arabidopsis. *Plant Cell* 23, 3533–3546. doi: 10.1105/tpc.111.086314

Sakamoto, T., Tsujimoto-Inui, Y., Sotta, N., Hirakawa, T., Matsunaga, T. M., Fukao, Y., et al. (2018). Proteasomal degradation of BRAHMA promotes boron tolerance in arabidopsis. *Nat. Commun.* 9, 5285. doi: 10.1038/s41467-018-07393-6

Schindelin, J., Arganda-Carreras, I., Frise, E., Kaynig, V., Longair, M., Pietzsch, T., et al. (2012). Fiji: An open-source platform for biological-image analysis. *Nat. Methods* 9, 676–682. doi: 10.1038/nmeth.2019

Sinha, P., Dube, B., Singh, M., and Chatterjee, C. (2006). Effect of boron stress on yield, biochemical parameters and quality of tomato. *Indian J. Horticulture* 63, 39–43.

Smalle, J., and Vierstra, R. D. (2004). The ubiquitin 26S proteasome proteolytic pathway. *Annu. Rev. Plant Biol.* 55, 555–590. doi: 10.1146/annurev.arplant.55.031903.141801

Sun, L., Yang, Z., Song, Z., Wang, M., Sun, L., Lu, S., et al. (2013). The plant-specific transcription factor gene NAC103 is induced by bZIP60 through a new cis-regulatory element to modulate the unfolded protein response in arabidopsis. *Plant J.* 76, 274–286. doi: 10.1111/tpj.12287

Vierstra, R. D. (2003). The ubiquitin/26S proteasome pathway, the complex last chapter in the life of many plant proteins. *Trends Plant Sci.* 8, 135–142. doi: 10.1016/S1360-1385(03)00014-1

Warington, K. (1923). The effect of boric acid and borax on the broad bean and certain other plants. *Ann. Bot.* 37, 629–672. doi: 10.1093/oxfordjournals.aob.a089871

Wolf, D. H., and Hilt, W. (2004). The proteasome: a proteolytic nanomachine of cell regulation and waste disposal. *Biochim. Biophys. Acta (BBA)-Molecular Cell Res.* 1695, 19–31. doi: 10.1016/j.bbamcr.2004.10.007

Yamaguchi, M., Nagahage, I. S. P., Ohtani, M., Ishikawa, T., Uchimiya, H., Kawai-Yamada, M., et al. (2015). Arabidopsis NAC domain proteins VND-INTERACTING1 and ANAC103 interact with multiple NAC domain proteins. *Plant Biotechnol* 32.2:119–123. doi: 10.5511/plantbiotechnology.15.0208a

Yi, D., Alvim Kamei, C. L., Cools, T., Vanderauwera, S., Takahashi, N., Okushima, Y., et al. (2014). The arabidopsis SIAMESE-RELATED cyclin-dependent kinase inhibitors SMR5 and SMR7 regulate the DNA damage checkpoint in response to reactive oxygen species. *Plant Cell* 26, 296–309. doi: 10.1105/tpc.113.118943

Yoshiyama, K., Conklin, P. A., Huefner, N. D., and Britt, A. B. (2009). Suppressor of gamma response 1 (SOG1) encodes a putative transcription factor governing multiple responses to DNA damage. *Proc. Natl. Acad. Sci. USA* 106, 12843–12848. doi: 10.1073/pnas.0810304106

frontiers | Frontiers in Plant Science

TYPE Original Research
PUBLISHED 08 June 2023
DOI 10.3389/fpls.2023.1201129

OPEN ACCESS

EDITED BY
Ali Ferjani,
Tokyo Gakugei University, Japan

REVIEWED BY
Mingshu Cao,
AgResearch Ltd, New Zealand
Jianxin Shi,
Shanghai Jiao Tong University, China

*CORRESPONDENCE
Keiichi Mochida
keiichi.mochida@riken.jp
Masami Yokota Hirai
masami.hirai@riken.jp

†These authors have contributed equally to this work and share last authorship

RECEIVED 06 April 2023
ACCEPTED 24 May 2023
PUBLISHED 08 June 2023

CITATION
Uchida K, Kim J-S, Sato M, Tabeta H, Mochida K and Hirai MY (2023) A metabolome genome-wide association study implicates histidine *N*-pi-methyltransferase as a key enzyme in *N*-methylhistidine biosynthesis in *Arabidopsis thaliana*. *Front. Plant Sci.* 14:1201129. doi: 10.3389/fpls.2023.1201129

A metabolome genome-wide association study implicates histidine *N*-pi-methyltransferase as a key enzyme in *N*-methylhistidine biosynthesis in *Arabidopsis thaliana*

Kai Uchida[1], June-Sik Kim[1,2], Muneo Sato[1], Hiromitsu Tabeta[1], Keiichi Mochida[1,3,4,5*†] and Masami Yokota Hirai[1,6*†]

[1]RIKEN Center for Sustainable Resource Science, Yokohama, Kanagawa, Japan, [2]Institute of Plant Science and Resources, Okayama University, Kurashiki, Okayama, Japan, [3]Kihara Institute for Biological Research, Yokohama City University, Yokohama, Kanagawa, Japan, [4]School of Information and Data Sciences, Nagasaki University, Nagasaki, Nagasaki, Japan, [5]RIKEN Baton Zone Program, Yokohama, Kanagawa, Japan, [6]Department of Applied Biosciences, Graduate School of Bioagricultural Science, Nagoya University, Nagoya, Japan

A genome-wide association study (GWAS), which uses information on single nucleotide polymorphisms (SNPs) from many accessions, has become a powerful approach to gene identification. A metabolome GWAS (mGWAS), which relies on phenotypic information based on metabolite accumulation, can identify genes that contribute to primary and secondary metabolite contents. In this study, we carried out a mGWAS using seed metabolomic data from *Arabidopsis thaliana* accessions obtained by liquid chromatography–mass spectrometry to identify SNPs highly associated with the contents of metabolites such as glucosinolates. These SNPs were present in genes known to be involved in glucosinolate biosynthesis, thus confirming the effectiveness of our analysis. We subsequently focused on SNPs detected in an unknown methyltransferase gene associated with *N*-methylhistidine content. Knockout and overexpression of *A. thaliana* lines of this gene had significantly decreased and increased *N*-methylhistidine contents, respectively. We confirmed that the overexpressing line exclusively accumulated histidine methylated at the pi position, not at the tau position. Our findings suggest that the identified methyltransferase gene encodes a key enzyme for *N*-methylhistidine biosynthesis in *A. thaliana*.

KEYWORDS

GWAS, metabolomic analysis, *N*-methylhistidine, methyltransferase, LC-MS/MS

Introduction

Plants accumulate a wide variety of metabolites. Plant-produced metabolites differ among species, and recent studies suggest that within-species metabolism is highly variable, both qualitatively and quantitatively, as well (Fernie and Tohge, 2017). To identify genes responsible for the variable accumulation of metabolites in plants, quantitative trait locus (QTL) analysis based on progenies of two parental strains that differ in a quantitative phenotype of interest has often been used. In recent years, genomes of representative accessions of single plant species as well as hundreds to thousands of accession-specific genomes have been determined, thereby providing a rich source of information on within-species genome-wide genetic variations, such as single nucleotide polymorphisms (SNPs). As a consequence, interest in population genomics has greatly increased.

A genome-wide association study (GWAS) is a method for identifying causative genetic loci of phenotypic variations through testing of genetic associations between genome-scale polymorphisms and phenotypic datasets. Compared with QTL mapping, which only assesses allelic diversity segregated between particular parents, the GWAS approach provides a higher resolution of causal coordinates and more fully explores phenotypic diversity in a natural population. As an extension, metabolic or metabolome GWAS (mGWAS), which uses metabolomic data for phenotypic information, has been applied to identify genes related to specific metabolites (Riedelsheimer et al., 2012; Angelovici et al., 2013; Chen et al., 2014; Matsuda et al., 2015; Slaten et al., 2020; Zeng et al., 2020; Wei et al., 2021; Zhao et al., 2023). Like a conventional QTL analysis, a GWAS can be used to find a causative gene of a specific phenotype of interest and thus serve as a hypothesis-driven approach to functional genomics. In addition, a GWAS can be applied as a data-driven approach, where a large number of phenotypes are first analyzed without setting any objective and a hypothesis is then formulated based on the results. Because it is not hypothesis-based, data-driven research has the potential to yield unexpected results. In fact, a number of cases have been reported in which GWASs have led to novel findings. For instance, a GWAS using osmotic tolerance as an indicator revealed the involvement of genes participating in pathogen resistance (Ariga et al., 2017). As another example, a study using glutamine-related traits in seeds revealed a trait association with aliphatic glucosinolate biosynthesis genes (Slaten et al., 2020).

In the present study, we performed a mGWAS using SNP information and metabolomic data from seeds of *Arabidopsis thaliana* accessions. This mGWAS revealed the association of many metabolites with SNPs. For example, the accumulation of glucosinolates, which are Brassicales-specific specialized metabolites, was associated with SNPs in known glucosinolate biosynthetic genes, thus validating our GWAS method. In many cases, however, functional characterization of genes showing associations with accumulations of some metabolites based solely on annotations was difficult. We subsequently focused on SNPs highly associated with the accumulation of pi-methyl histidine (πMH or 3-methyl-L-histidine) that were present in a gene (AT2G32160) annotated as a methyltransferase gene. Overexpression and knockout lines of this gene exhibited significantly increased and decreased πMH contents, respectively. This methyltransferase gene may thus be involved in the biosynthesis of πMH in *A. thaliana*. Our results demonstrate that data-driven mGWAS is a useful way to identify unexpected novel genes.

Materials and methods

Plants

Seeds of 245 *A. thaliana* accessions were purchased from the Arabidopsis Biological Resource Center. For the mGWAS, plants were grown from the original seeds in a greenhouse at 22°C under fluorescent light (16-h light/8-h dark), and mature seeds were harvested.

Seeds of SALK lines (Alonso et al., 2003) (AT2G32160, SALK_077267 and SALK_118137; AT2G32170, SALK_046329) (Supplementary Figure 1) were also purchased from the Arabidopsis Biological Resource Center. Homozygous mutants were confirmed by genomic PCR using primers obtained from T-DNA Express (http://signal.salk.edu/cgi-bin/tdnaexpress). The transgenic lines named *MT160*-OE and *MT170*-OE were established in the Col-0 background by introducing the CDS of AT2G32160.3 or AT2G32170.1 driven by the Cauliflower mosaic virus 35S promoter by the floral dip method (Clough and Bent, 1998) using *Agrobacterium tumefaciens* strain GV3101 (pMP90) transformed with vectors created as described below (under "Cloning").

Transgenic plants were selected using GFP fluorescence as an indicator, and T_3 seeds with confirmed fluorescence were used in subsequent experiments. Plants for the expression analysis were grown on half-strength Murashige and Skoog (MS) medium (10 g l^{-1} sucrose, 8 g l^{-1} agar, 1 g l^{-1} MES, and MS vitamin solution, pH 5.7) at 22°C under 16-h light/8-h dark conditions. After 3 weeks, aerial parts were sampled.

AT2G32160-OE plants for πMH analysis were cultured hydroponically as follows. Hydroponic sponges (2.5 × 2.5 × 2.5 cm; Kyowa, Osaka, Japan) were cut horizontally into thirds (2.5 × 2.5 × 0.8 cm), and a slit was introduced into each section. The divided sponges were then soaked in 1× Hyponica hydroponic liquid fertilizer (Kyowa). Water-absorbing sheets (Miki Tokushu Paper Mfg., Ehime, Japan) were soaked in the same medium. Roots of plants grown for 2 weeks under the above-mentioned conditions were placed between a half-folded absorbent sheet, placed in the sponge cutouts, and transferred to 50-ml amber conical tubes (Eppendorf, Hamburg, Germany) filled with the same liquid medium. The plants in each tube were lightly covered with plastic wrap and grown for 1 week. Col-0 plants were grown next to each OE plant as a control. Six grown plants each for different genotypes were used for the metabolomic analysis. A photograph of plants before sampling is shown in Supplementary Figure 2.

Chemicals

πMH and tau-methyl-L-histidine (τMH) for GC-MS/MS structural analyses were purchased from Fujifilm Wako Pure Chemical Corporation (Osaka, Japan) as 3-methyl-L-histidine (product code 139-17851) and 1-methyl-L-histidine (product code 136-17861), respectively.

Metabolomic analysis

To obtain metabolomic data for the mGWAS, seed samples were prepared by scooping approximately 50 seeds with a seed spoon (Bio Medical Science, Tokyo, Japan). Except for 10 accessions with insufficient seeds, prepared in triplicate, six replicates were prepared per accession. Metabolite extraction was performed according to previous studies (Sawada et al., 2009; Uchida et al., 2020). A metabolomic analysis for mGWAS was performed on a liquid chromatography–tandem quadruple mass spectrometry system (UPLC-TQS, Waters, Milford, MA, USA) according to previously reported methods (Sawada et al., 2009; Sawada et al., 2012) using the multiple reaction monitoring (MRM) conditions listed in Supplementary Table 2. The metabolome analysis included blank samples (only the extraction solvent) and the average intensity of the blank samples was used as the basal noise level. We generated six metabolomic datasets: three with data from 245 accessions, and three with data from 235 accessions.

For the metabolomic analysis, plant samples (aerial parts and roots) and seeds were suspended in 80% (v/v) methanol with 0.1% (v/v) formic acid and internal standards (8.4 nM of lidocaine and 210 nM of 10-camphorsulfonic acid) to a concentration of 4 mg/ml and approximately 50 seeds/ml, respectively, and extracted as described above. Quantification of πMH in plant samples and seeds of *MT160*- and *MT170*-OE and SALK lines was performed using LC-QqQ-MS (LCMS-8050, Shimadzu, Kyoto, Japan). The analysis was carried out according to our previous study (Uchida et al., 2020) using the MRM conditions detailed in Supplementary Table 3.

mGWAS

We retrieved a publicly available, genome-wide polymorphism dataset of Arabidopsis accessions genotyped with the Arabidopsis 250k-SNP chip (Atwell et al., 2010) and generated a custom variation dataset comprising 213,925 biallelic SNP loci for these 220 accessions (Supplementary Table 1). To conduct a GWAS based on the six metabolome datasets, we used the multiple loci mixed linear model of GAPIT v3.1.0 (Wang and Zhang, 2021) in R v4.1.3. More specifically, we estimated the genetic relationship using a Multiple Loci Mixed Linear Model. Initially, we listed SNPs with p-value less than 1×10^{-5} and from the coding regions of genes overlapping these SNPs, we complied 1,683 genes. We displayed the results as quantile–quantile and Manhattan plots using the R package qqman v0.1.8 (Turner, 2018). The in-house Python and R scripts used to build the custom dataset and perform the GWAS are available at a GitHub repository (https://github.com/junesk9/).

Cloning

The coding sequence (CDS) of AT2G32160.3 was amplified by nested PCR using two sets of primers (first PCR: 5′-CTTCGTGTATACGAGGAACC-3′ and 5′-CTTAAAAACAAATGCAACAG-3′; second PCR: 5′-CACCATGATTTCATCGTCAGAGAT-3′ and 5′-TTAAGTTGTTGTTATAGCACAC-3′) and PrimeSTAR MAX DNA polymerase (Takara, Shiga, Japan) using cDNA derived from Col-0 rosettes. The amplified CDS was then cloned into a pENTR-D-TOPO vector (Thermo Fisher Scientific, Waltham, MA, USA). The AT2G32170.1 CDS was amplified in the same way using two primer sets (first PCR: 5′-ACCGAAGAGCCACCACC-3′ and 5′-CAGACACAAATAAAGAGAGTC-3′; second PCR: 5′-ATGGTTTCGCCGTCAGAGAGATG-3′ and 5′-TTAAGTTGTTGTTATAGCAC-3′). We attempted to clone the generated amplicon into a pCR8/GW/TOPO vector (Thermo Fisher Scientific); however, most of the resulting insertions were in the reverse direction, probably because the CDS in the desired orientation was toxic to *E. coli* strain DH5α. In addition, sequences cloned from amplicons inserted in the correct direction were complete aside from the introns. As an alternative, we first amplified the full-length vector sequence without introns using a cloned vector containing one intron in the correct direction as a template, PrimeSTAR MAX DNA polymerase (Takara), and primers for mutagenesis (5′-AATGATACACTGCCATGGGTCATGATT-3′ and 5′- TGGCAGTGTATCATTTTCATCCCAT-3′). Next, the Dpn I-treated amplified product was used to transform *E. coli*, resulting in the successful cloning of a vector with the CDS in the correct direction. Compared with non-transformed colonies, the colonies of bacteria carrying the vector in the correct direction were very small. The generated AT2G32160.3 (pENTR-D-TOPO) and AT2G32170.1 (pCR8/GW/TOPO) constructs were respectively introduced into overexpression vectors pASG-GW and pAKG-GW (Uchida et al., 2020) using Gateway LR Clonase II Enzyme mix (Thermo Fisher Scientific).

GC-MS/MS analysis of MHs

For GC-MS/MS analysis, 100 µl aliquots of 250 µM πMH and τMH solutions were dispensed into separate 1.5 ml tubes. After evaporation of the solution using a centrifuge evaporator (SpeedVac, Thermo Fisher Scientific) and addition of 100 µl Mox regent (2% methoxyamine in pyridine, Thermo) to each tube, the metabolites were methoxylated at 30°C for approximately 6 h with shaking at 1,200 rpm using a thermo shaker (BSR-MSC100, Biomedical Sciences). Next, 50 µl of 1% (v/v) trimethylchlorosilane (TMS, Thermo Fisher Scientific) was added, and TMS derivatization was carried out by incubating the mixture at 37°C for 30 min with shaking at 1,200 rpm. Finally, 50-µl aliquots of the derivatized samples were dispensed into vials for GC-MS/MS analysis (AOC-5000 Plus with GCMS-TQ8040, Shimadzu). πMH-

2TMS and τMH-2TMS were annotated using total ion chromatographs obtained by GC-MS/MS in scan mode, and MRM transitions (parent ion > daughter ion) were determined to be 218.00 > 73.10 for πMH-2TMS and 196.00 > 73.10 for τMH-2TMS. Plant extracts were derivatized in the same manner as used for πMH and τMH, and MHs in the extracts were analyzed by GC-MS/MS in MRM mode. Raw data collection was performed using GCMS Solution software (Shimadzu). GC-MS/MS parameters have been detailed previously (Tabeta et al., 2021).

Expression analysis

The samples used for expression analysis were aerial parts of 3-week-old plants grown on agar-solidified half-strength MS medium (see the Plants section). Total RNA extraction, cDNA synthesis, and real-time PCR expression analysis were performed according to our previous study (Uchida et al., 2020). The primers used were as follows: 5′-TGATTGGTTGGATTCTTCGTTA-3′ and 5′-TTCCTTATTACCCAACGAACCTT-3′ for AT2G32160, 5′-GGTTGATGTAGATAAGGTTCGTTGT-3′ and 5′-AGGCTTGTAGCATTGATCTCG-3′ for AT2G32170, and 5′-GTTGGGATGAACCAGAAGGA-3′ and 5′-AAGAATACCTCTCTTGGATTGTGC-3′ for actin, the internal control.

Results

mGWAS and selection of novel candidate genes

We first conducted a preliminary metabolomic analysis based on LC-MS/MS using all *A. thaliana* seed accessions and selected 147 metabolites that were detected with high signal-to-noise ratios (> 3) and small relative standard deviation (< 10%) for a more detailed metabolomic analysis (Supplementary Tables 4–9). Next, we analyzed the metabolomes of seeds of 245 accessions and performed a GWAS of the metabolomic data to find associations ($p < 1 \times 10^{-5}$, Supplementary Figure 3) between contents of 140 metabolites and SNPs (Supplementary Table 10). We then examined associations between metabolites and SNPs located in gene regions and found 1,683 candidate genes. As an example, the gene encoding methylthioalkylmalate synthase (MAM) showed associations with a number of glucosinolates with different side chains. In this study, we focused on AT2G32160, which was annotated as a methyltransferase gene and showed an association with 3-methyl-histidine (πMH), as methyltransferase was likely to be directly related to the biosynthesis of πMH, a methylated metabolite. Detected SNPs with low *p*-values ($p < 1 \times 10^{-9}$) had no apparent effect on the gene function of AT2G32160 because they were located in introns or did not result in amino acid substitutions in exons. In contrast, SNPs with high *p*-values ($p > 1 \times 10^{-2}$ in all batch) gave rise to nonsense mutations (i.e., TGG to TGA) (Supplementary Table 11).

The gene next to AT2G32160, AT2G32170, was annotated as a methyltransferase gene as well (Supplementary Figure 4). The functions of AT2G32160 and AT2G32170 have not been previously determined. In this study, we analyzed AT2G32170 in addition to AT2G32160 associated with πMH. For convenience, AT2G32160 and AT2G32170 are hereafter referred to as *MT160* and *MT170*, respectively.

Expression analysis of *MT160* and *MT170*

Expression levels of *MT160* and *MT170* in aerial parts of 3-week-old plants of the transgenic lines named *MT160*-OE and *MT170*-OE (see Materials and Methods) were analyzed by real-time PCR. According to the analysis, expression levels of *MT160* were increased by 19–28 fold in *MT160*-OE lines, whereas those of *MT170* were almost identical between *MT170*-OE lines and wild-type Col-0 (Figure 1). In addition, overexpression and disruption of *MT160* had no effect on *MT170* expression, and expression levels of *MT160* and *MT170* in SALK lines were respectively less than 1% and approximately 30% of those in Col-0.

Structural analysis of MH in *A. thaliana* seeds by GC-MS/MS

Two types of MH, which differ in the position of the methyl group, have been found in living organisms: πMH and τMH (Figure 2). Because these two isomers could not be easily

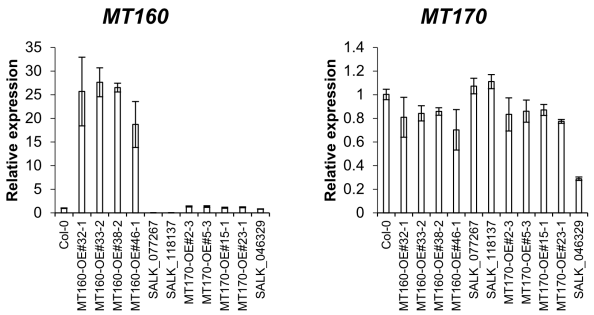

FIGURE 1
Expression analysis of *MT160* and *MT170* in aerial parts of 3-week-old *A. thaliana* plants based on real-time PCR. Bars indicate means ± standard error based on three biological replicates.

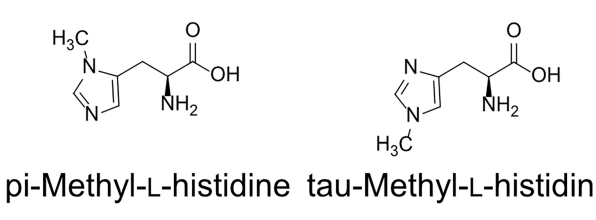

FIGURE 2
Structures of methylhistidine isomers.

distinguished by our LC-MS/MS platform, the chemical structure of the metabolite detected in *A. thaliana* by LC-MS/MS was confirmed to be πMH by GC-MS/MS using TMS-derivatized extracts. The TMS-derivatized standard MH compounds were clearly separated in the GC-MS/MS chromatogram (Figure 3A). Comparison of the chromatograms of the seed extracts with those of the two MH standards revealed that the peak corresponding to πMH-2TMS (m/z 218.00 > 73.10), but not that corresponding to τMH-2TMS (m/z 196.00 > 73.10), was present in all samples (Figure 3B). This result confirms that the metabolite detected by LC-MS/MS was actually πMH.

Quantification of πMH in *MT160*- and *MT170*-OE and knockout lines

πMH contents of seeds of *MT160*-OE and -knockout lines were respectively approximately 3.7-fold higher and one-tenth lower than those of Col-0 (Figure 4; Supplementary Table 12). Although expression levels of *MT170* in *MT170*-OE lines were unchanged relative to those in Col-0, seeds of some lines had increased πMH contents (Figure 5; Supplementary Table 12). The amount of πMH in aerial parts and roots of hydroponically grown plants was increased by 20–35-fold and 12–28-fold, respectively, in *MT160*-OE lines

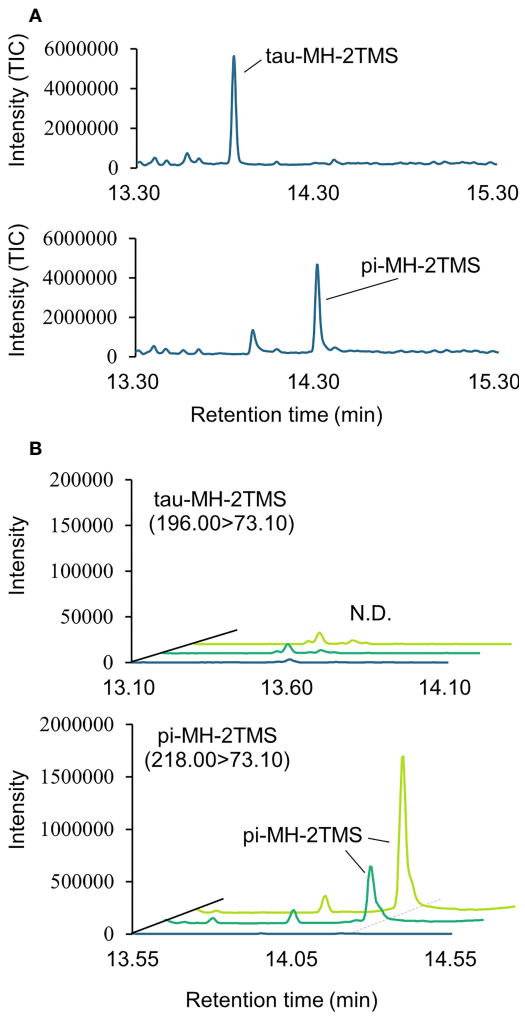

FIGURE 3
Determination of isomeric structures of methylhistidine (MH) in seeds of *Arabidopsis* lines by GC-MS/MS. **(A)** Chromatographs of τMH and πMH. Trimethylsilyl (TMS) standard samples were analyzed by GC-MS/MS in full scan mode. The total ion chromatograph (TIC) is indicated in blue. **(B)** Chromatographs obtained by GC-MS/MS in MRM mode. τMH-2TMS (196.00 > 73.10) and πMH-2TMS (218.00 > 73.10) were analyzed in the Col-0 (green), the overexpressing line *MT160*-OE#32-1 (lime yellow), and extraction buffer (blue). N.D., not detected.

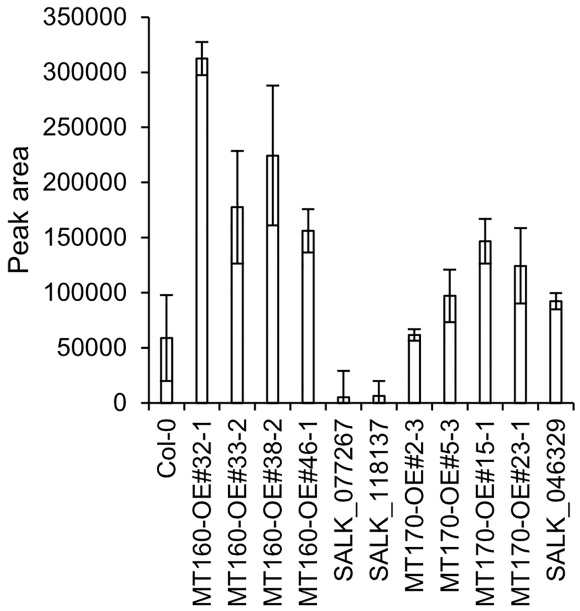

FIGURE 4
πMH content of seeds of *Arabidopsis* lines. Bars indicate means ± standard error based on three replicates, each comprising approximately 50 seeds.

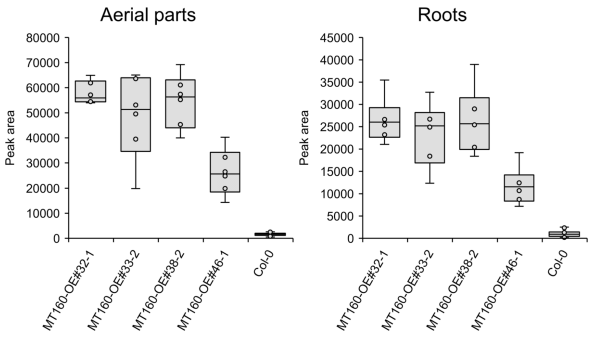

FIGURE 5
Box plots of the πMH content of aerial parts and roots of *MT160*-OE lines and the Col-0 wild type. The number of biological replicates is as follows: *n* = 6 (*MT160*-OEs); *n* = 24 (Col-0; four independent experiments with six individuals each).

compared with Col-0 (Figure 5; Supplementary Table 13). In contrast, πMH contents of *MT160*- and *MT170*-knockout lines and *MT170*-OE lines were unchanged (Supplementary Figure 5; Supplementary Tables 14, 15).

Discussion

In this study, we conducted a completely data-driven mGWAS using *A. thaliana* seeds without any preliminary information. We detected many SNPs associated with the accumulation of various metabolites and found associations between aliphatic glucosinolate compounds and SNPs on MAM genes. Given that MAMs are essential enzymes for the side-chain elongation of aliphatic glucosinolates, these uncovered associations can be considered to constitute a positive control for the mGWAS and thus validate the results of our study. As a target for further investigation, we focused on a methyltransferase gene of unknown function showing an association with πMH accumulation. Because *MT160* is an enzyme gene, we expected nonsense mutations to have the highest impact on πMH content. We discovered, however, πMH contents of accessions carrying the nonsense mutation were not significantly different from those in accessions harboring other SNPs, and therefore the *p*-value of the SNP causing the nonsense mutation was higher than that of SNPs located in introns or those responsible for silent mutations (Supplementary Table 11; Supplementary Figure 6). The absence of a significant influence on the phenotype, despite nonsense mutations detected, could potentially be attributed to factors such as latent redundant genes that bypass such nonfunctional mutations, or mechanisms like stop codon read-through, which suppresses the termination of translation. The TGA (UGA) codon, also generated by the nonsense mutation of *MT160* gene, is reported to be the stop codon most prone to read-through in recent studies in *A. thaliana* (Xu et al., 2020; Sahoo et al., 2022). Regarding the candidates of the causative mutation that could impact πMH content, our study, which utilized polymorphism data derived from the 250K SNP-Chip, could not rule out the possibility of undetectable polymorphisms in the *MT160* region. In this study, we demonstrated that our mGWAS-based approach identified the gene encoding methyltransferase, a key enzyme for *N*-methylhistidine biosynthesis in *A. thaliana*, while our results also illustrated the challenges of identifying causative mutations for the metabolic phenotypes observed in the population. Alongside ensuring exhaustive coverage of genetic variations within the population, efforts towards exploring genes that could potentially bypass metabolic networks, as well as enriching the annotation for polymorphic sites—including those involving potential stop codon read-through—may prove beneficial in further elucidating the genetic basis of metabolic diversity in *A. thaliana*.

Histidine methyltransferases have been found in yeast (Hpma1p or YIL110W) and mammals (SETD3, UPF0586, and METTL9) and respectively methylate the π- or τ-position of histidine (Webb et al., 2010; Kwiatkowski et al., 2018; Wilkinson et al., 2019; Davydova et al., 2021). Although amino acid sequence identity among YIL110W (yeast), UPF0586 (rat), and MT160 is low, all of these proteins have an N-2227 domain (Drozak et al., 2015). In our study, overexpression of *MT160* increased the content of histidine methylated at the π-, but not τ-, position, similar to YIL110W and UPF0586. All enzymes with an N-2227 domain are thus considered to methylate the pi-position of histidine in all species, and MT160 most likely functions as a histidine N_{π}-methyltransferase. Given that πMH content respectively increased and decreased in *MT160*-OE and knockout lines in our study, MT160 certainly appears to be involved in πMH biosynthesis in *A. thaliana*.

Methylated amino acids have been found in various plant species (Eloff, 1980; Fourré and Lhoest, 1989; Tyihák et al., 1989; Waterborg, 1993). To our knowledge, however, MH has only been reported in calli of barley and seashore paspalum (*Paspalum vaginatum*) (Katoh, 1990; Shi et al., 2020). In the present study, recombinant protein of MT160 could not be purified because the protein was not produced in the *E. coli* expression system (data not shown). The detailed enzymatic properties of MT160 are thus still unknown, and whether the target molecule of MT160 is free histidine or a histidine residue within proteins is unclear. Future work is needed to identify the target molecule of MT160.

In contrast to *MT160*, disruption of *MT170* did not affect plant MH contents. In addition, *MT170*-OE lines did not overexpress *MT170* for some unknown reason. One possible reason is that overexpression of *MT170* may have negatively affected *Arabidopsis* growth and thus overexpressing line could not be obtained. Moreover, a small amount of πMH was detected in *MT160*-knockout lines and some accessions with nonsense mutations in the *MT160* gene. These facts suggest that other factors besides *MT160* and *MT170* are involved in the variation in πMH content in response to environmental conditions. Furthermore, genes of unknown function harboring SNPs very strongly associated with πMH content were found on chromosome 5 (Supplementary Figure 3; Supplementary Table 10) and may have an effect on πMH content.

The significance of methylation of free histidine or histidine residues in proteins is currently unclear. According to a recent study, METTL9 may participate in mammalian immune response by pi-methylating the proinflammatory protein S100A9 (Daitoku et al., 2021; Davydova et al., 2021), and METTL18 regulates the rate of translation by tau-methylating histidines in ribosomes (Matsuura-Suzuki et al., 2022). In plants, however, the function of πMH has not been clarified. Our study findings thus provide useful new insights into the role of histidine methylation in plants.

Data availability statement

The original contributions presented in the study are included in the article/Supplementary Material. Further inquiries can be directed to the corresponding authors.

Author contributions

KU generated the overexpression lines and carried out the expression analysis. J-SK and KM performed the GWAS. MS conducted the metabolomic analysis. HT carried out the GC-MS

analysis. KU and MH wrote the manuscript. All authors contributed to the article and approved the submitted version.

Acknowledgments

We thank the Salk Institute Genomic Analysis Laboratory for providing sequence-indexed Arabidopsis T-DNA insertion mutants (SALK_077267, SALK_118137, and SALK_046329). We thank Ms. Akane Sakata, Ms. Junko Takanobu, Ms. Jun Inaba, Dr. Yuji Sawada, and Mr. Yutaka Yamada at RIKEN CSRS for technical support. We thank Edanz (https://jp.edanz.com/ac) for editing the English text of a draft of this manuscript.

Conflict of interest

The authors declare that the research was conducted in the absence of any commercial or financial relationships that could be construed as a potential conflict of interest.

The editor AF declared a past collaboration with the authors MH and HT at the time of review.

Publisher's note

All claims expressed in this article are solely those of the authors and do not necessarily represent those of their affiliated organizations, or those of the publisher, the editors and the reviewers. Any product that may be evaluated in this article, or claim that may be made by its manufacturer, is not guaranteed or endorsed by the publisher.

Supplementary material

The Supplementary Material for this article can be found online at: https://www.frontiersin.org/articles/10.3389/fpls.2023.1201129/full#supplementary-material

References

Alonso, J. M., Stepanova, A. N., Leisse, T. J., Kim, C. J., Chen, H., Shinn, P., et al. (2003). Genome-wide insertional mutagenesis of *Arabidopsis thaliana*. *Science* 301, 653–657. doi: 10.1126/science.1086391

Angelovici, R., Lipka, A. E., Deason, N., Gonzalez-Jorge, S., Lin, H., Cepela, J., et al. (2013). Genome-wide analysis of branched-chain amino acid levels in arabidopsis seeds. *Plant Cell* 25, 4827–4843. doi: 10.1105/tpc.113.119370

Ariga, H., Katori, T., Tsuchimatsu, T., Hirase, T., Tajima, Y., Parker, J. E., et al. (2017). NLR locus-mediated trade-off between abiotic and biotic stress adaptation in arabidopsis. *Nat. Plants* 3, 17072. doi: 10.1038/nplants.2017.72

Atwell, S., Huang, Y. S., Vilhjalmsson, B. J., Willems, G., Horton, M., Li, Y., et al. (2010). Genome-wide association study of 107 phenotypes in *Arabidopsis thaliana* inbred lines. *Nature* 465, 627–631. doi: 10.1038/nature08800

Chen, W., Gao, Y., Xie, W., Gong, L., Lu, K., Wang, W., et al. (2014). Genome-wide association analyses provide genetic and biochemical insights into natural variation in rice metabolism. *Nat. Genet.* 46, 714–721. doi: 10.1038/ng.3007

Clough, S. J., and Bent, A. F. (1998). Floral dip: a simplified method for *Agrobacterium*-mediated transformation of *Arabidopsis thaliana*. *Plant J.* 16, 735–743. doi: 10.1046/j.1365-313x.1998.00343.x

Daitoku, H., Someya, M., Kako, K., Hayashi, T., Tajima, T., Haruki, H., et al. (2021). siRNA screening identifies METTL9 as a histidine *N*π-methyltransferase that targets the proinflammatory protein S100A9. *J. Biol. Chem.* 297, 101230. doi: 10.1016/j.jbc.2021.101230

Davydova, E., Shimazu, T., Schuhmacher, M. K., Jakobsson, M. E., Willemen, H., Liu, T., et al. (2021). The methyltransferase METTL9 mediates pervasive 1-methylhistidine modification in mammalian proteomes. *Nat. Commun.* 12, 891. doi: 10.1038/s41467-020-20670-7

Drozak, J., Piecuch, M., Poleszak, O., Kozlowski, P., Chrobok, L., Baelde, H. J., et al. (2015). UPF0586 protein C9orf41 homolog is anserine-producing methyltransferase. *J. Biol. Chem.* 290, 17190–17205. doi: 10.1074/jbc.M115.640037

Eloff, J. N. (1980). The amino acid metabolism of *Dichapetalum cymosum* (Engl.) (Gifblaar) i. the biosynthesis of n-methyl-L-alanine and n-methyl-L-serine. *Z. für Pflanzenphysiologie* 98, 403–410. doi: 10.1016/S0044-328X(80)80193-0

Fernie, A. R., and Tohge, T. (2017). The genetics of plant metabolism. *Annu. Rev. Genet.* 51, 287–310. doi: 10.1146/annurev-genet-120116-024640

Fourré, J. L., and Lhoest, J. (1989). Protein synthesis and modification by heat in rice cell culture. *Plant Sci.* 61, 69–74. doi: 10.1016/0168-9452(89)90120-9

Katoh, Y. (1990). Changes in the contents of s-adenosylmethionine and 1-methyl-histidine in hiproly barley callus after auxin withdrawal. *Agric. Biol. Chem.* 54, 3117–3122. doi: 10.1271/bbb1961.54.3117

Kwiatkowski, S., Seliga, A. K., Vertommen, D., Terreri, M., Ishikawa, T., Grabowska, I., et al. (2018). SETD3 protein is the actin-specific histidine n-methyltransferase. *Elife* 7, e37921. doi: 10.7554/eLife.37921.048

Matsuda, F., Nakabayashi, R., Yang, Z., Okazaki, Y., Yonemaru, J., Ebana, K., et al. (2015). Metabolome-genome-wide association study dissects genetic architecture for generating natural variation in rice secondary metabolism. *Plant J.* 81, 13–23. doi: 10.1111/tpj.12681

Matsuura-Suzuki, E., Shimazu, T., Takahashi, M., Kotoshiba, K., Suzuki, T., Kashiwagi, K., et al. (2022). METTL18-mediated histidine methylation of RPL3 modulates translation elongation for proteostasis maintenance. *Elife* 11, e72780. doi: 10.7554/eLife.72780.sa2

Riedelsheimer, C., Lisec, J., Czedik-Eysenberg, A., Sulpice, R., Flis, A., Grieder, C., et al. (2012). Genome-wide association mapping of leaf metabolic profiles for dissecting complex traits in maize. *Proc. Natl. Acad. Sci. U.S.A.* 109, 8872–8877. doi: 10.1073/pnas.1120813109

Sahoo, S., Singh, D., Singh, A., Pandit, M., Vasu, K., Som, S., et al. (2022). Identification and functional characterization of mRNAs that exhibit stop codon readthrough in *Arabidopsis thaliana*. *J. Biol. Chem.* 298, 102173. doi: 10.1016/j.jbc.2022.102173

Sawada, Y., Akiyama, K., Sakata, A., Kuwahara, A., Otsuki, H., Sakurai, T., et al. (2009). Widely targeted metabolomics based on large-scale MS/MS data for elucidating metabolite accumulation patterns in plants. *Plant Cell Physiol.* 50, 37–47. doi: 10.1093/pcp/pcn183

Sawada, Y., Nakabayashi, R., Yamada, Y., Suzuki, M., Sato, M., Sakata, A., et al. (2012). RIKEN tandem mass spectral database (ReSpect) for phytochemicals: a plant-specific MS/MS-based data resource and database. *Phytochemistry* 82, 38–45. doi: 10.1016/j.phytochem.2012.07.007

Shi, H., Huang, R., Liu, Y., Chen, X., Lu, S., and Guo, Z. (2020). Identification of a cold tolerant mutant in seashore paspalum (*Paspalum vaginatum*). *Plant Cell Tissue Organ Culture (PCTOC)* 140, 379–387. doi: 10.1007/s11240-019-01734-z

Slaten, M. L., Yobi, A., Bagaza, C., Chan, Y. O., Shrestha, V., Holden, S., et al. (2020). mGWAS uncovers gln-glucosinolate seed-specific interaction and its role in metabolic homeostasis. *Plant Physiol.* 183, 483–500. doi: 10.1104/pp.20.00039

Tabeta, H., Watanabe, S., Fukuda, K., Gunji, S., Asaoka, M., Hirai, M. Y., et al. (2021). An auxin signaling network translates low-sugar-state input into compensated cell enlargement in the *fugu5* cotyledon. *PloS Genet.* 17, e1009674. doi: 10.1371/journal.pgen.1009674

Turner, S. D. (2018). Qqman: an r package for visualizing GWAS results using q-q and Manhattan plots. *J. Open Source Soft.* 3, 731. doi: 10.21105/joss.00731

Tyihák, E., Király, Z., Gullner, G., and Szarvas, T. (1989). Temperature-dependent formaldehyde metabolism in bean plants. the heat shock response. *Plant Sci.* 59, 133–139. doi: 10.1016/0168-9452(89)90130-1

Uchida, K., Sawada, Y., Ochiai, K., Sato, M., Inaba, J., and Hirai, M. Y. (2020). Identification of a unique type of isoflavone *O*-methyltransferase, GmIOMT1, based on multi-omics analysis of soybean under biotic stress. *Plant Cell Physiol.* 61, 1974–1985. doi: 10.1093/pcp/pcaa112

Wang, J., and Zhang, Z. (2021). GAPIT version 3: boosting power and accuracy for genomic association and prediction. *Genom. Proteom. Bioinform.* 19, 629–640. doi: 10.1016/j.gpb.2021.08.005

Waterborg, J. H. (1993). Dynamic methylation of alfalfa histone H3. *J. Biol. Chem.* 268, 4918–4921. doi: 10.1016/S0021-9258(18)53483-9

Webb, K. J., Zurita-Lopez, C. I., Al-Hadid, Q., Laganowsky, A., Young, B. D., Lipson, R. S., et al. (2010). A novel 3-methylhistidine modification of yeast ribosomal protein Rpl3 is dependent upon the YIL110W methyltransferase. *J. Biol. Chem.* 285, 37598–37606. doi: 10.1074/jbc.M110.170787

Wei, W., Li, S., Wang, Y., Wang, B., Fan, G., Zeng, Q., et al. (2021). Metabolome-based genome-wide association study provides genetic insights into the natural variation of foxtail millet. *Front. Plant Sci.* 12, 665530. doi: 10.3389/fpls.2021.665530

Wilkinson, A. W., Diep, J., Dai, S., Liu, S., Ooi, Y. S., Song, D., et al. (2019). SETD3 is an actin histidine methyltransferase that prevents primary dystocia. *Nature* 565, 372–376. doi: 10.1038/s41586-018-0821-8

Xu, L., Liu, T., Xiong, X., Liu, W., Yu, Y., and Cao, J. (2020). AtC3H18L is a stop-codon read-through gene and encodes a novel non-tandem CCCH zinc-finger protein that can form cytoplasmic foci similar to mRNP granules. *Biochem. Biophys. Res. Commun.* 528, 140–145. doi: 10.1016/j.bbrc.2020.05.081

Zeng, X., Yuan, H., Dong, X., Peng, M., Jing, X., Xu, Q., et al. (2020). Genome-wide dissection of Co-selected UV-b responsive pathways in the UV-b adaptation of qingke. *Mol. Plant* 13, 112–127. doi: 10.1016/j.molp.2019.10.009

Zhao, H., He, Y., Zhang, K., Li, S., Chen, Y., He, M., et al. (2023). Rewiring of the seed metabolome during tartary buckwheat domestication. *Plant Biotechnol. J.* 21, 150–164. doi: 10.1111/pbi.13932

frontiers | Frontiers in Plant Science

TYPE Original Research
PUBLISHED 17 August 2023
DOI 10.3389/fpls.2023.1255486

OPEN ACCESS

EDITED BY
Ali Ferjani,
Tokyo Gakugei University, Japan

REVIEWED BY
Akira Yoshinari,
Nagoya University, Japan
Jozef Mravec,
University of Copenhagen, Denmark

*CORRESPONDENCE
Kyoko Miwa
miwakyoko@ees.hokudai.ac.jp

RECEIVED 08 July 2023
ACCEPTED 31 July 2023
PUBLISHED 17 August 2023

CITATION
Onuh AF and Miwa K (2023) Mutations in type II Golgi-localized proton pyrophosphatase *AVP2;1/VHP2;1* affect pectic polysaccharide rhamnogalacturonan-II and alter root growth under low boron condition in *Arabidopsis thaliana*.
Front. Plant Sci. 14:1255486.
doi: 10.3389/fpls.2023.1255486

Mutations in type II Golgi-localized proton pyrophosphatase *AVP2;1/VHP2;1* affect pectic polysaccharide rhamnogalacturonan-II and alter root growth under low boron condition in *Arabidopsis thaliana*

Amarachukwu Faith Onuh and Kyoko Miwa*

Graduate School of Environmental Science, Hokkaido University, Sapporo, Japan

The essential plant nutrient boron is required for the crosslinking of the pectin polysaccharide, rhamnogalacturonan II (RG-II). The synthesis of the pectic polysaccharides takes place in the Golgi apparatus, acidified by proton pumps. AVP2;1/VHP2;1 is a type II proton pyrophosphatase localized in the Golgi apparatus, which possesses proton pumping activity coupled with pyrophosphate hydrolysis. Its activity and expression patterns have been previously revealed but its role in plants remains unknown. The aim of the present work therefore was to explore the physiological role of AVP2;1 in *Arabidopsis thaliana*. In the screening of mutants under low boron, a mutant carrying a missense mutation in *AVP2;1* was isolated. This mutant showed increased primary root growth under low boron conditions but no significant difference under normal boron condition compared to wild type plants. T-DNA insertion caused similar growth, suggesting that reduced function of AVP2;1 was responsible. Root cell observation revealed an increase in meristematic zone length, cell number in meristem and length of matured cell in *avp2;1* mutants compared to wild type under low boron. Calcium concentration was reduced in mutant root cell wall under low boron. RG-II specific sugars also tended to be decreased in mutant root cell wall under low and normal boron conditions. These results suggest that changes in cell wall component by mutations in *AVP2;1* may possibly explain the increased root length of mutants under low boron. This supports the idea that AVP2;1 plays a role in pH homoeostasis in Golgi apparatus for pectin synthesis.

KEYWORDS

***Arabidopsis thaliana*, boron, cell wall, proton pyrophosphatase, rhamnogalacturonan-II (RG-II)**

Introduction

Boron (B) is one of the essential micronutrients of plants. Its deficiency is widespread and various mitigatory approaches such as management of nutrient condition by fertilizer application have been explored. The application of borate fertilizers to make up for the insufficient soil boron is limited by its cost and effectiveness (Güneş et al., 2003; Duran et al., 2018; Fujiyama et al., 2019). Its ineffectiveness is due to the difficulty to ascertain the optimum required fertilizer amount because of the wide range of boron requirement among plant species (Gupta et al., 1985). There is a narrow window between boron deficiency and toxicity and hence inappropriate application of borate fertilizer may lead to toxicity. On the other hand, the use of molecular approach as a mitigatory measure for boron deficiency has been exploited. This involves the overexpression of the boron transporters BOR1, BOR2 and NIP5;1 in plant species like *Brassica napus*, *Zea mays*, *Arabidopsis thaliana*, *Oryza sativa* etc. to improve boron deficiency tolerance (Onuh and Miwa, 2021). Though this approach is useful for the reduction of boron fertilizer application, it still does not completely solve the problem of low-boron stress. This is because upregulating these boron transporters would increase boron uptake thereby leading to a depletion of the limited soil boron in long term. There is therefore a need for a better measure to mitigate low-boron stress.

The primary cell wall is composed of cellulose, hemicellulose, pectin and soluble proteins. Its major component is pectin making up 30-50% of the primary cell wall (Cosgrove and Jarvis, 2012). The pectin component is structurally heterogenous, consisting of three different types of polysaccharide domains: homogalacturonan (HG), rhamnogalacturonan-I (RG-I) and rhamnogalacturonan-II (RG-II) (Mohnen, 2008; Alba and Kontogiorgos, 2017). Minerals such as calcium (Ca) and boron (B) in the pectin, are essential for the crosslinking of HG and RG-II, respectively, which forms the pectin network and aids the overall stability of the primary cell wall. RG-II has HG as a backbone and six distinct side chains A-F (Ndeh et al., 2017; Voxeur et al., 2017) and it has been experimentally demonstrated that RG-II exists as a dimer crosslinked by a borate diester in the plant cell wall (Kobayashi et al., 1996). The major function of boron discovered and experimentally shown so far is its stability of the primary cell wall by crosslinking of RG-II (Matoh et al., 1993; O'Neill et al., 2001).

The pectic polysaccharides of the plant cell wall are synthesized in the Golgi apparatus by the activity of Golgi-localized proteins (Driouich et al., 1993; Lerouxel et al., 2006) and subsequently transported through the TGN (trans-Golgi network) in an acidic condition. With the use of pH sensors, estimated pH was 6.8 and 6.3 in cis-Golgi and TGN in *A. thaliana* protoplasts, respectively (Shen et al., 2013), and it was 6.3 and 5.6 in trans-Golgi and TGN/EE (early endosome) in *A. thaliana* root cells, respectively (Luo et al., 2015). The presence of two types of proton pumps in the Golgi apparatus and TGN which are possibly responsible for its acidification and ion homeostasis has been established in plants. These proton pumps are the vacuolar type ATPase (V-ATPase) (Luo et al., 2015) and proton pyrophosphatase (H^+-PPase). The H^+-PPase has a dual function of hydrolysis of pyrophosphate (PPi) into two ortho-phosphates in the cytosol and proton pumping into the Golgi apparatus. The energy generated from the hydrolysis of PPi by this enzyme is what powers its translocation of proton into the Golgi apparatus.

Generally, two types of H^+-PPase, the type I and type II exist in plants (Drozdowicz et al., 2000). In *A. thaliana*, there are three genes which encode this enzyme. Type I is encoded by *AVP1/VHP1/FUGU5* (At1g15690) and type II by *AVP2;1/VHP2;1* (At1g78920) and *AVP2;2/VHP2;2* (At1g16780). AVP2;1 and AVP1 share 33% amino acid sequence identity whereas AVP2;1 and AVP2;2 share 94% amino acid sequence identity (Segami et al., 2010). The AVP2s, which have a Mg^{2+}-binding motif, have been reported to have an obligatory requirement for Mg^{2+} and an insensitivity to potassium ions (K^+) for their PPi hydrolytic enzymatic activities (Drozdowicz et al., 2000). According to Segami et al. (2010), AVP2s also show characteristics of Zn^{2+} dependency for its enzymatic activity. Segami et al. (2010) have revealed that the AVP1 and the AVP2s whose protein levels are less than 0.3% of AVP1, are localized to the tonoplast (AVP1) and the Golgi apparatus and TGN (AVP2s). So far it has also been found that AVP1 is abundant in shoot apical meristem, leaf primordia and pollen in *A. thaliana* while AVP2s are abundant in young roots, buds, flowers and siliques (Segami et al., 2010; Segami et al., 2014). The functional characterization of AVP1 in *A. thaliana* has been established by studies in mutants and overexpression lines. Some of its known roles are regulation of auxin-mediated organ development and involvement in various abiotic stress tolerance (Li et al., 2005; Kim et al., 2014; Nepal et al., 2020; Zhang et al., 2023). It has also been shown that rather than proton pumping, PPi hydrolysis activity is the major contribution of AVP1 in organ development as demonstrated using *fugu5* mutants (Ferjani et al., 2011; Asaoka et al., 2016). However, little is known about the AVP2s and their mutant phenotype.

In this study, we focused on AVP2;1 and from the screening of *A. thaliana* mutants with enhanced root growth under low boron, a mutant carrying a missense mutation in *AVP2;1* was isolated. T-DNA lines of *AVP2;1* showed similar root growth suggesting that the reduced function of AVP2;1 was responsible for the phenotype. Here we report the phenotypic unveiling of *avp2;1* mutants and the possible effect of *AVP2;1* mutation on cell wall synthesis. These findings give insight into the possible function(s) of AVP2;1 in plants with regards to boron nutrition.

Materials and methods

Plant materials and growth conditions

Columbia-0 (Col-0), an ecotype of *Arabidopsis thaliana* (L.) Heynh was used as wildtype (WT) in this study. The mutant number 31A hereafter referred to as *avp2;1-4/vhp2;1-4* used in this study was obtained via the screening of Col-0 seeds mutagenized with ethyl methanesulfonate (EMS) (Hiroguchi et al., 2021). This screening was performed under severe boron deficient (0.03 μM) condition and the mutant showed longer root than Col-0 under this condition and no difference from Col-0 under normal (100 μM) boron condition. This mutant carries a base

substitution of guanine to adenine (G800A in CDS and G2492A in full length genomic sequence from the transcriptional start site) which caused an amino acid substitution (G267D in protein). *AVP2;1* (At1g78920) T-DNA insertion mutants SALK_0542912 in Col-0 background (Alonso et al., 2003) and SAIL_165F07 in Col-3 background (Sessions et al., 2002) hereafter referred to as *avp2;1-2/vhp2;1-2* and *avp2;1-3/vhp2;1-3*, respectively, were also used. T-DNA insertion position for both lines is the 6th intron of At1g78920. These T-DNA insertion mutants were obtained from the Arabidopsis Biological Resource Center (ABRC). To determine homozygosity of T-DNA insertion, PCR was performed using the sets of primers listed in Table S1.

Seeds were surface sterilized using a washing solution containing 30 mL tap water, 3 mL of bleach (5-10% hypochlorous acid) and 3 drops of detergent, rinsed five times with sterilized ultra-pure water, suspended in ultra-pure water and stored in the dark at 4°C for 4 days before being sown. Plants were cultured in solidified MGRL media (Fujiwara et al., 1992) in which boron concentration was adjusted with boric acid. Growth conditions of 0.06 µM and 0.1 µM boric acid for low boron condition, 0.2 µM, 0.3 µM and 1 µM boric acid for mildly low boron condition, 100 µM boric acid for normal boron condition and 3000 µM boric acid for toxic boron condition were set. The MGRL solid media contained 1% (w/v) sucrose and 1% (w/v) gellan gum (Wako Pure Chemicals). Plants were incubated in a vertical position at 22°C under a 16-hour light/8-hour dark cycle.

Quantitative reverse-transcription PCR (qRT-PCR)

Surface-sterilized seeds of Col-0 and *avp2;1* mutants were sown in solid medium containing different concentrations of boric acid for 9 days. Roots were harvested and immediately frozen using liquid nitrogen for RNA extraction. The frozen samples were homogenized at 1700 rpm for 15 sec four times using Multi beads shocker (YASUI KIKAI) in a 3 mL tube. Total RNA was extracted using RNeasy Plant Mini Kit (Qiagen, Germany) and treated with RNase-free DNase (Qiagen, Germany) for 30 mins to eliminate genomic DNA contamination. cDNA was synthesized from 0.25 µg total RNA using the PrimeScript RT reagent kit (TAKARA). Expression level of *AVP2;1*, *NIP5;1*, *BOR1*, and *BOR2* was analyzed by qRT-PCR using Thermal Cycle Dice (TAKARA, Japan) with SYBR premix Ex Taq II (TAKARA, Japan). The mRNA level of *AVP2;1* was detected at the 5' (upstream) portion and 3' (downstream) portion of T-DNA insertion. *EF1α* was used as a reference gene for normalization of the target mRNA level. Primers used are listed in Table S1.

Measurement of primary root length

For the measurement of primary root length, photographs of 9-day-old seedlings grown under 0.06 µM, 0.1 µM, 0.2 µM, 0.3 µM, 100 µM and 3000 µM boric acid were taken and the digital image was analyzed using an imaging processing software, ImageJ.

Observation of primary root under stereomicroscopy

Surfaced sterilized seeds of Col-0 and *avp2;1* mutants were grown under 0.1 µM boric acid (low boron), 0.3 µM boric acid (mildly low boron) and 100 µM boric acid (normal boron) in solid media for 5 days. Root tips of plant lines were observed and photographed using a stereomicroscope (OLYMPUS SZX12) equipped with Moticam1080 (Shimadzu).

Measurement of root cell length and number

Col-0 and *avp2;1-4* mutant were grown under low boron (0.1 µM) and normal boron (100 µM) in MGRL solid media for 5 days. The plant roots were stained with 10 mgL^{-1} propidium iodide (PI: FUJIFILM Wako Pure Chemical, Japan). The imaging data was obtained using a LSM980 (Zeiss, Germany) confocal laser scanning microscope at an excitation and emission wavelength of 543 nm and 543nm-694nm. The obtained images were exported with the Carl Zeiss ZEN 3 blue edition software. The length of fully elongated cortical cells and root apical meristem (RAM) length were measured using ImageJ software. The fully elongated cortical cells or matured cortical cells were defined as the cells within regions of fully developed root hairs (Pacheco-Escobedo et al., 2016). The RAM length was defined as the distance between quiescent center and first elongating cortical cells and the number of cortical cells within the RAM length were counted using the cell counter ImageJ plugin (https://imagej.nih.gov/ij/plugins/cell-counter.html) and regarded as the number of cells in the RAM (Pacheco-Escobedo et al., 2016).

Dry weight measurement

To obtain root and rosette leaf samples for dry weight measurement, surface sterilized seeds were first grown on rockwool with ultra-pure water and incubated for 7 days at 22°C under a 10-hour light/14-hour dark cycle (short day) and 70% relative humidity. Seedlings were transferred to liquid MGRL media containing 0.15 µM boric acid (low boron), 0.3 µM boric acid (mildly low boron) and 100 µM boric acid (normal boron) and grown for 28 days. Liquid culture was changed weekly during the initial 14 days after transfer, and subsequently changed twice in a week. The rosette leaves and roots of plant lines were harvested and rinsed with ultra-pure water. They were dried at 60°C for 15 days and the dry weight of both rosette leaves and roots was measured.

Cell wall extraction from root samples

For the analysis of cell wall properties, plants were grown in solid media containing 0.1 µM boric acid (low boron), 0.3 µM boric acid (mildly low boron) and 100 µM boric acid (normal boron) for 9 days and alcohol insoluble residues (AIR) were extracted from their

frozen root as described (Matsunaga et al., 2004). About 600-900 root samples were harvested as a single sample for low boron condition and about 300-450, as a single sample for mildly low boron and normal boron conditions. The frozen root tissues were crushed at 1700 rpm for 15 sec in a total of 4 cycles using a multi bead shocker (YASUI KIKAI) and then homogenized with 80% (v/v) ethanol. The homogenates were shaken using a rotator and centrifuged. The insoluble pellets were washed twice with 80% (v/v) ethanol, once with 99.5% (v/v) ethanol, twice with methanol/chloroform (1:1, v/v), once with acetone and twice with ultrapure water. The insoluble residues obtained were freeze-dried using FDU-1200 (EYELA, Japan) for 25 h and treated as cell wall samples.

Measurement of boron and calcium concentration

To measure total boron and calcium concentration in the rosette leaves and roots, plants were grown in a hydroponic culture system (the same system as dry weight measurement) under 0.1 µM boric acid (low boron), 0.3 µM boric acid (mildly low boron) and 100 µM boric acid (normal boron) and grown for 42 days (7 days in ultra-pure water and 35 days in liquid MGRL media). The concentration for low boron was increased to 0.15 µM boric acid after 19 days of culture in liquid MGRL media due to the severity of boron deficiency. The rosette leaves and roots were then harvested and rinsed with ultrapure water. The harvested samples were dried at 60°C for 9 days (at least more than 3 days) and dry weight was measured. The dried samples were submerged in concentrated HNO_3 for 3 days at room temperature and first digested at 110°C for about 2 h followed by digestion with H_2O_2 for 10 mins. The digested samples were dissolved in 2% HNO_3. For the measurement of cell wall boron and calcium concentration, about 2 mg of root AIR extracted from 9-d-old plants were treated with HNO_3 at room temperature for 3 days. The samples were then digested and dissolved in 2% HNO_3 as described above. Boron and calcium concentrations were measured by inductively coupled plasma mass spectrometry (ELAN DRC-e, PerkinElmer, USA).

Measurement of RG-II specific sugars

To estimate the amount of RG-II present in root cell wall of plant lines, the measurement of 2-keto-3-deoxy sugars as RG-II specific sugars was performed following a modified thiobarbituric acid protocol described by York et al. (1985). About 1.5 mg of AIR were treated with 5 U of endo-polygalacturnanase from *Pectobacterium carotovorum*, (E-PGALPC, Megazyme, Ireland) in 300 µL of 0.1 M sodium acetate buffer at pH 5.5 for 89 h at 40°C for complete digestion. The enzyme was dialyzed in 0.1 M sodium acetate buffer before use. The suspension was centrifuged three times to remove insoluble residues completely and the supernatant was collected after each centrifuge. To hydrolyze the polysaccharide sugar, 200 µL of the supernatant was mixed with 100 µL of 0.5 M H_2SO_4, vortexed and incubated at 100°C for 30 mins. This was followed by cooling down the solution at room temperature for 10 mins, then the addition of 250 µL of 40 mM HIO_4 dissolved in 62.5 mM H_2SO_4, vortexing and incubation at room temperature for 20 mins for a cleavage reaction to generate formylpyruvic acid. 600 µL of 2% Na_2SO_3 dissolved in 0.5 M HCl was subsequently added to neutralize excess HIO_4 and vortexed. A brown coloration was formed upon this addition but quickly disappeared. 500 µL of 25 mM thiobarbituric acid was added, and the mixture was vortexed and incubated at 100°C for 15 mins for pigment generation. 1 mL of DMSO (99.5%) was added to the solution for pigment stabilization and then the mixture was incubated at 24°C for 7 mins. To quantify generated pigments, an absorbance at 548 nm was measured using a spectrophotometer (U-2910, HITACHI High Technologies Corp., Japan). The concentration of 2-keto-3-deoxy sugars were estimated using 2-keto-3-deoxyoctonate ammonium salt (Sigma-Aldrich, USA) as a standard.

Statistical analysis

Comparisons between the wildtype Col-0 and *avp2;1* mutants were performed using the Dunnett's test and Student's t-test.

Results

Mutations in *AVP2;1* increased primary root length under low boron

To explore the factors that modulate root growth under boron limitation, *A. thaliana* mutants were screened which showed increased primary root length under low boron supply from EMS-treated Col-0. One of these mutants named number 31A, represented as *avp2;1-4*, showed an enhanced primary root length under a limited supply of boron (0.06 µM and 0.1 µM, Figures 1A, D) although the primary root length was not statistically different from Col-0 under normal boron condition (100 µM, Figures 1A, D). Through genetic mapping and genomic sequencing, it was revealed that the longer primary root was caused by a single recessive locus and this mutant was found to carry a missense mutation in the 7th exon of *AVP2;1* which encodes a Golgi-localized proton pyrophosphatase (Figure 1B). This missense mutation (G800A in CDS) led to an amino acid substitution of glycine to aspartic acid (G267D in protein). G267 is predicted to be located close to the 6th transmembrane domain, and is conserved among AVP1, AVP2;1 and AVP2;2 (Segami et al., 2010; Tojo et al., 2023). To examine if the mutant phenotype was because of its mutation in *AVP2;1*, two T-DNA lines of *AVP2;1* were obtained. These two lines represented as *avp2;1-2* and *avp2;1-3* respectively, carry a T-DNA insertion in the 6th intron of *AVP2;1* (Figure 1B). Both T-DNA lines showed increased primary root under low boron but no differences under normal boron supply similar to *avp2;1-4* (Figures 1A, D), supporting that the mutations in *AVP2;1* were responsible for the increased primary root length under low boron conditions.

To check *AVP2;1* mRNA expression in the mutants, *AVP2;1* mRNA was quantified by qRT-PCR using two sets of primers to

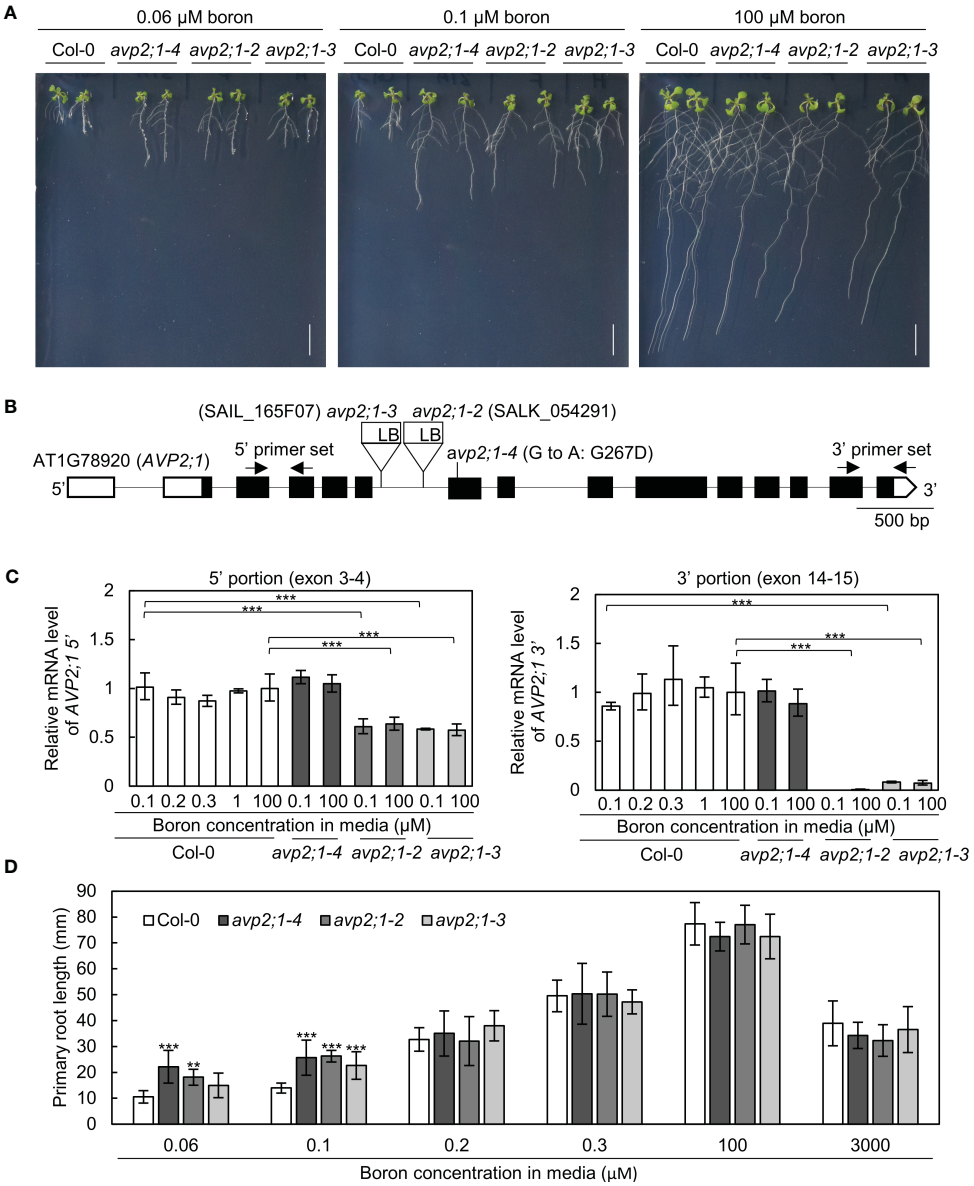

FIGURE 1
Growth analysis and mRNA level in wildtype Col-0 and *avp2;1* mutants. **(A)** Photos of plants under 0.06 µM (very low), 0.1 µM (low) and 100 µM (normal) boron conditions. (scale bar: 10 mm). **(B)** *AVP2;1* gene structure showing the point mutation, T-DNA insertion positions and primer positions used for mRNA quantification. White and black boxes indicate UTRs and coding regions while the connecting black line indicates the intron. **(C)** mRNA quantification of *AVP2;1* in roots of wildtype Col-0 and *avp2;1* mutants using primers at the 5' portion and 3' portion respectively under various concentrations of boron. *EF1α* was used for normalization. Means ± SD are shown (n=3-4). Statistical analysis was not performed for *avp2;1-2* under 0.1 µM at the 3' portion because it was below detection limit. **(D)** Primary root length of wildtype Col-0 and *avp2;1* mutant lines under various boron concentrations. Means ± SD are shown (n=6-11). All the analysis in Figure 1 were done using 9-d-old plants grown in solid media. ***$P < 0.001$,**$P < 0.01$, compared with wildtype Col-0 under the same boron conditions (Dunnett's test).

detect the upstream portion (5', exon 3-4) and downstream (3', exon 14-15) of T-DNA insertion. In Col-0, with the use of both sets of primers, *AVP2;1* mRNA level was not obviously changed under various boron concentrations (Figure 1C) suggesting that the mRNA expression of *AVP2;1* in roots is not dependent on boron nutrition. Under low (0.1 µM) and normal (100 µM) boron, *AVP2;1* mRNA was not changed in *avp2;1-4* when compared to Col-0 using both upstream and downstream primers. However, in *avp2;1-2* and *avp2;1-3*, *AVP2;1* mRNA was reduced to 60% in the upstream portion of the T-DNA insertion. In the downstream portion of insertion, *AVP2;1* mRNA level was reduced to 0.5% and 7-10% in *avp2;1-2* and *avp2;1-3*, respectively under both boron conditions compared to Col-0 (Figure 1C). This suggests that although the destabilized 5' incomplete portion of mRNA was likely expressed, *AVP2;1* mRNA is not at least overexpressed in T-DNA insertion lines. This shows that the T-DNA insertion mutants, *avp2;1-2* and *avp2;1-3*, are knockdown mutants suggesting that reduced function of AVP2;1 is responsible for the mutant phenotype.

To examine the growth response of the *avp2;1* mutants to different boron conditions, plants were grown under various range

of boron concentration. *avp2;1* mutants exhibited longer primary roots only under low boron conditions (0.06 and 0.1 μM) compared to Col-0 but showed no significant differences under mildly low (0.2 and 0.3 μM), normal (100 μM) and even toxic (3000 μM) boron conditions (Figure 1D).

To check the possibility of the involvement of *AVP2;1* in root growth under other stress conditions, mutant lines were grown under low phosphorus and low pH, respectively. No differences were found between the *avp2;1* mutants and Col-0 under these conditions (Figures S1A, B). Taken together, these results indicate that the reduced expression or function of *AVP2;1* causes an increase in the primary root length under a limited supply of boron and this increase is likely observed specifically under low boron.

Alleviated inhibition of both cell division and elongation was observed in *avp2;1* mutants

To characterize the effects of *avp2;1* mutations on root cells, the root tips of 5-d-old plants grown under low (0.1 μM), mildly low (0.3 μM), and normal (100 μM) boron were first observed under a stereomicroscope. Although primary root length was not obviously different between Col-0 and *avp2;1* mutants at this age under all the boron conditions (Figure S2A), longer meristematic and elongation zones were observed in *avp2;1* mutants compared to Col-0 under low (0.1 μM) boron condition (Figure 2A) and no difference was observed under mildly low (0.3 μM) boron (Figure S2B) and normal (100 μM) boron condition (Figure 2B). There were also no distinguishing differences in the root hair distribution between wildtype Col-0 and *avp2;1* mutant lines under both low and normal boron conditions. The root cells of Col-0 and *avp2;1-4* mutant was further examined using a confocal microscope in 5-d-old plants. Under low (0.1 μM) boron, the shape of the root cells of Col-0 were collapsed and the root cell arrangement was damaged; however, *avp2;1-4* root cells showed a mitigated inhibition in cell shape and cell arrangement (Figure 2B). In addition, an increase in meristematic zone length, cell number in root apical meristem (RAM), and length of matured cortical cell was observed in *avp2;1-4* compared to Col-0 under low boron condition, and no differences was found under normal (100 μM) boron condition (Figure 2C). These observations suggest that inhibition of both root cell elongation and division caused by low boron was alleviated by *avp2;1* mutation accounting for the enhanced primary root growth.

Boron concentration in roots and rosette leaves was not different between Col-0 and *avp2;1* mutants

To explore the mechanisms behind the increased root length of *avp2;1* mutants under limited supply of boron, the possibility of an enhancement in boron uptake or transport in mutant lines was considered. To measure tissue boron concentration, plants were hydroponically grown so that plant roots can freely access the media. In hydroponic culture, *avp2;1* mutants also exhibited longer root length compared to the wildtype Col-0 under low (0.15 μM) boron condition when Col-0 root elongation was inhibited. No obvious difference in root length was found among plant lines under mildly low (0.3 μM) and normal (100 μM) boron conditions (Figure 3A). This shows the consistency of the mutant phenotype irrespective of the plant culture system. In both root and rosette leaf dry weight, no significant differences were observed between Col-0 and *avp2;1* mutants (Figure 3B). In the concentration of total boron in roots and rosette leaves, no differences were observed between the wildtype Col-0 and *avp2;1* mutant lines irrespective of the boron concentration in the media (Figure 3C). This suggests that the mutations in *AVP2;1* did not primarily affect the boron transport.

To further examine the effects of *avp2;1* mutation in boron transport, the mRNA expression of *NIP5;1*, *BOR1* and *BOR2* were checked in wildtype Col-0 and *avp2;1* mutant lines under low (0.1 μM) and normal (100 μM) boron conditions. *NIP5;1*, *BOR1* and *BOR2* encode major boron transporters required for root growth under low boron (Onuh and Miwa, 2021). No increase was detected in the mRNAs of these transporter genes in the mutant lines under low and normal boron conditions (Figures 4A–C). *NIP5;1* mRNA is induced by low boron (Tanaka et al., 2011). *NIP5;1* mRNA levels in all the three *avp2;1* mutants were rather reduced to 73-74% of that of Col-0 under low boron (Figure 4A). This decrease in *NIP5;1* mRNA in roots could be an indirect consequence of the increased root length in *avp2;1* mutants under low boron (Figure 1A). *NIP5;1* promoter activity is more strongly detected in the elongation zone compared to the mature portion of the roots (Takano et al., 2006). Compared to Col-0 in which root elongation was severely inhibited (Figure 1A), the relative proportion of the elongation zone to the entire root could be smaller in *avp2;1* mutants, resulting in the reduction in relative level of *NIP5;1* mRNA under low boron.

Taken together, these results suggest that the upregulation of boron transport was not likely the cause of the enhanced root length exhibited by the *avp2;1* mutant lines under low boron.

Reduced calcium and RG-II specific sugars were observed in root cell wall of *avp2;1* mutants

Due to the role of boron in plant cell wall stability by crosslinking of two monomers of RG-II, changes in cell wall components were considered as a possible mechanism of the enhanced root growth of *avp2;1* mutants under a low boron supply. To explore this possibility, concentrations of the cell wall minerals, calcium, and boron, were measured in root cell wall under low (0.1 μM), mildly low (0.3 μM), and normal (100 μM) boron conditions. No difference was found in boron concentration in cell wall under low and mildly low boron condition, but *avp2;1* mutant lines showed a slight tendency of reduction compared to the wildtype Col-0 under normal boron conditions (Figure 5A). Since boron binding to RG-II is assumed to be saturated when sufficient boron is supplied, this suggests a possibility of a reduced boron binding capacity in *avp2;1* mutant cell wall. On the other hand, the concentration of calcium in the cell wall was generally increased in all the plant lines under low boron

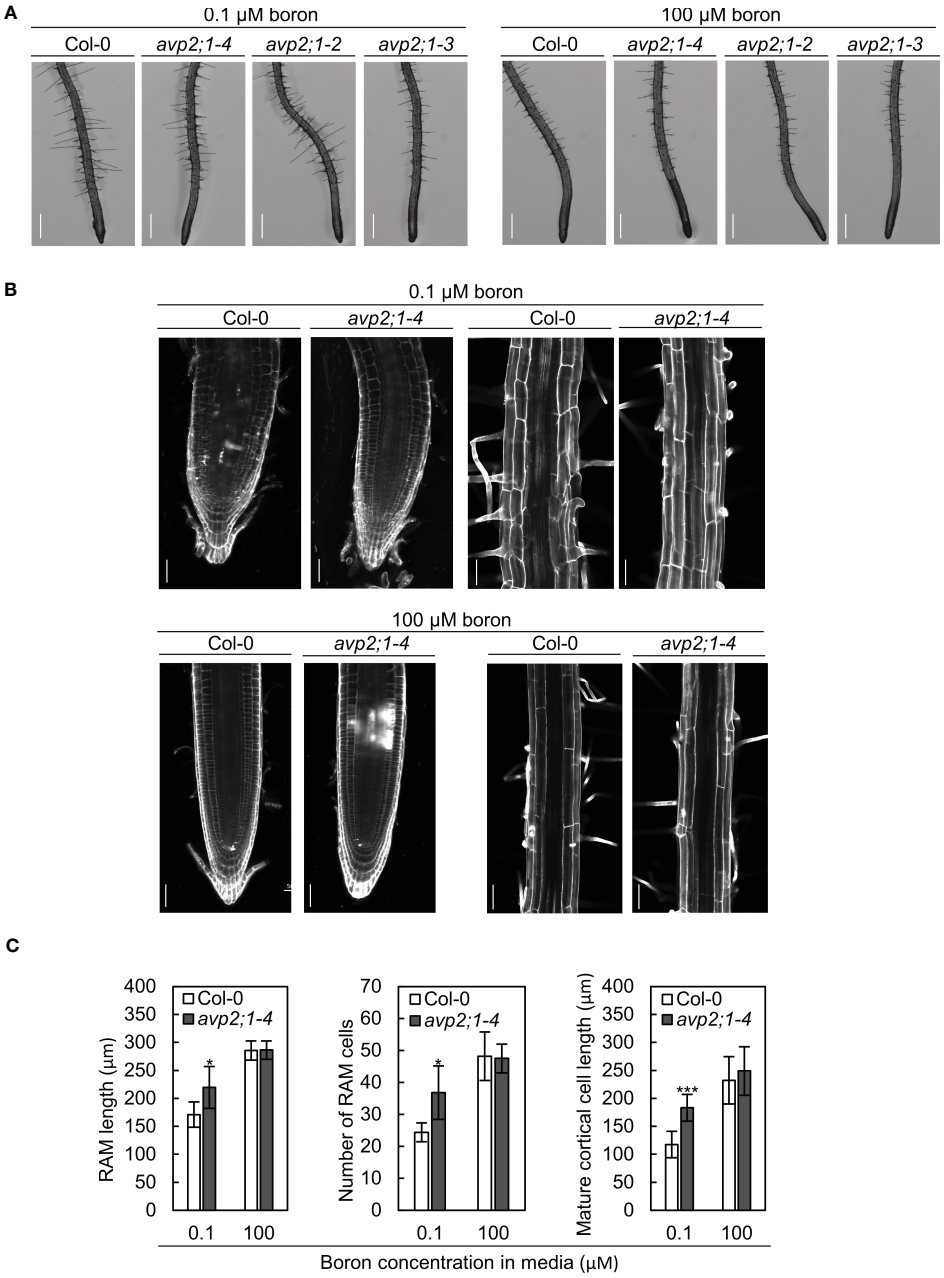

FIGURE 2
Observation of the root cells of Col-0 and *avp2;1* mutants. **(A)** Stereomicroscopic images of root tips of wildtype Col-0 and *avp2;1* mutants grown under low (0.1 µM) and normal (100 µM) boron conditions. (scale bar: 400 µm). **(B)** Confocal images of roots of wildtype Col-0 and *avp2;1-4* grown under low (0.1 µM) and normal (100 µM) boron conditions showing its meristematic zone and mature zone. (scale bar: 50 µm). **(C)** Root apical meristem (RAM) length (n=5-7 plants), number of RAM cells (n=5-7 plants), and mature cortical cell length (n=5-7 plants, means of 2-12 cells per plant were taken) of wildtype Col-0 and *avp2;1-4* under 0.1 µM and 100 µM boron conditions. Means ± SD are shown. All the analysis in Figure 2 were done using 5-d-old plants grown in solid media. ***$P < 0.001$,*$P < 0.05$, compared with wildtype Col-0 under the same boron conditions (Student's t-test).

compared to mildly low and normal boron (Figure 5B), probably as a compensation of the reduced borate crosslinking in the cell wall. Under low boron, *avp2;1* mutant lines showed a significant decrease by15-18% in cell wall calcium concentration (Figure 5B), but there were no differences under mildly low and normal boron conditions.

To further confirm the possibility of a reduced boron binding capacity in *avp2;1* mutant root cell wall, RG-II amount was estimated by measuring 2-keto-3-deoxy sugars which are RG-II specific sugars. There was a 6-17% decrease of RG-II specific sugars in *avp2;1* mutant lines compared to wildtype Col-0 under all the three boron conditions although a statistical difference was found only in *avp2;1-4* under low B (Figure 5C).

These results support that a*vp2;1* mutations did affect cell wall components and possibly cell wall stability. This change could probably explain the increased root growth of *avp2;1* mutants under a limited boron supply.

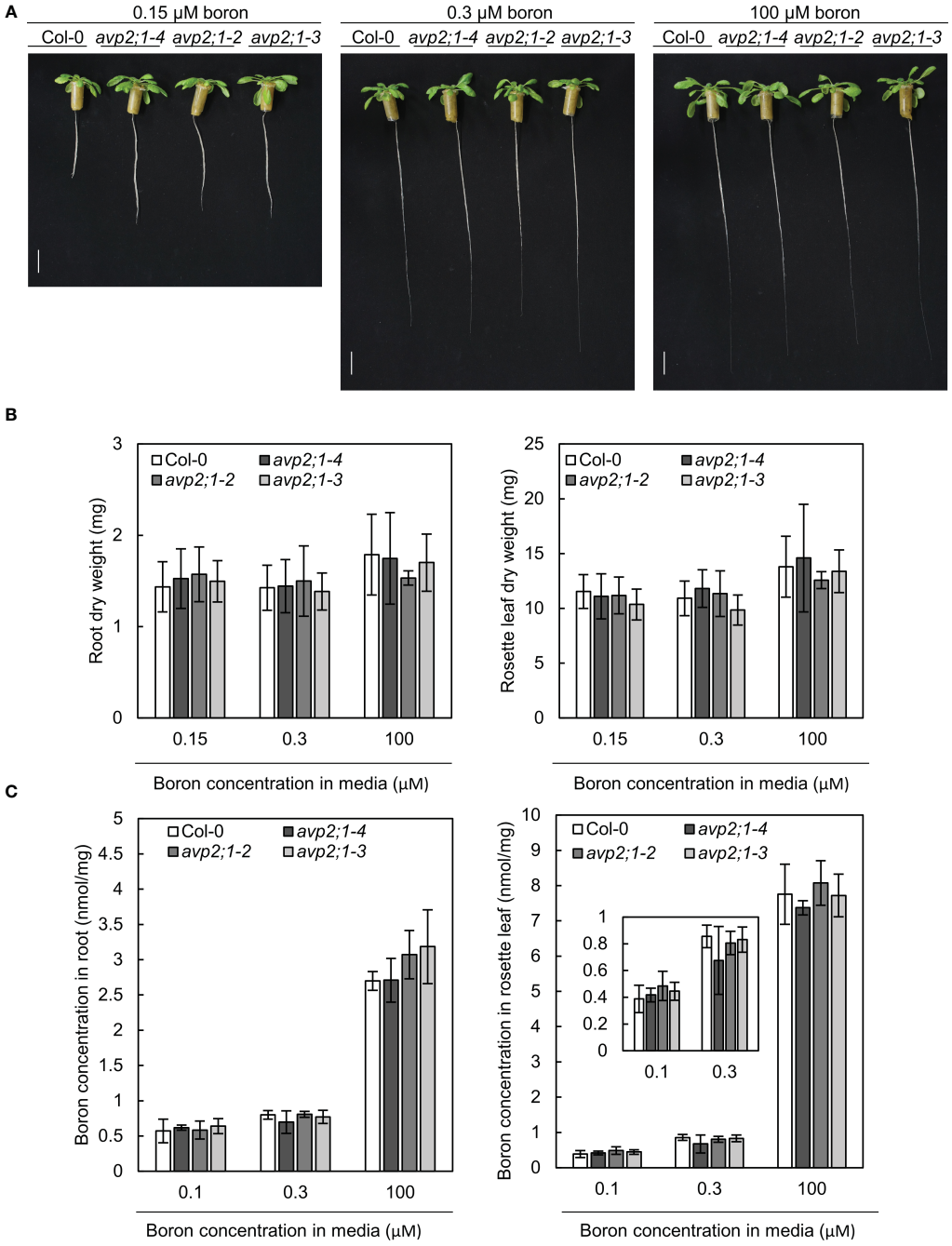

FIGURE 3
Growth in hydroponic culture and boron concentration in root and rosette leaves. **(A)** Representatives of wildtype Col-0 and *avp2;1* mutants grown in a hydroponic culture under low (0.15 µM), mildly low (0.3 µM) and normal (100 µM) boron conditions for 35 days. (scale bar: 20 mm). **(B)** Dry weight of wildtype Col-0 and mutant roots and rosette leaves grown under the same condition as **(A)**. **(C)** Boron concentration in root and rosette leaves of wildtype Col-0 and *avp2;1* mutants grown for 42 days under low (0.1 µM, the B concentration in media was increased to 0.15 µM after 19 days of culture in liquid MGRL media), mildly low (0.3 µM) and normal (100 µM) boron conditions using hydroponic culture. Means ± SD are shown (n=5-6). $P > 0.05$, compared with wildtype Col-0 under the same boron conditions (Dunnett's test).

Discussion

Previous studies have successfully identified and characterized the *A. thaliana* type II H^+-PPase, AVP2;1 as a proton pump localized to the Golgi apparatus and TGN (Segami et al., 2010). However, its physiological role and their mutant phenotype remains poorly understood in plants. In this study, we characterized *avp2;1* mutants from the view of boron deficiency stress and found that mutations in *AVP2;1* affected plant growth under low boron conditions and cell wall components under low and normal boron conditions. To describe the mechanism behind this, we propose that a reduction of AVP2;1 decreases pH pumping activity in Golgi apparatus and this possibly leads to the changes in biological processes in Golgi apparatus such as reduction in

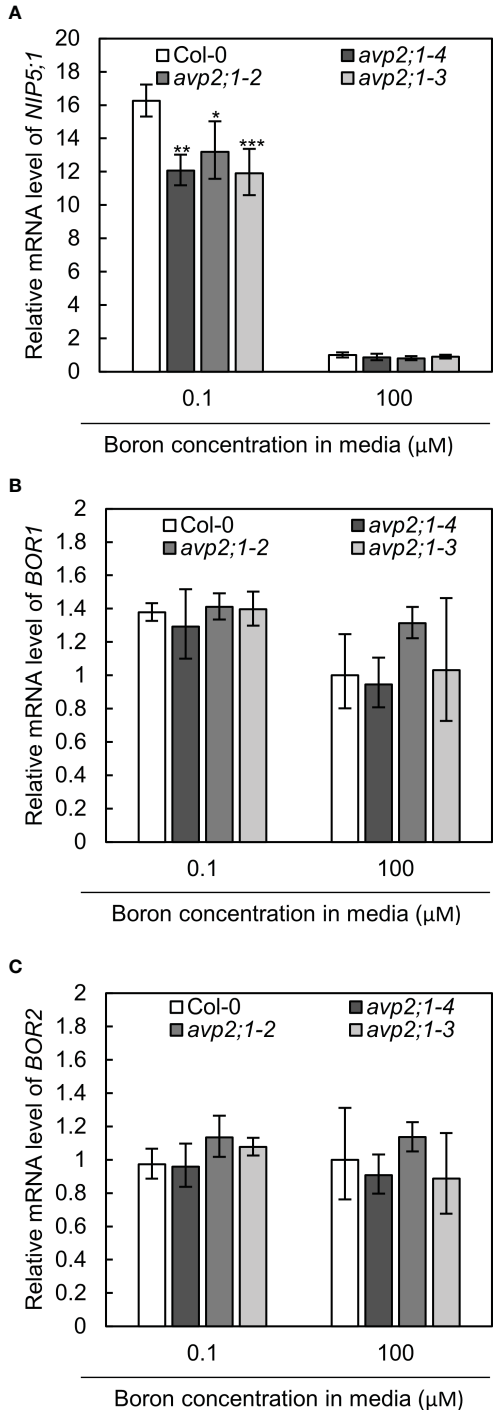

FIGURE 4
mRNA levels of boron transporter genes. **(A–C)** Relative mRNA quantification of *NIP5;1* **(A)** *BOR1* **(B)** and *BOR2* **(C)** in root of wildtype Col-0 and *avp2;1* mutant lines under low (0.1 μM) and normal (100 μM) boron condition. mRNA extracted from 9-d-old plants grown in solid media were used for all analysis. *EF1α* was used for normalization. The data was standardized by the value of Col-0 under normal (100 μM) boron condition which was set as 1. Means ± SD are shown (n=3-4). ***$P < 0.001$, **$P < 0.01$, *$P < 0.05$ compared with wildtype Col-0 under the same boron conditions (Dunnett's test).

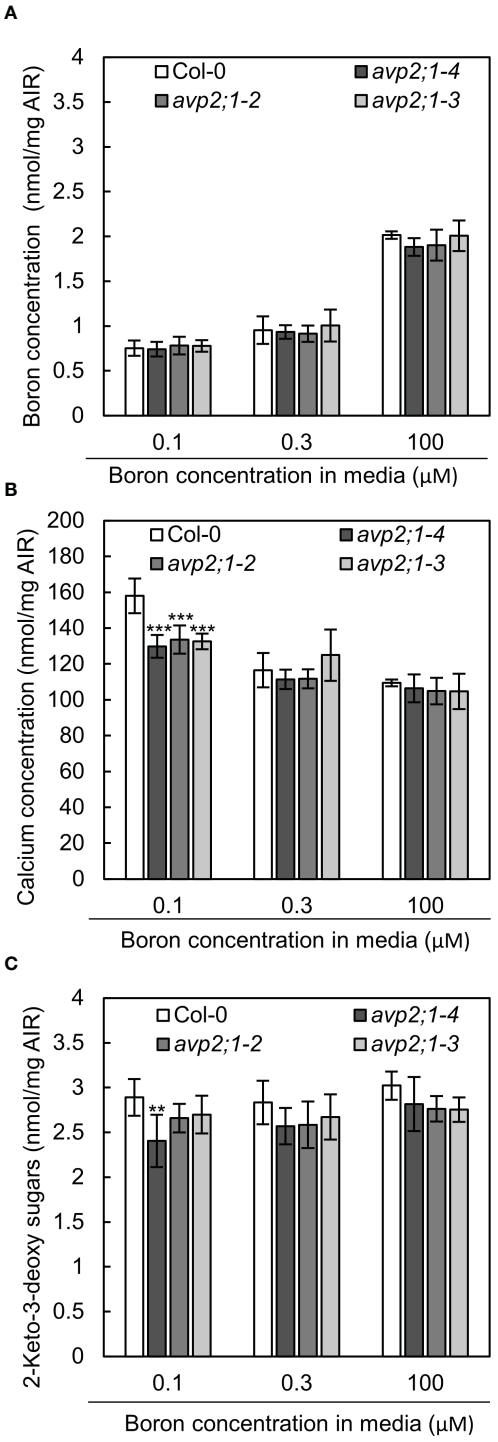

FIGURE 5
Boron, calcium and RG-II specific sugars in root cell wall extracted as alcohol insoluble residue (AIR). **(A-C)** Concentration of boron **(A)** calcium **(B)** and RG-II specific sugar, 2-keto-3-deoxy sugars **(C)** in root AIR of wildtype Col-0 and *avp2;1* mutants. The same AIR extracted from 9-d-old plants grown under low (0.1 μM), mildly low (0.3 μM) and normal (100 μM) boron conditions in solid media were used for all analysis. Means ± SD are shown (n=4-6). ***$P < 0.001$, **$P < 0.01$, compared with wildtype Col-0 under the same boron conditions (Dunnett's test).

pectin synthesis, which causes reduced sensitivity to low boron by a reduced boron requirement.

H^+ pumping rather than PPi hydrolysis is likely a key for *avp2;1* mutant root growth

AVP2;1 like other H^+ -PPases has the dual role of PPi hydrolysis and proton pumping. To have a holistic picture of the functioning of AVP2;1 in plants, it is important to understand which role of AVP2;1 causes the observed mutant phenotypes. In the case of AVP1/VHP1, *fugu5* mutant was used to demonstrate this. The *fugu5-1* is a loss-of-function *AVP1* mutant which has a null PPase activity resulting in reduced shoot growth, impaired size and shape of cotyledon, and reduced hypocotyl length of etiolated seedlings (Ferjani et al., 2011; Asaoka et al., 2016). The introduction of cytosolic soluble inorganic pyrophosphatase (IPP) of *S. cerevisiae* under the control of the *AVP1* promoter into the *fugu5-1* mutant, was able to rescue these phenotypes (Ferjani et al., 2011). This suggested that rather than proton pumping, hydrolysis of cytosolic PPi is the major physiological role of AVP1. This was further confirmed using an uncoupling mutated variant of AVP1 that could hydrolyze PPi but had no proton pumping activity. The introduction of this mutant variant into *fugu5-3* rescued shoot growth as when native H^+-PPase (AVP1) was introduced (Asaoka et al., 2016), thereby supporting that the hydrolytic role rather than proton pumping of AVP1, is essential for plant growth. On the other hand, Tojo et al. (2023) has revealed the negligible contribution of PPi hydrolytic role of AVP2;1 in growth of *A. thaliana* seedling. This was done by phenotypic characterization of the *AVP2;1* mutant, *vhp2;1-1/avp2;1-1* (SAIL_512_B02) and *fugu5-1vhp2;1-1* double mutant. Phenotypes related to loss of PPase activity such as alterations in cotyledon shape and hypocotyl elongation defects in etiolated seedlings were not observed in *vhp2;1-1* and neither was any additional effect observed in *fugu5-1vhp2;1* compared to *fugu5-1*. We also tested the response of *avp1-4* (Yang et al., 2018) to low boron stress. However, no difference from Col-0 was observed (Figure S3) in contrast to *avp2;1* mutants. Considering the minimal contribution of AVP2;1 in PPi hydrolysis for the growth of *A. thaliana* and the plant growth observed in *avp1-4*, we suggest that rather than the hydrolysis of cytosolic PPi, proton pumping into the Golgi apparatus is the primary component driving the *avp2;1* mutant root growth under low boron conditions.

Change of H^+ pumping activity in the Golgi apparatus possibly affects pectin synthesis including RG-II

The Golgi apparatus is involved in sorting and transporting proteins to cellular compartments as well as assembling and exporting the non-cellulosic polysaccharides of the cell wall matrix including pectin in plants (Driouich et al., 2012). For non-cellulosic cell wall polysaccharide synthesis in Golgi apparatus, by the activity of the nucleotide sugar transporter (NST), nucleoside di-phosphate sugar (NDP-sugar) is imported from the cytosol into the Golgi lumen, supplying substrate for glycosyltransferase (Figure 6). The sugar moiety is then transferred to a building chain of polysaccharide via the action of glycosyltransferase and the resulting NDP is hydrolyzed by NDPase to nucleoside monophosphate (NMP) and inorganic phosphate. The NMP concentration gradient drives transport of NDP-sugar via NSTs as NDP-sugar/NMP antiporters. The inorganic phosphate released from NDP hydrolysis is exported into the cytosol from Golgi apparatus via a phosphate transporter (Reyes and Orellana, 2008; Figure 6).

Assuming H^+ pumping activity of AVP2;1 as its key contribution to plant growth, we propose that a reduced function of AVP2;1 would increase pH and affect ion homeostasis in the Golgi apparatus. The effect of these changes would likely affect biochemical processes in the Golgi apparatus including pectin synthesis (Figure 6) and in this study, we have observed a tendency of a reduction in RG-II amount under various boron concentrations in *avp2;1* mutant cell wall (Figure 5). This proposition is in line with Reyes and Orellana (2008) hypothesis that the activity of glycosyltransferase could be affected by ion homeostasis and pH. pH dependent activity of some *A. thaliana* glycosyltransferases such as RG-I: galacturonsyltransferase (RGGAT1) (Amos et al., 2023), HG: galacturonosyltransferase (GAUT1:GAUT7) (Amos et al., 2018), RG-I: rhamnosyltransferase (RRT1) (Takenaka et al., 2018), RG-II: xylosyltransferase (RGXT1) (Petersen et al., 2009) involved in pectin synthesis has been reported. These *in vitro* analyses showed an optimal pH for these glycosyltransferases to be pH 6.5 (RGGAT1), pH 7.2 (GAUT1:GAUT7), pH 7 (RRT1) and around pH 7 (RGXT1). However, this may be different from the actual activity within the cell considering the pH range of the Golgi apparatus. In addition, it has been shown in human cancer cells that a slight increase in the Golgi pH affects the formation of glycosyltransferase complexes and also induces mislocalization of glycosyltransferase from the Golgi apparatus into endosomal compartments (Kellokumpu, 2019).

The Golgi-localized inorganic phosphate transporter, PHT4;6 in *A. thaliana* has been identified to release inorganic phosphate (Pi) into the cytosol from the Golgi lumen (Guo et al., 2007). Although it has not been experimentally demonstrated, it is hypothesized that the release of the lumenal Pi by PHT4;6 is dependent on proton gradients (Guo et al., 2007). The lumenal Pi if not released, could hamper activities in the Golgi apparatus including pectin synthesis.

Considering the localization of AVP2;1 to the TGN, there is also a possibility that the pectin trafficking is hampered/affected by a reduced function of AVP2;1. This probably could lead to a reduced amount of pectin which is trafficked or deposited to the cell wall.

We also observed the reduction of calcium concentration in cell wall of *avp2;1* mutants under low boron compared to wildtype Col-0 (Figure 5). The HG is crosslinked by calcium and hence, a reduction in cell wall calcium concentration could imply a reduced HG. We propose that in addition to RG-II polysaccharide, HG polysaccharide could be also affected by changes in the state of the Golgi apparatus caused by the reduced H^+ pumping activity of AVP2;1. It is also possible that the reduction of calcium-crosslinked HG is due to a

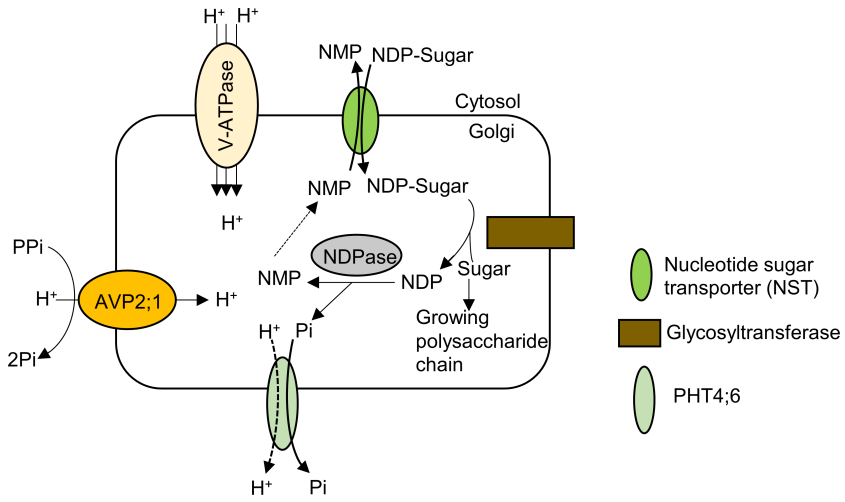

FIGURE 6
Model of pectin synthesis and the contribution of AVP2;1 to the maintenance of ion homeostasis in the Golgi apparatus. By the activity of the nucleotide sugar transporter (NST) which is an NDP-sugar/NMP antiporter, nucleoside di-phosphate sugar (NDP-sugar) is imported from the cytosol into the Golgi lumen. The sugar moiety is then transferred to a growing chain of polysaccharide via the action of glycosyltransferase and the resulting NDP is hydrolyzed by NDPase to nucleoside monophosphate (NMP) and inorganic phosphate. The NMP concentration gradient drives transport of NDP-sugar via NSTs as NDP-sugar/NMP antiporters. The inorganic phosphate released from NDP hydrolysis is exported into the cytosol from Golgi apparatus via a phosphate transporter (PHT4;6). AVP2;1 helps to maintain ionic homeostasis and acidic state of the Golgi apparatus via its proton pumping activity thereby enhancing the process of pectic polysaccharide synthesis.

secondary effect induced by growth change in mutants rather than a direct effect of reduction in H^+ pumping activity of AVP2;1. Pectin methylesterase (PME) catalyzes the demethylesterification of HG thereby increasing calcium crosslinking. It has been found that the activity of PME is induced by boron deficiency (Yan et al., 2021) possibly for compensation of borate-RG-II crosslinking. Hence, due to relieved severity of boron deficiency in *avp2;1* mutants under low boron supply, the demethylesterification activity of the PME could be reduced resulting in the decrease of cell wall calcium concentration.

Decrease in RG-II amount may possibly reduce boron requirement in *avp2;1* mutants

One of the major effects of boron deficiency on plants is the damage of growing points, which include inhibition of root cell elongation and division leading to a cessation of root elongation (Dell and Huang, 1997). However, *avp2;1* mutant lines showed less sensitivity to this (Figure 2). Following the observed tendency of reduced amount of RG-II by 6-17% in these mutants (Figure 5), we suggest that this reduced sensitivity to low boron is because of a reduction in boron requirement. Reduced boron requirement means that a smaller amount of boron can satisfy the boron demand possibly due to the reduced boron binding sites for RG-II in *avp2;1* mutants. In line with our study, Hiroguchi et al. (2021) has also shown that 20-30% reduction in RG-II enhances root elongation under limited supply of boron. In this case, increased root meristem was not clearly observed under low boron condition in *tmn1* mutants at 4 days compared to this current study of *avp2;1* mutants at 5 days (Figure 2). However, a tendency of an increased root meristem was observed in the *tmn1* mutant still at 4 days and at a longer incubation time under low boron condition in hydroponic culture (Hiroguchi et al., 2021).

It has also been reported that there is a positive correlation between pectin amount and cell wall boron concentration which may represent amount of boron required by plants for tissue development among different plant species (Hu et al., 1996). More directly, a positive correlation between cell wall boron concentration and RG-II amount has been revealed (Matoh et al., 1996). This implies pectin amount or RG-II amount determines sensitivity to boron deficiency hence the reduced sensitivity to low boron in *avp2;1* mutants. We suggest that cell wall modification would be another approach for conferring low-boron tolerance.

The contribution of AVP2;1 to pH homeostasis in Golgi apparatus may be minimal

In our study, *avp2;1* mutants showed a significant increase in primary root growth accompanied by increased root cell division and elongation when compared to wildtype Col-0 under low boron. This increment of growth was however not observed in the leaves of *avp2;1* mutants (Figures 1, 3) possibly because AVP2s protein is predominately expressed in roots but not in young and mature leaves (Segami et al., 2010). Again, differences between the wildtype Col-0 and *avp2;1* mutants were not observed under normal boron condition. One possible explanation to this could be a minor contribution of AVP2;1 to pH homeostasis in Golgi apparatus because it is assumed that V-ATPase is the major proton pump in the Golgi apparatus. Result of the analysis of RG-II specific sugars revealed a 6-7% consistent reduction in *avp2;1* mutants compared to wildtype Col-0 under both low and normal boron condition

except for *avp2;1-4* which showed 17% reduction under low boron condition. Under normal boron conditions, most of RG-II is crosslinked by sufficient supply of boron therefore, a 6-7% reduction of RG-II may not greatly affect the plant growth. However, under low boron conditions, when borate crosslinking of RG-II is likely a major determinant for cell division and elongation, this slight change of RG-II could affect the plant growth.

AVP2;2 is an isoform of AVP2;1 and shares about 94% amino acid sequence identity (Segami et al., 2010). Based on the amino acid sequence identity of the two proteins, we examined *avp2;2* mutants to check if AVP2;2 has a similar role in low boron as AVP2;1. The analysis of the growth of *avp2;2* mutants, however, revealed that unlike *avp2;1* mutants, *avp2;2* mutants showed no significant differences from Col-0 under low and normal boron conditions (Figure S4). This could be because of its very low transcript amount compared to *AVP2;1* hence no noticeable change in *avp2;2* mutants. Another possibility is that though AVP2;1 and AVP2;2 share great similarities, their functions do not overlap, and reduction of low boron sensitivity may be specific to AVP2;1.

In conclusion, this study supports an idea that AVP2;1 plays a role in proton pumping and acidification of Golgi apparatus for maintenance of pectin synthesis by examination of *avp2;1* mutants. It also proposes the reduction of boron requirement by molecular approach as a sustainable strategy against low boron stress.

Data availability statement

The original contributions presented in the study are included in the article/Supplementary Material. Further inquiries can be directed to the corresponding author.

Author contributions

AO: Conceptualization, Data curation, Formal Analysis, Funding acquisition, Investigation, Methodology, Resources, Validation, Writing – review & editing, Writing – original draft. KM: Conceptualization, Data curation, Formal Analysis, Funding acquisition, Investigation, Methodology, Resources, Validation, Writing – review & editing, Project administration, Supervision.

Funding

This work was supported by MEXT KAKENHI and JSPS KAKENHI to KM [grant number JP18H05490, JP19H05637] and by JST SPRING to AO [JPMJSP2119].

Acknowledgments

We sincerely appreciate Michiko Tsukamoto and Yuko Kawara for their technical assistance. We also appreciate Prof. Toshirio Watanabe for his technical support in ICP-MS.

Conflict of interest

The authors declare that the research was conducted in the absence of any commercial or financial relationships that could be construed as a potential conflict of interest.

Publisher's note

Supplementary material

The Supplementary Material for this article can be found online at: https://www.frontiersin.org/articles/10.3389/fpls.2023.1255486/full#supplementary-material

References

Alba, K., and Kontogiorgos, V. (2017). Pectin at the oil-water interface: Relationship of molecular composition and structure to functionality. *Food Hydrocoll.* 68, 211–218. doi: 10.1016/j.foodhyd.2016.07.026

Alonso, J. M., Stepanova, A. N., Leisse, T. J., Kim, C. J., Chen, H., Shinn, P., et al. (2003). Genome-wide insertional mutagenesis of *Arabidopsis thaliana*. *Science* 301, 653–657. doi: 10.1126/science.1086391

Amos, R. A., Atmodjo, M. A., Huang, C., Gao, Z., Venkat, A., Taujale, R., et al. (2023). Polymerization of the backbone of the pectic polysaccharide rhamnogalacturonan I. *Nat. Plants* 4, 673. doi: 10.1038/s41477-022-01270-3

Amos, R. A., Pattathil, S., Yang, J. Y., Atmodjo, M. A., Urbanowicz, B. R., Moremen, K. W., et al. (2018). A two-phase model for the non-processive biosynthesis of homogalacturonan polysaccharides by the GAUT1:GAUT7 complex. *J. Biol. Chem.* 49, 19047–19063. doi: 10.1074/jbc.RA118.004463

Asaoka, M., Segami, S., Ferjani, A., and Maeshima, M. (2016). Contribution of PPi-hydrolyzing function of vacuolar H^+-pyrophosphatase in vegetative growth of *Arabidopsis*: Evidenced by expression of uncoupling mutated enzymes. *Front. Plant Sci.* 7. doi: 10.3389/fpls.2016.00415

Cosgrove, D. J., and Jarvis, M. C. (2012). Comparative structure and biomechanics of plant primary and secondary cell walls. *Front. Plant Sci.* 3. doi: 10.3389/fpls.2012.00204

Dell, B., and Huang, L. (1997). Physiological response of plants to low boron. *Plant Soil* 193, 103–120. doi: 10.1023/A:1004264009230

Driouich, A., Faye, L., and Staehelin, A. (1993). The plant Golgi apparatus: a factory for complex polysaccharides and glycoproteins. *Trends Biochem. Sci.* 18, 210–214. doi: 10.1016/0968-0004(93)90191-O

Driouich, A., Follet-Gueye, M. L., Bernard, S., Kousar, S., Chevalier, L., Vicré-Gibouin, M., et al. (2012). Golgi-mediated synthesis and secretion of matrix polysaccharides of the primary cell wall of higher plants. *Front. Plant Sci.* 3. doi: 10.3389/fpls.2012.00079

Drozdowicz, Y. M., Kissinger, J. C., and Rea, P. A. (2000). AVP2, a sequence-divergent, K^+-insensitive H^+-translocating inorganic pyrophosphatase from Arabidopsis. *Plant Physiol.* 123, 353–362. doi: 10.1104/pp.123.1.353

Duran, C., Arce-Johnson, P., and Aquea, F. (2018). Methylboronic acid fertilization alleviates boron deficiency symptoms in *Arabidopsis thaliana*. *Planta* 248, 221–229. doi: 10.1007/S00425-018-2903-0

Ferjani, A., Segami, S., Horiguchi, G., Muto, Y., Maeshima, M., and Tsukaya, H. (2011). Keep an eye on PPi: The vacuolar-type H^+-pyrophosphatase regulates postgerminative development in *Arabidopsis*. *Plant Cell* 23, 2895–2908. doi: 10.1105/tpc.111.085415

Fujiwara, T., Hirai, M. Y., Chino, M., Komeda, Y., and Naito, S. (1992). Effects of sulfur nutrition on expression of the soybean seed storage protein genes in transgenic petunia. *Plant Physiol.* 99, 263–268. doi: 10.1104/pp.99.1.263

Fujiyama, B. S., Silva, A. R. B., Silva Júnior, M. L., Cardoso, N. R. P., Fonseca, A. B., Viana, R. G., et al. (2019). Boron fertilization enhances photosynthesis and water use efficiency in soybean at vegetative growth stage. *J. Plant Nutr.* 42, 2498–2506. doi: 10.1080/01904167.2019.1659326

Güneş, A., Alpaslan, M., İnal, A., Saıt Adak, M., Eraslan, F., and Çiçek, N. (2003). Effects of boron fertilization on the yield and some yield components of bread and durum wheat. *Turk. J. Agric.* 27, 329–335.

Guo, B., Jin, Y., Wussler, C., Blancaflor, E. B., Motes, C. M., Versaw, W. K., et al. (2007). Functional analysis of the *Arabidopsis* PHT4 family of intracellular phosphate transporters. *New Phytol.* 177, 889–898. doi: 10.1111/j.1469-8137.2007.02331.x

Gupta, U. C., Jame, Y. W., Campbell, C. A., Leyshon, A. J., and Nicholaichuk, W. (1985). Boron toxicity and deficiency: a review. *Can. J. Soil Sci.* 65, 381–409. doi: 10.4141/cjss85-044

Hiroguchi, A., Sakamoto, S., Mitsuda, N., and Miwa, K. (2021). Golgi-localized membrane protein AtTMN1/EMP12 functions in the deposition of rhamnogalacturonan II and I for cell growth in Arabidopsis. *J. Exp. Bot.* 72, 3611–3629. doi: 10.1093/jxb/erab065

Hu, H., Brown, P. H., and Labavitch, J. M. (1996). Species variability in boron requirement is correlated with cell wall pectin. *J. Exp. Bot.* 47, 227–232. doi: 10.1093/jxb/47.2.227

Kellokumpu, S. (2019). Golgi pH, ion and redox homeostasis: how much do they really matter? *Front. Cell Dev. Biol.* 7. doi: 10.3389/fcell.2019.00093

Kim, Y. S., Kim, I. S., Choe, Y. H., Bae, M. J., Shin, S. Y., Park, S. K., et al. (2014). Overexpression of the *Arabidopsis* vacuolar H^+-pyrophosphatase AVP1 gene in rice plants improves grain yield under paddy field conditions. *J. Agric. Sci.* 152, 941–953. doi: 10.1017/S0021859613000671

Kobayashi, M., Matoh, T., and Azuma, J. I. (1996). Two chains of rhamnogalacturonan II are cross-linked by borate-diol ester bonds in higher plant cell walls. *Plant Physiol.* 110, 1017–1020. doi: 10.1104/pp.110.3.1017

Lerouxel, O., Cavalier, D. M., Liepman, A. H., and Keegstra, K. (2006). Biosynthesis of plant cell wall polysaccharides - a complex process. *Curr. Opin. Plant Biol.* 9, 621–630. doi: 10.1016/j.pbi.2006.09.009

Li, J., Yang, H., Peer, W. A., Richter, G., Blakeslee, J., Bandyopadhyay, A., et al. (2005). *Arabidopsis* H^+-PPase AVP1 regulates auxin-mediated organ development. *Science* 310, 121–125. doi: 10.1126/science.1115711

Luo, Y., Scholl, S., Doering, A., Zhang, Y., Irani, N. G., Di Rubbo, S., et al. (2015). V-ATPase activity in the TGN/EE is required for exocytosis and recycling in *Arabidopsis*. *Nat. Plants* 1, 15094. doi: 10.1038/nplants.2015.94

Matoh, T., Ishigaki, K., Ohno, K., and Azuma, J. (1993). Isolation and characterization of a boron-polysaccharide complex from radish roots. *Plant Cell Physiol.* 34, 639–642. doi: 10.1093/oxfordjournals.pcp.a078465

Matoh, T., Kawaguchi, S., and Kobayashi, M. (1996). Ubiquity of a borate-rhamnogalacturonan II complex in the cell walls of higher plants. *Plant Cell Physiol.* 37, 636–640. doi: 10.1093/oxfordjournals.pcp.a028992

Matsunaga, T., Ishii, T., Matsumoto, S., Higuchi, M., Darvill, A., Albersheim, P., et al. (2004). Occurrence of the primary cell wall polysaccharide rhamnogalacturonan II in pteridophytes, lycophytes, and bryophytes. implications for the evolution of vascular plants. *Plant Physiol.* 134, 339–351. doi: 10.1104/pp.103.030072

Mohnen, D. (2008). Pectin structure and biosynthesis. *Curr. Opin. Plant Biol.* 11, 266–277. doi: 10.1016/j.pbi.2008.03.006

Ndeh, D., Rogowski, A., Cartmell, A., Luis, A. S., Basle, A., Gray, J., et al. (2017). Complex pectin metabolism by gut bacteria reveals novel catalytic functions. *Nature* 544, 65–70. doi: 10.1038/nature21725

Nepal, N., Yactayo-Chang, J. P., Gable, R., Wilkie, A., Martin, J., Aniemena, C. L., et al. (2020). Phenotypic characterization of *Arabidopsis thaliana* lines overexpressing AVP1 and MIOX4 in response to abiotic stresses. *Appl. Plant Sci.* 8, e11384. doi: 10.1002/aps3.11384

O'Neill, M. A., Eberhard, S., Albersheim, P., and Darvill, A. G. (2001). Requirement of borate cross-linking of cell wall rhamnogalacturonan II for *Arabidopsis* Growth. *Science* 294, 846–849. doi: 10.1126/science.1062319

Onuh, A. F., and Miwa, K. (2021). Regulation, diversity and evolution of boron transporters in plants. *Plant Cell Physiol.* 62, 590–599. doi: 10.1093/pcp/pcab025

Pacheco-Escobedo, M. A., Ivanov, V. B., Ransom-Rodríguez, I., Arriaga-Mejía, G., Ávila, H., Baklanov, I. A., et al. (2016). Longitudinal zonation pattern in *Arabidopsis* root tip defined by a multiple structural change algorithm. *Ann. Bot.* 118, 763–776. doi: 10.1093/aob/mcw101

Petersen, B. L., Egelund, J., Damager, I., Kirsten, F., Jacob, K. J., Zhang, Y., et al. (2009). Assay and heterologous expression in *Pichia pastoris* of plant cell wall type-II membrane anchored glycosyltransferases. *Glycoconj. J.* 26, 1235–1246. doi: 10.1007/s10719-009-9242-0

Reyes, F., and Orellana, A. (2008). Golgi transporters: opening the gate to cell wall polysaccharide biosynthesis. *Curr. Opin. Plant Biol.* 11, 244–251. doi: 10.1016/j.pbi.2008.03.008

Segami, S., Makino, S., Miyake, A., Asaoka, M., and Maeshima, M. (2014). Dynamics of vacuoles and H^+-pyrophosphatase visualized by monomeric green fluorescent protein in *Arabidopsis*: Artifactual bulbs and native intravacuolar spherical structures. *Plant Cell* 26, 3416–3434. doi: 10.1105/tpc.114.127571

Segami, S., Nakanishi, Y., Sato, M. H., and Maeshima, M. (2010). Quantification, organ-specific accumulation and intracellular localization of type II H^+-pyrophosphatase in Arabidopsis thaliana. *Plant Cell Physiol.* 51, 1350–1360. doi: 10.1093/pcp/pcq096

Sessions, A., Burke, E., Presting, G., Aux, G., McElver, J., Patton, D., et al. (2002). A high-throughput *Arabidopsis* reverse genetics system. *Plant Cell* 14, 2985–2994. doi: 10.1105/TPC.004630

Shen, J., Zeng, Y., Zhuang, X., Sun, L., Yao, X., Pimpl, P., et al. (2013). Organelle pH in the *Arabidopsis* endomembrane system. *Mol. Plant* 6, 1419–1437. doi: 10.1093/mp/sst079

Takano, J., Wada, M., Ludewig, U., Schaaf, G., von Wirén, N., and Fujiwara, T. (2006). The *Arabidopsis* major intrinsic protein NIP5;1 is essential for efficient boron uptake and plant development under boron limitation. *Plant Cell* 18, 1498–1509. doi: 10.1105/tpc.106.041640

Takenaka, Y., Kato, K., Ogawa-Ohnishi, M., Tsuruhama, K., Kajiura, H., Yagyu, K., et al. (2018). Pectin RG-I rhamnosyltransferases represent a novel plant-specific glycosyltransferase family. *Nat. Plants* 4, 669–676. doi: 10.1038/s41477-018-0217-7

Tanaka, M., Takano, J., Chiba, Y., Lombardo, F., Ogasawara, Y., Onouchi, H., et al. (2011). Boron-dependent degradation of NIP5;1 mRNA for acclimation to excess boron conditions in *Arabidopsis*. *Plant Cell* 23, 3547–3559. doi: 10.1105/tpc.111.088351

Tojo, H., Tabeta, H., Gunji, S., Hirai, M. Y., David, P., Javot, H., et al. (2023). Roles of type II H^+-PPases and PPsPase1/PECP2 in early developmental stages and PPi homeostasis of *Arabidopsis thaliana*. *Front. Plant Sci.* 14. doi: 10.3389/fpls.2023.1031426

Voxeur, A., Soubigou-Taconnat, L., Legée, F., Sakai, K., Antelme, S., Durand-Tardif, M., et al. (2017). Altered lignification in *mur1-1* a mutant deficient in GDP-L-fucose synthesis with reduced RG-II cross linking. *PloS One* 12, e0184820. doi: 10.1371/journal.pone.0184820

Yan, L., Riaz, M., Liu, J., Liu, Y., Zeng, Y., and Jiang, C. (2021). Boron reduces aluminum deposition in alkali-soluble pectin and cytoplasm to release aluminum toxicity. *J. Hazard. Mater.* 401, 123388. doi: 10.1016/j.jhazmat.2020.123388

Yang, Y., Tang, R. J., Mu, B., Ferjani, A., Shi, J., Zhang, H., et al. (2018). Vacuolar proton pyrophosphatase is required for high magnesium tolerance in *Arabidopsis*. *Int. J. Mol. Sci.* 19, 3617. doi: 10.3390/ijms19113617

York, W., Darvill, A. G., Mcneil, M., and Albersheim., P. (1985). 3-deoxy-D-*manno*-2-octulosonic acid (KDO) is a component of rhamnogalacturonan II, a pectic polysaccharide in the primary cell walls of plants. *Carbohydr. Res.* 138, 109–126. doi: 10.1016/0008-6215(85)85228-9

Zhang, H., Chen, M., Xu, C., Liu, R., Tang, W., Chen, K., et al. (2023). H^+-pyrophosphatases enhance low nitrogen stress tolerance in transgenic *Arabidopsis* and wheat by interacting with a receptor-like protein kinase. *Front. Plant Sci.* 14. doi: 10.3389/fpls.2023.1096091

frontiers | Frontiers in Plant Science

TYPE Original Research
PUBLISHED 23 August 2023
DOI 10.3389/fpls.2023.1221436

OPEN ACCESS

EDITED BY
Ali Ferjani,
Tokyo Gakugei University, Japan

REVIEWED BY
Kengo Kanamaru,
Kobe University, Japan
Jeeyon Jeong,
Amherst College, United States

*CORRESPONDENCE
Cornelia Spetea
cornelia.spetea.wiklund@bioenv.gu.se

†These authors have contributed equally to this work and share first authorship

RECEIVED 12 May 2023
ACCEPTED 07 July 2023
PUBLISHED 23 August 2023

CITATION
Dukic E, van Maldegem KA, Shaikh KM, Fukuda K, Töpel M, Solymosi K, Hellsten J, Hansen TH, Husted S, Higgins J, Sano S, Ishijima S and Spetea C (2023) Chloroplast magnesium transporters play essential but differential roles in maintaining magnesium homeostasis. *Front. Plant Sci.* 14:1221436. doi: 10.3389/fpls.2023.1221436

Chloroplast magnesium transporters play essential but differential roles in maintaining magnesium homeostasis

Emilija Dukic[1†], Kim A. van Maldegem[1†], Kashif Mohd Shaikh[1†], Kento Fukuda[2], Mats Töpel[3,4], Katalin Solymosi[5], Jonna Hellsten[1], Thomas Hesselhøj Hansen[6], Søren Husted[6], John Higgins[7], Satoshi Sano[2], Sumio Ishijima[2] and Cornelia Spetea[1*]

[1]Department of Biological and Environmental Sciences, University of Gothenburg, Gothenburg, Sweden, [2]Graduate School of Life and Environmental Sciences, Kyoto Prefectural University, Kyoto, Japan, [3]Department of Marine Sciences, University of Gothenburg, Gothenburg, Sweden, [4]IVL Swedish Environmental Research Institute, Gothenburg, Sweden, [5]Department of Plant Anatomy, ELTE Eötvös Loránd University, Budapest, Hungary, [6]Copenhagen Plant Science Centre, Department of Plant and Environmental Sciences, University of Copenhagen, Copenhagen, Denmark, [7]Department of Geosciences, Princeton University, Princeton, NJ, United States

Magnesium (Mg^{2+}) is essential for photosynthesis in the chloroplasts of land plants and algae. Being the central ion of chlorophyll, cofactor and activator of many photosynthetic enzymes including RuBisCO, magnesium-deficient plants may suffer from leaf chlorosis symptoms and retarded growth. Therefore, the chloroplast Mg^{2+} concentration is tightly controlled by magnesium transport proteins. Recently, three different transporters from two distinct families have been identified in the chloroplast inner envelope of the model plant *Arabidopsis thaliana*: MGT10, MGR8, and MGR9. Here, we assess the individual roles of these three proteins in maintaining chloroplast Mg^{2+} homeostasis and regulating photosynthesis, and if their role is conserved in the model green alga *Chlamydomonas reinhardtii*. Phylogenetic analysis and heterologous expression revealed that the CorC-like MGR8 and MGR9 transport Mg^{2+} by a different mechanism than the CorA-like MGT10. *MGR8* and *MGT10* genes are highest expressed in leaves, indicating a function in chloroplast Mg^{2+} transport. MGR9 is important for chloroplast function and plant adaptation in conditions of deficiency or excess of Mg^{2+}. Transmission electron microscopy indicated that MGT10 plays a differential role in thylakoid stacking than MGR8 and MGR9. Furthermore, we report that MGR8, MGR9, and MGT10 are involved in building up the pH gradient across the thylakoid membrane and activating photoprotection in conditions of excess light, however the mechanism has not been resolved yet. While there are no chloroplast MGR-like transporters in Chlamydomonas, we show that MRS4 is a homolog of MGT10, that is required for photosynthesis and cell growth. Taken together, our findings reveal that the studied Mg^{2+} transporters play essential but differential roles in maintaining chloroplast Mg^{2+} homeostasis.

KEYWORDS

***Arabidopsis thaliana*, *Chlamydomonas reinhardtii*, chloroplast, magnesium homeostasis, magnesium transporter, chlorophyll fluorescence, photosynthesis**

1 Introduction

Magnesium (Mg^{2+}) is an abundant and essential mineral nutrient for all living organisms. In plants, Mg^{2+} critically contributes to the process of photosynthesis since it is required as the central ion of the chlorophyll (Chl) molecule and as an activator of RuBisCO as well as for thylakoid stacking and counterbalancing of the H^+ gradient across the thylakoid membrane (Szabò and Spetea, 2017; Tang and Luan, 2017). A significant proportion (15-35%) of the total Mg^{2+} content in plants is allocated to the chloroplast (Chen et al., 2018). In *Arabidopsis thaliana* (hereafter Arabidopsis), Mg^{2+} is taken up from the soil by the roots, loaded into the xylem, and transported throughout the shoots into the leaf chloroplasts (Hermans et al., 2013). Due to its charge, Mg^{2+} cannot move freely across membranes, and transport is tightly controlled by specialized transport proteins.

Even though no thylakoid-located Mg^{2+} transporter has been identified so far, two distinct families of proteins are known to transport Mg^{2+} across the inner envelope membrane. MGT10 was localized to the chloroplast envelope (Drummond et al., 2006), proven to transport Mg^{2+}, and to play an essential role in chloroplast development and photosynthesis (Liang et al., 2017; Sun et al., 2017). MGT10 belongs to a major family of magnesium transporters in plants (MGTs) that are related to the well-characterized family of bacterial CorA-type Mg^{2+} ion channels (Li et al., 2001; Lunin et al., 2006; Guskov et al., 2012). Most recently, two magnesium release transporters, MGR8 and MGR9, from a distant clade of cyclin M (CNNMs) from yeast and humans, were localized to the chloroplast inner envelope (Zhang et al., 2022). MGR8 and MGR9 share 78% amino acid sequence identity and their Mg^{2+} uptake activity was demonstrated by functional complementation of a *Salmonella typhimurium* mutant (Zhang et al., 2022). Both families of Mg^{2+} transporters play an essential role for the plant since the single knockout of *MGR10* and the double knockout of *MGR8* and *MGR9* result in impaired chloroplast development (Sun et al., 2017; Zhang et al., 2022). At present, the individual roles of these transporters remain largely unknown.

Mg^{2+} is also essential for photosynthesis and growth in algae, and although there are homologs in the genomes of green algae, no Mg^{2+} transporter has been characterized so far (Marchand et al., 2018). In this study, we aimed to assess the role of MGR8, MGR9, and MGT10 in maintaining magnesium homeostasis in the chloroplast of Arabidopsis and if their role is conserved in the model green alga *Chlamydomonas reinhardtii* (hereafter Chlamydomonas). To reach this aim, we analyzed and compared gene expression, Mg^{2+} content, proton motive force (PMF) size and partitioning, non-photochemical quenching (NPQ), chloroplast ultrastructure, and biomass in wild type, corresponding single and double mutants when cultivated hydroponically in standard as well as low and high Mg^{2+} conditions. Using functional complementation assays in *Escherichia coli* (*E. coli*), we show that MGR8 and MGR9 are capable of mediating Mg^{2+} transport although with different affinities. In Arabidopsis leaves, together with MGT10, they regulate photosynthetic electron transport and photoprotection in response to excess light. Chlamydomonas does not have chloroplast MGRs, but the MGT10 homolog (MRS4) is required for photosynthesis and cell growth.

Abbreviations: CBS, cystathione-beta-synthase; Chl, chlorophyll; CNBH, cyclic nucleotide–binding homology; CNMM, cyclin M; DUF, domain of unknown function; ECS, electrochromic shift; ETR, electron transport rate; F_v/F_m, maximal quantum yield of photosystem II photochemistry; ICP-MS/OES, inductively coupled plasma mass/optical emission spectrometry; MGR, magnesium release protein; MGT, magnesium transporter; *Mr*, molecular weight; NPQ, non-photochemical quenching; PMF, proton motive force; PSII, photosystem II; Y (I), quantum yield of PSI photochemistry; Y(II), quantum yield of PSII photochemistry; ΔpH, H^+ concentration gradient; TEM, transmission electron microscopy.

2 Results

2.1 MGR8 and MGR9 resemble CorC-like transporters, whereas MGT10 is a CorA-like channel

To assess the evolutionary relationships among MGT10, MGR8, and MGR9, we compared their protein sequences with those of several well-characterized magnesium transporters. Phylogenetic analyses showed that MGT10 shared the closest evolutionary history with the *E. coli* CorA, whereas MGR8 and MGR9 clustered together with the CorC proteins of *Thermus parvatiensis* and *E. coli* (Supplementary Figure S1A). The magnesium transport function of CorA protein family members depends on the Gly-Met-Asn (GMN) motif located in the extracellular loop of the channel (Guskov et al., 2012; Ishijima et al., 2021). This motif could be found in the MGT10 sequence, whereas it was absent in MGR8 and MGR9 sequences (Supplementary Figure S1B). Previous work reported that MGR8 and MGR9 belong to a separate clade of the plant MGR family, which is most distant from CNNMs (Tang et al., 2022; Zhang et al., 2022). Our phylogenetic analyses confirmed that MGR8 and MGR9 cluster together in a MGR sub-family (Figure 1). Interestingly, this cluster does not include CNNMs and MGR1–7 and does include the bacterial Mg^{2+} transporter CorC (Figure 1, Supplementary Figure S1A). Structurally, CNNMs consist of an N-terminal extracellular domain, a transmembrane domain of unknown function (DUF21), a large cytosolic region containing a cystathionine-synthase (CBS) pair domain, and a putative cytosolic cyclic nucleotide–binding homology (CNBH) domain at the C-terminus. Our sequence alignment shows that while MGR8 and MGT9 also harbor the DUF21 and the CBS-pair domain, the C-terminus is distinct from the CNBH domain of CNNMs and shares a considerable number of identical amino acids with the C-terminal CorC-HlyC domain of bacterial CorC (Supplementary Figure S1B). Members of the CorC Mg^{2+} transporter family were shown to be Na^+ dependent since depletion of Na^+ resulted in loss of their Mg^{2+} transport activity (Yamazaki et al., 2013; Jin et al., 2022). The Asparagine residue Asn94 in the transmembrane domain of the CorC protein from *Thermus parvatiensis* was identified as important for Na^+

10.3389/fpls.2023.1221436

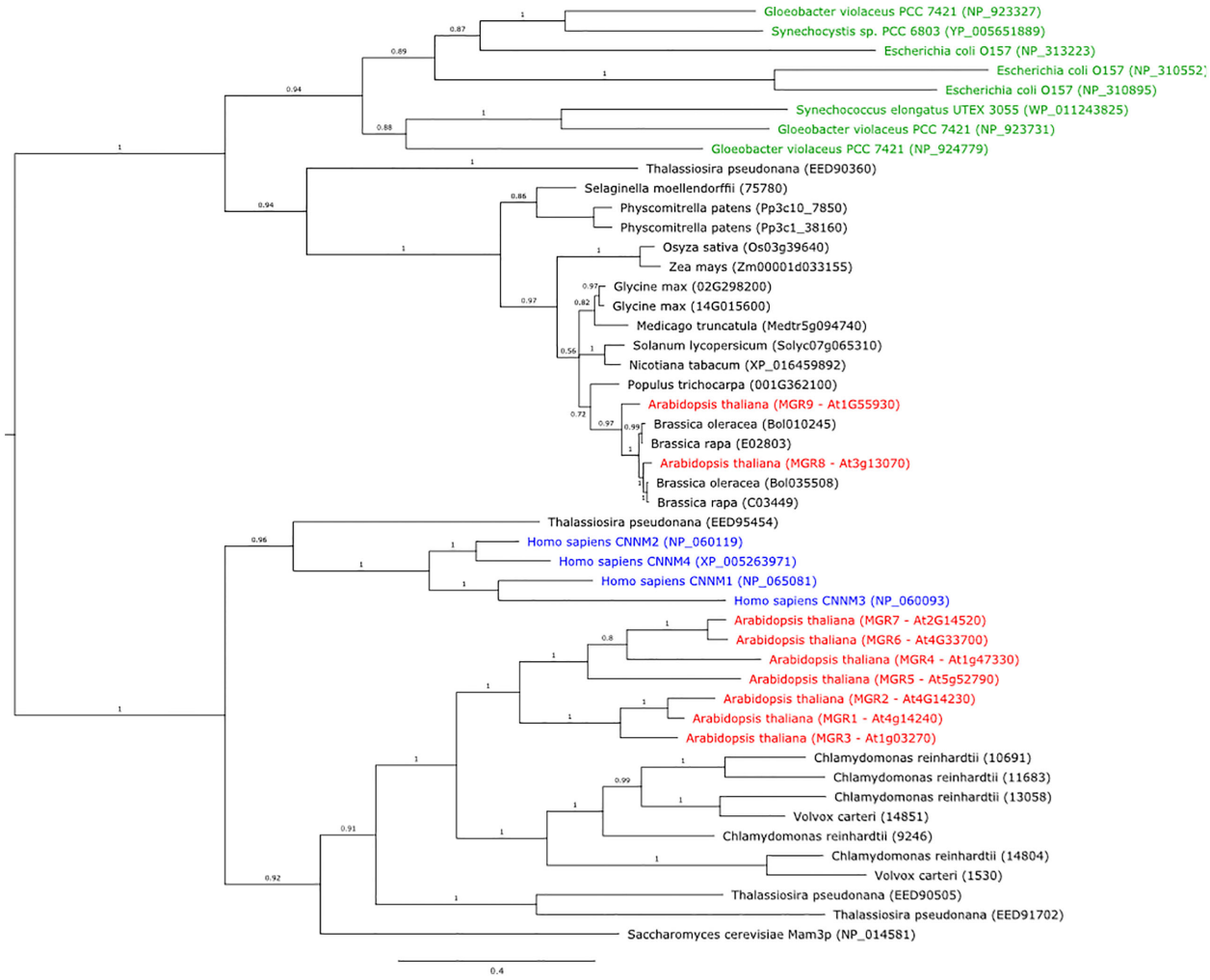

FIGURE 1
Phylogenetic tree of protein sequences from plants, bacteria, green algae, diatoms, yeast, and humans, that are homologs of the Arabidopsis MGR8 and MGR9. The tree was constructed using MrBayes v3.2.6. Bacteria are indicated in green text, the human CNNM1–4 homologs in blue, and all Arabidopsis MGRs in red. Numbers above branches indicate posterior probability values and the expected number of changes per site along the branches is indicated by the scale bar.

sensitivity (Huang et al., 2021). Interestingly, both MGR8 and MGR9 also contain this residue in their transmembrane DUF21 domain (Supplementary Figure S1B), suggesting possible coordination of transport between Mg^{2+} and Na^{+} across the chloroplast inner envelope. Taken together, these data indicate that MGR8 and MGR9 may function as CorC-like transporters, whereas MGT10 shares the closest evolutionary history with the CorA channel.

Phylogenetic analysis of MGR8 and MGR9 homologs revealed that both proteins are distributed amongst land plants, algae, and cyanobacteria. Within the plant genus *Brassicaceae*, MGR8 and MGR9 proteins form two well-supported clades and all investigated species code for 2–3 copies each (Supplementary Figure S2). However, species from *Brassica*, *Eruca*, *Crambe*, and *Sinapis*, only carry the MGR8-like protein, albeit in multiple distinct copies, resulting from gene duplication. There are 1–2 copies of MGR8- and MGR9-related proteins in other plant species and cyanobacteria species like *Synechocystis* sp., *Synechoccocus elongatus*, and *Gloeobacter violaceus* (Figure 1). In diatoms (e.g., *Thalassiosira pseudonana*), we could find homologs for CNNMs and MGR1–7 but not for MGR8 and MGR9. These findings indicate that MGR8 and MGR9 share evolutionary histories but are not evenly distributed in nature.

To assess if the Mg^{2+} transport protein sequences of Arabidopsis MGR8, MGR9, and MGT10 are conserved in green algae, we have searched for homologs in the unicellular *Chlamydomonas reinhardtii* and the multicellular *Volvox carteri*. While there was no AtMGR8 or AtMGR9 homolog, we identified one MRS4 sequence in each green algae species as close homologs of AtMGT10 (Supplementary Figure 3). MRS4 shares the highest sequence identity with MGT10 in the N-terminal long loop and in the transmembrane region (Supplementary Figure S4). In addition, the protein sequences of both CrMRS4 and VcMRS4 contain the characteristic GMN motif.

2.2 MGR8 and MGR9 transport Mg^{2+} in *E. coli* by a different mechanism than MGT10 and CNNMs

Using heterologous expression in the Mg^{2+} uptake-deficient *E. coli* strain TM2 (Δ*corA* Δ*mgtA* Δ*yhiD*), we assessed the magnesium transport activity of MGR8 and MGR9 and compared it with that of MGT10. Under standard conditions, the growth of TM2 requires the addition of at least 10 mM Mg^{2+} to the LB medium (Ishijima et al., 2015). TM2 cells expressing either *MGR8* or *MGR9* cDNA grew optimally in LB medium supplemented with 1 mM Mg^{2+} but not in the absence of added Mg^{2+}, while the cells with an empty vector did not grow in either absence or presence of up to 1 mM Mg^{2+} (Figures 2A, B). Interestingly, TM2 cells expressing *MGR9* could grow well in LB medium supplemented with 0.5 mM Mg^{2+}, while *MGR8*-expressing cells failed to grow (Figures 2A, B). In addition, when 0.8 mM or less Mg^{2+} was added, the growth of cells expressing *MGR8* but not of cells expressing *MGR9* was reduced (Supplementary Figures S5A, B). At 10 mM Mg^{2+}, the cells expressing *MGR8* grew much faster and better than the *MGR9*-expressing cells and the cells with an empty vector (Supplementary Figure S5C). As previously reported by Ishijima and colleagues (2015; 2021), we observed that TM2 cells expressing *MGT10* could readily grow in LB medium without Mg^{2+} supplementation (Supplementary Figure S5D). These results indicate that MGR8, MGR9, and MGT10 functionally complement the Mg^{2+} auxotrophy of the TM2 cells and that the expressed proteins are capable of transporting Mg^{2+} without any additional protein partners. The ability of TM2 cells expressing *MGR9* to grow at lower external Mg^{2+} concentration than the cells expressing *MGR8* indicates a broader concentration range at which MGR9 may be active.

We found that $AlCl_3$ inhibited the growth of TM2 cells expressing *MGT10* (Supplementary Figure S5D) as previously reported (Ishijima et al., 2015), likely due to Al^{3+} uptake into the cells (Ishijima et al., 2018). In contrast, no growth inhibition of TM2 cells expressing either *MGR8* or *MGR9* was observed with 1 mM $AlCl_3$ in combination with 1 mM Mg^{2+} (Figures 2C, D). These results indicate that the Mg^{2+} transport activity of MGR8 and MGR9 is not inhibited by Al^{3+} and that they do not transport Al^{3+} into the *E. coli* cells under these conditions. Taken together, we propose that MGR8 and MGR9 transport Mg^{2+} by a different mechanism than MGT10.

Human CNNMs contain evolutionarily conserved residues, whose mutations cause hypomagnesemia and associated congenital diseases (Stuiver et al., 2011; Giménez-Mascarell et al., 2019; Chen Y.S. et al., 2020). Disease-causing mutations include E357K from the DUF21 domain of CNNM2, R407L, P409L, and T495I from the ATP-binding site within the CBS domain of CNNM4 (Chen Y.S. et al., 2020), demonstrating the importance of these four residues for CNNM transport activity. In addition, the residues corresponding to G466, E471, and D472 of MGR8 are conserved near the end of the CBS domain in the CNNM family (Zhang et al., 2022). To test whether these seven residues (Supplementary Figure S1B) are important for the Mg^{2+} transport activity of MGR8, we introduced point mutations (E261K, R388L, P390A, P390L, G466A, T469A, T469I, E471A, and D472A) and expressed the constructs in TM2 cells. The TM2 cells expressing the MGR8 G466A mutant did not grow in LB medium supplemented with 1 mM Mg^{2+} (Figure 2E). All other mutants grew similarly to the cells expressing the wild type MGR8 (Figures 2E, F). These results indicate that, among the mutated residues conserved in CNNMs, only G466 in the CBS domain is critical for the Mg^{2+} transport activity of MGR8. Based on these findings and the notion that all mutated residues are also conserved in MGR9 (Supplementary Figure S1B), we postulate that MGR8 and MGR9 transport Mg^{2+} by a different mechanism than CNNMs.

2.3 *MGR9* gene expression is upregulated at low and high Mg^{2+} concentrations

The tissue-specific expression pattern of the *MGT10* gene was previously analysed by GUS-staining (Drummond et al., 2006; Sun et al., 2017). Recently, the more sensitive quantitative RT-PCR method was used to analyze the expression of *MGR8* and *MGR9* genes (Zhang et al., 2022). In our quantitative RT-PCR analysis we included all three transporter genes and investigated their tissue expression pattern in Arabidopsis plants grown at 0.75 mM Mg^{2+} (standard conditions). *MGR8* exhibited high expression in all vegetative organs and lower expression in flowers (Figure 3A). *MGT10* was highest expressed in mature organs, in contrast to *MGR9* which was predominantly expressed in seedlings. Notably, expression levels of *MGR8* and *MGT10* genes were highest in leaves.

Considering the observed activity of MGR9 in TM2 cells under low Mg^{2+} conditions, we postulated the possible involvement of MGR9 in Arabidopsis growth at such levels. Accordingly, we evaluated gene expression in response to three different Mg^{2+} concentrations. Plants were grown for two weeks at 0.75 mM Mg^{2+} and then transferred for 3–4 weeks at either no (0 mM), standard (0.75 mM), or high (3 mM) Mg^{2+}. At 0 mM Mg^{2+}, expression of the *MGR9* gene in leaves was upregulated 20-fold, while expression of *MGR8* and *MGT10* was downregulated as compared to standard conditions (Figure 3B). *MGR9* expression was also upregulated at 3 mM Mg^{2+} (2-fold), while the expression of the other two genes was unaltered relative to 0.75 mM Mg^{2+}. These results indicate that *MGR8* and *MGT10* are the mainly expressed Mg^{2+} transporters in the leaves of Arabidopsis plants grown at standard Mg^{2+} concentration, whereas *MGR9* expression is elevated in conditions of deficiency or excess Mg^{2+}.

To further investigate the gene expression patterns of the three magnesium transporters under Mg^{2+}-deficient conditions, we obtained two independent homozygous T-DNA insertion knockout mutants for *MGR8* (*mgr8-1* and *mgr8-2*) and *MGR9* (*mgr9-1* and *mgr9-2*), and a heterozygous knockdown mutant for *MGT10* (*mgt10*) (Supplementary Figure S6). We speculate that these mutant plants might compensate for the loss of one transporter by upregulating the expression of the other magnesium transporter genes. The expression of *MGR9* was similar in *mgr8* and *mgt10* mutants grown hydroponically at 0.75 mM Mg^{2+}, whereas *MGR8* was more expressed in *mgt10* than in

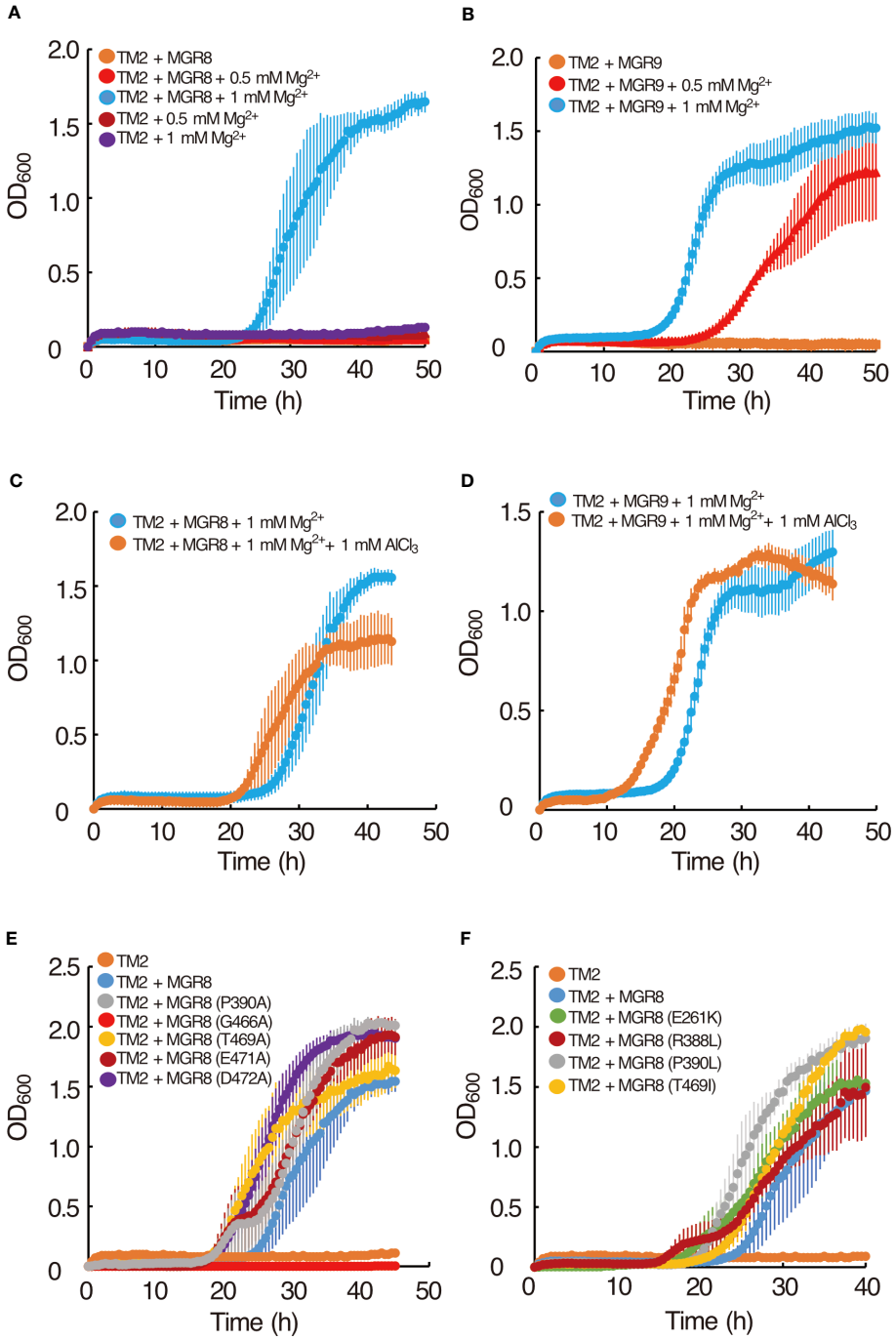

FIGURE 2
Complementation of the *E. coli* TM2 Mg^{2+} auxotrophy with *MGR8* and *MGR9* and Al^{3+} inhibition. **(A)** Growth curves of TM2 transformed with the pTV118N vector containing *MGR8* cDNA and with the empty vector. **(B)** Growth curves of TM2 transformed with the plasmid containing *MGR9* cDNA. Cells were grown at 37°C on LB medium supplemented with different concentrations of $MgSO_4$. LB medium without added $MgSO_4$ contained 0.17 mM Mg^{2+} (Ishijima et al., 2015). **(C, D)** Effect of Al^{3+} on the growth curves of TM2 transformed with the plasmid containing *MGR8* **(C)** and *MGR9* **(D)** cDNA. Cells were grown at 37°C on LB medium supplemented with 1 mM $MgSO_4$. $AlCl_3$ was added at 0 mM and 1 mM concentration. **(E, F)** Growth curves of TM2 transformed with the plasmid containing *MGR8* wild type, P390A, G466A, T469A, E471A, and D472A **(E)**, E261K, R388L, P390L, and T469I **(F)** mutant cDNA and with the empty pTV118N vector. Cells were grown at 37°C on LB medium supplemented with 1 mM $MgSO_4$. The OD_{600} was measured every 0.5 h. Data are average values of three or more independent experiments, and bars indicate means ± S.E.M.

mgr9 (Supplementary Figure S7). When grown at 0 mM Mg^{2+}, *MGR9* was upregulated 2-fold in *mgr8* and slightly upregulated in *mgt10*, whereas *MGT10* and *MGR8* expression was downregulated or unaltered in *mgr9* and *mgt10* mutants relative to 0.75 mM Mg^{2+} (Figure 3C). These results strengthen the evidence for a role of MGR9 in Mg^{2+}-deficient conditions.

Knowing a protein's subcellular localization is a pivotal element in unravelling its functional role within the cell. Sun and colleagues

10.3389/fpls.2023.1221436

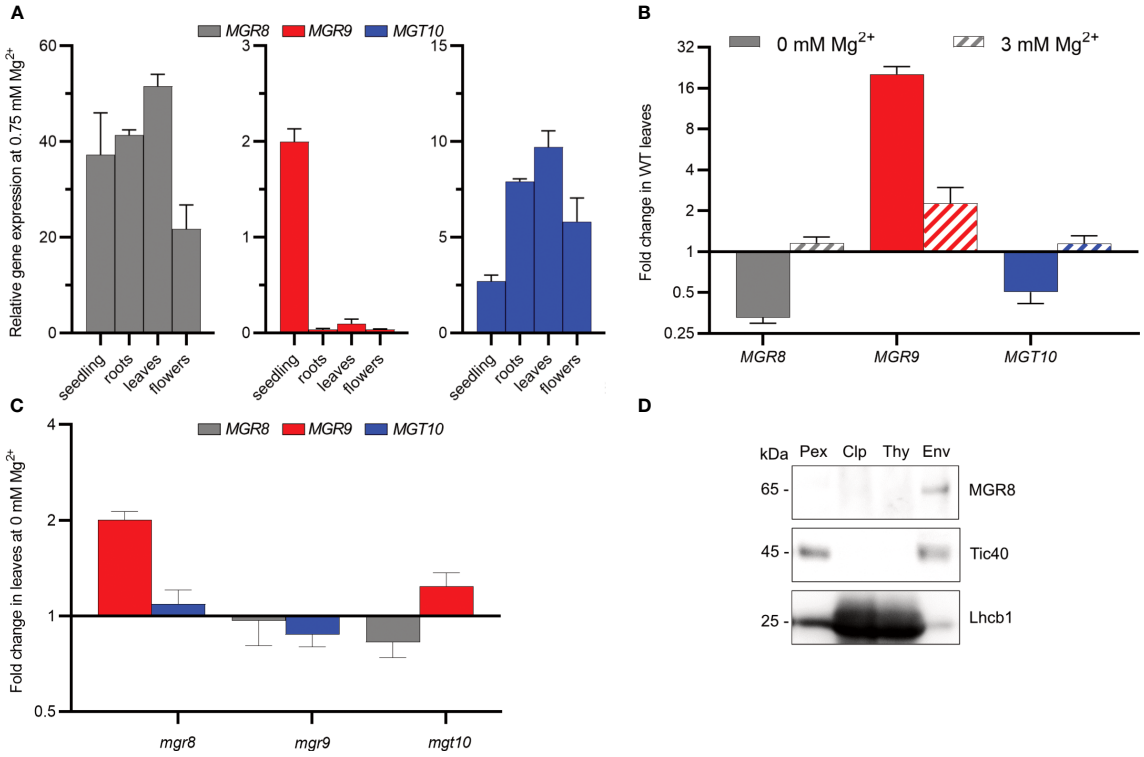

FIGURE 3
Expression pattern and chloroplast localization in Arabidopsis. **(A)** Relative expression in 2-week-old seedlings and roots, leaves, and flowers of 6-week-old wild type plants grown hydroponically at 0.75 mM Mg^{2+} was determined using quantitative RT-PCR. *ACTIN8* and *PEX4* were used as internal standards. **(B, C)** Wild type (WT) plants **(B)** and mutants **(C)** were grown first for two weeks at 0.75 mM Mg^{2+} and then for three to four weeks at either 0 or 3 mM Mg^{2+}. The plotted data represent expression fold change relative to the expression at 0.75 mM Mg^{2+} in the same genotype. Where two independent lines were available, the obtained data are presented as averages. The scale on the Y-axis in **(B, C)** is log_2, whereas the fold change values are non-log_2-transformed. The data presented in **(A–C)** are means ± S.E.M (n = 4 plants). **(D)** Total protein extracts (Pex), Chloroplasts (Clp), thylakoid (Thy), and envelope (Env) membranes were prepared from wild type leaves. Localization of MGR8 in chloroplast and subfractions was performed by immunoblotting with an MGR8-peptide-specific antibody. Purity of fractions was confirmed using antibodies against marker proteins for the respective compartment: inner envelope translocon complex Tic40 protein and the light harvesting Chl *a/b* binding thylakoid protein Lhcb1. Uncropped version of the immunoblots is shown in Supplementary Figure S8.

(2017) localized MGT10 to the chloroplast envelope by western blot analysis. Recently, MGR8 and MGR9 were also localized to the chloroplast envelope by using a GFP-fluorescence approach (Zhang et al., 2022). In our study, we raised an antibody against an MGR8-specific C-terminal peptide (Supplementary Figure S1B). The generated antibody detected a band at a relative molecular weight (*Mr*) of 65 kDa in total protein extracts from wild type (WT) leaves and in mutant lines *mgr9-1* and *mgr9-2*, but not in *mgr8-1* and *mgr8-2*. The *Mr* is in good agreement with the theoretical MW of 65.65 kDa for the protein lacking the chloroplast transit peptide (amino acids 1-71, Supplementary Figure S1B). Immunoblot analyses of purified chloroplasts membrane subfractions, thylakoid- and envelope membranes confirmed an envelope location of the MGR8 protein (Figure 3D and Supplementary Figure S8).

2.4 MGR8, MGR9, and MGT10 are required for regular thylakoid stacking in Arabidopsis

Thylakoid stacking, also referred to as overall grana size, is stabilized by Mg^{2+} ions. We, therefore, examined the chloroplast ultrastructure and thylakoid stacking in three single mutant lines using transmission electron microscopy (TEM). Regular WT-like chloroplast and thylakoid morphology were observed in 6-week-old *mgr8* and *mgr9* mutants (Figures 4A–C). Interestingly, it was reported that the homozygous double mutant *mgr8mgr9* had impaired chloroplast development (Zhang et al., 2022). This double mutant had no thylakoid stacks in two-week-old plants and short and inflated thylakoid stacks in 3-week-old plants.

The *mgt10* mutant had a peculiar leaf phenotype with yellow vein leaves (Supplementary Figure S9), in agreement with previously published results (Liang et al., 2017; Sun et al., 2017). The green interveinal regions contained chloroplasts with regular grana (Figure 4D), whereas the yellow vein regions contained normal chloroplasts with regular grana and peculiar plastids with macro-grana (Figures 4E, F). Macro-grana are unusually wide grana consisting of a high number of stacked thylakoid lamellae and are associated with an overall underdeveloped stroma thylakoid membrane system. Macro-grana were especially abundant in the bundle sheath cells, although they could be also observed in palisade and spongy parenchyma cells sampled from the vein region. Taken together, these results in combination with the results from Zhang and colleagues (2022) suggest that both families are required for

10.3389/fpls.2023.1221436

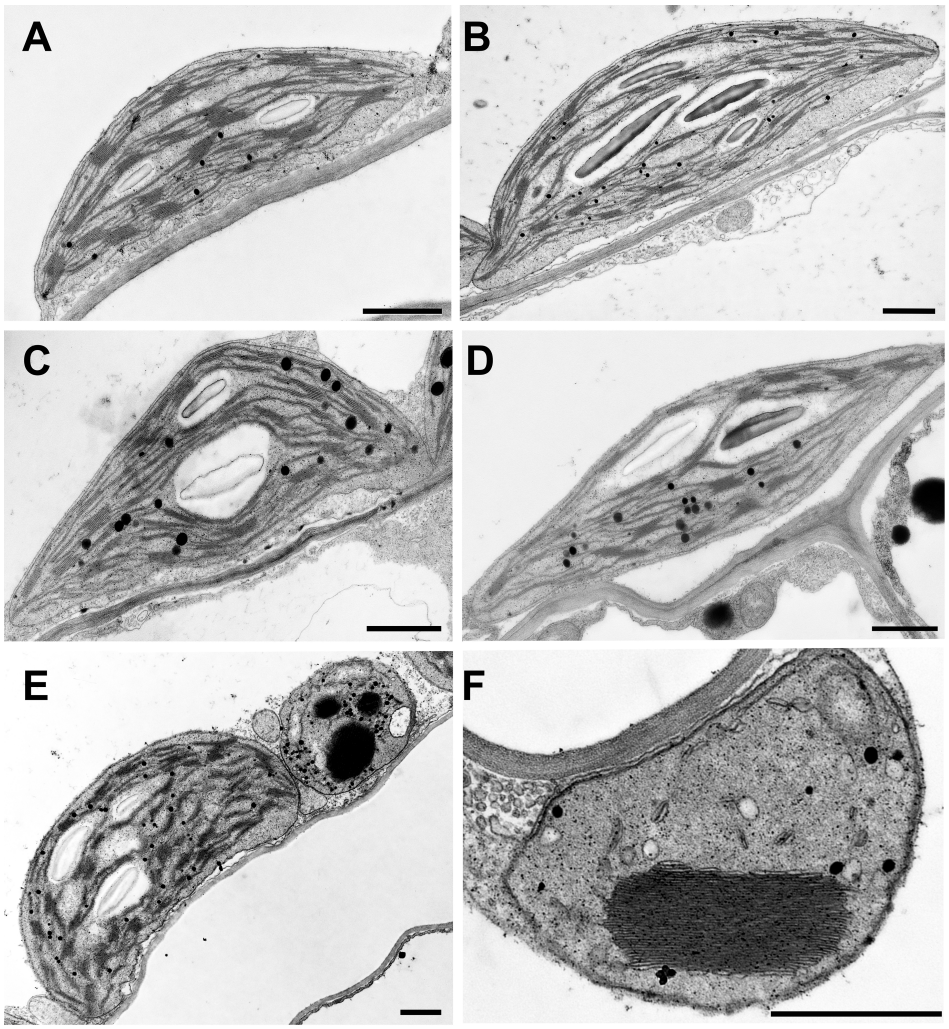

FIGURE 4
Chloroplast ultrastructure in Arabidopsis. Wild type plants and mutants were grown in standard Mg^{2+} conditions for six weeks. Representative TEM photos of chloroplasts are shown. **(A)** Wild-type, **(B)** *mgr8-2*, **(C)** *mgr9-1*, **(D)** *mgt10* green interveinal region, **(E, F)** *mgt10* chlorotic, yellow vein region. **(E)** Mesophyll cell with normal chloroplast and peculiar plastid. **(F)** peculiar plastid with macro-granum, vesicles, and no stroma thylakoids typical for bundle sheath cells. Scale bar: 1 µm.

regular thylakoid stacking and chloroplast development. However, the opposite pattern in grana size, i.e., smaller in *mgr8mgr9* (Zhang et al., 2022) and larger in the peculiar plastids observed in *mgt10* (Figure 4F, Sun et al., 2017), implies differential roles of the two families of transporters.

2.5 MGR8, MGR9, and MGT10 participate in building the pH gradient required for photoprotection in fluctuating light

To understand the role of MGR8, MGR9, and MGT10 in photosynthetic reactions in the thylakoid membrane, we grew plants at three different concentrations of Mg^{2+} (0, 0.75, and 3 mM) and measured the slow kinetics of chlorophyll fluorescence induction in fluctuating light. In addition to the single mutants, we investigated the impact of a double mutant of the two most expressed transporters on photosynthetic performance. We crossed the *mgr8-2* and *mgt10* mutant lines, resulting in the *mgt10mgr8-2* double mutant. All mutant lines grew like WT and displayed similar shoot and root weight at all three Mg^{2+} concentrations (Supplementary Figure S9). We first determined the maximum quantum yield of photosystem II (PSII) photochemistry (F_v/F_m). Our results show that the F_v/F_m yield was slightly but significantly lower in both *mgr9* lines and *mgt10* at 0 mM Mg^{2+}, indicating a reduced maximum photosynthetic efficiency in terms of electron transport (Supplementary Table S1).

In plants grown at 0 and 0.75 mM Mg^{2+}, on transition from low to high light, NPQ was induced slower in all mutants as compared to WT (Figures 5A, B). The steady-state NPQ was the lowest in *mgt10* and *mgt10mgr8-2*, intermediate in *mgr8*, and the least affected in the *mgr9* mutants. Following the transition from high to low light, NPQ relaxed similarly in all genotypes. The electron transport through both photosystems, indicated by Y(II) and Y(I),

10.3389/fpls.2023.1221436

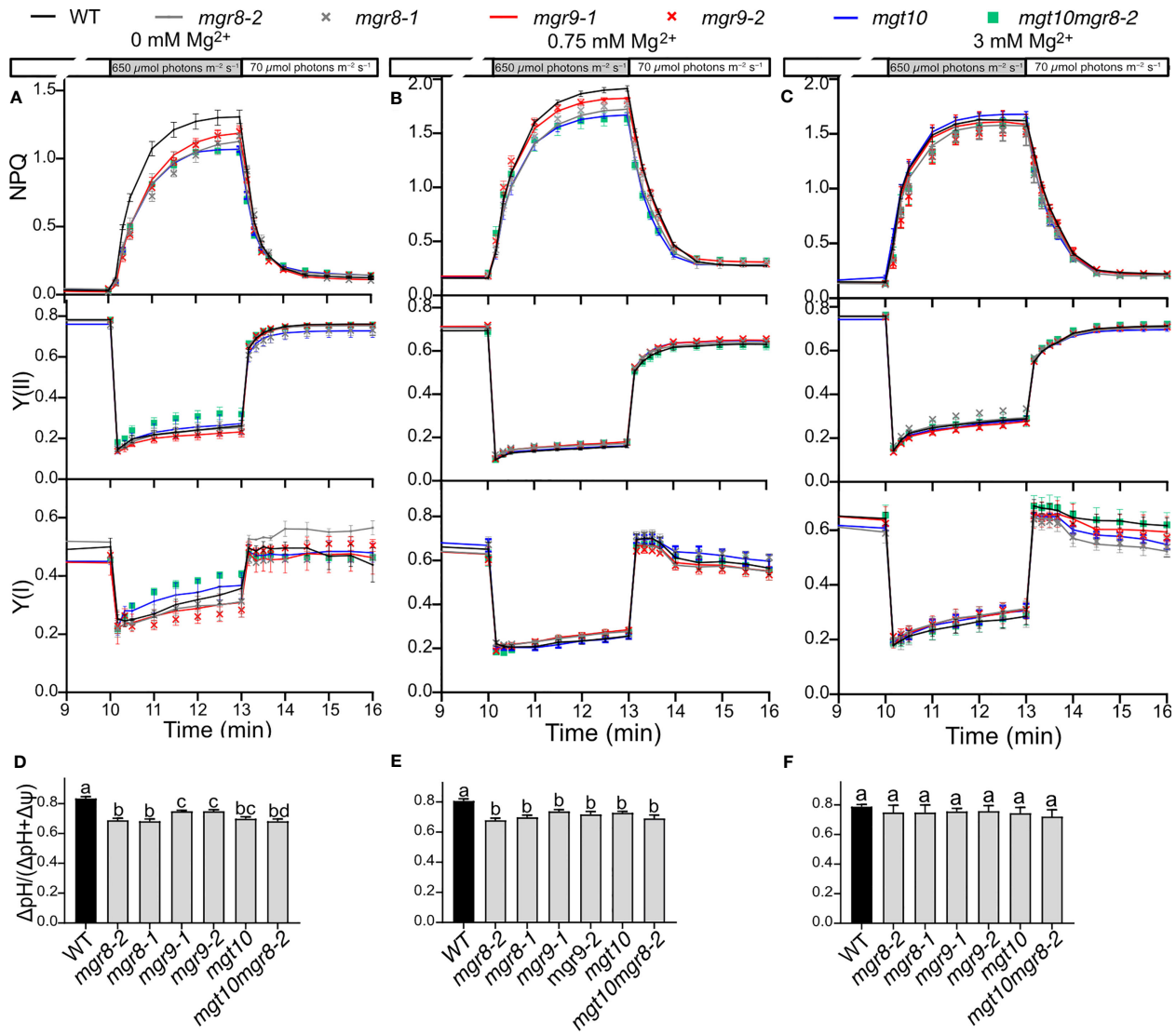

FIGURE 5
Dynamics of photosynthesis and photoprotection in fluctuating light. Wild type (WT) plants and mutants were grown hydroponically first for two weeks at 0.75 mM Mg^{2+} and then for four to five weeks at the indicated Mg^{2+} concentrations. Plants were dark adapted for 20 min, illuminated for 10 min with low light, then for 3 min with high light, and then again for 3 min in low light. Chl fluorescence and electrochromic shift were recorded with Dual-PAM-100. The plots in **(A–C)** show non-photochemical quenching (NPQ), PSII, and PSI quantum yields (Y(II) and (YI)). The plots in **(D–F)** show the partitioning of the proton motive force to ΔpH as determined from ECS measurements at the end of transition from low to high light. The plotted data are means ± S.E.M. (n = 4-7 plants). Different letters indicate statistically significant differences among the genotypes according to Tukey one-way ANOVA ($P < 0.05$).

was like WT in all mutants and conditions (Figures 5A, B). In parallel experiments, we recorded electrochromic shift (ECS) kinetics at the end of each low-to-high light and high-to-low light transition to estimate the total PMF and its partitioning. The PMF size was alike WT at the end of each transition (Supplementary Figure S10A). The ΔpH, also known as the H^+ concentration gradient, in transition from low to high light significantly decreased in all mutants grown at 0 and 0.75 mM Mg^{2+} (Figures 5D, E), and was like WT in transition from high to low light (Supplementary Figure S10B). These data indicate that MGR8, MGR9, and MGT10 are involved in building up the pH gradient to rapidly activate NPQ without largely affecting the electron transport through photosystems and overall PMF size. Plants grown at 3 mM Mg^{2+} did not differ in any of the studied parameters (Figures 5C, F, Supplementary Figures S10A, B).

To test whether the observed reduced NPQ and altered thylakoid ultrastructure could be a result of altered magnesium homeostasis, we measured the mineral content in shoots and isolated chloroplasts using inductively coupled plasma optical emission spectrometry (ICP-OES) and inductively coupled plasma mass spectrometry (ICP-MS), respectively. When grown in the absence of Mg^{2+}, all mutants had a slightly but significantly higher Mg^{2+} content in the shoots compared to WT (Supplementary Figure S11). At standard Mg^{2+} concentration (0.75 mM), shoots of all single mutants had less whereas the double mutant *mgt10mgr8-2* had a WT-like Mg^{2+} content. At 3 mM Mg^{2+}, all mutant shoots had WT levels of Mg^{2+} except for *mgt10* which had a

10.3389/fpls.2023.1221436

significantly higher content. In chloroplasts isolated from plants grown at standard Mg^{2+} concentration, *mgr8-2* and *mgt10* had a Mg^{2+} content reduced by 38%, *mgr9* by 21%, whereas *mgt10mgr8-2* displayed a 17% increase relative to WT (Figure 6A). The chloroplast Na^+ and K^+ contents in most single mutant lines were similar to those in the WT (Figures 6B, C). Nevertheless, *mgt10mgr8-2* contained significantly higher levels of both Na^+ and K^+, suggesting that the double loss of MGR10 and MGR8 also impacts other ion transporters.

To investigate whether the observed differences in the chloroplast Mg^{2+} content have impacted RuBisCO activity in CO_2 fixation, we have measured net photosynthesis at the growth light and at a higher light intensity. As shown in Supplementary Figure S12, this activity was not significantly different among the genotypes at neither light intensity, in line with the WT-like growth and biomass data (Supplementary Figure S9).

2.6 The Chlamydomonas MRS4 transporter is required for photosynthesis and cell growth

We identified CrMRS4 and VcMRS4 proteins as close homologs of AtMGT10 (Supplementary Figures S3, S4). To explore the function of MRS4, we characterized a Chlamydomonas knock-out mutant from the CLiP library (*mrs4*) and complemented this mutant with the *VcMRS4* gene (*mrs4*::*MRS4*) (Supplementary Figure S13). The knockout mutant grew poorly in light on minimum TP medium, but supplementation with Mg^{2+} or complementation with *VcMRS4* considerably improved its growth (Figure 7A). Growth of *mrs4* in TAP medium in darkness did not impact growth (Figure 7A), indicating that MRS4 is involved in autotrophic growth.

To further investigate the cause of the reduced growth of *mrs4*, we examined various parameters of photosynthetic reactions in the thylakoid membrane. The knockout mutant *mrs4* had a significantly reduced F_v/F_m relative to WT due to a higher F_0. These results indicate that *mrs4* had a higher proportion of closed PSII centers already in the dark-adapted state (Figures 7B, C). In addition, *mrs4* had reduced electron transport rates throughout the range of tested light intensities, indicating enhanced light sensitivity (Figure 7D). When exposed to high light (2500 µmol photons m^{-2} s^{-1}), the knockout mutant was able to induce NPQ in the first minute of illumination, but it decreased to 0 after 3 min. The NPQ in the supplemented and complemented lines were higher than in *mrs4* and more stable over time, but still lower than WT (Figure 7E). In addition, the PSII activity, indicated by Y(II), was lower in all mutants (Figure 7F). The total PMF across the thylakoid membrane was slightly but significantly higher in *mrs4* and in *mrs4*::*MRS4* at two time points in high light (660 µmol photons m^{-2} s^{-1}), and like WT in the supplemented line (Figure 7G). The *mrs4* mutant PMF was dominated by ΔpH, whereas the complemented line and the Mg^{2+} supplemented mutant had intermediate ΔpH levels between WT and mutant (Figure 7H, Supplementary Figure S14). The observed high ΔpH in the *mrs4* mutant is likely to cause lower PSII activity due to photoinhibition. Notably, despite the high ΔpH, the NPQ levels in the mutant were low, indicating a reduced capacity for photoprotection (Figures 7D, F). Taken together, these results suggest that the *mrs4* mutant has an enhanced sensitivity to light due to photoinhibition and malfunctioning of the PSII complex.

To test if the observed lower PSII activity is linked to an altered thylakoid structure, WT and *mrs4* morphology were analyzed using TEM. Chlamydomonas cultures grown in TAP medium in darkness revealed no major differences between WT and *mrs4* (Supplementary Figure S15A). In addition, a similar overall cell ultrastructure was observed in WT and the *mrs4* mutant after 3 h or 4 days of illumination at 100 µmol photons m^{-2} s^{-1} on minimal TP medium. However, inside the chloroplast, the *mrs4* thylakoids were more stacked and consisted of more layers (Supplementary Figures S15A, B).

To investigate if the decrease in photoprotective capacity, increased ΔpH and altered grana stacking could be a result of altered mineral content in the cell, we measured the Mg^{2+}/Na^+, $K^+/$

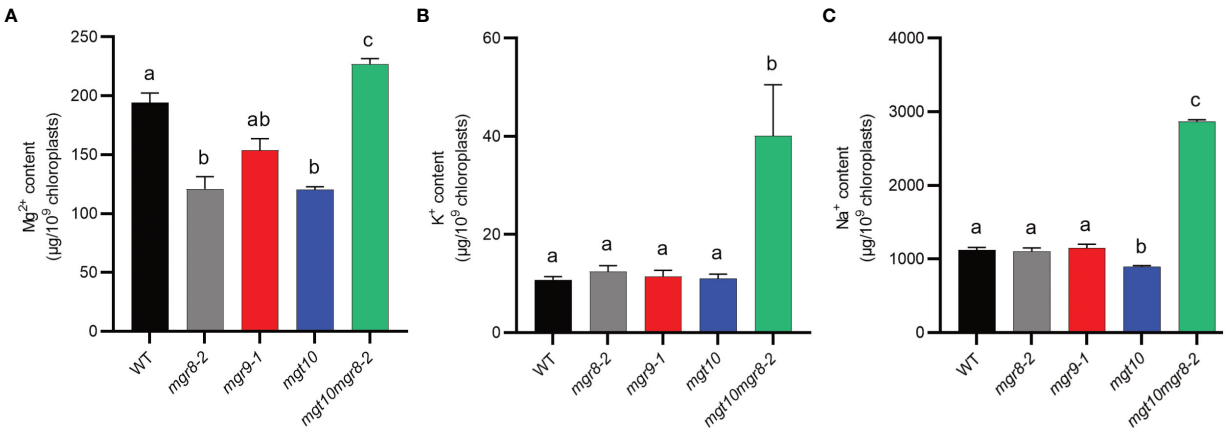

FIGURE 6
Mineral content of Arabidopsis chloroplasts. Intact chloroplasts were prepared from shoots of plants grown at 0.75 mM Mg^{2+} and their mineral content was determined using ICP-MS. **(A)** Mg^{2+}, **(B)** K^+, and **(C)** Na^+ content of Arabidopsis chloroplasts. The presented data are expressed as means ± S.E.M. (n = 3 chloroplast preparations). Different letters indicate statistically significant differences among the genotypes according to Tukey one-way ANOVA ($P < 0.05$).

10.3389/fpls.2023.1221436

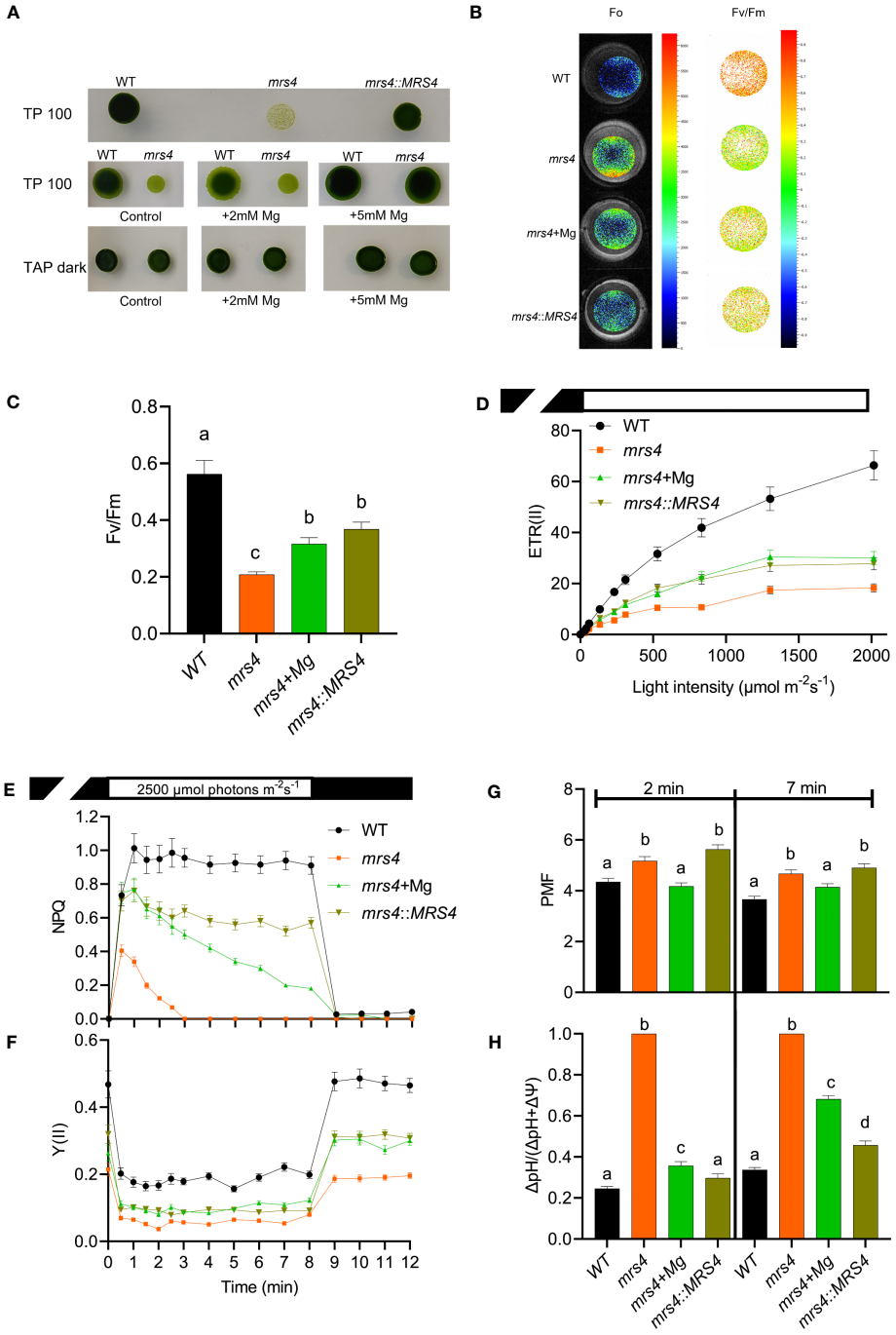

FIGURE 7
Chlamydomonas *mrs4* experiences light stress. Wild type (WT), *mrs4*, and complemented *mrs4:MRS4* were grown in the light (100 µmol photons m^{-2} s^{-1}) on TP medium (TP100) or in darkness on TAP (TAP dark), and where indicated supplemented with 5 mM Mg^{2+}. **(A)** Spot tests on agar plates showing that complementation with *VcMRS4* and Mg^{2+} supplementation improve the growth of the mutant. **(B, C)** Chl fluorescence imaging using FluorCam shows significantly reduced maximum quantum yield of PSII photochemistry (F_v/F_m) in *mrs4* due to enhanced minimum fluorescence (F_0). Complementation with *VcMRS4* and Mg^{2+} supplementation improved the photosynthetic efficiency of the mutant. Chl fluorescence and electrochromic shift were recorded with a Dual-Pam-100. **(D)** Rapid light response curves of electron transport rates of PSII (ETR(II)). **(E, F)** Slow kinetics of Chl fluorescence induction during 8 min of illumination followed by 4 min in darkness. The data show reduced ETR(II), NPQ, and Y(II) in *mrs4* and improvement by complementation with *VcMRS4* and Mg^{2+} supplementation of cells grown in TP100. **(G, H)** The total proton motive force (PMF) and partitioning to ΔpH were determined from ECS decay kinetics in darkness of cells grown in TAP dark and pre-exposed at 660 µmol photons m^{-2} s^{-1} for 2 or 7 min. The data in **(C–G)** are means ± S.E.M. (n = 3 replicates). Different letters indicate significant differences among the genotypes according to Tukey one-way ANOVA ($P < 0.05$). The PMF in the *mrs4* mutant consists of 100% ΔpH, indicating that the cells experience high light stress.

Na^+, and Ca^{2+}/Na^+ ratios of *mrs4* and WT using ICP-MS. There were no significant differences in the mineral content ratios for cells grown on TAP in darkness (Supplementary Figure S16). However, we found that *mrs4* cells grown at 100 µmol photons m^{-2} s^{-1} in minimal TP medium had significantly elevated Mg^{2+}/Na^+ and Ca^{2+}/Na^+ ratios as compared to WT (Supplementary Figure S16). These results indicate that *mrs4* accumulated higher levels of Mg^{2+} and Ca^{2+} inside the cell. An excess of Mg^{2+} could explain the increased grana size, as it was proposed for MGT10 in Arabidopsis (Sun et al., 2017). Taken together with the observed altered thylakoid ultrastructure and associated reactions, our data suggests that MRS4 ensures an optimal Mg^{2+} concentration in the chloroplast for photosynthesis and cell growth.

3 Discussion

Plants require Mg^{2+} inside the chloroplast for chlorophyll synthesis, RuBisCO enzyme activation, and thylakoid stacking. As a result, this ion plays a pivotal role in both light-dependent and light-independent photosynthetic reactions. The inner envelope of the chloroplast contains three different Mg^{2+} transporters from two distinct families, the CorA-like MGT10 and the CorC-like MGR8 and MGR9. Both families play an essential role for the plant since the single knockout of MGR10 and the double knockout mutation MGR8 and MGR9 result in impaired chloroplast development. Nevertheless, how Mg^{2+} homeostasis is regulated by MGR8, MGR9, and MGT10 in the plant chloroplast and if their function is conserved in algae remained unknown. Our study provides several lines of evidence for a differential role of the three transporters in the chloroplast function. In addition, we identified an MGT10 homolog in Chlamydomonas, MRS4, that is essential for photosynthesis and cell growth.

Firstly, we demonstrate distinct expression patterns of the three transporters in Arabidopsis plants grown under different external Mg^{2+} concentrations. Their expression pattern in various organs was previously analyzed in WT plants grown at standard Mg^{2+} supply (Drummond et al., 2006; Sun et al., 2017; Zhang et al., 2022), but neither at low or high concentrations nor in mutants. In plants grown at standard Mg^{2+} concentration, *MGR8* and *MGT10* genes were highest expressed in leaves (Figure 3A), indicating a function in chloroplast Mg^{2+} transport. *MGR9* was upregulated in Arabidopsis plants grown in conditions of Mg^{2+} deficiency (Figures 3B, C). Heterologous expression of MGR9 rescued the growth of *E. coli* TM2 cells at a lower Mg^{2+} concentration than MGR8 (Figures 2A, B). Therefore, we propose that MGR9 is required for chloroplast function in low Mg^{2+} environments.

The Mg^{2+} concentration in the chloroplast stroma is important for regulation of RuBisCO enzyme activity (Mott and Berry, 1986). In our study, we observed a 38-21% reduced Mg^{2+} content in the chloroplast of *mgr8, mgr9*, and *mgt10*, suggesting a role for all three transporters in magnesium uptake into the chloroplast. However, this suggestion does not explain why the Mg^{2+} content of *mgt10mgr8-2* was 17% higher than that of WT (Figure 6). Therefore, further studies are required to elucidate the directionality of transport for the three proteins in Arabidopsis. The CO_2 fixation activity and plant biomass were non-significantly different among genotypes (Supplementary Figures S9, S12). We postulate that the observed alterations in the Mg^{2+} content in the mutant chloroplasts were mild, and therefore did not impact the carboxylase activity of RuBisCO. All studied mutants displayed a lower NPQ due to a lower ΔpH at increasing light intensities when grown at low and standard Mg^{2+} concentrations (Figures 5A, B, D, E). These data indicate that MGR8, MGR9, and MGT10 are involved in building up the pH gradient to rapidly activate NPQ without largely affecting the electron transport through photosystems and overall PMF size. The observation of a lower ΔpH in all analyzed mutants lacks an obvious explanation, as MGTs and MGRs are known to facilitate the direct transport of Mg^{2+} ions and not H^+. From previous studies, we know that a Mg^{2+} influx can lower the pH of the stroma due to the activation of a reversible $(Na^+)K^+/H^+$ exchange across the envelope (Huber and Maury, 1980; Wu et al., 1991; Wu and Berkowitz, 1992). Our data show altered Na^+ and K^+ homeostasis in the chloroplasts of the *mgt10mgr8-2* double mutant (Figures 6B, C), which also displayed the most different NPQ and ΔpH from WT in conditions of excess light (Figures 5A, B, D, E). Thus, potentially the studied envelope Mg^{2+} transporters affected the PMF partitioning to ΔpH indirectly *via* cation/H^+ exchangers. Such a possibility is supported by reduced NPQ and ΔpH in loss of function Arabidopsis mutants for the envelope K^+/H^+ exchangers KEA1 and KEA2 in conditions of excess light (Kunz et al., 2014). Future studies with double mutants of an Mg^{2+} transporter and cation/H^+ exchanger may provide more insights into the potential coordination of ion transport across the chloroplast envelope impacting pH homeostasis.

An alternative explanation for the altered mineral content could be related to the phylogenetic grouping of MGR8, MGR9 and MGT10. Our protein sequence alignment indicates that MGR8 and MGR9 are not CNNM- but CorC-like transporters, whereas MGT10 shares the closest evolutionary history with CorA (Figure 1, Supplementary Figure S1A). MGR8 transports Mg^{2+} by a distinct mechanism as compared to CNNMs, as evidenced by the heterologous expression of several mutant lines (Figures 2E, F). Furthermore, we demonstrate that in contrast to MGT10, the Mg^{2+} transport activity of MGR8 and MGR9 was not inhibited by Al^{3+} (Figures 2C, D), implying a distinct transport mechanism than for CorA-like members. Structurally, CorC is a Na^+-dependent transporter, whereas CorA adopts a channel-like architecture with an ion-conducting pore (Franken et al., 2022; Jin et al., 2022). The Mg^{2+} transport activity of CorC is driven by the Na^+ gradient, and an Asparagine residue was identified to play an essential role (Huang et al., 2021). Both MGR8 and MGR9 contain this residue (Supplementary Figure S1B), indicating possible coordination of transport between Mg^{2+} and Na^+ across the chloroplast inner envelope. Based on our protein sequence alignment, we postulate that MGT10 might function as a Mg^{2+} ion channel, whereas MGR8 and MGR9 function as Na^+-dependent Mg^{2+} transporters. Future structural and functional analyses are required to fully understand the transport mechanism of all three transporters.

Chloroplasts are organelles with a high demand for Mg^{2+} to ensure the maintenance of photosynthetic activity. So far, no Mg^{2+} transporter is known in the chloroplast of unicellular or multicellular algae. Our study found one MGT10-like homolog (MRS4) in *Chlamydomonas reinhardtii* and *Volvox carteri* (Supplementary Figure S3) but no chloroplast MGR8 or MGR9-like sequences. Our findings from the

analyses of CrMRS4 provide strong support for a Mg^{2+} transport function and critical role in photosynthesis and cell growth. We found a low NPQ induction and thus reduced capacity for photoprotection in the *mrs4* mutant (Figure 7E). We propose that this enhanced sensitivity to light is a result of a higher proportion of closed PSII centers and the potential malfunctioning of the PSII complex (Figures 7B–D). The partial rescue of the *mrs4* phenotype (Figure 7) by complementation with the *VcMRS4* implies that the functionality of the two MRS4 proteins may be partly different. Even supplementation with excess Mg^{2+} during growth did not fully rescue the *mrs4* phenotype, potentially due to the presence of excess Mg^{2+} inside the chloroplast (Supplementary Figure S16).

Our TEM results show that thylakoid stacking was affected in *mgt10* but not in *mgr8* or *mgr9* (Figure 4). Interestingly, the observation of an opposite pattern in grana size, i.e., smaller in *mgr8mgr9* (Zhang et al., 2022) and larger in the peculiar plastids in *mgt10* (Figures 4D, F; Sun et al., 2017), implies different roles of the two families of transporters. Knock-out of the MGT10 homolog *MRS4* in Chlamydomonas resulted in more stacked thylakoids that contained more layers (Supplementary Figure S15). This morphotype is very similar to the macro-grana observed in the Arabidopsis *mgt10* mutant, indicating an evolutionarily conserved function for members of this protein family. There are several other common features between the *mgt10* and *mrs4* mutants, including the reduced F_v/F_m and NPQ (Figures 4A, B, 7C, E and Supplementary Table S1). These perturbations in photosynthetic efficiency can be attributed to the macro-grana thylakoid ultrastructure, which likely disturbs the organization of LHCII-PSII complexes and movement of damaged complexes during repair in light conditions (Sun et al., 2017). Taken together, our results demonstrate that the three Arabidopsis magnesium transporters have differential roles in maintaining chloroplast magnesium homeostasis. Future research should focus on investigating the mechanisms underlying the functional coordination among these three magnesium transporters, as well as their interactions with other chloroplast transporters, to provide a more comprehensive understanding of magnesium homeostasis in plant cells.

4 Materials and methods

4.1 Plant material and growth conditions

Arabidopsis thaliana wild type (Columbia-0) and the T-DNA insertion lines *mgr8-1* (SALK_074964), *mgr8-2* (SALK_007335), *mgr9-1* (SALK_061515), and *mgr9-2* (SALK_087652) were obtained from the SALK collection (Alonso et al., 2003), and have been described by Zhang et al. (2022). The *mgt10* (GABI_764F12) was obtained from the GABI-KAT collection (Rosso et al., 2003) and is a heterozygous knockdown mutant. Genotyping of the T-DNA insertion lines was done by PCR/RT-PCR with gene-specific primers (Supplementary Table S2). The double *mgt10mgr8-2* mutant was obtained by crossing *mgt10* and *mgr8-2*. Wild type (WT) plants and mutants were grown hydroponically for 6-7 weeks in a growth chamber (CLF PlantMaster; Plant Climatics, Wertingen, Germany) using a daily cycle of 16 h of light (120 µmol photons m^{-2} s^{-1}) at 21°C and 8 h of dark at 19°C at a relative humidity of 70%. The nutrient solution was prepared as described (Gibeaut et al., 1997; Conn et al., 2013) with the modification that $MgSO_4$ was used at the concentration of 0 (low Mg^{2+}), 0.75 (standard Mg^{2+}) and 3 mM (high Mg^{2+}).

4.2 *Chlamydomonas reinhardtii* material and cultivation conditions

Wild type *Chlamydomonas reinhardtii* (strain CC-4533) and the *mrs4* mutant (strain LMJ.RY0402.244553) were obtained from the CLiP library of the Chlamydomonas Resource Centre (https://www.chlamylibrary.org/). The strains were maintained in darkness on agar plates (1.2% w/v) prepared with Tris-Acetate-Phosphate (TAP) containing 0.4 mM $MgSO_4$. For genotyping, DNA was extracted, and PCR was performed with the appropriate combination of primers (Supplementary Table S2). For the spot tests, a loopful of culture was transferred to TAP medium and grown in darkness for 2 days. The cells were then resuspended to a density of 5 x 10^5 cells mL^{-1} in TAP which was enriched or not with 2 or 5 mM $MgSO_4$, spotted at different dilutions on TAP agar plates containing corresponding $MgSO_4$ concentration, and allowed to grow in darkness at 20°C. From the same inoculum, cells were resuspended in minimal Tris-Phosphate (TP) medium which was enriched or not with 2 or 5 mM $MgSO_4$, spotted on TP plates, and allowed to grow at 20°C using a daily cycle of 16 h of light (100 µmol photons m^{-2} s^{-1}) and 8 h of dark. For photosynthetic analyses, strains were grown in liquid TP medium at an initial density of 1x 10^6 cells mL^{-1} in a volume of 50 ml for 4 days using a daily cycle of 16 h of light (100 µmol photons m^{-2} s^{-1}) and 8 h of dark.

4.3 Phylogenetic analysis

Whole genome sequence data from a representative set of plant species were downloaded from Phytozome v13 (https://phytozome-next.jgi.doe.gov/). Bacterial data were downloaded from NCBI (https://www.ncbi.nlm.nih.gov/) and sequences of the diatom *Thalassiosira pseudonana* from the JGI Genome portal (https://genome.jgi.doe.gov/portal/). The amino acid sequences were then queried using BLASTp v2.2.28+ (Camacho et al., 2009) and MAFFTv6.843b (Katoh and Toh, 2008) to identify homologs of the Arabidopsis MGR9 (At1g55930) and MGR8 (At3g13070) (https://github.com/topel-research-group/misc/blob/master/blast_and_align.py). Phylogenetic analyses of the identified homologs were then performed using MrBayes v3.2.6 (Ronquist et al., 2012) for 1 million generations (Brassicacese analysis) and 2 million generations (Plants, bacteria, diatom, green algae and human sequences), respectively, after which the Average Standard Deviation (AvgStdDev) was significantly low, and the analyses were assumed to have converged. The first 25% of the tree samples were discarded and the remaining trees were summarized in majority consensus trees (see Figure 1, Supplementary Figure S2).

The following protein sequences were used for constructing the phylogenetic tree in Supplementary Figure S1A: AtMGT10 (NP_568424.1), EcCorA (P0ABI4), EcCorC (P0AE78), TpCorC

(WP_060384576.1), AtMGR8 (NP_187914.1), AtMGR9 (NP_187914.1), hCNNM2 (Q9H8M5) and hCNNM4 (Q6P4Q7). For the construction of the phylogenetic tree of CrMRS4 (Cre50g761497), amino acid sequences for Mg^{2+} transporters were downloaded from the plant membrane protein database (http://aramemnon.uni-koeln.de/) for *Arabidopsis thaliana*, and from Phytozome v13 (https://phytozome-next.jgi.doe.gov/) for *Chlamydomonas reinhardtii* (v6.1) and *Volvox carteri* (v2.1). The sequences were aligned using ClustalW in MEGA11 (Tamura et al., 2021) and the phylogenetic trees were generated using the neighbor-joining method with 500 bootstraps and the default settings of MEGA11.

4.4 Complementation of *E. coli* TM2 mutant with Arabidopsis *MGR8* and *MGR9*

The Arabidopsis sequences that encode for MGR8 (stock no. GPSO-0186) and MGR9 (BRC no. pda13388) were obtained from the Arabidopsis Biological Resource Center (http://abrc.osu.edu/) and the RIKEN BRC through the National BioResource Project of the MEXT/AMED, Japan, respectively. The MGR8 and MGR9 proteins contain N-terminal extensions. The ChloroP1.1 algorithms predicted a chloroplast leader and transit peptide cleavage sites at amino acid 71 of MGR8 and amino acid 72 of MGR9, respectively (Supplementary Figure S1B). The cDNA fragments that encode MGR8 from F72 to the C-terminal Q661 residue and MGR9 from L73 to the C-terminal E653 residue were subcloned in frame at the *Nco*I site of the pTV118N vector (TakaraBio, Japan) for the *E. coli* complementation assay (Ishijima et al., 2015). To generate various mutants, inverse PCR-based mutagenesis was performed using appropriate primer sets (Supplementary Table S2), and the obtained mutant cDNAs were subcloned into the pTV118N vector. All plasmid sequences were confirmed by DNA sequencing.

The plasmids containing the *MGR8* and *MGR9* wild type and mutant cDNAs were transformed into *E. coli* mutant TM2 (Δ*corA* Δ*mgtA* Δ*yhiD*) cells (Ishijima et al., 2015). TM2 transformed with an empty pTV118N vector was used as a negative control. Culture growth was monitored at 37°C with an ODBOX-c OD-Monitor (TAITEC, Japan).

4.5 Quantitative real-time PCR analysis

Total RNA was isolated from two-week-old seedlings and plant tissues of 6-week-old plants with an E.Z.N.A. R6827-01 Plant RNA kit (Omega Bio-Tek, GA, USA) and residual DNA was removed with E1091 DNAse (Omega Bio-Tek). cDNA was synthesized using 500 ng of total RNA through iScript cDNA Synthesis Kit (Bio-Rad, Hercules, CA, USA). Quantitative real-time PCR analyses were conducted with a SsoAdvanced Universal SYBR Green Supermix on a CFX96 Touch Thermal Cycler (Bio-Rad). Fifty ng of cDNA was used as qPCR template in 10 µl reactions. Amplifications were done in a two-step PCR with the following conditions: initial denaturation for 2 min at 95°C, followed by 40 cycles of denaturation for 5 s at 95°C, annealing for 30 s at 60°C, and extension for 10 s at 72°C. After amplification, melt-curve analyses were performed for all primers. Gene-specific primers used were ordered from Bio-Rad (Supplementary Table S3). ΔCq method ($2^{-\Delta Cq}$) was used to calculate relative expression using *PEX4* and *ACTIN8* as the reference genes.

4.6 Immunoblotting

Total protein extracts were prepared from 100 mg snap frozen leaves ground in 500 µL PEB buffer (AS08300, Agrisera, Umeå, Sweden) and centrifuged to remove insolubilized material. Intact chloroplasts were prepared from 50 g fresh leaves ground in 50 mM HEPES-KOH (pH 7.8), 300 mM sorbitol, 2 mM Na_2EDTA, and 5 mM ascorbic acid, centrifuged and loaded on Percoll 40/75% gradients. Intact chloroplasts were collected following centrifugation of the gradients at the 40%-75% interface, washed, and resuspended in 50 mM HEPES-KOH (pH 7.8), 300 mM sorbitol, and 2 mM Na_2EDTA. Intactness was verified by microscopy and the number of chloroplasts was counted using a hemocytometer. Thylakoid and envelope membranes were prepared from lysed chloroplasts, and centrifuged at 3000 *g* and 150,000 *g*, respectively. Protein concentration was determined using a Bradford assay (Bio-Rad). Equal amounts of protein (8 µg) were separated on 4-15% (w/v) SDS-PAGE gels (Bio-Rad) and transferred to polyvinylidene difluoride (PVDF) membranes. Nonspecific bindings on the membranes were blocked with 5% (w/v) milk. An antibody was generated by Agrisera in rabbit against the EHVLADNSKKQQ C-terminal peptide of MGR8 (Supplementary Figure S1B). The rabbit anti-Tic40 and Lhcb1 antibodies were purchased from Agrisera (AS10709, AS01004). Following incubation with a goat anti-rabbit secondary antibody (Bio-Rad), the chemiluminescent signal on the blots was detected using Clarity and Clarity Max ECL substrates (Bio-Rad).

4.7 Transmission electron microscopy

The fixation and embedding of 1 x 2 mm Arabidopsis leaf pieces for TEM were carried out as described (Böszörményi et al., 2020). In the case of WT and *mgt10*, TEM samples close to leaf veins were also fixed. Fixation and embedding of Chlamydomonas cells were done following the protocol of Skepper (2000), with gentle centrifugation following each step to collect the cells. Briefly, the Chlamydomonas cells of the liquid media were centrifuged at 1000 *g* for 5 min at room temperature, washed with 10 mL fresh TAP/TP medium, then centrifuged again as described above. The pellet was then resuspended in 1 mL of 2.5% glutaraldehyde in 50 mM HEPES (pH 7.4) and fixed for 1 h at room temperature on a tube rotator. Cells were then centrifuged at 5000 *g* for 3 min at room temperature. The pellet was washed for 3 x 5 min with ddH_2O, with centrifugation with the above parameters after each washing step. Samples were postfixed for 1-2 hrs at 4°C in 1 mL 1% OsO_4, 1.5% (w/v) $K_3[Fe(CN)_6]$, and 2 mM $CaCl_2$. After centrifugation as above, samples were washed 4 x 5 min with ddH_2O. Samples were

then stained for 1-2 h at room temperature in 1 mL Bulk Stain solution (2% uranyl acetate in 0.05 M maleate buffer, pH 5.5). After staining, samples were again centrifuged as above and then washed 3 x 5min with ddH_2O. After dehydration in graded ethanol series, samples were transferred to acetonitrile and then embedded in epoxy resin (Quetol 651, nonenyl succinic anhydride - NSA, methyl-5-norbornene-2,3-dicarboxylic anhydride - NMA, and catalyst dimethylbenzylamine - BDMA). The resin-embedded Chlamydomonas pellet samples were polymerized in Eppendorf tubes that were then cut into smaller pieces which were then re-embedded in Durcupan ACM epoxy resin (Fluka Chemie AG) in blocks suitable for ultrathin sectioning. A Reichert Jung ULTRACUT E microtome was used for ultrathin (70 nm) sectioning of all resin-embedded samples. After a 5-min staining with 5% uranyl acetate dissolved in methanol, and a subsequent 5-min-long treatment with Reynold's lead citrate solution, the copper grids holding the sections were investigated using a JEOL JEM 1011 (JEOL Ltd., Japan) at 80 kV accelerating voltage as described (Dukic et al., 2019). An Olympus Morada CCD camera (Olympus Optical Co. Ltd., Japan) was used to take digital images. At least 25 randomly chosen cell sections were studied for each sample and representative images for all samples were chosen for the preparation of Figure 4 and Supplementary Figure S15.

4.8 Kinetics of chlorophyll *a* fluorescence induction

Fast kinetics of Chl *a* induction in Arabidopsis leaves were recorded on 30 min dark-adapted plants by applying saturating red actinic light of 3,600 µmol photons m^{-2} s^{-1} for 1 s using a Handy-PEA (Hansatech, UK) fluorometer. Initial F_0 and F_m fluorescence values were determined by the saturating pulse. The maximal quantum yield of PSII photochemistry (F_v/F_m) was calculated as (F_m-F_0)/F_m using Hansatech PEA Plus v1.10 software according to Strasser et al. (2004). The slow kinetics of Chl fluorescence induction and P700 oxidation-reduction of Arabidopsis were simultaneously recorded with a Dual-PAM-100 equipped with DUAL-DB and DUAL-E emitter-detector module (Walz, Effeltrich, Germany). The kinetics were recorded on attached leaves of 30 min dark-adapted plants exposed to fluctuating red actinic light as follows: 10 min in low light (70 µmol photons m^{-2} s^{-1}) followed by 3 min in high light (650 µmol photons m^{-2} s^{-1}) and then again 3 min in low light. Saturating red pulses of 5,000 µmol photons m^{-2} s^{-1} and 800 ms duration were applied for determination of the maximal fluorescence yield in the dark state (F_m) and during the period with actinic light (F_m'). NPQ and Y(II) were calculated based on changes in Chl fluorescence as (F_m–F_m')/F_m' and (F_m'–F)/F_m', respectively, according to Genty et al. (1989). Y(I) was calculated from absorbance changes at 830 nm according to Klughammer and Schreiber (1994).

To measure PSII activity in Chlamydomonas, cells grown in TP in the light were resuspended to 30 µg Chl mL^{-1} and incubated with agitation at 50 rpm in darkness for 15 min. Kinetics of Chl fluorescence induction were recorded using DUAL-PAM-100 during actinic illumination at 2,500 µmol m^{-2} s^{-1} for 8 min followed by 4 min of dark relaxation. Saturating red pulses of 3,000 µmol photons m^{-2} s^{-1} were applied to the samples in a cuvette under continuous stirring for determination of F_m and F_m'. The maximal photochemical efficiency of PSII (F_v/F_m), NPQ and Y(II) were calculated as above. Rapid light response curves of electron transport rate were recorded using photosynthetically active radiation increasing stepwise from 26 to 2,015 µmol photons m^{-2} s^{-1}.

For imaging analysis of Chl fluorescence using FluorCam 800 MF (Photon System Instruments, Drasow, Czech Republic), 1 mL of Chlamydomonas cells containing 30 µg Chl were dark-adapted, transferred onto a 12-well cell culture plate (Nunc, Thermo Fisher Scientific, USA) and analyzed using default quenching 1 protocol with actinic white light at 100 µmol photons m^{-2} s^{-1} exposure for 6 min followed by 2 min in darkness. Saturating flashes of white light at 3,000 µmol photons m^{-2} s^{-1} were applied after every min of light/dark with a shutter speed of 10 µs and sensitivity of 50%.

4.9 Electrochromic shift

ECS measurements were carried out using the Dual-PAM-100 system equipped with a P515/535 module. Arabidopsis plants were first 30 min dark-adapted and then exposed to fluctuating red light as described in section 4.8. ECS was measured at the end of each low-to-high light and high-to-low light transition. PMF size was calculated as the difference between the ECS signal in light and the minimum value of the ECS signal after the light was turned off. Calculation of PMF partitioning to ΔpH and ΔΨ was performed using the steady-state time point of the ECS signal in darkness (Cruz et al., 2001). Before each ECS measurement, three saturating 50-µs actinic red flashes of 200,000 µmol photons m^{-2} s^{-1} were applied to determine the ECS_{ST}; subsequently, the ECS_{ST} amplitude was used to normalize the ECS signal before the calculation of PMF size and partitioning values.

For ECS in Chlamydomonas, cells grown in TAP in darkness were resuspended at 30 µg Chl mL^{-1} and incubated with agitation at 50 rpm in darkness for 15 min before being layered on a glass slide and exposed to actinic red light for 2 and 7 min. The light was switched off and decay kinetics were measured to calculate ECSt, ECSst, PMF size and partitioning to ΔpH and ΔΨ as for Arabidopsis.

4.10 Mineral content measurement by inductively coupled plasma mass/optical emission spectrometry

Plant shoot samples were collected directly from the hydroponic system after 6-7 weeks, washed twice with double distilled water (ddH_2O), and then dried in the oven for 3 days at 80°C. The dried sample was crushed to a fine powder using a ceramic mortar and pestle. A 100 mg subsample was digested with 70% (v/v) HNO_3 and 30% (v/v) H_2O_2 in a ratio of 3:1 (Chen A. et al., 2020) at 240°C and 200 bars for 15 min in a pressurized microwave oven (Milestones SRL, Italy). After dilution to 3.5% acid, the element concentrations were determined using ICP-OES (5100; Agilent Technologies) and data were processed using Agilent ICP Expert software (Hansen et al., 2009). Similarly, a subsample of

chloroplasts purified on a 40%/75% Percoll gradient and adjusted to contain 10^9 chloroplasts mL^{-1} were digested and analyzed using ICP-MS (7900; Agilent Technologies) and data were processed using Agilent Masshunter software, as the low element concentrations required a more sensitive detector than the one used for plant tissues.

To determine the mineral content in Chlamydomonas, cell colonies maintained on 1.2% (w/v) agar TAP plates were used to inoculate liquid TAP medium for growth in darkness and shaking for three days. Early log phase cultures were harvested and washed with either TAP or TP medium followed by resuspension in the corresponding medium to reach 0.5 x10^5 cells mL^{-1}. The cells were grown either in TAP in darkness or TP under continuous illumination (100 µmol photons m^{-2} s^{-1}) and shaking for four days. Samples (in triplicate) containing 2 x10^7 cells (~800 mg) were harvested and washed twice in 5 mM HEPES (pH 7.0) and 2 mM EDTA before collection and air-drying of the cell pellet. Pelletized cells were digested in screw-capped Teflon vials on a hot plate at elevated temperatures (25-75°C) using a 5:2 mixture of HNO_3 (68-70% v/v) and H_2O_2 (30% v/v)). Samples were then dissolved in 2% HNO_3 and analyzed for cation ratios (Mg^{2+}/Na^+, K^+/Na^+, and Ca^{2+}/Na^+) on an ICP-MS (ICAP-Q; ThermoScientific). Elemental ratios were quantified using a series of externally calibrated standards (Inorganic Ventures Co.) and analytical uncertainties were estimated at ~5-10% (1σ) based on repeat measurements of the calibration standards.

4.11 CO_2 fixation

Net photosynthesis rates in terms of CO_2 fixation were determined using Li-COR portable Photosynthesis System Li-6400 (Lincoln, Nebraska, USA). Plants were first light-adapted for at least 1 h in the growth chamber and then exposed in the gas exchange chamber to broad spectrum light generated with red, green, and blue LEDs at 120 and 700 µmol photons m^{-2} s^{-1} in atmospheric CO_2 (440 µmol mol^{-1}) for approximately 5 min or until a steady state was reached. Data were normalized to leaf area determined using ImageJ.

4.12 Complementation experiments of Chlamydomonas *mrs4* mutant with Volvox *MRS4*

The Chlamydomonas *MRS4* gene was incomplete in the v5.5 genome (Cre50.g761497), and trials to obtain it by TAIL-PCR have failed. For complementation experiments of *mrs4*, we have chosen to clone its homolog in *Volvox carteri* (Vocar.0040s0086) using the pipeline described by Mackinder et al. (2017). Briefly, the open reading frame was amplified from Volvox genomic DNA by PCR from two fragments (2-3 kbp each) using Phusion High-Fidelity DNA polymerase (New England BioLabs) and primers given in Supplementary Table S2. The PCR products were purified from agarose gels, re-assembled, and cloned in-frame with a C-terminal Venus-3×FLAG in pLM005 by Gibson assembly (New England BioLabs). The construct was linearized by EcoRV-HF and verified by sequencing. For transformation of the *mrs4* mutant, cells were cultured in TAP liquid medium at 23°C under light at 150 µmol photons m^{-2} s^{-1} to 1-2 x 10^6 cells mL^{-1}. The cells were washed and suspended at 2 x 10^8 cells mL^{-1} in MAX Efficiency Transformation reagent (Invitrogen) together with the linearized plasmid and by electroporation using a NEPA21 electroporator (NEPA GENE). The transformants were plated on TP agar supplemented with 25 µg mL^{-1} and grown under light (150 µmol photons m^{-2} s^{-1}) for 7 days. Those transformants showing better growth than the *mrs4* mutant were screened by PCR with primers given in Supplementary Table S2 to verify the correct insertion of *VcMRS4*.

Data availability statement

The original contributions presented in the study are included in the article/Supplementary Material. Further inquiries can be directed to the corresponding author.

Author contributions

ED, SI, and CS conceived the study and designed the experiments. ED carried out the ECS, Chl fluorescence, CO_2 fixation measurements, and qRT-PCR. KAvM carried out the localization western blots. KMS and CS performed the Chlamydomonas work. KvM, KMS, and MT performed the phylogenetic analyses. KF, SS, and SI run the heterologous characterization in *E. coli*. ED and CS fixed and embedded the samples for TEM. KS performed the TEM analyses. JHe generated the *mgt10mgr8-2* double mutant. TH and SH performed mineral analyses of Arabidopsis samples. JHi performed the mineral analyses of Chlamydomonas cells. ED, KvM, and KMS performed the statistical analyses. KvM, SI, ED, KMS, and CS wrote the manuscript. All authors helped to edit the manuscript and approved the submitted version

Funding

This work was supported by grants from the Swedish Research Council to CS (VR 2016-03836 and 2021-03790) and JSPS KAKENHI to SI (JP15K07399). KMS was recipient of a postdoctoral fellowship from the Carl Tryggers Foundation (CTS 20:406). KS would like to acknowledge the Bolyai János Research Scholarship of the Hungarian Academy of Sciences and the National Research Development and Innovation Office of Hungary (grant OTKA FK 124748) for support.

Acknowledgments

CS acknowledges the sabbatical program at the Faculty of Science, University of Gothenburg. CS also thanks Dr. Lianyong Wang for help with Chlamydomonas transformation, Dr. Moritz T. Meyer

for help with the fixation of Chlamydomonas cells for TEM, and Prof. Martin C. Jonikas for the Chlamydomonas experiments performed in his laboratory at Princeton University. Authors are grateful to Csilla Gergely (Eötvös Loránd University) for skillful technical assistance with ultrathin sectioning and Dr. Stephen Miller (University of Maryland, Baltimore) for the gift of Volvox genomic DNA.

Conflict of interest

The authors declare that the research was conducted in the absence of any commercial or financial relationships that could be construed as a potential conflict of interest.

Publisher's note

Supplementary material

The Supplementary Material for this article can be found online at: https://www.frontiersin.org/articles/10.3389/fpls.2023.1221436/full#supplementary-material

References

Alonso, J. M., Stepanova, A. N., Leisse, T. J., Kim, C. J., Chen, H., Shinn, P., et al. (2003). Genome-wide insertional mutagenesis of *Arabidopsis thaliana*. *Science* 301, 653–657. doi: 10.1126/science.1086391

Böszörményi, A., Dobi, A., Skribanek, A., Pávai, M., and Solymosi, K. (2020). The effect of light on plastid differentiation, chlorophyll biosynthesis, and essential oil composition in rosemary (*Rosmarinus officinalis*) leaves and cotyledons. *Front. Plant Sci.* 11, 196. doi: 10.3389/fpls.2020.00196

Camacho, C., Coulouris, G., Avagyan, V., Ma, N., Papadopoulos, J., Bealer, K., et al. (2009). BLAST+: architecture and applications. *BMC Bioinf.* 10, 1–9. doi: 10.1186/1471-2105-10-421

Chen, A., Hansen, T. H., Olsen, L. I., Palmgren, M., Husted, S., Schjoerring, J. K., et al. (2020). Towards single-cell ionomics: A novel micro-scaled method for multi-element analysis of nanogram-sized biological samples. *Plant Methods* 16, 1–13. doi: 10.1186/S13007-020-00566-9

Chen, Y. S., Kozlov, G., Fakih, R., Yang, M., Zhang, Z., Kovrigin, E. L., et al. (2020). Mg^{2+}-ATP sensing in CNNM, a putative magnesium transporter. *Structure* 28, 324–335.e4. doi: 10.1016/j.str.2019.11.016

Chen, Z. C., Peng, W. T., Li, J., and Liao, H. (2018). Functional dissection and transport mechanism of magnesium in plants. *Semin. Cell Dev. Biol.* 74, 142–152. doi: 10.1016/.semcdb.2017.08.005

Conn, S. J., Hocking, B., Dayod, M., Xu, B., Athman, A., Henderson, S., et al. (2013). Protocol: Optimising hydroponic growth systems for nutritional and physiological analysis of *Arabidopsis thaliana* and other plants. *Plant Methods* 9, 4. doi: 10.1186/1746-4811-9-4

Cruz, J. A., Sacksteder, C. A., Kanazawa, A., and Kramer, D. M. (2001). Contribution of electric field (Delta psi) to steady-state transthylakoid proton motive force (pmf) in *vitro* and in *vivo*. control of pmf parsing into Delta psi and Delta pH by ionic strength. *Biochemistry* 40, 1226–1237. doi: 10.1021/bi0018741

Drummond, R. S. M., Tutone, A., Li, Y. C., and Gardner, R. C. (2006). A putative magnesium transporter AtMRS2-11 is localized to the plant chloroplast envelope membrane system. *Plant Sci.* 170, 78–89. doi: 10.1016/j.plantsci.2005.08.018

Dukic, E., Herdean, A., Cheregi, O., Sharma, A., Nziengui, H., Dmitruk, D., et al. (2019). K^+ and Cl^- channels/transporters independently fine-tune photosynthesis in plants. *Sci. Rep.* 9, 1–12. doi: 10.1038/s41598-019-44972-z

Franken, G. A. C., Huynen, M. A., Martínez-Cruz, L. A., Bindels, R. J. M., and de Baaij, J. H. F. (2022). Structural and functional comparison of magnesium transporters throughout evolution. *Cell. Mol. Life Sci.* 79, 418. doi: 10.1007/S00018-022-04442-8

Genty, B., Briantais, J. M., and Baker, N. R. (1989). The relationship between the quantum yield of photosynthetic electron transport and quenching of chlorophyll fluorescence. *Biochim. Biophys. Acta* 990, 87–92. doi: 10.1016/S0304-4165(89)80016-9

Gibeaut, D. M., Hulett, J., Cramer, G. R., and Seemann, J. R. (1997). Maximal biomass of *Arabidopsis thaliana* using a simple, low-maintenance hydroponic method and favorable environmental conditions. *Plant Physiol.* 115, 317–319. doi: 10.1104/pp.115.2.317

Giménez-Mascarell, P., Oyenarte, I., González-Recio, I., Fernández-Rodríguez, C., Corral-Rodríguez, M.Á., Campos-Zarraga, I., et al. (2019). Structural insights into the intracellular region of the human magnesium transport mediator CNNM4. *Int. J. Mol. Sci.* 20, 6279. doi: 10.3390/ijms20246279

Guskov, A., Nordin, N., Reynaud, A., Engman, H., Lundbäck, A.-K., Jin, A., et al. (2012). Structural insights into the mechanisms of Mg^{2+} uptake, transport, and gating by CorA. *Proc. Natl. Acad. Sci. U.S.A.* 109, 18459–18464. doi: 10.1073/pnas.1210076109

Hansen, T. H., Laursen, K. H., Persson, D. P., Pedas, P., Husted, S., and Schjoerring, J. K. (2009). Micro-scaled high-throughput digestion of plant tissue samples for multi-elemental analysis. *Plant Methods* 5, 12. doi: 10.1186/1746-4811-5-12

Hermans, C., Conn, S. J., Chen, J., Xiao, Q., and Verbruggen, N. (2013). An update on magnesium homeostasis mechanisms in plants. *Metallomics* 5, 1170–1183. doi: 10.1039/c3mt20223b

Huang, Y., Jin, F., Funato, Y., Xu, Z., Zhu, W., Wang, J., et al. (2021). Structural basis for the Mg^{2+} recognition and regulation of the CorC Mg^{2+} transporter. *Sci. Adv.* 7, 6140. doi: 10.1126/sciadv.abe6140

Huber, S. C., and Maury, W. (1980). Effects of magnesium on intact chloroplasts: I. evidence for activation of (sodium) potassium/proton exchange across the chloroplast envelope. *Plant Physiol.* 65, 350–354. doi: 10.1104/pp.65.2.350

Ishijima, S., Manabe, Y., Shinkawa, Y., Hotta, A., Tokumasu, A., Ida, M., et al. (2018). The homologous Arabidopsis MRS2/MGT/CorA-type Mg^{2+} channels, AtMRS2-10 and AtMRS2-1 exhibit different aluminum transport activity. *Biochim. Biophys. Acta* 1860, 2184–2191. doi: 10.1016/j.bbamem.2018.08.016

Ishijima, S., Shiomi, R., and Sagami, I. (2021). Functional analysis of whether the glycine residue of the GMN motif of the Arabidopsis MRS2/MGT/CorA-type Mg^{2+} channel protein AtMRS2-11 is critical for Mg^{2+} transport activity. *Arch. Biochem. Biophys.* 697, 108673. doi: 10.1016/j.abb.2020.108673

Ishijima, S., Uda, M., Hirata, T., Shibata, M., Kitagawa, N., and Sagami, I. (2015). Magnesium uptake of Arabidopsis transporters, AtMRS2-10 and AtMRS2-11, expressed in *Escherichia coli* mutants: Complementation and growth inhibition by aluminum. *Biochim. Biophys. Acta* 1848, 1376–1382. doi: 10.1016/j.bbamem.2015.03.005

Jin, F., Huang, Y., and Hattori, M. (2022). Recent advances in the structural biology of Mg^{2+} channels and transporters. *J. Mol. Biol.* 434, 167729. doi: 10.1016/j.jmb.2022.167729

Katoh, K., and Toh, H. (2008). Recent developments in the MAFFT multiple sequence alignment program. *Brief Bioinform.* 9, 286–298. doi: 10.1093/bib/bbn013

Klughammer, C., and Schreiber, U. (1994). An improved method, using saturating light pulses, for the determination of photosystem I quantum yield *via* P700+-absorbance changes at 830 nm. *Planta* 192, 261–268. doi: 10.1007/bf01089043

Kunz, H. H., Gierth, M., Herdean, A., Satoh-Cruz, M., Kramer, D. M., Spetea, C., et al. (2014). Plastidial transporters KEA1, -2, and -3 are essential for chloroplast osmoregulation, integrity, and pH regulation in Arabidopsis. *Proc. Natl. Acad. Sci. U.S.A.* 111, 7480–7485. doi: 10.1073/pnas.1323899111

Li, L., Tutone, A. F., Drummond, R. S. M., Gardner, R. C., and Luan, S. (2001). A novel family of magnesium transport genes in Arabidopsis. *Plant Cell* 13, 2761. doi: 10.1105/tpc.010352

Liang, S., Qi, Y., Zhao, J., Li, Y., Wang, R., Shao, J., et al. (2017). Mutations in the Arabidopsis AtMRS2-11/AtMGT10/VAR5 gene cause leaf reticulation. *Front. Plant Sci.* 8, 2007. doi: 10.3389/fpls.2017.02007

Lunin, V. V., Dobrovetsky, E., Khutoreskaya, G., Zhang, R., Joachimiak, A., Doyle, D. A., et al. (2006). Crystal structure of the CorA Mg^{2+} transporter. *Nature* 440, 833–837. doi: 10.1038/nature04642

Mackinder, L. C. M., Chen, C., Leib, R. D., Patena, W., Blum, S. R., Rodman, M., et al. (2017). A spatial interactome reveals the protein organization of the algal CO_2-concentrating mechanism. *Cell* 171, 133–147.e14. doi: 10.1016/j.cell.2017.08.044

Marchand, J., Heydarizadeh, P., Schoefs, B., and Spetea, C. (2018). Ion and metabolite transport in the chloroplast of algae: lessons from land plants. *Cell. Mol. Life Sci.* 75, 2153–2176. doi: 10.1007/S00018-018-2793-0

Mott, K. A., and Berry, J. A. (1986). Effects of pH on activity and activation of ribulose 1,5-bisphosphate carboxylase at air level CO_2. *Plant Physiol.* 82, 77. doi: 10.1104/pp.82.1.77

Ronquist, F., Teslenko, M., van der Mark, P., Ayres, D. L., Darling, A., Höhna, S., et al. (2012). MrBayes 3.2: efficient Bayesian phylogenetic inference and model choice across a large model space. *Syst. Biol.* 61, 539–542. doi: 10.1093/sysbio/syS029

Rosso, M. G., Li, Y., Strizhov, N., Reiss, B., Dekker, K., and Weisshaar, B. (2003). An *Arabidopsis thaliana* T-DNA mutagenized population (GABI-Kat) for flanking sequence tag-based reverse genetics. *Plant Mol. Biol.* 53, 247–259. doi: 10.1023/B:PLAN.0000009297.37235.4a

Skepper, J. N. (2000). Immunocytochemical strategies for electron microscopy: choice or compromise. *J. Microsc.* 199, 1–36. doi: 10.1046/J.1365-2818.2000.00704.X

Strasser, R. J., Tsimilli-Michael, M., and Srivastava, A. (2004). Analysis of the chlorophyll a fluorescence transient. In: G. C. Papageorgiou and Govindjee Eds. *Chlorophyll a fluorescence. Advances in Photosynthesis and Respiration*. Dordrecht: Springer, vol. 19, pp. 321–362. doi: 10.1007/978-1-4020-3218-9_12

Stuiver, M., Lainez, S., Will, C., Terryn, S., Günzel, D., Debaix, H., et al. (2011). CNNM2, encoding a basolateral protein required for renal Mg^{2+} handling, is mutated in dominant hypomagnesemia. *Am. J. Hum. Genet.* 88, 333–343. doi: 10.1016/j.ajhg.2011.02.005

Sun, Y., Yang, R., Li, L., and Huang, J. (2017). The magnesium transporter MGT10 is essential for chloroplast development and photosynthesis in *Arabidopsis thaliana*. *Mol. Plant* 10, 1584–1587. doi: 10.1016/j.molp.2017.09.017

Szabò, I., and Spetea, C. (2017). Impact of the ion transportome of chloroplasts on the optimization of photosynthesis. *J. Exp. Bot.* 68, 3115–3128. doi: 10.1093/jxb/erx063

Tamura, K., Stecher, G., and Kumar, S. (2021). MEGA11: molecular evolutionary genetics analysis version 11. *Mol. Biol. Evol.* 38, 3022–3027. doi: 10.1093/molbev/msab120

Tang, R. J., and Luan, S. (2017). Regulation of calcium and magnesium homeostasis in plants: from transporters to signaling network. *Curr. Opin. Plant Biol.* 39, 97–105. doi: 10.1016/j.pbi.2017.06.009

Tang, R.-J., Meng, S.-F., Zheng, X.-J., Zhang, B., Yang, Y., Wang, C., et al. (2022). Conserved mechanism for vacuolar magnesium sequestration in yeast and plant cells. *Nat. Plants* 8, 181–190. doi: 10.1038/s41477-021-01087-6

Wu, W., and Berkowitz, G. A. (1992). Stromal pH and photosynthesis are affected by electroneutral K and H exchange through chloroplast envelope ion channels. *Plant Physiol.* 98, 666–672. doi: 10.1104/pp.98.2.666

Wu, W., Peters, J., and Berkowitz, G. A. (1991). Surface charge-mediated effects of Mg^{2+} on K^+ flux across the chloroplast envelope are associated with regulation of stromal pH and photosynthesis. *Plant Physiol.* 97, 580–587. doi: 10.1104/pp.97.2.580

Yamazaki, D., Funato, Y., Miura, J., Sato, S., Toyosawa, S., Furutani, K., et al. (2013). Basolateral Mg^{2+} extrusion *via* CNNM4 mediates transcellular Mg^{2+} transport across epithelia: a mouse model. *PloS Genet.* 9, 1003983. doi: 10.1371/journal.pgen.1003983

Zhang, B., Zhang, C., Tang, R., Zheng, X., Zhao, F., Fu, A., et al. (2022). Two magnesium transporters in the chloroplast inner envelope essential for thylakoid biogenesis in Arabidopsis. *New Phytol.* 236, 464–478. doi: 10.1111/nph.18349

Frontiers in
Plant Science

Cultivates the science of plant biology and its applications

The most cited plant science journal, which advances our understanding of plant biology for sustainable food security, functional ecosystems and human health.

Discover the latest Research Topics

See more →

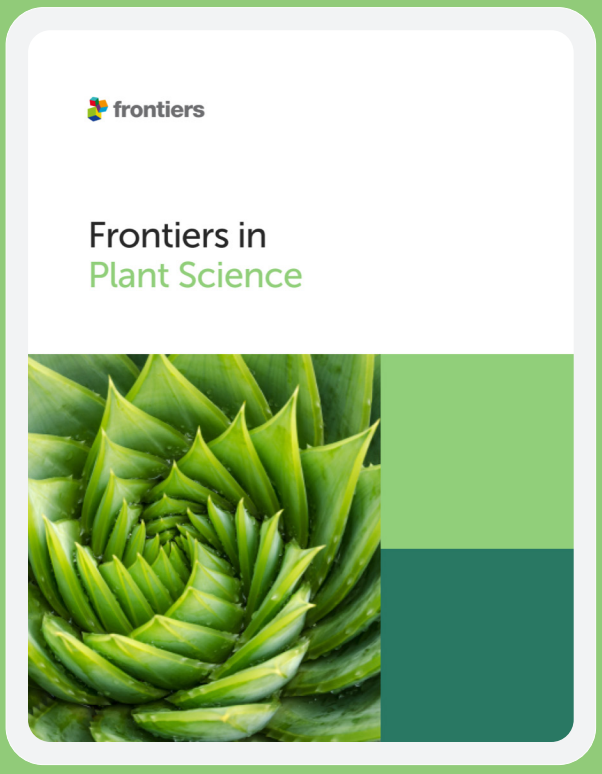

Frontiers

Avenue du Tribunal-Fédéral 34
1005 Lausanne, Switzerland
frontiersin.org

Contact us

+41 (0)21 510 17 00
frontiersin.org/about/contact